# STATUS GO FOR PRECLINICAL IMAGING

EDITED BY: Claudia Kuntner, Bernhard Baumann, Adriana Tavares and Andreas Hess

PUBLISHED IN: Frontiers in Physics and Frontiers in Physiology

frontiers Research Topics

ISSN 1664-8714
ISBN 978-2-88966-172-5
DOI 10.3389/978-2-88966-172-5

## About Frontiers

Frontiers is more than just an open-access publisher of scholarly articles: it is a pioneering approach to the world of academia, radically improving the way scholarly research is managed. The grand vision of Frontiers is a world where all people have an equal opportunity to seek, share and generate knowledge. Frontiers provides immediate and permanent online open access to all its publications, but this alone is not enough to realize our grand goals.

## Frontiers Journal Series

The Frontiers Journal Series is a multi-tier and interdisciplinary set of open-access, online journals, promising a paradigm shift from the current review, selection and dissemination processes in academic publishing. All Frontiers journals are driven by researchers for researchers; therefore, they constitute a service to the scholarly community. At the same time, the Frontiers Journal Series operates on a revolutionary invention, the tiered publishing system, initially addressing specific communities of scholars, and gradually climbing up to broader public understanding, thus serving the interests of the lay society, too.

## Dedication to Quality

Each Frontiers article is a landmark of the highest quality, thanks to genuinely collaborative interactions between authors and review editors, who include some of the world's best academicians. Research must be certified by peers before entering a stream of knowledge that may eventually reach the public - and shape society; therefore, Frontiers only applies the most rigorous and unbiased reviews.
Frontiers revolutionizes research publishing by freely delivering the most outstanding research, evaluated with no bias from both the academic and social point of view. By applying the most advanced information technologies, Frontiers is catapulting scholarly publishing into a new generation.

## What are Frontiers Research Topics?

Frontiers Research Topics are very popular trademarks of the Frontiers Journals Series: they are collections of at least ten articles, all centered on a particular subject. With their unique mix of varied contributions from Original Research to Review Articles, Frontiers Research Topics unify the most influential researchers, the latest key findings and historical advances in a hot research area! Find out more on how to host your own Frontiers Research Topic or contribute to one as an author by contacting the Frontiers Editorial Office: researchtopics@frontiersin.org

# STATUS GO FOR PRECLINICAL IMAGING

Topic Editors:
**Claudia Kuntner,** Austrian Institute of Technology (AIT), Austria
**Bernhard Baumann,** Medical University of Vienna, Austria
**Adriana Tavares,** University of Edinburgh, United Kingdom
**Andreas Hess,** University of Erlangen Nuremberg, Germany

**Citation:** Kuntner, C., Baumann, B., Tavares, A., Hess, A., eds. (2020). Status Go for Preclinical Imaging. Lausanne: Frontiers Media SA. doi: 10.3389/978-2-88966-172-5

# Table of Contents

frontiers in Physics

EDITORIAL
published: 25 September 2020
doi: 10.3389/fphy.2020.00344

Check for updates

# Editorial: Status Go for Preclinical Imaging

*Claudia Kuntner[1]*, Bernhard Baumann[2], Adriana A. S. Tavares[3] and Andreas Hess[4]*

[1] Preclinical Molecular Imaging, AIT Austrian Institute of Technology GmbH, Seibersdorf, Austria, [2] Center for Medical Physics and Biomedical Engineering, Medical University of Vienna, Vienna, Austria, [3] Edinburgh Preclinical Imaging, University of Edinburgh, Edinburgh, United Kingdom, [4] Institute of Experimental and Clinical Pharmacology and Toxicology, Friedrich-Alexander University Erlangen-Nuernberg, Erlangen, Germany

**Keywords: preclinical imaging, PET, SPECT, MRI, ultrasound, microscopy, quantification**

**Editorial on the Research Topic**

**Status Go for Preclinical Imaging**

This special Research Topic includes a collection of reviews and original articles on preclinical imaging. Preclinical imaging encompasses the use of imaging methods to study animal models, tissue samples, and other unique specimens, such as eggs (*in ovo*). Preclinical imaging is driven by advances in medical physics and instrumentation as well as by active research in biology and medicine. Given the multi-disciplinary nature of preclinical imaging, some articles from this collection appear in the journal Frontiers in Physics whereas others appear in the journal Frontiers in Physiology.

Over time, preclinical imaging has evolved from a technique perceived to be niche and of limited value to an established workhorse in medical research, supporting drug discovery programs, mechanistic studies focused on understanding (patho-)physiology and disease development as well as progression, and aiding the development of paradigms for clinical imaging. Preclinical imaging also encompasses scales of different orders of magnitude, from molecular/microscopic to structural/macroscopic as well as organismic scale, thus providing not only superb anatomical detail but also excellent quantitative functional information. Despite the tremendous and ever-expanding role of preclinical imaging in medical research, its full potential can only be delivered if preclinical researchers apply the same amount of effort and rigor to their preclinical protocols as is used in clinical settings. This means that thoughtful study planning and use of established standardized protocols, accompanied by careful handling of the subjects (e.g., animals, eggs, or tissue samples) is of paramount importance to generate preclinical imaging datasets with translational value. Furthermore, there is a need to implement robust image analysis approaches, including reliable and reproducible methods to obtain quantitative data. Finally, state-of-the-art statistical testing and controlling must be applied.

In the present Research Topic, 13 articles are divided into 6 reviews, 1 mini-review, 4 original research articles, 1 perspective, and 1 brief research report, covering some of the latest research activities on diverse topics including microscopy, positron emission tomography (PET) quantification, single photon emission computed tomography (SPECT) for neuroimaging, small animal magnetic resonance imaging (MRI), ultrasound, *in ovo* imaging, *in vivo* cell tracking using multiple imaging methods and correlated multimodal imaging (CMI).

The review article by Walter et al. provides a comprehensive overview of the challenges of CMI, where information from the same specimen with two or more modalities is combined to create a composite view of the sample. In this review paper, the different imaging techniques available for CMI, including correlated light microscopy, electron microscopy, and biological hybrid imaging, are described alongside the advantages and disadvantages of each modality.



***Edited and reviewed by:***
*Thomas Beyer, Medical University of Vienna, Austria*

****Correspondence:***
*Claudia Kuntner*
*claudia.kuntner@ait.ac.at*

***Specialty section:***
*This article was submitted to Medical Physics and Imaging, a section of the journal Frontiers in Physics*

***Received:*** *21 July 2020*
***Accepted:*** *22 July 2020*
***Published:*** *25 September 2020*

***Citation:***
*Kuntner C, Baumann B, Tavares AAS and Hess A (2020) Editorial: Status Go for Preclinical Imaging. Front. Phys. 8:344. doi: 10.3389/fphy.2020.00344*

In this Frontiers special issue, five papers discuss the latest research in nuclear imaging techniques. The paper by He et al. describes strategies for the extraction of an arterial or image-derived input function for quantification of the adenosine type 1 receptors (A1) with PET. The impact of attenuation correction on [$^{18}$F]FDG PET imaging is described by Wanek et al. using data from phantom and rat studies. Oelschlegel and Goldschmidt's paper focuses on describing the use of cerebral blood flow SPECT imaging to study brain-wide activation patterns in awake rodents. Dual tracer PET/SPECT studies are reported by Blower et al. using phantoms to investigate the cross-contamination of PET signal on SPECT measurements and vice-versa. Finally, a perspective article by Jones et al. provides an outlook at the possibilities of how preclinical imaging might be instrumental to deliver the full potential of the clinical total-body PET technology.

Traditionally, hybrid radionuclide imaging has been used to study the physiology and pathophysiology in humans and rodents. However, it can also be used to examine tumoral uptake of radiotracers together with anatomical information in the Hen's Egg Test Chorioallantoic-Membrane (HET-CAM) model by so-called *in ovo* imaging (Winter et al.). This is an emerging new application for preclinical imaging. Another more routine application of preclinical imaging involves the use of imaging technology to track cells *in vivo* and consequently help with the development of novel cancer immunotherapies. Imaging methods used to track cells are applied as summarized in the review by Iafrate and Fruhwirth.

This special issue on preclinical imaging also covers the utility of preclinical MRI as a promising diagnostic tool to monitor disease progression and response to therapy in preclinical models. Technical aspects of *in vivo* small animal cardiovascular MRI are summarized in the review by Li et al. whereas Anderson et al. describe the development of MR diffusion imaging protocols for structural connectomics analysis in mouse models of human disease.

Finally, the Research Topic is further complemented by a review on preclinical ultrasound imaging techniques and applications (Moran and Thomson) and a mini-review on recent technological and methodological advances in the field of multiphoton microscopy (Pozzi et al.).

The Research Topic editors greatly appreciate the amount of work from contributors, reviewers, and Frontiers staff. We believe that the articles published in this Research Topic provide further evidence that preclinical imaging is an invaluable tool in medical and biological research and will continue to supply the field with new critical knowledge on the causes, consequences, and treatment options of multiple diseases. This is a moment when the preclinical imaging community needs to go further, continuing to push the limits of this tool.

## AUTHOR CONTRIBUTIONS

All authors listed have made a substantial, direct and intellectual contribution to the work, and approved it for publication.

**Conflict of Interest:** The authors declare that the research was conducted in the absence of any commercial or financial relationships that could be construed as a potential conflict of interest.

frontiers in Physiology

ORIGINAL RESEARCH
published: 29 January 2020
doi: 10.3389/fphys.2019.01617

# Image-Derived Input Functions for Quantification of $A_1$ Adenosine Receptors Availability in Mice Brains Using PET and [$^{18}$F]CPFPX

*Xuan He[1,2], Franziska Wedekind[1], Tina Kroll[1], Angela Oskamp[1], Simone Beer[1], Alexander Drzezga[1,3], Johannes Ermert[4], Bernd Neumaier[4], Andreas Bauer[1,5] and David Elmenhorst[1,6]**

*[1] Institut für Neurowissenschaften und Medizin (INM-2), Forschungszentrum Jülich, Jülich, Germany, [2] Department of Neurophysiology, Institute of Zoology (Bio-II), RWTH Aachen University, Aachen, Germany, [3] Department of Nuclear Medicine, University Hospital of Cologne, Cologne, Germany, [4] Institut für Neurowissenschaften und Medizin (INM-5), Forschungszentrum Jülich, Jülich, Germany, [5] Neurological Department, Medical Faculty, Heinrich Heine University Düsseldorf, Düsseldorf, Germany, [6] Division of Medical Psychology, University of Bonn, Bonn, Germany*

OPEN ACCESS

***Edited by:***
*Claudia Kuntner, Austrian Institute of Technology (AIT), Austria*

***Reviewed by:***
*Jens P. Bankstahl, Hannover Medical School, Germany*
*David B. Stout, Independent Researcher, Culver City, United States*

****Correspondence:***
*David Elmenhorst*
*d.elmenhorst@fz-juelich.de*

***Specialty section:***
*This article was submitted to Medical Physics and Imaging, a section of the journal Frontiers in Physiology*

***Received:*** *30 October 2019*
***Accepted:*** *23 December 2019*
***Published:*** *29 January 2020*

***Citation:***
*He X, Wedekind F, Kroll T, Oskamp A, Beer S, Drzezga A, Ermert J, Neumaier B, Bauer A and Elmenhorst D (2020) Image-Derived Input Functions for Quantification of $A_1$ Adenosine Receptors Availability in Mice Brains Using PET and [$^{18}$F]CPFPX. Front. Physiol. 10:1617. doi: 10.3389/fphys.2019.01617*

**Purpose:** *In vivo* imaging for the $A_1$ adenosine receptors ($A_1$ARs) with positron emission tomography (PET) using 8-cyclopentyl-3-(3-[$^{18}$F]fluoropropyl)-1-propylxanthine ([$^{18}$F]CPFPX) has become an important tool for studying physiological processes quantitatively in mice. However, the measurement of arterial input functions (AIFs) on mice is a method with restricted applicability because of the small total blood volume and the related difficulties in withdrawing blood. Therefore, the aim of this study was to extract an appropriate [$^{18}$F]CPFPX image-derived input function (IDIF) from dynamic PET images of mice.

**Procedures:** In this study, five mice were scanned with [$^{18}$F]CPFPX for 60 min. Arterial blood samples ($n$ = 7 per animal) were collected from the femoral artery and corrected for metabolites. To generate IDIFs, three different approaches were selected: (A) volume of interest (VOI) placed over the heart (cube, 10 mm); (B) VOI set over abdominal vena cava/aorta region with a cuboid (5 × 5 × 15 mm); and (C) with 1 × 1 × 1 mm voxels on five consecutive slices. A calculated scaling factor (α) was used to correct for partial volume effect; the method of obtaining the total metabolite correction of [$^{18}$F]CPFPX for IDIFs was developed. Three IDIFs were validated by comparison with AIF. Validation included the following: visual performance; computing area under the curve (AUC) ratios (IDIF/AIF) of whole-blood curves and parent curves; and the mean distribution volume ($V_T$) ratios (IDIF/AIF) of $A_1$ARs calculated by Logan plot and two-tissue compartment model.

**Results:** Compared with the AIF, the IDIF with VOI over heart showed the best performance among the three IDIFs after scaling by 1.77 (α) in terms of visual analysis, AUC ratios (IDIF/AIF; whole-blood AUC ratio, 1.03 ± 0.06; parent curve AUC ratio, 1.01 ± 0.10) and $V_T$ ratios (IDIF/AIF; Logan $V_T$ ratio, 1.00 ± 0.17; two-tissue compartment model $V_T$ ratio, 1.00 ± 0.13) evaluation. The $A_1$ARs distribution of average parametric images was in good accordance to autoradiography of the mouse brain.

**Conclusion:** The proposed study provides evidence that IDIF with VOI over heart can replace AIF effectively for quantification of $A_1$ARs using PET and [$^{18}$F]CPFPX in mice brains.

**Keywords: image-derived input function, positron emission tomography, $A_1$ adenosine receptors, [$^{18}$F]CPFPX, mice brains**

## INTRODUCTION

The $A_1$ adenosine receptors ($A_1$ARs) are involved in various neurological as well as psychiatric disorders (Paul et al., 2011), and play significant role in processes such as sleep–wake regulation (Porkka-Heiskanen and Kalinchuk, 2011) and memory consolidation (Gessi et al., 2011; Paul et al., 2011). At present, multiple antagonists, agonists, and allosteric modulators are under development to explore the therapeutic effect of adenosine receptors (Kiesman et al., 2009). Small animal imaging could simplify the evaluation process of these compounds; moreover, various mice models of adenosine-related diseases might help to identify potential applications (Elmenhorst et al., 2013). Therefore, there is a high interest in *in vivo* imaging techniques for the $A_1$AR with positron emission tomography (PET) in mice to visualize molecular processes quantitatively. PET with the radiotracer 8-cyclopentyl-3-(3-[$^{18}$F]fluoropropyl)-1-propylxanthine ([$^{18}$F]CPFPX) can be used to quantify the *in vivo* concentration of $A_1$ARs in the brain (Bauer et al., 2003). For this quantification, the concentration of parent radiotracer in plasma is necessary as the input function to the brain. The arterial input function (AIF) is still the gold standard (Meyer et al., 2006; Chen et al., 2007; Zanotti-Fregonara et al., 2009a) for quantification of target receptors via the invasive procedure of arterial cannulation. However, in mice, the total blood volume is small, and continuous blood sampling during the whole experiment is relatively difficult and technically challenging (Laforest et al., 2005; Yee et al., 2005). In addition, measuring the AIF might affect the physiological function of the small animal. Multiple blood samplings in mice have often conducted as a terminal procedure preventing longitudinal studies within individual (Kim et al., 2006; Ferl et al., 2007; Wu et al., 2007).

Several methods have therefore been developed to overcome the difficulties of arterial blood sampling including image-derived input functions (IDIFs) (Chen et al., 1998; Naganawa et al., 2005; Su et al., 2005; Fang and Muzic, 2008; Mourik et al., 2008), which became an attractive non-invasive alternative compared to AIF. The high spatial resolution of modern small-animal PET scanners (Lecomte et al., 1994; Cherry et al., 1997; Chatziioannou et al., 1999) allows to acquire IDIFs even from small anatomical regions. In brain PET studies from mice, only a few organs such as heart and abdominal vena cava/aorta are expected to be directly visible from initial time frames after injection. Accordingly, IDIFs were successfully established in "large" ($\sim$2 mm diameter) blood vessels in mice (Lanz et al., 2014).

Most studies, however, reported the extraction of the IDIFs from rodent hearts because outlining blood vessels was challenging (Parker and Feng, 2005; Zanotti-Fregonara et al., 2009b; Croteau et al., 2010). When using heart muscle cells or liver, however, the spill-over effects have to be considered. Compared with heart, IDIFs from "large" blood vessel are less influenced by spill-in effects from surrounding tissues (Lanz et al., 2014), while partial volume effects caused by limited resolution and difficult delineation have to be considered carefully.

According to the previous results and the specific distribution pattern of $A_1$AR, we extracted IDIFs over both heart as well as abdominal vena cava/aorta in mice scanned with PET and [$^{18}$F]CPFPX. For quantification of $A_1$AR availability in mice brains, three different approaches for volume of interest (VOI) definition for respective IDIFs were selected.

Since the radioligand we used in this study showed fast metabolization, namely, the parent radioligand accounted for only $\sim$18% of total radioactivity in whole blood 60 min after radiotracer injection, data were corrected for metabolites.

To evaluate the accuracy and precision of the different image-derived input approaches, AIFs from the same animals were used as reference standard.

Thus, the aim of this present study was to define appropriate IDIFs for dynamic [$^{18}$F]CPFPX PET in mice.

## MATERIALS AND METHODS

### Animal Preparation

All procedures were approved by German regional authorities (Landesamt für Natur, Umwelt und Verbraucherschutz) and performed on the basis of the German Animal Welfare Act. The animal experimental data reported in this study are in compliance with the Animal Research: Reporting *in vivo* Experiments guidelines. Five healthy male C57BL/6 mice (28 weeks; 37.80 $\pm$ 5.42 g, mean $\pm$ SD) with free access to standard mouse food and water were housed in a 12 h light/dark cycle at 22°C.

Anesthesia was introduced with 5% isoflurane in 2 L/min oxygen and maintained at 1.5–2% isoflurane in 1 L/min oxygen. The surgical cannulation (PE10, Becton Dickinson, Sparks, MD, United States) of the femoral artery and heparin-coated microtubes served for blood sampling; another catheter placed in the tail vein was used for a bolus injection of [$^{18}$F]CPFPX. The dead volume of the catheter was 14.17 $\pm$ 2.09 μl.

Breathing rate (pressure pad, 41 $\pm$ 10 bpm) and body temperature (rectal probe) were used to continuously monitor all animals throughout the PET scans (BioVet System, m2m Imaging, Salisbury, QLD, Australia). A constant body temperature (37.17 ± 0.58°C) was maintained by a heating lamp.

## [$^{18}$F]CPFPX PET Scan and Image-Derived Input Function Extraction Methods

Radiosynthesis and formulation of [$^{18}$F]CPFPX were performed as described earlier (Holschbach et al., 2002). [$^{18}$F]CPFPX was routinely obtained ready for injection with a radiochemical yield of 20 ± 5%, a radiochemical purity of 99.5 ± 0.3%, and a molar activity of 396 ± 114 GBq/mol.

All PET data were acquired on a Siemens Inveon Multimodality PET scanner (Siemens, Knoxville, TN, United States) with Inveon Acquisition Workplace 1.5 (Siemens). The mice were positioned supine (to allow blood sampling) with their heads fixed by the nose cone of the anesthesia system.

A dual-source $^{57}$Co transmission scan was processed for 10 min to correct attenuation before emission scans. Directly afterward, a bolus of [$^{18}$F]CPFPX (0.83 ± 0.18 MBq) was injected over 1 min via a syringe pump (model 44, Harvard Apparatus, Holliston, MA, United States) at time of scan start.

List-mode PET data were acquired for 60 min after tracer application and framed into a dynamic sequence of 12 × 10, 3 × 20, 3 × 30, 3 × 60, 3 × 150, and 9 × 300 s frames. One hundred fifty-nine slices were reconstructed by filtered back projection (Ramp filter, cutoff = 0.5) after Fourier rebinning into 2D sinograms. All PET images were corrected for attenuation and scatter radiation.

Postprocessing of PET images and activity extraction from the VOIs were performed with PMOD 3.408 software (version 3.408, PMOD Group, Zurich, Switzerland). To explore an appropriate image-derived input, three different approaches were selected (**Figure 1**) using the first time frames after [$^{18}$F]CPFPX injection (image of the first 10 s) as a guide. For method A (**Figure 1A**), a large VOI covering the whole organ was placed over the heart (cube, 10 mm), and for method B (**Figure 1B**), over the abdominal vena cava/aorta region (cuboid, 5 × 5 × 15 mm). In a second step, an automatic algorithm from PMOD was utilized to identify only those voxels, within these volumes exceeding 50% of the total activity inside the VOI for subsequent read out. For method C (**Figure 1C**), 1 × 1 × 1 mm voxels on five consecutive slices (Lanz et al., 2014) were manually placed over the abdominal vena cava/aorta region (also centered on highest activity spot).

In this study, an optimal calculated scaling factor (α) was calculated to correct the partial volume effects of regions for IDIF effectively using the equation below:

$$\text{Sum} = \sum_{i=1}^{7} \left[C_{\text{AIF}}(t_i) - C_{\text{raw\_IDIF}}(t_i) \times \alpha\right]^2 \quad (1)$$

where α is the scaling factor used in this study for the three different approaches, $C_{\text{AIF}}$ is the radioactivity concentration (kBq/cc) of AIF at any time point ($t_i$), and $C_{\text{raw\_IDIF}}$ is the raw radioactivity concentration of the three different IDIFs used in this study at the same time points. The optimal scaling factor α

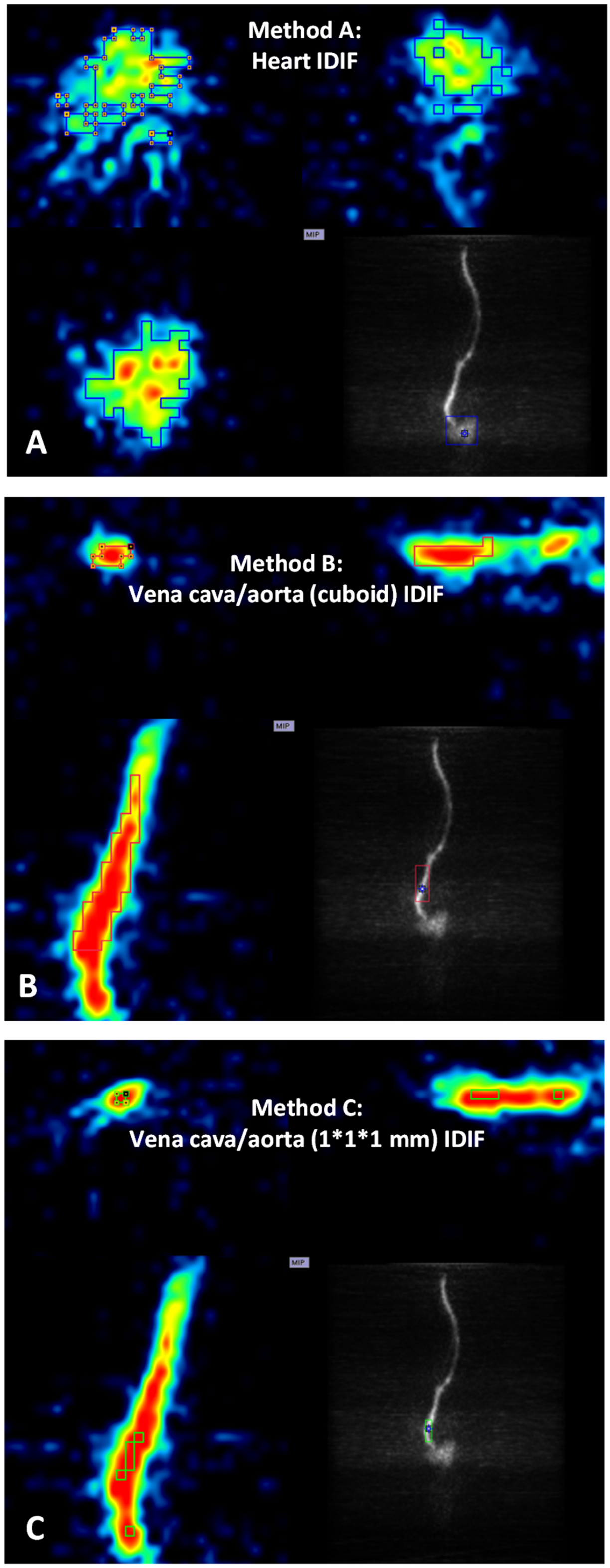


**FIGURE 1 |** Positron emission tomography images of heart and abdominal vena cava/aorta in a representative mouse during the first 10 s after [$^{18}$F]CPFPX bolus injection were used to define different volumes of interest *(Continued)*

**FIGURE 1 |** Continued
(VOIs) with image-derived input functions (IDIFs). Each image has three planes: coronal plane (upper left), sagittal plane (upper right), and horizontal plane (lower left). The lower right of each image shows a maximum-intensity-projection (MIP) map on the coronal plane. **(A)** VOI placed over the heart (cube, 10 mm). **(B)** VOI placed over abdominal vena cava/aorta region (cuboid, 5 × 5 × 15 mm). **(C)** VOI (1 × 1 × 1 mm voxels with five consecutive slices) delineated on abdominal vena cava/aorta region (centered on the highest activity spot).

is obtained by minimizing Sum, namely, the difference between arterial inputs and corrected image-inputs is lowest with the optimized α. More detailed information about Eq. (1) is discussed in section "Discussion."

## Arterial Blood Sampling and Metabolite Correction

During PET acquisition, blood samples (20.51 ± 5.78 μl per time point) were taken from the femoral artery at 1, 10, 20, 30, 40, 50, and 60 min after tracer injection. After blood sampling, heparinized saline solution was used to prevent coagulation inside of the catheter by flushing. All whole-blood and plasma samples were weighed in preweighted tubes, then measured in a high-sensitivity γ-counter (ISOMED 2100; Medizintechnik Dresden, Germany) to calibrate the activity concentration with radioactive decay correction (relative to the start of the acquisition). The fraction of unchanged radioligand in total plasma activity (parent curve) was determined using a previously published approach (Meyer et al., 2004) using thin layer chromatography.

Since the radiometabolite fraction of [$^{18}$F]CPFPX is high (Bier et al., 2006; Matusch et al., 2006), data were corrected for metabolism, and the extraction of the parent radioligand was corrected for residual activity in the precipitate after protein extraction (extraction correction). The following equation was used for data interpolation:

$$\text{Total metabolite correction } (t) = \frac{1}{(1 + a \times (t-d)^{b})^{c}} \times \frac{1}{(1 + e \times t^{2})^{f}} \quad (2)$$

where $a$, $b$, $c$, and $d$ are fitted to describe the metabolite fraction; $e$ and $f$ are fitted to describe the extraction fraction. More detailed information about Eq. (2) is discussed in section "Discussion."

## Accuracy of Image-Derived Input Functions

The accuracy and precision of the different image-derived extraction methods of input functions were evaluated by comparison with AIF.

### Visual Comparison

After using the scaling factor on image inputs, time–activity curves of whole-blood and parent tracer obtained with each method were compared with standard arterial whole-blood and parent time–activity curves. The comparison considered overall shape of the curves, the height of the peaks, as well as the slope of the tails.

### Area Under Curve Ratios

In addition to the visual comparison, a quantitative analysis was performed using area under curve (AUC) ratios between the image- and arterial-derived curves (Zanotti-Fregonara et al., 2011). The image/arterial ratios of both whole-blood time–activity curves and metabolite-corrected parent time–activity curves were calculated. The image-derived parent curve of each mouse was estimated by multiplying the image-derived whole-blood time–activity curve with group average parent/whole blood ratios at the same time points.

### Kinetic Modeling

After postprocessing with scaling factor α, PET data were analyzed with both the Logan plot model (Logan et al., 1990) and the two-tissue compartment model (2TCM) (Leenders et al., 1990; Koeppe et al., 1991). Logan analysis was implemented with $t^{*}$ = 20 min and with no weighting. 2TCM analysis used "prescribed weighting" (standard deviation of the pixel values in the VOI is used for the calculation of the weights) in all IDIF methods. For AIF, the three-term exponentials function was applied in the configuration of blood activity fitting and interpolation.

All distribution volumes ($V_{\mathrm{T}}$) with different input functions were obtained for brain regions, such as cortex, hippocampus, and thalamus for each mouse. The mean $V_{\mathrm{T}}$ ratios (image-derived input/arterial input) based on three different IDIFs were calculated and compared. The linear regression was used to show the correlation between image-derived input and arterial input, while the Bland-Altman plot was introduced to describe agreement between image-derived input and arterial input.

## Parametric Images and Autoradiography

Average parametric images ($n$ = 5) of $V_{\mathrm{T}}$ in mice brains were calculated by application of Logan plot for both AIF and IDIF over heart (method A). Logan plot was set up with $t^{*}$ = 20 min, and with no masking.

The results of *in vivo* binding by different PET input functions were further verified by *in vitro* autoradiography. After decapitation, the mouse brain was removed, frozen in 2-methylbutane (−40°C) and stored at −80°C. Brain sections (20-μm thickness) were mounted on slides. Preincubation was conducted in 170 mM Tris–HCl buffer (pH 7.4) and 2 U/L adenosine deaminase for 15 min at 4°C. Later on, main incubation lasted for 2 h at room temperature with the same buffer including [$^{3}$H]CPFPX (0.99 nM; molar activity, 2,009 GBq/mmol) (Holschbach et al., 2003), 100 μM Gpp(NH)p and 2 U/L adenosine deaminase. After washing with preincubation buffer and a rapid rinse in ice-cold water, sections were dried with a stream of air (room temperature) and exposed against phosphor-imaging plates (BAS2025; Fuji, Japan) with tritium activity standards (Amersham Biosciences, Piscataway, United States). For further processing of digital autoradiography, an image plate reader (spatial resolution of 50 μm; BAS 5000;

Fuji, Japan) and image analysis software (Image Gauge 4.0; Fuji, Japan) were used. To get less background noise image in Image Gauge 4.0, 32-color type (displays in 32 pseudo-colors) was used with linear method (adjusts contrast with a linear curve).

# RESULTS

## Blood Sample Analysis

The whole-blood activity curves reached at highest value at ∼60 s among the seven blood sampling time points, followed by a rapid drop (**Supplementary Figure 1A**). Plasma activity showed a stable percentage of whole-blood activity with a mean plasma/whole blood ratio of 1.67 ± 0.04. Metabolite correction of [$^{18}$F]CPFPX was done (Eq. 2) with parameters set to $a$ (0.18), $b$ (1.84), $c$ (0.34), $d$ (0.30), $e$ (0.19), and $f$ (0.02). Group mean parent/whole blood ratio [(plasma/whole blood ratio) × total metabolite correction] over time was calculated (**Supplementary Figure 1B**) based on Eq. (2).

## Visual Analysis

After extraction of IDIFs with different methods, a calculated scaling factor (α = 1.77) was used to correct for partial volume effects in whole-blood curves (**Figure 2A**).

The tails of whole-blood curves obtained by three different IDIF approaches generally matched closely with the reference arterial inputs. The image-derived whole-blood curve with the VOI over the heart performed best.

Compared with the arterial parent compound curves (**Figure 2B**), the image-derived parent compound curves performed equally well. The shape of the image-derived input over heart (method A) was smoother than vena cava/aorta (cuboid) VOI (method B) and 1 × 1 × 1 mm VOI (method C).

## Ratios of Area Under Curves

After scaling, the mean AUC ratio between image-derived and arterial inputs of both whole-blood and corrected parent curves were estimated. As given in **Table 1**, the mean AUC ratio was smaller for heart (method A) and aorta (1 × 1 × 1 mm)

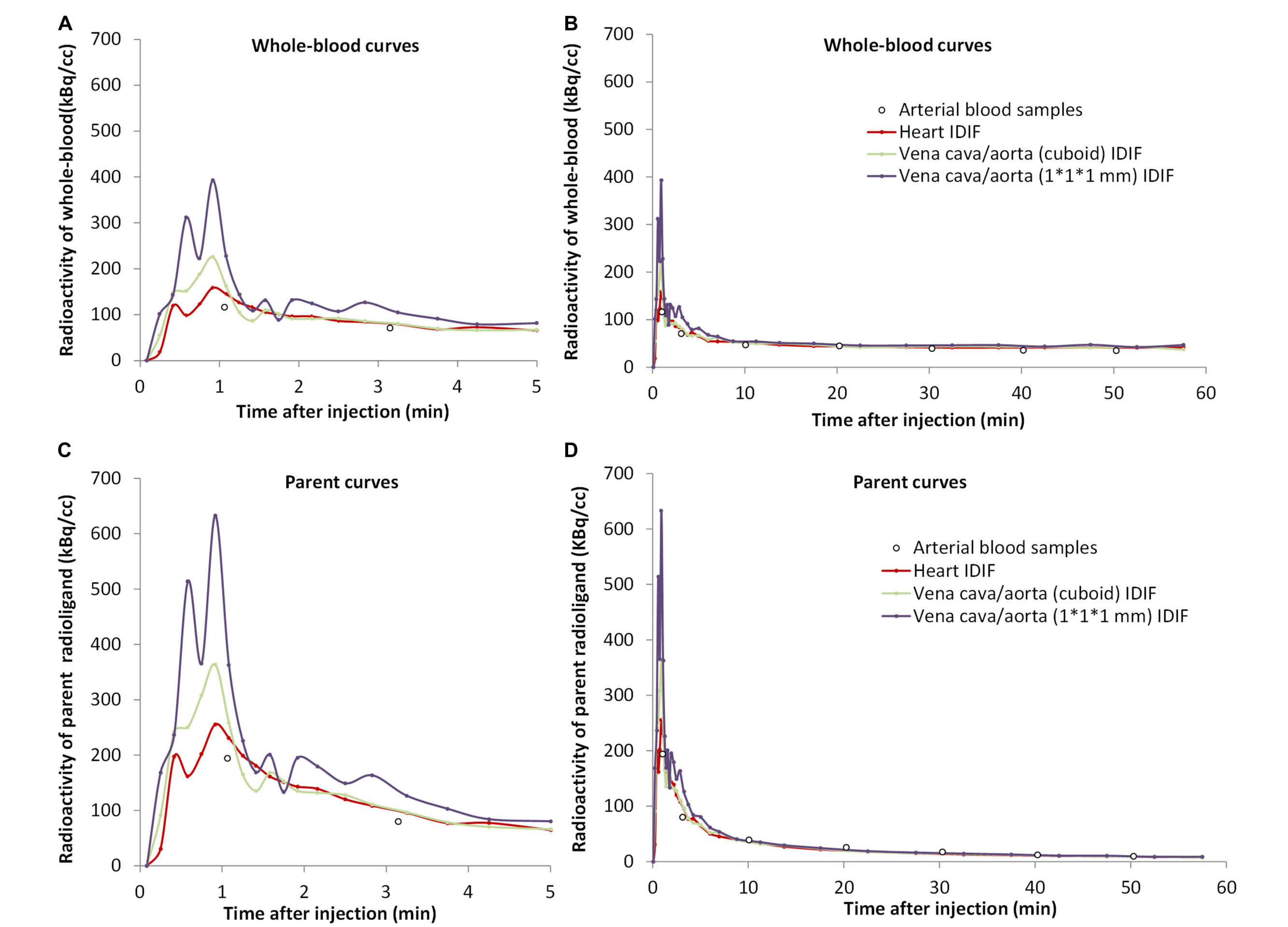


**FIGURE 2 |** The concentrations over time of [$^{18}$F]CPFPX in whole-blood **(A,B)** and parent radioligand **(C,D)** (with metabolite correction) curves from the arterial input function (white dots) and from the three image-derived input functions (IDIFs) with different volumes of interest (VOIs) (colored lines) in a representative animal. The left curves **(A,C)** are excerpts of the first 5 min of the total curves **(B,D)**.

**TABLE 1 |** Mean AUC ratios (IDIF/AIF) for each VOI related IDIF in both whole-blood and parent curves.

| | Method A Heart (mean ± SD) | Method B Vena cava/aorta (cuboid) (mean ± SD) | Method C Vena cava/aorta (1 × 1 × 1 mm) (mean ± SD) |
|---|---|---|---|
| Whole-blood AUC ratio | 1.03 ± 0.06 | 1.11 ± 0.14 | 1.08 ± 0.10 |
| Parent curve AUC ratio | 1.01 ± 0.10 | 1.04 ± 0.14 | 1.06 ± 0.23 |

*n = 5. AUC, area under curve; VOI, volume of interest; IDIF, image-derived input function; AIF, arterial input function.*

(method C) VOIs than for aorta (cuboid) VOI (method B). Specifically, the difference in the whole-blood arterial AUC and image-derived AUC was ≤10% for both methods A and C. Moreover, method A had a whole-blood AUC ratio (1.03) that was closest to identity with a low standard deviation (SD) of 0.06.

On the other hand, the AUC ratio of parent curve in the aorta (1 × 1 × 1 mm; method C) was worse than in the heart (method A) and cuboid aorta (method B) VOIs (**Table 1**). The high ratio and SD in method C (1.06 ± 0.23) indicated that the results from this image-derived approach were inconstant and not fitted ideally among all tested mice, while method A performed best with an AUC ratio close to 1 and a low SD value (1.01 ± 0.10).

## Kinetic Modeling (Logan and 2TCM Analysis)

In **Figure 3**, the $V_T$ values of image-derived and arterial inputs generated by both Logan graphical and 2TCM analysis are presented for the following brain regions: striatum (STR), cortex (CTX), hippocampus (HIP), thalamus (THA), cerebellum (CB), hypothalamus (HYP), amygdala (AMY), olfactory bulb (OLF), and midbrain (MID).

The $V_T$ values of each mouse obtained by the Logan graphical analysis (**Figures 3A–C**) show better correlations between arterial and image-derived inputs $V_T$ in all three IDIF extraction methods, while the $V_T$ values with the 2TCM model were more dispersed around the identity line (**Figures 3D–F**).

As seen in Bland–Altman plots (**Figure 4**), according to the comparison between AIF and IDIF over heart (method A) (**Figures 4A,D**), 0% (0/45) and 4.44% (2/45) difference dots were located outside of the 95% limits of agreement by Logan and 2TCM analysis, respectively; in comparison between AIF and method B, 2.22% (1/45) difference dots (**Figures 4B,E**) were located out of the 95% limits of agreement with both

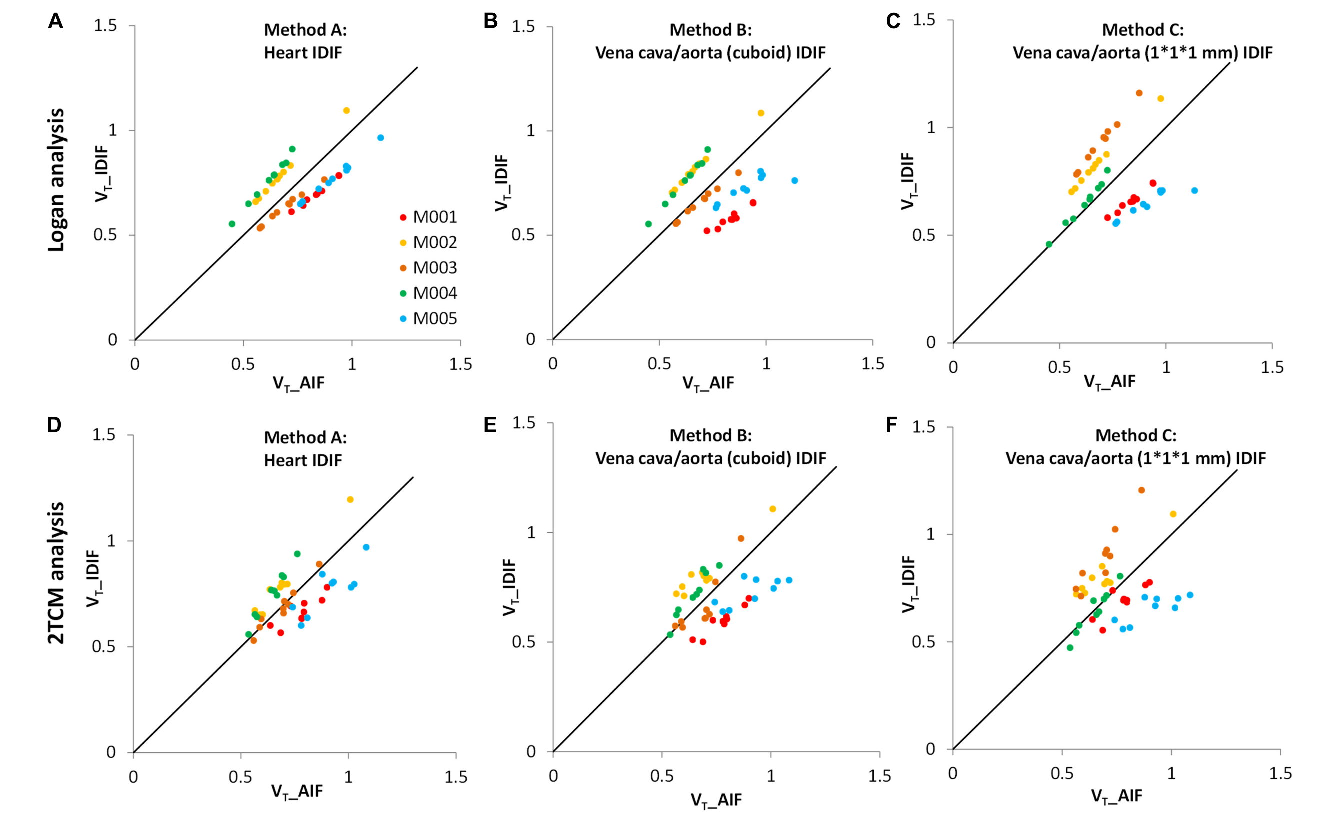


**FIGURE 3 |** Comparison of distribution volumes ($V_T$) values between image-derived input function (IDIF) and arterial input function (AIF). All $V_T$ values of different input functions in various brain regions were generated by two kinetic models: the Logan graphical model (upper) and the 2TCM model (lower). **(A,D)** The IDIF with the volume of interest (VOI) placed over the heart (method A); **(B,E)** the IDIF with the VOI set over abdominal vena cava/aorta region with a cuboid (method B); **(C,F)** the IDIF with the VOI delineated with 1 × 1 × 1 mm voxels on five consecutive slices over the abdominal vena cava/aorta region (method C). Different dots represent different brain regions (*n* = 9). Different colors represent different mice (*n* = 5). The solid line is the line of identity.

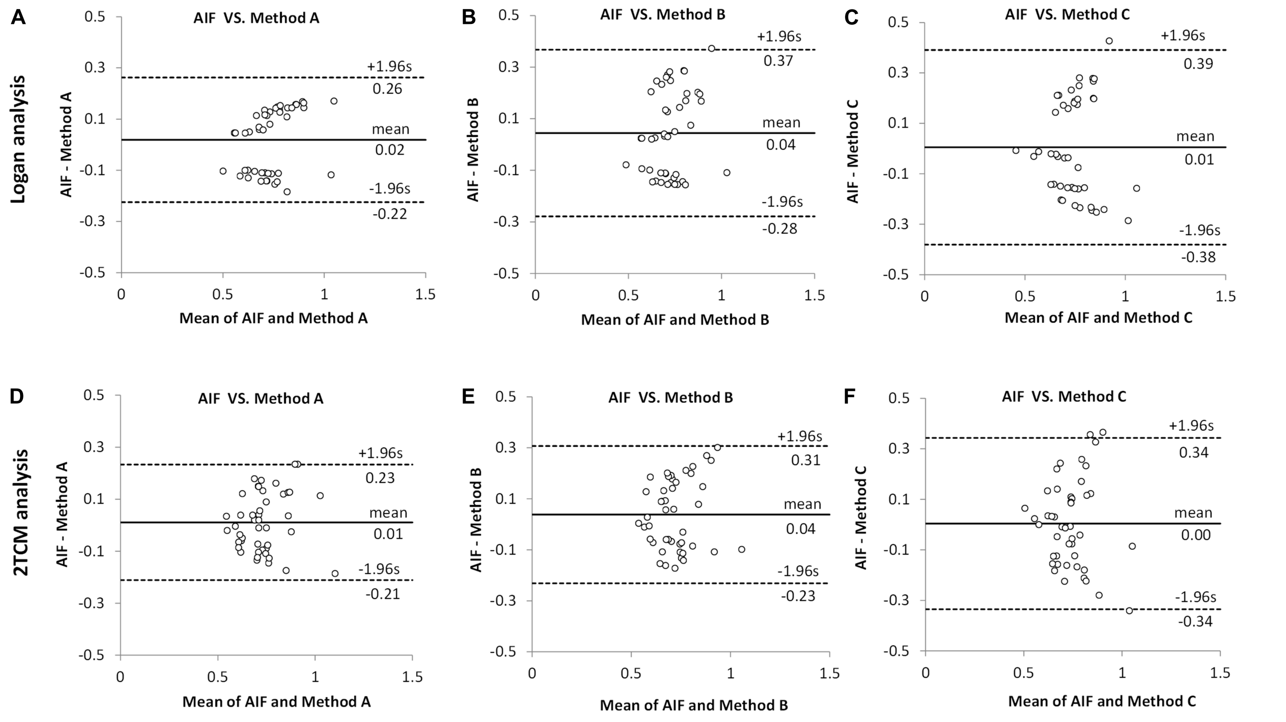


**FIGURE 4 |** Comparison between arterial input function (AIF) and image-derived input function (IDIF) of distribution volumes ($V_T$) by Bland–Altman analysis. All $V_T$ values obtained by Logan and 2TCM kinetic modeling were the same as the data in **Figure 3**. **(A,D)** The IDIF with the volume of interest (VOI) placed over the heart (method A) compared with AIF. **(B,E)** The IDIF with the VOI set over abdominal vena cava/aorta region with a cuboid (method B) compared with AIF. **(C,F)** the IDIF with the VOI delineated with 1 × 1 × 1 mm voxels on five consecutive slices over the abdominal vena cava/aorta region (method C) compared with AIF. Different dots represent different brain regions ($n$ = 9) in all mice ($n$ = 5).

Logan and 2TCM analysis; as for method C, 2.22% (1/45) and 6.67% (3/45) difference dots (**Figures 4C,F**) were located out of the limits by Logan and 2TCM analysis, respectively. Moreover, based on the comparison between AIF and method A (**Figures 4A,D**), the ratios of the maximum difference to the mean within the 95% limits of agreement were 25.01% (0.1849/0.7390) and 25.26% (0.1860/0.7363) by Logan and 2TCM analysis, respectively. However, ratios were higher in comparison between AIF and other input functions (methods B and C): 39.33% (0.2856/0.7261), 37.27% (0.2694/0.7227), 38.42% (0.2865/0.7457), and 44.21% (0.3270/0.7396) in **Figures 4B,C,E,F**, respectively.

Therefore, irrespective of Logan or 2TCM analysis, the best $V_T$ performance of the IDIFs were found qualitatively with the heart (method A) VOI (**Figure 3A**).

In detail, the mean $V_T$ ratios between image-derived and arterial inputs for method A (**Table 2**) were 1.00 ± 0.17 by Logan and 1.00 ± 0.13 by 2TCM analysis, respectively. Both modeling results were approaching unity. Specific $V_T$ values of different brain regions obtained with method A by Logan and 2TCM models are given in **Supplementary Table 1**.

**Figure 5** shows the average parametric images ($n$ = 5) of $V_T$ with Logan plot for both AIF and IDIF over heart (method A). **Figures 5A,D** present the typical distribution of $A_1$AR in mice brains, which is in good accordance to the distribution pattern in autoradiography (**Figure 5G**).

## DISCUSSION

The main goal of the present study was to establish an optimal [18F]CPFPX IDIF which can replace AIF requiring blood sampling in mice. Three non-invasive IDIFs were tested using different VOI-based approaches: (A) VOI placed over the heart (cube, 10 mm); (B) VOI set over abdominal vena cava/aorta region with a cuboid (5 × 5 × 15 mm); and (C) VOI delineated with 1 × 1 × 1 mm voxels on five consecutive slices, also over the abdominal vena cava/aorta region (centered on highest activity spot). We evaluated all the image-derived input results by

**TABLE 2 |** Mean $V_T$ ratios (IDIF/AIF) obtained from striatum, cortex, hippocampus, thalamus, cerebellum, hypothalamus, amygdala, olfactory bulb, and midbrain for each VOI related image-derived approach in both Logan graphical and 2TCM analysis.

| | Method A Heart (mean ± SD) | Method B Vena cava/aorta (cuboid) (mean ± SD) | Method C Vena cava/aorta (1 × 1 × 1 mm) (mean ± SD) |
|---|---|---|---|
| Logan $V_T$ ratio | 1.00 ± 0.17 | 0.97 ± 0.21 | 1.02 ± 0.25 |
| 2TCM $V_T$ ratio | 1.00 ± 0.13 | 0.97 ± 0.16 | 1.02 ± 0.21 |

*n = 5. $V_T$, total distribution volume; VOI, volume of interest; 2TCM, two-tissue compartment model; IDIF, image-derived input function; AIF, arterial input function.*

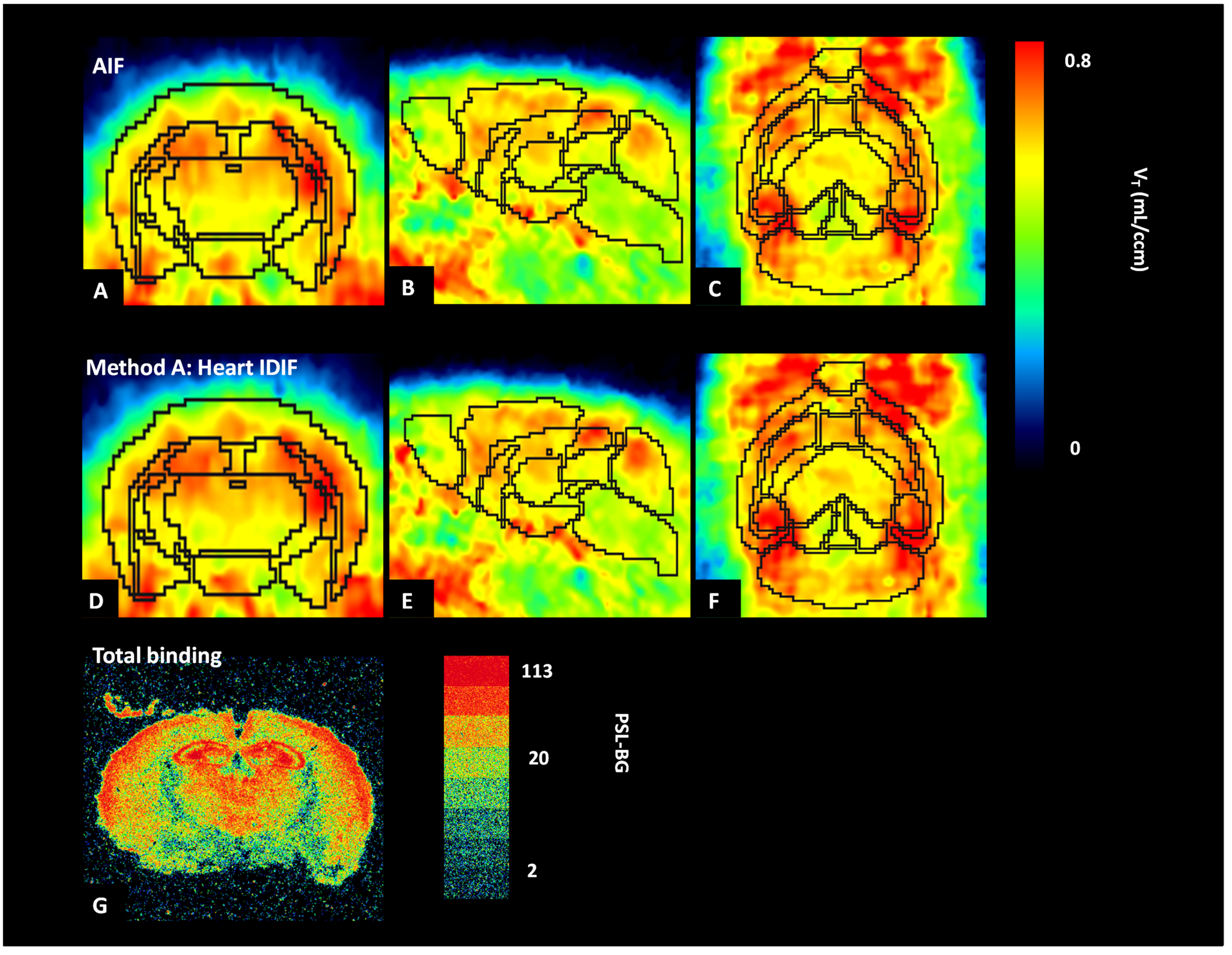


**FIGURE 5 |** Average parametric images (*n* = 5) of $A_1$ adenosine receptors ($A_1$ARs) distribution in mice brains calculated by application of Logan plot in PET: coronal plane (left column), sagittal plane (middle column), and horizontal plane (right column) images representing cerebral $A_1$AR using the arterial input function (AIF) **(A–C)** and the image-derived input function over the heart (heart IDIF) **(D–F)**. Mouse brain autoradiograph (at 0.99 nM concentration of [$^3$H]CPFPX) shows receptor total binding **(G)**.

comparison with standard AIF. We found that method A (VOI placed over the heart) closely follows the AIF. It also showed more accurate, stable and more reliable results than methods B and C in terms of AUC ratios and kinetic modeling of both Logan plot and 2TCM analysis.

As shown in **Figures 3**, **4**, **Table 2**, and **Supplementary Table 1**, all results of kinetic modeling analysis with all three image-derived approaches were calculated with both Logan plot and 2TCM. Considering the three different image-derived and the AIFs applied in this study, the Logan-derived $V_T$ values of a 60-min scan were very similar to those obtained with 2TCM analysis, with a difference of <5% (**Supplementary Figure 2**). Therefore, in further studies, we propose to directly select Logan analysis for kinetic modeling not only because it is more robust regarding the modeling parameters but also because it is less sensitive than 2TCM modeling analysis toward extraction of the first part of the input curve. Logan analysis based on the AUC of the input function is less sensitive than 2TCM analysis to the initial shape of the input function. The radioactivity concentration of the initial part of whole-blood curve changes rapidly, and consequently, it is difficult to acquire a correct curve from the image data (Zanotti-Fregonara et al., 2011). Under these circumstances, $V_T$ values are sometimes poorly obtained with 2TCM.

Except from the gold-standard approach of arterial plasma input function and IDIF, the input function for kinetic models can also be acquired by applying a reference region method. When studying brain receptors, cerebellum is used as reference region for some neuroreceptor quantifications. Unfortunately, there often is no reference region for other neuroreceptors, for example, the studies for nicotinic receptors with tracer: (2-[$^{18}$F]fluoro-A-85380) (Zanotti-Fregonara et al., 2012) and mGluR1 with ([$^{11}$C]ITDM) (Bertoglio et al., 2019) in mice.

Different suggestions have been put forward to deal with partial volume as well as spill-out and spill-in effects, respectively. According to Chen et al. (2007) and Kang et al. (2018), the activity $C_{\text{measured}}$ from VOIs can be considered as a combination of two components: the true radioactivity in the blood vessel and the radioactivity from surrounding regions:

$$C_{\text{measured}}(t) = \text{PV} \times C_{\text{vessel}}(t) + \text{SO} \times C_{\text{surrounding}}(t) \quad (3)$$

where $C_{\text{measured}}(t)$ is the measured radioactivity in the blood obtained from PET, $C_{\text{vessel}}(t)$ is the true radioactivity in the blood vessel, and $C_{\text{surrounding}}(t)$ is radioactivity from surrounding tissues; PV is the determined partial volume correction coefficient, and SO represents the experimental spill-over correction coefficient required to consider the spatial resolution of the small-animal PET scanner and the reconstruction methodology. Lanz et al. (2014) proposed another method for the "spill-out effect" correction of the imaged-derived inputs by a double-exponential function. However, instead of one scaling factor (α), this convolution operation needs four parameter optimizations and a modified Levenberg–Marquardt non-linear regression method. Compared with the above-mentioned studies, we simplified the equations and functions to correct the radioactivity concentration of IDIFs. The main reason for that is that [$^{18}$F]CPFPX rarely showed obvious affinity for myocardium, so that the spill-over effect could be ignored. In our study, because of spill-out and related partial volume effects, the raw image-derived activity of whole blood was always lower than the measured AIF ($p < 0.05$, by $t$ test). To correct the above-mentioned effects in IDIFs, an optimal scaling factor ($\alpha = 1.77$) was calculated (see Eq. 1) and subsequently used for scaling of different IDIFs.

Metabolite correction for IDIF is another important aspect for tracers with high radiometabolite fractions. So far, the majority of studies about the IDIFs prefer to use tracers with negligible metabolism, such as Sari et al. (2017) who discussed image-derived methods for [$^{18}$F]FDG only focusing on partial volume effects and not metabolite correction. For radiotracers with fast metabolism, such as [$^{18}$F]CPFPX, one key part of obtaining IDIFs is the total metabolite correction. In the present study, we not only explored how to solve partial volume effects with a scaling factor (α) but also developed a method of obtaining the total metabolite correction (Eq. 2) of [$^{18}$F]CPFPX for image-derived input approaches. Specifically, after scaling with factor α, the parent $\text{curve}_{(\text{IDIF})}$ was obtained by following formulas: parent $\text{curve}_{(\text{IDIF})}$ = whole-blood $\text{curve}_{(\text{IDIF})}$ × (mean parent/whole-blood ratio), mean parent/whole-blood ratio = plasma $\text{curve}_{(\text{IDIF})}$ × total metabolite correction ($t$)/whole-blood $\text{curve}_{(\text{IDIF})}$, plasma $\text{curve}_{(\text{IDIF})} = 1.67 \times$ whole-blood $\text{curve}_{(\text{IDIF})}$.

Although this study required a small amount of blood samples for calculating the scaling factor (α) and the parameters ($a$–$f$) of total metabolite correction equation (Eq. 2), there are still opportunities to achieve completely blood-free IDIFs for acquiring parent curves for future [$^{18}$F]CPFPX or other tracer studies in mice. On the other hand, we can use blood-based methods to optimize the accuracy of the IDIFs. For example, Lanz et al. (2014) tried to decrease the effect of tracer dispersion in blood during the first minute after the [$^{18}$F]FDG bolus injection. They estimated the average scaling parameter using a single blood sample at 1.5 min, which resulted in higher accuracy for the extraction of IDIFs in animals.

There is a potential drawback of the evaluation regarding the AUC ratio. Since the first blood sample was collected 1–2 min after tracer injection, it is possible that the peaks of the arterial blood curves were lower than the peaks of image-derived curves (**Figure 2**). Taking this into account when using the AUC ratios between image-derived and arterial curves, resulting values would be bigger. This may explain why all AUC ratios in **Table 1** were $>1$. Another limitation of the present study is the relatively low number of mice. However, even though we used only five animals and there were individual differences, we strongly believe in the representativeness of our results. For instance, in **Figures 3A–C**, although every mouse performed significant correlations ($R^2$) between arterial and image-derived inputs $V_T$ values by Logan analysis, there was still no perfect overlay with the line of identity because of the individual slopes and intercepts. However, when we did the average of all five mice, the $V_T$ values of image-derived inputs got much closer to arterial inputs (**Table 2**). Notwithstanding these findings, an increased study power will undoubtedly help optimizing the data in further non-invasive input function studies.

In the present study, autoradiography was used for qualitative analysis of $A_1AR$ with [$^3$H]CPFPX. Compared with parametric PET images from [$^{18}$F]CPFPX of arterial and IDIF (**Figures 5A,D**), the distribution of $A_1AR$ in autoradiography (**Figure 5G**) showed the same binding patterns. For example, high concentrations of $A_1AR$ in cortex, hippocampus, and thalamus were detected by both PET and autoradiography, and the qualitative distribution of $A_1AR$ labeled with [$^3$H]CPFPX (0.99 nM) in coronal sections was similar to previous data of Bailey et al. (2003).

A potential improvement of our image-derived input approach might derive from a closer look at heartbeat affects. Previously, only the left ventricle was used as the region of interest to reduce the motion of heart and improve the precision. Recently, Herraiz et al. (2016) and Verhaeghe et al. (2018) showed that the left ventricle volume can be estimated by means of cardiac gating during PET acquisition. For this purpose, PET raw data were divided into time subsets according to the different phases of the heart activity. Thus, a more accurate measurement and verification of whole-heart image-derived inputs might be obtained in future studies when gated PET imaging will be applied (Locke et al., 2011; Mabrouk et al., 2012).

## CONCLUSION

The present study provides evidence that a non-invasive IDIF can validly replace the standard AIF in quantification of $A_1AR$ PET using the fast metabolizing radioligand [$^{18}$F]CPFPX in mice. Furthermore, a VOI over the heart is the best choice to extract the IDIF after comparing different VOI placements regarding image-derived curves, AUC ratios, and kinetic modeling results ($V_T$).

## DATA AVAILABILITY STATEMENT

The datasets analyzed during the current study are available from the corresponding author on reasonable request.

## ETHICS STATEMENT

The animal study was reviewed and approved by the German regional authorities (Landesamt für Natur, Umwelt und Verbraucherschutz) and performed on the basis of the German Animal Welfare Act.

## AUTHOR CONTRIBUTIONS

DE, AB, and TK designed the study. FW, TK, AO, and DE were responsible for experiments and data collection. XH did analysis and interpretation of data, and drafted and revised the manuscript. DE, TK, SB, and AD made contribution to the data interpretation. JE and BN contributed with tracer synthesis. All authors critically revised the manuscript and approved the final version.

## ACKNOWLEDGMENTS

The authors would like to thank Magdalene Vögeling and Nikola Kornadt-Beck for excellent technical assistance, and Judith Fronczek-Poncelet for proofreading an early version of the manuscript. XH would like to thank the China Scholarship Council (CSC) for financial support under grant no. 201606240119.

## SUPPLEMENTARY MATERIAL

The Supplementary Material for this article can be found online at: https://www.frontiersin.org/articles/10.3389/fphys.2019.01617/full#supplementary-material

## REFERENCES

Bailey, A., Hawkins, R. M., Hourani, S. M., and Kitchen, I. (2003). Quantitative autoradiography of adenosine receptors in brains of chronic naltrexone-treated mice. *Br. J. Pharmacol.* 139, 1187–1195. doi: 10.1038/sj.bjp.0705340

Bauer, A., Holschbach, M. H., Meyer, P. T., Boy, C., Herzog, H., Olsson, R. A., et al. (2003). In vivo imaging of adenosine A1 receptors in the human brain with [18F]CPFPX and positron emission tomography. *Neuroimage* 19, 1760–1769. doi: 10.1016/s1053-8119(03)00241-6

Bertoglio, D., Verhaeghe, J., Korat, S., Miranda, A., Wyffels, L., Stroobants, S., et al. (2019). *In vitro* and *In vivo* assessment of suitable reference region and kinetic modelling for the mGluR1 radioligand [(11)C]ITDM in mice. *Mol. Imaging Biol.* doi: 10.1007/s11307-019-01435-1 [Epub ahead of print].

Bier, D., Holschbach, M. H., Wutz, W., Olsson, R. A., and Coenen, H. H. (2006). Metabolism of the A(1)1 adenosine receptor positron emission tomography ligand [18F]8-cyclopentyl-3-(3-fluoropropyl)-1-propylxanthine ([18F]CPFPX) in rodents and humans. *Drug Metab. Dispos.* 34, 570–576. doi: 10.1124/dmd.105.006411

Chatziioannou, A. F., Cherry, S. R., Shao, Y. P., Silverman, R. W., Meadors, K., Farquhar, T. H., et al. (1999). Performance evaluation of microPET: a high-resolution lutetium oxyorthosilicate PET scanner for animal imaging. *J. Nucl. Med.* 40, 1164–1175.

Chen, K., Bandy, D., Reiman, E., Huang, S. C., Lawson, M., Feng, D., et al. (1998). Noninvasive quantification of the cerebral metabolic rate for glucose using positron emission tomography, 18F-fluoro-2-deoxyglucose, the Patlak method, and an image-derived input function. *J. Cereb. Blood Flow Metab.* 18, 716–723. doi: 10.1097/00004647-199807000-00002

Chen, K., Chen, X., Renaut, R., Alexander, G. E., Bandy, D., Guo, H., et al. (2007). Characterization of the image-derived carotid artery input function using independent component analysis for the quantitation of [18F] fluorodeoxyglucose positron emission tomography images. *Phys. Med. Biol.* 52, 7055–7071. doi: 10.1088/0031-9155/52/23/019

Cherry, S. R., Shao, Y., Silverman, R. W., Meadors, K., Siegel, S., Chatziioannou, A., et al. (1997). MicroPET: a high resolution PET scanner for imaging small animals. *IEEE Trans. Nucl. Sci.* 44, 1161–1166. doi: 10.1109/23.596981

Croteau, E., Lavallee, E., Labbe, S. M., Hubert, L., Pifferi, F., Rousseau, J. A., et al. (2010). Image-derived input function in dynamic human PET/CT: methodology and validation with 11C-acetate and 18F-fluorothioheptadecanoic acid in muscle and 18F-fluorodeoxyglucose in brain. *Eur. J. Nucl. Med. Mol. Imaging* 37, 1539–1550. doi: 10.1007/s00259-010-1443-z

Elmenhorst, D., Kroll, T., Wedekind, F., Weisshaupt, A., Beer, S., and Bauer, A. (2013). In vivo kinetic and steady-state quantification of 18F-CPFPX binding to rat cerebral A1 adenosine receptors: validation by displacement and autoradiographic experiments. *J. Nucl. Med.* 54, 1411–1419. doi: 10.2967/jnumed.112.115576

Fang, Y. H., and Muzic, R. F. Jr. (2008). Spillover and partial-volume correction for image-derived input functions for small-animal 18F-FDG PET studies. *J. Nucl. Med.* 49, 606–614. doi: 10.2967/jnumed.107.047613

Ferl, G. Z., Zhang, X., Wu, H. M., Kreissl, M. C., and Huang, S. C. (2007). Estimation of the 18F-FDG input function in mice by use of dynamic small-animal PET and minimal blood sample data. *J. Nucl. Med.* 48, 2037–2045. doi: 10.2967/jnumed.107.041061

Gessi, S., Merighi, S., Varani, K., and Borea, P. A. (2011). Adenosine receptors in health and disease. *Adv. Pharmacol.* 61, 41–75. doi: 10.1016/B978-0-12-385526-8.00002-3

Herraiz, J. L., Herranz, E., Cal-Gonzalez, J., Vaquero, J. J., Desco, M., Cusso, L., et al. (2016). Automatic cardiac self-gating of small-animal PET data. *Mol. Imaging Biol.* 18, 109–116. doi: 10.1007/s11307-015-0868-y

Holschbach, M. H., Olsson, R. A., Bier, D., Wutz, W., Sihver, W., Schuller, M., et al. (2002). Synthesis and evaluation of no-carrier-added 8-cyclopentyl-3-(3-[F-18]fluoropropyl)-1-propylxanthine ([F-18]CPFPX): a potent and selective A(1)-adenosine receptor antagonist for in vivo imaging. *J. Med. Chem.* 45, 5150–5156. doi: 10.1021/jm020905i

Holschbach, M. H., Wutz, W., Schuller, M., Bier, D., and Coenen, H. H. (2003). Tritium-labelled 8-cyclopentyl-3-(3-fluoropropyl)-1-propylxanthine ([H-3]CPFPX), a potent and selective antagonist for the A(1) adenosine receptor. *J. Labelled Comp. Radiopharm.* 46, 365–372. doi: 10.1002/jlcr.679

Kang, Y., Mozley, P. D., Verma, A., Schlyer, D., Henchcliffe, C., Gauthier, S. A., et al. (2018). Noninvasive PK11195-PET image analysis techniques can detect abnormal cerebral microglial activation in Parkinson's disease. *J. Neuroimaging* 28, 496–505. doi: 10.1111/jon.12519

Kiesman, W. F., Elzein, E., and Zablocki, J. (2009). A1 adenosine receptor antagonists, agonists, and allosteric enhancers. *Handb. Exp. Pharmacol.* 193, 25–58. doi: 10.1007/978-3-540-89615-9_2

Kim, J., Herrero, P., Sharp, T., Laforest, R., Rowland, D. J., Tai, Y. C., et al. (2006). Minimally invasive method of determining blood input function from PET images in rodents. *J. Nucl. Med.* 47, 330–336.

Koeppe, R. A., Holthoff, V. A., Frey, K. A., Kilbourn, M. R., and Kuhl, D. E. (1991). Compartmental analysis of [11C]flumazenil kinetics for the estimation of ligand transport rate and receptor distribution using positron emission tomography. *J. Cereb. Blood Flow Metab.* 11, 735–744. doi: 10.1038/jcbfm.1991.130

Laforest, R., Sharp, T. L., Engelbach, J. A., Fettig, N. M., Herrero, P., Kim, J., et al. (2005). Measurement of input functions in rodents: challenges and solutions. *Nucl. Med. Biol.* 32, 679–685. doi: 10.1016/j.nucmedbio.2005.06.012

Lanz, B., Poitry-Yamate, C., and Gruetter, R. (2014). Image-derived input function from the vena cava for 18F-FDG PET studies in rats and mice. *J. Nucl. Med.* 55, 1380–1388. doi: 10.2967/jnumed.113.127381

Lecomte, R., Cadorette, J., Richard, P., Rodrigue, S., and Rouleau, D. (1994). Design and engineering aspects of a high-resolution positron tomograph for small animal imaging. *IEEE Trans. Nucl. Sci.* 41, 1446–1452. doi: 10.1109/23.322930

Leenders, K. L., Perani, D., Lammertsma, A. A., Heather, J. D., Buckingham, P., Healy, M. J., et al. (1990). Cerebral blood flow, blood volume and oxygen utilization. Normal values and effect of age. *Brain* 113(Pt 1), 27–47. doi: 10.1093/brain/113.1.27

Locke, L. W., Berr, S. S., and Kundu, B. K. (2011). Image-derived input function from cardiac gated maximum a posteriori reconstructed PET images in mice. *Mol. Imaging Biol.* 13, 342–347. doi: 10.1007/s11307-010-0347-4

Logan, J., Fowler, J. S., Volkow, N. D., Wolf, A. P., Dewey, S. L., Schlyer, D. J., et al. (1990). Graphical analysis of reversible radioligand binding from time-activity measurements applied to [N-11C-methyl]-(-)-cocaine PET studies in human subjects. *J. Cereb Blood Flow Metab.* 10, 740–747. doi: 10.1038/jcbfm.1990.127

Mabrouk, R., Dubeau, F., Bentourkia, M., and Bentabet, L. (2012). Extraction of time activity curves from gated FDG-PET images for small animals' heart studies. *Comput. Med. Imaging Graph* 36, 484–491. doi: 10.1016/j.compmedimag.2012.05.002

Matusch, A., Meyer, P. T., Bier, D., Holschbach, M. H., Woitalla, D., Elmenhorst, D., et al. (2006). Metabolism of the A1 adenosine receptor PET ligand [18F]CPFPX by CYP1A2: implications for bolus/infusion PET studies. *Nucl. Med. Biol.* 33, 891–898. doi: 10.1016/j.nucmedbio.2006.07.006

Meyer, P. T., Bier, D., Holschbach, M. H., Boy, C., Olsson, R. A., Coenen, H. H., et al. (2004). Quantification of cerebral A1 adenosine receptors in humans using [18F]CPFPX and PET. *J. Cereb. Blood Flow Metab.* 24, 323–333. doi: 10.1097/01.wcb.0000110531.48786.9d

Meyer, P. T., Circiumaru, V., Cardi, C. A., Thomas, D. H., Bal, H., and Acton, P. D. (2006). Simplified quantification of small animal [18F]FDG PET studies using a standard arterial input function. *Eur. J. Nucl. Med. Mol. Imaging* 33, 948–954. doi: 10.1007/s00259-006-0121-7

Mourik, J. E., Lubberink, M., Klumpers, U. M., Comans, E. F., Lammertsma, A. A., and Boellaard, R. (2008). Partial volume corrected image derived input functions for dynamic PET brain studies: methodology and validation for [11C]flumazenil. *Neuroimage* 39, 1041–1050. doi: 10.1016/j.neuroimage.2007.10.022

Naganawa, M., Kimura, Y., Ishii, K., Oda, K., Ishiwata, K., and Matani, A. (2005). Extraction of a plasma time-activity curve from dynamic brain PET images based on independent component analysis. *IEEE Trans. Biomed. Eng.* 52, 201–210. doi: 10.1109/tbme.2004.840193

Parker, B. J., and Feng, D. G. (2005). Graph-based Mumford-Shah segmentation of dynamic PET with application to input function estimation. *IEEE Trans. Nucl. Sci.* 52, 79–89. doi: 10.1109/tns.2004.843133

Paul, S., Elsinga, P. H., Ishiwata, K., Dierckx, R. A., and Van Waarde, A. (2011). Adenosine A(1) receptors in the central nervous system: their functions in health and disease, and possible elucidation by PET imaging. *Curr. Med. Chem.* 18, 4820–4835. doi: 10.2174/092986711797535335

Porkka-Heiskanen, T., and Kalinchuk, A. V. (2011). Adenosine, energy metabolism and sleep homeostasis. *Sleep Med. Rev.* 15, 123–135. doi: 10.1016/j.smrv.2010.06.005

Sari, H., Erlandsson, K., Law, I., Larsson, H. B., Ourselin, S., Arridge, S., et al. (2017). Estimation of an image derived input function with MR-defined carotid arteries in FDG-PET human studies using a novel partial volume correction method. *J. Cereb. Blood Flow Metab.* 37, 1398–1409. doi: 10.1177/0271678X16656197

Su, K. H., Wu, L. C., Liu, R. S., Wang, S. J., and Chen, J. C. (2005). Quantification method in [18F]fluorodeoxyglucose brain positron emission tomography using independent component analysis. *Nucl. Med. Commun.* 26, 995–1004. doi: 10.1097/01.mnm.0000184999.81203.5c

Verhaeghe, J., Bertoglio, D., Kosten, L., Thomae, D., Verhoye, M., Van Der Linden, A., et al. (2018). Noninvasive relative quantification of [(11)C]ABP688 PET imaging in mice versus an input function measured over an arteriovenous shunt. *Front. Neurol.* 9:516. doi: 10.3389/fneur.2018.00516

Wu, H. M., Sui, G., Lee, C. C., Prins, M. L., Ladno, W., Lin, H. D., et al. (2007). In vivo quantitation of glucose metabolism in mice using small-animal PET and a microfluidic device. *J. Nucl. Med.* 48, 837–845. doi: 10.2967/jnumed.106.038182

Yee, S. H., Jerabek, P. A., and Fox, P. T. (2005). Non-invasive quantification of cerebral blood flow for rats by microPET imaging of 15O labelled water: the application of a cardiac time-activity curve for the tracer arterial input function. *Nucl. Med. Commun.* 26, 903–911. doi: 10.1097/00006231-200510000-00009

Zanotti-Fregonara, P., Fadaili El, M., Maroy, R., Comtat, C., Souloumiac, A., Jan, S., et al. (2009a). Comparison of eight methods for the estimation of the image-derived input function in dynamic [(18)F]-FDG PET human brain studies. *J. Cereb. Blood Flow Metab.* 29, 1825–1835. doi: 10.1038/jcbfm.2009.93

Zanotti-Fregonara, P., Maroy, R., Comtat, C., Jan, S., Gaura, V., Bar-Hen, A., et al. (2009b). Comparison of 3 methods of automated internal carotid segmentation in human brain PET studies: application to the estimation of arterial input function. *J. Nucl. Med.* 50, 461–467. doi: 10.2967/jnumed.108.059642

Zanotti-Fregonara, P., Maroy, R., Peyronneau, M. A., Trebossen, R., and Bottlaender, M. (2012). Minimally invasive input function for 2-18F-fluoro-A-85380 brain PET studies. *Eur. J. Nucl. Med. Mol. Imaging* 39, 651–659. doi: 10.1007/s00259-011-2004-9

Zanotti-Fregonara, P., Zoghbi, S. S., Liow, J. S., Luong, E., Boellaard, R., Gladding, R. L., et al. (2011). Kinetic analysis in human brain of [11C](R)-rolipram, a positron emission tomographic radioligand to image phosphodiesterase 4: a retest study and use of an image-derived input function. *Neuroimage* 54, 1903–1909. doi: 10.1016/j.neuroimage.2010.10.064

**Conflict of Interest:** The authors declare that the research was conducted in the absence of any commercial or financial relationships that could be construed as a potential conflict of interest.

frontiers in Physics

ORIGINAL RESEARCH
published: 11 February 2020
doi: 10.3389/fphy.2020.00021

# Study of the Cumulative Dose Between Fractions of Lung Cancer Radiotherapy Based on CT and CBCT Image Deformable Registration Technology

*Judong Luo[1], Changdong Ma[2], Shuang Yu[2], Zhenjiang Li[3] and Changsheng Ma[3]**

[1] Department of Oncology, The Affiliated Changzhou No.2 People's Hospital of Nanjing Medical University, Changzhou, China, [2] Department of Radiation Therapy, Qilu Hospital of Shandong University, Jinan, China, [3] Department of Radiotherapy, Shandong Cancer Hospital and Institute, Shandong First Medical University and Shandong Academy of Medical Sciences, Jinan, China

OPEN ACCESS

**Edited by:**
Andreas Hess,
Friedrich-Alexander University Erlangen-Nürnberg, Germany

**Reviewed by:**
Wazir Muhammad,
Yale University, United States
Fei Geng,
McMaster University, Canada

***Correspondence:**
Changsheng Ma
machangsheng_2000@126.com

**Specialty section:**
This article was submitted to Medical Physics and Imaging, a section of the journal Frontiers in Physics

**Received:** 15 July 2019
**Accepted:** 24 January 2020
**Published:** 11 February 2020

**Citation:**
Luo J, Ma C, Yu S, Li Z and Ma C (2020) Study of the Cumulative Dose Between Fractions of Lung Cancer Radiotherapy Based on CT and CBCT Image Deformable Registration Technology. Front. Phys. 8:21. doi: 10.3389/fphy.2020.00021

**Objective:** To analyze the difference between planned dose and delivered dose by accumulating the dose based on CT and CBCT image deformable registration.

**Methods:** The clinical data of 24 NSCLC (non-small cell lung cancer) patients receiving conformal radiotherapy or intensity-modulated radiotherapy (IMRT) were retrospectively analyzed. With the CBCT image of each week as the target image, we performed the deformation registration for CBCT images and planning CT images in RayStation. The delivered dose of CBCT images compared to the planning CT images was accumulated with the use of mapping relationships in registration. The differences in planned dose and accumulative dose of target and at-risk organs were compared.

**Results:** The average planned and accumulative doses of GTV in 24 patients were 5832.45 ± 645.42 and 5750.65 ± 630.27 cGy, respectively ($P < 0.05$). The average planning target volume (PTV) in CT plans and accumulation plans reaching the prescription dose was 95.59 and 81.47% of the PTV ($P > 0.05$). At the stage of treatment, the volumes of the at-risk organs in CBCT images were not significantly different. There were no statistically significant differences in the probability of complications in the right lung, left lung, heart, total lung, or spinal cord ($P > 0.05$).

**Conclusion:** With the dose deformable registration method, the dose caused by changes in the target anatomical structure of NSCLC patients was found. The dose to organs did not change much. However, in some patients, the received radiation in the target organ was less than the prescribed dose.

**Keywords: non-small cell lung cancer, dose-volume histogram, fraction delivered dose, deformable registration, accumulative dose**

## INTRODUCTION

In current radiotherapy practice IMRT technology can significantly improve the rate of tumor control and reduce complications. Therefore, IMRT is widely used in some complex target radiotherapies [1]. Multiple factors can affect the precise implementation of radiotherapy. There will be changes in the location of the target for each radiotherapy fraction, which can lead to difference between the planned dose and cumulative dose. For example, a target volume reduction will lead to bad dose distribution, and the surrounding normal tissue into the high dose area can increase the normal tissue radiation dose [2]. Therefore, it is necessary to analyze these changes during the process of fraction radiotherapy.

Adaptive radiation therapy (ART) is based on image data, cumulative dose, and other dose information to understand the various changes in patients, make timely adjustments to the planning target volume (PTV) and clinical target volume (CTV), and modify the prescribed dose and treatment plan to improve follow-up treatment and more accurately apply radiation therapy. Generally speaking, image-guided radiotherapy, volume-guided radiotherapy, and dose-guided radiotherapy are part of ART [3]. In this study, we analyzed the difference between planned dose and delivered dose by calculating the accumulated dose based on deformable registration, and we analyzed the changes in the volume and dose of targets and organs-at-risk by comparing cone beam CT (CBCT) images and planning CT images of patients with non-small cell lung cancer (NSCLC). We initially studied the actual dose volume histogram of target and OARs in NSCLC radiotherapy.

## MATERIALS AND METHODS

### Plan CT Acquisition and Target Contour

A total of 24 patients with NSCLC who underwent CRT or IMRT (24 sets of CT images and CBCT images) were retrospectively analyzed from January 2014 to January 2015 in Shandong Tumor Hospital. 18 patients were male, and the others were female. The median age was 58 years (range, 47–65 years). General clinical data of patients were as shown in **Table 1**. The pCT was obtained with a fan-beam helical CT scanner (Philips Brilliance Big Bore 16 slice CT, Philips Medical Systems, Eindhoven, The Netherlands) with 3 mm slice thickness and 512 × 512 pixels. The pCT was imported into the RayStation radiotherapy planning system via the network. The target and OARs were contoured on pCT. The target of radiotherapy included the gross tumor target (GTV), the clinical target (CTV) with the small lesion, the inner target (ITV) edge of the target movement, and the margin of the PTV. When the lung cancer target was outlined, the width and window position of the CT window were 1,600 and −600 HU, respectively, and the window width and window position of the Mediastinum window were 400 and 20 HU, respectively. Unless, there was evidence of invasion, CTV should not have exceeded the anatomical range. The lung cancer primary tumor was GTV + (6 ∼ 8) mm + respiratory mobility + setup error. The mediastinal lymph node was PTV for GTV + (3 ∼ 5) mm + respiratory mobility + setup error. The doctor could base the dose on the normal structure around the target to modify it as appropriate. The OARs included the lungs, spinal cord, heart, and esophagus.

**TABLE 1 |** General clinical data of patients.

| Characteristics | Value |
|---|---|
| **Gender** | |
| Male | 18 |
| Female | 6 |
| Age | 47–65 y, median 58 |
| **Stage** | |
| IIIA | 14 |
| IIIB | 10 |
| Squamous | 16 |
| Adenocarcinoma | 8 |
| GTV/$cm^3$ | 17.6 ± 8.1 $cm^3$ Range (8.69–36.58) |
| PTV/$cm^3$ | 98.59 ± 30.27 $cm^3$ Range (744.65–2197.43) |
| Left lung/$cm^3$ | 1355.52 ± 744.65 $cm^3$ Range (744.65–2197.43) |
| Right lung/cm3 | 1738.77 ± 890.12 $cm^3$ Range (1047.76–2424.55) |

### The Radiotherapy Plan Design

The physicians used the RayStation treatment planning system, and the conformal plans generally included a 6 MV X-ray and 4–6 fixed conformal fields. The lateral angle was adjusted as far as possible to make its long axis parallel to the target, reducing the volume through the lung tissue, to ensure that at least one field completely avoided the spinal cord, and all the field angle intervals should have been as high as 40°. It was common to have 5 fields for lung tumors. Conventional IMRTs typically consisted of 5–7 fields, and the separation angles were the same. When IMRT was applied to lung cancer, the number of fields and the angle separation tended to be adjusted according to the actual situation. The prescription dose was 2.0 Gy × 30 fractions; V30 < 20% or average lung dose (Dmean) ≤ 20 Gy; heart V30 ≤ 46% or Dmean <26 Gy; esophageal V50 ≤ 30% or Dmean ≤ (34 ∼ 40) Gy, maximum dose (Dmax) ≤ (58 ∼ 74) Gy.

### CBCT Image Acquisition

Twenty-four patients underwent CBCT scanning before treatment. According to the scanning range, the reference center level was selected. In the three-dimensional laser light, the front and the left and right sides of the center of the body were marked. The Elekta Synergy (Elekta Oncology Systems, Crawley, UK) accelerator XVI system acquired the CBCT images. The system consists of a high-level X-ray tube and a large, amorphous silicon X-ray detection board through the telescopic robot arm installed on both sides of the linear accelerator rack. The scan mode was half-phan mode, and the rotation angle was 200°. The scanning parameters were as follows: tube voltage 120 kV, tube current 25 mA, acquisition rate 5.5 frames/s, plus bowtie filter, and S20 collimator. The process of XVI acquisition was issued by the tube pulsed X-ray (frequency fixed to 5.75 Hz). The radiation went through the scanning object, and then the signal was read and stored by the plate detector. The above process was repeated to collect data. The image reconstruction matrix was 512 × 512, the reconstructed layer thickness was 3 mm, and the CBCT image was 88 layers. The CBCT scan was done once every time the patient was treated, and the image registration and the setup error were corrected. Finally, all CT and CBCT images were imported into the RayStation treatment planning system.

## CT and CBCT Image Deformable Registration

CBCT image targets and OARs were outlined by the function of automatic profiling in the RayStation treatment planning system. The outlines were then manually corrected by the clinicians. The CT image was used as the reference image, and the daily CBCT image was used as the target image. The rigid registration was based on the outer contour of the body, and then the deformation registration was applied based on the gray-value information. If necessary, we manually modified the result of the rigid registration. We applied the target mapping to the planned CT target and OAR to the CBCT image.

## CBCT Fractional Dose Calculation and Accumulation

Using dose tracking and cumulative doses in the Adaptive Radiation module in the RayStation treatment planning system, the individual CBCT electronic density tables obtained from each patient's CT image map were selected for CBCT images. Based on the CBCT image, the fractional dose was calculated, and the fractional dose was added to the planned CT image to obtain the cumulative dose.

## Normal Tissue Complication Probability (NTCP)

Normal tissue complication probability (NTCP) values were also calculated for each OAR with the Lyman-Kutcher-Burman (LKB) model. The three parameters were derived according to Burman identification: several parameters, including mean hepatic dose, percentage volume of normal lung with a radiation dose more than 20 Gy (V20 Gy), and normal tissue complication probability (NTCP), were calculated from DVH. The NTCP model of Lyman was used. In the NTCP model,

$$NTCP = 1/\sqrt{2\pi} \int_{-\infty}^{t} \exp(-t^2/2)dt \quad (1)$$

$$\mathrm{t} = (D - TD_{50}(v))/(m \times TD_{50}(v)) \quad (2)$$

$$v = V/V_{ref} \quad (3)$$

$$\mathrm{TD}\ (2) = \mathrm{TD}\ (\mathrm{v}) \times \mathrm{v}^{\mathrm{n}} \quad (4)$$

where TD50(v) is the 50% tolerance dose for uniform irradiation of the partial volume V. The partial- and whole-lung radiation tolerance doses were related by a power law relationship:

Where Vref is the volume of normal lung. The parameter n is the volume effect parameter, for which the value of 0.87 from the literature was applied. The parameter m is the steepness of the dose-complication curve for a fixed partial volume, and an estimate of 0.18 was used. The TD50 of 24.5 Gy was applied in the calculation. The effective-volume method of Kutcher and Burman was used to provide estimates of equivalent doses and volume pairs for uniform partial organ irradiation from the DVHs summarizing the non-uniform irradiation. The three parameters were derived according to Burman's identification: lung (TD50 = 24.5 Gy, $n$ = 0.87, m = 0.18), heart (TD50 = 48.0 Gy, $n$ = 0.35, m = 0.10) and spinal cord (TD50 = 66.5 Gy, $n$ = 0.05, m = 0.175).

## Statistical Analysis

Statistical analysis was carried out using the statistical software SPSS version 19.0. Data are expressed as mean ± standard deviation and were compared using the $t$-test. $P < 0.05$ was statistically significant.

# RESULTS

## Target and OAR Volume Changes

The mean volume change of the tumor target in 24 patients was 88.26% of the original volume on the CBCT image. CBCT automatically outlined the results, and the CT automatically outlined results were not very different. The results of the CBCT in the third patient showed an increase in volume, while the CBCT in the fifth patient showed a reduction in volume. Due to respiratory movement caused by the tumor target and the surrounding tissue movement, there was an error in the target of the radiotherapy and the plan target, resulting in changes in the dose.

The CBCT showed that the volume of the lungs changed relative to the fraction of treatment, and the volume of the lungs in most patients changed greatly with the fraction of treatment. The treated left and right lung were reduced to 93.39 and 96.79% of the original volume, respectively. At the end of treatment, the mean volume of the left and right lungs in 24 patients with CBCT images was 88.95 and 80.32% of the original volume, respectively. Comparison of CT and CBCT images showed the same changes in the left and right lung volumes. Besides the first case of a patient with a larger left lung volume, the remaining volumes were reduced. This shows that CBCT to analyze the pulmonary deformation of the registration was still more accurate and automatically showed that the method could better reflect the changes in lung volume.

## Target and OAR Dose Changes

**Figure 1** shows little change in CT and CBCT images with the fraction dose of the target. Most of the target volumes on the CT images and CBCT were not very different, and the impact on the dose was not large. The dose of PTV was not significantly different in any of the 24 patients, and the error was within 5%, indicating that the target was in a high-dose area during each fraction.

**Figure 2** shows the change in CT and CBCT images with the fraction of dose to the OARs. The left and right lungs of 24 patients showed a substantially reduced lung volume and a mean increase in lung dose as a result of CT and CBCT calculation. The patient CBCT was used to sketch the results, and the left and right lung doses in the course of treatment were much greater than the CT image doses. The left and right lung CBCT


**FIGURE 1 |** DVH changes of the target area, the GTV and PTV.

of the 24 patients showed 167.31 ± 165.75 and 79.33 ± 54.11 cGy, respectively, and the cumulative dose was 164.63 ± 164.96 and 77.63 ± 53.36 cGy, respectively. Most of the 24 patients showed the same dose treatment progress, gradually decreased lung volume, and gradually increased lung dose, indicating that the reduction in lung volume and its dose increase have a certain relevance to whether the treatment at the original dose will cause excessive exposure.

**Figure 3** shows the change in atelectasis on CT images with the fraction dose. There were four plans: Plan0327, Plan0403, Plan0410, and Plan0417. This patient had cT4N2M0 NSCLC and was treated with 30 fraction × 2.0 Gy. Two IGRT specialists, independent of each other, visually evaluated every MVCT. For each MVCT, the observed changes in atelectasis were scored. This result shows that it is very important to use image-guided radiotherapy (IGRT).

## The Cumulative Dose Changes of Targets and OARs

**Table 2** shows the cumulative dose of GTV D99. In addition to the first and fifth cases of patients with GTV, the cumulative dose was lower than the planned dose, but it was still within the clinical requirements to achieve the lowest dose. The other target did not show significant changes. No dose to the target showed any significant changes, indicating that the target had been under high dose coverage. In addition, there was no significant difference between CT and CBCT cumulative doses. When the target was reduced, we had to give the original target a sufficient dose to ensure the control rate of the tumor, indicating that the target was in the high-dose area.

The basic clinical information of the order, age, sex, and staging of 24 patients is shown in **Table 2**, and the volumes of GTV, PTV, left lung, and right lung as measured by CT images before treatment are listed.

**Table 2** shows the results of GTV D95, D50, average, and PTV planned dose and cumulative dose changes and some evaluation parameters of the paired *t*-test analysis. The average dose changes yielded t values of 1.919, 2.299, 2.372, 2.197 in the course of treatment. The respective *P* values were 0.096, 0.055, 0.049, and 0.064. The CT plan and cumulative plan of the target PTV V100 reached the prescription dose of average volumes 95.59 and 81.47%. For GTV, the difference between planned dose and cumulative dose was statistically significant ($P < 0.05$).

**Table 3** shows some of the differences in the assessment parameters of the lungs and the spinal cord and the difference between the planned dose and the applied cumulative dose. The cumulative dose to the lung and spinal cord in 24 patients decreased compared with the planned dose, and the cardiac Dmean accumulation showed an increase. Paired *t*-test analysis showed that the mean values of Dmean, left lung Dmean, heart Dmean, whole lung Dmean and spinal Dmax were 1.222, 0.480, −0.291, 0.786, and 1.683, respectively, and the *P* values were 0.261, 0.646, 0.780, 0.457, and 0.136, which were not statistically significant.

## DISCUSSION

There are many important organs around a radiotherapy target. The control rate of lung cancer and the radiation therapy dose is related to the surrounding normal tissue dose limit and has become the biggest obstacle for conventional radiotherapy to

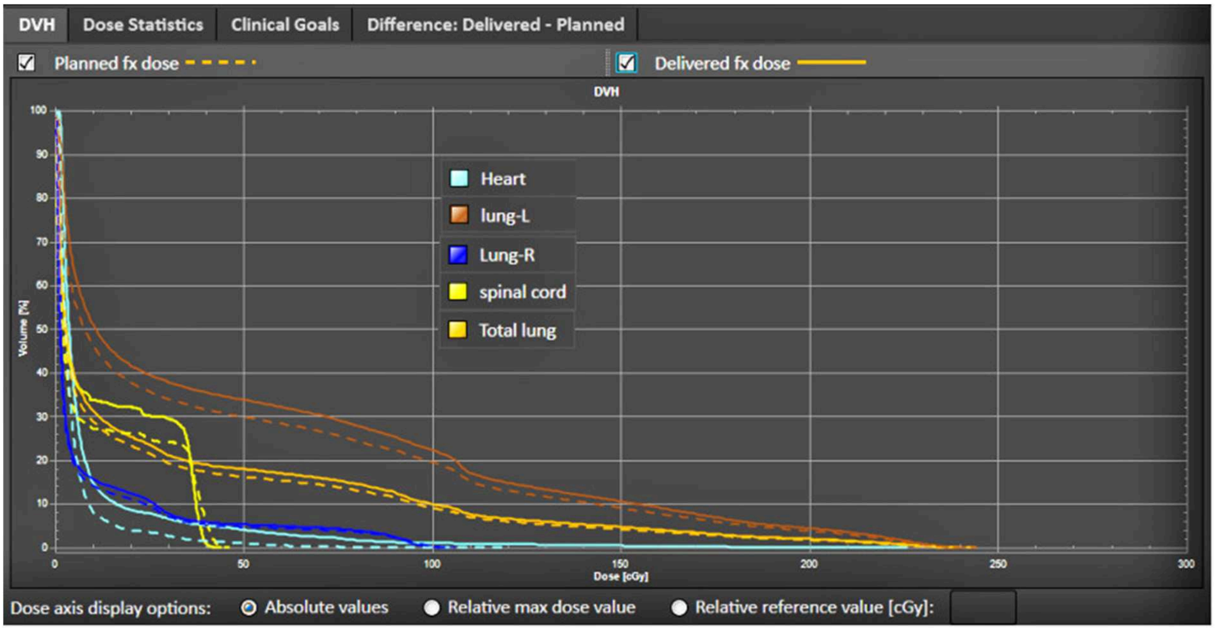


**FIGURE 2 |** DVH changes of the OARs, including the heart, spinal cord, and lungs.

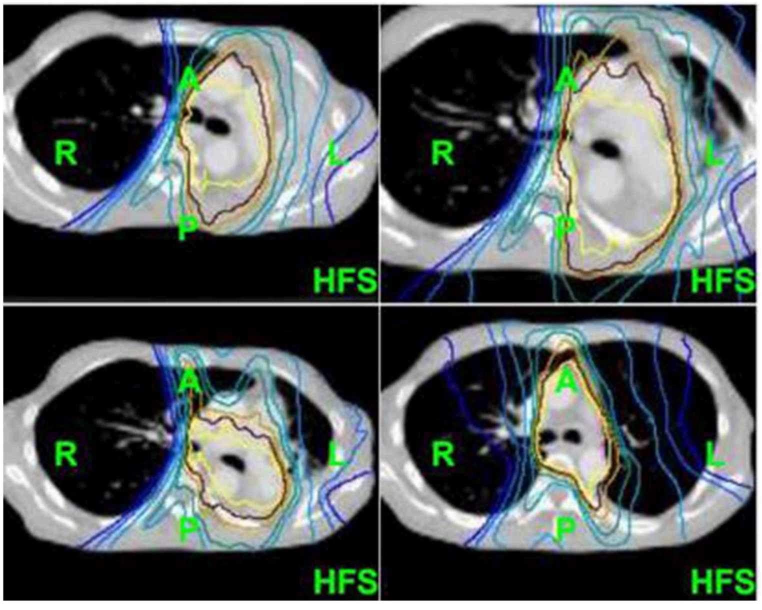


**FIGURE 3 |** The change in atelectasis on CT images with the fraction dose.

improve the tumor dose. CRT or IMRT radiotherapy can produce a dose distribution that is highly suitable for the shape of the target, reducing the surrounding normal tissue exposure and limiting the organ's dose, but from the pretreatment planning through the entire course of treatment [4], the dose distribution of the initial treatment plan changes during the actual treatment, and the difference between the administered dose and the planned dose is conducive to adjusting the radiotherapy plan for better and more accurate radiotherapy.

In this study, GTV Dmean decreased significantly during the course of treatment, indicating that the experience of the outgoing boundary may not have met the requirements. Kwong et al. [5] indicated that the results of the lung cancer GTV center for the displacement of the head and foot direction were

**TABLE 2 |** Differences in exposure dose between CT plan and accumulation plan.

| GTV | CT plan | Accumulation plan | *t*-value | *P*-value |
|---|---|---|---|---|
| $D_{95}$ | 6179.00 ± 616.24 | 6156.35 ± 614.94 | 1.935 | 0.086 |
| $D_{50}$ | 6308.90 ± 656.02 | 6662.25 ± 629.93 | 2.467 | 0.067 |
| Average | 6307.45 ± 624.22 | 5753.90 ± 630.27 | 2.254 | 0.039 |
| PTV ($V_{100}$) | 96.59 ± 2.29% | 89.67 ± 18.71% | 2.456 | 0.067 |

**TABLE 3 |** Differences in organs-at-risk dose between CT plan and accumulation plan.

| Organs (Gy) | CT plan | Accumulation plan | *t* value | *P* value |
|---|---|---|---|---|
| Right lung $D_{mean}$ | 793.30 ± 54.11 | 776.3 ± 53.36 | 1.222 | 0.261 |
| Left lung $D_{mean}$ | 1673.10 ± 165.75 | 1646.3 ± 164.96 | 0.480 | 0.646 |
| Heart $D_{mean}$ | 618.80 ± 66.70 | 683.8 ± 60.91 | −0.291 | 0.780 |
| Total lung $D_{mean}$ | 1181.40 ± 67.22 | 1158.7 ± 66.19 | 0.786 | 0.457 |
| Spinal cord $D_{max}$ | 3726.20 ± 185.91 | 3600.0 ± 173.14 | 1.683 | 0.136 |
| NTCP of right lung (%) | 1.60 ± 0.74 | 1.33 ± 0.86 | 1.702 | 0.085 |
| NTCP of left lung (%) | 6.00 ± 1.94 | 5.34 ± 1.76 | 0.897 | 0.124 |
| NTCP of heart (%) | 4.77 ± 2.15 | 4.55 ± 2.37 | −0.532 | 0.112 |
| NTCP of total lung (%) | 2.53 ± 1.32 | 1.95 ± 1.22 | 1.023 | 0.075 |
| NTCP of spinal-cord (%) | 2.03 ± 0.72 | 1.81 ± 0.94 | 1.224 | 0.090 |

significantly smaller than those of the corresponding direction of the diaphragm. Therefore, the expansion of the safety boundary according to experience may cause excessive exposure of normal tissue. PTV reached as low as 81.47% of the prescribed dose volume. In three selected middle esophageal cancer patients with three-dimensional conformal radiotherapy, Brown et al. [6] illustrated the need to replan during the course of treatment.

Replanning should be done only at the right time. Ding et al. [7] studied 87 patients with IMRT and three-dimensional adaptive radiotherapy, followed by 18F-FDG PET/CT scans after 40 Gy irradiation, and mapped the target. Zhang et al. [8] studied 40 cases of NSCLC radiotherapy target volume changes. Comparing the number of irradiations $\leq$ 20 times the reset and 20 times after the reduction of the GTV reduction ratio and Dmean decline ratio in the ipsilateral lung and whole lung, they concluded that 40 Gy/20 replanning is the most reasonable, but different individuals should be differentially planned using PET and CT fusion images. The tumors subsided significantly in their patients.

Because the soft-tissue contrast of CT images is high, the soft-tissue contrast of CBCT is poor. In a previous study, we used CT scanning to repeat the changes that doctors made in target and normal tissues. In this study, we used CT and multiple CBCT to outline the results. The lungs and target changed as the treatment progressed, and to varying degrees. CBCT images were used to outline the tumors. The lungs and spinal cord permitted a better sketch effect, and for targets with a low surrounding tissue contrast, the algorithm still needs to continue to be improved [9]. The image algorithm mainly includes the frequency domain Contourlet transform, wavelet transform and spatial domain non-local mean filtering [10–12]. These algorithms have much room for development.

By the use of deformation registration, we can outline the CT image profile to the kilovolt-like CBCT image, decomposed into multiple CBCT calculations, and the CBCT dose is added each time. The total dose will be transplanted to the planning CT image. The obtained results will reduce the patient position changes, organ volume changes, and other uncertain factors. The results of dose uptake using CBCT showed that there was some difference between the delivered dose and the planned dose during the treatment of the lungs, while the dose to the heart increased and the dose to the spinal cord decreased slightly. More cases are needed to supplement the data and confirm the conclusions of this study.

Since we need to superimpose each dose on the original CT and compare it with the planning CT, we need to calibrate the CBCT's HU-RED table accurately to obtain a more accurate cumulative dose [13]. In this study, we used RayStation software to automatically divide the HU values by the different tissue densities. The accuracy of the method was improved compared to the traditional method of calibration. Another method is to map the ROIs between CT and CBCT, but due to positioning errors and CBCT image quality, these two methods cannot completely eliminate the error [14–19], but they can meet the current clinical requirements.

In summary, this NSCLC radiotherapy target and an OAR real DVH preliminary study was based on the offline artificial correction method, and the process took much more time. In addition, whether the accuracy of the two image target regions and normal tissue deformation registration affects the calculation of DVH parameters remains to be verified. By improving the speed and accuracy of deformation registration, we can achieve rapid online correction of radiotherapy targets and adaptive radiotherapy.

## CONCLUSION

The doses to the lung and to other normal organs did not change much, and there was no statistically significant difference in the probability of complications in normal tissues. However, in some patients, the radiation dose in the target area was reduced, which may have led to missed targets.

## DATA AVAILABILITY STATEMENT

The datasets generated for this study are available on request to the corresponding author.

## ETHICS STATEMENT

This study was carried out in accordance with the recommendations of Ethics Committee Approval at Shandong Cancer Hospital and Institute. The protocol was approved by Ethics Committee of the Shandong Cancer Hospital and

Institute. As the study is retrospective, the need for written informed consent from participants was waived.

## AUTHOR CONTRIBUTIONS

JL and CdM drafted conception and design and draft the manuscript. ZL and CsM contributed to acquire, analyze, and interpret data. SY contributed to acquire data and enhanced its intellectual content. All authors read and approved the final manuscript.

## FUNDING

This work was supported by Natural Science Foundation of Shandong Province (ZR2019MH136, ZR2017BA024), Projects of Medical and Health Technology Development Program in Shandong Province (2017WS110, 2017WS306), Project funded by China Postdoctoral Science Foundation (2019M652356), The National Nature Science Foundation of China (81800156, 81974467).

## REFERENCES


1. Endo M, Tsunoo T, Kandatsu S, Tanada S, Aradate H, Saito Y. Four-dimensional computed tomography (4D CT)–concepts and preliminary development. *Radiat Med*. (2003) **21**:17–22.
2. Zhao JD, Xu ZY, Zhu J, Qiu JJ, Hu WG, Cheng LF, et al. Application of active breathing control in 3-dimensional conformal radiation therapy for hepatocellular carcinoma: the feasibility and benefit. *Radiother Oncol*. (2008) **87**:439–44. doi: 10.1016/j.radonc.2007.12.006
3. Ma C, Hou Y, Li H, Li D, Zhang Y, Chen S, et al. A Study of the anatomic changes and dosimetric consequences in adaptive CRT of non-small-cell lung cancer using deformable CT and CBCT image registration. *Technol Cancer Res Treat*. (2014) **13**:95–100. doi: 10.7785/tcrt.2012.500365
4. Xi M, Liu MZ, Deng XW, Zhang L, Huang XY, Liu H, et al. Defining internal target volume (ITV) for hepatocellular carcinoma using four-dimensional CT. *Radiother Oncol*. (2007) **84**:272–8. doi: 10.1016/j.radonc.2007.07.021
5. Kwong Y, Mel AO, Wheeler G, Troupis JM. Four-dimensional computed tomography (4DCT): a review of the current status and applications. *J Med Imaging Radiat Oncol*. (2015) **59**:545–54. doi: 10.1111/1754-9485.12326
6. Brown E, Owen R, Harden F, Mengersen K, Oestreich K, Houghton W, et al. Head and neck adaptive radiotherapy: predicting the time to replan. *Asia Pac J Clin Oncol*. (2016) **12**:460–7. doi: 10.1111/ajco.12516
7. Ding X, Li H, Wang Z, Huang W, Li B, Zang R, et al. A clinical study of shrinking field radiation therapy based on F-18-FDG PET/CT for stage III non-small cell lung cancer. *Technol Cancer Res Treat*. (2013) **12**:251–7. doi: 10.7785/tcrt.2012.500310
8. Zhang YJ, Li JB, Lu J, Liu TH, Gong GZ, Ma CS, et al. Study on modification of radiotherapy plan for three dimensional conformal radiotherapy for non small cell lung cancer. *Chin J Cancer Prev Treat*. (2010) **17**:1852–4.
9. Dobashi S, Sugane T, Mori S, Asakura H, Yamamoto N, Kumagai M, et al. Intrafractional respiratory motion for charged particle lung therapy with immobilization assessed by four-dimensional computed tomography. *J Radiat Res*. (2011) **52**:96–102. doi: 10.1269/jrr.10019
10. Chen X, Gilkeson RC, Fei B. Automatic 3D-to-2D registration for CT and dual-energy digital radiography for calcification detection. *Med Phys*. (2007) **34**:4934–43. doi: 10.1118/1.2805994
11. Lu X, Zhang S, Su H, Chen Y. Mutual information-based multimodal imageregistration using a novel joint histogram estimation. *Comput Med Imaging Graph*. (2008) **32**:202–9. doi: 10.1016/j.compmedimag.2007.12.001
12. Ren L, Godfrey DJ, Yan H, Wu QJ, Yin FF. Automatic registration between reference and on-board digital tomosynthesis images for positioning verification. *Med Phys*. (2008) **35**:664–72. doi: 10.1118/1.2831903
13. Ma C, Cao J, Yin Y, Zhu J. Radiotherapy dose calculation on KV cone-beam CT image for lung tumor using the CIRS calibration. *Thorac Cancer*. (2014) **5**:68–73. doi: 10.1111/1759-7714.12055
14. Nithiananthan S, Brock KK, Daly MJ, Chan H, Irish JC, Siewerdsen JH. Demons deformable registration for CBCT-guided procedures in the head and neck: convergence and accuracy. *Med Phys*. (2009) **36**:4755. doi: 10.1118/1.3223631
15. Wang H, Dong L, O'Daniel J, Mohan R, Garden AS, Ang KK, et al. Validation of an accelerated'demons' algorithm for deformable image registration in radiation therapy. *Phys Med Biol*. (2005) **50**:2887. doi: 10.1088/0031-9155/50/12/011
16. Lou Y, Niu T, Jia X, Vela PA, Zhu L, Tannenbaum AR. Joint CT/CBCT deformable registration and CBCT enhancement for cancer radiotherapy. *Med Image Anal*. (2013) **17**:387–400. doi: 10.1016/j.media.2013.01.005
17. Yu G, Liang Y, Yang G, Shu H, Li B, Yin Y, et al. Accelerated gradient-based free form deformable registration for online adaptive radiotherapy. *Phys Med Biol*. (2015) **60**:2765–83. doi: 10.1088/0031-9155/60/7/2765
18. Li N, Zarepisheh M, Uribe-Sanchez A, Moore K, Tian Z, Zhen X, et al. Automatic treatment plan re-optimization for adaptive radiotherapy guided with the initial plan DVHs. *Phys Med Biol*. (2013) **58**:8725–38. doi: 10.1088/0031-9155/58/24/8725
19. Zarepisheh M, Long T, Li N, Tian Z, Romeijn HE, Jia X, et al. A DVH-guided IMRT optimization algorithm for automatic treatment planning and adaptive radiotherapy replanning. *Med Phys*. (2014) **41**:061711. doi: 10.1118/1.4875700


**Conflict of Interest:** The authors declare that the research was conducted in the absence of any commercial or financial relationships that could be construed as a potential conflict of interest.

frontiers in Physics

MINI REVIEW
published: 13 February 2020
doi: 10.3389/fphy.2020.00026

# Scattering Compensation for Deep Brain Microscopy: The Long Road to Get Proper Images

*Paolo Pozzi* [1†], *Daniela Gandolfi* [1,2†], *Carlo Adolfo Porro* [1], *Albertino Bigiani* [1] and *Jonathan Mapelli* [1*]

[1] Dipartimento di Scienze Biomediche, Metaboliche e Neuroscienze, Centro di Neuroscienze e Neurotecnologie, Università di Modena e Reggio Emilia, Modena, Italy, [2] Dipartimento di Scienze del Comportamento e del Sistema Nervoso, Università di Pavia, Pavia, Italy

Multiphoton microscopy is the most widespread method for preclinical brain imaging when sub-micrometer resolution is required. Nonetheless, even in the case of optimal experimental conditions, only a few hundred micrometers under the brain surface can be imaged by multiphoton microscopy. The main limitation preventing the acquisition of images from deep brain structures is the random light scattering which, until recently, was considered an unsurmountable obstacle. When in 2007 a breakthrough work by Vellekoop and Mosk [1] proved it is indeed possible to compensate for random scattering by using high resolution phase modulators, the neuro-photonics community started chasing the dream of a multiphoton microscopy capable of reaching arbitrary depths within the brain. Unfortunately, more than 10 years later, despite a massive improvement of technologies for scattering compensation in terms of speed, performances and reliability, clear images from deep layers of biological tissues are still lacking. In this work, we review recent technological and methodological advances in the field of multiphoton microscopy analyzing the big issue of scattering compensation. We will highlight the limits hampering image acquisition, and we will try to analyze the road scientists must tackle to target one of the most challenging issue in the field of biomedical imaging.

**Keywords: two photon microscopy, scattering compensation, *in vivo* brain imaging, adaptive optics in biomedical imaging, subcellular and synaptic imaging, neurophotonics**

OPEN ACCESS

***Edited by:***
*Bernhard Baumann, Medical University of Vienna, Austria*

***Reviewed by:***
*Boran Han, Harvard University, United States*
*Dustin Ryan Osborne, The University of Tennessee, Knoxville, United States*

***Correspondence:**
*Jonathan Mapelli*
*jonathan.mapelli@unimore.it*

† *These authors have contributed equally to this work*

***Specialty section:***
*This article was submitted to Medical Physics and Imaging, a section of the journal Frontiers in Physics*

***Received:*** *14 October 2019*
***Accepted:*** *27 January 2020*
***Published:*** *13 February 2020*

***Citation:***
*Pozzi P, Gandolfi D, Porro CA, Bigiani A and Mapelli J (2020) Scattering Compensation for Deep Brain Microscopy: The Long Road to Get Proper Images. Front. Phys. 8:26. doi: 10.3389/fphy.2020.00026*

## INTRODUCTION

The analysis of brain function and dysfunction is inherently bound to the visualization of neuronal morphology in intact tissues and most importantly is tightly related to the investigation of synaptic and cellular activity in extended neuronal networks [2]. The first disruptive advancement in the field of neurophotonics arrived at the beginning of the 90's, when in the Webb laboratory [3] it was proven that the two-photon microscopy (2PM), only theoretically envisaged more than 50 years before [4], was indeed feasible. The advent of femtosecond-pulsed infrared laser sources and the development of advanced scanning methods opened new routes to researchers aiming to perform imaging of thick biological samples [5]. A deeper light penetration, a reduced photodamage together with the possibility to detect non-ballistic fluorescence photons because of the intrinsic confocality of multiphoton excitation, allowed 2PM to become the gold standard technique for *in vivo* brain imaging. Unfortunately, the strongly turbid media distorting incident light avoids clear and fully resolved images from deeper layer in the brain to be obtained, even in small animals. The maximum imaging depth is in fact related to the ability of incident light to target the focal plane (ballistic photons) in a diffraction limited volume. In particular, the repeated scattering of the incident wavefront is, most of the time, so robust that the spatial coherence is completely lost beyond a small volume with a radius comparable to the wavelength of light [1, 6–8]. While purely morphological imaging of structures deep within a three-dimensional sample can easily be achieved by chemically fixing and optically clearing the tissue [9], functional imaging requires the preservation of physiological condition, and inevitably requires more complex solutions.

Two non-exclusive strategies are currently adopted to overcome the physical limitations preventing image formation in deep brain layers: (i) changing the laser source to increase the probability of the excitation process to occur; (ii) inserting Adaptive Optics (AO) in the light path to correct the incident wavefront after its determination [10]. In the first case, longer wavelengths, either in the form of two [8] or three photon excitation (3PM) can yield a substantial increase [11] in the penetration depth mainly taking advantage of the lower ratios between scattering and molecule absorption in the mid infrared (see below). In analogy to what was done with astronomy, the second approach proposes the adjustment of the incident wavefront based on the feedback coming from the sample, either through the aid of wavefront sensors or not.

## MODULATING THE INCIDENT LIGHT TO IMPROVE MULTI-PHOTON PERFORMANCES

An extensive analysis of 2PM signal degradation by brain tissues has been conducted by Theer and Denk [12]. In this work, the authors showed that signal rapidly fades during the travel across tissues to disappear when the signal to background ratio (SBR) becomes unitary [12]. This condition typically occurs between 5 and 6 effective attenuation lengths ($l_a$) below the surface of the tissue. For instance, in the mouse cortex at 775-nm excitation wavelength the 2PM $l_a$ is about 130 μm and the resulting penetration depth is 700∼ μm [13]. This means that, in adult mice, 2PM imaging is limited to cortical layers. The access to subcortical structures is thus restricted to technical approaches encompassing invasive optical probes or the removal of the overlying tissues. A few years after the work by Theer and Denk, in 2013 Horton and colleagues calculated the trade-off between tissue scattering and molecule absorption [13], the two main determinants of signal degradation. This work allowed to determine the optimal spectral window for two-photon excitation. The minimal reduction of 2PE due to brain scattering was in fact registered at wavelengths centered on two narrow regions around 1,300 and 1,700 nm. In addition, the imaging depth scales linearly with the attenuation coefficient, but it scales logarithmically with the average power incident on the tissue surface and on the duty cycle [8]. In 2003 Theer et al. had tried to lower the repetition rate of the laser to increase the pulse power impinging on the sample and therefore limiting the attenuation coefficient [14]. This trick allowed researchers to image down to 1 mm in the mouse brain, with a significant improvement of 2PM performances. Despite the increase in the penetration depth, near infrared excitation wavelengths do not preserve from the strong attenuation due to brain scattering. To further improve the overall image quality, Kobat et al. [8] exploited the 1,300 nm window by performing long wavelength 2PM. The excitation of brain vasculatures filled with dextran molecules allowed researchers to collect signals down to 1.2 mm below the brain surface. The same authors [15], a couple of years later showed images at a depth of 1.6 mm with a relatively low power (120 mW) at the brain surface. Beside the effective increase in the penetration depth, these methods collectively suffer from a few limitations (see **Table 1**): (I) The phototoxicity scales with the incident average power; (II) long wavelengths coupled with 2PM strongly limit the number of excitable fluorophores, especially excluding the widely employed green fluorescent protein and most of its derivates; (III) the image resolution scales down with the excitation wavelength; (IV) longer wavelength sources are more expensive and sophisticated than a single mode-locked pulsed infrared laser.

Some of these constraints can be overcome by exploiting three-photon absorption at long wavelength (>1,300 nm). In the early 90's two separate demonstrations of the feasibility of 3PE were independently reported [11, 16]. Besides a better penetration depth due to the reduced scattering, 3PM also provides an improvement of image quality through an overall better excitation localization [16]. The emitted fluorescence of 3PE in fact fades off as $1/z^4$ compared to $1/z^2$ of 2PM (where z is the distance from the focal plane). This, in turn brings a tremendous increase of the signal to noise ratio. Moreover, the use of long wavelength (>1,500 nm) gives the possibility to employ a large spectrum of fluorescent molecules commonly used with single photon fluorescence imaging. Finally, long wavelength and high-pulse energy excitation at a low repetition rate significantly increases the amount of excited molecules. The main disadvantage of such technique is the light source needed to properly excite fluorophores with three photons [17] which necessarily has to be a high-power laser with an optical parametric amplifier (OPA). Furthermore, the low repetition rate most likely to be used for 3PE may require long scanning procedures to obtain at least one pulse per effective image pixel.

## THE IMPACT OF ADAPTIVE OPTICS ON 2PM PERFORMANCES

From a physical standpoint, the effect of a turbid medium on the propagation of light can be described as a spatially dependent phase retardation of the wavefront. While an ideal spherical wavefront, such as that generated by the objective would focus in a diffraction limited spot, any distortion from a spherical form would subtract power from the intended focus and redirect it elsewhere in the sample, reducing excitation efficiency and increasing background noise. The techniques aimed at mitigating such problems are known as adaptive optics (AO). The

**TABLE 1 |** Strategies for improving 2PM deep brain imaging.

| Strategy | Method | Advantage | Disadvantage | References |
|---|---|---|---|---|
| Laser source change | Long-wavelength 2PM | - >1 mm penetration depth | - Increased phototoxicity<br>- Fewer fluorophores<br>- Lower resolution<br>- Sophisticated laser sources | [8, 12, 14, 15] |
| | 3PM | - >1 mm depth<br>- Large number of fluorophores<br>- Low energy incident light | - Expensive laser source<br>- Slow scanning procedures | [13, 16, 17] |
| Adaptive optics | Wavefront sensor | - Wide choice of adaptive elements | - Exogenous guide star<br>- Anisoplanatism | [18–24] |
| | Sensorless | - Endogenous fluorescence | - Numerous iterations | [6, 7, 19, 25–28] |
| | OPC | Low cost adaptive elements | Requires coherent signals | [29–31] |

principle at the basis of adaptive methods is that, by exploiting phase modulating optical components, the incident wavefront impinging onto the surface of a turbid medium, can be shaped until matches the wavefront in the focal plane affected by the medium itself [10]. This is particularly important because the precise focusing of light into the medium at a desired depth is fundamental not only for high-resolution imaging [32] but also for optogenetics [33], functional imaging [34] or photo-dependent therapies [35].

Traditional AO is performed with smooth phase modulators, such as deformable mirrors, capable of compensating relatively low-resolution aberrations defined as a continuous function in the optical system's pupil. The two main roads to get to wavefront determination and correction are with a wavefront sensor of any kind, or "sensorless." The first group draws inspiration from astronomy, the field which drove the development of AO, where a deformable mirror corrects the wave profile following the feedback given by a wavefront sensor. *In vivo* wavefront sensing AO must necessarily be guided by a point-like light source in the focal plane inside the sample itself, serving as a guide star for the wavefront sensor. The wavefront from the guide star is then measured by a sensor (e.g., Shack-Hartmann-SHWS) to implement the active correction performed by the adjustable optical components.

In this configuration, the incident wavefront is determined by the acquisition of a de-scanned guidestar that can have the form of exogenous fluorescence molecules [1], second-harmonic radiating nanoparticles [36], photo-acoustic feedback [37], focused ultrasonic waves [29] or kinematics targets to extrapolate intrinsic dynamics [38]. Recently [18], in the Kleinfeld laboratory has been developed a method to perform 2PM imaging 800 $\mu$m under the brain surface with the correction of optical aberration through signals coming from brain microvessels labeled with Cy5.5, a strongly red shifted molecule. The robust measurement of aberration is achieved through a descanned Shack Hartmann wavefront sensor (formed by a microlens array and an Electron-Multiplying CCD) producing a spot pattern that feeds the algorithm piloting the shape of a deformable mirror [18]. This method allowed researchers not only to generate high quality images deep inside mouse brain but also to collect functional signals (calcium and glutamate changes) during *in vivo* sensori-motor tasks. In a different approach, the two-photon emission of previously labeled fluorescent neurons is collected by a SHWS and used to implement an iterative correction of the wavefront through a Liquid Crystal Spatial Light Modulator (LC-SLM) over subsets of large brain volumes [19]. Alternatively, multiple laser lines have been added in the optical setup to excite fluorescent microspheres injected into brain tissue [20] while keeping similar adaptive schemes (SHWS and deformable mirror). Beside the use of SLM and DM, researchers have developed algorithms to control other optical components such as Micromirrors [21, 22], adaptive lenses [23] or ferroelectric SLM [24].

In the case of a sensorless approach, the modulation of the incident beam wavefront is performed through an optimization procedure of the two-photon emission (2PE) intensity as a function of the wavefront correction [25]. The 2PE signal can be also used to measure the quality of images degraded by a priori known trial aberrations [6]. This scheme requires a model-based optimization describing the aberration effect on the chosen metric. Sensorless methods have the main advantage that it is not necessary to introduce neither additional optical components in the detection part of the microscope, nor guide star sources in the sample. On the contrary, these methods typically suffer from longer optimization times compared to wavefront sensing [19], requiring the acquisition of a minimum of $N + 1$ images in order to achieve optimal correction with an adaptive element with $N$ actuators [6, 39, 40], small volumes of proper correction [26], the introduction of fluorescent beads in the scattering medium [27] and may require serial images acquisition [28]. Interestingly, to speed up the optimization process, Galwaduge et al. [7] iteratively determined the correction across the whole pupil instead of working on a subset of pixels. Furthermore, differently from previous approaches, the "whole pupil" scheme takes advantage only on the 2PE intensity to correct the wavefront without image acquisition.

A substantial problem in the application of adaptive optics in microscopy is given by the fact that when scanning, light directed to different areas of the field of view travels through different parts of the sample, and needs therefore a different correction, a phenomenon known as anisoplanatism [41]. Adaptive optics systems generally only correct an average aberration through all the field of view and are effective only on relatively small regions. An approach to mitigate this problem is to conjugate the adaptive element to a plane between the objective and the sample, instead of the pupil of the system [30], or splitting the pupil in multiple subregions for different areas of the field of view [42]. These approaches however require high resolution correctors, which are either very expensive or slow in their correction.

## DYNAMIC SCATTERING COMPENSATION

Traditionally, only correction of smooth wavefronts was considered possible with adaptive optics, and scattering was considered an unsolvable problem. The work by Vellekoop and Mosk proved [1] that scattering can indeed be compensated through the application of a high resolution, discontinuous phase modulation by means of a high resolution spatial light modulator. While groundbreaking in concept, scattering compensation has a number of technical difficulties which make application in multiphoton microscopy challenging. Due to the discontinuous nature of the correction pattern, Shack Hartmann wavefront sensors cannot be used, while sensorless approaches can require millions of measurements to iteratively adjust the wavefront due to the high number of degrees of freedom of the correction. This is incompatible with microscopy usage, as the brain tissue can rapidly change during measurement on a sub-second timescale [43]. An alternative strategy widely adopted is to measure the scattering response in a parallel manner by adopting the principle of time reversal or "optical phase conjugation" (OPC). The recording of propagating scattered light field both in phase and amplitude should in fact allow the reproduction of a backpropagating phase conjugated field. This field, in turn could retrace its trajectory through the medium and return to the original input light field [31]. The main disadvantage of this approach is that interferometry or alternatively coherent waves mixing is necessary. It is therefore difficult to implement with fluorescence signals which are incoherent unless coupled with ultrasound waves [29].

## DISCUSSION

A massive technological effort by the photonics community has produced the development of sophisticated imaging tools. However, the holy grail of neurophotonics has yet to be discovered: it is still almost impossible to perform sub-cellular resolution imaging in deep brain structure without invasive approaches. A proper compensation of scattering in a three-dimensional turbid medium is in fact still an unresolved issue, despite most of the required technologies are available. It is our opinion that the ideal corrector should be a high resolution spatial light modulator, with enough speed to provide sensorless optimization on time scales compatible with experimental needs. While wavefront-sensing correction has long been considered the state of the art in adaptive optics for microscopy, its technical complexity, inability to effectively compensate for anisoplanatism, and its unreliability for high-order aberrations, make it, in our opinion, unsuitable for the future challenges we described in this manuscript. Recent development in pixel overdrive technologies [44] have started reaching the commercial market, providing the scientific community with tools capable of hundreds of Hz modulation. Very fast SLMs would in turn require high performing optimization procedures. In addition, real-time optimization of scattering compensation in dynamically changing scattering media was recently proven possible through an FPGA implementation [45]. Finally, a conjugate adaptive optics configuration, such as the one reported by Park and colleagues [42], would need to be used in order to achieve the widest possible field of view.

Still, the extremely anisoplanatic nature of scattering correction would, in the end, require some form of parallelized correction in multiple, small fields of view. This would require focusing in multiple diffraction limited spots over an extensive field of view (which was already proven possible in the original Vellekoop publication in 2007) and, most importantly, a reliable method to independently collect the fluorescence signal from multiple foci. This last critical step is still an open question while promising initial results have been achieved by exploiting the temporal separation of excitation pulses [46] and, more recently, through speckle demixing [47]. An additional problem is due to the even more pronounced anisoplanatism of the correction, where the size of the corrected field of view can be as small as the resolution itself, if the correction is applied in the pupil.

To our knowledge, the most successful application of scattering compensation reported to date in multiphoton microscopy was performed by conjugating a high speed, high resolution deformable mirror with the highly scattering, but relatively thin intact skull of an adult mice, to image microglial cells underneath [42]. Unfortunately, while extremely impressive, the proposed method cannot be generalized to thicker scattering layers.

Acquiring high quality images with subcellular resolution of deep brain structure is a goal that has not yet been realized. However, the combination of incident scattering compensation with deconvolution algorithms widely adopted in conventional imaging to compensate isotropic emission can substantially improve the performances of 2P systems, giving hope that this dream can be converted into reality into the next few years.

## AUTHOR CONTRIBUTIONS

All authors contributed in the preparation and revision of the manuscript.

## FUNDING

This work was supported by: Italian Ministry of Education, University and Research (MIUR): Dipartimenti di Eccellenza Program (2018–2022)—Department of Biomedical, Metabolic and Neural Sciences, University of Modena and Reggio Emilia to CP, and by the University of Modena and Reggio Emilia: FAR 2017 to JM.

## REFERENCES

1. Vellekoop M, Mosk AP. Focusing coherent light through opaque strongly scattering media. *Opt Lett.* (2007) **32**:2309. doi: 10.1364/OL.32.002309
2. Gandolfi D, Pozzi P, Tognolina M, Chirico G, Mapelli J, D'Angelo E. The spatiotemporal organization of cerebellar network activity resolved by two-photon imaging of multiple single neurons. *Front Cell Neurosci.* (2014) **8**:92. doi: 10.3389/fncel.2014.00092
3. Denk W, Strickler JH, Webb WW. Two-photon laser scanning fluorescence microscopy. *Science.* (1990) **248**:73–6. doi: 10.1126/science.2321027
4. Göppert-Mayer M. *Über Elementarakte mit zwei Quantensprüngen* (Ph.D. dissertation). John Wiley & Sons, Inc., Göttingen, Germany (1931). doi: 10.1002/andp.19314010303
5. Svoboda K, Yasuda R. Principles of two-photon excitation microscopy and its applications to neuroscience. *Neuron.* (2006). **50**:823–39. doi: 10.1016/j.neuron.2006.05.019
6. Débarre D, Botcherby EJ, Watanabe T, Srinivas S, Booth MJ, Wilson T. Image-based adaptive optics for two-photon microscopy. *Opt Lett.* (2009) **34**:2495–7. doi: 10.1364/OL.34.002495
7. Galwaduge PT, Kim SH, Grosberg LE, Hillman EMC. Simple wavefront correction framework for twophoton microscopy of *in-vivo* brain. *Biomed Opt Exp.* (2015) **6**:2997. doi: 10.1364/BOE.6.002997
8. Kobat D, Durst ME, Nishimura N, Wong AW. Deep tissue multiphoton microscopy using longer wavelength excitation. *Opt Exp.* (2009) **17**:13354. doi: 10.1364/OE.17.013354
9. Chung K, Wallace J, Kim SY, Kalyanasundaram S, Andalman AS, Davidson TJ, et al. Structural and molecular interrogation of intact biological systems. *Nature.* (2013) **497**:332–7. doi: 10.1038/nature12107
10. Kubby JA. *Adaptive Optics for Biological Imaging*. Boca Raton, FL: CRC Press; Taylor & Francis Group (2013). doi: 10.1201/b14898
11. Hell SW, Bahlmann K, Schrader M, Soini M, Malak H, Gryczynski I, et al. Three-photon excitation in fluorescence microscopy. *J Biomed Opt.* (1996) **1**:71–4. doi: 10.1117/12.229062
12. Theer P, Denk W. On the fundamental imaging-depth limit in two-photon microscopy. *J Opt Soc Am.* (2006) **23**:3139–49. doi: 10.1364/JOSAA.23.003139
13. Horton NG, Wang K, Kobat D, Clark CG, Wise FW, Schaffer CB, et al. *In vivo* three-photon microscopy of subcortical structures within an intact mouse brain. *Nat Photonics.* (2013) **7**:205–9. doi: 10.1038/nphoton.2012.336
14. Theer P, Hasan MT, Denk W. Two-photon imaging to a depth of 1000 μm in living brains by use of a Ti:$Al_2O_3$ regenerative amplifier. *Opt Lett.* (2003) **28**:2003. doi: 10.1364/OL.28.001022
15. Kobat D, Horton NG, Xu C. *In vivo* two-photon microscopy to 1.6 μm depth in mouse cortex. *J Biomed Opt.* (2011) **6**:106014. doi: 10.1117/1.3646209
16. Xu C, Zipfel W, Shear JB, Williams RM, Webb WW. Multiphoton fluorescence excitation: New spectral windows for biological nonlinear microscopy *Proc Natl Acad Sci USA.* (1996) **93**:10763–8. doi: 10.1073/pnas.93.20.10763
17. Guesmi K, Abdeladim L, Tozer S, Mahou P, Kumamoto T, Jurkus K, et al. Dual-color deep-tissue three-photon microscopy with a multiband infrared laser. *Light Sci Appl.* (2018) **7**:12. doi: 10.1038/s41377-018-0012-2
18. Liu R, Li Z, Marvin JS, Kleinfeld D. Direct wavefront sensing enables functional imaging of infragranular axons and spines. *Nat Methods.* (2019) **16**:615–8. doi: 10.1038/s41592-019-0434-7
19. Wang C, Liu R, Milkie DE, Sun W, Tan Z, Kerlin A, et al. Multiplexed aberration measurement for deep tissue imaging *in vivo*. *Nat Methods.* (2014) **11**:1037–40. doi: 10.1038/nmeth.3068
20. Tao X, Fernandez BM, Azucena O, Fu M, Garcia D, Zuo Y, et al. Adaptive optics confocal microscopy using direct wavefront sensing. *Opt Lett.* (2011) **36**:2011. doi: 10.1364/OL.36.001062
21. Albert O, Sherman L, Mourou G, Norris TB, Vdovin G. Smart microscope:an adaptive optics learning system for aberration correction in multiphoton confocal microscopy. *Opt Lett.* (2000) **25**:52–4. doi: 10.1364/OL.25.000052
22. Sherman L, Ye JY, Albert O, Norris TB. Adaptive correction of depth-induced aberrations in multiphoton scanning microscopy using a deformable mirror. *J Microsc.* (2002) **206**:65–71. doi: 10.1046/j.1365-2818.2002.01004.x
23. Bueno JM, Skorsetz M, Bonora S, Artali P. Wavefront correction in two-photon microscopy with a multi-actuator adaptive lens. *Opt Exp.* (2018) **26**:14278. doi: 10.1364/OE.26.014278
24. Neil MAA, Kaitis J, Booth MJ, Wilson T, Tanaka T, Kawata S. Adaptive aberration correction in a two-photon microscope. *J Microsc.* (2000) **200**:105–8. doi: 10.1046/j.1365-2818.2000.00770.x
25. Wang K, Sun W, Richie CT, Harvey BK, Betzig E, Ji N. Direct wavefront sensing for high-resolution *in vivo* imaging in scattering tissue. *Nat Commun.* (2015) **6**:7276. doi: 10.1038/ncomms8276
26. Tang J, Germaina RN, Cuib M. Superpenetration optical microscopy by iterative multiphoton adaptive compensation technique. *Proc Natl Acad Sci USA.* (2012) **109**:22. doi: 10.1073/pnas.1119590109
27. Ji N, Milkie DE, Betzig E. Adaptive optics via pupil segmentation for high-resolution imaging in biological tissues. *Nat Methods.* (2010) **7**:141–7. doi: 10.1038/nmeth.1411
28. Milkie DE, Betzig E, Ji N. Pupil-segmentation-based adaptive optical microscopy with full-pupil illumination. *Opt Lett.* (2011) **36**:4206–8. doi: 10.1364/OL.36.004206
29. Xu X, Liu H, Wang LV. Time-reversed ultrasonically encoded optical focusing into scattering media. *Nat Photon.* (2011) **5**:154–7. doi: 10.1038/nphoton.2010.306
30. Mertz J, Paudel H, Bifano TG. Field of view advantage of conjugate adaptive optics in microscopy applications. *Appl Opt.* (2015) **101**:3498–506. doi: 10.1364/AO.54.003498
31. Yaqoob Z, Psaltis D, Feld MS, Yang C. Optical phase conjugation for turbidity suppression in biological samples. *Nat Photon.* (2008) **2**:110–15. doi: 10.1038/nphoton.2007.297
32. Doi A, Oketani R, Nawa Y, Fujita K. High-resolution imaging in two-photon excitation microscopy using in situ estimations of the point spread function. *Biomed Opt Exp.* (2018) **9**:202. doi: 10.1364/BOE.9.000202
33. Wen-Chen I, Ronzitti E, Lee BR, Daigle TL, Dalkara D, Zeng XH, et al. *In vivo* submillisecond two-photon optogenetics with temporally focused patterned light. *J Neurosci.* (2019) **39**:3484–97. doi: 10.1523/JNEUROSCI.1785-18.2018
34. Pozzi P, Gandolfi D, Tognolina M, Chirico G, Mapelli J, D'Angelo E. High-throughput spatial light modulation two-photon microscopy for fast functional imaging *Neurophotonics.* (2015) **2**:015005. doi: 10.1117/1.NPh.2.1.015005
35. Sironi L, Freddi S, Caccia M, Pozzi P, Rossetti L, Pallavicini P, et al. Gold branched nanoparticles for cellular treatments. *J Phys Chem C.* (2012) **116**:18407–18. doi: 10.1021/jp305021k
36. Hsieh CL, Pu Y, Grange R, Psaltis D. Digital phase conjugation of second harmonic radiation emitted by nanoparticles in turbid media. *Opt Exp.* (2014) **18**:12283. doi: 10.1364/OE.18.012283
37. Chaigne T, Katz O, Boccara AC, Fink M, Gigan BS. Controlling light in scattering media noninvasively using the photo-acoustic transmission-matrix. *Nat Photon.* (2014) **8**:58–64. doi: 10.1038/nphoton.2013.307
38. Ma C, Xu X, Liu Y, Wang LV. Time-reversed adapted-perturbation (TRAP) optical focusing onto dynamic objects inside scattering media. *Nat Photonics.* (2014) **8**:931–6. doi: 10.1038/nphoton.2014.251
39. Débarre D, Booth MJ, Wilson T. Image-based adaptive optics through optimisation of low spatial frequencies. *Opt Exp.* (2007) **15**:8176–90. doi: 10.1364/OE.15.008176
40. Pozzi. P, Soloviev O, Wilding D, Vdovin G, Verhagen M. Optimal model-based sensorless adaptive optics for epifluorescence microscopy. *PLoS ONE.* (2018) **13**:e0194523. doi: 10.1371/journal.pone.0194523
41. Fried DL. Anisoplanatism in adaptive optics. *JOSA.* (1982) **72**:52–61. doi: 10.1364/JOSA.72.000052
42. Park JH, Sun W, Cui M. High-resolution *in vivo* imaging of mouse brain through the intact skull. *Proc Natl Acad Sci USA.* (2015) **112**:9236–41. doi: 10.1073/pnas.1505939112
43. Horstmeyer R, Ruan H, Yang C. Guidestar-assisted wavefront-shaping methods for focusing light into biological tissue. *Nat Photon.* (2015) **9**:563–71. doi: 10.1038/nphoton.2015.140
44. Thalhammer G, Bowman RW, Love GD, Padgett MJ, Ritsch-Marte M. Speeding up liquid crystal SLMs using overdrive with phase change reduction. *Opt Exp.* (2013) **21**:1779–97. doi: 10.1364/OE.21.001779

45. Blochet B, Bourdieu L, Gigan S. Focusing light through dynamical samples using fast continuous wavefront optimization. *Opt Lett.* (2017) **42**:4994–7. doi: 10.1364/OL.42.004994
46. David N, Fittinghoff P, Wiseman W, Squier JA. Widefield multiphoton and temporally decorrelated multifocal multiphoton microscopy. *Opt Exp.* (2000) **7**:273–9. doi: 10.1364/OE.7.000273
47. Moretti C, Gigan S. Readout of fluorescence functional signals through highly scattering tissue. *arXiv*. (2019). asXiv:1906.02604

**Conflict of Interest:** The authors declare that the research was conducted in the absence of any commercial or financial relationships that could be construed as a potential conflict of interest.

frontiers in Physics

PERSPECTIVE
published: 03 April 2020
doi: 10.3389/fphy.2020.00077

# Total Body PET Imaging From Mice to Humans

*Terry Jones**

*Department of Radiology, Medical Center, University of California, Davis, Sacramento, CA, United States*

The technology of Total Body PET scanning has been recently established. To advance its application for undertaking across body research in humans, small animal PET scanning is positioned to undertake programs of the pre-clinical development of paradigms and protocols that would be translatable to human total body studies.

**Keywords: positron emission tomography, total body PET, small animal PET, systems biology, molecular imaging**

## INTRODUCTION

Positron emission tomography (PET) is the most specific and sensitive method for imaging regional tissue molecular interactions and pathways in humans [1]. The specificity comes from the range of imaging biomarkers that can be used labeled with positron emitting radionuclides. These range from the short lived of minutes radioactive half-life, to longer lived of hours to days half-life. The radiochemists have overcome the challenges of radiosyntheses labeling with radionuclides such as carbon-11 and fluorine-18 to chelation radio labeling with longer lived metals such as zirconium-89. The sensitivity for detecting low mass, i.e., truly tracer levels of biomarkers arises through:

i) radiolabeling procedures that provide high specific activity of the tracer compound,
ii) the use of imaging based upon coincident detection which offers highly efficient, electronic collimation for recording regional tissue concentrations of tracer.

Exploiting the electronic collimation through 3D PET by extending the axial length of PET scanners, evolved cautiously in the early years. This was initially restrained both by cost and ensuring the important need to record quantitative scan data that can be processed to derive meaningful quantitative parameters of regional tissue function. Initial clinical research and healthcare applications of PET focused on individual organs of the body e.g., brain or heart and oncology focused on static [$^{18}$F]FDG imaging for tumor detection within the torso. Hence, there was little immediate incentive to embrace the cost of extending the axial length of PET scanners beyond a typical 24 cm axial length. For a review of the development of human PET scanners see Jones and Townsend [2].

## SMALL ANIMAL PET SCANNERS

Preclinical small animal PET scanners arose both from the need to support the pre-clinical development of imaging biomarkers and the advances initially made to maximize the use of electronic collimation in humans. It was realized that the efficiency offered by wide axial coincidence detection resulted in the sensitivity needed to achieve high spatial resolution when scanning small laboratory animals. Since the early 1990's, small animal PET scanners have undergone a number of technical advances in order to improve the spatial resolution along with the accompanying sensitivity to support the statistical demands of increasing the spatial resolution see Miyaoka and Lehnert [3]. Total body imaging in mice is well-established as most of the preclinical scanners provide axial field



**Edited by:**
*Claudia Kuntner,*
*Austrian Institute of Technology (AIT), Austria*

**Reviewed by:**
*Daniele De Paula Faria,*
*University of São Paulo, Brazil*
*Timothy DeGrado,*
*Mayo Clinic, United States*

***Correspondence:**
*Terry Jones*
*terry.jones40@googlemail.com*

**Specialty section:**
*This article was submitted to Medical Physics and Imaging, a section of the journal Frontiers in Physics*

**Received:** *16 December 2019*
**Accepted:** *04 March 2020*
**Published:** *03 April 2020*

**Citation:**
*Jones T (2020) Total Body PET Imaging From Mice to Humans. Front. Phys. 8:77. doi: 10.3389/fphy.2020.00077*

of views covering the whole body of mice. As such in preclinical research it is common to examine radiotracer distribution at a whole-body level in mice. Moreover, in preclinical imaging, researchers have also profited from dynamic imaging to obtain quantitative results by kinetic modeling [4, 5]. However, in human imaging the first total body scanner became available in 2018 and total body based kinetic modeling still in its infancies.

## HUMAN TOTAL BODY PET SCANNER (TBP)

A human total body PET scanner (TBP) of some near 2 meters axial length has been developed that is destined to become transformative for molecular imaging in humans [6–8]. The first human results have been obtained demonstrating; images of high statistical quality, total body regional kinetics which, when processed, produce total body quantitative parametric images of tissue function [8, 9] as shown in **Figures 1**, **2**. An alternative design of TBP scanner, using non-Anger logic detectors, is under construction with a projected overall length of 1.4 meters [10, 11].

The projected applications of TBP are in both clinical healthcare and research with iteration between both areas.

### Clinical Healthcare Procedures With TBP

In standard clinical healthcare, TBP will enable current examinations to be undertaken much better with advantages in quality and practicability:

A. The quality advantages of TBP are:

i) Significantly improved image quality,
ii) Quantitative imaging, based upon kinetic modeling is much more easily, and non-invasively undertaken using high quality image derived arterial input functions,
iii) Widening the applications of PET—translating from the new clinical research areas developed with TBP,
iv) Increased range of imaging bio-markers available in a given imaging center, from wider and further afield commercial distribution centers because of longer effective shelf lives.

B. The practical advantages of TBP in healthcare are:

i) Scan times of minutes: more patient throughput per unit of time,
ii) Scan times of minutes resulting in less movement induced blurring,
iii) Remove the need for arterial blood sampling,
iv) Could do the clinical load of 3–4 conventional scanners: space and staff saving,
v) Prescribe scans with lower radiation dose to patients and staff, and offering opportunities for screening,

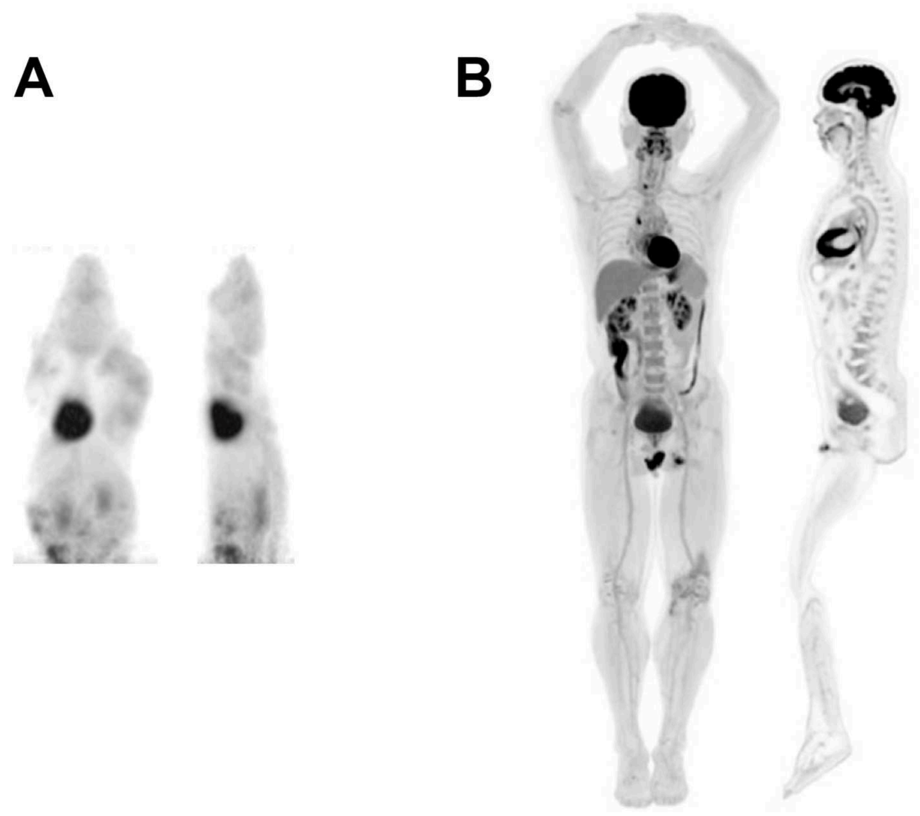


**FIGURE 1 |** Selected views from a **(A)** mouse and **(B)** human total-body scan showing total-body MIP and total-body sagittal view. Mouse image was acquired using the micro PET Focus 220 scanner whereas the human image was acquired using the EXPLORER total body PET scanner. This research was originally published in JNM [8]. © SNMMI.

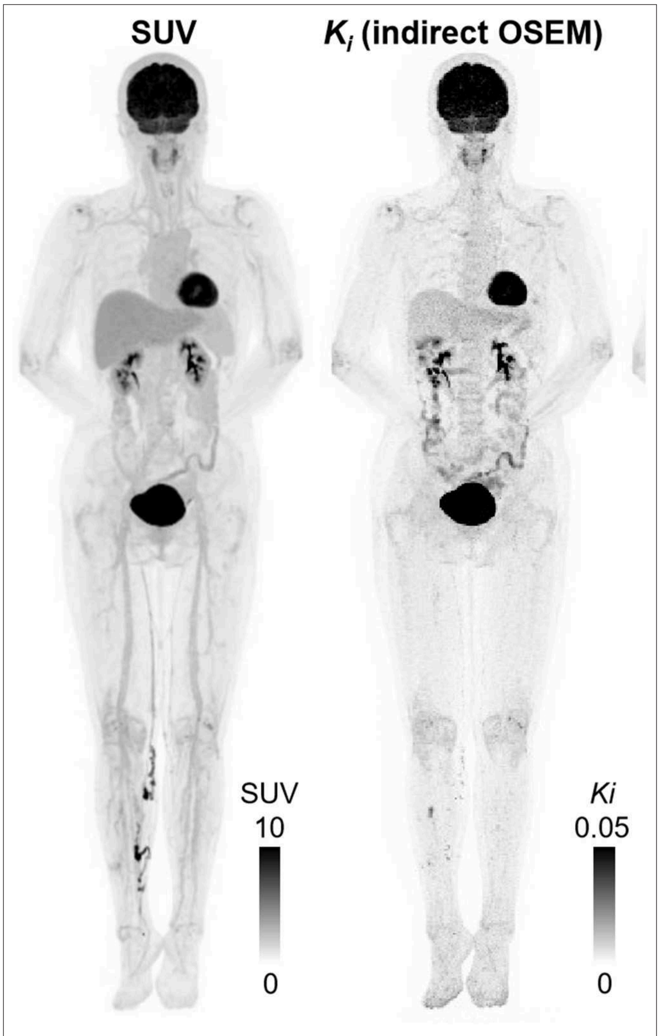


**FIGURE 2 |** Maximum intensity projection (MIP) using last 30 min of data (left to right): SUV; indirect OSEM Patlak slope $K_i$ (3 iterations 10 subsets); This research was originally published in JNM [9]. © SNMMI.

vi) Longer shelf life of radiolabelled tracers from distribution centers-avoiding the cost of in-house GMP production of new tracers labeled with fluorine-18, and, across cities, carbon-11.

### Clinical Research Applications With TBP

The clinical research applications with TBP rests to some extent on the underlying means to study lower levels of occult pathology e.g., in cancer, inflammation and infection but also the "Systems Biology" of human beings. Such studies are destined to cover: pharmacokinetics, pharmacodynamics, oncology, cardiovascular, endocrinology, immunology, maternal-fetal studies, and brain-body interactions e.g., in psychiatry, neurology, and inflammatory diseases.

## OUTLOOK ON TBP IMAGING

From the outset, the take up of TBP is facing numbers of challenges. In the first instance this is the cost of such an instrument. However, "Since the 1970's, the technical developments in PET instrumentation have resulted in major improvements in image quality for patient studies. These advances, although initially seen to be somewhat costly, have, by opening up new clinical applications, proved ultimately to be cost-effective" [2]. Never-the-less, funders at this time are asking for proof-of-concept pilot data that demonstrates that transformative studies will be made possible. Hence the pressure on the few operational TBP scanners to provide for early proof-of-concept data. To advance the new investigative field of total body PET, it will be necessary to formulate, validate/characterize, suitable paradigms and corresponding protocols. TBP based "systems biology" research is in its infancy. Such research would cover for example measures of: The whole-body's functioning of the vascular system and regional variations and changes therein. Physiological and endocrinology interactions between different organs of the body. Movement of cells from within and across the body. Pharmacokinetics and pharmacodynamic effects throughout the body. Physiological and metabolic interaction and exchange within and between the mother and fetus.

While some pilot human studies are envisaged, in order, to address the broad scope for such investigations, there is clearly a need to explore and consolidate such pilots at the pre-clinical level. This is where small animal PET scanner technology, which is already in place for total body PET studies of mice and rats, is destined to play a significant role in establishing paradigms and protocols that are translatable to human TBP. It is estimated that there are ~400 small animal PET scanners worldwide. These already existing extensive pre-clinical small animal PET programs represent a major resource within the molecular imaging community. They are well-positioned to develop, characterize and validate the paradigms and protocols for the more advanced total body PET scanning based "system biology" human studies. Inevitably there will be some reverse translation not least asking for more performance of the small animal PET technology and effecting quantitative parametric imaging.

## ETHICS STATEMENT

The study protocol was approved by the Zhongshan Hospital Shanghai Ethics Committee. The patients/participants provided their written informed consent to participate in this study.

## AUTHOR CONTRIBUTIONS

The author confirms being the sole contributor of this work and has approved it for publication.

## FUNDING

The EXPLORER scanner was developed with support from NCI, NIBIB, and the NIH Office of the Director through Transformative R01 CA 206187, with additional support from United Imaging Healthcare.

## ACKNOWLEDGMENTS

The author acknowledges the generous invitation to join in the development of the EXPLORER Total Body PET scanner project received from Simon Cherry and Ramsey Badawi at UC Davis. In formulating the projected clinical research and healthcare applications Total Body PET, the contribution is acknowledged of Pat Price in oncology along with many other clinical researchers in internal medicine.

## REFERENCES

1. Jones T. The role of positron emission tomography within the spectrum of medical imaging. *Eur J Nucl Med*. (1996) 23:207–11. doi: 10.1007/BF01731847
2. Jones T, Townsend D. History and future technical innovation in positron emission tomography. *J Med Imaging*. (2017) 4:011013. doi: 10.1117/1.JMI.4.1.011013
3. Miyaoka RS, Lehnert AL. Small Animal PET: Review of what have we done and where we are going. *Phys Med Biol.* (in press).
4. Dupont P, Warwick J. Kinetic modelling in small animal imaging with PET. *Methods*. (2009) 48:98–103. doi: 10.1016/j.ymeth.2009.03.008
5. Zheng X, Wen L, Yu SJ, Huang SC, Feng DD. A study of non-invasive Patlak quantification for whole-body dynamic FDG-PET studies of mice. *Biomed Signal Process Control*. (2012) 7:438–46. doi: 10.1016/j.bspc.2011.11.005
6. Cherry SR, Badawi RD, Karp JS, Moses WW, Price P, Jones T. Total-body imaging: Transforming the role of positron emission tomography. *Sci Transl Med*. (2017) 9:eaaf6169. doi: 10.1126/scitranslmed.aaf6169
7. Cherry SR, Jones T, Karp JS, Qi J, Moses WW, Badawi RD. Total-body PET: maximizing sensitivity to create new opportunities for clinical research and patient care. *J Nucl Med*. (2018) 59:3–12. doi: 10.2967/jnumed.116.184028
8. Badawi RD, Shi H, Hu P, Chen S, Xu T, Price PM, et al. First human imaging studies with the EXPLORER total-body PET scanner. *J Nucl Med*. (2019) 60:299–303. doi: 10.2967/jnumed.119.226498
9. Zhang X, Xie Z, Berg E, Judenhofer MS, Liu W, Xu T, et al. Total-body dynamic reconstruction and parametric imaging on the uEXPLORER. *J Nucl Med*. (2019) 61:285–91. doi: 10.2967/jnumed.119.230565
10. Karp JS, Vishwanath V, Geagan M, Muehllehner G, Pantel A, Parma M, et al. PennPET explorer: design and preliminary performance of a whole-body imager. *J Nucl Med*. (2020) 61:136–43. doi: 10.2967/jnumed.119.229997
11. Pantel AR, Viswanath V, Daube-Witherspoon ME, Dubroff JG, Muehllehner G, Parma MJ, et al. PennPET explorer: human imaging on a whole-body imager. *J Nucl Med*. (2020) 61:144–51. doi: 10.2967/jnumed.119.231845

**Conflict of Interest:** The University of California, Davis and United Imaging Healthcare have a research agreement and a revenue sharing agreement.

The author declares that the research was conducted in the absence of any commercial or financial relationships that could be construed as a potential conflict of interest.

frontiers in Physiology

REVIEW
published: 03 April 2020
doi: 10.3389/fphys.2020.00154

Check for updates

# How Non-invasive *in vivo* Cell Tracking Supports the Development and Translation of Cancer Immunotherapies

***Madeleine Iafrate and Gilbert O. Fruhwirth****

*Imaging Therapy and Cancer Group, Department of Imaging Chemistry and Biology, School of Biomedical Engineering & Imaging Sciences, King's College London, London, United Kingdom*

OPEN ACCESS

**Edited by:**
*Claudia Kuntner,*
*Austrian Institute of Technology, Austria*

**Reviewed by:**
*Ann Ager,*
*Cardiff University, United Kingdom*
*Shu-Chi A. Yeh,*
*Wellman Center for Photomedicine, Massachusetts General Hospital, United States*

***Correspondence:**
*Gilbert O. Fruhwirth*
*gilbert.fruhwirth@kcl.ac.uk*

**Specialty section:**
*This article was submitted to Medical Physics and Imaging, a section of the journal Frontiers in Physiology*

***Received:*** *26 November 2019*
***Accepted:*** *12 February 2020*
***Published:*** *03 April 2020*

**Citation:**
*Iafrate M and Fruhwirth GO (2020) How Non-invasive in vivo Cell Tracking Supports the Development and Translation of Cancer Immunotherapies. Front. Physiol. 11:154. doi: 10.3389/fphys.2020.00154*

Immunotherapy is a relatively new treatment regimen for cancer, and it is based on the modulation of the immune system to battle cancer. Immunotherapies can be classified as either molecular or cell-based immunotherapies, and both types have demonstrated promising results in a growing number of cancers. Indeed, several immunotherapies representing both classes are already approved for clinical use in oncology. While spectacular treatment successes have been reported, particularly for so-called immune checkpoint inhibitors and certain cell-based immunotherapies, they have also been accompanied by a variety of severe, sometimes life-threatening side effects. Furthermore, not all patients respond to immunotherapy. Hence, there is the need for more research to render these promising therapeutics more efficacious, more widely applicable, and safer to use. Whole-body *in vivo* imaging technologies that can interrogate cancers and/or immunotherapies are highly beneficial tools for immunotherapy development and translation to the clinic. In this review, we explain how *in vivo* imaging can aid the development of molecular and cell-based anti-cancer immunotherapies. We describe the principles of imaging host T-cells and adoptively transferred therapeutic T-cells as well as the value of traceable cancer cell models in immunotherapy development. Our emphasis is on *in vivo* cell tracking methodology, including important aspects and caveats specific to immunotherapies. We discuss a variety of associated experimental design aspects including parameters such as cell type, observation times/intervals, and detection sensitivity. The focus is on non-invasive 3D cell tracking on the whole-body level including aspects relevant for both preclinical experimentation and clinical translatability of the underlying methodologies.

**Keywords: adoptive cell therapy, cell tracking, drug development, molecular imaging, multi-modal whole-body imaging, positron emission tomography, reporter gene**

## INTRODUCTION

Immunotherapy is a relatively new concept that is increasingly applied to a variety of conditions. Most of the currently approved or emerging immunotherapy approaches are in the oncology arena. In some cases, they were curative, which represents a major leap over most previous treatment concepts. Mechanistically, they modulate the immune system to better attack the cancer. There are two types of anti-cancer immunotherapy, molecular and cell-based immunotherapy. Both approaches are already in clinical use, whereby molecular immunotherapies currently are further developed with more applications and more approved therapeutics.

Molecular immunotherapies usually modulate the immune system by targeting immune checkpoints using antibodies or antibody-derived molecules. Examples include ICIs targeted at CTLA-4 (e.g. ipilimumab) or the PD-1/PD-L1 axis (e.g. nivolumab, atezolizumab, and pembrolizumab) (Hodi et al., 2010; Topalian et al., 2012; Larkin et al., 2015; Darvin et al., 2018). These immunotherapeutics were largely developed using similar regulatory approval frameworks to other receptor-targeting drugs. Although in several cases the whole-body distribution of these therapeutics would be accessible through imaging the molecular immunotherapy itself, this is not routinely performed. Only very recently did studies report the whole-body distribution of radiolabeled checkpoint inhibitors in man (e.g. atezolizumab, Bensch et al., 2018; Jauw et al., 2019) to assess whether imaging them might reveal prognostic information. Despite molecular immunotherapies changing the landscape of cancer treatment (Ledford et al., 2018), significant challenges remain. These include non-responding patients (Feng et al., 2013), severe immune-related adverse events (IrAE, i.e., ICI weakening the normal physiological barriers against autoimmunity resulting in various local and systemic autoimmune responses), and the development of resistance (Darvin et al., 2018).

Cell-based immunotherapies consist of live immune cells that are administered to patients. The anti-tumor properties are either intrinsic to these therapeutic cells or conferred to them through genetic engineering. The therapeutic immune cells are either taken from a different human donor (allogeneic) or are isolated from the patient (autologous) before undergoing manipulations that transform the cells into immunotherapeutic cells. A historic lack of clarity surrounding the regulatory aspect of live cell-based therapy resulted in debates on what constitutes manipulations requiring regulatory approval (Anon, 2014), but it is now accepted that any cells that have been cultured with any drugs are subject to regulatory approval. The new paradigm of cell-based immunotherapy has forced regulatory agencies to re-evaluate their approval processes to accommodate for living drugs and to avoid slowing progress; for example, the new ATMP framework accelerates the approval process if there is demonstrable clinical need (Marks and Gottlieb, 2018). The first ever clinically approved cell-based anti-cancer immunotherapies were the chimeric antigen receptor T-cell (CAR-T) therapies tisagenlecleucel and axicabtagene ciloleucel, both of which are autologous CD19-targeted CAR-T immunotherapies for the treatment of certain hematological malignancies (B-cell lymphomas; U.S. Food and Drug Administration, 2017). While spectacular treatment successes have been reported for CAR-T immunotherapies, alike molecular immunotherapeutics, not all patients responded and sometimes the effects were only temporary (Neelapu et al., 2017; Schuster et al., 2017; Maude et al., 2018), and these therapeutics have also been associated with severe side-effects and fatalities during trials (Linette et al., 2013; Saudemont et al., 2018). In addition, CAR-T immunotherapy has generally yielded disappointing results in solid tumors (Martinez and Moon, 2019). Nonetheless, the portfolio of immune cells envisaged for cell-based anti-cancer immunotherapy is increasing and now includes T-cell receptor-modified T-cells (TCR-T), γδ T-cells, NK and dendritic cells (DC). Importantly, there are several unknowns including the *in vivo* distribution, persistence and survival of cell-based immunotherapies as well as their efficacy at target and non-target sites, and there is a need to investigate these aspects during their development and translation into the clinics.

**Abbreviations:** ATMP, advanced therapy medicinal products; BLI, bioluminescence imaging, a preclinical imaging technology; CAR, chimeric antigen receptor, an artificial molecule; CAR-T, chimeric antigen receptor T-cell therapy; CD2, cluster of differentiation 2, a cell adhesion molecule found on the surface of T-cells and natural killer cells; also known as T-cell surface antigen T11/Leu-5, LFA-2, LFA-3 receptor, erythrocyte receptor and rosette receptor; CD3, cluster of differentiation 3, a T-cell co-receptor; CD4, cluster of differentiation 4, a glycoprotein found on the surface of immune cells such as T helper cells, monocytes, macrophages, and dendritic cells; CD7, cluster of differentiation 7, found on thymocytes and mature T-cells; CD8, cluster of differentiation 8, a glycoprotein that serves as a co-receptor for the T-cell receptor; predominantly expressed on the surface of cytotoxic T-cells; CD19, cluster of differentiation 19, also known as B-Lymphocyte Surface Antigen B4, T-Cell Surface Antigen Leu-12 and CVID3 is a transmembrane protein; CD25, cluster of differentiation 25, also known as IL-2 receptor alpha chain, a part of the high-affinity IL receptor; CT, computed tomography, a whole-body imaging technology employing X–rays; CTLA-4, cytotoxic T-lymphocyte-associated protein 4, also known as cluster of differentiation 152; a molecule that is part of an immune checkpoint axis; DC, dendritic cell, a type of immune cell; DFO, desferrioxamine, a chelator for metal ions; FDA, U.S. Food and Drug Administration; [$^{18}$F]FHBG, 9-(4-[$^{18}$F]-Fluoro-3-[hydroxymethyl]butyl)guanine, a radiotracer for the reporter gene HSV1-*tk*; FMT, fluorescence mediated tomography, a fluorescence-based whole-body imaging technology; HMPAO, hexamethylene-propyleneamine oxime, an agent to label cells directly with $^{99m}$Tc; HSV1-*tk*, Herpes Simplex Virus 1 thymidine kinase, an enzyme that can be exploited as a reporter gene; ICI, immune checkpoint inhibitor; IL, IL, immune mediators; specified by a number to identify the individual molecule (e.g. IL-2 and IL-12); IrAE, immune related adverse event; LAG-3, lymphocyte-activation gene 3, an immune checkpoint molecule; MRI, magnetic resonance imaging, an imaging technology; MSOT, multispectral optoacoustic tomography, an advanced form of PAT imaging; NET, norepinephrine transporter, a mammalian protein that can be used as a host reporter gene; NIS, sodium iodide symporter, a mammalian protein that can be used as a host reporter gene; NK, natural killer cell, a type of immune cell; OCT, optical coherence tomography, an optical imaging technology; OPT, optical projection tomography, a preclinical optical imaging technology; OVA, ovalbumin, main protein found in egg white; widely used as a model antigen in T-cell biology; Numerous mouse cancer models have been modified to express OVA to aid in enhancing and tracking tumor-specific T-cell responses; PAT, photoacoustic tomography, an imaging technology; PD-1, programed cell death protein 1, an immune checkpoint molecule; PD-L1, programed death ligand 1, also known as cluster of differentiation 274 or B7 homolog 1 (B7-H1); constitutes an immune checkpoint axis together with PD-1; PET, positron emission tomography, a whole-body imaging technology detecting γ-photons produced by the annihilation of positrons stemming from the decay of certain radioisotopes; PSMA, prostate-specific membrane antigen, a glutamate carboxypeptidase 2 also known as folate hydrolase 1; qPCR, quantitative polymerase chain reaction, an analysis technique to determine specific DNA amounts in biological samples; RSOM, raster-scanning optoacoustic mesoscopy, a preclinical imaging technology exploiting the photoacoustic effect; SPECT, single photon emission computed tomography, a whole-body imaging technology detecting radioisotope location in 3D; TCR, T-cell receptor, a multi-protein complex responsible for many T-cell activation mechanisms; TCR-T, T-cell receptor-modified T-cell therapy; TIL, tumor infiltrating lymphocyte; US, ultrasound imaging, a cheap standard imaging technology.

## THE NEED FOR IMAGING IN IMMUNOTHERAPY DEVELOPMENT

During the early stages of drug development, animal models are frequently employed to investigate the efficacies of drug candidates in defined disease settings. For instance, multiple animal tumor models have been used in the development of chemotherapeutics and targeted therapies (Cekanova and Rathore, 2014). Similar experimentation has also been necessary for the development of immunotherapies to establish targeting efficiencies, pharmacokinetics/pharmacodynamics, whether there is spatial heterogeneity to therapy delivery, and whether therapy presence is related to efficacy. Novel and accurate biomarkers are also essential to guide immunotherapy development to ensure optimal benefit for cancer patients. Notably, imaging biomarkers differ from conventional tissue/blood-based biomarkers in several important aspects (O'Connor et al., 2017). Foremost, imaging biomarkers are non-invasive, thus overcoming sampling limitations and associated tissue morbidities of conventional tissue/blood biomarkers, and they provide whole-body information albeit usually for only one target at the time. Furthermore, dynamic imaging can provide pharmacokinetic information. As with other biomarkers, imaging biomarkers should be standardized across multiple centers to unleash their full potential for diagnosis, patient stratification and treatment monitoring. Pathways for the development and standardization of dedicated imaging biomarkers have been structured and excellently described by a large team of cancer researchers (O'Connor et al., 2017), and we refer the reader to this publication for specific details.

Whole-body *in vivo* imaging technologies (**Figure 1**) that can interrogate cancers and therapeutics in preclinical models are very valuable tools in this context. They show great potential to provide answers to various challenges central to immunotherapy:

(1) Which immune cell classes are present in tumors and are they critical for response?
(2) What role do other components of the tumor microenvironment play?
(3) What are the consequences of heterogeneity within tumors and between lesions?
(4) What are biomarkers of true response and true progression?
(5) What is the relationship between target expression levels, affinity, and response?
(6) Can resistance be detected early or even be predicted?
(7) How can the distribution, fate, persistence and efficacy of cell-based immunotherapies be tracked *in vivo*?
(8) Can off-target effects and associated toxicities be detected early or be predicted?
(9) How can combination treatments be designed in a rational and effective manner?

Given that metastasis is responsible for >90% of cancer mortality, novel immunotherapy treatments need also to be evaluated for their efficacies against secondary lesions. Metastases can significantly differ from the primary tumor because of tumor evolution, and consequently can show a different therapy response compared to the primary lesion (Caswell and Swanton, 2017; Kim et al., 2019). While anti-metastatic endpoints have long been regarded impractical, it is noteworthy that an anti-metastatic prostate cancer drug, apalutamide, recently received FDA approval on the basis of metastasis-free survival as a new endpoint (measuring the length of time that tumors did not spread to other parts of the body or that death occurred after starting treatment, U.S. Food and Drug Administration, 2018). This raised the prospects for further such research, not least in the context of immunotherapy, and if immunotherapy were to be used as a treatment at earlier stages of cancer. Thus, preclinical models of metastasis employing *in vivo* traceable cancer cells have also a role to play in the development of immunotherapies (Gomez-Cuadrado et al., 2017).

## IMAGING APPROACHES IN IMMUNOTHERAPY DEVELOPMENT

### Brief Overview of Relevant Imaging Technologies

Medical imaging revolutionized the diagnosis and treatment of human disease by providing anatomical, physiological and molecular information (Mankoff, 2007). Imaging technologies differ in their capabilities and limitations. **Figure 1** details the properties of those imaging technologies relevant to this review. Notably, several modalities are already in routine clinical use, for example US, magnetic resonance imaging (MRI), the radionuclide imaging modalities SPECT and PET, and X–ray computed tomography (CT). PAT and MSOT are two closely related relatively new modalities and have recently been translated into the clinical for special applications. PAT/MSOT delivers near infrared laser pulses into biological tissues with the latter absorbing and converting some of the laser pulse energy into heat, leading to transient thermoelastic expansion and thus wideband ultrasonic emission, which is used to compute an image (Ntziachristos et al., 2005; Wang and Yao, 2016). A purely optical imaging approach that is currently used in the clinical setting is OCT with applications in ophthalmology (Jung et al., 2011; Tao et al., 2013) and dermatology (Mogensen et al., 2009; Olsen et al., 2015). In general, the various imaging technologies can be categorized into modalities that subject the patient to a radiation dose (CT, PET, and SPECT) and modalities that are employing non-ionizing radiation (MRI, OCT, PAT/MSOT, and US). Depending on the research/clinical question, CT, MRI, PAT/MSOT, and US can be used with or without a contrast agent. In contrast, PET and SPECT strictly require contrast agents for image formation; these are often termed radiotracers, not least in reference to the very small concentrations required ("tracer levels;" picomolar concentration range) as both PET and SPECT are orders of magnitude more sensitive than the other clinically useable imaging technologies (**Figure 1**).

In preclinical settings, BLI can compete in sensitivity with radionuclide imaging modalities, but at much reduced experimental complexity and cost (instrument cost and running

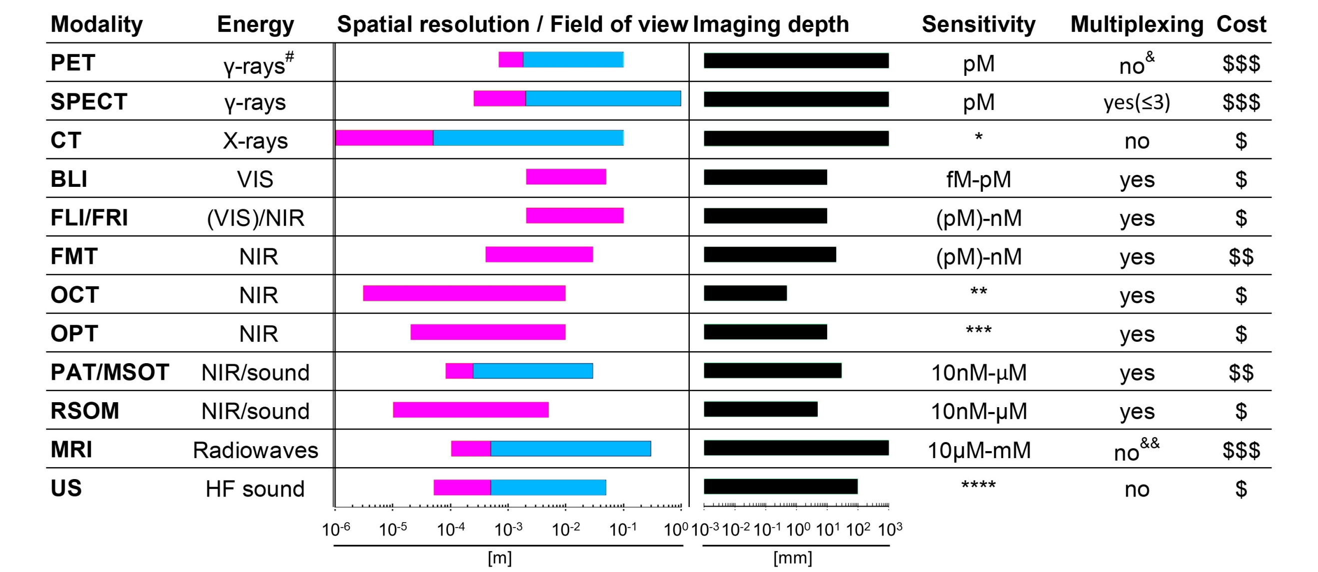


**FIGURE 1 |** Properties of various whole-body imaging modalities. Imaging modalities are ordered according to the electromagnetic spectrum they exploit for imaging (top, high energy; bottom, low energy). Routinely achievable spatial resolution (left end) and fields of view (right end) are shown in red. Where bars are blue, they overlap red bars and indicate the same parameters but achievable with instruments used routinely in the clinic. Imaging depth is shown in black alongside next to sensitivity ranges. Instrument cost estimations are classified as ($) < 125,000 $, ($$) 125-300,000 $ and ($$$) > 300,000 $. #Generated by positron annihilation (511keV). *Contrast agents sometimes used to obtain different anatomical/functional information. **In "emission mode" comparable to other fluorescence modalities (~nM). ***Fluorophore detection can suffer from photobleaching by excitation light. ****Highly dependent on contrast agent. & Dual isotope PET is feasible but not routinely in use; it requires two tracers, one with a positron emitter (e.g. $^{18}$F and $^{89}$Zr) and the other with a positron-gamma emitter (e.g. $^{124}$I, $^{76}$Br, and $^{86}$Y), and is based on recent reconstruction algorithms to differentiate the two isotopes based on the prompt-gamma emission (Andreyev and Celler, 2011; Cal-Gonzalez et al., 2015; Lage et al., 2015). &&Multichannel MRI imaging has been shown to be feasible (Zabow et al., 2008). PET, positron emission tomography; SPECT, single photon emission computed tomography; CT, computed tomography; BLI, bioluminescence imaging; FLI, fluorescent lifetime imaging; FRI, fluorescent reflectance imaging; FMT, fluorescence molecular tomography; OCT, optical coherence tomography; OPT, optical projection tomography; PAT, photoacoustic tomography; MSOT, multispectral optoacoustic tomography; RSOM, raster-scan optoacoustic mesoscopy; MRI, magnetic resonance imaging; US, ultrasound.

cost), which renders it a widely used tool. It relies on the presence of luciferase reporter proteins, which convert an administered chemical substrate into light that is then collected by highly sensitive cameras. As luciferase proteins are of non-mammalian origin, BLI is not translatable to the human setting. Another disadvantage is that BLI relies on light emitted within tissues which in turn is subject to absorption and scatter within the tissue matrix, thereby precluding reliable 3D quantification (Li et al., 2013; Dunlap, 2014; Jiang et al., 2016). Fluorescence-based whole-body imaging has also been developed (FLI/FRI), whereby fluorescence light is generated within a thick samples/small animal through excitation light; the approach has the same issues as BLI but is far less sensitive. To obtain true 3D data a tomographic design is required. Among the optical modalities listed in **Figure 1**, this is provided by optical projection tomography (OPT), which can be considered as the optical analog of CT. OPT operates on the micrometer to millimeter scales (Sharpe et al., 2002; Cheddad et al., 2012) thereby bridging the scale gap between classical whole-body imaging technologies and microscopy. It can either provide tomographic data on light absorption or fluorescence signals, and has been used in live zebrafish (Bassi et al., 2011; McGinty et al., 2011), fruit flies (Vinegoni et al., 2008; Arranz et al., 2014) and for whole organ imaging in mice (Alanentalo et al., 2008; Gleave et al., 2012; Gupta et al., 2013). An alternative approach offering larger fields of view in the centimeter range is diffuse optical tomography or FMT, which exploits photon tissue propagation theory to allow for 3D reconstruction at centimeter depth but its resolution is affected by weak signals and high tissues scattering (**Figure 1**; Graves et al., 2004; Ntziachristos, 2006; Venugopal et al., 2010; Zacharakis et al., 2011; Wang et al., 2015; Lian et al., 2017). In this review we lay emphasize on methodologies that are providing reliable quantifiable 3D information and have the potential to be clinically translatable.

As imaging modalities differ in their capabilities and limitations (**Figure 1**), combination technologies have become particularly important. For example, PET offers excellent sensitivity and provides absolute quantitative data (Lajtos et al., 2014) but can only detect signals at millimeter resolution. Hence, PET imaging was combined with other modalities providing higher anatomical resolution, such as CT (Basu et al., 2014) or MRI (Catana, 2017). This resulted in multi-modal whole-body imaging approaches adding anatomical context (from CT, MRI) to molecular imaging information (e.g. from PET or SPECT). Very recently, ultrafast US was combined with PET technology to form a new hybrid technology with the potential to provide molecular, anatomical and functional imaging data (Provost et al., 2018). Multi-modal imaging technologies are extremely useful to obtain maximal information from imaging, whereby the recent work of Bensch et al. provides a very good example for its power in the context of immunotherapy (Bensch et al., 2018).

## The Role of Anatomical Imaging

Anatomical imaging methods such as computed tomography (CT) or MRI provide excellent 3D resolution *in vivo* and enable quantification of tumor size and growth if the tumor differs sufficiently in contrast from surrounding tissues. Importantly, these techniques are non-specific and do not quantify tumor or immune cells specifically, but can account for the entirety of the tumor mass or reveal parameters such as texture (Lambin et al., 2012). This can cause issues for treatment monitoring if tumor size or radiomic features are not correlated to treatment response. If efficacy assessment is based on tumor shrinkage (cf. RECIST criteria in humans, Eisenhauer et al., 2009), then anatomical imaging is not appropriate for the assessment of immunotherapeutics, which initially can cause tumor sizes to increase or plateau before tumor regression occurs. This phenomenon is termed "pseudo-progression" and is evident in both molecular and cell-based immunotherapeutics (Nishino et al., 2017). It is caused by the very mechanisms of immunotherapy, which re-educates the immune system to detect and attack cancer cells, thereby resulting in immune cell infiltration/expansion, and tumors initially enlarging rather than regressing. Pseudo-progression has been recognized and is being accounted for in new criteria relevant for immunotherapy monitoring (Wolchok et al., 2009; Seymour et al., 2017).

## Molecular Imaging and Immunotherapy

Molecular imaging differs from anatomical imaging in that it provides specific molecular information on the whole-body level. Molecular imaging can be exploited to visualize and quantify the presence of a target of interest at a given time on the whole-body level. This can be used to diagnose and guide patient stratification and treatment decisions. *Via* molecular imaging, the heterogeneity of target expression can be assessed, for example, between primary and secondary lesions or within individual tumors (Alizadeh et al., 2015; Kurland et al., 2017; Bensch et al., 2018). Importantly, molecular imaging can support treatment monitoring, for example, inform on target engagement, therapy efficacy, and in certain cases can be used to probe the activity of a therapeutic. Molecular imaging employs a broad variety of different contrast agent classes based on target-specific small molecules as well as a variety of biomolecules. The latter include full-length antibodies, bivalent $F(ab')_2$ fragments, minibodies, monovalent Fab fragments, diabodies, single-chain variable fragments (scFv), nanobodies, affibodies (listed in order of decreasing molecular weight). Strategies for developing and optimizing such targeted probes for non-invasive imaging using radioactive, optical, magnetic resonance, and ultrasound approaches have been recently summarized by Freise and Wu (Freise and Wu, 2015). The imaging of T-cell effector molecules such as the PD-L1/PD1 axis has been shown to be a successful approach to study T-cell *in vivo* distribution in preclinical models (Natarajan et al., 2015; Heskamp et al., 2019) and in humans (Jauw et al., 2019). However, a caveat of molecular imaging is its reliance on one chosen molecular target, because its expression might change during tumor progression, and with these changes also the imaging read-outs would change. Recently, the predictive power of molecular imaging for treatment outcome was demonstrated through visualization of the radiolabeled ICI atezolizumab by multimodal PET/CT imaging (combined molecular and anatomical imaging, Bensch et al., 2018; **Figure 2**). In this study, clinical responses were better correlated with pre-treatment [$^{89}$Zr]Zr-desferrioxamine (DFO)-atezolizumab PET signals than with immunohistochemistry- or RNA-sequencing-based predictive biomarkers. [$^{89}$Zr]Zr-DFO-pembrolizumab, which targets PD-1 on T-cells, is currently being tested in clinical trials involving non-small cell lung cancer or metastatic melanoma patients (NCT02760225, NCT03065764). Similarly, the T-cell expressed ICI target CTLA-4 has been imaged in preclinical mouse models of colon cancer to better understand target expression and therapy side effects (Higashikawa et al., 2014). Additionally, $^{89}$Zr-labeled ipilimumab targeting CTLA-4 in humans is in phase II trials (NCT03313323) to better comprehend the pharmacodynamics/pharamacokinetics of this antibody-based immunotherapeutic and its IrAEs. Other imaging targets related to T-cell effector functions include interferon-$\gamma$ and granzyme B, which have both been studied in mice (Larimer et al., 2017, 2019; Gibson et al., 2018).

In preclinical models, the use of reporter genes to detect cancer cells *in vivo* (see Section "Non-invasive Whole-Body *in vivo* Cell Tracking") can overcome specificity issues of anatomical imaging. Cancer cell tracking by means of reporter gene imaging is frequently performed using bioluminescence technology which is cost-effective and fast but suffers from the limitations of optical imaging, which preclude accurate quantification (**Figure 1**, see Section "Brief Overview of Relevant Imaging Technologies"). A recent article comparing BLI alone with combined BLI and radionuclide imaging demonstrated such aspects providing real-life examples in the context of cancer cell tracking (Vandergaast et al., 2019). It is noteworthy that other imaging technologies can fare well in some specialized cases. For example, metastasis tracking of melanin-producing murine melanoma cells was achieved in mice at reasonable sensitivity and resolution compared to the study aims by using PAT (Lavaud et al., 2017). Alternatively, radionuclide cancer cell tracking methodologies have been developed but they are more expensive and lower throughput techniques but provide 3D tomographic and fully quantitative information (e.g. Fruhwirth et al., 2014; Diocou et al., 2017; Volpe et al., 2018). The latter is currently being tackled by the development of multi-animal radionuclide imaging beds (e.g. four-mouse hotels, Greenwood et al., 2019).

# *IN VIVO* IMAGING OF T-CELL POPULATIONS

Specific cell surface markers on T-cells are attractive imaging targets as they enable the *in vivo* visualization of either all T-cells or distinct T-cell sub-populations. They can also be exploited for the quantification of therapeutic responses affecting T-cell presence (or absence) in cancerous tissues. For example, targeting T-cell receptors (TCR) is attractive

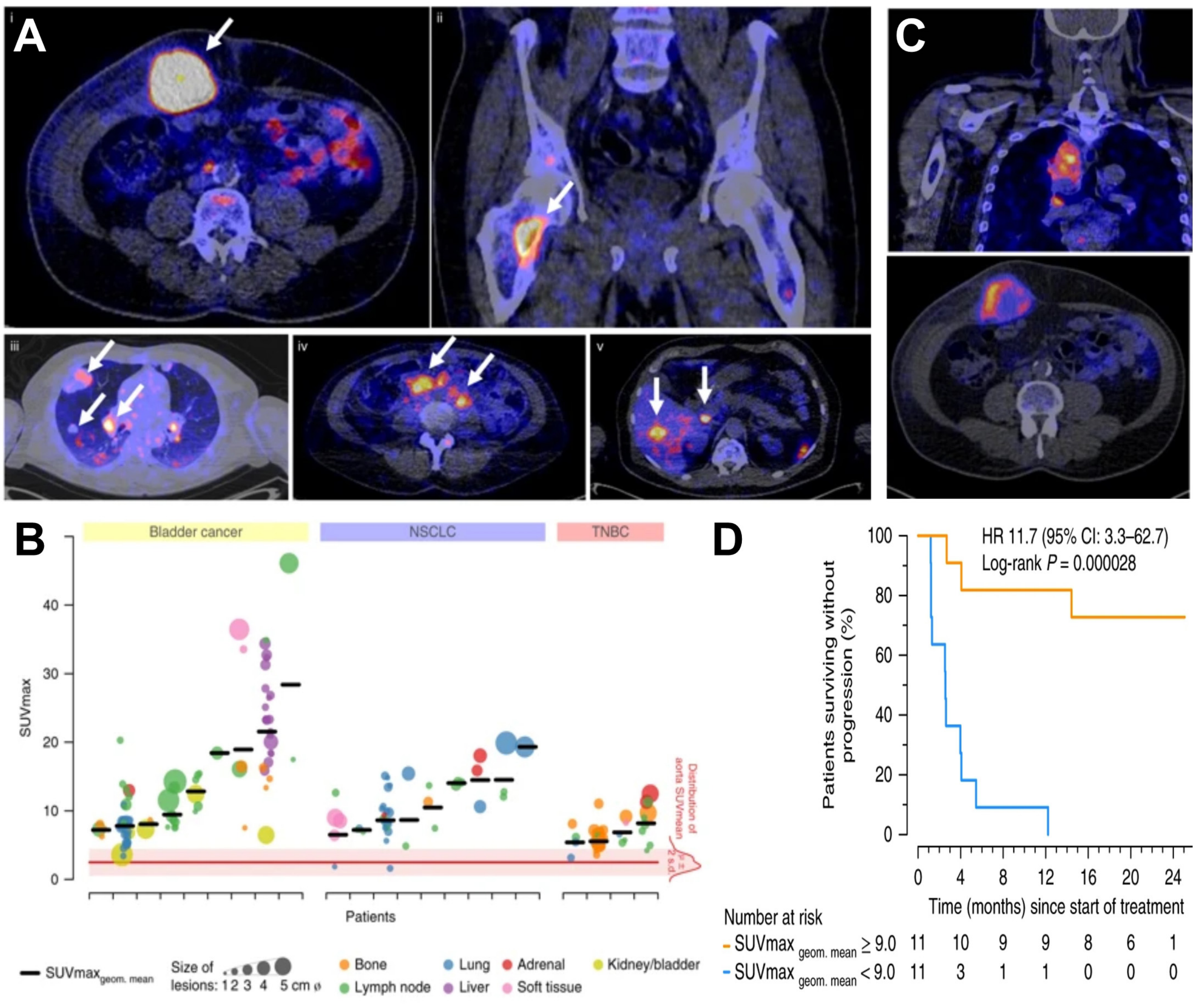


**FIGURE 2 |** Molecular imaging can be used as a non-invasive tool to predict clinical response of immunotherapy. **(A)** Examples of PET/CT images of four patients illustrating $^{89}$Zr-atezolizumab tumor uptake in five different locations on day 7 post-contrast agent administration (white arrows indicate tumor lesions; PET scans were performed once per patient and time point). Images (i) and (ii) are from the same patient, whereas images (iii), (iv), and (v) are each from a separate patient. **(B)** Overview of $^{89}$Zr-atezolizumab uptake as $SUV_{max}$ at day 7 post-contrast agent administration in 196 tumor lesions with a diameter >2 cm grouped per tumor type and ordered by increasing geometric mean SUVmax per patient, visualizing tumor size and site, and with the distribution of aorta for blood pool background uptake as reference. Horizontal bars indicate geometric mean SUVmax per patient. **(C)** PET/CT images of lesions of two patients with heterogeneous intralesional $^{89}$Zr-atezolizumab uptake on day 7 post contrast agent administration. *(Top)* Mediastinal lesion of a NSCLC patient ($SUV_{max}$ 19.9) and *(Bottom)* abdominal wall metastases of a bladder cancer patient ($SUV_{max}$ 36.4). **(D)** Progression-free survival according to the geometric mean standard uptake value ($SUV_{max}$) per patient obtained by non-invasive PET imaging using $^{89}$Zr-labeled atezolizumab (orange, above-median geometric mean uptake; blue, below-median geometric mean uptake; *N* = 22 patients; two-sided log-rank test). For comparison, Hazard Ratios (HR) were only 2.6 and 1.3 for two different PD-L1 antibodies used in histology. For details see Bensch et al. (2018). (Reproduced with modifications from the indicated reference).

because due to their high turnover on the plasma membrane, the bound radiotracers can gradually accumulate within the T-cells. In one preclinical study, TCRs were targeted using a $^{89}$Zr-conjugated anti-murine TCR F(ab')2 fragment selective for the murine TCR beta domain. Using PET/CT imaging, this radiotracer was shown to track the location of adoptively transferred engineered T-cells *in vivo*; notably, imaging data and *ex vivo* quantification of transgenic T-cell numbers in tumors correlated well (Yusufi et al., 2017). Additionally, using a $^{64}$Cu-labeled anti-chicken OVA-TCR antibody, it was demonstrated that associated TCR internalization neither impaired antigen recognition *via* the TCR, nor did it diminish T-cell viability or function in mice (Griessinger et al., 2015).

Alternatively, targeting CD3, a T-cell surface glycoprotein and pan-T-cell marker, has been suggested. Therefore, a radiometal-chelated antibody against CD3 ([$^{89}$Zr]Zr-DFO-CD3) was designed to quantify T-cell infiltration during anti-CTLA-4 treatment in colon cancer xenograft models. As the host species were mice, a murine anti-CD3 antibody was required in this case, and large amounts of infiltrated T-cells were found in the tumor prior to regression (Larimer et al., 2016). The LAG-3 was similarly exploited to image T-cells in xenografts established in transgene mice expressing human LAG-3 as host strains (Kelly et al., 2018).The radiolabelling strategy also utilized the siderophore-based chelator DFO, and this $^{89}$Zr-based radiotracer is now in clinical development. Moreover, $^{89}$Zr-LAG-3 PET is currently investigated in patients suffering from head and neck cancer or non-small cell lung cancer (NCT03780725). Notably, both anti-CD4 and anti-CD8 cys-diabodies have been radiometal-labeled ($^{89}$Zr, $^{64}$Cu) to track the corresponding T-cell sub-populations in preclinical models. Using these radiotracers, researchers imaged treatment responses of immunotherapies, for example response to checkpoint inhibitors such as anti-PD-1 (Seo et al., 2018) or anti-PD-L1 (alone or in combination with adoptive cell therapy) (Tavare et al., 2016; Freise et al., 2017; Zettlitz et al., 2017). The advantage of incorporating antibody fragments rather than full-length antibodies into the design of *in vivo* imaging agents is that the end product will reach its target more quickly, and it will be excreted faster (Bates et al., 2019). Such engineered antibody fragments targeting CD8 have already progressed into clinical trials (NCT03107663, NCT03802123, and NCT03610061). To increase specificity and reduce liver toxicity and Fc $\gamma$ receptor binding, bispecific antibodies targeting both T-cells (e.g. *via* 4-1BB) and either tumor antigens (e.g. CD19) or tumor stroma (e.g. FAP) have been developed. The bispecific antibodies have also been conjugated to radioisotopes to track their *in vivo* distribution in rodents by SPECT or PET imaging (Claus et al., 2019).

The mentioned approaches are applicable to the development of various molecular immunotherapies and cell-based immunotherapies. A general limitation is that the obtained imaging signals cannot be used to back-calculate precise T-cell numbers because the precise expression levels of T-cell surface marker molecules are unknown at the point of imaging. All above described methods probe T-cell presence but not their activities. As for cell-based immunotherapies, there is an additional limitation, namely the lack of discrimination between adoptively transferred and resident cells. To overcome this the adoptively transferred cells would need to be labeled to distinguish them from the resident ones (cf. Section "Non-invasive Whole-Body *in vivo* Cell Tracking").

## IMAGING THE ACTIVATION OF T-CELLS

Upon antigen-recognition and co-stimulation, naïve T-cells become activated in secondary lymphoid organs, which results in the expression of various cell surface markers of T-cell activation. The latter can be imaged using specific antibodies or antibody-fragments. For example, OX40 (CD134/TNFRSF4) is such a cell surface-expressed marker of T-cell activation and it has been used to image the spatiotemporal dynamics of T-cell activation following *in situ* vaccination with CpG oligodeoxynucleotide in a dual tumor-bearing mouse model (Alam et al., 2018). Moreover, it was shown that OX40 imaging using $^{64}$Cu-DOTA-AbOX40 as a contrast agent for PET predicted tumor responses with greater accuracy than both blood-based measurements for early response (i.e., Luminex analyses including interferon-$\gamma$, tumor necrosis factor $\alpha$, MCP1, MIP1B etc.) and anatomical measurements in this mouse model. Another example is the trimeric IL -2 receptor (CD25/IL-2Ra), which was exploited to visualize activated T-cells in immune-compromised mice by PET imaging using the contrast agent *N*-(4-[$^{18}$F]fluorobenzoyl)- IL -2 (Di Gialleonardo et al., 2012). IL-12 has also been implicated as a specific target for T-cell activation. Consequently, $^{99m}$Tc-labeled IL-12 has been used to detect T-cell activation *in vivo* in mice, albeit in colitis and not yet in tumor models (Annovazzi et al., 2006). Moreover, bioluminescence and radionuclide imaging tools to assess TCR-specific activation of T-cells have been developed (Ponomarev et al., 2001; Kleinovink et al., 2018), however, these approaches are still in preclinical development and are based on genetic engineering of T-cells and thus constitute specialized variants of cell tracking as described in Section "Non-invasive Whole-Body *in vivo* Cell Tracking".

Alternatively, it is possible to exploit the observation that T-cells undergo metabolic changes upon activation in tissues (van der Windt and Pearce, 2012; Buck et al., 2016) resulting in the influx of substrates not normally present in non-activated T-cells. While targeting metabolic pathways with imaging agents can distinguish activated from non-activated T-cells, this approach can suffer from competing signals generated by different cells in close vicinity. A very promising PET tracer in this context is 2′-deoxy-2′-[$^{18}$F]fluoro-9-β-D-arabinofuranosylguanine ([$^{18}$F]F-AraG), which accumulates in activated T-cells predominantly *via* two salvage kinase pathways (Ronald et al., 2017). Notably, the unlabeled compound has previously been used as a T-cell depleting drug in refractory T-cell acute lymphoblastic leukemia. [$^{18}$F]F-AraG PET imaging in a murine acute graft-vs.-host-disease (GvHD) model enabled visualization of secondary lymphoid organs harboring activated donor T-cells prior to clinical symptoms of GvHD. Notably, the biodistribution of [$^{18}$F]F-AraG was favorable and it may be useful for imaging activated T-cells in the context of immunooncology, which is currently investigated in several clinical trials (NCT03311672, NCT03142204, and NCT03007719).

## NON-INVASIVE WHOLE-BODY *IN VIVO* CELL TRACKING

The exploitation of molecular imaging has also enabled spatiotemporal whole-body *in vivo* tracking of administered cells (Kircher et al., 2011). One form of *in vivo* cell tracking has long been used to localize occult infections in patients (de Vries et al., 2010; Roca et al., 2010). Technological and methodological advances over the last decade led to a resurgence of cell tracking, this time in conjunction with the emergence of live cell therapeutics. For their development, several important questions remain largely elusive and require attention;

(i) the whole-body distribution of therapeutic cells;
(ii) their potential for re-location during treatment and the kinetics of this process;
(iii) whether on-target off-site toxicities occur;
(iv) how long the administered cells survive; and
(v) which biomarkers are best suited to predict and monitor cell therapy efficacy.

Traditional approaches in preclinical cell therapy development relied on dose escalation with toxicity evaluation, tumorigenicity tests, and qPCR-based persistence determination. Whole-body imaging-based *in vivo* cell tracking can inform on questions (i)-(iv) of these aspects in a truly non-invasive manner. However, many clinical trials are still performed largely without knowledge of the *in vivo* distribution and fate of the administered therapeutic cells, making it impossible to adequately monitor and assess their safety, thereby raising ethical questions when considering complications in clinical trials that could have been averted or mitigated if whole-body imaging had been used (Linette et al., 2013; Saudemont et al., 2018). With cell-based anti-cancer immunotherapies currently centered on adoptively transferred T-cells, either subjected to genetic engineering or *ex vivo* expansion only, there was a need to develop corresponding imaging tools to quantify T-cells *in vivo* on the whole-body level.

## Methods of *in vivo* Cell Tracking

*In vivo* cell tracking rests on the principles and mechanisms of molecular imaging to achieve contrast between cells of interest and the other cells of the organism. In some cases, there are intrinsic features of the cells of interest that can be exploited for generating contrast, for example, when cells produce targetable molecules that show low or no expression in other tissues. Under these circumstances, conventional molecular imaging offers cell tracking possibilities both preclinically and clinically. Examples demonstrating this are; tracking thyroid cancer metastases using the NIS (Kogai and Brent, 2012; Portulano et al., 2014), exploiting the PSMA to image prostate cancer and its spread (Perera et al., 2016; Oliveira et al., 2017), carcinoembryonic antigen (CEA) for colorectal cancer imaging (Tiernan et al., 2013), or melanin imaging in melanomas (Tsao et al., 2012). However, in most *in vivo* cell tracking scenarios, including all reported cases of cell-based immunotherapy, contrast agents or contrast-generating features must be introduced to the cells of interest. Fundamentally, cell labels can be introduced to cells *via* two different methodologies, direct or indirect cell labeling.

### Direct Cell Labeling for Cell-Based Immunotherapies

Direct cell labeling is performed upon cells *ex vivo*, and the subsequently labeled cells are re-administered into subjects, where they can be tracked using the relevant imaging technology (**Figure 3A**). Cells can either take up the contrast agents on their own (e.g. through phagocytosis, *via* internalizing receptors etc.) or are labeled through assisted contrast agent uptake (e.g. using cell permeant contrast agents, transfection etc.). There is a large variety of ready-to-use contrast agents available including chelated radiometals (for PET or SPECT), $^{19}F$-fluorinated nanoparticles and iron oxide nanoparticles (for various MRI types), as well as organic fluorophores and fluorescent nanoparticles (for optical imaging); for more details the reader is referred to a recent review by Kircher et al. (2011). One strength of MRI imaging is its excellent whole-body resolution. Consequently, various nanoparticles have been used to label and track adoptively transferred cells in preclinical models by MRI (Qiu et al., 2018). When applied to cell-based immunotherapy in humans, $^{19}F$-fluorinated nanoparticles have been proven effective cell-tracking contrast agents for MRI (Srinivas et al., 2013), as $^{19}F$ is naturally almost absent in tissues. Unfortunately, the detection sensitivity of $^{19}F$ is very low and requires specialized equipment. Attempts to improve detection sensitivities included the use of molecules and nanoparticles incorporating many $^{19}F$ atoms (Srinivas et al., 2012). Longitudinal tracking of activated T-cells *in vivo* was reported for a period of nearly three weeks in mice (Srinivas et al., 2009), but others found only limited utility for *in vivo* tracking of similarly labeled $CD4^+$/$CD8^+$ T-cells (in a murine diabetes model, Saini et al., 2019). Despite multiple optical contrast agents available for cell labeling, whole-body *in vivo* cell tracking using optical methodologies is very limited. This is caused by the intrinsic shortcomings of optical imaging including high tissue absorption and scatter precluding accurate *in vivo* localization and quantification. This includes 3D fluorescence molecular tomography (FMT), which also suffers from poor resolution, limited depth penetration and low sensitivity compared to other modalities (**Figure 1**). In the following, we focus on direct cell labeling with radioisotopes, because radionuclide imaging is currently the most sensitive tool for *in vivo* tracking of directly labeled cells in mammals. When co-registered with CT or MRI for additional anatomical detail, SPECT/PET-MRI/CT images are most promising to aid clinical translation of cell-based immunotherapies. Radioisotope can be used for cell labeling by either (i) exposing cells to chelating agents such as radiometal-complexed hydroxyquinolines (oxines) resulting in cellular uptake *via* diffusion or transport-mediated processes, or by (ii) linking radioisotopes onto cell surfaces, either electrostatically (e.g. using cell insertion peptides) or covalently.

In inflammatory conditions and infectious disease, the radiometal chelators [$^{111}$In]In-oxine and [$^{99m}$Tc]Tc-HMPAO have been routinely used clinically for tracking *ex vivo* labeled cells, e.g. white blood cells (Roca et al., 2010; de Vries et al., 2010). This decades-old methodology has more recently been applied to clinical studies of $CD4^+$ T-cells in Hodgkin's lymphoma (Grimfors et al., 1989), to assess penetrance of tumor-infiltrating lymphocytes in melanoma (Fisher et al., 1989; Griffith et al., 1989) or autologous $CD8^+$ T-cells in early stage non-small cell lung cancer patients who receive anti-PD-L1 immunotherapy in a neo-adjuvant setting (NCT03853187). Both $^{111}$In and $^{99m}$Tc are compatible with SPECT imaging or scintigraphy, an imaging technology which has previously been shown to be insufficiently sensitive in clinical studies (James and Gambhir, 2012). Although technological advances in SPECT instrumentation are improving the situation somewhat, PET imaging remains the method of choice, since it offers absolute quantification and higher sensitivity on clinical instrumentation.

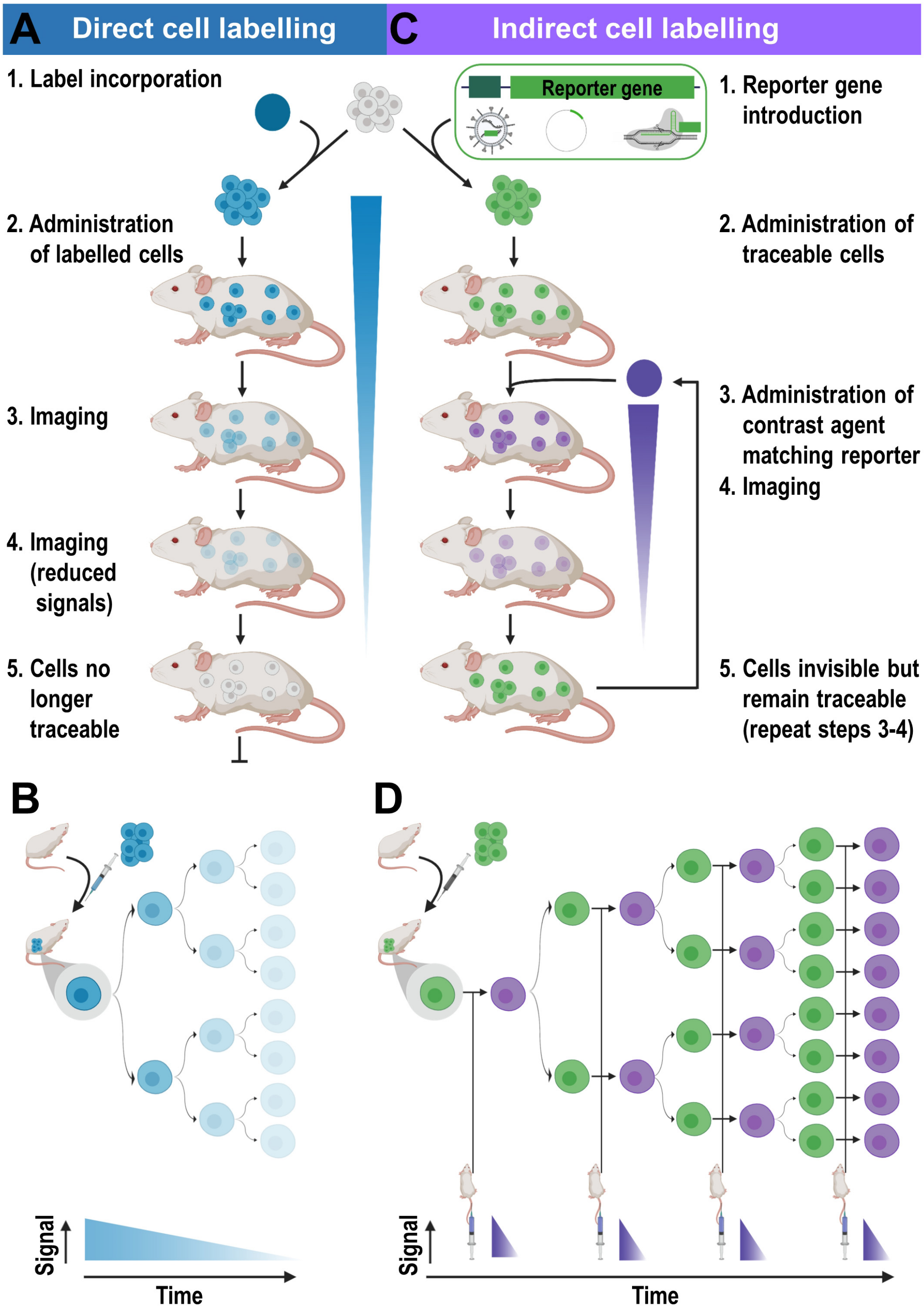


**FIGURE 3 |** Cell labeling approaches and their consequences for *in vivo* detectability of cells. **(A)** Cells are directly labeled by incorporation of a contrast agent (blue) matching the desired imaging technology. Cells can either take up the contrast agent on their own (e.g. through phagocytosis, *via* internalizing receptors etc.) or are labeled through assisted contrast agent uptake (e.g. cell permeant contrast agents, transfection etc.). The labeled cells (blue) are administered to animals and remain traceable until the contrast agent concentration per cell becomes too dilute to be detectable. Several processes including label efflux, label dilution through cell division, and in the case of radioisotopes also radioactive decay contribute and limit the maximum observation time *in vivo*. **(B)** Scheme depicting the effects of label dilution on cell detectability. **(C)** Indirect cell labeling requires the incorporation of a reporter gene (green) under the control of a suitable promoter (dark green). Reporter genes are frequently introduced using viruses but can also be incorporated *via* episomal plasmids or gene editing. Engineered cells (green) are administered to animals and can be visualized *in vivo via* administration of corresponding contrast agents (purple) followed by imaging, which can be repeated to enable long-term tracking. **(D)** Filial generations of reporter gene expressing cells remain traceable, hence indirectly labeled cells are *in vivo* traceable indefinitely.

The PET isotope equivalent of $^{111}$In (τ = 2.8 days) is $^{89}$Zr (τ = 3.3 days), which has a similar half-life but different decay properties ($^{89}$Zr: 23% positron emission, higher energy γ–rays than $^{111}$In but lacking Auger electron emission). Like $^{111}$In, cell labeling with $^{89}$Zr became possible with oxine chelators (Charoenphun et al., 2015; Sato et al., 2015), and it was shown to be better retained inside cells than [$^{111}$In]In-oxine (Charoenphun et al., 2015). This is a major advantage because the images correspond to the locations of the radioisotope; if labels leak out of cells rapidly they are more likely to give unreliable results. [$^{89}$Zr]Zr-oxine has been widely applied preclinically for immune cell labeling of cytotoxic T lymphocytes (CTL), γδ T-cells, DC and CAR-T (Sato et al., 2015; Weist et al., 2018; Man et al., 2019). With GMP-compatible protocols now available, [$^{89}$Zr]Zr-oxine is on a trajectory toward clinical translation and ultimately it will replace [$^{111}$In]In-oxine, which has become increasingly scarce in the EU due to economic reasons (Dhawan and Peters, 2014). A limitation of PET is its restricted spatial resolution (**Figure 1**) which is fundamentally limited by the radioisotope-dependent average positron range in matter (Phelps et al., 1975; Cal-Gonzalez et al., 2013). A way to mitigate its low resolution is to combine it with anatomical imaging methods that feature higher resolution (PET/MRI and PET/CT). For cell tracking applications also nanoparticle-based, multimodal PET/MRI probes have been envisaged, for example iron oxide nanoparticles that are cross-linked to radioisotopes (Garcia et al., 2015).

An alternative direct cell labeling methodology is to link contrast agents to the cell surface of cells. For example, [$^{89}$Zr]Zr-DFO-NCS was used to label human mesenchymal stem cells and while retained on the cell surface for about a week, cell viability appeared to be unaffected (Bansal et al., 2015). This approach is constrained by the availability of cell surface reactive groups that can be exploited, in this case primary amines, and it has the potential to interfere with cell surface proteins and impair cell function. This could restrict its use, particularly if tracer-level concentrations are superseded to achieve high *ex vivo* cell labeling to expand the cell tracking time (cf. **Figures 3A,B**). However, no systematic comparative studies between cell uptake and cell surface linking of radiometals in lymphocytes have so far been reported.

### Indirect Cell Labeling Applied to Immunotherapy Development

Indirect cell labeling is based on genetic engineering of cells to ectopically express a reporter, which serves as an imaging target (**Figure 3C**). This imaging target is then imaged *in vivo* after administration of suitable contrast agents, for example short half-life radiotracers, in a process that can be repeated to detect the traceable reporter-expressing cells over time (**Figures 3C,D**). Introduction of genetically encoded reporters is most frequently performed by viral transduction to ensure genomic integration and long-term expression. In some cases, episomal plasmids have been used (e.g. delivered by transfection or electroporation; Lufino et al., 2008; Ronald et al., 2013). Lately, gene editing approaches have been exploited for reporter insertion as they can be advantageous to viral transduction because they offer precise control over the genomic site of reporter insertion (Bressan et al., 2017). With feasibility having been demonstrated, this approach is likely to receive greater attention in the cell therapy field in future. Contrast formation relies on one of several mechanisms (**Figure 4**): either

(a) label uptake into cells by transporters,
(b) label binding to cell surface-expressed reporters, or
(c) expression of contrast-forming proteins, which either (i) produce a label through enzymatic action (e.g. luciferases, tyrosinase), or (ii) act as labels themselves (e.g. fluorescent proteins).

All these mechanisms can be useful for preclinical cell tracking and a variety of corresponding reporter genes are listed in **Table 1**. For clinical cell tracking, the emphasis must lies on the mechanisms (a) and (b), because the contrast-forming proteins are either not of human origin or produce toxic products if expressed outside their original context (e.g. tyrosinase; Urabe et al., 1994) and thus not clinically translatable. Alongside improvements of imaging technologies, also the corresponding reporter genes have been developed and optimized. A fundamental drawback of indirect cell labeling is that it requires genetic engineering. However, this is neither a concern for preclinical experimentation nor for cell therapies already reliant on it (e.g. CAR-T) (Saudemont et al., 2018). Several factors require careful consideration when planning reporter gene-afforded *in vivo* cell tracking experiments, particularly in the context of immunotherapies (see Section "Experimental Design Considerations for *in vivo* Cell Tracking").

## Multiplex Cell Tracking

It would be highly beneficial to track both primary tumors and metastases alongside the therapeutic in preclinical models. Combining preclinical whole-body cancer cell tracking with imaging of molecular or cell-based immunotherapeutics could enable image-based quantification of the extent a labeled/traceable immunotherapy reaches *in vivo* traceable cancers, and whether the immunotherapy is delivered to all primary/secondary lesions. Dual-modality approaches would be required for this, ideally both tomographic in nature to enable the 3D quantification of metastasis burden alongside the immunotherapy. While almost every well-performed preclinical immunotherapy imaging study cross-correlates tumor targeting of the traceable therapeutic with either anatomical or molecular imaging in the primary tumor, metastases have rarely been accounted for. One example of such a study evaluating also the metastatic sites involved was performed by Edmonds *et al.* (Edmonds et al., 2016) in a preclinical breast cancer model. The authors employed dual-radioisotope imaging to co-track cancer metastases and a liposomally encapsulated immunomodulatory drug with the aim to optimize the time between liposome administration and the subsequent adoptive transfer of γδ T-cell immunotherapy involving both primary and secondary lesions. In a subsequent preclinical study, the same authors co-tracked $^{89}$Zr-oxine labeled γδ T-cells (direct labeling approach) to NIS reporter expressing breast cancer cells (indirect labeling approach

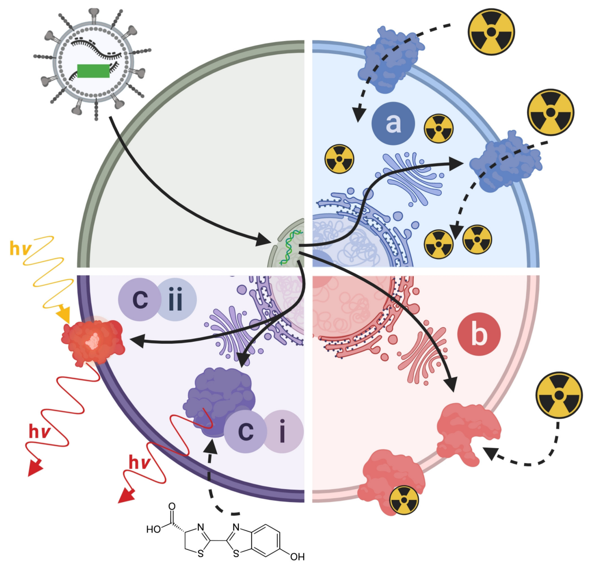


**FIGURE 4 |** Molecular imaging mechanisms relevant to reporter genes for indirect cell labeling. Cartoon showing the three main molecular imaging mechanism that are exploited for indirect cell labeling. **(a)** Transport (blue): these reporters are expressed at the plasma membrane of cells and each expressed reporter can transport several contrast agent molecules into the cell, which constitutes a signal amplification mechanism. The radionuclide transporters NIS and NET belong to this class of reporters. **(b)** Protein binding (red): these reporters are also normally expressed at the plasma membrane of cells and contrast agents bind directly to them; minor levels of signal amplification are theoretically possible if several contrast agents could bind to the reporter, or if several contrast agents could be fused to a reporter binding molecule; however, signal amplification is inferior compared to transporters. Examples for this reporter class are PSMA and SSTR2. **(c)** Contrast forming reporters (purple) can be sub-divided into two categories; enzymes that can generate contrast, and proteins that act as labels with intrinsic contrast. **($c_i$)** Enzymatic contrast formation: such reporters either entrap a molecular probe or generate a contrast agent from a precursor that needs to be either supplied externally or is available within the cell. Thymidine kinases such as HSV1-*tk* are examples for enzymes that entrap a radiotracer through its phosphorylation, and thereby generate contrast. Firefly luciferases are examples of reporters that convert an externally supplied substrate [shown: luciferin light (hν)]. Tyrosinase is an example of a reporter which converts cell-intrinsic precursors to the contrast agent melanin. **($c_{ii}$)** Intrinsic contrast: these reporters produce a signal on their own, normally upon stimulation. Classical examples are all fluorescent proteins, which generate specific light emissions upon excitation with light matching their excitation spectra. For details and literature references to relevant reporter genes see **Tables 1**, **2**. NIS, sodium/iodide symporter; NET, norepinephrine transporter; PSMA, prostate specific membrane antigen; SSTR2, somatostatin receptor 2.

using $^{99m}TcO_4^-$ as a NIS radiotracer) employing sequential multi-modal PET-SPECT-CT imaging (Man et al., 2019).

## EXPERIMENTAL DESIGN CONSIDERATIONS FOR *in vivo* CELL TRACKING

To ensure immunotherapy development benefits from cell tracking, it is imperative that the cell labeling approaches for therapeutic and/or cancer cells are chosen with the experimental goals in mind. Considerations must include a variety of different aspects such as cell tracking time, cell tracking interval, experimental setting (preclinical or clinical), use of immunocompetent or immunocompromised host organisms, imaging technology, and contrast agent properties and availability. To detect cells, the employed cell label must match the envisaged imaging technology to be used. The choice of the imaging technology dictates the achievable spatial resolution and imaging depth (**Figure 1**), impacts on minimal temporal resolution through image acquisition speeds, and contributes majorly to detection sensitivity and cost. Availability of the imaging technology and the necessary label further impact on the feasibility of collaborative across different institutions, which is of particular importance for clinical translation of a methodology and the chances of its subsequent adoption in clinical practice.

## Imaging Technology and Its Impact on Cell Detection Sensitivity

### Considerations for the Selection of the Imaging Technology

Exquisite detection sensitivity is required for *in vivo* cell tracking applications. In practice, this means sensitivities should be within or below the picomolar concentration range (**Figure 1**), which can be achieved best with bioluminescence and radionuclide imaging modalities. Unlike radionuclide imaging technologies, BLI neither provides absolute quantitative data nor true 3D information and is applicable only preclinically. However, despite its shortcomings, BLI has so far been the most frequently used preclinical approach to measure the impact of immunotherapeutics on *in vivo* traceable bioluminescent tumors; most likely due to BLI being relatively cheap and fast. In special cases, BLI can currently provide unique information relevant to immunotherapy development on the preclinical level. For example, dual-luciferase reporter methodology enabled the quantification of *in vivo* T-cell activation in specifically engineered transgene mice (Mezzanotte et al., 2011; Kleinovink et al., 2018). While it is fundamentally possible to perform such preclinical experiments with more quantitative 3D radionuclide tomography, it has not been reported so far; most likely due to more complex logistics and higher costs associated with this approach (e.g. two different radiotracers with similar pharmacokinetics/pharmacodynamics would be needed for each individual imaging session).

In many cases, 3D tomographic whole-body imaging data is required in rodents or larger mammals, i.e., non-translucent organisms. This generally limits the use of optical imaging technologies due to their inherent limitations relating to tissue light absorption and scatter. Hence, radionuclide imaging modalities are preferred for such purposes, but they require dedicated reporter genes, which are scarce compared to the plethora of different fluorescent proteins or luciferases that have been developed (Thorn, 2017; Shcherbakova et al., 2018; Mezzanotte et al., 2017). If clinical translation is the main goal for cell tracking applications, then radionuclide imaging is the

**TABLE 1 |** Reporter gene classes according to their molecular imaging mechanisms (cf. **Figure 4**) including selected examples.

| Mechanism [cf. Figure 4] | Reporter | Properties | Matching imaging modality | References |
|---|---|---|---|---|
| Transporter [a] | Mammalian transporters | Sodium iodide symporter (NIS, SLC5A5); Norepinephrin transporter (NET, SLC6A2); Dopamine transporter (DAT, SLC6A3). | Various radiotracers for PET and SPECT for all reporters listed. | (Dai et al., 1996; Moroz et al., 2007; Jauregui-Osoro et al., 2010; Khoshnevisan et al., 2016, 2017; UCL Business PLC, 2017; Jiang et al., 2018) |
| | Ion transporter from magnetotatic bacteria | MS-1 magA. | MRI (Endogenous or exogenous iron). | (Nakamura et al., 1995; Zurkiya et al., 2008; Cho et al., 2014) |
| | Polypeptides | Sodium-Taurocholate Co-transporting Polypeptide (NTCP). | Fluorescence and MRI. | (Wu et al., 2019) |
| Cell surface protein binding [b] | G-protein-coupled receptors | Somatostatin receptor type 2 (SSTR2); Dopamine receptor ($D_2R$). | PET and SPECT radiotracers available; PET radiotracers available. | (Satyamurthy et al., 1990; MacLaren et al., 1999; Rogers et al., 1999, 2000; Zinn et al., 2000a; Chaudhuri et al., 2001; Liang et al., 2001; Hwang et al., 2007) |
| | Recycling receptor | Transferrin receptor. | MRI (SPIO). | (Weissleder et al., 2000) |
| | Cell-surface antigen-based reporter | Human carcino-embryonic antigen-based reporters are recombinant proteins based on CEA minigene (N-A3) fused to extracellular and transmembrane domains of human FcγRIIb receptor, CD5 or TfR carboxyterminal domain. | PET and SPECT radiotracers available. | (Hammarstrom, 1999; Hong et al., 2008; Kenanova et al., 2009; Barat et al., 2011; Girgis et al., 2011) |
| | Mammalian cell surface protein | PSMA and mutants; radiotracers bind to the protein using it as a cell surface protein and not exploiting its enzymatic properties. | PET and SPECT radiotracers available. | (Castanares et al., 2014; Minn et al., 2019) |
| Enzymes [ci] | Bacterial enzymes | *E. coli* dihydrofolate reductase (eDHFR); *E. coli* β-galactosidase. | PET; Various including OPTICAL (chemiluminescence), MRI, PET and SPECT. | (Fowler and Zabin, 1977; Louie et al., 2000; Li et al., 2007; Liu and Mason, 2010; Green et al., 2017; Sellmyer et al., 2017, 2019; Guo et al., 2019; Krueger et al., 2019) |
| | Mammalian and non-viral kinases | Pyruvate kinase M2, thymidine kinases (viral such as HSV1-*tk* and mammalian variants), deoxycytodine kinases. | Various PET tracers for the individual kinases. | (Tjuvajev et al., 1995; Ponomarev et al., 2007; Jang et al., 2010, 2012; Likar et al., 2010; Park et al., 2015; Lee et al., 2017; Haywood et al., 2019; Seo et al., 2019). |
| | Other mammalian enzymes | Tyrosinase | PAT/MSOT, MRI, PET. | (Weissleder et al., 1997; Ponomarev et al., 2004; Krumholz et al., 2011) |
| | Luciferases | Various luciferases including Firefly, Green Click Beetle; Gaussia, Renilla; and NanoLuc. | OPTICAL (bioluminescence): Firefly, Green Click Beetle: D-luciferin; Gaussia, Renilla: coeloenterazine; NanoLuc: imidazopyrazinone. | (Lorenz et al., 1991; Loening et al., 2006; Tannous, 2009; Inoue et al., 2011; Hall et al., 2012; Schaub et al., 2015; Germain-Genevois et al., 2016; La Barbera et al., 2017; Mezzanotte et al., 2014, 2017; Hunt et al., 2016; Aswendt et al., 2019; Weihs and Dacres, 2019; Zhang et al., 2019) |
| Fluorescent Proteins [cii] | Proteins with intrinsic fluorophores | Red fluorescent: E2-Crimson/mTagRFP/mPlum/mNeptune; Infrared fluorescent: iRFP 670/iRFP 720. | OPTICAL (fluorescence upon appropriate excitation): (emission $\lambda_{max}$): 543/584/649/650; (emission $\lambda_{max}$): 670/720. | (Merzlyak et al., 2007; Kremers et al., 2009; Lin et al., 2009; Filonov et al., 2011; Liu et al., 2013; Shcherbakova and Verkhusha, 2013; Deliolanis et al., 2014; Isomura et al., 2017; Zhou et al., 2018; Fukuda et al., 2019) |
| Frequency-selective contrast/other | Artificial protein | Contrast based on transfer of radiofrequency labeling from the reporter's amide protons to water protons. | MRI (CEST). | (Gilad et al., 2007; Farrar et al., 2015) |
| Formation of gas vesicles/other | Mammalian acoustic reporter gene (mARG) | Gas vesicles are produced which generate US contrast. | US (3.2 MPa insonation). | (Farhadi et al., 2019) |

most suitable approach to address the questions raised in Section "Non-invasive Whole-Body *in vivo* Cell Tracking."

## Detection Sensitivity and the Duration of Cell Tracking

Detection sensitivity of labeled cells depends on the cellular label concentration and the matched imaging technology. The different labeling methodologies affect the cellular label concentration in different ways (see Section "Non-invasive Whole-Body *in vivo* Cell Tracking"). Label dilution, label efflux and in the case of radioactive labels dosimetry, can be severe limitations of direct cell labeling methodologies. The impact of label dilution has been discussed above (Section "Direct Cell Labeling for Cell-Based Immunotherapies"). Copper isotopes are the main example wherein label efflux causes issues. $^{64}Cu$ ($\tau$ = 12 h) had been suggested as a shorter half-life PET isotope (Adonai et al., 2002; Li et al., 2009; Bhargava et al., 2009) potentially competing with the SPECT isotope $^{99m}Tc$ ($\tau$ = 6.0 h). However, its unfavorably high cellular efflux (>50% per 4-5 h) paired with efficient liver uptake resulted in low signal-to-background ratios *in vivo* (Adonai et al., 2002; Bhargava et al., 2009; Li et al., 2009; Griessinger et al., 2014). High label efflux also limited the use of the long half-life PET radiometal $^{52}Mn$ for cell tracking (Gawne et al., 2018). For considerations regarding dosimetry see Section "Impact of Cell Labeling Methodology on Cell Function."

For indirectly labeled cells, the molecular imaging mechanism of the used reporter gene and the cellular expression level of the reporter gene are crucial, while the label dilution aspect plays no significant role (**Figure 3D**). Reporter genes which enzymatically entrap radiotracers that are taken up into cells offer high cell detection sensitivities. Examples are thymidine kinases, which phosphorylate and thereby entrap radiotracers in the cells, e.g. HSV1-*tk* is detected through its corresponding PET radiotracer [$^{18}$F]FHBG. Transporters (e.g. NET or NIS) provide signal amplification as each reporter protein can transport several radiotracer molecules into the cell. It is noteworthy that ectopic expression of reporters can affect the fate of their substrates. For example, NIS is normally expressed in thyroid follicular cells and its regular substrate, iodide, is metabolized into thyroid hormones after cell import. Upon ectopic expression in non-thyroidal cells, e.g. cancer cells or immune cells, this downstream mechanism affecting the equilibrium of the imported iodide is non-existent resulting in iodide not being accumulated to the same extent compared to thyroid tissues. To apply radioiodide for cell tracking in humans, it would be necessary to counteract high thyroid uptake and radioiodide metabolization there as this could lead to thyroid damage. The latter is possible by prior administration of non-radioactive iodide, but this also impacts on detection sensitivity of the traceable cells of interest. Non-iodide NIS radiotracers, which are not metabolized and wash out of thyroid cells would thus be preferable. As NIS is not very selective regarding its anion substrates (Paroder-Belenitsky et al., 2011) anionic radiotracers that are roughly similar in size and shape were developed for NIS imaging; they include $^{99m}TcO_4^-$, [$^{18}$F]$BF_4^-$, [$^{18}$F]$SO_3^-$ or [$^{18}$F]$PF_6^-$ (Jauregui-Osoro et al., 2010; Khoshnevisan et al., 2017; Jiang et al., 2018). They are not entrapped in cells, neither in thyroidal tissues nor in cells ectopically expressing NIS. Therefore, it would be advantageous to use non-iodide NIS radiotracers for clinical cell tracking. Another advantage of the new NIS PET radiotracers is that they are based on $^{18}$F, which has superior decay properties compared to $^{124}$I. $^{18}$F decays with a half-life of 109.8 min to $^{18}$O with 96.9% positrons ($E_{mean}$ = 0.250 MeV and 0.6 mm average positron range), while $^{124}$I decays with a half-life of 4.18 days to $^{124}$Te with only 22.7% positrons (11.7% $\beta_2^+$ at $E_{mean}$ = 975 MeV and 4.4 mm mean range, and 10.7% $\beta_1^+$ at $E_{mean}$ = 0.687 MeV and mean 2.8 mm range, plus a minor 0.3% $\beta_3^+$ at 0.367 MeV and 1.1 mm mean range) accompanied by several $\gamma$–rays and a high proportion of electron capture (Conti and Eriksson, 2016). Consequently, $^{18}$F produces more positrons per decay resulting in better detectability. It is noteworthy that $^{18}$F positrons also have a lower mean energy than those of $^{124}$I resulting in lower mean positron ranges (until annihilation and emission of detectable $\gamma$–rays) and therefore enabling better PET resolution. While free positron range considerations are currently irrelevant for clinical PET imaging (instrument resolution with 3-4 mm larger than most average free positron ranges of relevant PET isotopes), they are of concern for preclinical PET imaging (instruments can provide resolution even below 1 mm with the right isotope) (Deleye et al., 2013; Nagy et al., 2013). Notably, first-in-man clinical studies using [$^{18}$F]$BF_4^-$ to image NIS have already been completed (O'Doherty et al., 2017), thereby lowering the hurdles for NIS-afforded PET reporter gene imaging as a means of cell tracking in humans. Such considerations regarding the selection of radioisotopes as part of an individual reporter:contrast agent pair are transferable also to other reporters for which contrast agents with different radioisotopes are available (see **Table 2**). Selection of the best suited reporter:contrast agent pair is paramount.

The detection sensitivities of NIS-expressing extra-thyroidal cells have been reported preclinically to be as good as hundreds/thousands for cancer cells expressing NIS (Fruhwirth et al., 2014; Diocou et al., 2017) and CAR-T expressing PSMA *in vitro* (Minn et al., 2019), or tens of thousands for effector T-cells using various different reporter genes *in vivo* (Moroz et al., 2015) (**Figure 5**). Comparative studies aiming at the evaluation of how different reporter genes impact on T-cell detectability have been performed in the past (Moroz et al., 2015). Importantly, since this study new reporter gene:contrast agent pairs have become available, for example PSMA paired with its high-affinity PET ligand [$^{18}$F]DCFPyL (Minn et al., 2019) or NIS paired with its PET radiotracer [$^{18}$F]$BF_4^-$ (see above). Consequently, new comparative studies are needed to conclude on relative reporter:contrast agent performance in relevant immune cells; ideally performed such that also reporter expression levels and their intracellular availabilities for interaction with their contrast agents are precisely controlled. As reporter expression levels are cell type-dependent, it is highly recommended to determine detection sensitivities of indirectly labeled cells in each case and also on the available instrumentation before designing *in vivo* cell tracking experiments.

**TABLE 2 |** Promising host-compatible reporter genes and their corresponding imaging tracers.

| Reporter | | | Reporter *in vivo* detection | | |
|---|---|---|---|---|---|
| **Class** | **Name** | **Properties** | **Imaging modality and contrast agent** | **Contrast agent properties** | **References** |
| Transporter | Sodium iodide symporter (NIS) | Symports $Na^+$ alongside various anions. Endogenous expression in thyroid, stomach, lacrimal, salivary and lactating mammary glands, small intestine, choroid plexus and testicles. | PET: $^{124}I^-$, $[^{18}F]BF_4{}^-$, $[^{18}F]SO_3F^-$, $[^{18}F]PF_6{}^-$. SPECT: $^{99m}TcO_4{}^-$, $^{123}I^-$. | Tracers do not cross BBB. | (Dai et al., 1996; Jauregui-Osoro et al., 2010; Khoshnevisan et al., 2016, 2017; Jiang et al., 2018) |
| | Norepinephrine transporter (NET) | NaCl-dependent monoamine transporter. Endogenously expressed in organs with sympathetic innervation (heart, brain), | PET: [$^{124}$I]MIBG**; [$^{11}$C]hydroxyephedrine. SPECT: [$^{123}$I]MIBG**. | Tracers do not cross BBB. | (Moroz et al., 2007) |
| | Dopamine transporter (DAT) | NaCl-dependent. | PET: [$^{11}$C]CFT, [$^{11}$C]PE2I, [$^{18}$F]FP-CIT. SPECT: $^{123}$I-β-CIT**, $^{123}$I-FP-CIT**, $^{123}$I-Ioflupane**, $^{99m}$TRODAT. | Few data in public domain. Tracers cross BBB. | (UCL Business PLC, 2017) |
| Enzyme | Pyruvate kinase M2 | Expression during development, also in cancers. | PET: [$^{18}$F]DASA-23. | Background in organs of excretion route. Suggested for cell tracking within brain. Tracer crosses BBB. | (Haywood et al., 2019) |
| | Thymidine kinase (hmtk2/hΔTK2) | Human kinase causing cellular tracer trapping. | PET: [$^{124}$I]FIAU**, [$^{18}$F]FEAU, [$^{18}$F]FMAU (for hTK2-N93D/L109F). | Tracers do not cross the BBB; Endogenous signals in gall bladder, intestine and organs involved in clearance. | (Ponomarev et al., 2007) |
| | Deoxycytidine kinase (hdCK) | Human kinase causing cellular tracer trapping. | PET: [$^{124}$I]FIAU**, [$^{18}$F]FEAU. | Tracers do not cross the BBB; Endogenous signals in gall bladder, intestine and organs involved in clearance. | (Likar et al., 2010; Lee et al., 2017) |
| Cell surface receptor | Somatostatin receptor type 2 (SSTr2) | G-protein-coupled receptor. Endogenous expression in brain, adrenal glands, kidneys, spleen, stomach and many tumors (i.e., SCLC, pituitary, endocrine, pancreatic, paraganglioma, medullary thyroid carcinoma, pheochromocytoma); | PET: $^{68}$Ga-DOTATOC, $^{68}$Ga-DOTATATE. SPECT: $^{111}$In-DOTA-BASS. (best tracers selected here). | Tracers may cause cell signaling, change proliferation and might inhibit impair cell function. Non-metal octreotide radiotracers can cross blood brain barrier (BBB). | (Rogers et al., 1999, 2000; Zinn et al., 2000a,b; Chaudhuri et al., 2001) |
| | Dopamine receptor ($D_2R$) | G-protein-coupled receptor. High endogenous expression in pituitary gland and striatum. | PET: [$^{18}$F]FESP, [$^{11}$C]Raclopride, [$^{11}$C]N-methylspiperone. | Slow clearance of [$^{18}$F]FESP; Tracers cross BBB. | (Satyamurthy et al., 1990; MacLaren et al., 1999; Liang et al., 2001; Hwang et al., 2007) |
| | Transferrin receptor (TfR) | Fast recycling receptor. | MRI: Transferrin-conjugated SPIO. | Transferrin-conjugated SPIOs are internalized by cells. | (Weissleder et al., 2000) |
| Cell surface protein | Glutamate carboxy-peptidase 2 (PSMA) and variant tPSMA$^{N9del}$ | tPSMA$^{N9del}$ has higher plasma membrane concentration. High expression in prostate. | PET: [$^{18}$F]DCFPyL, [$^{18}$F]DCFBC. SPECT: [$^{125}$I]DCFPyL**.anti-PSMA antibodies and ligands can be flexibly labeled*, e.g. J951-IR800. | Background signal in kidneys. Tracers do not cross BBB. | (Castanares et al., 2014; Minn et al., 2019) |
| Cell surface antigen | Human carcino-embryonic antigen (hCEA) | Overexpressed in pancreatic, gastric, colorectal and medullary thyroid cancers. | PET: $^{124}$I-anti-CEA scFv-Fc H310A**, [$^{18}$F]FB-T84.66 diabody SPECT: $^{99m}$Tc-anti-CEA Fab' (approved), $^{111}$In-ZCE-025, $^{111}$In-anti-CEA F023C5i. | Tracers do not cross BBB. | (Griffin et al., 1991; Hammarstrom, 1999; Hong et al., 2008; Kenanova et al., 2009) |

*(Continued)*

**TABLE 2** | Continued

| Reporter | | | Reporter *in vivo* detection | | |
|---|---|---|---|---|---|
| **Class** | **Name** | **Properties** | **Imaging modality and contrast agent** | **Contrast agent properties** | **References** |
| Artificial cell surface molecule | DOTA antibody reporter 1 (DAbR1) | ScFv of anti-DOTA antibody 2D12.5/G54C fused to human CD4 TM domain. | PET: $^{86}$Y-AABD. | Tracer is a DOTA complex that binds irreversibly to a cysteine residue in the 2D12.5/G54C antibody. Tracer does not cross BBB. | (Wei et al., 2008) |
| | Estrogen receptor α ligand binding domain | No reported physiological function. | PET: [$^{18}$F]FES. | Tracer is clinically used estrogen receptor imaging agent. | (Qin et al., 2013) |
| | Anti-PEG Fab fragment* | Some tracers cross BBB; PEG is non-toxic and approved by FDA. | PET: $^{124}$I-PEG-SHPP*,**. MRI: SPIO-PEG. Fluorescence: e.g. NIR797-PEG. | Iodine tracers bear risk of deiodination. Some tracers cross BBB. | (Chuang et al., 2010) |
| Carrier protein | Ferritin | | MRI: iron. | Iron is not equally distributed across the brain and therefore may cause local susceptibility shifts that are above the MRI detection limit. | (Cohen et al., 2005; Genove et al., 2005) |

*Promise was evaluated based on (i) host-compatibility of the reporter and (ii) availability of contrast agents. *Any other modality can be used provided a suitable contrast forming moiety will be attached to PEG and the CEA antibodies, respectively. **Radioiodinated tracers can become de-iodinated in vivo resulting in free iodide that is subsequently taken up into NIS expressing organs.*

## Proliferation of Traceable Cells and *in vivo* Tracking Time

Paramount for choosing the cell labeling approach is how rapid the traceable cells divide and how long-term an observer wishes to track them *in vivo*. Tracking cancer cells in preclinical tumor models normally entails following them over multiple cell divisions, spreading over weeks if not months. To evaluate cell-based anti-cancer immunotherapies, cell engraftment, expansion and survival are of interest, whereby observation times, usually several days up to several weeks, are long-term compared to division/expansion events of therapeutic cells.

For direct cell labeling applications label efflux and label dilution are limiting (**Figures 3B,D**). If radioisotopes are used for direct cell labeling then their half-lives additionally limit achievable tracking times with 4-5 half-lives being realistic with existing small-animal PET instrumentation; e.g. about two weeks for $^{89}$Zr (Khoshnevisan et al., 2017) depending on the amount of radiolabel loading and instrument sensitivity. As the continued presence of the radioisotope in direct cell labeling results in a radiation dose to the cell and consequently radiation damage accumulation, a compromise must be reached between the maximum label concentration, which should not impair cell function (see Section "Impact of Cell Labeling Methodology on Cell Function"), and the maximum achievable tracking time.

In contrast, indirect cell labeling does not suffer from label dilution as the genetically encoded reporter is passed on to filial generations, thereby rendering the observation time theoretically indefinite. Indirect cell labeling relies on repeat administration of contrast agents, if radioactive then short half-live radioisotopes. This adds complexity as for example radiotracers need to be freshly prepared for every imaging session (**Figure 3D**), but it is certainly advantageous that the overall received doses are smaller than in direct cell labeling when compared over the same tracking periods. Consequently, indirect cell labeling is the preferred method of choice for long-term cell tracking, including cancer cell tracking in spontaneous metastasis models or the long-term evaluation of cell-based immunotherapies.

## *In vivo* Cell Tracking Interval

During tracking of directly labeled cells, the imaging interval is not linked to the imaging technology other than that animal welfare considerations must be considered (e.g. minimum interval of repeat-anesthesia). However, for indirect cell labeling approaches with radionuclide reporter gene and corresponding radiotracers, the choice of radioisotope affects the minimum imaging interval because the radiotracer from an earlier imaging session must have had time to sufficiently decay before a new batch can be administered to enable a subsequent imaging session (**Figure 3D**). For example, there are various radiotracers for the radionuclide reporter NIS, which have differing radioisotope half-lives; these include $^{99m}TcO_4^-$ ($\tau$ = 6.01 h) and $^{123}I^-$ ($\tau$ = 13.2 h) for SPECT or $^{124}I^-$ ($\tau$ = 101 h) and $[^{18}F]BF_4^-$ ($\tau$ = 1.83 h) for PET. Again, ~4-5 half-lives are needed for sufficient radiotracer decay and this defines the minimum time interval acceptable between imaging sessions. It was previously shown that repeat-imaging of NIS-expressing cells is possible after four half-lives using $^{99m}TcO_4^-$, i.e., after 24 h (Diocou et al., 2017); however, this would not be possible for over two weeks when using $^{124}I^-$, while $[^{18}F]BF_4^-$ would allow ~8 h intervals.

As for radionuclide imaging-afforded cell tracking it is noteworthy that radiotracer concentrations are very low, generally below target saturation, hence presence of prior administered radiotracers is normally negligible for later imaging sessions due to very low picomolar radiotracer concentrations, even if they would stay intact and not be excreted. A special case in this context is $^{99m}Tc$, which decays to long-lived $^{99}Tc$ and consequently remains in the same chemical form after its decay. Thus, it could accumulate over repeat imaging sessions unless excreted. For example, in preclinical NIS imaging experiments in mice the radiotracer $^{99m}TcO_4^-$ is administered at 15 – 30 MBq per animal. This equates to about 0.5 – 1.0 pmol of the total pertechnetate species (sum of $^{99m}TcO_4^-$ and $^{99}TcO_4^-$) taking into account a typical $^{99m}TcO_4^-$ generator elution regimen and $^{99}TcO_4^-$ carrier presence (Lamson et al., 1975). Even in an unrealistic worst-case scenario excluding its renal excretion, each repeat NIS imaging session would add this amount to the animal. However, the overall pertechnetate concentration would still be far below NIS saturation as its Michaelis-Menten constant for pertechnetate is likely very similar to those reported for $ReO_4^-$ or $ClO_4^-$ (Paroder-Belenitsky et al., 2011) and hence in the low micromolar range. Others repeatedly imaged animals with NIS-expressing cancer cells by $^{99m}TcO_4^-$ -SPECT and found no impact of earlier imaging sessions on subsequent ones (Diocou et al., 2017). For radiotracers that decompose chemically following radioisotope decay this consideration is irrelevant. Such an example is the NIS PET radiotracer $[^{18}F]BF_4^-$, in which $^{18}F$ decays to $^{18}O$ resulting in a chemically instable product ultimately generating borate, which is no longer a substrate for NIS (Khoshnevisan et al., 2016). While presented using the example of NIS here, such considerations can also be relevant for other reporter gene:radiotracer pairs.

## Cell Viability and Its Impact on Detected Cell Tracking Signals

Signals from directly labeled cells do not report on whether the cells are alive. Moreover, recorded signals might not even stem from the initially labeled cell population (e.g. due to label efflux or cell death and subsequent deposition or uptake into different cells). In contrast, indirect cell labeling is fundamentally linked to cell viability as the reporter is encoded in the DNA of the traceable cells. However, signal loss in reporter expressing cells is also a possibility, for example, when the reporter gene expression cassettes become epigenetically silenced. Notably, so-called 'safe harbor locations' have been discovered in mammalian genomes (Pellenz et al., 2019), and reporter genes can be inserted into such locations using gene editing methodologies. The latter has recently be demonstrated in different stem cell types even with large reporter genes such as NIS (Wolfs et al., 2017; Ashmore-Harris et al., 2019).

Stem cell tracking experiments conducted with cells that were both iron oxide nanoparticle-labeled ("direct" cell label) and expressing luciferase and the fluorescent protein GFP ("indirect" reporter genes) elegantly demonstrated the differences between the two different cell labeling methodologies (**Figure 6**). Even though MRI signals from the iron oxide nanoparticle were detectable for four weeks, these signals were found through *ex vivo* validation by histology to stem from resident macrophages that had phagocytosed the nanoparticles, which were released from dying stem cells. In contrast, luciferase signals were recorded only from living cells and were validated *ex vivo* also by histology (Li et al., 2008). This study highlighted comprehensively that reporter gene imaging much better reflects cell viability and that great care must be taken to avoid ascribing signals from directly labeled cells to the wrong cell populations. Consequently, employing direct cell labeling necessitates independent cross-validation, which could include e.g. *in vivo* co-tracking by reporter gene imaging and *ex vivo* validation by histology or flow cytometry.

Within indirect cell tracking, there can be variations in how reporter genes reflect cell viability. Differences can arise due to the steady-state concentrations of certain reporter proteins in cells, determined by the production and degradation rate of the reporter. These turnover parameters have not been systematically studied for most reporter genes except some fluorescent proteins (Khmelinskii et al., 2016). In certain conditions, turnover can be manipulated, for example through genetic modification with oxygen degradation domains to speed up reporter degradation in normoxic conditions (Goldman et al., 2011; Misra et al., 2017). In general, both fluorescent proteins and reporters relying on contrast agent binding are likely to produce signals if present. Dying traceable cells or cell debris from them will remain detectable until the reporter proteins are cleared or destroyed. In contrast, reporters with enzyme or transporter functions need to be active to generate contrast in cells, and this requires a form of cellular energy to drive the transport. For example in the case of NIS, the $Na^+/K^+$ gradient (Dohan et al., 2003) is critical and its breakdown results in loss of NIS transporter activity, which is the basis for the high sensitivity of NIS to cell death. Consequently, if cell viability is central to the goals of a study, an activity-dependent reporter may yield more reliable data than a reporter which signal relies merely on protein presence.

## Impact of Cell Labeling Methodology on Cell Function

It is obvious that there should be no impact of the cell labeling methodology on the function and long-term fate of the labeled cell. Contrast agents for direct cell labeling that are compatible with highly sensitive *in vivo* detection of labeled cells are often radiotracers. While chemical/biological toxicity is mostly irrelevant due to very low tracer-level concentrations (picomolar), they have the potential to exert radio-damage to the cells depending on their cellular concentration and location, their half-life and type of radioactive decay. For example, despite their short range the Auger electrons emitted by $^{111}In$ and to a lesser extent by $^{99m}Tc$ have the potential to exert significant DNA damage if they come in close proximity with DNA within

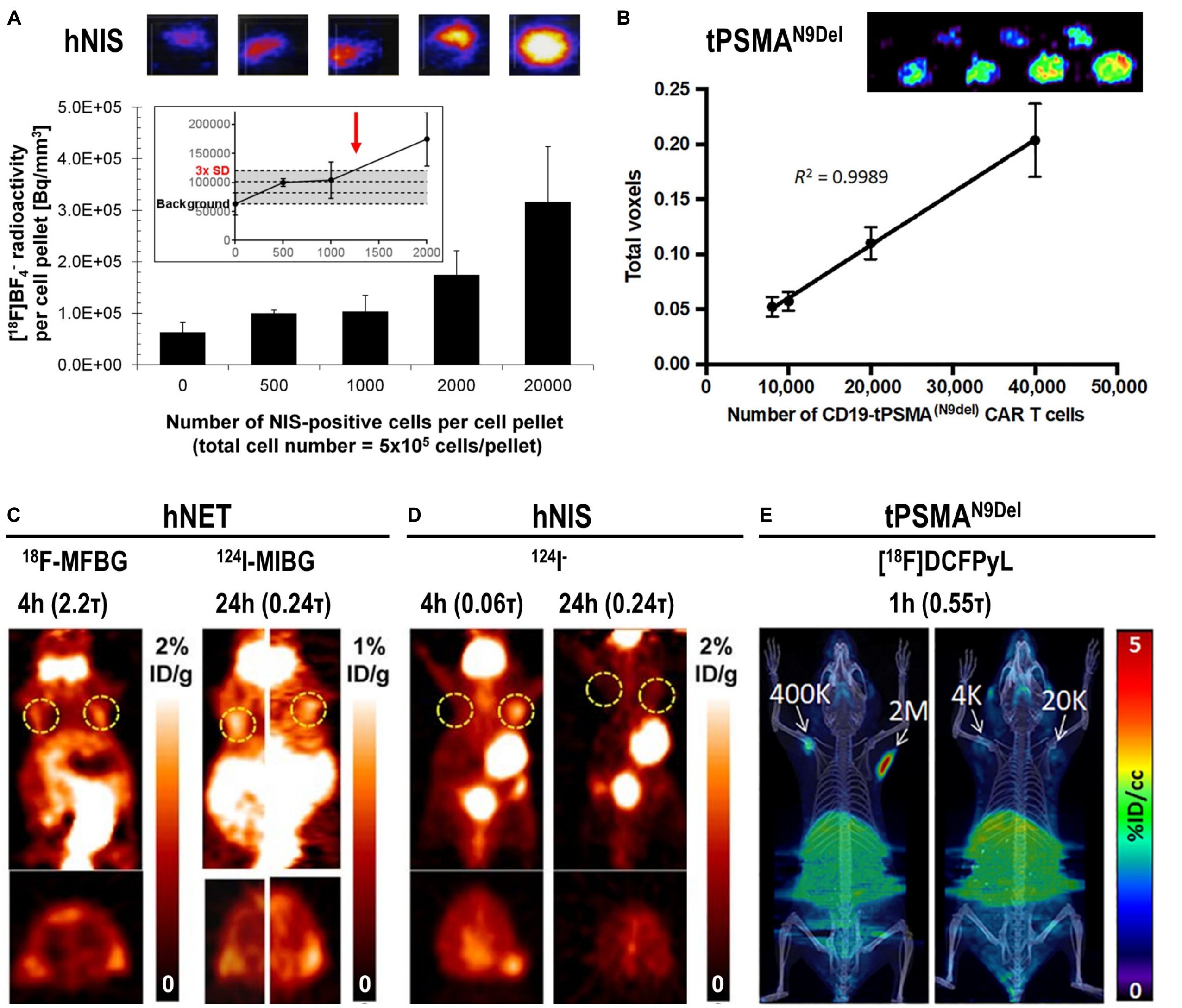


**FIGURE 5 |** *In vitro* and *in vivo* detection sensitivity of reporter gene expressing cells. **(A)** *In vitro* determination of the detection limit of NIS-positive cells within a cell pellet of NIS-negative cells for the NIS radio tracer [$^{18}$F]BF$_4^-$ using nanoPET/CT equipment from Mediso. For experimental details see Diocou et al. (2017) (*top*) Typical results of nanoPET/CT imaging of cell pellets and *(bottom)* quantitative analysis of imaging experiments. The limit of detection was determined to be ~1,250 NIS-positive cells (inset, red arrow). **(B)** Standard curve demonstrating a linear relationship between the PET signal and the number of CD19-tPSMA$^{N9del}$ CAR-T. *(top) In vitro* phantom from which the standard curve was derived. The *in vitro* phantom used varying numbers of CD19-tPSMA$^{(N9del)}$ CAR T cells incubated with [$^{18}$F]DCFPyL, a high affinity, positron-emitting ligand targeting PSMA; cell numbers were in the top row $10^3$, $2 \cdot 10^3$, $4 \cdot 10^3$, and $6 \cdot 10^3$, and in the bottom row $8 \cdot 10^3$, $10^4$, $2 \cdot 10^4$, and $4 \cdot 10^4$. Images were acquired using a SuperArgus small-animal PET/CT instrument from Sedecal. The data in the graph show results from the bottom row of images. The detection limit was determined to be around 2,000 cells. For experimental details see Minn et al. (2019). **(C,D)** PET *in vivo* imaging of human primary T-cells transduced with hNET **(C)** or hNIS **(D)** reporter genes. Different numbers of T-cells were injected subcutaneously, followed by systemic administration of indicated corresponding radiopharmaceuticals. PET imaging at indicated time points after radiotracer administration was performed using a Focus 120 microPET scanner from Siemens. Number of T-cells injected is (left dashed ring) $3 \cdot 10^5$ and (right dashed ring) $10^6$. No potentially interfering signals were thresholded and data are expressed as percentage injected dose per gram (%ID/g). For experimental details see Moroz et al. (2015). **(E)** NSG mice injected with the indicated number of CD19-tPSMA$^{N9del}$ CAR-T in 50 μL (50% Matrigel) in the shoulders (white arrows). Mice were *in vivo* imaged on the Sedecal's SuperArgus small-animal PET/CT at 1 h after administration of the corresponding radiotracer [$^{18}$F]DCFPyL. PET data are expressed in percentage of injected dose per cubic centimeter of tissue imaged (%ID/cc). To improve the display contrast of the *in vivo* images, relatively high renal radiotracer uptake was masked using a thresholding method. For experimental details see Minn et al. (2019). (Figure combined from the publications referenced in the legend above; permissions from corresponding publishers obtained).

the cell nucleus (Sahu et al., 1995). Consequently, cell labeling with agents directly releasing them into the cytosol such as [$^{111}$In]In-oxine could be more harmful than agents linking them to the cell surface. However, systematic comparative and quantitative studies on such radiobiological effects are not yet available in lymphocytes. Nevertheless, it can be safely assumed

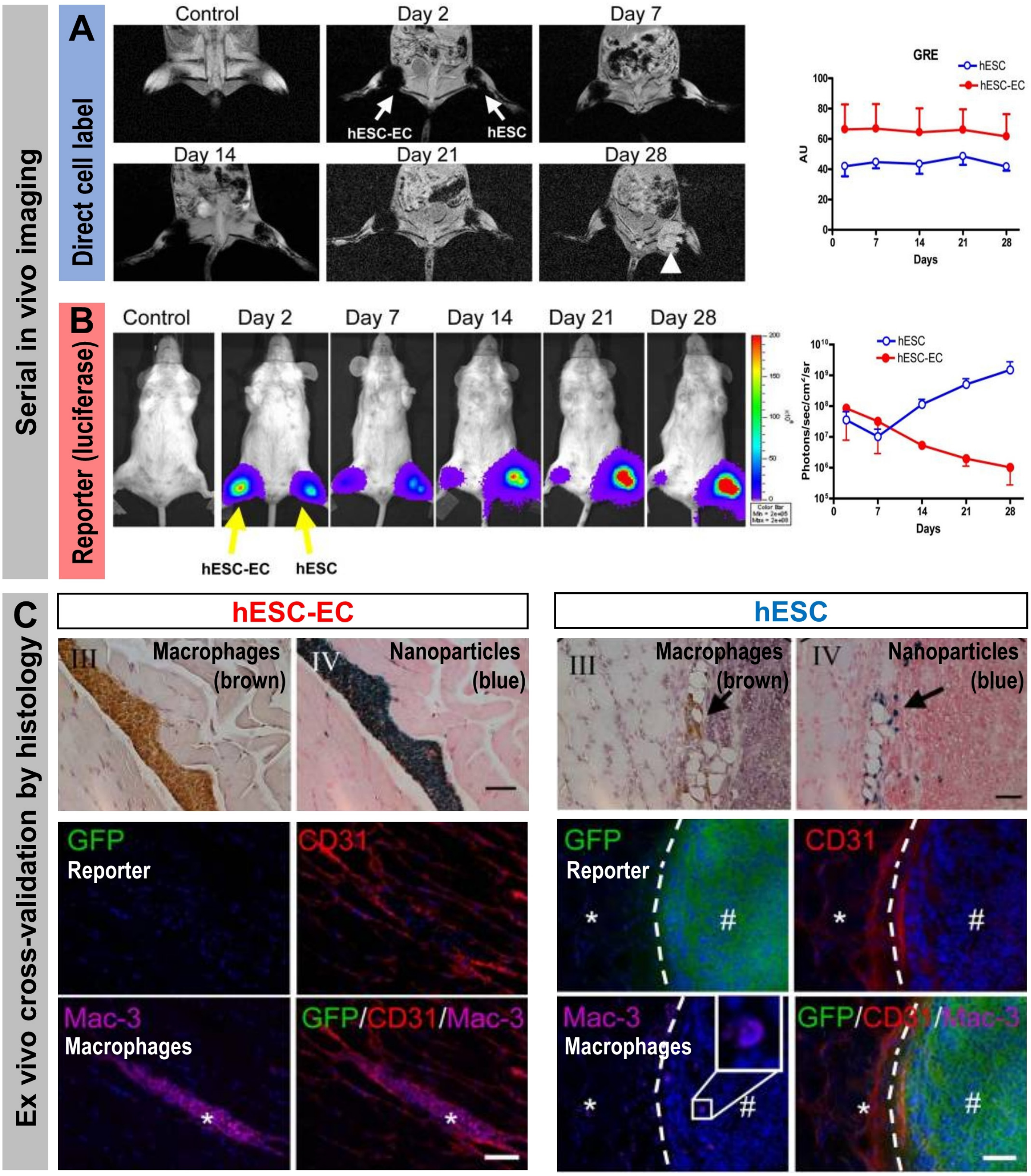


**FIGURE 6 |** How the type of cell labeling impacts on conclusions drawn from signals obtained from serial imaging. Cell viability can be assessed better from indirectly labeled cells than from directly labeled cells as shown by a cross-validation study using both direct and indirect cell labeling within the same cells. Reporter gene (luciferase and GFP)-expressing human embryonic stem cells (hES) or human embryonic stem cells differentiated to endothelial cells (hESC-EC) were directly labeled using iron oxide nanoparticles. **(A)** MRI imaging to track the directly loaded nanoparticle cell label *(A/left)* Serial *in vivo* MR [gradient-recalled echo (GRE)] images of iron oxide nanoparticles. No hypointense signal was found in control animals injected with unlabeled cells. MR signals showed no significant difference from day 2 to day 28 (the white arrow indicates teratoma formation in the hind limb injected with hES cells). *(A/right)* Quantitative analysis of GRE signals from all animals transplanted with hES cells and hESC-ECs [signal activity is expressed as authority unit (AU)]. **(B)** Tracking of the cells by virtue of reporter gene imaging (indirect cell labeling). *(B/left)* Planar bioluminescence imaging reveals differences in signals obtained from hind limbs that received either hES or hESC-EC cells. After initial similar signal decreases in both limbs, the signals from limbs with hES increased significantly over time, coinciding with teratoma formation in these limbs. *(B/right)* Quantification of 2D bioluminescence signals from each limb (photons/sec/cm$^2$/sr; note the log10 scale). **(C**, top**)** Immunohistochemical (IHC) analysis of initially double labeled hES cells and hESC-ECs clearly reveals iron oxide (by Prussian Blue) co-localizing with a macrophage stain (by specific antibody Mac-3); IHC counterstains were Nuclear Fast Red and Hematoxylin, respectively. Note that macrophages loaded with iron particles can be found in between muscle bundles.

*(Continued)*

**FIGURE 6 |** Continued
(**C**, bottom) Immunofluorescence staining of GFP for transplanted luciferase co-expressing hESC-ECs (left) or hESC (right). Other panels show respective counterstains for microvasculature (CD31) or macrophages (Mac-3); nuclei were stained with DAPI (blue) in merged images. All images are from four weeks after transplantation. There were no transplanted $GFP^+$ hESC-ECs found nearby macrophages. In tissues that received hES cells, $GFP^+$ hESC were found to form teratoma (#) but no Prussian Blue-stained nanoparticles were found in corresponding IHC regions. The dashed line separates teratoma from normal muscle fibers (*). All scale bars are 20 μm. (Figure modified with permission from Li et al., 2008).

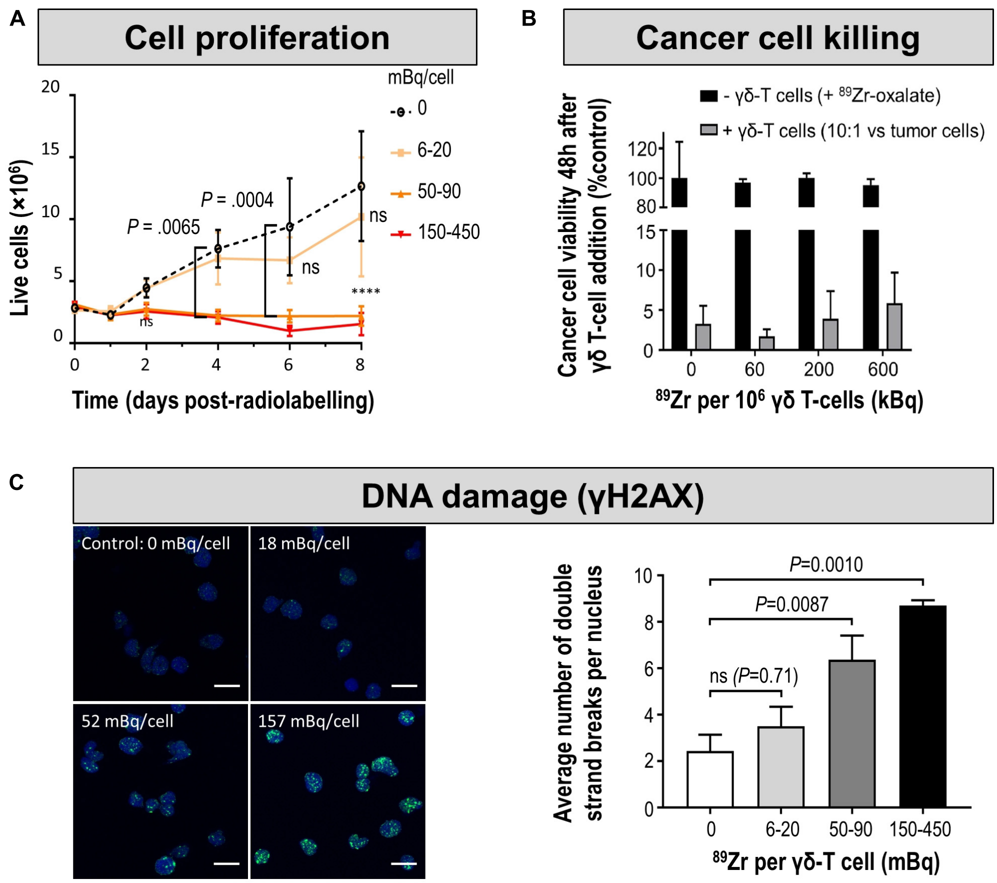


**FIGURE 7 |** Cell characterization after direct labeling of T-cells with [$^{89}$Zr]Zr-oxine. **(A)** *In vitro* proliferation of differently radiolabeled human γδ T-cells demonstrates that with higher amounts of cell label per cell, the capacity to proliferate diminishes. As expansion capacity is crucial for cell-based immunotherapy applications, it is paramount to perform such proliferation assays for sufficiently long times and quantify any differences even if they happen several days after cell labeling. **(B)** Tumor cell killing assay demonstrates that even γδ T-cells containing radioactivity levels incompatible with further expansion still retain at least part of their tumor killing function if supplied in sufficiently high amounts. Here, the authors reported this using a triple negative breast cancer cell line *in vitro* by quantifying tumor cell viability 48 h after immune cell addition. Notably, unchelated $^{89}$Zr supplied to tumor cells did not kill them and served as one of the controls. **(C)** *(left)* DNA damage analysis in radiolabeled human γδ T-cells. Representative images of γ-H2AX foci (green) and nuclei (blue); scale bars are 10 μm. *(right)* Cumulative data from the quantification of γ-H2AX foci per nuclei after radiolabelling. For statistical analysis of all data see Man et al. (2019), from where this figure is reproduced with modification and permission.

that great care must be taken when radiolabelling e.g. T-cells with radiometals, because irradiation is a successful method to deplete the immune system of lymphocytes indicating their distinct sensitivity to radiation (Manda et al., 2012; Piotrowski et al., 2018). Generally, the longer the half-life the larger the dose the labeled cells receive; and this is also valid for their *in vivo* environment which experiences crossfire from the labeled cells. Consequently, careful consideration of dosimetry is required as well as biological evaluation of radiation effects in radiolabeled cells. For example, [$^{89}$Zr]Zr-oxine labeled γδ T-cells were tracked to NIS-reporter gene expressing tumors visualized by $^{99m}TcO_4^-$ in breast xenograft murine models to determine if the immunostimulatory drug alendronate would result in enhanced tumor targeting by the administered γδ T-cells (Man et al., 2019). To achieve this, the authors first titrated cellular radioactivity amounts delivered into γδ T-cells and validated its impact on γδ T-cell viability/proliferation, occurrence of DNA double strand breaks and retention of tumor cell killing function (**Figure 7**). This resulted in an optimized radiolabelling regimen that was then used for *in vivo* cell tracking. Using a similar approach, others determined tumor targeting and tumor retention of [$^{89}$Zr]Zr-oxine-labeled CAR-T in a glioblastoma and prostate cancer animal model (Weist et al., 2018). The reported tolerated radioactivity levels in labeled cells were 20 mBq/cell for γδ T-cell and 70-80 mBq/cell for effector T-cells/CAR-T in these studies. Fundamentally, the tolerated radioactivity amounts limit the possible tracking time for such labeled cells.

As indirect cell tracking is based on repeat administration of short half-life radioisotopes (**Figure 3C**), total received doses are lower compared to direct cell labeling-afforded cell tracking over equivalent time spans. While radio damage is likely less of concern in this context, there are currently no systematic studies on radio damage of reporter-expressing lymphocytes incubated repeatedly with short half-life radiotracers available.

Another important aspect relates to the question of whether there is any impact of the typically very small administered radiotracer amounts ("tracer levels," "microdoses") on the corresponding target biology/physiology; in the context of this article for example whether imaging affects adoptively transferred immunotherapies. Generally accepted is the use of tracer level amounts, whereby a microdose is defined as "less than 1/100 of the dose of a test substance calculated (based on animal data) to yield a pharmacological effect of the test substance with a maximum dose of ≤100 μg or, in the case of biological agents, ≤30 nmol" (European Medicines Agency, 2004; VanBrocklin, 2008). However, there are studies available now, which should serve as a primer to investigate this matter more closely as molecules emerged that have biological effects at administered doses comparable to what is generally accepted as tracer level/microdose amounts. First, in a study aimed at radiotherapeutic evaluation of the human somatostatin receptor (hSSTr2) agonist [$^{90}$Y]Y-DOTATOC, it was found that the agonist impaired immune function in humans (Barsegian et al., 2015). Hence, it cannot be ruled out at this point that other somatostatin-related imaging agents also have effects on the immune system, and consequently this imaging agent might not be suitable to *in vivo* track hSSTr2 reporter expressing adoptively transferred T-cells. Moreover, a recent study reported that immunoPET performed to *in vivo* track adoptively transferred T-cells in tumor-bearing mice impacted on immunotherapy outcome (Mayer et al., 2018). The authors used $^{89}$Zr-DFO-conjugated anti-CD7 and anti-CD2 antibody fragments (F(ab')$_2$), respectively, to quantify adoptively transferred T-cell populations in tumors. While they did not find any impact of both imaging tracers on T-cells *in vitro*, they found that the anti-CD2 radiotracer caused severe T-cell depletion and abrogated the effects of the adoptively transferred T-cell immunotherapy (the anti-CD7 radiotracer performed as expected and had no impact on adoptively transferred T-cells). The amounts of radiolabeled antibody fragment used in this study were ∼9 μmol/kg [1 mg/kg F(ab')$_2$], which was, for example, about five times less compared to what was used in the seminal immunoPET study that originally developed the anti-CD8 *cis*-diabody (∼50 μmol/kg ≈ 3 mg/kg), which is now in clinical development (see Section "*In vivo* Imaging of T-Cell Populations"). From these two examples follows clearly that great care must be taken with imaging agents in the context of immunology even when used at amounts generally accepted to be in the range of what normally constitutes tracer levels/microdoses, because there can be effects on immune cells and their functions *in vivo*, depending on the chosen imaging target. Furthermore, this is strong evidence that *in vitro* experimentation might not be indicative of such effects. Moreover, this is also an argument for the need of careful comprehensive *in vivo* validation experiments in relevant animal models during the development of imaging agents, irrespective of whether envisaged to aid immunotherapy development or intended for future immunotherapy monitoring in the clinics.

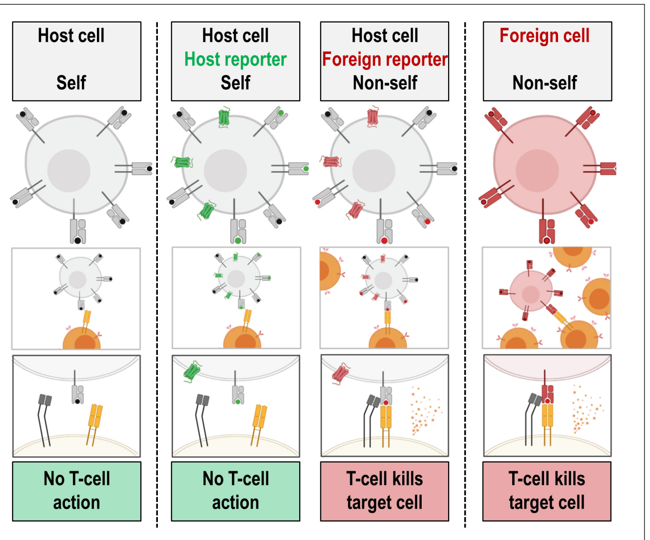


**FIGURE 8 |** Simplified cartoon illustrating one way of cytotoxic T-cells to recognize foreign reporter antigens. A variety of immune recognition mechanisms exist in mammals as part of their innate and adaptive immune system. Here, as a simplified example, recognition of antigen-presenting MHC class I molecules on target cells by a cytotoxic CD8$^{+}$ T-cells is visualized. The TCR (orange) of the cytotoxic CD8$^{+}$ T-cells recognizes foreign antigen presented on host MHC class I molecules (light gray with red foreign antigen) but not host antigen on host MHC class I molecules (green: antigen from host reporter; black: any other host antigen). Foreign MHC class I molecules are also recognized by CD8$^{+}$ T-cells. The T-cell co-receptor CD8 (dark gray) binds to MHC class I molecules upon TCR binding and the overall process activates CD8$^{+}$ T-cells. CD8$^{+}$ T-cell action results in granzyme and perforin release, and consequent killing of the corresponding target cell. Several mechanisms ensure that host antigens are not recognized; they include deletion of self-recognizing T-cells and tolerance conferred by regulatory T-cells. This simplified scheme demonstrates the importance to employ host reporters in experiments involving species with intact adaptive immunity.

## Immunogenicity and Contrast Are Linked in Reporter Gene Applications

For *in vivo* tracking of cell-based immunotherapies using reporter genes, immunogenicity of the reporter represents another very important aspect. It is linked to the achievable contrast at different body locations, which we explain in the following. For best contrast, a foreign reporter would appear ideal as it is expressed nowhere in the host organism guaranteeing good contrast. In animal disease models, such reporters are, for example, fluorescent proteins, luciferases (Mezzanotte et al., 2017) or the PET reporter herpes simplex virus 1 thymidine kinase (HSV1-*tk*) (Gambhir et al., 2000; Yaghoubi and Gambhir, 2006; Likar et al., 2009). All of them provide excellent contrast *in vivo* with varying sensitivities and spatial resolutions depending on the imaging modality used to probe them (cf. **Figure 1**). However, all of them are proteins foreign to mammals and consequently any cell expressing them in mammals can be detected and cleared by an intact host immune system (**Figure 8**). While this might represent only a minor issue if heavily immunocompromised animals are used, for example in human tumor xenograft models, it cannot be ignored in syngeneic models or the human clinical setting. While the foreign reporter (HSV1-*tk*) was used in the first proof-of-principle clinical reporter gene imaging study (Keu et al., 2017), this was performed in the setting of late-stage glioblastoma in heavily pre-treated patients, all of whom died within a year of the study start. In fact, immunogenicity of HSV1-*tk* has been well documented (Berger et al., 2006) and consequently HSV1-*tk* has been ruled out for reporter gene-afforded routine cell tracking of adoptive cell-based immunotherapies in humans; it should also not be considered for research in preclinical syngeneic models.

Immunogenicity issues can best be overcome by using host reporter proteins (**Table 2**) that are normally endogenously expressed in the organism of interest. Importantly, these host reporters should be endogenously expressed in only a very limited number of host tissues, only in tissues where signals do not interfere with the experimental goals, and ideally at low levels to ensure favorable contrast in adjacent organs (cf. different background patterns in **Figure 5**).

Mammalian NIS has been found to be useful as a radionuclide reporter if used together with non-iodine radiotracers, which results in better signal-to-background (Diocou et al., 2017). Generally in mammals, NIS is endogenously expressed at high levels in the thyroid gland and at lower levels in few extrathyroidal tissues (salivary glands, mammary glands, stomach and small intestine, testes) (Portulano et al., 2014). This means that for cell tracking applications in other organs the host reporter gene NIS provides excellent signal-to-background ratios when exogenously expressed in cells of interest. NIS has been used to track many different cell types preclinically (Sieger et al., 2003; Groot-Wassink et al., 2004; Che et al., 2005; Dingli et al., 2006; Merron et al., 2007; Terrovitis et al., 2008; Carlson et al., 2009; Higuchi et al., 2009; Fruhwirth et al., 2014; Diocou et al., 2017) including stem cell and CAR-T-cell therapies (Emami-Shahri et al., 2018; Kurtys et al., 2018; Ashmore-Harris et al., 2019). It has not yet been used in the clinic but due to its favorable properties and the readily available corresponding radiotracers for both PET and SPECT for its detection, it is a promising candidate for use in future clinical trials.

The human somatostatin receptor subtype 2 (hSSTr2) is another reporter with some potential for cell tracking using clinically approved PET tracers based on somatostatin analogs [e.g. [$^{68}$Ga]Ga-DOTATATE (antagonist) or [$^{68}$Ga]Ga-DOTATOC (agonist)] and it has been used preclinically for CAR-T tracking (Zhang et al., 2011; Vedvyas et al., 2016). A significant pitfall of hSSTr2 use as a reporter for immunotherapies is that it is expressed endogenously on various immune cell types including T-cells, B-cells and macrophages (Elliott et al., 1999). This negatively affects imaging specificity in immunocompetent models and likely humans. It is also expressed in the cerebrum, kidneys and also the gastrointestinal tract (Yamada et al., 1992). Moreover, it was found that the hSSTr2 agonist [$^{90}$Y]Y-DOTATOC impaired immune function in humans (Barsegian et al., 2015). Whilst radioactive contrast agent concentrations are very low, it cannot be ruled out without further studies that somatostatin analogs and their derivatives might also impair some immune system functions. Another important caveat of hSSTr2 use as a reporter is that it internalizes upon substrate binding (Oomen et al., 2001; Cescato et al., 2006) and this is likely to affect the detection sensitivity of hSSTr2-expressing cells through reduction of its steady-state concentration on the plasma membrane.

A very promising host reporter gene with very limited endogenous expression is PSMA (Castanares et al., 2014). It has been developed alongside PET radiotracers that were originally intended for molecular imaging of PSMA-expressing prostate cancer. PSMA is a type II plasma membrane protein that can be internalized upon ligand binding. It has a short cytoplasmic N-terminal tail, which is responsible for its internalization (Rajasekaran et al., 2003). N-terminally modified PSMA variants, $PSMA^{W2G}$ and $tPSMA^{N9del}$, were recently designed to prevent receptor internalization and to increase PSMA surface expression with the authors hypothesizing that would increase PET radiotracer binding and overall imaging sensitivity (Minn et al., 2019). Moreover, the $tPSMA^{N9del}$ variant lacks putative intracellular signaling motifs rendering it less likely to affect normal T-cell function. $tPSMA^{N9del}$ was used as a reporter to track CAR-T cells in a preclinical model of acute lymphoblastic leukemia by PET imaging with the radiotracer [$^{18}$F]DCFPyL (Minn et al., 2019). [$^{18}$F]DCFPyL is a radiotracer for PSMA, in fact a high-affinity PSMA ligand that can be produced in good quantities and with high specific activity (Ravert et al., 2016), and it has already been used in humans and is currently also in a phase II clinical trial for the detection of metastatic prostate cancer *via* PSMA (NCT03173924), another application that requires the detection of small amounts of cells.

Despite some notable advances in recent years, there is still significant room for improvement to optimize host reporter/tracer pairs, for example to improve signal-to-background, tailor them better to application in specific immune cells, and enhance the steady-state concentrations in traceable cells and thereby cell tracking sensitivity.

## CONCLUSION AND OUTLOOK

The development of both molecular and cell-based immunotherapies can be greatly assisted by *in vivo* imaging, which provided valuable insight into spatiotemporal dynamics of immune responses and the complex interactions of the tumor microenvironment. *In vivo* imaging has earned itself a place among the indispensable tools for immunotherapy development at preclinical stages, and many available molecular imaging technologies can be used for understanding the mechanisms governing immunotherapy function and to improve immunotherapy efficacy and safety. Newly identified relevant targets will require some degree of molecular imaging development to generate the relevant contrast agent, but multiple robust methodologies for turning target-specific biomolecules such as antibodies, antibody fragments/derivatives or peptides into contrast agents are already available. Various molecular imaging techniques aiding immunotherapy are currently at the brink of clinical application, mostly still in explorative studies, some in clinical trials, and they focus on early response monitoring with response prediction representing a major goal. Individual response monitoring at the patient level is particularly important as responses can be heterogeneous between lesions within the same individual and also between patients, rendering this a potential routine clinical application of molecular imaging in the future. A currently somewhat underexplored area is immunotherapy presence and action at secondary lesions. Preclinically, traceable cancer models would be very useful tools in this context, enabling *in vivo* quantification of therapy arrival and perhaps therapy action at the intended target sites. Clinically, molecular imaging will help inform on lesion heterogeneity as well as potential response heterogeneity in patients.

Cell-based immunotherapies represent an area in need of further development to unleash their full potential and render them more efficacious, safer to use, and more widely applicable. Therefore, it remains highly beneficial to better understand their *in vivo* distribution, behavior and fate, and to use such non-invasively acquired information to elucidate and tailor their mechanisms of action. Cell-based immunotherapies can be classified into two groups that (a) do not need genetic engineering for efficacy, and those that (b) fundamentally require genetic engineering (e.g. CAR-T, TCR-T).

The first group, which includes immunotherapies based on e.g. TILs and γδ T-cells, the choice between direct and indirect cell labeling depends on the precise research question, practicalities and of course whether clinical translation of the tracking methodology is envisaged and for what purpose. Implementing genetic engineering to enable indirect cell labeling to these therapies adds a significant regulatory burden and it is certainly difficult to justify the additional efforts required for the sole purpose of *in vivo* cell therapy tracking. Consequently, recently developed direct cell labeling approaches involving cell tracking by PET (e.g. γδ T-cell labeling with [$^{89}$Zr]Zr-oxine) are promising tools despite their obvious limitations caused by the cell labeling methodology itself (label efflux, label dilution, complex dosimetry, limited observation times). However, the situation is likely to improve through the development of total-body PET, which has been reported to be 40-times more sensitive than conventional PET (Cherry et al., 2018). This sensitivity advantage could either be invested into faster PET scanning or scanning with much less radioactivity. *In vivo* cell tracking studies using this new technology will reveal to what extent the sensitivity advantage of total-body PET can be used to extend the tracking time of directly labeled cells.

For cell-based immunotherapies that require genetic engineering, an immunocompatible host reporter gene can be implemented without adding to the regulatory burden. Indirect cell labeling is clearly advantageous over direct cell labeling in such cases as it enables longer-term monitoring, reflects cell proliferation/survival, and avoids complex dosimetry considerations during cell labeling. Genetic engineering technologies have been steadily advanced and include now viral as well as non-viral delivery methods as well as site-specific integration via gene editing approaches (**Figure 3C**). Moreover, the reporter gene can be co-delivered with other relevant components during genetic engineering of the cells as was previously demonstrated rendering CAR-T traceable by SPECT or PET (Emami-Shahri et al., 2018; Kurtys et al., 2018; Minn et al., 2019). If contrast agents can be used that match the reporter and are already clinically approved, this is obviously beneficial. Importantly, it is unlikely that a one-fits-all approach across cancers involving only one immunocompatible host reporter gene is viable. More likely, various cancers at different body locations with varying endogenous host reporter expression levels will be targeted by genetically engineered cell-based immunotherapies in which the targeting moiety as well as the host reporter must be tailored. Undoubtedly, more research into host reporter/contrast agent pairs is warranted to provide the most flexible tools to render these immunotherapies *in vivo* traceable with best contrast in a quantitative manner.

In summary, we described how *in vivo* imaging can aid the development of molecular and cell-based anti-cancer immunotherapies and explained a variety of methodological and experimental design aspects. Notably, these concepts can also be extrapolated to immunotherapies intended to treat other conditions, for example, in the fields of regenerative medicine (Naumova et al., 2014), transplantation (Afzali et al., 2013; Safinia et al., 2016), diabetes type I (Alhadj Ali et al., 2017; Smith and Peakman, 2018), multiple sclerosis (Chataway et al., 2018), and infectious diseases (Hotchkiss and Moldawer, 2014).

## AUTHOR CONTRIBUTIONS

GF contributed the article concept. Both authors compiled the figures, wrote the manuscript, and contributed to manuscript revision, read, and approved the submitted version.

## FUNDING

The authors received support from the Cancer Research UK (Multidisciplinary Project Award C48390/A21153 to GF) and EPSRC and GE Healthcare (Ph.D. studentship to MI). Further they are supported by the King's College London and UCL Comprehensive Cancer Imaging Centre, funded by Cancer Research UK and EPSRC; the National Institute for Health Research (NIHR) Biomedical Research Centre based at Guy's and

St Thomas' NHS Foundation Trust and King's College London; and the Wellcome/EPSRC Centre for Medical Engineering at King's College London [WT 203148/Z/16/Z]. Institutional Open Access funds to support article publication were also received. The views expressed are those of the authors and not necessarily those of the NHS, the NIHR, or the DoH.

## ACKNOWLEDGMENTS

We would like to thank Professsor Paul Marsden (King's College London) for his very helpful suggestions in editing the manuscript. **Figures 3**, **4**, **8** contain graphics that were created using software accessed on BioRender.com *via* MI's paid subscription.

## REFERENCES


Adonai, N., Adonai, N., Nguyen, K. N., Walsh, J., Iyer, M., Toyokuni, T., et al. (2002). Ex vivo cell labeling with 64Cu-pyruvaldehyde-bis(N4-methylthiosemicarbazone) for imaging cell trafficking in mice with positron-emission tomography. *Proc. Natl. Acad. Sci. U.S.A.* 99, 3030–3035. doi: 10.1073/pnas.052709599

Afzali, B., Edozie, F. C., Fazekasova, H., Scotta, C., Mitchell, P. J., Canavan, J. B., et al. (2013). Comparison of regulatory T cells in hemodialysis patients and healthy controls, implications for cell therapy in transplantation. *Clin. J. Am. Soc. Nephrol.* 8, 1396–1405. doi: 10.2215/CJN.12931212

Alam, I. S., Mayer, A. T., Sagiv-Barfi, I., Wang, K., Vermesh, O., Czerwinski, D. K., et al. (2018). Imaging activated T cells predicts response to cancer vaccines. *J. Clin. Invest.* 128, 2569–2580. doi: 10.1172/JCI98509

Alanentalo, T., Loren, C. E., Larefalk, A., Sharpe, J., Holmberg, D., and Ahlgren, U. (2008). High-resolution three-dimensional imaging of islet-infiltrate interactions based on optical projection tomography assessments of the intact adult mouse pancreas. *J. Biomed. Opt.* 13:054070. doi: 10.1117/1.3000430

Alhadj Ali, M., Liu, Y. F., Arif, S., Tatovic, D., Shariff, H., Gibson, V. B., et al. (2017). Metabolic and immune effects of immunotherapy with proinsulin peptide in human new-onset type 1 diabetes. *Sci. Transl. Med.* 9:eaaf7779. doi: 10.1126/scitranslmed.aaf7779

Alizadeh, A. A., Aranda, V., Bardelli, A., Blanpain, C., Bock, C., Borowski, C., et al. (2015). Toward understanding and exploiting tumor heterogeneity. *Nat. Med.* 21, 846–853. doi: 10.1038/nm.3915

Andreyev, A., and Celler, A. (2011). Dual-isotope PET using positron-gamma emitters. *Phys. Med, Biol.* 56, 4539–4556. doi: 10.1088/0031-9155/56/14/020

Anon (2014). *UNITED STATES of America, Appellee v. REGENERATIVE SCIENCES, LLC, A Corporation, et al., Appellants*. Toronto: Thomson Reuters.

Annovazzi, A., D'Alessandria, C., Bonanno, E., Mather, S. J., Cornelissen, B., van de Wiele, C., et al. (2006). Synthesis of 99mTc-HYNIC-interleukin-12, a new specific radiopharmaceutical for imaging T lymphocytes. *Eur. J. Nucl. Med. Mol. Imaging* 33, 474–482. doi: 10.1007/s00259-005-0001-6

Arranz, A., Dong, D., Zhu, S., Savakis, C., Tian, J., and Ripoll, J. (2014). In-vivo optical tomography of small scattering specimens, time-lapse 3D imaging of the head eversion process in Drosophila melanogaster. *Sci. Rep.* 4:7325. doi: 10.1038/srep07325

Ashmore-Harris, C., Blackford, S. J., Grimsdell, B., Kurtys, E., Glatz, M. C., Rashid, T. S., et al. (2019). Reporter gene-engineering of human induced pluripotent stem cells during differentiation renders in vivo traceable hepatocyte-like cells accessible. *Stem Cell Res.* 41:101599. doi: 10.1016/j.scr.2019.101599

Aswendt, M., Vogel, S., Schäfer, C., Jathoul, A., Pule, M., and Hoehn, M. (2019). Quantitative in vivo dual-color bioluminescence imaging in the mouse brain. *Neurophotonics* 6, 1–11.

Bansal, A., Pandey, M. K., Demirhan, Y. E., Nesbitt, J. J., Crespo-Diaz, R. J., Terzic, A., et al. (2015). Novel (89)Zr cell labeling approach for PET-based cell trafficking studies. *EJNMMI Res.* 5:19. doi: 10.1186/s13550-015-0098-y

Barat, B., Kenanova, V. E., Olafsen, T., and Wu, A. M. (2011). Evaluation of two internalizing carcinoembryonic antigen reporter genes for molecular imaging. *Mol. Imaging Biol.* 13, 526–535. doi: 10.1007/s11307-010-0375-0

Barsegian, V., Hueben, C., Mueller, S. P., Poeppel, T. D., Horn, P. A., Bockisch, A., et al. (2015). Impairment of lymphocyte function following yttrium-90 DOTATOC therapy. *Cancer Immunol. Immunother.* 64, 755–764. doi: 10.1007/s00262-015-1687-3

Bassi, A., Fieramonti, L., D'Andrea, C., Mione, M., and Valentini, G. (2011). In vivo label-free three-dimensional imaging of zebrafish vasculature with optical projection tomography. *J. Biomed. Opt.* 16:100502. doi: 10.1117/1.3640808

Basu, S., Hess, S., Nielsen Braad, P. E., Olsen, B. B., Inglev, S., and Hoilund-Carlsen, P. F. (2014). The Basic Principles of FDG-PET/CT Imaging. *PET Clin.* 9, 355–370. doi: 10.1016/j.cpet.2014.07.006

Bates, A., Power, C. A., and David, V. S. (2019). Goliath, the structure, function, and clinical prospects of antibody fragments. *Antibodies* 8:28. doi: 10.3390/antib8020028

Bensch, F., van der Veen, E. L., Lub-de Hooge, M. N., Jorritsma-Smit, A., Boellaard, R., Kok, I. C., et al. (2018). (89)Zr-atezolizumab imaging as a non-invasive approach to assess clinical response to PD-L1 blockade in cancer. *Nat. Med.* 24, 1852–1858. doi: 10.1038/s41591-018-0255-8

Berger, C., Flowers, M. E., Warren, E. H., and Riddell, S. R. (2006). Analysis of transgene-specific immune responses that limit the in vivo persistence of adoptively transferred HSV-TK-modified donor T cells after allogeneic hematopoietic cell transplantation. *Blood* 107, 2294–2302. doi: 10.1182/blood-2005-08-3503

Bhargava, K. K., Gupta, R. K., Nichols, K. J., and Palestro, C. J. (2009). In vitro human leukocyte labeling with (64)Cu, an intraindividual comparison with (111)In-oxine and (18)F-FDG. *Nucl. Med. Biol.* 36, 545–549. doi: 10.1016/j.nucmedbio.2009.03.001

Bressan, R. B., Dewari, P. S., Kalantzaki, M., Gangoso, E., Matjusaitis, M., Garcia-Diaz, C., et al. (2017). Efficient CRISPR/Cas9-assisted gene targeting enables rapid and precise genetic manipulation of mammalian neural stem cells. *Development* 144, 635–648. doi: 10.1242/dev.140855

Buck, M. D., O'Sullivan, D., Klein Geltink, R. I., Curtis, J. D., Chang, C. H., Sanin, D. E., et al. (2016). Mitochondrial dynamics controls T cell fate through metabolic programming. *Cell* 166, 63–76. doi: 10.1016/j.cell.2016.05.035

Cal-Gonzalez, J., Herraiz, J. L., Espana, S., Corzo, P. M., Vaquero, J. J., Desco, M., et al. (2013). Positron range estimations with PeneloPET. *Phys. Med. Biol.* 58, 5127–5152. doi: 10.1088/0031-9155/58/15/5127

Cal-Gonzalez, J., Lage, E., Herranz, E., Vicente, E., Udias, J. M., Moore, S. C., et al. (2015). Simulation of triple coincidences in PET. *Phys. Med. Biol.* 60, 117–136. doi: 10.1088/0031-9155/60/1/117

Carlson, S. K., Classic, K. L., Hadac, E. M., Dingli, D., Bender, C. E., Kemp, B. J., et al. (2009). Quantitative molecular imaging of viral therapy for pancreatic cancer using an engineered measles virus expressing the sodium-iodide symporter reporter gene. *AJR Am. J. Roentgenol.* 192, 279–287. doi: 10.2214/AJR.08.1205

Castanares, M. A., Mukherjee, A., Chowdhury, W. H., Liu, M., Chen, Y., Mease, R. C., et al. (2014). Evaluation of prostate-specific membrane antigen as an imaging reporter. *J. Nucl. Med.* 55, 805–811. doi: 10.2967/jnumed.113.134031

Caswell, D. R., and Swanton, C. (2017). The role of tumour heterogeneity and clonal cooperativity in metastasis, immune evasion and clinical outcome. *BMC Med.* 15:133. doi: 10.1186/s12916-017-0900-y

Catana, C. (2017). Principles of Simultaneous PET/MR Imaging. *Magn. Reson. Imaging Clin. N. Am.* 25, 231–243. doi: 10.1016/j.mric.2017.01.002

Cekanova, M., and Rathore, K. (2014). Animal models and therapeutic molecular targets of cancer, utility and limitations. *Drug Des. Devel. Ther.* 8, 1911–1921. doi: 10.2147/DDDT.S49584

Cescato, R., Schulz, S., Waser, B., Eltschinger, V., Rivier, J. E., Wester, H. J., et al. (2006). Internalization of sst2, sst3, and sst5 receptors, effects of somatostatin agonists and antagonists. *J. Nucl. Med.* 47, 502–511.

Charoenphun, P., Meszaros, L. K., Chuamsaamarkkee, K., Sharif-Paghaleh, E., Ballinger, J. R., Ferris, T. J., et al. (2015). [(89)Zr]oxinate4 for long-term in vivo cell tracking by positron emission tomography. *Eur. J. Nucl. Med. Mol. Imaging* 42, 278–287. doi: 10.1007/s00259-014-2945-x

Chataway, J., Martin, K., Barrell, K., Sharrack, B., Stolt, P., Wraith, D. C., et al. (2018). Effects of ATX-MS-1467 immunotherapy over 16 weeks in relapsing multiple sclerosis. *Neurology* 90, e955–e962. doi: 10.1212/WNL.0000000000005118

Chaudhuri, T. R., Rogers, B. E., Buchsbaum, D. J., Mountz, J. M., and Zinn, K. R. (2001). A noninvasive reporter system to image adenoviral-mediated gene transfer to ovarian cancer xenografts. *Gynecol. Oncol.* 83, 432–438. doi: 10.1006/gyno.2001.6333

Che, J., Doubrovin, M., Serganova, I., Ageyeva, L., Zanzonico, P., and Blasberg, R. (2005). hNIS-IRES-eGFP dual reporter gene imaging. *Mol. Imaging* 4, 128–136.

Cheddad, A., Svensson, C., Sharpe, J., Georgsson, F., and Ahlgren, U. (2012). Image processing assisted algorithms for optical projection tomography. *IEEE Trans. Med. Imaging* 31, 1–15. doi: 10.1109/TMI.2011.2161590

Cherry, S. R., Jones, T., Karp, J. S., Qi, J., Moses, W. W., and Badawi, R. D. (2018). Total-body PET, maximizing sensitivity to create new opportunities for clinical research and patient care. *J. Nucl. Med.* 59, 3–12. doi: 10.2967/jnumed.116.184028

Cho, I. K., Moran, S. P., Paudyal, R., Piotrowska-Nitsche, K., Cheng, P.-H., Zhang, X., et al. (2014). Longitudinal monitoring of stem cell grafts in vivo using magnetic resonance imaging with inducible maga as a genetic reporter. *Theranostics* 4, 972–989. doi: 10.7150/thno.9436

Chuang, K. H., Wang, H. E., Cheng, T. C., Tzou, S. C., Tseng, W. L., Hung, W. C., et al. (2010). Development of a universal anti-polyethylene glycol reporter gene for noninvasive imaging of PEGylated probes. *J. Nucl. Med.* 51, 933–941. doi: 10.2967/jnumed.109.071977

Claus, C., Ferrara, C., Xu, W., Sam, J., Lang, S., Uhlenbrock, F., et al. (2019). Tumor-targeted 4-1BB agonists for combination with T cell bispecific antibodies as off-the-shelf therapy. *Sci. Transl. Med.* 11: eaav5989. doi: 10.1126/scitranslmed.aav5989

Cohen, B., Dafni, H., Meir, G., Harmelin, A., and Neeman, M. (2005). Ferritin as an endogenous MRI reporter for noninvasive imaging of gene expression in C6 glioma tumors. *Neoplasia* 7, 109–117. doi: 10.1593/neo.04436

Conti, M., and Eriksson, L. (2016). Physics of pure and non-pure positron emitters for PET, a review and a discussion. *EJNMMI Phys.* 3:8. doi: 10.1186/s40658-016-0144-5

Dai, G., Levy, O., and Carrasco, N. (1996). Cloning and characterization of the thyroid iodide transporter. *Nature* 379, 458–460. doi: 10.1038/379458a0

Darvin, P., Toor, S. M., Sasidharan Nair, V., and Elkord, E. (2018). Immune checkpoint inhibitors, recent progress and potential biomarkers. *Exp. Mol. Med.* 50:165. doi: 10.1038/s12276-018-0191-1

de Vries, E. F., Roca, M., Jamar, F., Israel, O., and Signore, A. (2010). Guidelines for the labelling of leucocytes with (99m)Tc-HMPAO. Inflammation/Infection Taskgroup of the European Association of Nuclear Medicine. *Eur. J. Nucl. Med. Mol. Imaging* 37, 842–848. doi: 10.1007/s00259-010-1394-4

Deleye, S., Van Holen, R., Verhaeghe, J., Vandenberghe, S., Stroobants, S., and Staelens, S. (2013). Performance evaluation of small-animal multipinhole muSPECT scanners for mouse imaging. *Eur. J. Nucl. Med Mol Imaging.* 40, 744–758. doi: 10.1007/s00259-012-2326-2

Deliolanis, N. C., Ale, A., Morscher, S., Burton, N. C., Schaefer, K., Radrich, K., et al. (2014). Deep-tissue reporter-gene imaging with fluorescence and optoacoustic tomography, a performance overview. *Mol. Imaging Biol.* 16, 652–660. doi: 10.1007/s11307-014-0728-1

Dhawan, R. T., and Peters, A. M. (2014). Withdrawal of indium-111, implications for white-cell imaging. The nuclear medicine community must act. *Nucl. Med. Commun.* 35, 789–791. doi: 10.1097/mnm.0000000000000138

Di Gialleonardo, V., Signore, A., Glaudemans, A. W., Dierckx, R. A., and De Vries, E. F. (2012). N-(4-18F-fluorobenzoyl)interleukin-2 for PET of human-activated T lymphocytes. *J. Nucl. Med.* 53, 679–686. doi: 10.2967/jnumed.111.091306

Dingli, D., Kemp, B. J., O'Connor, M. K., Morris, J. C., Russell, S. J., and Lowe, V. J. (2006). Combined I-124 positron emission tomography/computed tomography imaging of NIS gene expression in animal models of stably transfected and intravenously transfected tumor. *Mol. Imaging Biol.* 8, 16–23. doi: 10.1007/s11307-005-0025-0

Diocou, S., Volpe, A., Jauregui-Osoro, M., Boudjemeline, M., Chuamsaamarkkee, K., Man, F., et al. (2017). [(18)F]tetrafluoroborate-PET/CT enables sensitive tumor and metastasis in vivo imaging in a sodium iodide symporter-expressing tumor model. *Sci. Rep.* 7:946. doi: 10.1038/s41598-017-01044-4

Dohan, O., De la Vieja, A., Paroder, V., Riedel, C., Artani, M., Reed, M., et al. (2003). The sodium/iodide Symporter (NIS), characterization, regulation, and medical significance. *Endocr. Rev.* 24, 48–77. doi: 10.1210/er.2001-0029

Dunlap, P. (2014). Biochemistry and genetics of bacterial bioluminescence. *Adv. Biochem. Eng. Biotechnol.* 144, 37–64. doi: 10.1007/978-3-662-43385-0_2

Edmonds, S., Volpe, A., Shmeeda, H., Parente-Pereira, A. C., Radia, R., Baguna-Torres, J., et al. (2016). Exploiting the metal-chelating properties of the drug cargo for in vivo positron emission tomography imaging of liposomal nanomedicines. *ACS Nano* 10, 10294–10307. doi: 10.1021/acsnano.6b05935

Eisenhauer, E. A., Therasse, P., Bogaerts, J., Schwartz, L. H., Sargent, D., Ford, R., et al. (2009). New response evaluation criteria in solid tumours, revised RECIST guideline (version 1.1). *Eur. J. Cancer* 45, 228–247. doi: 10.1016/j.ejca.2008.10.026

Elliott, D. E., Li, J., Blum, A. M., Metwali, A., Patel, Y. C., and Weinstock, J. V. (1999). SSTR2A is the dominant somatostatin receptor subtype expressed by inflammatory cells, is widely expressed and directly regulates T cell IFN-gamma release. *Eur. J. Immunol.* 29, 2454–2463. doi: 10.1002/(sici)1521-4141(199908)29:08<2454::aid-immu2454>3.0.co;2-h

Emami-Shahri, N., Foster, J., Kashani, R., Gazinska, P., Cook, C., Sosabowski, J., et al. (2018). Clinically compliant spatial and temporal imaging of chimeric antigen receptor T-cells. *Nat. Commun.* 9:1081. doi: 10.1038/s41467-018-03524-1

European Medicines Agency. (2004). *Position Paper on Non-Clinical Safety Studies to Support Clinical Trials with A Single Microdose*. Amsterdam: European Medicines Agency

Farhadi, A., Ho, G. H., Sawyer, D. P., Bourdeau, R. W., and Shapiro, M. G. (2019). Ultrasound imaging of gene expression in mammalian cells. *Science* 365:1469. doi: 10.1126/science.aax4804

Farrar, C. T., Buhrman, J. S., Liu, G., Kleijn, A., Lamfers, M. L., McMahon, M. T., et al. (2015). Establishing the lysine-rich protein CEST reporter gene as a CEST MR imaging detector for oncolytic virotherapy. *Radiology* 275, 746–754. doi: 10.1148/radiol.14140251

Feng, Y., Roy, A., Masson, E., Chen, T. T., Humphrey, R., and Weber, J. S. (2013). Exposure-response relationships of the efficacy and safety of ipilimumab in patients with advanced melanoma. *Clin. Cancer Res.* 19, 3977–3986. doi: 10.1158/1078-0432.CCR-12-3243

Filonov, G. S., Piatkevich, K. D., Ting, L.-M., Zhang, J., Kim, K., and Verkhusha, V. V. (2011). Bright and stable near-infrared fluorescent protein for in vivo imaging. *Nat. Biotechnol.* 29:757. doi: 10.1038/nbt.1918

Fisher, B., Packard, B. S., Read, E. J., Carrasquillo, J. A., Carter, C. S., Topalian, S. L., et al. (1989). Tumor localization of adoptively transferred indium-111 labeled tumor infiltrating lymphocytes in patients with metastatic melanoma. *J. Clin. Oncol.* 7, 250–261. doi: 10.1200/jco.1989.7.2.250

Fowler, A. V., and Zabin, I. (1977). The amino acid sequence of beta-galactosidase of *Escherichia coli*. *Proc. Natl Acad. Sci. U. S. A.* 74, 1507–1510. doi: 10.1073/pnas.74.4.1507

Freise, A. C., and Wu, A. M. (2015). In vivo imaging with antibodies and engineered fragments. *Mol. Immunol.* 67, 142–152. doi: 10.1016/j.molimm.2015.04.001

Freise, A. C., Zettlitz, K. A., Salazar, F. B., Lu, X., Tavare, R., and Wu, A. M. (2017). ImmunoPET Imaging of Murine CD4(+) T Cells Using Anti-CD4 Cys-Diabody, Effects of Protein Dose on T Cell Function and Imaging. *Mol. Imaging Biol.* 19, 599–609. doi: 10.1007/s11307-016-1032-z

Fruhwirth, G. O., Diocou, S., Blower, P. J., Ng, T., and Mullen, G. E. (2014). A whole-body dual-modality radionuclide optical strategy for preclinical imaging of metastasis and heterogeneous treatment response in different microenvironments. *J. Nucl. Med.* 55, 686–694. doi: 10.2967/jnumed.113.127480

Fukuda, A., Honda, S., Fujioka, N., Sekiguchi, Y., Mizuno, S., Miwa, Y., et al. (2019). Non-invasive in vivo imaging of UCP1 expression in live mice via near-infrared fluorescent protein iRFP720. *PLoS One* 14:e0225213. doi: 10.1371/journal.pone.0225213

Gambhir, S. S., Bauer, E., Black, M. E., Liang, Q., Kokoris, M. S., Barrio, J. R., et al. (2000). A mutant herpes simplex virus type 1 thymidine kinase reporter gene shows improved sensitivity for imaging reporter gene expression with positron emission tomography. *Proc. Natl. Acad. Sci. U.S.A.* 97, 2785–2790. doi: 10.1073/pnas.97.6.2785

Garcia, J., Tang, T., and Louie, A. Y. (2015). Nanoparticle-based multimodal PET/MRI probes. *Nanomedicine* 10, 1343–1359. doi: 10.2217/nnm.14.224

Gawne, P., Man, F., Fonslet, J., Radia, R., Bordoloi, J., Cleveland, M., et al. (2018). Manganese-52, applications in cell radiolabelling and liposomal nanomedicine PET imaging using oxine (8-hydroxyquinoline) as an ionophore. *Dalton. Trans.* 47, 9283–9293. doi: 10.1039/c8dt00100f

Genove, G., DeMarco, U., Xu, H., Goins, W. F., and Ahrens, E. T. (2005). A new transgene reporter for in vivo magnetic resonance imaging. *Nat. Med.* 11, 450–454. doi: 10.1038/nm1208

Germain-Genevois, C., Garandeau, O., and Couillaud, F. (2016). Detection of brain tumors and systemic metastases using NanoLuc and fluc for dual reporter imaging. *Mol. Imaging Biol.* 18, 62–69. doi: 10.1007/s11307-015-0864-2

Gibson, H. M., McKnight, B. N., Malysa, A., Dyson, G., Wiesend, W. N., McCarthy, C. E., et al. (2018). IFNgamma PET imaging as a predictive tool for monitoring response to tumor immunotherapy. *Cancer Res.* 78, 5706–5717. doi: 10.1158/0008-5472.CAN-18-0253

Gilad, A. A., McMahon, M. T., Walczak, P., Winnard, P. T. Jr., Raman, V., Van Laarhoven, H. W., et al. (2007). Artificial reporter gene providing MRI contrast based on proton exchange. *Nat. Biotechnol.* 25:217. doi: 10.1038/nbt1277

Girgis, M. D., Olafsen, T., Kenanova, V., McCabe, K. E., Wu, A. M., and Tomlinson, J. S. (2011). Targeting CEA in pancreas cancer xenografts with a mutated scFv-Fc antibody fragment. *EJNMMI Res.* 1, 24. doi: 10.1186/2191-219X-1-24

Gleave, J. A., Wong, M. D., Dazai, J., Altaf, M., Henkelman, R. M., Lerch, J. P., et al. (2012). Neuroanatomical phenotyping of the mouse brain with three-dimensional autofluorescence imaging. *Physiol. Genomics* 44, 778–785. doi: 10.1152/physiolgenomics.00055.2012

Goldman, S. J., Chen, E., Taylor, R., Zhang, S., Petrosky, W., Reiss, M., et al. (2011). Use of the ODD-luciferase transgene for the non-invasive imaging of spontaneous tumors in mice. *PLoS One* 6:e18269. doi: 10.1371/journal.pone.0018269

Gomez-Cuadrado, L., Tracey, N., Ma, R., Qian, B., and Brunton, V. G. (2017). Mouse models of metastasis, progress and prospects. *Dis. Model Mech.* 10, 1061–1074. doi: 10.1242/dmm.030403

Graves, E. E., Weissleder, R., and Ntziachristos, V. (2004). Fluorescence molecular imaging of small animal tumor models. *Curr. Mol. Med.* 4, 419–430. doi: 10.2174/1566524043360555

Green, O., Gnaim, S., Blau, R., Eldar-Boock, A., Satchi-Fainaro, R., and Shabat, D. (2017). Near-infrared dioxetane luminophores with direct chemiluminescence emission mode. *J. Am. Chem. Soc.* 139, 13243–13248. doi: 10.1021/jacs.7b08446

Greenwood, H. E., Nyitrai, Z., Mocsai, G., Hobor, S., and Witney, T. H. (2019). High throughput PET/CT imaging using a multiple mouse imaging system. *J. Nucl. Med.* 61, 292–297. doi: 10.2967/jnumed.119.228692

Griessinger, C. M., Kehlbach, R., Bukala, D., Wiehr, S., Bantleon, R., Cay, F., et al. (2014). In vivo tracking of Th1 cells by PET reveals quantitative and temporal distribution and specific homing in lymphatic tissue. *J. Nucl. Med.* 55, 301–307. doi: 10.2967/jnumed.113.126318

Griessinger, C. M., Maurer, A., Kesenheimer, C., Kehlbach, R., Reischl, G., Ehrlichmann, W., et al. (2015). 64Cu antibody-targeting of the T-cell receptor and subsequent internalization enables in vivo tracking of lymphocytes by PET. *Proc. Natl. Acad. Sci. U.S.A* 112, 1161–1166. doi: 10.1073/pnas.1418391112

Griffin, T. W., Brill, A. B., Stevens, S., Collins, J. A., Bokhari, F., Bushe, H., et al. (1991). Initial clinical study of indium-111-labeled clone 110 anticarcinoembryonic antigen antibody in patients with colorectal cancer. *J. Clin. Oncol.* 9, 631–640. doi: 10.1200/jco.1991.9.4.631

Griffith, K. D., Read, E. J., Carrasquillo, J. A., Carter, C. S., Yang, J. C., Fisher, B., et al. (1989). In vivo distribution of adoptively transferred indium-111-labeled tumor infiltrating lymphocytes and peripheral blood lymphocytes in patients with metastatic melanoma. *J. Natl. Cancer Inst.* 81, 1709–1717. doi: 10.1093/jnci/81.22.1709

Grimfors, G., Schnell, P. O., Holm, G., Johansson, B., Mellstedt, H., Pihlstedt, P., et al. (1989). Tumour imaging of indium-111 oxine-labelled autologous lymphocytes as a staging method in Hodgkin's disease. *Eur. J. Haematol.* 42, 276–283. doi: 10.1111/j.1600-0609.1989.tb00112.x

Groot-Wassink, T., Aboagye, E. O., Wang, Y., Lemoine, N. R., Keith, W. N., and Vassaux, G. (2004). Noninvasive imaging of the transcriptional activities of human telomerase promoter fragments in mice. *Cancer Res.* 64, 4906–4911. doi: 10.1158/0008-5472.can-04-0426

Guo, Y., Hui, C.-Y., Liu, L., Zheng, H.-Q., and Wu, H.-M. (2019). Improved Monitoring of Low-Level Transcription in *Escherichia coli* by a β-Galactosidase α-Complementation System. *Front. Microbiol.* 10:1454. doi: 10.3389/fmicb.2019.01454

Gupta, S., Utoft, R., Hasseldam, H., Schmidt-Christensen, A., Hannibal, T. D., Hansen, L., et al. (2013). Global and 3D spatial assessment of neuroinflammation in rodent models of Multiple Sclerosis. *PLoS One* 8:e76330. doi: 10.1371/journal.pone.0076330

Hall, M. P., Unch, J., Binkowski, B. F., Valley, M. P., Butler, B. L., Wood, M. G., et al. (2012). Engineered luciferase reporter from a deep sea shrimp utilizing a novel imidazopyrazinone substrate. *ACS Chem. Biol.* 7, 1848–1857. doi: 10.1021/cb3002478

Hammarstrom, S. (1999). The carcinoembryonic antigen (CEA) family, structures, suggested functions and expression in normal and malignant tissues. *Semin. Cancer Biol.* 9, 67–81. doi: 10.1006/scbi.1998.0119

Haywood, T., Beinat, C., Gowrishankar, G., Patel, C. B., Alam, I. S., Murty, S., et al. (2019). Positron emission tomography reporter gene strategy for use in the central nervous system. *Proc. Natl. Acad. Sci. U.S.A.* 116, 11402–11407. doi: 10.1073/pnas.1901645116

Heskamp, S., Wierstra, P. J., Molkenboer-Kuenen, J. D. M., Sandker, G. W., Thordardottir, S., Cany, J., et al. (2019). PD-L1 microSPECT/CT imaging for longitudinal monitoring of PD-L1 expression in syngeneic and humanized mouse models for cancer. *Cancer Immunol. Res.* 7, 150–161. doi: 10.1158/2326-6066.CIR-18-0280

Higashikawa, K., Yagi, K., Watanabe, K., Kamino, S., Ueda, M., Hiromura, M., et al. (2014). 64Cu-DOTA-anti-CTLA-4 mAb enabled PET visualization of CTLA-4 on the T-cell infiltrating tumor tissues. *PLoS One* 9:e109866. doi: 10.1371/journal.pone.0109866

Higuchi, T., Anton, M., Saraste, A., Dumler, K., Pelisek, J., Nekolla, S. G., et al. (2009). Reporter gene PET for monitoring survival of transplanted endothelial progenitor cells in the rat heart after pretreatment with VEGF and atorvastatin. *J. Nucl. Med.* 50, 1881–1886. doi: 10.2967/jnumed.109.067801

Hodi, F. S., O'Day, S. J., McDermott, D. F., Weber, R. W., Sosman, J. A., Haanen, J. B., et al. (2010). Improved survival with ipilimumab in patients with metastatic melanoma. *N. Engl. J. Med.* 363, 711–723. doi: 10.1056/NEJMoa1003466

Hong, H., Sun, J., and Cai, W. (2008). Radionuclide-based cancer imaging targeting the carcinoembryonic antigen. *Biomark Insights* 3, 435–451.

Hotchkiss, R. S., and Moldawer, L. L. (2014). Parallels between cancer and infectious disease. *N. Engl. J. Med.* 371, 380–383. doi: 10.1056/nejmcibr1404664

Hunt, E. A., Moutsiopoulou, A., Ioannou, S., Ahern, K., Woodward, K., Dikici, E., et al. (2016). Truncated variants of gaussia luciferase with tyrosine linker for site-specific bioconjugate applications. *Sci. Rep.* 6:26814. doi: 10.1038/srep26814

Hwang, D. W., Kang, J. H., Chang, Y. S., Jeong, J. M., Chung, J. K., Lee, M. C., et al. (2007). Development of a dual membrane protein reporter system using sodium iodide symporter and mutant dopamine D2 receptor transgenes. *J. Nucl. Med.* 48, 588–595. doi: 10.2967/jnumed.106.036533

Inoue, Y., Sheng, F., Kiryu, S., Watanabe, M., Ratanakanit, H., Izawa, K., et al. (2011). Gaussia luciferase for bioluminescence tumor monitoring in comparison with firefly luciferase. *Mol. Imaging* 10:7290. doi: 10.2310/7290.2010.00057

Isomura, M., Yamada, K., Noguchi, K., and Nishizono, A. (2017). Near-infrared fluorescent protein iRFP720 is optimal for in vivo fluorescence imaging of rabies virus infection. *J. Gen. Virol.* 98, 2689–2698. doi: 10.1099/jgv.0.000950

James, M. L., and Gambhir, S. S. (2012). A molecular imaging primer, modalities, imaging agents, and applications. *Physiol. Rev.* 92, 897–965. doi: 10.1152/physrev.00049.2010

Jang, S. J., Kang, J. H., Kim, K. I., Lee, T. S., Lee, Y. J., Lee, K. C., et al. (2010). Application of bioluminescence imaging to therapeutic intervention of herpes simplex virus type I–Thymidine kinase/ganciclovir in glioma. *Cancer Lett.* 297, 84–90. doi: 10.1016/j.canlet.2010.04.028

Jang, S. J., Lee, Y. J., Lim, S., Kim, K. I., Lee, K. C., An, G. I., et al. (2012). Imaging of a localized bacterial infection with endogenous thymidine kinase using radioisotope-labeled nucleosides. *Int. J. Med. Microbio.* 302, 101–107. doi: 10.1016/j.ijmm.2011.11.002

Jauregui-Osoro, M., Sunassee, K., Weeks, A. J., Berry, D. J., Paul, R. L., Cleij, M., et al. (2010). Synthesis and biological evaluation of [F-18]tetrafluoroborate, a PET imaging agent for thyroid disease and reporter gene imaging of the sodium/iodide symporter. *Eur. J. Nucl. Med. Mol. Imaging* 37, 2108–2116. doi: 10.1007/s00259-010-1523-0

Jauw, Y. W. S., Bensch, F., Brouwers, A. H., Hoekstra, O. S., Zijlstra, J. M., Pieplenbosch, S., et al. (2019). Interobserver reproducibility of tumor uptake quantification with (89)Zr-immuno-PET, a multicenter analysis. *Eur. J. Nucl. Med. Mol. Imaging* 46, 1840–1849. doi: 10.1007/s00259-019-04377-6

Jiang, H., Bansal, A., Goyal, R., Peng, K.-W., Russell, S. J., and DeGrado, T. R. (2018). Synthesis and evaluation of 18F-hexafluorophosphate as a novel PET probe for imaging of sodium/iodide symporter in a murine C6-glioma tumor model. *Bioorg. Med. Chem.* 26, 225–231. doi: 10.1016/j.bmc.2017.11.034

Jiang, T., Du, L., and Li, M. (2016). Lighting up bioluminescence with coelenterazine, strategies and applications. *Photochem. Photobiol. Sci.* 15, 466–480. doi: 10.1039/c5pp00456j

Jung, W., Kim, J., Jeon, M., Chaney, E. J., Stewart, C. N., and Boppart, S. A. (2011). Handheld optical coherence tomography scanner for primary care diagnostics. *IEEE Trans. Biomed. Eng.* 58, 741–744. doi: 10.1109/TBME.2010.2096816

Kelly, M. P., Tavare, R., Giurleo, J., Makonnen, S., Hickey, C., Danton, M., et al. (2018). "Immuno-PET detection of LAG-3 expressing intratumoral lymphocytes using the zirconium-89 radiolabeled fully human anti-LAG-3 antibody REGN3767," in *American Association for Cancer Research Annual Meeting*, Chicago.

Kenanova, V., Barat, B., Olafsen, T., Chatziioannou, A., Herschman, H. R., Braun, J., et al. (2009). Recombinant carcinoembryonic antigen as a reporter gene for molecular imaging. *Eur. J. Nucl. Med. Mol. Imaging* 36, 104–114. doi: 10.1007/s00259-008-0921-z

Keu, K. V., Witney, T. H., Yaghoubi, S., Rosenberg, J., Kurien, A., Magnusson, R., et al. (2017). Reporter gene imaging of targeted T cell immunotherapy in recurrent glioma. *Sci. Transl. Med.* 9: eaag2196. doi: 10.1126/scitranslmed.aag2196

Khmelinskii, A., Meurer, M., Ho, C. T., Besenbeck, B., Fuller, J., Lemberg, M. K., et al. (2016). Incomplete proteasomal degradation of green fluorescent proteins in the context of tandem fluorescent protein timers. *Mol. Biol. Cell* 27, 360–370. doi: 10.1091/mbc.E15-07-0525

Khoshnevisan, A., Chuamsaamarkkee, K., Boudjemeline, M., Jackson, A., Smith, G. E., Gee, A. D., et al. (2017). 18F-Fluorosulfate for PET Imaging of the sodium-iodide symporter, synthesis and biologic evaluation in vitro and in vivo. *J. Nucl. Med.* 58, 156–161. doi: 10.2967/jnumed.116.177519

Khoshnevisan, A., Jauregui-Osoro, M., Shaw, K., Torres, J. B., Young, J. D., Ramakrishnan, N. K., et al. (2016). [(18)F]tetrafluoroborate as a PET tracer for the sodium/iodide symporter, the importance of specific activity. *EJNMMI Res.* 6:34. doi: 10.1186/s13550-016-0188-5

Kim, R., Keam, B., Kim, S., Kim, M., Kim, S. H., Kim, J. W., et al. (2019). Differences in tumor microenvironments between primary lung tumors and brain metastases in lung cancer patients, therapeutic implications for immune checkpoint inhibitors. *BMC Cancer* 19:19. doi: 10.1186/s12885-018-5214-8

Kircher, M. F., Gambhir, S. S., and Grimm, J. (2011). Noninvasive cell-tracking methods. *Nat. Rev. Clin. Oncol.* 8, 677–688. doi: 10.1038/nrclinonc.2011.141

Kleinovink, J. W., Mezzanotte, L., Zambito, G., Fransen, M. F., Cruz, L. J., Verbeek, J. S., et al. (2018). A dual-color bioluminescence reporter mouse for simultaneous in vivo imaging of t cell localization and function. *Front. Immunol.* 9:3097. doi: 10.3389/fimmu.2018.03097

Kogai, T., and Brent, G. A. (2012). The sodium iodide symporter (NIS), regulation and approaches to targeting for cancer therapeutics. *Pharmacol. Ther.* 135, 355–370. doi: 10.1016/j.pharmthera.2012.06.007

Kremers, G.-J., Hazelwood, K. L., Murphy, C. S., Davidson, M. W., and Piston, D. W. (2009). Photoconversion in orange and red fluorescent proteins. *Nature Methods* 6:355. doi: 10.1038/nmeth.1319

Krueger, M. A., Cotton, J. M., Zhou, B., Wolter, K., Schwenck, J., Kuehn, A., et al. (2019). Abstract 1146, [18F]FPyGal, A novel ß-galactosidase specific PET tracer for in vivo imaging of tumor senescence. *Cancer Res.* 79, 1118–1146.

Krumholz, A., VanVickle-Chavez, S. J., Yao, J., Fleming, T. P., Gillanders, W. E., and Wang, L. V. (2011). Photoacoustic microscopy of tyrosinase reporter gene in vivo. *J. Biomed. Opt.* 16:080503. doi: 10.1117/1.3606568

Kurland, B. F., Peterson, L. M., Lee, J. H., Schubert, E. K., Currin, E. R., Link, J. M., et al. (2017). Estrogen receptor binding (18F-FES PET) and glycolytic activity (18F-FDG PET) predict progression-free survival on endocrine therapy in patients with ER+ breast cancer. *Clin. Cancer Res.* 23, 407–415. doi: 10.1158/1078-0432.CCR-16-0362

Kurtys, E., Lim, L., Man, F., Volpe, A., and Fruhwirth, G. (2018). In vivo tracking of CAR-T by [18f]BF4- PET/CT in human breast cancer xenografts reveals differences in CAR-T tumour retention. *Cytotherapy* 20:S20.

La Barbera, G., Capriotti, A. L., Michelini, E., Piovesana, S., Calabretta, M. M., Zenezini Chiozzi, R., et al. (2017). Proteomic analysis and bioluminescent reporter gene assays to investigate effects of simulated microgravity on Caco-2 cells. *Proteomics* 17:1700081. doi: 10.1002/pmic.201700081

Lage, E., Parot, V., Moore, S. C., Sitek, A., Udias, J. M., Dave, S. R., et al. (2015). Recovery and normalization of triple coincidences in PET. *Med. Phys.* 42, 1398–1410. doi: 10.1118/1.4908226

Lajtos, I., Czernin, J., Dahlbom, M., Daver, F., Emri, M., Farshchi-Heydari, S., et al. (2014). Cold wall effect eliminating method to determine the contrast recovery coefficient for small animal PET scanners using the NEMA NU-4 image quality phantom. *Phys. Med. Biol.* 59, 2727–2746. doi: 10.1088/0031-9155/59/11/2727

Lambin, P., Rios-Velazquez, E., Leijenaar, R., Carvalho, S., van Stiphout, R. G., Granton, P., et al. (2012). Radiomics, extracting more information from medical images using advanced feature analysis. *Eur. J. Cancer* 48, 441–446. doi: 10.1016/j.ejca.2011.11.036

Lamson, M. L. III, Kirschner, A. S., Hotte, C. E., Lipsitz, E. L., and Ice, R. D. (1975). Generator-produced 99m TcO4-, carrier free. *J. Nucl. Med.* 16, 639–641.

Larimer, B. M., Bloch, E., Nesti, S., Austin, E. E., Wehrenberg-Klee, E., Boland, G., et al. (2019). The Effectiveness of Checkpoint Inhibitor Combinations and Administration Timing Can Be Measured by Granzyme B PET Imaging. *Clin. Cancer Res.* 25, 1196–1205. doi: 10.1158/1078-0432.CCR-18-2407

Larimer, B. M., Wehrenberg-Klee, E., Caraballo, A., and Mahmood, U. (2016). Quantitative CD3 PET imaging predicts tumor growth response to Anti-CTLA-4 therapy. *J. Nucl. Med.* 57, 1607–1611. doi: 10.2967/jnumed.116.173930

Larimer, B. M., Wehrenberg-Klee, E., Dubois, F., Mehta, A., Kalomeris, T., Flaherty, K., et al. (2017). Granzyme B PET imaging as a predictive biomarker of immunotherapy response. *Cancer Res.* 77, 2318–2327. doi: 10.1158/0008-5472.CAN-16-3346

Larkin, J., Chiarion-Sileni, V., Gonzalez, R., Grob, J. J., Cowey, C. L., Lao, C. D., et al. (2015). Combined nivolumab and ipilimumab or monotherapy in untreated melanoma. *N. Engl. J. Med.* 373, 23–34. doi: 10.1056/NEJMoa1504030

Lavaud, J., Henry, M., Coll, J. L., and Josserand, V. (2017). Exploration of melanoma metastases in mice brains using endogenous contrast photoacoustic imaging. *Int. J. Pharm.* 532, 704–709. doi: 10.1016/j.ijpharm.2017.08.104

Ledford, H., Else, H., and Warren, M. (2018). Cancer immunologists scoop medicine Nobel prize. *Nature* 562, 20–21. doi: 10.1038/d41586-018-06751-0

Lee, J. T., Zhang, H., Moroz, M. A., Likar, Y., Shenker, L., Sumzin, N., et al. (2017). Comparative analysis of human nucleoside kinase-based reporter systems for PET imaging. *Mol. Imaging Biol.* 19, 100–108. doi: 10.1007/s11307-016-0981-6

Li, J., Chen, L., Du, L., and Li, M. (2013). Cage the firefly luciferin! - a strategy for developing bioluminescent probes. *Chem. Soc. Rev.* 42, 662–676. doi: 10.1039/c2cs35249d

Li, L., Zemp, R. J., Lungu, G. F., Stoica, G., and Wang, L. V. (2007). Photoacoustic imaging of lacZ gene expression in vivo. *J. Biomed. Opt.* 12:020504. doi: 10.1117/1.2717531

Li, Z., Suzuki, Y., Huang, M., Cao, F., Xie, X., Connolly, A. J., et al. (2008). Comparison of reporter gene and iron particle labeling for tracking fate of human embryonic stem cells and differentiated endothelial cells in living subjects. *Stem. Cell* 26, 864–873. doi: 10.1634/stemcells.2007-0843

Li, Z. B., Chen, K., Wu, Z., Wang, H., Niu, G., and Chen, X. (2009). 64Cu-labeled PEGylated polyethylenimine for cell trafficking and tumor imaging. *Mol/ Imaging Biol.* 11, 415–423. doi: 10.1007/s11307-009-0228-x

Lian, L., Deng, Y., Xie, W., Xu, G., Yang, X., Zhang, Z., et al. (2017). Enhancement of the localization and quantitative performance of fluorescence molecular tomography by using linear nBorn method. *Opt. Express* 25, 2063–2079. doi: 10.1364/OE.25.002063

Liang, Q., Satyamurthy, N., Barrio, J. R., Toyokuni, T., Phelps, M. P., Gambhir, S. S., et al. (2001). Noninvasive, quantitative imaging in living animals of a mutant dopamine D2 receptor reporter gene in which ligand binding is uncoupled from signal transduction. *Gene Ther.* 8, 1490–1498. doi: 10.1038/sj.gt.3301542

Likar, Y., Dobrenkov, K., Olszewska, M., Shenker, L., Cai, S., Hricak, H., et al. (2009). PET imaging of HSV1-tk mutants with acquired specificity toward pyrimidine- and acycloguanosine-based radiotracers. *Eur. J. Nucl. Med. Mol. Imaging* 36, 1273–1282. doi: 10.1007/s00259-009-1089-x

Likar, Y., Zurita, J., Dobrenkov, K., Shenker, L., Cai, S., Neschadim, A., et al. (2010). A new pyrimidine-specific reporter gene, a mutated human deoxycytidine kinase suitable for PET during treatment with acycloguanosine-based cytotoxic drugs. *J. Nucl. Med.* 51, 1395–1403. doi: 10.2967/jnumed.109.074344

Lin, M. Z., McKeown, M. R., Ng, H.-L., Aguilera, T. A., Shaner, N. C., Campbell, R. E., et al. (2009). Autofluorescent proteins with excitation in the optical window for intravital imaging in mammals. *Chem. Biol.* 16, 1169–1179. doi: 10.1016/j.chembiol.2009.10.009

Linette, G. P., Stadtmauer, E. A., Maus, M. V., Rapoport, A. P., Levine, B. L., Emery, L., et al. (2013). Cardiovascular toxicity and titin cross-reactivity of affinity-enhanced T cells in myeloma and melanoma. *Blood* 122, 863–871. doi: 10.1182/blood-2013-03-490565

Liu, L., and Mason, R. P. (2010). Imaging β-galactosidase activity in human tumor xenografts and transgenic mice using a chemiluminescent substrate. *PLoS One* 5:e12024. doi: 10.1371/journal.pone.0012024

Liu, M., Schmitner, N., Sandrian, M. G., Zabihian, B., Hermann, B., Salvenmoser, W., et al. (2013). In vivo three dimensional dual wavelength photoacoustic tomography imaging of the far red fluorescent protein E2-Crimson expressed in adult zebrafish. *Biomed. Opt. Express* 4, 1846–1855. doi: 10.1364/BOE.4.001846

Loening, A. M., Fenn, T. D., Wu, A. M., and Gambhir, S. S. (2006). Consensus guided mutagenesis of Renilla luciferase yields enhanced stability and light output. *Protein Eng., Design Select.* 19, 391–400. doi: 10.1093/protein/gzl023

Lorenz, W. W., McCann, R. O., Longiaru, M., and Cormier, M. J. (1991). Isolation and expression of a cDNA encoding Renilla reniformis luciferase. *Proc. Natl. Acad. Sci. U.S.A.* 88, 4438–4442. doi: 10.1073/pnas.88.10.4438

Louie, A. Y., Hüber, M. M., Ahrens, E. T., Rothbächer, U., Moats, R., Jacobs, R. E., et al. (2000). In vivo visualization of gene expression using magnetic resonance imaging. *Nat. Biotechnol.*18:321. doi: 10.1038/73780

Lufino, M. M., Edser, P. A., and Wade-Martins, R. (2008). Advances in high-capacity extrachromosomal vector technology, episomal maintenance, vector delivery, and transgene expression. *Mol. Ther.* 16, 1525–1538. doi: 10.1038/mt.2008.156

MacLaren, D. C., Gambhir, S. S., Satyamurthy, N., Barrio, J. R., Sharfstein, S., Toyokuni, T., et al. (1999). Repetitive, non-invasive imaging of the dopamine D2 receptor as a reporter gene in living animals. *Gene Ther.* 6, 785–791. doi: 10.1038/sj.gt.3300877

Man, F., Lim, L., Volpe, A., Gabizon, A., Shmeeda, H., Draper, B., et al. (2019). In Vivo PET Tracking of (89)Zr-Labeled Vgamma9Vdelta2 T cells to mouse xenograft breast tumors activated with liposomal alendronate. *Mol. Ther.* 27, 219–229. doi: 10.1016/j.ymthe.2018.10.006

Manda, K., Glasow, A., Paape, D., and Hildebrandt, G. (2012). Effects of ionizing radiation on the immune system with special emphasis on the interaction of dendritic and T cells. *Front. Oncol.* 2:102. doi: 10.3389/fonc.2012.00102

Mankoff, D. A. (2007). A definition of molecular imaging. *J. Nucl. Med* 48, 18N–21N.

Marks, P., and Gottlieb, S. (2018). Balancing safety and innovation for cell-based regenerative medicine. *N. Engl. J. Med.* 378, 954–959. doi: 10.1056/nejmsr1715626

Martinez, M., and Moon, E. K. (2019). CAR T cells for solid tumors, new strategies for finding, infiltrating, and surviving in the tumor microenvironment. *Front. Immunol.* 10:128. doi: 10.3389/fimmu.2019.00128

Maude, S. L., Laetsch, T. W., Buechner, J., Rives, S., Boyer, M., Bittencourt, H., et al. (2018). Tisagenlecleucel in CHILDREN AND YOUNG ADUlts with B-Cell LYMPHOBLASTIC LEUKEMIA. *N. Engl. J. Med.* 378, 439–448. doi: 10.1056/NEJMoa1709866

Mayer, K. E., Mall, S., Yusufi, N., Gosmann, D., Steiger, K., Russelli, L., et al. (2018). T-cell functionality testing is highly relevant to developing novel immuno-tracers monitoring T cells in the context of immunotherapies and revealed CD7 as an attractive target. *Theranostics* 8, 6070–6087. doi: 10.7150/thno.27275

McGinty, J., Taylor, H. B., Chen, L., Bugeon, L., Lamb, J. R., Dallman, M. J., et al. (2011). In vivo fluorescence lifetime optical projection tomography. *Biomed. Opt. Express* 2, 1340–1350. doi: 10.1364/BOE.2.001340

Merron, A., Peerlinck, I., Martin-Duque, P., Burnet, J., Quintanilla, M., Mather, S., et al. (2007). SPECT/CT imaging of oncolytic adenovirus propagation in tumours in vivo using the Na/I symporter as a reporter gene. *Gene Ther.* 14, 1731–1738. doi: 10.1038/sj.gt.3303043

Merzlyak, E. M., Goedhart, J., Shcherbo, D., Bulina, M. E., Shcheglov, A. S., Fradkov, A. F., et al. (2007). Bright monomeric red fluorescent protein with an extended fluorescence lifetime. *Nature Methods* 4:555. doi: 10.1038/nmeth1062

Mezzanotte, L., An, N., Mol, I. M., Löwik, C. W., and Kaijzel, E. L. (2014). A new multicolor bioluminescence imaging platform to investigate NF-κB activity and apoptosis in human breast cancer cells. *PloS One* 9:e85550. doi: 10.1371/journal.pone.0085550.<PMID<PMID:NOPMID</PMID<

Mezzanotte, L., Que, I., Kaijzel, E., Branchini, B., Roda, A., and Lowik, C. (2011). Sensitive dual color in vivo bioluminescence imaging using a new red codon optimized firefly luciferase and a green click beetle luciferase. *PLoS One* 6:e19277. doi: 10.1371/journal.pone.0019277

Mezzanotte, L., van 't Root, M., Karatas, H., Goun, E. A., and Lowik, C. (2017). In vivo molecular bioluminescence imaging, new tools and applications. *Trends Biotechnol*35, 640–652. doi: 10.1016/j.tibtech.2017.03.012

Minn, I., Huss, D. J., Ahn, H. H., Chinn, T. M., Park, A., Jones, J., et al. (2019). Imaging CAR T cell therapy with PSMA-targeted positron emission tomography. *Sci. Adv.* 5:eaaw5096. doi: 10.1126/sciadv.aaw5096

Misra, T., Baccino-Calace, M., Meyenhofer, F., Rodriguez-Crespo, D., Akarsu, H., Armenta-Calderon, R., et al. (2017). A genetically encoded biosensor for visualising hypoxia responses in vivo. *Biol. Open* 6, 296–304. doi: 10.1242/bio.018226

Mogensen, M., Thrane, L., Jorgensen, T. M., Andersen, P. E., and Jemec, G. B. (2009). OCT imaging of skin cancer and other dermatological diseases. *J. Biophotonics* 2, 442–451. doi: 10.1002/jbio.200910020

Moroz, M. A., Serganova, I., Zanzonico, P., Ageyeva, L., Beresten, T., Dyomina, E., et al. (2007). Imaging hNET reporter gene expression with 124I-MIBG. *J. Nucl. Med.* 48, 827–836. doi: 10.2967/jnumed.106.037812

Moroz, M. A., Zhang, H., Lee, J., Moroz, E., Zurita, J., Shenker, L., et al. (2015). Comparative analysis of T cell imaging with human nuclear reporter genes. *J. Nucl. Med.* 56, 1055–1060. doi: 10.2967/jnumed.115.159855

Nagy, K., Toth, M., Major, P., Patay, G., Egri, G., Haggkvist, J., et al. (2013). Performance evaluation of the small-animal nanoScan PET/MRI system. *J. Nucl. Med.* 54, 1825–1832. doi: 10.2967/jnumed.112.119065

Nakamura, C., Burgess, J. G., Sode, K., and Matsunaga, T. (1995). An iron-regulated gene, magA, encoding an iron transport protein of *Magnetospirillum* sp. strain AMB-1. *J. Biol. Chem.* 270, 28392–28396. doi: 10.1074/jbc.270.47.28392

Natarajan, A., Mayer, A. T., Xu, L., Reeves, R. E., Gano, J., and Gambhir, S. S. (2015). Novel radiotracer for ImmunoPET imaging of PD-1 checkpoint expression on tumor infiltrating lymphocytes. *Bioconjug Chem.* 26, 2062–2069. doi: 10.1021/acs.bioconjchem.5b00318

Naumova, A. V., Modo, M., Moore, A., Murry, C. E., and Frank, J. A. (2014). Clinical imaging in regenerative medicine. *Nat. Biotechnol.* 32, 804–818. doi: 10.1038/nbt.2993

Neelapu, S. S., Locke, F. L., Bartlett, N. L., Lekakis, L. J., Miklos, D. B., Jacobson, C. A., et al. (2017). Axicabtagene ciloleucel CAR T-Cell therapy in refractory large B-Cell lymphoma. *N. Engl. J. Med.* 377, 2531–2544. doi: 10.1056/NEJMoa1707447

Nishino, M., Ramaiya, N. H., Hatabu, H., and Hodi, F. S. (2017). Monitoring immune-checkpoint blockade, response evaluation and biomarker development. *Nat. Rev. Clin. Oncol.* 14, 655–668. doi: 10.1038/nrclinonc.2017.88

Ntziachristos, V. (2006). Fluorescence molecular imaging. *Annu. Rev. Biomed. Eng.* 8, 1–33.

Ntziachristos, V., Ripoll, J., Wang, L. V., and Weissleder, R. (2005). Looking and listening to light, the evolution of whole-body photonic imaging. *Nat,. Biotechnol.* 23, 313–320. doi: 10.1038/nbt1074

O'Connor, J. P., Aboagye, E. O., Adams, J. E., Aerts, H. J., Barrington, S. F., Beer, A. J., et al. (2017). Imaging biomarker roadmap for cancer studies. *Nat. Rev. Clin. Oncol.* 14, 169–186. doi: 10.1038/nrclinonc.2016.162

O'Doherty, J., Jauregui-Osoro, M., Brothwood, T., Szyszko, T., Marsden, P. K., O'Doherty, M. J., et al. (2017). (18)F-Tetrafluoroborate, a PET probe for imaging sodium/iodide symporter expression, whole-body biodistribution, safety, and radiation dosimetry in thyroid cancer patients. *J. Nucl. Med.* 58, 1666–1671. doi: 10.2967/jnumed.117.192252

Oliveira, J. M., Gomes, C., Faria, D. B., Vieira, T. S., Silva, F. A., Vale, J., et al. (2017). (68)Ga-prostate-specific membrane antigen positron emission tomography/computed tomography for prostate cancer imaging, a narrative literature review. *World J. Nucl. Med.* 16, 3–7. doi: 10.4103/1450-1147.198237

Olsen, J., Themstrup, L., and Jemec, G. B. (2015). Optical coherence tomography in dermatology. *G Ital Dermatol Venereol* 150, 603–615.

Oomen, S. P., Hofland, L. J., Lamberts, S. W., Lowenberg, B., and Touw, I. P. (2001). Internalization-defective mutants of somatostatin receptor subtype 2 exert normal signaling functions in hematopoietic cells. *FEBS Lett.* 503, 163–167. doi: 10.1016/s0014-5793(01)02729-6

Park, J. H., Kim, K. I., Lee, K. C., Lee, Y. J., Lee, T. S., Chung, W. S., et al. (2015). Assessment of α-fetoprotein targeted HSV1-tk expression in hepatocellular carcinoma with in vivo imaging. *Cancer Biother. Radiopharm.* 30, 8–15. doi: 10.1089/cbr.2014.1716

Paroder-Belenitsky, M., Maestas, M. J., Dohan, O., Nicola, J. P., Reyna-Neyra, A., Follenzi, A., et al. (2011). Mechanism of anion selectivity and stoichiometry of the Na+/I- symporter (NIS). *Proc. Natl. Acad. Sci. U.S.A.* 108, 17933–17938. doi: 10.1073/pnas.1108278108

Pellenz, S., Phelps, M., Tang, W., Hovde, B. T., Sinit, R. B., Fu, W., et al. (2019). New human chromosomal sites with "Safe Harbor" potential for targeted transgene insertion. *Hum. Gene Ther.* 30, 814–828. doi: 10.1089/hum.2018.169

Perera, M., Papa, N., Christidis, D., Wetherell, D., Hofman, M. S., Murphy, D. G., et al. (2016). Sensitivity, specificity, and predictors of positive (68)Ga-Prostate-specific membrane antigen positron emission tomography in advanced prostate cancer, a systematic review and meta-analysis. *Eur. Urol.* 70, 926–937. doi: 10.1016/j.eururo.2016.06.021

Phelps, M. E., Hoffman, E. J., Huang, S. C., and Ter-Pogossian, M. M. (1975). Effect of positron range on spatial resolution. *J. Nucl. Med.* 16, 649–652.

Piotrowski, A. F., Nirschl, T. R., Velarde, E., Blosser, L., Ganguly, S., Burns, K. H., et al. (2018). Systemic depletion of lymphocytes following focal radiation to the brain in a murine model. *Oncoimmunology* 7:e1445951. doi: 10.1080/2162402X.2018.1445951

Ponomarev, V., Doubrovin, M., Lyddane, C., Beresten, T., Balatoni, J., Bornman, W., et al. (2001). Imaging TCR-dependent NFAT-mediated T-cell activation with positron emission tomography in vivo. *Neoplasia* 3, 480–488. doi: 10.1038/sj.neo.7900204

Ponomarev, V., Doubrovin, M., Serganova, I., Vider, J., Shavrin, A., Beresten, T., et al. (2004). A novel triple-modality reporter gene for whole-body fluorescent, bioluminescent, and nuclear noninvasive imaging. *Eur. J. Nucl. Med. Mol. Imaging* 31, 740–751. doi: 10.1007/s00259-003-1441-5

Ponomarev, V., Doubrovin, M., Shavrin, A., Serganova, I., Beresten, T., Ageyeva, L., et al. (2007). A human-derived reporter gene for noninvasive imaging in humans, mitochondrial thymidine kinase type 2. *J. Nucl. Med.* 48, 819–826. doi: 10.2967/jnumed.106.036962

Portulano, C., Paroder-Belenitsky, M., and Carrasco, N. (2014). The Na+/I-symporter (NIS), mechanism and medical impact. *Endocr. Rev.* 35, 106–149. doi: 10.1210/er.2012-1036

Provost, J., Garofalakis, A., Sourdon, J., Bouda, D., Berthon, B., Viel, T., et al. (2018). Simultaneous positron emission tomography and ultrafast ultrasound for hybrid molecular, anatomical and functional imaging. *Nat. Biomed. Eng.* 2, 85–94. doi: 10.1038/s41551-018-0188-z

Qin, C., Lan, X., He, J., Xia, X., Tian, Y., Pei, Z., et al. (2013). An in vitro and in vivo evaluation of a reporter gene/probe system hERL/(18)F-FES. *PLoS One* 8:e61911. doi: 10.1371/journal.pone.0061911

Qiu, L., Valente, M., Dolen, Y., Jager, E., Beest, M. T., Zheng, L., et al. (2018). Endolysosomal-escape nanovaccines through adjuvant-induced tumor antigen assembly for enhanced effector CD8(+) T cell activation. *Small* 14:e1703539. doi: 10.1002/smll.201703539

Rajasekaran, S. A., Anilkumar, G., Oshima, E., Bowie, J. U., Liu, H., Heston, W., et al. (2003). A novel cytoplasmic tail MXXXL motif mediates the internalization of prostate-specific membrane antigen. *Mol. Biol. Cell* 14, 4835–4845. doi: 10.1091/mbc.e02-11-0731

Ravert, H. T., Holt, D. P., Chen, Y., Mease, R. C., Fan, H., Pomper, M. G., et al. (2016). An improved synthesis of the radiolabeled prostate-specific membrane antigen inhibitor, [(18) F]DCFPyL. *J. Labelled Comp. Radiopharm.* 59, 439–450. doi: 10.1002/jlcr.3430

Roca, M., de Vries, E. F., Jamar, F., Israel, O., and Signore, A. (2010). Guidelines for the labelling of leucocytes with (111)In-oxine. Inflammation/Infection Taskgroup of the European Association of Nuclear Medicine. *Eur. J. Nucl. Med. Mol. Imaging* 37, 835–841. doi: 10.1007/s00259-010-1393-5

Rogers, B. E., McLean, S. F., Kirkman, R. L., Della Manna, D., Bright, S. J., Olsen, C. C., et al. (1999). In vivo localization of [(111)In]-DTPA-D-Phe1-octreotide to human ovarian tumor xenografts induced to express the somatostatin receptor subtype 2 using an adenoviral vector. *Clin. Cancer Res.* 5, 383–393.

Rogers, B. E., Zinn, K. R., and Buchsbaum, D. J. (2000). Gene transfer strategies for improving radiolabeled peptide imaging and therapy. *Q. J. Nucl. Med.* 44, 208–223.

Ronald, J. A., Cusso, L., Chuang, H. Y., Yan, X., Dragulescu-Andrasi, A., and Gambhir, S. S. (2013). Development and validation of non-integrative, self-limited, and replicating minicircles for safe reporter gene imaging of cell-based therapies. *PLoS One* 8:e73138. doi: 10.1371/journal.pone.0073138

Ronald, J. A., Kim, B. S., Gowrishankar, G., Namavari, M., Alam, I. S., D'Souza, A., et al. (2017). A PET imaging strategy to visualize activated T Cells in acute graft-versus-host disease elicited by allogenic hematopoietic cell transplant. *Cancer Res.* 77, 2893–2902. doi: 10.1158/0008-5472.CAN-16-2953

Safinia, N., Vaikunthanathan, T., Fraser, H., Thirkell, S., Lowe, K., Blackmore, L., et al. (2016). Successful expansion of functional and stable regulatory T cells for immunotherapy in liver transplantation. *Oncotarget* 7, 7563–7577. doi: 10.18632/oncotarget.6927

Sahu, S. K., Kassis, A. I., Makrigiorgos, G. M., Baranowska-Kortylewicz, J., and Adelstein, S. J. (1995). The effects of indium-111 decay on pBR322 DNA. *Radiat. Res.* 141, 193–198.

Saini, S., Korf, H., Liang, S., Verbeke, R., Manshian, B., Raemdonck, K., et al. (2019). Challenges for labeling and longitudinal tracking of adoptively transferred autoreactive T lymphocytes in an experimental type-1 diabetes model. *MAGMA* 32, 295–305. doi: 10.1007/s10334-018-0720-x

Sato, N., Wu, H., Asiedu, K. O., Szajek, L. P., Griffiths, G. L., and Choyke, P. L. (2015). (89)Zr-oxine complex PET cell imaging in monitoring cell-based therapies. *Radiology* 275, 490–500. doi: 10.1148/radiol.15142849

Satyamurthy, N., Barrio, J. R., Bida, G. T., Huang, S. C., Mazziotta, J. C., and Phelps, M. E. (1990). 3-(2'-[18F]fluoroethyl)spiperone, a potent dopamine antagonist, synthesis, structural analysis and in-vivo utilization in humans. *Int. J. Rad. Appl. Instrum. A* 41, 113–129. doi: 10.1016/0883-2889(90)90096-y

Saudemont, A., Jespers, L., and Clay, T. (2018). Current status of gene engineering cell therapeutics. *Front. Immunol.* 9:153. doi: 10.3389/fimmu.2018.00153

Schaub, F. X., Reza, M. S., Flaveny, C. A., Li, W., Musicant, A. M., Hoxha, S., et al. (2015). Fluorophore-NanoLuc BRET reporters enable sensitive <em>In Vivo</em> optical imaging and flow cytometry for monitoring tumorigenesis. *Cancer Res.* 75, 5023–5033. doi: 10.1158/0008-5472.can-14-3538

Schuster, S. J., Svoboda, J., Chong, E. A., Nasta, S. D., Mato, A. R., Anak, O., et al. (2017). Chimeric antigen receptor T Cells in refractory B-Cell lymphomas. *N. Engl. J. Med.* 377, 2545–2554. doi: 10.1056/NEJMoa1708566

Sellmyer, M. A., Lee, I., Hou, C., Lieberman, B. P., Zeng, C., Mankoff, D. A., et al. (2017). Quantitative PET reporter gene imaging with [11C] trimethoprim. *Mol. Ther.* 25, 120–126. doi: 10.1016/j.ymthe.2016.10.018

Sellmyer, M. A., Richman, S. A., Lohith, K., Hou, C., Weng, C.-C., Mach, R. H., et al. (2019). Imaging CAR T cell trafficking with eDHFR as a PET reporter gene. *Mol. Ther.* 28, 42–51. doi: 10.1016/j.ymthe.2019.10.007

Seo, J. W., Tavare, R., Mahakian, L. M., Silvestrini, M. T., Tam, S., Ingham, E. S., et al. (2018). CD8(+) T-Cell density imaging with (64)Cu-Labeled Cys-Diabody informs immunotherapy protocols. *Clin. Cancer Res.* 24, 4976–4987.

Seo, M.-J., Park, J. H., Lee, K. C., Lee, Y. J., Lee, T. S., Choi, T. H., et al. (2019). Small animal PET imaging of hTERT RNA-Targeted HSV1-tk gene expression with trans-splicing ribozyme. *Cancer Biother. Radiopharm.* 35, 26–32. doi: 10.1089/cbr.2019.2839

Seymour, L., Bogaerts, J., Perrone, A., Ford, R., Schwartz, L. H., Mandrekar, S., et al. (2017). iRECIST, guidelines for response criteria for use in trials testing immunotherapeutics. *Lancet Oncol.* 18, e143–e152. doi: 10.1016/S1470-2045(17)30074-8

Sharpe, J., Ahlgren, U., Perry, P., Hill, B., Ross, A., Hecksher-Sorensen, J., et al. (2002). Optical projection tomography as a tool for 3D microscopy and gene expression studies. *Science* 296, 541–545. doi: 10.1126/science.1068206

Shcherbakova, D. M., Stepanenko, O. V., Turoverov, K. K., and Verkhusha, V. V. (2018). Near-infrared fluorescent proteins, multiplexing and optogenetics across scales. *Trends Biotechnol.* 36, 1230–1243. doi: 10.1016/j.tibtech.2018.06.011

Shcherbakova, D. M., and Verkhusha, V. V. (2013). Near-infrared fluorescent proteins for multicolor in vivo imaging. *Nature Methods.* 10:751. doi: 10.1038/nmeth.2521

Sieger, S., Jiang, S., Schonsiegel, F., Eskerski, H., Kubler, W., Altmann, A., et al. (2003). Tumour-specific activation of the sodium/iodide symporter gene under control of the glucose transporter gene 1 promoter (GTI-1.3). *Eur. J. Nucl. Med. Mol. Imaging* 30, 748–756. doi: 10.1007/s00259-002-1099-4

Smith, E. L., and Peakman, M. (2018). Peptide immunotherapy for type 1 diabetes-clinical advances. *Front. Immunol.* 9:392. doi: 10.3389/fimmu.2018.00392

Srinivas, M., Boehm-Sturm, P., Figdor, C. G., de Vries, I. J., and Hoehn, M. (2012). Labeling cells for in vivo tracking using (19)F MRI. *Biomaterials* 33, 8830–8840. doi: 10.1016/j.biomaterials.2012.08.048

Srinivas, M., Turner, M. S., Janjic, J. M., Morel, P. A., Laidlaw, D. H., and Ahrens, E. T. (2009). In vivo cytometry of antigen-specific t cells using 19F MRI. *Magn. Reson. Med.* 62, 747–753. doi: 10.1002/mrm.22063

Srinivas, M., Boehm-Sturm, P., Aswendt, M., Pracht, E. D., Figdor, C. G., de Vries, I. J., et al. (2013). In vivo 19F MRI for cell tracking. *J. Vis. Exp.* e50802. doi: 10.3791/50802

Tannous, B. A. (2009). Gaussia luciferase reporter assay for monitoring biological processes in culture and in vivo. *Nature Protoc.*4:582. doi: 10.1038/nprot.2009.28

Tao, A., Shao, Y., Zhong, J., Jiang, H., Shen, M., and Wang, J. (2013). Versatile optical coherence tomography for imaging the human eye. *Biomed. Opt. Express* 4, 1031–1044. doi: 10.1364/BOE.4.001031

Tavare, R., Escuin-Ordinas, H., Mok, S., McCracken, M. N., Zettlitz, K. A., Salazar, F. B., et al. (2016). An effective immuno-PET imaging method to monitor CD8-dependent responses to immunotherapy. *Cancer Res.* 76, 73–82. doi: 10.1158/0008-5472.CAN-15-1707

Terrovitis, J., Kwok, K. F., Lautamaki, R., Engles, J. M., Barth, A. S., Kizana, E., et al. (2008). Ectopic expression of the sodium-iodide symporter enables imaging of transplanted cardiac stem cells in vivo by single-photon emission computed tomography or positron emission tomography. *J. Am. Coll Cardiol.* 52, 1652–1660. doi: 10.1016/j.jacc.2008.06.051

Thorn, K. (2017). Genetically encoded fluorescent tags. *Mol. Biol. Cell* 28, 848–857. doi: 10.1091/mbc.E16-07-0504

Tiernan, J. P., Perry, S. L., Verghese, E. T., West, N. P., Yeluri, S., Jayne, D. G., et al. (2013). Carcinoembryonic antigen is the preferred biomarker for in vivo colorectal cancer targeting. *Br. J. Cancer* 108, 662–667. doi: 10.1038/bjc.2012.605

Tjuvajev, J. G., Stockhammer, G., Desai, R., Uehara, H., Watanabe, K., Gansbacher, B., et al. (1995). Imaging the expression of transfected genes in vivo. *Cancer Res.* 55, 6126–6132.

Topalian, S. L., Hodi, F. S., Brahmer, J. R., Gettinger, S. N., Smith, D. C., McDermott, D. F., et al. (2012). Safety, activity, and immune correlates of anti-PD-1 antibody in cancer. *N. Engl. J. Med.* 366, 2443–2454. doi: 10.1056/NEJMoa1200690

Tsao, H., Chin, L., Garraway, L. A., and Fisher, D. E. (2012). Melanoma, from mutations to medicine. *Genes Dev.* 26, 1131–1155. doi: 10.1101/gad.191999.112

UCL Business PLC (2017). *Detecting a Therapeutic Cell.* Patent No 20170056534. Mountain View, CA: JUSTIA.

U.S. Food and Drug Administration, (2018). *FDA Approves new Treatment for a Certain type of Prostate Cancer Using Novel Clinical Trial Endpoint*. FDA News Release.

Urabe, K., Aroca, P., Tsukamoto, K., Mascagna, D., Palumbo, A., Prota, G., et al. (1994). The inherent cytotoxicity of melanin precursors, a revision. *Biochim. BiophysActa* 1221, 272–278. doi: 10.1016/0167-4889(94)90250-x

U.S. Food and Drug Administration, (2017). *FDA Approval Brings First Gene Therapy to the United States*. Silver Spring, MA: US Food and Drug Administration.

van der Windt, G. J., and Pearce, E. L. (2012). Metabolic switching and fuel choice during T-cell differentiation and memory development. *Immunol. Rev.* 249, 27–42. doi: 10.1111/j.1600-065X.2012.01150.x

VanBrocklin, H. F. (2008). Radiopharmaceuticals for drug development. United States regulatory perspective. *Curr. Radiopharm.*1, 2–6. doi: 10.2174/1874471010801010002

Vandergaast, R., Khongwichit, S., Jiang, H., DeGrado, T. R., Peng, K. W., Smith, D. R., et al. (2019). Enhanced noninvasive imaging of oncology models using the NIS reporter gene and bioluminescence imaging. *Cancer Gene Ther.*

Vedvyas, Y., Shevlin, E., Zaman, M., Min, I. M., Amor-Coarasa, A., Park, S., et al. (2016). Longitudinal PET imaging demonstrates biphasic CAR T cell responses in survivors. *JCI Insight* 1, e90064. doi: 10.1172/jci.insight.90064

Venugopal, V., Chen, J., Lesage, F., and Intes, X. (2010). Full-field time-resolved fluorescence tomography of small animals. *Opt. Lett.* 35, 3189–3191. doi: 10.1364/OL.35.003189

Vinegoni, C., Pitsouli, C., Razansky, D., Perrimon, N., and Ntziachristos, V. (2008). In vivo imaging of Drosophila melanogaster pupae with mesoscopic fluorescence tomography. *Nat. Methods* 5, 45–47. doi: 10.1038/nmeth1149

Volpe, A., Man, F., Lim, L., Khoshnevisan, A., Blower, J., Blower, P. J., et al. (2018). Radionuclide-fluorescence reporter gene imaging to track tumor progression in rodent tumor models. *J. Vis. Exp.* 133:e57088. doi: 10.3791/57088

Wang, K., Wang, Q., Luo, Q., and Yang, X. (2015). Fluorescence molecular tomography in the second near-infrared window. *Opt. Express* 23, 12669–12679.

Wang, L. V., and Yao, J. (2016). A practical guide to photoacoustic tomography in the life sciences. *Nat. Methods* 13, 627–638. doi: 10.1038/nmeth.3925

Wei, L. H., Olafsen, T., Radu, C., Hildebrandt, I. J., McCoy, M. R., Phelps, M. E., et al. (2008). Engineered antibody fragments with infinite affinity as reporter genes for PET imaging. *J. Nucl. Med.* 49, 1828–1835. doi: 10.2967/jnumed.108.054452

Weihs, F., and Dacres, H. (2019). Red-shifted bioluminescence resonance energy transfer, improved tools and materials for analytical in vivo approaches. *Trac Trends Anal. Chem.* 116, 61–73. doi: 10.1016/j.trac.2019.04.011

Weissleder, R., Moore, A., Mahmood, U., Bhorade, R., Benveniste, H., Chiocca, E. A., et al. (2000). In vivo magnetic resonance imaging of transgene expression. *Nat. Med.* 6, 351–355.

Weissleder, R., Simonova, M., Bogdanova, A., Bredow, S., Enochs, W. S., and Bogdanov, A. Jr. (1997). MR imaging and scintigraphy of gene expression through melanin induction. *Radiology* 204, 425–429. doi: 10.1148/radiology.204.2.9240530

Weist, M. R., Starr, R., Aguilar, B., Chea, J., Miles, J., Poku, E., et al. (2018). Positron emission tomography of adoptively transferred chimeric antigen receptor T cells with Zirconium-89 oxine. *J. Nucl. Med.* 59, 1531–1537. doi: 10.2967/jnumed.117.206714

Wolchok, J. D., Hoos, A., O'Day, S., Weber, J. S., Hamid, O., Lebbe, C., et al. (2009). Guidelines for the evaluation of immune therapy activity in solid tumors, immune-related response criteria. *Clin. Cancer Res.* 15, 7412–7420. doi: 10.1158/1078-0432.CCR-09-1624

Wolfs, E., Holvoet, B., Ordovas, L., Breuls, N., Helsen, N., Schonberger, M., et al. (2017). Molecular imaging of human embryonic stem cells stably expressing human PET reporter genes after zinc finger nuclease-mediated genome editing. *J. Nucl. Med.* 58, 1659–1665. doi: 10.2967/jnumed.117.189779

Wu, M.-R., Huang, Y.-Y., and Hsiao, J.-K. (2019). Use of indocyanine green (ICG), a medical near infrared dye, for enhanced fluorescent imaging—comparison of organic anion transporting polypeptide 1B3 (OATP1B3) and sodium-taurocholate cotransporting polypeptide (NTCP) reporter genes. *Molecules* 24:2295. doi: 10.3390/molecules24122295

Yaghoubi, S. S., and Gambhir, S. S. (2006). PET imaging of herpes simplex virus type 1 thymidine kinase (HSV1-tk) or mutant HSV1-sr39tk reporter gene expression in mice and humans using [18F]FHBG. *Nat. Protoc.* 1, 3069–3075.

Yamada, Y., Post, S. R., Wang, K., Tager, H. S., Bell, G. I., and Seino, S. (1992). Cloning and functional characterization of a family of human and mouse somatostatin receptors expressed in brain, gastrointestinal tract, and kidney. *Proc. Natl. Acad. Sci. U.S.A.* 89, 251–255. doi: 10.1073/pnas.89.1.251

Yusufi, N., Mall, S., Bianchi, H. O., Steiger, K., Reder, S., Klar, R., et al. (2017). In-depth characterization of a TCR-specific tracer for sensitive detection of tumor-directed transgenic T cells by immuno-PET. *Theranostics* 7, 2402–2416. doi: 10.7150/thno.17994

Zabow, G., Dodd, S., Moreland, J., and Koretsky, A. (2008). Micro-engineered local field control for high-sensitivity multispectral MRI. *Nature* 453:1058. doi: 10.1038/nature07048

Zacharakis, G., Favicchio, R., Simantiraki, M., and Ripoll, J. (2011). Spectroscopic detection improves multi-color quantification in fluorescence tomography. *Biomed. Opt. Express* 2, 431–439. doi: 10.1364/BOE.2.000431

Zettlitz, K. A., Tavare, R., Knowles, S. M., Steward, K. K., Timmerman, J. M., and Wu, A. M. (2017). ImmunoPET of malignant and normal B cells with (89)Zr- and (124)I-Labeled obinutuzumab antibody fragments reveals differential CD20 internalization in vivo. *Clin. Cancer Res.* 23, 7242–7252. doi: 10.1158/1078-0432.CCR-17-0855

Zhang, H., Moroz, M. A., Serganova, I., Ku, T., Huang, R., Vider, J., et al. (2011). Imaging expression of the human somatostatin receptor subtype-2 reporter gene with 68Ga-DOTATOC. *J. Nucl. Med.* 52, 123–131. doi: 10.2967/jnumed.110.079004

Zhang, Y., Wang, C., Gao, N., Zhang, X., Yu, X., Xu, J., et al. (2019). Determination of neutralization activities by a new versatile assay using an HIV-1 genome carrying the Gaussia luciferase gene. *J. Virol. Methods* 267, 22–28. doi: 10.1016/j.jviromet.2019.02.009

Zhou, J., Sharkey, J., Shukla, R., Plagge, A., and Murray, P. (2018). Assessing the effectiveness of a far-red fluorescent reporter for tracking stem cells in vivo. *Int. J. Mol. Sci.* 19:19. doi: 10.3390/ijms19010019

Zinn, K. R., Buchsbaum, D. J., Chaudhuri, T. R., Mountz, J. M., Grizzle, W. E., and Rogers, B. E. (2000a). Noninvasive monitoring of gene transfer using a reporter receptor imaged with a high-affinity peptide radiolabeled with 99mTc or 188Re. *J. Nucl. Med.* 41, 887–895.

Zinn, K. R., Buchsbaum, D. J., Chaudhuri, T. R., Mountz, J. M., Grizzle, W. E., and Rogers, B. E. (2000b). Simultaneous in vivo imaging of thymidine kinase and somatostatin receptor expression after gene transfer with an adenoviral vector encoding both genes. *Mol. Ther.* 2000:S44.

Zurkiya, O., Chan, A. W. S., and Hu, X. (2008). MagA is sufficient for producing magnetic nanoparticles in mammalian cells, making it an MRI reporter. *Mag. Res. Med.* 59, 1225–1231. doi: 10.1002/mrm.21606

**Conflict of Interest:** The authors declare that the research was conducted in the absence of any commercial or financial relationships that could be construed as a potential conflict of interest.

frontiers in Physics

REVIEW
published: 09 April 2020
doi: 10.3389/fphy.2020.00047

# Correlated Multimodal Imaging in Life Sciences: Expanding the Biomedical Horizon

*Andreas Walter[1]*, Perrine Paul-Gilloteaux[2,3], Birgit Plochberger[4], Ludek Sefc[5], Paul Verkade[6], Julia G. Mannheim[7,8,9], Paul Slezak[10], Angelika Unterhuber[11], Martina Marchetti-Deschmann[12], Manfred Ogris[13], Katja Bühler[14], Dror Fixler[15], Stefan H. Geyer[16], Wolfgang J. Weninger[16], Martin Glösmann[17], Stephan Handschuh[17] and Thomas Wanek[18]*

[1] BioImaging Austria/CMI, Vienna BioCenter Core Facilities, Vienna, Austria, [2] Université de Nantes, CNRS, INSERM, l'institut du thorax, Nantes, France, [3] Nantes Université, CHU Nantes, Inserm, CNRS, SFR Santé, Inserm UMS 016, CNRS UMS 3556, Nantes, France, [4] Upper Austria University of Applied Sciences, Medical Engineering, BioImaging Austria/CMI, Linz, Austria, [5] Center for Advanced Preclinical Imaging (CAPI), First Faculty of Medicine, Charles University, Prague, Czechia, [6] School of Biochemistry, University of Bristol, Bristol, United Kingdom, [7] Department of Preclinical Imaging and Radiopharmacy, Werner Siemens Imaging Center, Eberhard-Karls University Tübingen, Tübingen, Germany, [8] Department of Physics and Astronomy, University of British Columbia, Vancouver, BC, Canada, [9] Cluster of Excellence iFIT (EXC 2180) "Image Guided and Functionally Instructed Tumor Therapies", University of Tuebingen, Tübingen, Germany, [10] Ludwig Boltzmann Institute for Experimental and Clinical Traumatology, BioImaging Austria/CMI, Vienna, Austria, [11] Center for Medical Physics and Biomedical Engineering, BioImaging Austria/CMI, Medical University of Vienna, Vienna, Austria, [12] Mass Spectrometric Bio- and Polymeranalysis, Institute of Chemical Technologies and Analytics, BioImaging Austria/CMI, TU Wien, Vienna, Austria, [13] Laboratory of MacroMolecular Cancer Therapeutics (MMCT), Department of Pharmaceutical Chemistry, Center of Pharmaceutical Sciences, BioImaging Austria/CMI, University of Vienna, Vienna, Austria, [14] VRVis Zentrum für Virtual Reality und Visualisierung Forschungs GmbH, BioImaging Austria/CMI, Vienna, Austria, [15] Laboratory of Advance Microscopy LAB, Faculty of Engineering, Institute of Nanotechnology and Advanced Materials, Bar Ilan University, Ramat Gan, Israel, [16] Division of Anatomy, Center for Anatomy and Cell Biology, BioImaging Austria/CMI, Medical University of Vienna, Vienna, Austria, [17] VetCore Facility for Research, Imaging Unit, BioImaging Austria/CMI, University of Veterinary Medicine Vienna, Vienna, Austria, [18] Preclinical Molecular Imaging, BioImaging Austria/CMI, AIT Austrian Institute of Technology GmbH, Seibersdorf, Austria

OPEN ACCESS

**Edited by:**
*Andreas Hess, University of Erlangen Nuremberg, Germany*

**Reviewed by:**
*Maurits A. Jansen, University of Edinburgh, United Kingdom*
*Michael D. Noseworthy, McMaster University, Canada*

***Correspondence:**
*Andreas Walter*
*andreas.walter@vbcf.ac.at*

**Specialty section:**
*This article was submitted to Medical Physics and Imaging, a section of the journal Frontiers in Physics*

**Received:** *29 November 2019*
**Accepted:** *20 February 2020*
**Published:** *09 April 2020*

**Citation:**
*Walter A, Paul-Gilloteaux P, Plochberger B, Sefc L, Verkade P, Mannheim JG, Slezak P, Unterhuber A, Marchetti-Deschmann M, Ogris M, Bühler K, Fixler D, Geyer SH, Weninger WJ, Glösmann M, Handschuh S and Wanek T (2020) Correlated Multimodal Imaging in Life Sciences: Expanding the Biomedical Horizon. Front. Phys. 8:47. doi: 10.3389/fphy.2020.00047*

The frontiers of bioimaging are currently being pushed toward the integration and correlation of several modalities to tackle biomedical research questions holistically and across multiple scales. Correlated Multimodal Imaging (CMI) gathers information about exactly the same specimen with two or more complementary modalities that—in combination—create a composite and complementary view of the sample (including insights into structure, function, dynamics and molecular composition). CMI allows to describe biomedical processes within their overall spatio-temporal context and gain a mechanistic understanding of cells, tissues, diseases or organisms by untangling their molecular mechanisms within their native environment. The two best-established CMI implementations for small animals and model organisms are hardware-fused platforms in preclinical imaging (Hybrid Imaging) and Correlated Light and Electron Microscopy (CLEM) in biological imaging. Although the merits of Preclinical Hybrid Imaging (PHI) and CLEM are well-established, both approaches would benefit from standardization of protocols, ontologies and data handling, and the development of optimized and advanced implementations. Specifically, CMI pipelines that aim at bridging preclinical and biological imaging beyond CLEM and PHI are rare but bear great potential to substantially advance both bioimaging and biomedical research. CMI faces three main challenges for its routine use in biomedical research: (1) Sample handling and preparation procedures that are compatible across modalities without compromising data quality, (2) soft- and hardware solutions to relocate the same region of interest (ROI) after transfer between imaging platforms including fiducial markers, and (3) automated software solutions to correlate complex, multiscale, multimodal and volumetric image data including reconstruction, segmentation and visualization. This review goes beyond preclinical imaging and puts accessible information into a broader imaging context. We present a comprehensive overview of the field of CMI from preclinical hybrid imaging to correlative microscopy, highlight requirements for optimization and standardization, present a synopsis of current solutions to challenges of the field and focus on current efforts to bridge the gap between preclinical and biological imaging (from small animals down to single cells and molecules). The review is in line with major European initiatives, such as COMULIS (CA17121), a COST Action to promote and foster Correlated Multimodal Imaging in Life Sciences.

**Keywords: bioimaging, correlated multimodal imaging, CMI, COMULIS, CLEM, correlative microscopy, hybrid imaging, correlation software**

## INTRODUCTION

The ideal imaging setup would provide both (i) holistic and (ii) multiscale information about the same sample:

Holistic imaging refers to probing all relevant information spaces for the same sample, assessing both structural and functional information (**Figure 1**). Functional imaging allows to portray dynamic physiological, metabolic and biological processes within the sample, such as diffusion, perfusion or glucose uptake. This requires both sensitivity to low molecular concentrations and specificity, the number of potential molecules resolved per scan (**Figure 2**). Since these processes occur in a complex tissue environment, ideally, this information is acquired *in-vivo* or in a close-to-native context without damaging the sample by irradiation. This requires trade-offs in bioimaging using single modalities since usually either structural or functional information is gathered by a single modality, and high-resolution localization with protein or ultrastructural accuracy often requires sectioning the sample and prevents *in-vivo* studies.

Multiscale structural imaging visualizes the same sample across all relevant scales. Ideally, it combines high axial and lateral resolution with high penetration depths, and is able to image or scan a wide field of view in a reasonable time that allows the correlation of complementary parameters acquired across the entire sample. However, bioimaging is usually performed using single modalities, which restricts multiscale imaging: Either a large field of view is imaged at low magnification, which provides overview and tissue context but restricts localization, or the specimen is imaged at high resolution, which provides (sub)cellular insights but limits contextual information. Besides, penetration depth comes at the expense of lateral resolution (**Figure 3**) and is limited due to aberration and attenuation by scattering and absorption (with highly wavelength-dependent elastic (Rayleigh) scattering—the intensity of Rayleigh-scattered light is $I \propto 1/\lambda^4$), and hence restricts 3D *in-vivo* imaging. The achievable penetration depth is proportional to the scattering mean free path, and strongly depends on the composition of the biological tissue, such as the presence and organization of microvasculature or collagen [2].

No single modality can gain multiscale or holistic information and accurately and comprehensively decipher the inner working of cells or entire organisms. Only the combination and—importantly—the multimodal correlation of imaging technologies allow to overcome the limitations mentioned above by integrating the best features of the combined techniques (compare **Tables 1**, **2**, **3**). Correlated Multimodal Imaging (CMI) gathers information about the specimen with two or more complementary modalities that—in combination—create a composite view of the sample. It is a holistic multiscale approach that spans the entire resolution range from nano- to millimeters, and provides complementary information about structure, function, dynamics, and molecular composition of the sample. CMI can hence study biomedical processes within their overall spatio-temporal context, and mechanistically analyze pathologies, diseases and organisms down to the underlying molecular events. Correlative Light and Electron Microscopy (CLEM), as a well-established case of CMI, can for

**Abbreviations:** AFM, Atomic Force Microscopy; CARS, Coherent Anti-Stokes Raman Spectroscopy; CLEM, Correlative Light and Electron Microscopy; CMI, Correlated Multimodal Imaging; CT, Computed Tomography; EM, Electron Microscopy; FIB, Focused Ion Beam; FM, Fluorescence Microscopy; HREM, High Resolution Episcopic Microscopy; LM, Light Microscopy;LSFM, Light Sheet Fluorescence Microscopy; MPI, Magnetic Particle Imaging; MPM, MultiPhoton Microscopy; MRI, Magnetic Resonance Imaging; MSI, Mass Spec Imaging; OCT, Optical Coherence Tomography; OI, Optical Imaging; PAI, Photoacoustic Imaging; PET, Positron Emission Tomography; PHI, Preclinical Hybrid Imaging; RS, Raman Spectroscopy; SEM, Scanning Electron Microscopy; SHG, Second Harmonic Generation Microscopy; SPECT, Single Photon Emission Computed Tomography; Superresolution, Superresolution Microscopy (such as STORM, PALM, STED); SXT, Soft X-ray Tomography; TEM, Transmission Electron Microscopy; TPEF, Two-Photon Excited Fluorescence Microscopy; US, Ultrasound.

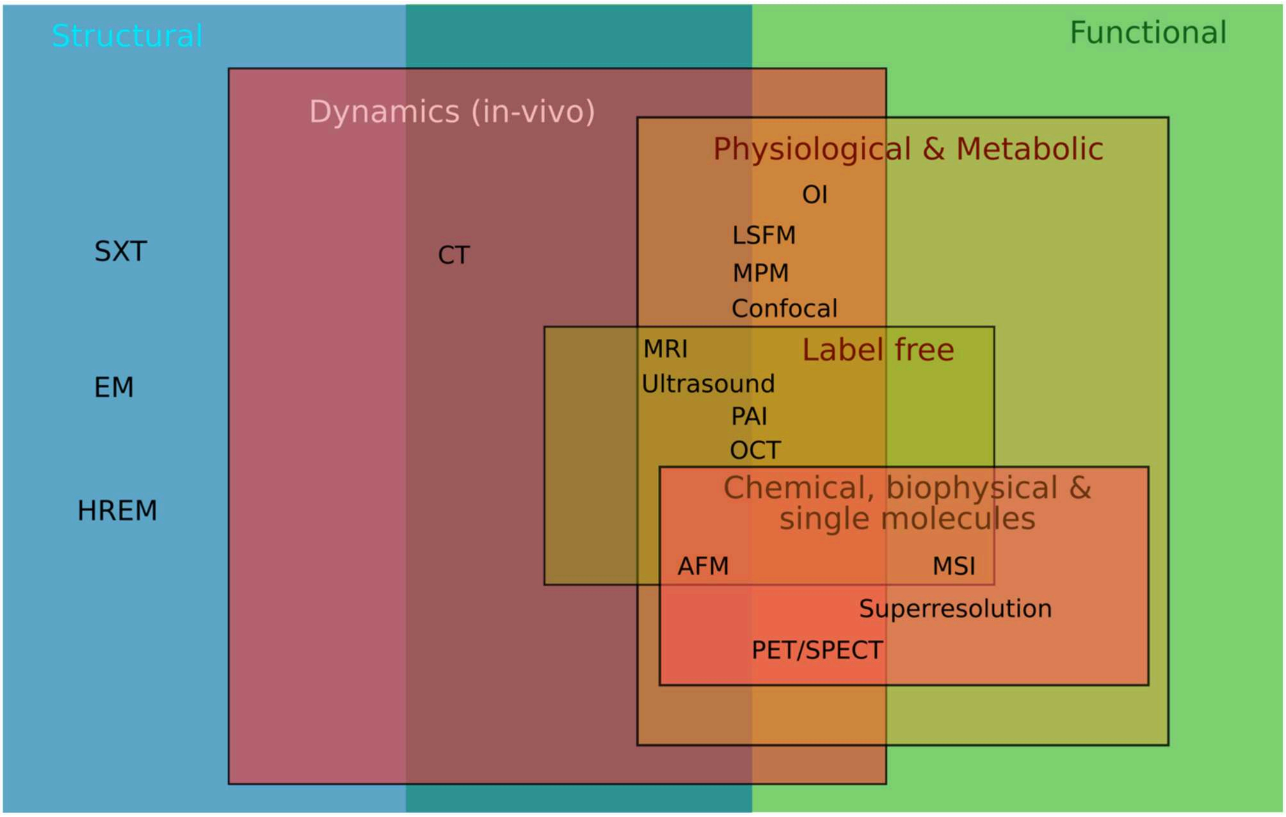


**FIGURE 1 |** Holistic imaging accessing all relevant information spaces from structural to functional imaging. Representation for the modalities mentioned in the text: SXT, Soft X-ray Tomography; HREM, High Resolution Episcopic Microscopy; EM, Electron Microscopy; CT, Computed Tomography; OI, Optical Imaging including bioluminescence and fluorescence imaging; LSFM, Light Sheet Fluorescence Microscopy; MPM, MultiPhoton Microscopy, Confocal, Confocal Microscopy; MRI, Magnetic Resonance Imaging; Ultrasound, PAI, Photoacoustic Imaging; OCT, Optical Coherence Tomography; AFM, Atomic Force Microscopy; MSI, Mass Spec Imaging; Superresolution, Microscopy such as STORM, PALM, STED; PET/SPECT, Positron Emission Tomography/Single Photon Emission Computed Tomography.

example gather both spatial (Electron Microscopy, EM) and functional information about a specific molecule (Fluorescence Microscopy, FM) within its subcellular context, and achieve near-atomic resolution (EM) within a relatively broad field of view (FM). Additionally, due to its complementarity and different contrast mechanisms, CMI allows to validate quantifications and conclusions drawn from any single modality.

For this review, we solely focus and distinguish between preclinical (imaging small animals and molecular processes *in-vivo*) and biological imaging (largely microscopy, *ex-vivo* visualization of subcellular processes and molecules, cells or tissues of model organisms). So far, CMI approaches in biological and preclinical research mainly focus on the correlation of two modalities [3]. There is one well-established example for each field: (1) Hardware-fused platforms for Hybrid Imaging [4] in preclinical research and diagnostics (which we refer to as **Preclinical Hybrid Imaging, PHI**), and (2) **Correlative Light and Electron Microscopy (CLEM)** in biological research [5]. The most prominent (and commercially available) implementations surely are micro-Positron Emission Tomography and micro-Computed Tomography (PET/CT) and Single Photon Emission Tomography (SPECT)/CT, but there is a large variety of other CMI combinations both in preclinical research and correlative microscopy which will broaden the accessible biomedical information significantly. The field of CMI is highly dynamic and heading toward more complex integrated implementations of multimodal workflows that also include advanced non-commercial setups, such as Soft X-Ray Tomography in biological imaging. Currently, however, there are only very few strategies that aim at bridging biological and preclinical imaging—even though these **Novel CMI Pipelines** reap the full potential of this approach in tackling biomedical research questions mechanistically. In this context, data handling and **Correlation Software** for diverse imaging data sets play a crucial role in CMI.

While the benefits of PHI and CLEM are more and more recognized in biomedical research, they lack gold standards for protocols or data handling and limit quantification. This includes for example the quantification of the correlation accuracy in CLEM or biomedical imaging ontologies. Apart from standardization, both PHI and CLEM leave room for optimization and the integration of advanced setups, such volume or super-resolution CLEM [6, 7] or hybrid preclinical multimodal platforms for Optical Coherence Tomography (OCT), Photoacoustic Imaging (PAI), and non-linear *in-vivo* microscopy [8]. For the routine implementation of CMI in biomedical research, several common bottlenecks need to be overcome, such as sample handling and preparation procedures that are compatible across modalities without compromising data quality, soft- and hardware solutions to relocate the same region of interest (ROI) after transfer between imaging platforms including fiducial markers, and automated software solutions to correlate complex, multiscale, multimodal and volumetric image data including reconstruction, segmentation and visualization. Due to these challenges and lack of gold standards, availability of CMI in routine biomedical research is limited. Specifically for novel CMI pipelines, the involved cutting-edge imaging technologies can be expensive and time-consuming—and simply not available to a single researcher. They require a broad range of interdisciplinary expertise across different imaging modalities from sample preparation to image processing. Besides, it is difficult for the user to keep track of the constantly expanding range of available modalities and their strengths and limitations. The use of CMI in biomedical research is also restricted by the lack of readily accessible commercial solutions that allow to address biomedical research questions without substantial technological R&D.

CMI will play a crucial role in the future of bioimaging and in life sciences, which is reflected by major European initiatives, such as the European Society for Hybrid Imaging or COMULIS, an EU-funded COST network that aims fostering CMI, disseminating its benefits, and accelerating its technological implementation as a versatile tool in biomedical research by addressing the mentioned challenges and bottlenecks.

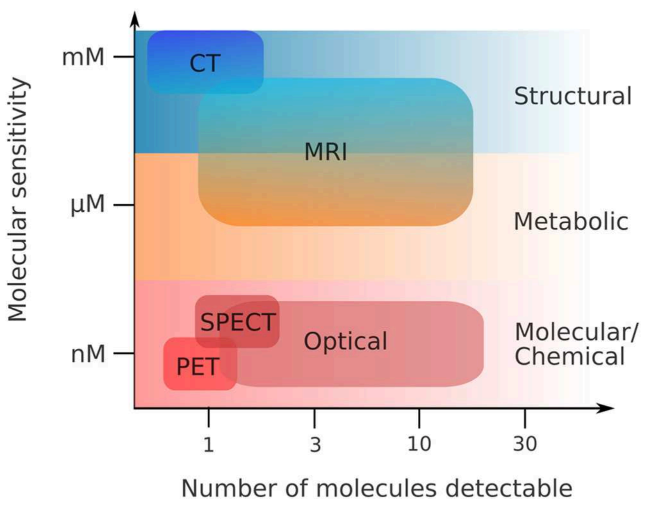


**FIGURE 2 |** Functional imaging—sensitivity vs. specificity. Same abbreviations as in **Figure 1**. Adapted from Pogue et al. [1], with permission from the American Journal of Roentgenology (copyright owner).

## STATE-OF-THE-ART

### CLEM and Correlative Microscopy

Ever since the first analysis of a biological sample using EM by Porter et al. [9], the light microscope was used first to target the cell of interest. This highlights one of the hallmarks of the power of CLEM: The identification of a specific event to

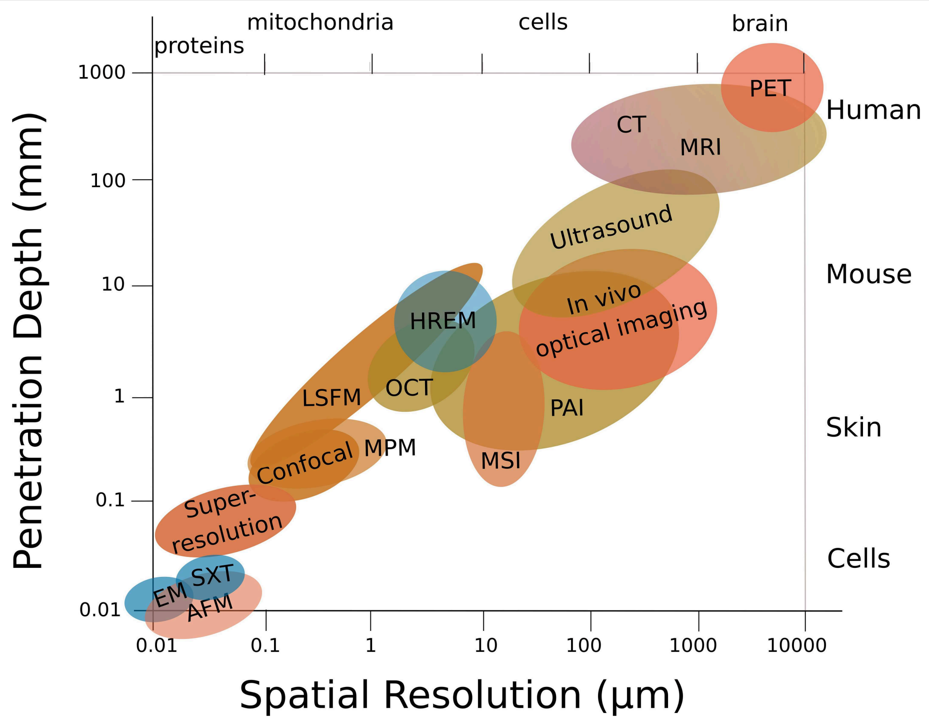


**FIGURE 3 |** Structural multiscale imaging. Penetration depth usually comes at the expense of lateral resolution. Same abbreviations as in **Figure 1**.

**TABLE 1 |** Imaging parameters, advantages and limitations of the most used *in-vivo* preclinical imaging techniques.

| Modality | CT | MRI | US | PET | SPECT | MPI | OI |
|---|---|---|---|---|---|---|---|
| Contrast mechanism | X-ray attenuation of tissues | Emitted RF signal after nuclear spin excitation | Acoustic impedance between tissue interfaces | Photon emission after positron annihilation | Emitted gamma-ray photons | Non-linear superparamagnetic nanoparticle magnetization changes | Fluorescence or bioluminescence light emission |
| Penetration | >500 mm | >500 mm | 10–150 mm | >500 mm | >500 mm | >500 mm | 1–10 mm |
| Intrinsic contrast | High (bone)<br>Low (soft tissues) | High | Low | None (Requires positron-emitting radioisotope labeled imaging agent) | None (Requires gamma-emitting radioisotope-labeled imaging agent) | None (Requires superparamagnetic nanoparticle contrast imaging agent) | Variable (autofluorescence)<br>None (bioluminescence- requires imaging agent) |
| Spatial resolution | ≤100 µm | ≤100 µm | 30–800 µm | 1–2 mm | 0.5–2 mm | 1 mm | 1 mm |
| Sensitivity (Imaging agent) | mM | µM—pM | n.a. | pM | pM-nM | pM | nM |
| Typical acquisition time | 10–25 min | 5–60 min | 5–15 min | 10–90 min | 30–90 min | 1–2 min | 2–10 min |
| Advantages | - excellent bone imaging | - non-ionizing radiation<br>- very good soft tissue contrast<br>- biochemical information (spectroscopy) | - high temporal and spatial resolution portable instrumentation<br>- cost efficient | - high sensitivity<br>- fully quantitative data<br>- high range of applications (imaging agent dependent)<br>- dynamic measurements | - high range of applications (imaging agent dependent)<br>- simultaneous radioisotope imaging possible | - non-ionizing radiation<br>- high speed<br>- high sensitivity<br>- fully quantitative data<br>- high range of applications<br>- dynamic measurements | - non-ionizing radiation<br>- high throughput<br>- cost effective |
| Limitations | - radiation dose<br>- low soft tissue contrast | - expensive equipment<br>- high maintenance costs<br>- lack of bone contrast | - limited tissue penetration<br>- poor contrast<br>- difficult to quantitate | - use of radioactive agents<br>- highly specialized equipment and staff required<br>- high costs | - use of radioactive agents<br>- semi-quantitative data<br>- costs | - limited commercially available contrast agents | - limited tissue penetration depth<br>- low spatial resolution<br>- semi-quantitativedata |
| Main application | - anatomical (bone)<br>- imaging | - anatomical (soft tissue)<br>- imaging *in vivo* MR spectroscopy | - blood vessel imaging | - diagnostic imaging (oncology, neurology, cardiology)<br>- pharmacokinetic and pharmacodynamic imaging | - diagnostic imaging (oncology, neurology, cardiology)<br>- drug development | - vascular imaging<br>- oncology<br>- cell tracking | - cancer imaging<br>- cell trafficking<br>- gene expression |

*CT, Computed Tomography; MRI, Magnetic Resonance Imaging; US, Ultrasound; PET, Positron Emission Tomography; SPECT, Single Photon Emission Computed Tomography; MPI, Magnetic Particle Imaging; OI, Optical Imaging including bioluminescence and fluorescence imaging.*

**TABLE 2 |** Imaging parameters, advantages and limitations of the most used *in-vivo* microscopy techniques in preclinical research.

| Modality | OCT | RS | MPM (CARS, TPEF, SHG) | PAI |
|---|---|---|---|---|
| Contrast mechanism | Optical scattering based on refractive index changes motion contrast (speckle and/or phase decorrelation) | Inelastic scattering of photons (Raman scattering) | - Molecular vibration (Raman scattering)<br>- Fluorescence<br>- Non-linear optical scattering | - Endogenous and/or exogenous optical absorption<br>- Photoacoustic effect |
| Penetration | ∼1–2 mm | ∼0.5 mm | ∼0.5 mm | ∼10 mm |
| Axial resolution | ≥0.5 μm (light source dependent) | ≥0.3 μm (diffraction limited) | ≥0.3 μm (diffraction limited) | ∼80 μm (implementation dependent) |
| Lateral resolution | ≥1 μm (diffraction limited) | ≥1 μm (diffraction limited) | ≥1 μm (diffraction limited) | ∼40 μm (photoacoustic wave) |
| Frame rate | 3D/1 Hz | 2D/1–10 s/point | 2D/<10 Hz | 3D/<10 mHz |
| ROI | 10 × 10 $mm^2$ | 1–100 $\mu m^2$ | 0.5 × 0.5 $mm^2$ | 10 × 10 $mm^2$ |
| Advantages | - *in vivo*<br>- fast<br>- non-invasive<br>- label-free<br>- morphology<br>- quantitative blood flow | Full molecular fingerprint | - *in vivo*<br>- endogenous contrast<br>- morphology -molecular fingerprint | - *in vivo*<br>- penetration depth<br>- endogenous and exogenous contrast |
| Limitations | - limited molecular information<br>- reduced subcellular resolution | - reduced penetration depth<br>- reduced FOV<br>- speed | - reduced penetration depth<br>- reduced field of view | - resolution<br>- speed<br>- structural contrast |

*OCT, Optical Coherence Tomography; RS, Raman Spectroscopy; MPM, MultiPhoton Microscopy; CARS, Coherent Anti-Stokes Raman Spectroscopy; TPEF, Two-Photon Excited Fluorescence Microscopy; SHG, Second Harmonic Generation Imaging; PAI, Photoacoustic Imaging.*

be analyzed at higher resolution in the electron microscope. Since then, CLEM has been applied to answer specific biological questions, most notably the seminal work by Rieder, using (live) Differential Interference Contrast (DIC) light microscopy to study microtubule organization during cell division [10]. CLEM took off shortly after the groundbreaking use of Green Fluorescent Protein (GFP) [11] that transformed life science research. The groups of Polishchuk et al. [12, 13] used the expression of GFP tagged to a viral protein (VSV-G) to first study the movement of post-Golgi transport carriers and subsequently analyze that exact same carrier at high resolution in EM. This workflow nicely exemplified that by combining the power of each technique, the sum is greater than its parts (1+1 = 3, [14]). Live imaging by FM provided the history of the carrier (originating from the Golgi) and EM not only showed the ultrastructure of the carrier but in addition provided information about its surrounding environment as a bonus, the so-called reference space. One of the great advantages of this workflow is its relative simplicity. It makes use of an imaging dish with a finder pattern embossed in it. The pattern can be recorded in the light microscope (LM) and as the finder pattern stands out from the rest of the glass coverslip, the pattern is also transferred to the resin block. This allows for trimming down the sample to only a very few cells around the cell of interest [15]. In principle, any lab with a light and an electron microscope will be able to perform this technique.

There are many different approaches to a CLEM experiment given the diversity of EM (TEM, SEM, electron tomography) and FM techniques (LSFM, MPM, super-resolution, confocal), which can be roughly classified in chemical fixation and embedding (in-resin) approaches, and cryo approaches (see e.g. **Table 3**). We have compiled a large number of those in a series of three books in the Methods in Cell Biology series (Volume 111, 124, and 140). Of particular interest for routine use is the preservation of in-resin fluorescence. This method retains the fluorescence (of GFP) after high pressure freezing and freeze substitution to Lowicryl [16–18]. So, after sectioning first, the fluorescence can be recorded with high Z-resolution because the section is only 70–100 nm thick and then can be mapped with high precision (50 nm) onto the underlying ultrastructure. An interesting development here is the integrated light and electron microscope that would allow for even better and more direct correlation as discussed later. It is important to highlight that the development of each of those techniques is driven by the need to answer a biological question and it should always be the case that this biological question is driving what kind of technology will be applied. As an example, we have been studying the formation of membrane tubules emanating from endosomes that transport and recycle cargo back to the plasma membrane. Chemical fixation as done by the pre-embedment approach described earlier [15] causes the tubules to fragment into smaller carriers, thus destroying the very object of study [19]. Hence a cryo-fixation method had to be developed that allows for capturing events observed live in the fluorescence light microscope on a time scale of seconds to be observed down the electron microscopy. This resulted in the development of the EMPACT2 + RTS with Leica Microsystems and allowed us and others to capture short-lived cellular events for study at the ultrastructural level [19–21]. Apart from CLEM, other well-established examples of correlative microscopy include the

**TABLE 3 |** Imaging parameters, advantages, and limitations of the most used *ex-vivo* microscopy techniques in biological research.

| Modality | AFM | TEM | Superresolution | Confocal | LSFM | Soft X-ray |
|---|---|---|---|---|---|---|
| Contrast mechanism/Working principle | Deflection of the cantilever is converted into force or lateral and vertical position.<br>Contrast: e.g., spring constant of cantilever | Electrons interact with the sample. Heavy atoms deviate electrons more from their path and generate contrast. Heavy metals are generally used to enhance contrast in biological samples | Uses the physical properties of statistically photoactivatable fluorophores (PALM) and selective deactivation of fluorophores (STED)<br>Contrast: e.g., quantum efficiency of fluorophore, labeling density | Fluorescent molecules are excited by lasers and emit at a longer wavelength<br>Contrast: e.g., quantum efficiency of fluorophore | LSFM scans a thin slice of the sample—optical sectioning—using a plane of light instead of a point | The sample is illuminated with 'water window' X-rays (2.3–4.4 nm), which are absorbed 10 times more strongly by carbon-containing biomolecules than by water (Beer-Lambert Law) |
| Penetration | Not specified: Material and AFM tip dependent ($< 20\,\mu$m) | $<1\,\mu$m | Technology dependent: $\sim10\,\mu$m | $<100\,\mu$m | $\geq1$ cm | $<20\,\mu$m (material dependent) |
| Axial resolution | $<1$ nm | $>2$ nm | Technology dependent: $>100$ nm | $\geq0.4\,\mu$m | $\geq0.4\,\mu$m | $\sim$ 50–20 nm |
| Lateral resolution | $<1$ nm | $<1$ nm | Technology dependent: $>5$ nm | $\sim$150–200 nm (wavelength dependent) | $\geq$500 nm (objective dependent) | $\sim$ 50–20 nm |
| ROI | $<100 \times 100\,\mu m^2$ | $<10 \times 10\,\mu m^2$ | Technology dependent: $\sim50 \times 50\,\mu m^2$ | $\sim$0.2–1 $mm^2$ | $\sim$0.2–1 $mm^2$ (limitation is the production of a uniform, thin light sheet over the volume) | $\sim15 \times 15\,\mu m^2$ |
| Advantages | - very high lateral and axial information<br>- live imaging possible<br>- no label<br>- physical/ chemical material properties<br>- manipulation/pipetting molecules | - ultrastructural information<br>- reference space in relation to structure of interest<br>- very high resolution | - highest resolution light microscopy techniques<br>- co-localization of single molecules | - Live imaging<br>- molecular interactions<br>- fast data collection | - Live imaging<br>- less photo damage to sample (longer imaging)<br>- *in vivo* volumetric imaging | - Close-to-native ultrastructural context in intact cells<br>- High throughput<br>- Niche technique between FM & EM |
| Limitations | - acquires mainly near surface information<br>- no real time imaging | - no live imaging<br>- usually elaborate processing (time consuming) | - no real time imaging<br>- applicable to nearly immobile molecules<br>- mostly not very suited for live imaging | - missing cellular context (only labels visible)<br>- diffraction limited resolution | - Special holders, limited specimen exchange | - Access to synchrotron radiation<br>- Molecular context missing<br>- no live imaging |

*AFM, Atomic Force Microscopy; TEM, Transmission Electron Microscopy; Superresolution, Microscopy such as STORM, PALM, STED; Confocal, Microscopy; LSFM, Light Sheet Fluorescence Microscopy; SXT, Soft X-ray Tomography.*

combination of FM and AFM. Besides, the combination of Soft X-ray Tomography (SXT) with FM and its super-resolution implementations allows to correlate two complementary contrast mechanisms at similar spatial resolution, and was used to study cell infections or the molecular distributions within the ultrastructural architecture [22, 23].

Advanced super-resolution FM circumvents the diffraction barrier with spatial resolution below 200 nm and has become a powerful tool for the observation of specific molecules in living cells, tissues, and even whole organisms. It is a valuable tool to study bio-molecular dynamics, interactions and co-localization via selective and specific labeling of certain components within cells and to provide biological information at the nanoscale by measuring forces of interacting objects. However, even with the recent implementation of high-speed AFM, the temporal resolution of fluorescence-based techniques cannot be reached. Likewise, the introduction of super-resolution microscopy cannot reach the spatial resolution of AFM. However, the combination of "Force-and-Light" allows to watch and simultaneously manipulate or control individual molecules. These two techniques in combination allow probing fundamental biological processes at a previously unrepresented level. In general, it is possible to combine all parameters gained from AFM techniques with those of FM ones (**Figure 4**). Nevertheless, it needs to be considered which combinations yield meaningful insights into the investigated system, and more importantly, which combinations do not influence each other—such as measuring of interaction forces and interaction kinetics as the kinetics will be directly altered by an applied force. Moreover, synchronized operations of both techniques instead of sequential ones are limited by the individual mechanical stability of each technique (e.g., thermal drift, acoustic disturbance, mechanical, and electronic noise/vibration).

To date, various combinations have been successfully confirmed to characterize previously inaccessible biological information. For example, the AFM tip was used as a nanopipette to supply targeted molecules to bio-membranes and its temporal interaction was described using FM [24, 25]. This approach allows for a so-called touch-and-watch experiment to study the uptake of foreign or active substances for example. Besides, there are a variety of correlative applications, which assessed combinations of the properties depicted in **Figure 4**: (i) Elasticity and diffusion using for example Förster Resonance Energy Transfer (FRET) between dye molecule [26–30]; (ii) interaction forces and diffusion using single molecule force spectroscopy and Total Internal Reflection Microscopy (TIRF), termed Single Molecule Cut and Paste, to assemble/split nucleotide-based aptamers individually [25, 31, 32]; (iii) interaction forces and localization using super-resolution FM to resolve the architecture of focal adhesion under physiological relevant conditions [33, 34]; and manipulation and localization to assemble single molecules patterns via the AFM to identify blinking parameters and maximal resolvable fluorophore density [35, 36].

## Preclinical Hybrid Imaging

Preclinical imaging of small laboratory animals covers all clinically used methods for human *in-vivo* imaging and also several methods that have not been implemented to humans yet. *In-vivo* imaging consists of **anatomical (structural) imaging** and **molecular (functional) imaging**.

Anatomical Imaging of body structures utilizes X-rays (CT—Computed Tomography), magnetic properties of tissues (MRI—Magnetic Resonance Imaging) or interacting of tissues with sound/pressure waves (US—ultrasonography or ultrasound imaging). CT images correspond to differential attenuation of X-rays depending on the density of interacting structures. CT images are characterized by very good spatial resolution but low contrast—so they are used preferentially for imaging of hard structures (bones). MRI imaging is based on nuclear magnetic resonance of hydrogen nuclei (protons) in oscillating magnetic fields. MRI provides inferior spatial resolution compared to CT but excellent soft tissue resolution [37]. Ultrasound waves penetrate soft tissues and form echoes on the boundary of tissues with different acoustic impedance. This allows for imaging of soft tissues such as muscle, tendon, veins, and inner organs. Higher frequency waves (40 to 70 MHz) penetrate little into the tissue (10–15 mm) but provide excellent spatial resolution down to 30 $\mu$m. US imaging is generally 2D but can be acquired and computed to form a 3D and 4D data set [38].

Molecular Imaging localizes a position of accumulated molecules (contrast agents). All three anatomical *in-vivo* techniques can be enhanced to molecular imaging by the use of contrast agents. Even without the use of contrast agents, MRI can track changes in blood flow and oxygenation of brain tissue connected to increased brain activity after stimulus and thus reveal the brain regions activated by such stimulus [39]. Ultrasound Doppler imaging can also detect functional changes in blood flow without contrast application.

Other pure molecular *in-vivo* imaging methods utilize radioisotopic, magnetic, optical or optoacoustic contrasts. The obtained images only show regions of contrast accumulation and must be co-registered with anatomical images to validate the exact position of the signal in the body, i.e. always require correlative or hybrid imaging approaches. Radioisotopic imaging methods include PET and SPECT. PET data acquisition is based on positron-emitting radioisotopes, in which the positron travels a short distance in the surrounding tissue, then annihilates with an electron forming a pair of high energy photons (511 keV), which travel in opposite directions and are detected by a ring of detectors surrounding the object of interest. The coincident signals are recorded and the position of radioisotopic contrast lays on the connecting line of the two detected photons. The mean distance of the emission and annihilation positions (positron range) is dependent on the energy of the PET isotope and the attenuation properties of the surrounding tissue [40]. In contrast to PET, SPECT imaging is based on single photon emitting isotopes that are detected by a gamma camera. To determine the direction from where the photon traveled, the collimator (typically made out of lead or tungsten) with single or multiple pinholes or slits must be placed between the imaged object and detector. Only photons that pass the collimator are detected. Based on the trajectory between the collimator and the detector, the position of annihilation can be reconstructed. SPECT isotope energies typically range between 30 and 300 keV

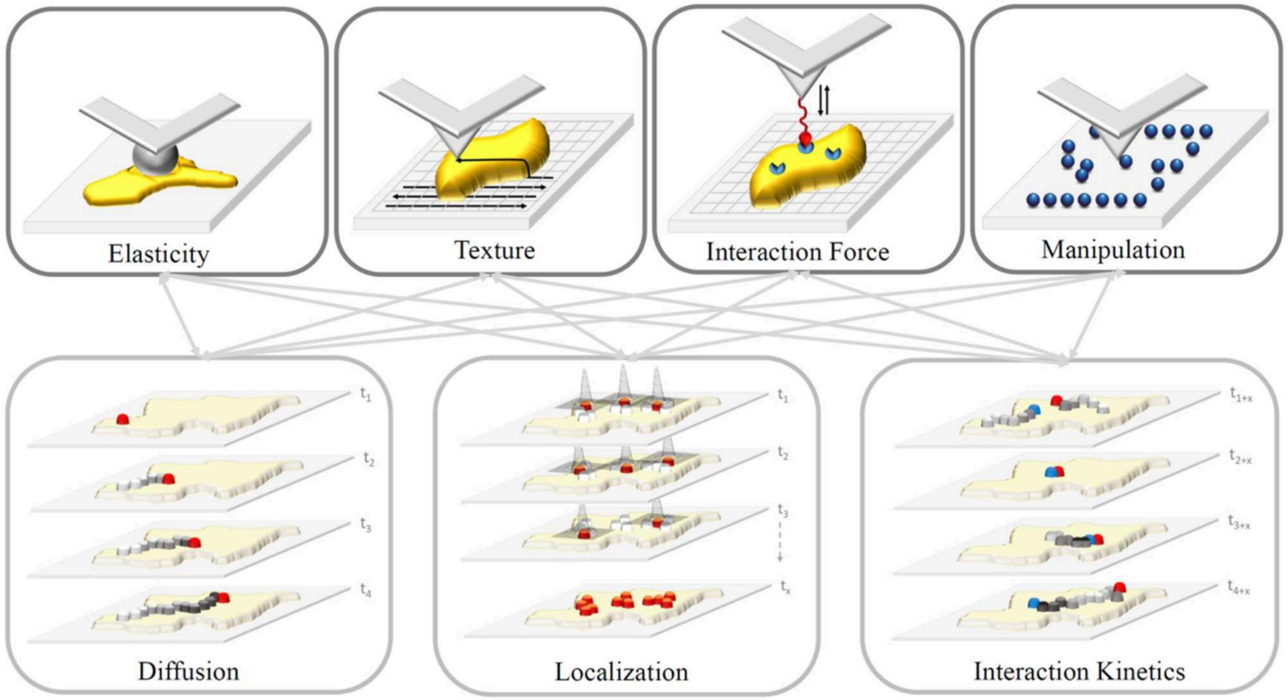


**FIGURE 4 |** Sketch of properties gained from AFM (upper row) and FM-based (lower row) techniques. Gray arrows depict possible combinations of properties. In general, we can differentiate acquired information premised on AFM, whether they are generated via force spectroscopy (measurement of interaction forces via functionalized tips or elasticity via ball-bearing tips) or by spatial scanning (sample texture or feature manipulation depending on the applied force) of the sample (yellow). In contrast, FM-based techniques study movement (e.g., diffusion) and interaction kinetics of molecules, and localize these particles down to an accuracy of a few nanometers depending on the number of detected photons.

and allow multi-isotope imaging when utilizing isotopes with no overlapping energy windows. SPECT and PET imaging have intrinsically different properties in terms of sensitivity and spatial resolution. While in SPECT, the collimator design vastly limits the number of detected photons and hence the sensitivity, PET imaging does not need a collimator and moreover, benefits from the ring design of detectors around the object of interest since the two photons are detected concomitantly by two detectors opposing the site of annihilation. Hence, sensitivity in PET is superior to SPECT sensitivity. Spatial resolution in PET, however, is limited by positron range and crystal size, whereas in SPECT, since the photon originates directly from the nucleus, spatial resolution is theoretically superior to PET resolution. However, spatial resolution and sensitivity are dependent on multiple factors, such as choice of isotope, crystal material, utilized detectors, etc. and especially in SPECT, collimator choice must be adapted based on the desired application. In order to diminish the effects of ionizing radiation, radioisotopes with short half-lives are used for PET and/or SPECT imaging. PET and SPECT scanners are usually constructed as hybrid devices (PET/CT, SPECT/CT, or PET/SPECT/CT). Recently, new PET detector materials compatible with magnetic resonance allowed the construction of PET/MRI hybrid scanners. The advantage of such scanners is excellent soft tissue contrast for precise localization of signal within organs, and the absence of CT imaging allows to diminish the radiation dose accumulated in imaged objects.

Magnetic properties of contrast agents are the basis for magnetic particle imaging (MPI) and electron paramagnetic resonance (EPR) imaging. MPI measures the position of superparamagnetic nanoparticles by detecting their non-linear magnetization response to oscillating magnetic fields [41]. The method ensures positive contrast localization with high spatial and temporal resolution. EPR imaging is similar to nuclear magnetic resonance; electron spins are affected instead of atomic nuclei spins. Different excitation frequencies are used compared to MRI (mostly in the microwave range). Absolute oxygen levels, reactive oxygen species (ROS), oxidative stress or spin probes can be determined *in vivo* by this method [42]. Magnetic molecular methods are usually co-registered with MRI or CT [43].

Optical imaging (OI) is fast and relatively cheap imaging of fluorescence and/or luminescence signals. Fluorescent probes are excited by matching wavelengths and emit fluorescent signal. The limitation of the method is the low light penetration through the tissues. The measured signal is thus not quantitative with more light loss for deeper probe localization. As hemoglobin (oxy- and deoxy-) absorbs the light in wavelengths below 650 nm, the optimal imaging window opens in the near-infrared (NIR) region (650–1,350 nm). Water absorbs at longer wavelengths [44]. Luminescence based on cellular expression of luciferase enzymes converting substrates to visible light gives superior images because it avoids illumination and corresponding tissue autofluorescence [45]. Fluorescent images are co-registered to hybrid images using brightfield or X-ray anatomical imaging. While OI was initially limited to 2D imaging, several technologies have been developed in recent years which allow 3D tomographic imaging in combination with morphological imaging based on CT. For preclinical OI, firefly luciferase is the most commonly used transgene allowing longitudinal studies on e.g., promoter activity in transgenic mice, growth and dissemination of implanted tumors [46] or biodistribution and proliferation of organisms in infection models [47]. Kuo et al. published the first tomographic imaging setup for luciferase imaging, termed diffuse luminescence imaging tomography (DLIT) [48]. Such systems are now also available with built-in CT capability, where CT data are used to determine surface topology. When implanting luciferase labeled tumor cells, this technology allows proper signal allocation to organs when combined with CT contrast agents. NIR fluorescence imaging (NIR) is not only applied in preclinical but also in clinical applications, e.g., for image guided surgery [49]. For the absorption range of 700–900 nm, several fluorophores, nanoprobes and reporter genes have been developed. Another emerging area in OI is the use of the so-called second NIR window (NIR-II) ranging from 1,000 to 1,700 nm [50]. This wavelength range enables imaging with improved tissue penetration depth and spatial resolution, but also minimized tissue autofluorescence and reduced scattering. Correlative imaging of NIR fluorescence and CT is enabled by applying fluorescence molecular tomography imaging (FMT, [51]). Using a commercialized system, tomographic imaging is achieved by acquiring multiple fluorescence images from different positions in transmission mode.

Another molecular imaging method is photoacoustic imaging (PAI). The laser NIR pulses penetrate into the tissue and deliver energy to photoacoustic contrast molecules which undergo a thermoelastic expansion [52]. This expansion then generates ultrasound waves detected by the ultrasound probe. There are specific endogenous contrasts (oxyhemoglobin, deoxyhemoglobin, melanin) and exogenously delivered photoacoustic contrasts for labeling of cells, vasculature, tumors etc. The contrasts give specific positive signal on the ultrasonic background. While other preclinical molecular imaging methods have a spatial resolution around 1 mm, photoacoustic imaging can produce images with a resolution of 50 $\mu$m or less. Nevertheless, the method is limited by the effective light penetration about 10 mm in soft tissues.

While CT has traditionally been used to assess morphologies in bone tissue, it holds more potential to the field of correlative imaging. Going beyond the depiction of mineralized tissues, it provides 3D reference volumes in integrated PET/CT, SPECT/CT or OI/CT devices that readily provide registered, multimodal data sets. Furthermore, CT can be used in a post-mortem, high-resolution, soft-tissue approach. Vascular structures can be visualized at high resolution in 3D via contrast agent perfusion [53], and contrast-enhanced microfocus CT (CE-CT) allows for simultaneous visualization of bone and soft tissues [54]. This makes CT a potent tool for both (a) integrated *in-vivo* applications providing longitudinal, registered 3D volumes in limited resolution and contrast, and (b) high-resolution post-mortem imaging with soft tissue contrast for 3D anatomical and pathological correlation.

Another important multimodal imaging approach that is gaining importance in preclinical settings as it preserves the tissue is label-free (optical) imaging and non-invasive, aseptic assessment of tissues and cells *in-vivo* at high resolution. While FM relies on specific contrast or the application of dyes or fluorescent proteins to highlight certain structures, most molecules do not exhibit intrinsic contrast and the application of dyes or fluorescent proteins might interfere with function and is typically limited to three to four colors due to spectral overlap, which makes it difficult to discriminate between the labeled structures or cells. Especially, optical coherence tomography (OCT) has matured over the last three decades to a potent non-invasive, high-resolution, label-free interferometric optical diagnostic imaging modality enabling video-rate *in vivo* cross-sectional tomographic visualization of structures with resolution comparable to histopathology, serving as *in vivo* optical biopsy [55, 56]. Despite the large potential of OCT, sensitivity and specificity to detect pathologic tissue is restricted and the correlation with other techniques is required. Raman spectroscopy (RS) complements OCT by giving a quantitative measure of the full molecular fingerprint of biomolecules such as lipids, proteins, carbohydrates, and nucleic acids, but is intrinsically slow. It relies on the effect of inelastic scattering of photons, stimulating molecular vibrations providing specific information on the chemical composition and molecular structure, and is an emerging technique in life sciences owing to its unique capability of generating spectroscopic fingerprints of cells and tissues in a non-destructive and label-free approach. It has been demonstrated that the combination OCT/RS on cancerous tissue can increase diagnostic sensitivity, specificity and accuracy compared to a single modality [57]. Two-photon excited fluorescence (TPEF) microscopy can be used to visualize endogenous fluorophores such as NADH and FAD giving information about redox states. Additionally, second harmonic generation (SHG) imaging is well-suited to image collagen fibers. Since SHG signals arise from induced polarization rather than from absorption, this leads to significantly reduced photobleaching and phototoxicity compared to fluorescence methods. SHG microscopy in combination with TPEF microscopy can monitor collagen structure changes and cellular metabolic activity *in vivo* during wound healing [58]. Hybrid multimodal multiphoton microscopy (MPM) [59] with single-photon sensitivity and submicron spatial resolution using the response of endogenous chemical biomarkers in skin, such as collagen or lipids acts as fast and label-free *in vivo* optical biopsy [60]. The synergistically combination of OCT with nonlinear optical imaging techniques such as TPEF, SHG, and CARS (Coherent Anti-Stokes Raman Spectroscopy) provides access to detailed information of tissue structure and molecular composition in a fast, label-free and non-invasive manner [61]. MPM offers high axial resolution with molecular contrast but limited speed and penetration depth. Combining MPM with OCT [62] adds wide-field morphologic information to the chemical fingerprint [63]. As described above, PAI can overcome penetration and scanning range limits of OCT, allowing imaging of deep vasculature [64, 65]. PAI can monitor angiogenesis, map blood oxygenation with sub-100 µm resolution and centimeter penetration depth. In combination with OCT it adds valuable vascular information in depth to the ultrahigh-resolution images [66, 67].

The combination of these optical modalities not only overcomes the limitations of isolated, standard imaging approaches, but also provides unique and complementary information (see **Tables 1**, **2**) which is only achievable through the correlation of these data.

## Novel CMI Pipelines

Since CMI allows to gain structural, functional, dynamical and chemical information about a single sample for a well-defined time point or even time lapse series across all relevant length scales and levels of biological organization, it is the most suitable approach to gain otherwise inaccessible insights into a huge variety of intricate biological processes and understand them within their complex (micro)environment. So far, common CMI approaches mainly focus on the combination of two modalities with two prevalent examples in biological imaging (CLEM) and preclinical research (PHI) that allow to combine functional with structural information from a singular event or within a single study (see Introduction). In PHI, two complementary imaging modalities are fused within a single setup, such as PET/CT or PET/MRI. PHI serves as a valuable diagnostic and research tool that can uncover molecular processes and biochemical pathways in living animals non-invasively within their anatomy, and has been used to study wide variety of biomedical questions, for example in cancer biology or brain research [68]. CLEM has become the method of choice to analyze rare and specific processes within tissues or cell lines, and has been used to study a wide variety of biological questions including membrane trafficking and viral pathways [17]. The maturity of the two fields is reflected in several commercial implementations for PHI (e.g., PET/CT or SPECT/CT), and a first commercially available integrated fluorescence and scanning electron microscope and commercial tools, ancillary equipment and software for CLEM to facilitate re-locating of the region of interest across modalities (see section State-of-the-Art). As illustrated in section State-of-the-Art, the limits of CLEM and PHI are currently pushed towards developing advanced implementation. For CLEM, these efforts include for example advanced FM approaches, such as (cryo)super-resolution or FM of thick tissues [6, 7]. Apart from CLEM, more and more other dual-modality combinations of microscopy technologies have been established during the last decade. Examples of these setups include various combinations of AFM with (advanced) FM (cp. section CLEM and Correlative Microscopy); combinations of soft X-ray tomography (SXT) and FM, for example to localize proteins involved in mitochondrial fission within their close-to-native subcellular context [22, 34, 69]; the correlation of mass spectrometry-based imaging (MSI) with EM to combine the inherently lower-resolution chemical images obtained from secondary ion mass spectrometry (SIMS) with the high-resolution ultrastructural images from EM [70]; and the combination of SIMS [71] and matrix-assisted laser desorption/ionization MSI (MALDI MSI) [72] with fluorescence *in-situ* hybridization (FISH) to link microbial phylogeny to metabolic activity at the single-cell level. Also, the newly developing field of molecular histology has to be mentioned that incorporates findings from MADLI MSI or infrared spectroscopy (IR) in classical histomorphology [73]. Besides, an increasing interest has arisen in research focused on elemental and molecular information that play crucial roles in both physiological and pathological metabolic processes. MALDI MSI was combined with laser-ablation inductively coupled plasma MS (LAICP MS) to study lipid changes colocalized with platinum, sulfur or phosphor distributions [74], and SIMS data were combined with topographical information from AFM to record accurate chemical 3D maps [75]. Advanced PHI includes R&D setups and pipelines that showcase combinations of *in-vivo* OI, OCT/PAI, US, MRI, CT, or PET [8, 76]. Examples as outlined in section Preclinical Hybrid Imaging include label-free imaging using OCT and RS [57], or the combination of MRI and OI [77].

Novel CMI pipelines go beyond correlative microscopy and PHI setups and usually include more than two complementary modalities. They aim at (1) bridging (preclinical) *in-vivo* imaging with *ex-vivo* biological microscopy to zoom in from a living sample to individual cellular structures and/or (2) adding localized spectroscopic [biophysical (e.g., mechanical properties or vibrational modes) or chemical (e.g., molecular or elemental)] information to the acquired structural and functional parameters. With all the electromagnetic spectrum explored for imaging, only incremental improvements in contrast, resolution, or sensitivity are expected for the available spectrum of imaging technologies (see e.g. **Tables 1–3**). To explore the multiple spatial and temporal scales necessary for a holistic understanding of organisms and their biology, novel CMI pipelines will be the method of choice. However, novel CMI pipelines with more than two modalities are in their infancy due to lack of access to a single researcher, the broad expertise required to oversee several modalities and due to lacking workflows and software solutions to track ROIs across modalities from living 3D tissue down to high lateral molecular resolution. While there are several EU-funded initiatives that aim at improving accessibility of advanced imaging technologies and interdisciplinary imaging expertise (such as Euro-BioImaging or COMULIS), such novel CMI pipelines nevertheless require substantial method development. Due to the diverse plethora of potential combinations of imaging technologies, setting up universal correlation protocols for CMI pipelines is not feasible. Sample preparation procedures for *ex-vivo* microscopy differ substantially across the technologies and even within a modality; AFM images alone, for example, can be acquired under various conditions (vacuum, atmosphere, and liquid). Correlative imaging usually requires modality-specific preparation and setup trade-offs, such as between preservation of fluorescence and subcellular architecture for CLEM, between the AFM laser and excitation spectra of the used fluorophores to avoid bleaching for correlative AFM [78], or between preservation of fluorescence and X-ray contrast for correlative

CT. Dependent on the used technology, the sample preparation needs to be adapted.

In respect to correlation strategies, universal protocols to assess correlation accuracy are not implemented and restrict finding the same ROI after relocation between imaging platforms or co-alignment of data sets. Strategies to improve correlation of different technologies include (1) resolution matching of the technologies and (2) correlative markers that can be visualized in different imaging technologies.

A common approach to improving correlation accuracy in correlative microscopy is to match the FM resolution to that of the microscopy technique with the highest resolution (EM, SXT, AFM) by integrating super-resolution FM. For CMI pipelines that bridge *in-vivo* with *ex-vivo* imaging, usually intermediate (mesoscopic) resolution steps need to be implemented—as for example mesoscopic *ex-vivo* MRI for the integration of macroscopic *in-vivo* MRI data and microscopic CT data [79]. A common example includes the emerging use of CT in a different context: As an intermediate imaging technology to create a 3D template of the sample after *in-vivo* imaging and before sectioning of the sample to probe the ROI. CT can visualize thick tissues in 3D at micrometer resolution, tracks distortions and morphological changes of the ROI after embedding and fixation, and allows ROI identification even without (preserving) fluorescence. CT is specifically suited as an intermediate technology between *in-vivo* optical microscopy and EM since it can also visualize the sample in resin blocks due to the heavy-metal stains used for EM sample preparation. It qualifies for other correlative microscopy approaches as well since it can reveal endogenous landmarks, such as the vasculature, after barium sulfate perfusion.

While there are a variety of fiducial markers that can be used and tracked in correlative microscopy (such as QDs or dye-labeled nanoparticles), there are currently no correlative markers that can be visualized with high accuracy both by microscopy and preclinical imaging technologies. Besides, robust fiducial markers that might withstand electron bombardment or high X-ray doses are also lacking. A common approach to facilitate correlation when using CT as an intermediate modality is near-infrared branding (NIRB). Prior to CT, a pulsed, near-infrared laser is used to create defined 3D marks in the fixed tissue that can be traced by both FM and EM, and hence facilitates dissecting the sample to assess the ROI in a biopsy. In Karreman et al. [80], the position of the ROI was predicted with an accuracy of below 5 $\mu$m.

A typical correlation workflow for a CMI pipeline including for example, *in-vivo* optical microscopy, CT and EM typically might include the following steps, and will need to be adapted for the specific biomedical research question: (1) *in-vivo* functional imaging of molecular dynamics using FM, such as spinning disk, light sheet or multi-photon microscopy, or *in-vivo* imaging of metabolic processes using advanced preclinical imaging technologies, such MRI or OCT; (2) (a) near-infrared branding, sample fixation, dissection, and further EM processing or (b) dissection, high pressure freezing, and freeze substitution; (3) resin embedding (lowicryl if fluorescence is to be preserved); (4) CT for identification of ROI; (5) volume EM. This workflow must be adapted according to the desired biomedical outcome. To preserve the native ultrastructure, cryo-fixation (high-pressure freezing) might be desired. This might be followed either by freeze substitution or by a cryo-workflow with the aim to perform cryo-EM. Surely, preserving the fluorescence (either with LR-white or HM20 acrylic resins and adapted EM protocols or by keeping the sample under cryo-conditions) can be of advantage to re-locate ROIs. If considering serial section EM (or on-section CLEM), fiducial markers can be added, and a commercial CLEM system can be used to re-identify the ROI in the fluorescence channel and retrieve it in the EM using e.g., SerialEM.

Several workflows have so far been established that solved the above-mentioned challenges on sample preparation, re-localization of ROIs, and data correlation. Recent examples for multiscale combinations of *in-vivo* and *ex-vivo* imaging include the correlation of intravital microscopy, CT and EM to study single tumor cells in the cerebral vasculature [81]; correlation of X-ray holographic nano-tomography, EM and FM to disentangle dense neuronal circuitry in *Drosophila melanogaster* and mammalian central and peripheral nervous tissue [82]; correlation of local neuronal and capillary responses by two-photon microscopy with mesoscopic responses detected by ultrasound (US) and BOLD-fMRI [83]; or extended CMI pipelines that include the correlation of a variety of imaging technologies, such as non-invasive US, CT and high-resolution episcopic microscopy (HREM) for phenotyping left/right asymmetries of all visceral organs in a mouse model of heterotaxy or combined OCT, PAI and HREM of chick embryos at multiple development stages [8, 84, 85]. Further examples of novel CMI pipelines that uncover biophysical or chemical information include the correlation of FM, molecular (MALDI MSI) and elemental imaging [X-ray fluorescence (XRF)] to analyze lipids and elements relevant to bone structures in the very same sample section of a chicken phalanx without tissue decalcification at the $\mu$m scales [86].

## Correlation Software

In addition to the experimental elements helping to bridge the different modalities mentioned in the previous sections, analyzing automated software solutions to correlate complex, multiscale, multimodal and volumetric image data including reconstruction, segmentation, and visualization are an essential pillar of CMI. Image processing and image analysis in biomedical imaging is a wide field of research, having their own conferences (such as ISBI, MICCAI, or NEUBIAS) and specialized journals (IEEE TMI or Medical Image Analysis for example), with thousands of new methods published every year. One common aspect defining the field is the cross expertise needed to develop new algorithms and software: The physics of the imaging modality, and the knowledge of the biological model or of the disease and organs beyond studies are usually important elements to be considered when developing an image processing or analysis method, making this field highly pluridisciplinary. Methods tackle different problems such as restoration (denoising and enhancing the quality and resolution of the acquired images), segmentation (identifying and spatially localizing objects in images), registration (aligning different images of the same or similar objects), and visualization (generating a comprehensive, potentially interactive, representation of the acquired imaging data). In this review, we focus on the two latter, in the context of CMI. Other main elements are mostly specific to one modality and we refer the reader to existing reviews for general approaches, for example, for the use of deep learning for all of these main components of image analysis [87] or for specific components for a specific modality (such as for EM image data restoration [88]). Note that one exception can be made regarding segmentation, where aligned volume can be sometimes used for what is called multimodal segmentation where information gathered from the different modalities refine the segmentation of the ROI [89]. This last category is actually one example of the interest of CMI from the image analysis point of view, where CMI helps image analysis and quantification.

Image (2D or 3D) registration is the process of computing the transformation linking two images or volumes to overlay matching structures (**Figure 5**). It is a prerequisite for joint quantitative evaluation of the data across modalities and scales for any kind of multimodal visualization of imaging data.

The model of transformation, i.e., the number of degrees of freedom allowed between the two images, is an important choice, relying on the knowledge of the physical relationship between the sample or the organ from one modality to the other modality. This transformation can be seen as a change of coordinate system if the organ or sample was not undergoing important deformation or deterioration between the two modalities. In that case, a rigid (rotations and translations), similarity (rigid plus uniform scaling), or affine (similarity plus shearing or reflection) may be sufficient. If there are deformations due to the sample evolution over time or due to the sample preparation step for the second modality, a more complex model allowing global and/or local deformation will have to be used (non-rigid or elastic models), according to the required accuracy. Currently, registration is often done in a semi-automated way in two steps: first, manual or automatic identification of landmarks or whole structures (segmentation) in the images to be correlated; second, manual definition of corresponding pairs of these features by the user. These landmarks serve then as an input to the registration process, that is computing an optimal transformation by maximizing the spatial matching of all defined features pairs.

In CLEM, mainly three software solutions are used to perform landmark- or segmentation-based registration: a plugin for FIJI [90] (distribution of ImageJ including many useful plugins) called BigWarp (initially developed to provide training and validation sets), a plugin for ICY called ec-CLEM [91], and the

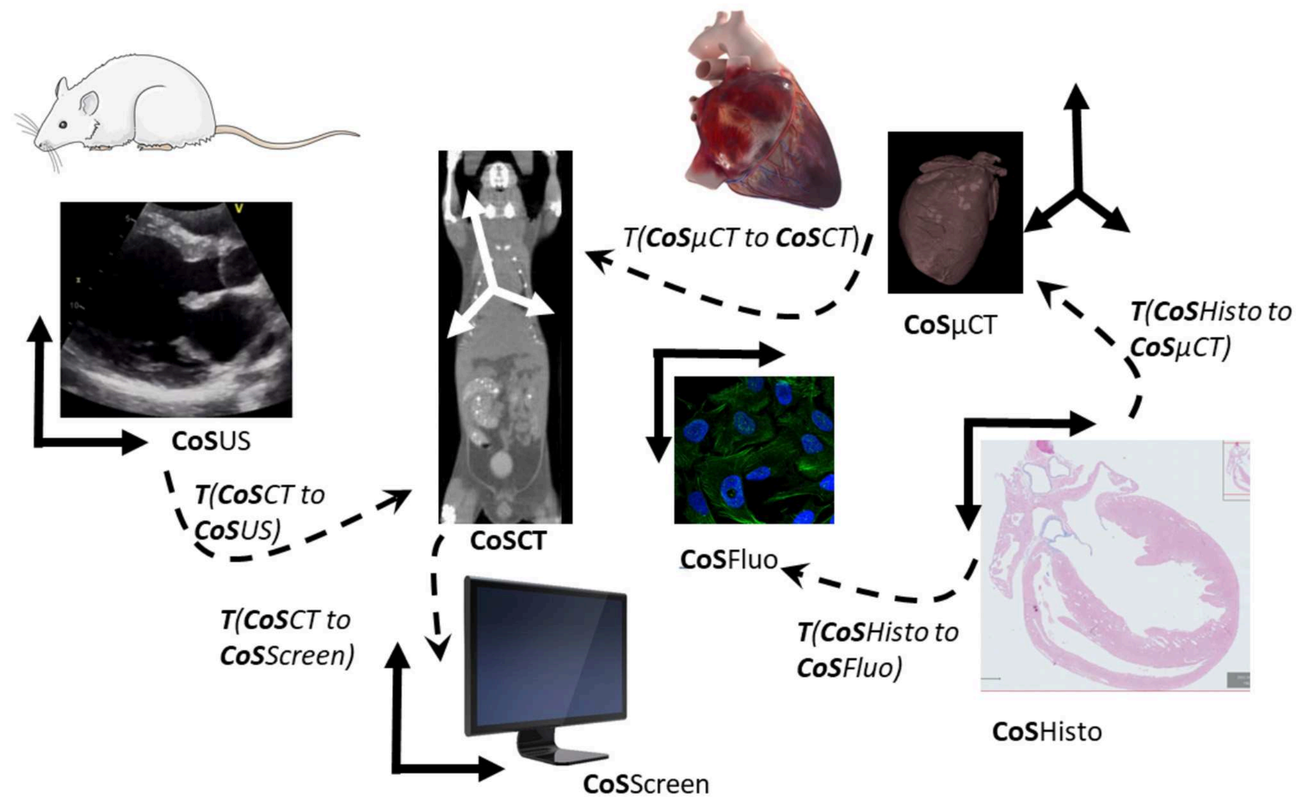


**FIGURE 5 |** Transformations and coordinate systems involved in the merging and visualization of multimodal data. All transformations between pair of images can be then combined to link all acquisitions and move between scales and modalities. CoS means Coordinate System. T (CoSUS to CoSCT) means the transformation spatially linking the two CoS, allowing for example to locate a US image in the CT volume. To compute the cell in the CT CoS, one can then combine transformations and apply it to the fluorescent cell images (CoSFluo) for example T (CoSFluo to CoSCT) = inverse [T (CoSHisto to CoSFluo)] × T (CoSHisto to CoSμCT) × T (CosμCT to CoSCT). Note that these changes of the coordinate system (or transformations) have to be computed in 3D to take into account possible changes of obliquity, and that they do not take into account deformations induced by sample preparation from one imaging modality to another one.

commercial software AMIRA (Thermofisher, Bordeaux France). Several structures have been used to correlate, including vessel, mitochondria, nuclei, added fiducials such as quantum dots (QDs) in the correlative microscopy field, or specific anatomical landmarks in the medical fields. Several other solutions exist in particular in the medical field, but are very dependent of the medical or biological question and of the workflow of imaging. One method will usually be composed based on a set of existing basic bricks performing one task to achieve the expected results [92].

The challenges in fully automated multimodal registration come from the discrepancy in the appearance of structures by different contrast mechanisms and resolution. While the specimen or sample undergoing imaging is usually kept the same size, imaging can focus on a very different field of view with a very different resolution. Algorithms then have to deal with what is called occlusion effect. The problem is usually tackled in a two-step process: first finding the coarse relationship between images, then doing a more accurate registration, that may take into account local deformation if any [93]. These local deformations are usually due to the sample preparation step (for instance, dehydration in histology, which makes the workflow of **Figure 5** very challenging without the use of fiducials). Two main approaches can be considered [94]:

(1) Considering the full content of the images and trying to find a common representation intensity space to be able to use monomodal approaches and metrics, or to define a metric that would take into account the possible discrepancy (a classical one is called mutual information, and is comparing joint histogram rather than intensity itself). These approaches are preferred when the different modalities present potentially similar content but with different aspects, for example, when matching bright field imaging with low magnification electronic images [95–97], when cell or nuclei edges are visible on both modalities, or CT with MRI where most of the anatomical structure will be appearing. An interesting approach in deep learning, rather than learning the common space between images, is to directly learn the transformation parameters linking two modalities by using pre-registered images undergoing a set of different parameters for one given transformation as a training set [98].

(2) Considering elements of interest extracted from both modalities, for example anatomical landmarks (points or shape of interest) or multimodal markers visible in both modalities (such as fluorescent QDs in CLEM). These approaches, generally called feature-based registration, are of particular interest when the relation between content is unknown or cannot be taken as an assumption (for example for the validation of a new probe or a new imaging modality). The method to find the matching and compute the transformation can be done with two main paradigms: transforming the image data in localizations with potential additional features using point-based registration ([89, 91] for the AutoFINDER part of ec-clem) or shape-based registration, potentially with intensity-based machine learning approaches [99]. Note that a plethora of variants exists for point-cloud registration, some of them sounding particularly promising for feature-based multimodal registration [100]. Interesting approaches mixed both feature-based and full registration by restraining the learning data set to registered features [101].

For both approaches one of the commonly used libraries for software implementation is ITK (https://itk.org) usually coupled with its visualization counterpart VTK (https://vtk.org).

Very powerful (command line) tools for landmark based or fully automatic image registration (rigid and deformable) are Elastix (http://elastix.isi.uu.nl), its derivative Simple Elastix (http://simpleelastix.github.io) and ANTs (http://picsl.upenn.edu/software/ants/). They allow the definition of fully parameterizable complex registration pipelines. Both libraries support the creation of so-called templates-standard reference spaces that enable the co-registration, comparison and joint analysis of images related to the same structure as represented on the template. These images can come either from the same or different subjects and, as long as there is enough joint information content to ensure registration, they can come from another modality. Multi-channel imaging, where one channel enables easy registration to the template, can support the integration of imaging data with complementary information to the template, like the integration of anatomical and functional images or spatial gene expression data. One prominent example for such standard spaces are standard brain templates that are used to spatially integrate collections of multi-modal brain data e.g., of humans or rodents like the Allen Brain (https://portal.brain-map.org/) or Human Brain Project (https://ebrains.eu) atlases, or the brain of adult [102] and larval [103] drosophila melanogaster.

Visualizing multimodal data, also referred as image fusion, require the knowledge of the spatial transformation linking the images, obtained by registration as explained above. Once this spatial relationship is known, there are several ways to fuse the image information for its interpretation by the user (**Figure 6**). Visualization *per se* is mainly categorized in two areas: image and volume rendering (for example using ray-casting algorithms), and region of interest rendering, using for example surface representation with meshes of polygons to match the ROI outside, after segmentation. One simple surface representation without proper identification is isosurface rendering, where a surface shape is defined by an intensity threshold and a surface mesh generated from it. A third way is to use slicing from a 3D volume and come back to a 2D visualization problem. One of the difficulties in multimodal visualization is the difference of spatial resolution between images, calling for interpolation, e.g., upsampling the images of the modalities with lower resolution to the same resolution as the images with the highest resolution. Most registration algorithms automatically resample the moving image to the resolution of the images to which it is registered (the fixed or target image), meaning pixels not existing in the original image have been created by interpolation.

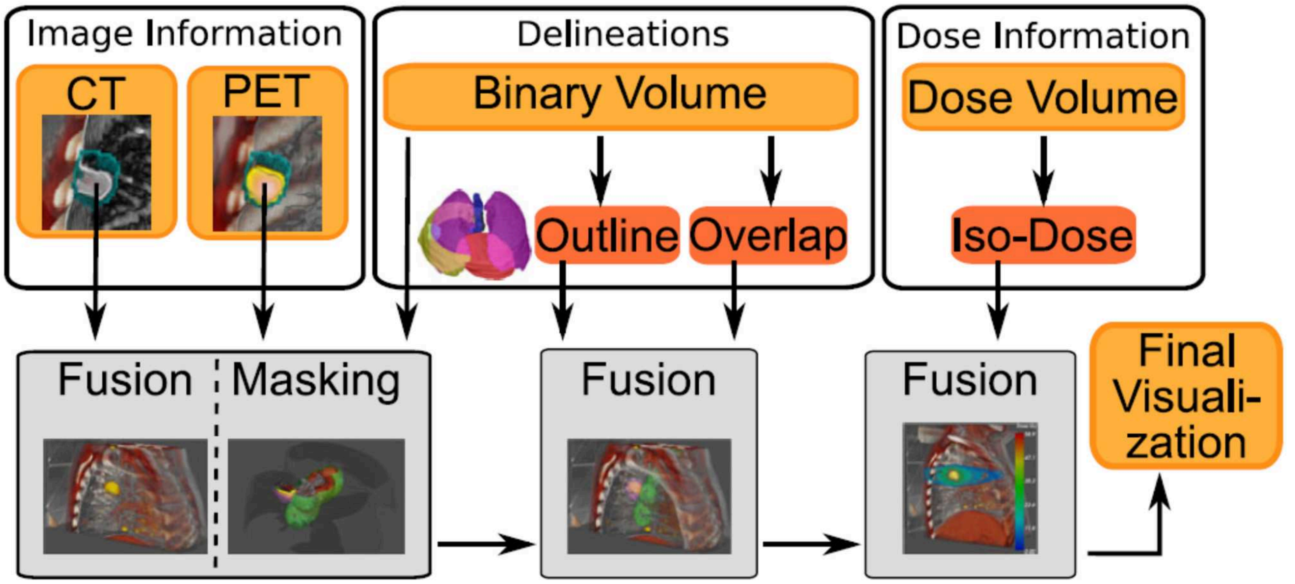


**FIGURE 6 |** Example of image sources (volume rendering or segmentation) from different modalities, where each type of modalities will be processed differently to provide the final visualization. Figure extracted from Schlachter et al. [104] under the Creative Commons Attribution License.

Efficient visualization of multimodal images will usually propose a combination of different visualization methods [104] and can add an additional channel of information related to the registration itself, such as the error in registration [105, 106]. One of the particular challenges is to deal with data that do not have the same dimensionality, such as time lapse vs. 3D or hyperspectral images, and heterogenous data [107]. To keep the full resolution of the biggest image, with data that can reach several terabytes in size for just one specimen, efforts are ongoing regarding efficient approaches of displaying and manipulating very big data, such as the big data viewer [108] as also used in the BigWarp Fiji Plugin.

For a more exhaustive list of software used in the field, the reader is invited to refer to a constantly updated list of software established in collaboration between the COST actions NEUBIAS (CA15124) and COMULIS (CA17121): www.comulis.eu & www.biii.eu.

# CHALLENGES OF THE FIELD AND CURRENT SOLUTIONS

## Standardization

### CLEM and Correlative Microscopy

As highlighted earlier, every biological question demands its own technological approach. This makes standardization difficult. There will never be one workflow to tackle every single question. It is important however, to try to avoid re-inventing the wheel all over again. Dissemination of established protocols and training the next generation of scientists in these protocols is therefore of the utmost importance. COMULIS is actively promoting such training and standardization where possible.

In CLEM, one of the areas where standardization would be possible is on the correlation precision. Where correlation down to around 50 nm is currently possible (e.g., [16]), for certain approaches an even more precise correlation would open up completely new possibilities. Can we map single fluorophores onto a single protein structure inside a crowded cellular environment? This is currently a dream scenario but will likely be possible in the future (see section CLEM and Correlative Microscopy).

For the moment we will have to do with internal or external added markers that can be used as fiducials for the alignment of the two datasets. If these dual-modality markers are used also to label specific proteins of interest, the first choice are quantum dots as they are fluorescent and their core, generally being made of Cadmium and Selenium, and is made of heavy metals for visualization in EM. Care must be taken however that the proteins coupled to such probes still fulfill its original function. We have shown that Transferrin coupled to QDs does not recycle anymore but, likely due to multiple receptors binding to one QD, is directed down the degradative pathway [109]. An alternative approach, using fluorescent moieties coupled next to a gold particle, has its own issues. It is well-known that fluorescent dyes can be quenched when in close proximity of gold particles [110]. We have recently shown that Alexafluor488 coupled to a 10 nm gold particle is quenched by 95% [111] rendering that particular probe useless as a true CLEM probe. One is probably better off using two individual probes, one tagged with fluorescence and one tagged with gold particles. In our experience a 1:10 ratio works well. Due to technical restraints we have not been able to measure the quenching effect of smaller gold particles yet. One can also add a fiducial marker from the outside. Kukulski et al. [16, 18] reported the use of 50 and 100 nm sized fluorescent beads that are added just before fixation and which are also readily identifiable in the electron microscope. The current methodology allows to correlate the LM and EM images from such experiments down to approximately 50 nm and would at the moment be considered as the standard. With the increasing integration of super-resolution FM technologies into CLEM workflows, this precision is most likely to improve. This does however warrant a remark. Again, it is all down to the underlying question what kind of precision is required. When one is for instance searching for a rare transfected cell amongst a field of untransfected cells all that is required is a correlation precision in the range of micrometers rather than nanometers.

In correlative AFM, first combinations studied the sample first using FM and then transferred it to the AFM [112], which restricted correlation. Early efforts imaged the fluorescence of labeled molecules and topographically imaged the same area. This was misleadingly termed as synchronized operation. The two high-resolution techniques can hardly operate simultaneously due to their reciprocal disturbances. Apart from the mechanical instability of the construction, FM excitation laser(s) can induce disturbances by influencing the detection system of the AFM and/or by short-time heating of the cantilever. Additionally, the AFM laser can lead to photobleaching of fluorescently labeled molecules. In general, these problems can be solved by carefully planning the performed experiments and adequately assembling the correlative setup. The biological material itself and the molecule of interest has to be immobile or immobilized as otherwise we would not be able to benefit from the merge. Most immobile samples are studied in combination of AFM with superresolution as both techniques demand immobile samples. Optical microscopy allows studying molecules within transparent samples in contrast to AFM, which is exclusively applicable on surfaces. TIRF excites fluorophores only close to an interface between different optical densities. To limit the influence of the optical excitation to the AFM system, it is convenient to combine these two methods.

## Preclinical Hybrid Imaging

Over the last decade, there has been an ongoing discussion about the ability to successfully translate preclinical findings into clinical practice [113–116]. Multiple studies have demonstrated that a bench-to-bedside translation from preclinical results into clinical practice is not as easy as anticipated [113, 115, 117]. **Figure 7** illustrates multiple biological, methodologic and technical factors inherently linked to the reproducibility, reliability, and comparability of preclinical imaging data. Each of these factors has a significant impact on the validity of the acquired data and hence can influence reproducibility and reliability of results. Furthermore, it has been shown that replication of already published results is not as straightforward as the scientific community would hope [113, 119, 120]. Hence, standardization of preclinical imaging protocols and techniques to overcome the "replication crisis" has been stated to be of utmost interest [121, 122].

In sharp comparison to the preclinical research field, clinical standardization is much further advanced and accreditation programs of scanners have been implemented together with unified quality control protocols to ensure reliable, comparable and reproducible results. Furthermore, standardized protocols are in place, which allow multi-center comparison and pooling of the data [123–125]. However, multi-center comparison is still not as easy as anticipated, but up to this point the efforts undertaken have clearly shown its benefit in clinical practice [126, 127].

It is important to emphasize that "over"- standardization in the preclinical environment is not the goal. The fast, dynamic pace of preclinical development is still a strength of one of its kind and should not be outmaneuvered. However, we have to ensure that preclinical findings can be translated more straightforward into clinical research and practice. Therefore, certain techniques, such as anesthesia protocols and animal handling, need to be unified. Furthermore, as has been stated multiple times, precise reporting of methods and techniques is of utmost importance to ensure feasible replication, as well as to facilitate findings from literature and build up based on the existing knowledge [128, 129]. Guidelines, such as the "Animals in Research: Reporting *in vivo* Experiments (ARRIVE)" guidelines help to improve the quality of reporting, and will consequently maximize the output and validity of published data [129]. In addition, multiple journals have updated their requirements for manuscript submission so that the respective authors either need to upload imaging data as well as all metadata, or to include a data availability statement during submission [130, 131]. An open access of the imaging data and respective metadata is certainly a huge step toward transparency and increased reproducibility and reliability of the data [132], as it has been demonstrated that image analysis is highly user- and software-dependent [133]. Randomized preclinical multi-center studies have been proposed to overcome the lack of reproducibility due to inadequate sample size, low significance, and low confidence of data [134–137]. However, the potential of multi-center studies cannot be fully accessed without proper standardization techniques in place in each participating institute. A recent study focusing on utilizing a basic [18F]fluorodeoxyglucose ([18F]FDG) imaging protocol in 4 different institutes demonstrated that the comparability among multiple institutes might be hampered due to, e.g., animal handling (each institute had different fasting protocols of animals in place; temperature regulation of animals during acquisition differed significantly), and animal facility environment or image analysis [133].

In regards to image analysis, the use of hybrid imaging technologies, with which anatomical co-registration data can be acquired using CT or MRI, significantly enhances the reliability of image analysis since this allows a precise definition of ROIs on the anatomical images that can be overlaid with functional imaging data (e.g., PET or OI data) to ensure the correct placement of ROIs, which is often difficult on functional data only [133]. Multimodal hybrid imaging can enhance reproducibility of results, but nevertheless precise standardized protocols to do so need to be implemented.

There is a huge demand for standardization in preclinical imaging and efforts to implement standardized protocols undertaken by initiatives, such as COMULIS, on a multi-center basis are certainly major steps toward more reproducibility and reliability of preclinical imaging data, as well as increased translation into clinical research and practice.

### Correlation Software

As seen from section Correlation Software, different methods have already been proposed in the literature for image registration or multimodal visualization. However, a few of them are actually used by researchers in life sciences, and one of the main reasons for this is the lack of user-friendly implementation and availability as software. In addition, as underlined in the other sections, every biological or medical questions comes with its own image analysis workflow [92]. In order to help with these workflows, but also to help data sharing and open science, a standardization of the representation of the multimodal spatial relationship and content types will be important. In the medical imaging field, such standards are in place, using Digital imaging and communications in medicine (DICOM), which includes guidelines for the representation of spatial transformation between multimodal images [linear (C20.2 DICOM) or deformable (C 20.3 DICOM)]. However, the list of metadata proposed by DICOM is really exhaustive and may prevent users and constructors to actually fill in this information, which represents 15% of major errors as reported in Gueld et al. [138]. In particular, this effort will be important for imaging modalities for which this standard is not in use now and information is not automatically filled in, or for third-party software or home-made methods to compute the spatial transformation that link two images or volumes. For this reason, there is ongoing effort associated with the deployment of public image archive [139–141] to define some minimal metadata requirement, and the one associated with CMI have still to be defined by the community.

Computing the accuracy and assessing the quality of the registration is one of the central problems of correlative microscopies or more generally CMI, in particular because the structure of interest is usually not marked in both modalities, and so it is essential to confirm the correlation is correct and not biased by user assumptions. This is of particular importance when dealing with largely multiscale approaches, since one pixel can be matched with a structure of hundreds of pixels in another modality, and then an error of one pixel could lead to erroneous conclusions. In previous publications [16, 142], an iterative leave-one-out method was used to assess the accuracy of the registration, where the registration error was computed as the average error of localization of beads not used for the registration and was therefore empirical. Recent work tried to find a theoretical estimation of the error, using the Cramer

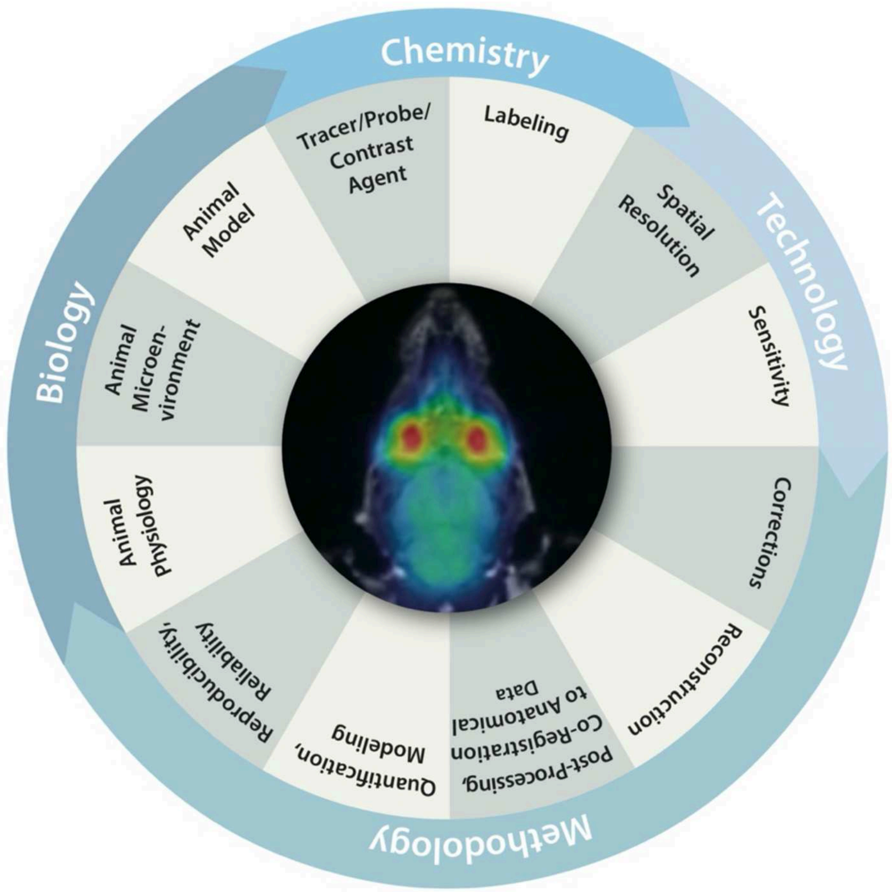


**FIGURE 7 |** Biological, chemical, methodological and technical factors inherently linked to the reproducibility, reliability and comparability of preclinical imaging data. Figure adapted from Figure 1 from Herfert et al. [118] with reprint permission from Springer according to their creative common license http://creativecommons.org/licenses/by/4.0/.

Rao limits [143] to estimate the transform error by taking into account the high resolution limit of accuracy. In ec-clem, the error is estimated using a formalism from the medical field for 2D and 3D rigid registration [144], originally developed for image guided surgery. It can be applied to correlative microscopy but is limited to a rigid-transformation point-based framework, and has the advantage of not requiring any ground truth matching in the images. In addition, this method may lack a proper mathematical formalism to demonstrate their usability in the fields. Note that metrics to compare images based on intensity may not be adapted in most of the case due to the discrepancy of image content (structures not present in both images). In the case of the absence of fiducials or anatomical landmarks to validate the registration, another currently used method to validate the accuracy of a registration is to use segmentation quality metrics, such as DICE metrics, to assess the overlap between known segmented structure.

Challenges are the competition of algorithms on a given dataset, where the ground truth is known in order to rank the algorithms according to a set of metrics designed for the challenge. Some challenges have been organized for the multimodal field, but usually focused on one particular problem (Anhir focused on multiplexed histological data or Curious for US to MRI brain images registration [145]). These challenges are of great interest since they provide a way to identify the actual level of accuracy state of the art and give direction for future research. They will also help define common and standard ways to assess the accuracy of the alignment of multimodal data, by defining community accepted stand error metrics.

## Requirements for Optimization and Challenges to the Field

### CLEM and Correlative Microscopy

In the recently published book "Correlative Imaging: Focusing on the Future," there was one over-arching theme that was highlighted in almost all chapters: Data. If handling data from a single modality can already create headaches for the data analysis and IT people, how about trying to combine datasets from different imaging modalities. Developments and possible solutions will be discussed in other parts of this review.

On the hardware side there are also clear trends visible and they almost seem to diverge from each other. On the one hand, there are the cryo-CLEM approaches trying to map protein structures in ultrastructural data, on the other, volume CLEM (a collection of techniques including FIB-SEM, SBF-SEM, array tomography, electron tomography) is more focused on large scale structures and mainly looks at connectivity between cells.

As with the integration of GFP in CLEM from 2000, the resolution revolution in cryoEM has now also been integrated into CLEM workflows, especially aided by the development of LM stages that can work under Liquid Nitrogen conditions [146–148]. These devices allow for the observation of fluorescent structures of plunge frozen samples and record their location for further studying in a cryo-TEM. Whereas, these stages are now fairly commonly in use, the development of cryo-CLEM workflows is still improving; e.g., super-resolution cryo-fluorescence has been recently shown [149]. One of the issues that needs to be dealt with in cellular cryoEM is the thickness of the sample. In most cases, only the outer edges of a cell can be directly imaged. Anything more inside will be too thick to image directly. Cryo-FIB-milling is currently the only way to acquire thin slices of frozen material for cryo-electron tomography (ET) [150]. Targeting the correct area in Z-height, the depth of the sample, is still one of the bottlenecks but acquiring fluorescence data in 3D using confocal cryo-fluorescence will further aid with this targeting problem.

Life is 3D, so also techniques falling under the quiet revolution banner (FIB-SEM, SBF-SEM, Array tomography, electron tomography) are being integrated more and more into CLEM approaches. Especially in these cases, finding the structure of interest adds another dimension of complexity. Resolution in z is generally lower than in x, y so targeting is even more difficult. Also acquisition of z-stacks acquired before processing for EM can be useful and essential but the coordinates may change during the processing. The addition of fiducials or endogenous tissue-existing landmarks, such as blood vessels, can be useful. In addition, a bridging step with intermediate resolution such as CT are relatively new additions to the CLEM workflows [80].

Fully integrated light and electron microscopes should be able to provide the best correlation between the two modalities and both integrated LM-TEM [151] and LM-SEM [111, 152] have been developed and are still improving. Of note here is that all these systems can only work with fixed samples and one of the hallmarks of light microscopy, live imaging, is lost. As before, it is the biological question that will determine what workflow and technology fits best.

In correlative AFM, correlative challenges and opportunities are faced by recent technological advancements, improving temporal and spatial resolution of already established techniques. The combination of these highly sophisticated setups is far from trivial and highly challenging. High-Speed Atomic Force Microscope, for example, allows studying dynamic processes at sub-molecular and sub-second scale and can be combined with STED to track molecular movement at nanometer resolution and in the millisecond range.

To enable a precise and simultaneous superposition, disturbances in correlative AFM must be sufficiently shielded. An acoustically shielded chamber around the FM including the AFM measuring head is suitable for this purpose. All components that can cause electronic or acoustic interference must be removed from the isolation chamber. Typically, water-cooled EM-CCD cameras are used here to minimize interference from the outset. During simultaneous applications, the problem arises that the measuring tip of the AFM is heated by the excitation laser. This problem cannot be prevented; in this case, combinations with TIRF or confocal microscopy are usually used. It is important to keep the excitation energy at the position of the cantilever low. If both techniques are used at the same time, a real time superposition of the images is currently not possible. In most cases, the images have to be adapted to each other by mathematically forced imaging errors.

For this purpose, a fluorescent grid is suitable which is taken before the actual measurement with both techniques at the same position and subsequently adapted to each other. Currently, the AFM manufacturers already offer their own software for superimposing the images. The measuring tip is moved to several different positions, which are recorded simultaneously on the microscope and then superimposed directly. However, the measuring tip in the fluorescence image cannot be superimposed more precisely than the resolution of the microscope. Of course, the resolution can be increased by fitting techniques, known from super-resolution microscopy, but the resolution of the AFM itself can never be achieved.

Further challenges will be the combination and further development of additional microscopy technologies, such as correlative SXT. Since imaging under cryo-conditions preserves a close-to-native environment (as for cryoEM) and in certain cases (as for SXT due to its operation in the water window) is the only possible implementation, the development of cryo-FM will play a crucial role in correlative microscopy. For correlative SXT, superresolution FM is specifically appealing since it matches the achievable spatial resolution, and further efforts will focus on its cryo-implementation [23].

## Preclinical Hybrid Imaging

One of the current bottlenecks for PHI lays in radiation doses for X-ray imaging together with radioisotopic imaging methods. CT, PET, and SPECT imaging delivers substantial radiation dose into the animal, and, of course, to the patient as well in clinics. The prolonged CT scanning times along with high doses of radioisotopes applied to the animal may interfere with the immune system, tumor growth and rapidly proliferating tissues (bone marrow, intestine) renewal. There are estimates that up to one percent of patients repeatedly scanned for possible metastases by whole body CT, PET/CT or SPECT/CT during a 5-years follow-up period may die because of new tumors induced by the imaging process [153, 154]. The significantly lower radiation load to the patient brings PET/MRI imaging; nevertheless, the high dose coming from high energy PET isotope injection cannot be avoided. Moreover, CT is excellent for hard tissue (bone) and contrast (e.g., angiography) imaging but soft tissue discrimination is rather poor. Several companies brought to the market so called spectral CT devices. They are usually based on dual energy X-ray sources, and the comparison of the energy-dependent attenuation of signal can improve the soft tissue recognition and distinguish contrasts and the bone, which is not possible in classical CT devices [155]. These CT machines can utilize slightly lower radiation dose compared to previous generation. Due to the recent progress in the development of novel radiation detectors, there occurred a possibility to introduce a completely new radiation detection approach. Under international collaboration in CERN, the photon counting TimePix detectors were developed. The current generation of TimePix3 detectors allows a simultaneous detection of the exact position, energy and time of the photon interaction. These properties can be used for true spectral CT detection. Novel detectors are much more sensitive and have a high spatial resolution of 55 $\mu$m. The CT image can be obtained very fast (in seconds compared to 20 to 30 min for high-resolution standard scans), thus significantly reducing the absorbed radiation dose. The filtering of noise allows to increase the signal-to-noise ratio. According to different attenuation tissue patterns, soft tissue recognition is easier even without contrast [156]. The high speed of TimePix3 detectors (1,700 images per second) and energy resolution is suitable for coincident event registration also in PET imaging [157]. The proof-of-principle of the use of the TimePix3 detectors has been published [158]. Several groups are testing the use of Compton cameras for SPECT imaging instead of collimated SPECT detection [159, 160]. Compton cameras allow to calculate the trajectory of incoming photons from original hit position and Compton scattering detected by a second detector layer. This allows to increase the sensitivity of SPECT from $<$0.1 to 80% for the most used SPECT isotope $^{99m}$Tc. SPECT imaging thus only requires a fraction of currently used radiation activity, and the absence of collimator facilitates the construction of combined CT/PET/SPECT devices with just one ring of detectors that can simultaneously record fast fully trimodal hybrid whole body imaging with very low radiation load. The main limitation is still the high price of detectors which could be in future substantially lowered by demand for production in large series.

Most of the optical imagers allow to detect fluorophores from visible light up to the NIR region with the longest wavelengths around 850 to 900 nm. This covers the close NIR region with relatively good light penetration. The signal loss in deeper tissues does not permit quantitative data nor fully tomographic imaging. Mouse tissues are much more transparent for shortwave infrared light (SWIR) with wavelengths between 1,000 and 2,000 m. No autofluorescence, reduced light scattering and lack of absorption by blood are the main advantages of imaging in the SWIR region [161]. The first commercial *in vivo* optical scanner allowing imaging of contrasts with longer excitation wavelengths than 1,000 nm appeared on the market in 2019. The method is still limited by the low availability of fluorescent contrast agents for use in the SWIR region.

Besides, there is the current challenge of correlating additional beneficial but not yet readily/commercially available imaging modalities (same challenge as faced by the biological microscopy community). For example, while fusion of optical tomography data (DLIT, FLIT, or FMT) with CT can be achieved using commercial imaging systems, co-registration of OI and MRI is still in the developmental state. As OI and MRI are recorded in separate systems, relocations of animals between the recording sessions have to be conducted with great diligence to avoid anatomical distortion and positional changes. Chehade developed a shuttle made of CT- and MRI- compatible material, which allowed the relocations of mice while keeping them properly in place [77].

These challenges hold also true for *in-vivo* microscopy—despite its impressive advances. It is still challenging to synergistically combine optical technologies in one platform since they do not match in imaging speed, size, resolution and contrast, and proper imaging pipelines have to be established. In this context, CMI platforms for label-free sample screening bear great potential, and working combinations of these modalities (such as OCT, RS, MPM, SHG—STATE-OF-THE-ART/Preclinical Hybrid Imaging) will need to be identified on the basis of their added value in tackling specific biomedical research questions.

## Novel CMI Pipelines

Novel CMI pipelines will continue to bridge *in-vivo* (preclinical) and *ex-vivo* (biological) imaging and allow to zoom in from physiological native tissue context to subcellular molecular resolution. This comes with several challenges to be tackled: (1) sample preparation that is compatible across imaging modalities without compromising data quality, (2) hard- and software solutions to relocate the same ROI after changing the imaging platform, (3) robust markers that can be detected in different imaging technologies, (4) lack of high throughput and automatization, (5) software solutions to correlate the imaging data and standards for data handling and storage, (6) availability of research infrastructure (i.e., cutting-edge imaging technologies from PET scanners down to cryo-EM).

(1) Sample preparation procedures are mainly an issue across *ex-vivo* imaging technologies since these require specific fixation and embedding that might be incompatible with other techniques. Typically, most *in-vivo* imaging protocols such as MRI, CT or US do not interfere with downstream processing for histologic and ultrastructural observation. This is true even when routine contrast agents are administered for *in-vivo* imaging. Typical example of incompatibility are the quenching of fluorophores by standard EM preparation protocols (compare section CLEM and Correlative Microscopy) or incompatibility of glutaraldehyde fixation or JB4 resin embedding with many protocols for immunohistochemistry. In general, fixation is a critical parameter in correlative workflows and requires optimization since it usually comes with sample-distorting artifacts, such as tissue shrinkage, swelling, hardening, and color change. Besides, it is of highest importance to fix the tissue or organism right after euthanasia to prevent autolysis and degradation of cellular structures [162]. To improve the penetration of fixatives, the tissue or sample might need to be incised. The sample should then be incubated in at least 20 times the sample volume, and, to facilitate correlation, be pre-embedded in 1% agarose using a casting mold prior to processing [163]. Ideally, both macroscopic and microscopic morphologies are preserved by the simultaneous stabilization of all cellular components as achieved by cryofixation. However, while preserving the close-to-native morphology, the drawback of cryofixation in comparison to chemical fixation is its limited depth to which samples can be well-frozen. High-pressure freezing allows to fix a thickness of maximally 0.6 mm. Continuing to work under cryo-conditions ensures close-to-native architecture, but poses additional challenges to potential follow-up microscopy technologies such as FM—since current cryo-objectives are limited in their optical performance (such as low numerical aperture) [164].

Importantly, all destructive staining needs to be avoided: An example is the perfusion of vasculature with heparin, formalin, NaCl and barium sulfate with gelatin to stain blood vessels via the ventricles after anesthesia in mice. Vasculature staining can be replaced in certain cases by post-mortem staining with Lugol's solution, a mixture of one part iodine and two parts potassium iodide in water [165].

Imaging thick tissues or entire organisms *in vivo* and subsequently zooming-in into the subcellular ultrastructure is facilitated by current advances in FM of non-transparent organisms, such as longer wavelengths for deeper penetrations depths [166], development of improved near-infrared probes [167], or photoacoustics [168]. While studying even thicker tissue—though *in-vitro*—will be facilitated by further advancements in clearing larger samples using lipid extraction to reduce light scattering, it is questionable whether this will also facilitate correlative microscopy approaches since clearance of larger samples might interfere with ultrastructural preservation.

(2) Identifying the same ROI across diverse in- and *ex-vivo* imaging platforms is currently an inherent bottleneck of novel CMI approaches. Specifically, the relocation of a ROI in thick living tissue at high subcellular or molecular resolution presents the biggest challenge faced by CMI when bridging *in-vivo* preclinical imaging and *ex-vivo* biological microscopy. As outlined in 2.3, current strategies focus on NIRB as an intermediate step for volume CLEM. If no additional processing step is foreseen between modalities (which might induce distortions or even require reduction of the volume by sectioning), the straightforward approach to correlate the ROI across modalities is to use a joint transferable coordinating system. A well-established example is the annotation of FM to define ROIs with a dedicated CLEM module and import and relocate these coordination lists into the cryo-EM microscope using SerialEM [169]. Other approaches focus on using the same holder for different imaging modalities. Examples include immobilization beds for preclinical imaging in mice using PET and CT (where additionally $^{22}$Na fiducial markers can be placed into stationary pegs at defined depths to provide a 3D references to simplify image registration), or the combination of x-ray spectromicroscopy with electron tomography, where Allende meteorite grains were deposited on a TEM grid and transferred between the electron microscope and the COSMIC soft x-ray beamline [170]. First "plug-and-play" holder solutions are being described that are compatible and even commercially available, which can fit in a variety of microscopes for correlative imaging without changing the holder. While it facilitates relocation of ROIs tremendously, this approach cannot overcome the main limits or CMI pipelines: To assess a ROI in thick tissue, the tissue will still need to be cut due to the limited penetration depths of most high-resolution *ex-vivo* microscopy techniques.

To facilitate ROI relocation, CMI also aims at setting up hardware-fused hybrid setups that inherently co-localize the same ROI due to their joint coordination system. Apart from well-known commercially available PHI scanners (such as PET/CT, SPECT/CT, or PET/MRI), as described in section State-of-the-Art, examples include (i) a variety of hybrid AFM and FM setups [30, 171, 172], (ii) first implementations of integrated EM-FM setups [111, 173], (iii) several combined setups of OCT with photoacoustics or non-linear microscopy [174], and (iv) diverse hardware-based approaches to combine OI techniques with CT or MRI [175]. Nevertheless, in certain cases, relocation across single modality systems using cross-platform transport beds for CMI may provide superior performance compared to hybrid systems where compromises may have been made in the integration process.

If hybrid setups are not available (as is mostly the case), correlation can be facilitated by imaging the exact same sample without intermediate processing steps. For example, instead of performing FM before EM fixation and embedding, EM sections could be imaged directly with FM if preserving fluorescence or immunolabeling them.

(3) There is a plethora of multimodal probes for correlative microscopy and preclinical imaging, but there are hardly any robust markers that can be detected across modalities when combining various contrast mechanism with high microscopic accuracy. For correlative microscopy, most commonly used markers include QDs or polymer beads. Other examples include biocompatible nanosized, fluorescent and electron-dense intracellular nanodiamonds (internalized in living cells via endocytosis) as probes for 3D CLEM [176]. For the combination of preclinical imaging modalities, mainly CT, MRI, and optical approaches, there is a variety of CMI probes: (1) Lipid-based markers, such as liposomes or lipoproteins as carriers; (2) macromolecular carriers where different contrast agents are attached to a common macromolecule (and its reactive amines, thiols, or carboxyls); (3) nanoparticles, such as QDs, iron oxide nanoparticles or nanoparticle carriers; or (4) small molecules where two or more probes are directly fused together with minimal intervening bonds [177]. Further examples include high-contrast, non-radioactive tungsten-based fiducial markers for multimodal brain imaging with MRI, PET and CT that are attached outside of the sample in close proximity of the ROI, and numerous dual PET and NIR fluorescence imaging probes [178, 179], such as fluorescence-labeled monoclonal antibodies (mAbs) and systemic applications of both mAbs and peptides in PET/SPECT *in-vivo*. While $^{64}$Cu the prevalent isotope for systemic mAb imaging, $^{18}$F and $^{68}$Ga isotopes better match the targeting half-lives of peptides. Although dual agents for PET and NIR imaging are in its infancy and no agent has been approved by the FDA so far, several preclinical applications have been reported [179]. Examples for markers for advanced CMI pipelines include photo- or chemically-convertible tags (such as miniSOG or APEX) that can be detected in FM, CT and EM and were used to identify the ROI across multiple imaging modalities [180–182].

Most multimodal probes are exogenous. The ultimate goal is to have the organism or cells express their own probes after transfection. Fusions of GFP for fluorescence imaging and herpes simplex virus thymidine kinase (HSV-TK) for PET have been reported in several studies. HSV-TK can also be fused to other optical reporters and constructs of luciferase. With QDs and (NIR) fluorophores being used across preclinical and biological imaging modalities, these two markers appear most promising for advanced CMI pipelines. While a single CMI marker will guarantee the same pharmacokinetics and colocalization of the signal for each modality and reduces the stress on the blood clearance mechanisms of small animals (as induced by multiple doses of agents), the variations of sensitivities of different imaging modalities need to be considered when aiming for the detection of a single probe correlatively. In certain cases, it may not be practical to simply add all functionalities to one molecule [177].

For a rough alignment of untreated samples between relocation of imaging platforms, registration marks such as gridded coverslips or finder grids [183], or deposition of metal structures or engraving of the surface are commonly used. To provide rough orientation when dissecting ROIs from living organisms for subsequent *ex-vivo* analysis, the margins of adjacent tissue are demarcated in their bodily orientation with surgical ink or notches on the skin. For advanced CMI pipelines from thick tissue to 2D sections, endogenous landmarks or NIRB can be used. In volume CLEM, blood vessels, nuclei or myelinated axons can be used as endogenous fiducials since they show sufficient contrast both in light and electron microscopy and are distinctive in size and shape—as demonstrated for mouse brain imaging using a CMI pipeline with *in-vivo* 2-photon microscopy and FIB/SEM [6].

(4) Nanometer-resolution of the subcellular architecture of tissues usually requires time-intensive scanning of the sample (as for FIB/SEM or AFM) since lateral resolution often comes at the expense of penetration depth and field of view. The selection of a volume of interest several orders of magnitude smaller than the sample imaged by FM is hence both crucial and challenging. Solutions to studying big volumes at high resolution and with high throughput include the use of multi-beam setups (such as multi-beam SEM [184]) with parallelized data collection, or the automation of the identification of ROIs and image acquisition [185]. Since advanced CMI setups require tedious protocol optimization, time-intensive image acquisitions and intermediate processing steps, in general, novel CMI pipelines suffer from lack of throughput, which restricts reproducibility and statistics. Currently, the focus of CMI pipelines is rather on identifying working combinations to address previously inaccessible biomedical research than on fostering throughput. Once those correlations have been showcased and are proven feasible by substantial R&D efforts, CMI will enter further automatization and simplification to generate throughput.

(5) Advances and current trends in correlation software are discussed in sections Correlation Software and Correlation Software. To expedite automated multimodal image

registrations and quantification, data handling specific to multimodality needs to be established, including universal imaging formats, ontologies, and data storage and repositories. While there is currently no universally established microscopy format with additional diversity between preclinical and biological imaging approaches, repositories and public archives for diverse imaging data are being implemented—from single molecules (EMPIAR) to tissues (Tissue-IDR). Correlative data sets (such as CLEM data to link functional information across spatial and temporal scales) will be included in the so-called added-value databases that are developed around the archive. They aim at gathering a greater understanding for specific biological areas through systematic integration of images [141]. Integration of such multimodal data sets and their interoperability will be facilitated by universal large-scale multi-granular imaging ontologies, whose need is being described in first publications [186, 187].

(6) Novel CMI pipelines require access to diverse imaging technologies. All these technologies and the necessary expertise are unlikely to be found in a single laboratory, which restricts the development and implementation of CMI. To facilitate access to complementary imaging technologies and exchange of knowledge, several initiatives have been established. Two prominent examples are (1) COMULIS (Correlated Multimodal Imaging in Life Sciences), a COST Action (CA17121) to foster CMI, and (2) Euro-BioImaging, a European Research Infrastructure Consortium providing open access to imaging technologies in biological and biomedical research.

### Correlation Software

As already underlined, most of the automated methods are developed *ad hoc* for a particular multimodal problem. Machine learning and deep learning are definitely moving the image analysis field a step forward [87] since their main interest is to create an ideal method of processing based on training data sets, translating the effort of developing *ad-hoc* computer vision or signal processing methods to the effort of annotating data and formalizing the problem as input/output. Note that deep learning is still in progress and a lot of research is still going on to optimize these methods and reduce the number of training datasets required, as well as taking into account the errors in annotations in training data sets [87]. Based on these approaches, a universal solution without any user input is not envisioned *per se*, but rather a universal framework for multimodal registration, or the creation of a giant bank of pretrained models. It could be envisioned to be set up with minimal user input, i.e., by providing registered data sets or at least identifying on both modalities what should be used for matching. There are ongoing approaches for a universal segmenting tool, based on deep learning, trained on different data, for example, for nuclei segmentation [188]. Interestingly, it has been shown that some of the models trained could be applied in a new different modality (even if all at the same microscopic scale), for example, with different staining without the need of further training.

Another challenge in the field is the integration of very heterogeneous data, such as CMI with very different dimensions (multiplexing or spectral data with hundreds of outputs for one spatial localization, temporal vs. static) with non-imaging data such as -omics data. This effort could be facilitated by two approaches: the single cells approaches, and the development of spatially localized proteomics or genomics which are now starting to appear as commercial platform and would facilitate these links. But then the analysis of this largely heterogeneous data still requires to develop new statistical tools.

Another trend is to use multimodal aligned images as training sets to construct inference models to reduce the needs for one or the other modality. For example, Li et al. [189] used a deep learning approach to generate PET images from MRI and demonstrated similar classification results using the generated PET images than the true PET images for Alzheimer Disease and Mild Cognitive impairment. In this preliminary study, a 3D convolutional neural network was trained with MRI patches as input and matching PET patches as output using half of a database of patients having both exams. The parameters of the network capture a relationship between both modalities. This trained network was then used to generate the predicted PET images from MRI images, and validated against the remaining half of the database. The same principles have been applied also to microscopy images, where for example restoration based on deep learning have shown impressive results [190], and even predicting fluorescent labeling from transmitted light images [191].

These approaches in the long term could then reduce the number of modalities required to answer a particular question. To achieve such a goal, sharing well-annotated aligned multimodal data is of particular importance. Efforts are on-going in this direction to share repositories and public archives ([141], Empiar, IDR).

## CONCLUSIONS AND OUTLOOK: FUTURE OF THE FIELD

To have an even bigger impact and to become a basic life science technology as FM is nowadays, it will be crucial for correlative microscopy to develop and disseminate automated workflows that can deal with huge amounts of data and seamlessly merge diverse data sets. This process will be facilitated by a number of factors: the improved capabilities of integrated systems, the adaption of standard file formats, and the deposition and sharing of these information-rich datasets.

For PHI, preclinical molecular *in-vivo* whole-body imaging is fully dependent on hybrid imaging and co-registration with anatomical images. Some devices are already multimodal in their hardware settings, but images from different techniques are taken sequentially and implemented automated co-registration often requires manual intervention to obtain the best results. Multimodal animal beds allow to scan the same anesthetized animal in different devices, co-register multiple imaging methods and obtain enhanced molecular information about the *in-vivo* processes. The implementation of new methods and contrast agents broadens the spectrum of imaging possibilities, and simultaneously acquired multiple hybrid images facilitate proper visualization. Besides, OI has seen significant expansion in biomedical and diagnostic applications, which go beyond simple visualization of the sample. Novel modalities allow label-free mapping of biomolecules *in vivo* providing a way to determine a stage of disease progression or enable tomographic assessment of deep tissue layers. Nevertheless, current research efforts are indicating that in many biomedical applications, a single modality is inadequate to provide a comprehensive picture of a disease. Instead a targeted combination of modalities, which give access to a set of (label-free) parameters is necessary.

In summary, CMI is a field under construction, relying on broad expertise. In particular, data processing, analysis and management need to be incorporated in the initial reflections leading to a project, and a continuous and iterative dialog has to take place during the whole project with image data analysts such that the communities can understand the requirements and needs of each other. Setting up standard approaches and sharing protocols and generated data will definitely be the key elements for achieving a smooth communication. A real holistic view will be achieved when other type of data will be also correlated with imaging data, but to reach such a goal the CMI community needs to develop its own solid ground.

Ideally, CMI will lead to multimodal platforms that allow to functionally and morphologically characterize the entire sample *in-vivo*, fast and non-destructively at high axial and lateral resolution and high penetration to gain a mechanistic understanding of organisms and diseases. By synergistically fusing complementary imaging techniques, CMI platforms can give insights into a variety of tissue properties during a single image acquisition, and better tissue characterization can be achieved than by the separate imaging modalities alone. Complementary information provided by the fused imaging modalities and machine-learning-assisted data analysis will ultimately yield novel biomarkers by a multi-dimensional classification accelerating the discovery and translation of novel therapeutic strategies. Such hybrid platforms of high accuracy will correlate the modalities instantly without the need for post-processing correlation software. Surely, 3D cellular, ultrastructural and molecular tissue maps as acquired by CMI will substantially transform biomedical research and diagnostics in the future.

## AUTHOR CONTRIBUTIONS

AW initiated, coordinated, and supervised the manuscript and wrote all CMI sections, Introduction, Conclusion, and Abstract. LS wrote main parts of the PHI sections. PP-G wrote all software sections. PV and BP main parts of the correlative microscopy sessions. JM, MO, BP, PS, AU, SH, DF, and MM-D contributed to each section. KB, SG, MG, TW, and WW provided feedback and edits.

## FUNDING

This work has been supported by the Federal State of Upper Austria and "Land OÖ Basisfinanzierung" and Timed Center Upper Austria TC-HyperChol.

## ACKNOWLEDGMENTS

PP-G acknowledges ANR-18-CE45-0015 and the France-BioImaging infrastructure supported by the French National Research Agency (ANR-10-INBS-04). LS acknowledges the large RI Project LM2015062 Czech-BioImaging funded by MEYS, Czech Republic. KB acknowledges the FFG COMET center project 854174. All authors acknowledge their collaboration facilitated by COST as members of COMULS (CA17121).

## REFERENCES


1. Pogue BW, Leblond F, Krishnaswamy V, Paulsen KD. Radiologic and near-infrared/optical spectroscopic imaging: where is the synergy? *Am J Roentgenol.* (2010) **195**:321–32. doi: 10.2214/AJR.10.5002
2. Helmchen F, Denk W. Deep tissue two-photon microscopy. *Nat Methods.* (2005) **2**:932–40. doi: 10.1038/nmeth818
3. Marti-Bonmati L, Sopena R, Bartumeus P, Sopena P. Multimodality imaging techniques. *Contrast Media Mol Imaging.* (2010) **5**:180–9. doi: 10.1002/cmmi.393
4. Beyer T, Freudenberg LS, Townsend DW, Czernin J. The future of hybrid imaging-part 1: hybrid imaging technologies and SPECT/CT. *Insights Imaging.* (2011) **2**:161–9. doi: 10.1007/s13244-010-0063-2
5. de Boer P, Hoogenboom JP, Giepmans BN. Correlated light and electron microscopy: ultrastructure lights up! *Nat Methods.* (2015) **12**:503–13. doi: 10.1038/nmeth.3400
6. Luckner M, Burgold S, Filser S, Scheungrab M, Niyaz Y, Hummel E, et al. Label-free 3D-CLEM using endogenous tissue landmarks. *iScience.* (2018) **6**:92–101. doi: 10.1016/j.isci.2018.07.012
7. Johnson E, Seiradake E, Jones EY, Davis I, Grunewald K, Kaufmann R. Correlative in-resin super-resolution and electron microscopy using standard fluorescent proteins. *Sci Rep.* (2015) **5**:9583. doi: 10.1038/srep09583
8. Liu M, Chen Z, Zabihian B, Sinz C, Zhang E, Beard PC, et al. Combined multi-modal photoacoustic tomography, optical coherence tomography (OCT) and OCT angiography system with an articulated probe for *in vivo* human skin structure and vasculature imaging. *Biomed Opt Express.* (2016) **7**:3390–402. doi: 10.1364/BOE.7.003390
9. Porter KR, Claude A, Fullam EF. A study of tissue culture cells by electron microscopy : methods and preliminary observations. *J Exp Med.* (1945) **81**:233–46. doi: 10.1084/jem.81.3.233
10. Rieder CL, Cole RW, Khodjakov A, Sluder G. The checkpoint delaying anaphase in response to chromosome monoorientation is mediated by an inhibitory signal produced by unattached kinetochores. *J Cell Biol.* (1995) **130**:941–8. doi: 10.1083/jcb.130.4.941
11. Heim R, Cubitt AB, Tsien RY, Porter KR, Claude A, Fullam EF. Improved green fluorescence. *Nature.* (1995) **373**:663–4. doi: 10.1038/373663b0
12. Polishchuk RS, Polishchuk EV, Marra P, Alberti S, Buccione R, Luini A, et al. Correlative light-electron microscopy reveals the tubular-saccular ultrastructure of carriers operating between Golgi apparatus and plasma membrane. *J Cell Biol.* (2000) **148**:45–58. doi: 10.1083/jcb.148.1.45
13. Polishchuk EV, Di Pentima A, Luini A, Polishchuk RS. Mechanism of constitutive export from the golgi: bulk flow via the formation, protrusion, and en bloc cleavage of large trans-golgi network tubular domains. *Mol Biol Cell.* (2003) **14**:4470–85. doi: 10.1091/mbc.e03-01-0033

14. Lees RM, Peddie CJ, Collinson LM, Ashby MC, Verkade P, Miles BT, et al. Correlative two-photon and serial block face scanning electron microscopy in neuronal tissue using 3D near-infrared branding maps. *Methods Cell Biol.* (2017) **140**:245–76. doi: 10.1016/bs.mcb.2017.03.007
15. Olmos Y, Hodgson L, Mantell J, Verkade P, Carlton JG. ESCRT-III controls nuclear envelope reformation. *Nature.* (2015) **522**:236–9. doi: 10.1038/nature14503
16. Kukulski W, Schorb M, Welsch S, Picco A, Kaksonen M, Briggs JA. Correlated fluorescence and 3D electron microscopy with high sensitivity and spatial precision. *J Cell Biol.* (2011) **192**:111–9. doi: 10.1083/jcb.201009037
17. Kukulski W, Schorb M, Kaksonen M, Briggs JA. Plasma membrane reshaping during endocytosis is revealed by time-resolved electron tomography. *Cell.* (2012) **150:**508–20. doi: 10.1016/j.cell.2012.05.046
18. Kukulski W, Schorb M, Welsch S, Picco A, Kaksonen M, Briggs JA. Precise, correlated fluorescence microscopy and electron tomography of lowicryl sections using fluorescent fiducial markers. *Methods Cell Biol.* (2012) **111**:235–57. doi: 10.1016/B978-0-12-416026-2.00013-3
19. Brown E, Van Weering J, Sharp T, Mantell J, Verkade P. Capturing endocytic segregation events with HPF-CLEM. *Methods Cell Biol.* (2012) **111**:175–201. doi: 10.1016/B978-0-12-416026-2.00010-8
20. Spiegelhalter C, Tosch V, Hentsch D, Koch M, Kessler P, Schwab Y, et al. From dynamic live cell imaging to 3D ultrastructure: novel integrated methods for high pressure freezing and correlative light-electron microscopy. *PLoS ONE.* (2010) **5**:e9014. doi: 10.1371/journal.pone.0009014
21. Verkade P. Moving EM: the rapid transfer system as a new tool for correlative light and electron microscopy and high throughput for high-pressure freezing. *J Microsc.* (2008) **230**(Pt. 2):317–28. doi: 10.1111/j.1365-2818.2008.01989.x
22. Elgass KD, Smith EA, LeGros MA, Larabell CA, Ryan MT. Analysis of ER-mitochondria contacts using correlative fluorescence microscopy and soft X-ray tomography of mammalian cells. *J Cell Sci.* (2015) **128**:2795–804. doi: 10.1242/jcs.169136
23. Pereiro E. Correlative cryo-soft X-ray tomography of cells. *Biophys Rev.* (2019) **11**:529–30. doi: 10.1007/s12551-019-00560-z
24. Axmann M, Sezgin E, Karner A, Novacek J, Brodesser MD, Rohrl C, et al. Receptor-Independent transfer of low density lipoprotein cargo to biomembranes. *Nano Lett.* (2019) **19**:2562–7. doi: 10.1021/acs.nanolett.9b00319
25. Plochberger B, Rohrl C, Preiner J, Rankl C, Brameshuber M, Madl J, et al. HDL particles incorporate into lipid bilayers - a combined AFM and single molecule fluorescence microscopy study. *Sci Rep.* (2017) **7**:15886. doi: 10.1038/s41598-017-15949-7
26. Spedden E, White JD, Naumova EN, Kaplan DL, Staii C. Elasticity maps of living neurons measured by combined fluorescence and atomic force microscopy. *Biophys J.* (2012) **103**:868–77. doi: 10.1016/j.bpj.2012.08.005
27. Kashef J, Franz CM. Quantitative methods for analyzing cell-cell adhesion in development. *Dev Biol.* (2015) **401**:165–74. doi: 10.1016/j.ydbio.2014.11.002
28. Christenson W, Yermolenko I, Plochberger B, Camacho-Alanis F, Ros A, Ugarova TP, et al. Combined single cell AFM manipulation and TIRFM for probing the molecular stability of multilayer fibrinogen matrices. *Ultramicroscopy.* (2014) **136**:211–5. doi: 10.1016/j.ultramic.2013.10.009
29. Staunton JR, Doss BL, Lindsay S, Ros R. Correlating confocal microscopy and atomic force indentation reveals metastatic cancer cells stiffen during invasion into collagen I matrices. *Sci Rep.* (2016) **6**:19686. doi: 10.1038/srep19686
30. Chaudhuri O, Parekh SH, Lam WA, Fletcher DA. Combined atomic force microscopy and side-view optical imaging for mechanical studies of cells. *Nat Methods.* (2009) **6**:383–7. doi: 10.1038/nmeth.1320
31. Chtcheglova LA, Hinterdorfer P. Simultaneous AFM topography and recognition imaging at the plasma membrane of mammalian cells. *Semin Cell Dev Biol.* (2018) **73**:45–56. doi: 10.1016/j.semcdb.2017.08.025
32. Cordes T, Strackharn M, Stahl SW, Summerer W, Steinhauer C, Forthmann C, et al. Resolving single-molecule assembled patterns with superresolution blink-microscopy. *Nano Lett.* (2010) **10**:645–51. doi: 10.1021/nl903730r
33. Franz CM, Muller DJ. Analyzing focal adhesion structure by atomic force microscopy. *J Cell Sci.* (2005) **118**:5315–23. doi: 10.1242/jcs.02653
34. Harke B, Chacko JV, Haschke H, Canale C, Diaspro A. A novel nanoscopic tool by combining AFM with STED microscopy. *Opt Nanoscopy.* (2012) 1:3. doi: 10.1186/2192-2853-1-3
35. Rief M, Gautel M, Gaub HE. Unfolding forces of titin and fibronectin domains directly measured by AFM. *Adv Exp Med Biol.* (2000) **481**:129–41. doi: 10.1007/978-1-4615-4267-4_8
36. Bek A, Jansen R, Ringler M, Mayilo S, Klar TA. Fluorescence enhancement in hot spots of AFM-designed gold nanoparticle sandwiches. *Nano Lett.* (2008) **8**:485–90. doi: 10.1021/nl072602n
37. Caldemeyer KS, Buckwalter KA. The basic principles of computed tomography and magnetic resonance imaging. *J Am Acad Dermatol.* (1999) **41**:768–71. doi: 10.1016/S0190-9622(99)70015-0
38. Damen FW, Berman AG, Soepriatna AH, Ellis JM, Buttars SD, Aasa KL, et al. High-frequency 4-Dimensional Ultrasound (4DUS): a reliable method for assessing murine cardiac function. *Tomography.* (2017) **3**:180–7. doi: 10.18383/j.tom.2017.00016
39. Chow MSM, Wu SL, Webb SE, Gluskin K, Yew DT. Functional magnetic resonance imaging and the brain: a brief review. *World J Radiol.* (2017) **9**:5–9. doi: 10.4329/wjr.v9.i1.5
40. Carter LM, Kesner AL, Pratt EC, Sanders VA, Massicano AVF, Cutler CS, et al. The impact of positron range on PET resolution, evaluated with phantoms and PHITS monte carlo simulations for conventional and non-conventional radionuclides. *Mol Imaging Biol.* (2020) **22**:73–84. doi: 10.1007/s11307-019-01337-2
41. Knopp T, Gdaniec N, Moddel M. Magnetic particle imaging: from proof of principle to preclinical applications. *Phys Med Biol.* (2017) **62**:R124–78. doi: 10.1088/1361-6560/aa6c99
42. Khramtsov VV. *In vivo* molecular electron paramagnetic resonance-based spectroscopy and imaging of tumor microenvironment and redox using functional paramagnetic probes. *Antioxid Redox Signal.* (2018) **28**:1365–77. doi: 10.1089/ars.2017.7329
43. Gonet M, Epel B, Halpern HJ, Elas M. Merging preclinical EPR tomography with other imaging techniques. *Cell Biochem Biophys.* (2019) **77**:187–96. doi: 10.1007/s12013-019-00880-7
44. Jiang Y, Pu K. Molecular fluorescence and photoacoustic imaging in the second near-infrared optical window using organic contrast agents. *Adv Biosyst.* (2018) **2**:1700262. doi: 10.1002/adbi.201700262
45. Yao Z, Zhang BS, Prescher JA. Advances in bioluminescence imaging: new probes from old recipes. *Curr Opin Chem Biol.* (2018) **45**:148–56. doi: 10.1016/j.cbpa.2018.05.009
46. Manni I, de Latouliere L, Gurtner A, Piaggio G. Transgenic animal models to visualize cancer-related cellular processes by bioluminescence imaging. *Front Pharmacol.* (2019) **10**:235. doi: 10.3389/fphar.2019.00235
47. Dorsaz S, Coste AT, Sanglard D. Red-shifted firefly luciferase optimized for *Candida albicans In vivo* bioluminescence imaging. *Front Microbiol.* (2017) **8**:1478. doi: 10.3389/fmicb.2017.01478
48. Kuo C, Coquoz O, Troy TL, Xu H, Rice BW. Three-dimensional reconstruction of *in vivo* bioluminescent sources based on multispectral imaging. *J Biomed Opt.* (2007) **12**:024007. doi: 10.1117/1.2717898
49. Vahrmeijer AL, Hutteman M, van der Vorst JR, van de Velde CJ, Frangioni JV. Image-guided cancer surgery using near-infrared fluorescence. *Nat Rev Clin Oncol.* (2013) **10**:507–18. doi: 10.1038/nrclinonc.2013.123
50. Kenry, Duan Y, Liu B. Recent advances of optical imaging in the second near-infrared window. *Adv Mater.* (2018) **30**:e1802394. doi: 10.1002/adma.201802394
51. Ale A, Ermolayev V, Herzog E, Cohrs C, de Angelis MH, Ntziachristos V. FMT-XCT: *in vivo* animal studies with hybrid fluorescence molecular tomography-X-ray computed tomography. *Nat Methods.* (2012) **9**:615–20. doi: 10.1038/nmeth.2014
52. Xu M, Wang LV. Photoacoustic imaging in biomedicine. *Rev Sci Instruments.* (2006) 77:041101. doi: 10.1063/1.2195024
53. Blery P, Pilet P, Bossche AV, Thery A, Guicheux J, Amouriq Y, et al. Vascular imaging with contrast agent in hard and soft tissues using microcomputed-tomography. *J Microsc.* (2016) **262**:40–9. doi: 10.1111/jmi.12339
54. Kerckhofs G, Stegen S, van Gastel N, Sap A, Falgayrac G, Penel G, et al. Simultaneous three-dimensional visualization

of mineralized and soft skeletal tissues by a novel microCT contrast agent with polyoxometalate structure. *Biomaterials.* (2018) **159**:1–12. doi: 10.1016/j.biomaterials.2017.12.016
55. Huang D, Swanson EA, Lin CP, Schuman JS, Stinson WG, Chang W, et al. Optical coherence tomography. *Science.* (1991) **254**:1178–81. doi: 10.1126/science.1957169
56. Drexler W, Fujimoto JG. *Optical Coherence Tomography: Technology and Applications*. Basel: Springer International Publishing Switzerland. (2015).
57. Bovenkamp D, Sentosa R, Rank E, Erkkilä M, Placzek F, Püls J, et al. Combination of high-resolution optical coherence tomography and raman spectroscopy for improved staging and grading in bladder cancer. *Appl Sci.* (2018) **8**:2371. doi: 10.3390/app8122371
58. Li J, Bower AJ, Vainstein V, Gluzman-Poltorak Z, Chaney EJ, Marjanovic M, et al. Effect of recombinant interleukin-12 on murine skin regeneration and cell dynamics using *in vivo* multimodal microscopy. *Biomed Opt Express.* (2015) **6**:4277–87. doi: 10.1364/BOE.6.004277
59. König K. Hybrid multiphoton multimodal tomography of *in vivo* human skin. *IntraVital.* (2012) **1**:11–26. doi: 10.4161/intv.21938
60. Hanson KM, Bardeen CJ. Application of nonlinear optical microscopy for imaging skin. *Photochem Photobiol.* (2009) **85**:33–44. doi: 10.1111/j.1751-1097.2008.00508.x
61. Andreana M, Sentosa R, Erkkilä MT, Drexler W, Unterhuber A. Depth resolved label-free multimodal optical imaging platform to study morpho-molecular composition of tissue. *Photochem Photobiol Sci.* (2019) **18**:997–1008. doi: 10.1039/C8PP00410B
62. Alex A, Weingast J, Weinigel M, Kellner-Höfer M, Nemecek R, Binder M, et al. Three-dimensional multiphoton/optical coherence tomography for diagnostic applications in dermatology. *J Biophotonics.* (2013) **6**:352–62. doi: 10.1002/jbio.201200085
63. Drexler W, Liu M, Kumar A, Kamali T, Unterhuber A, Leitgeb RA. Optical coherence tomography today: speed, contrast, and multimodality. *J Biomed Opt.* (2014) **19**:071412. doi: 10.1117/1.JBO.19.7.071412
64. Jun X, Wang LV. Small-animal whole-body photoacoustic tomography: a review. *IEEE Trans Biomed Eng.* (2014) **61**:1380–9. doi: 10.1109/TBME.2013.2283507
65. Zhou Y, Yao J, Wang LV. Tutorial on photoacoustic tomography. *J Biomed Opt.* (2016) **21**:061007. doi: 10.1117/1.JBO.21.6.061007
66. Zhang W, Li Y, Nguyen VP, Huang Z, Liu Z, Wang X, et al. High-resolution, *in vivo* multimodal photoacoustic microscopy, optical coherence tomography, and fluorescence microscopy imaging of rabbit retinal neovascularization. *Light Sci Appl.* (2018) **7**:103. doi: 10.1038/s41377-018-0093-y
67. Liu M, Drexler W. Optical coherence tomography angiography and photoacoustic imaging in dermatology. *Photochem Photobiol Sci.* (2019) **18**:945–62. doi: 10.1039/C8PP00471D
68. Cai W, Chen X. Multimodality molecular imaging of tumor angiogenesis. *J Nucl Med.* (2008) **49**(Suppl. 2):113–28S. doi: 10.2967/jnumed.107.045922
69. Labernadie A, Thibault C, Vieu C, Maridonneau-Parini I, Charriere GM. Dynamics of podosome stiffness revealed by atomic force microscopy. *Proc Natl Acad Sci USA.* (2010) **107**:21016–21. doi: 10.1073/pnas.1007835107
70. Vollnhals F, Audinot J-N, Wirtz T, Mercier-Bonin M, Fourquaux I, Schroeppel B, et al. Correlative microscopy combining secondary ion mass spectrometry and electron microscopy: comparison of intensity-hue-saturation and laplacian pyramid methods for image fusion. *Anal Chem.* (2017) **89**:10702–10. doi: 10.1021/acs.analchem.7b01256
71. Behrens S, Lösekann T, Pett-Ridge J, Weber PK, Ng WO, Stevenson BS, et al. Linking microbial phylogeny to metabolic activity at the single-cell level by using enhanced element labeling-catalyzed reporter deposition fluorescence in situ hybridization (EL-FISH) and NanoSIMS. *Appl Environ Microbiol.* (2008) **74**:3143–50. doi: 10.1128/AEM.00191-08
72. Geier BK, Sogin E, Michellod D, Janda M, Kompauer M, Spengler B, et al. Spatial metabolomics of *in situ*, host-microbe interactions. (2020) *bioRxiv* 2019:555045. doi: 10.1101/555045
73. Vachet RW. Molecular histology: More than a picture. *Nat Nanotechnol.* (2015) **10**:103–4. doi: 10.1038/nnano.2015.4.
74. Holzlechner M, Bonta M, Lohninger H, Limbeck A, Marchetti-Deschmann M. Multi-sensor Imaging - from sample preparation to integrated multimodal interpretation of LA-ICP-MS and MALDI MS imaging data. *Anal Chem.* (2018) **90**:8831–7. doi: 10.1021/acs.analchem.8b00816
75. Fleming Y, Wirtz T. High sensitivity and high resolution element 3D analysis by a combined SIMS-SPM instrument. *Beilstein J Nanotechnol.* (2015) **6**:1091–9. doi: 10.3762/bjnano.6.110
76. Menendez MI, Hettlich B, Wei L, Knopp MV. Preclinical multimodal molecular imaging using (18)F-FDG PET/CT and MRI in a phase i study of a knee osteoarthritis in *In vivo* canine Model. *Mol Imaging.* (2017) **16**:1536012117697443. doi: 10.1177/1536012117697443
77. Chehade M, Srivastava AK, Bulte JW. Co-registration of bioluminescence tomography, computed tomography, and magnetic resonance imaging for multimodal *in vivo* stem cell tracking. *Tomography.* (2016) **2**:159–65. doi: 10.18383/j.tom.2016.00160
78. Zhou L, Cai M, Tong T, Wang H. Progress in the correlative atomic force microscopy and optical microscopy. *Sensors.* (2017) **17**:938. doi: 10.3390/s17040938
79. Cebulla J, Kim E, Rhie K, Zhang J, Pathak AP. Multiscale and multi-modality visualization of angiogenesis in a human breast cancer model. *Angiogenesis.* (2014) **17**:695–709. doi: 10.1007/s10456-014-9429-2
80. Karreman MA, Mercier L, Schieber NL, Shibue T, Schwab Y, Goetz JG. Correlating intravital multi-photon microscopy to 3D electron microscopy of invading tumor cells using anatomical reference points. *PLoS ONE.* (2014) **9**:e114448. doi: 10.1371/journal.pone.0114448
81. Karreman MA, Mercier L, Schieber NL, Solecki G, Allio G, Winkler F, et al. Fast and precise targeting of single tumor cells *in vivo* by multimodal correlative microscopy. *J Cell Sci.* (2016) **129**:444–56. doi: 10.1242/jcs.181842
82. Pacureanu A, Maniates-Selvin J, Kuan AT, Thomas LA, Chen C-L, Cloetens P, et al. Dense neuronal reconstruction through X-ray holographic nano-tomography. *bioRxiv.* (2019) 653188. doi: 10.1101/653188
83. Boido D, Rungta RL, Osmanski BF, Roche M, Tsurugizawa T, Le Bihan D, et al. Mesoscopic and microscopic imaging of sensory responses in the same animal. *Nat Commun.* (2019) **10**:1110. doi: 10.1038/s41467-019-09082-4
84. Desgrange A, Lokmer J, Marchiol C, Houyel L, Meilhac SM. Standardised imaging pipeline for phenotyping mouse laterality defects and associated heart malformations, at multiple scales and multiple stages. *Dis Model Mech.* (2019) **12**:dmm038356. doi: 10.1101/516039
85. Liu M, Maurer B, Hermann B, Zabihian B, Sandrian MG, Unterhuber A, et al. Dual modality optical coherence and whole-body photoacoustic tomography imaging of chick embryos in multiple development stages. *Biomed Opt Express.* (2014) **5**:3150–9. doi: 10.1364/BOE.5.003150
86. Svirkova A, Turyanskaya A, Perneczky L, Streli C, Marchetti-Deschmann M. Multimodal imaging of undecalcified tissue sections by MALDI MS and muXRF. *Analyst.* (2018) **143**:2587–95. doi: 10.1039/C8AN00313K
87. Litjens G, Kooi T, Bejnordi BE, Setio AAA, Ciompi F, Ghafoorian M, et al. A survey on deep learning in medical image analysis. *Med Image Anal.* (2017) **42**:60–88. doi: 10.1016/j.media.2017.07.005
88. Roels J, Aelterman J, Luong HQ, Lippens S, Pižurica A, Saeys Y, et al. An overview of state-of-the-art image restoration in electron microscopy. *J Microsc.* (2018) **271**:239–54. doi: 10.1111/jmi.12716
89. Akselrod-Ballin A, Dafni H, Addadi Y, Biton I, Avni R, Brenner Y, et al. Multimodal correlative preclinical whole body imaging and segmentation. *Sci Rep.* (2016) **6**:27940. doi: 10.1038/srep27940
90. Schindelin J, Arganda-Carreras I, Frise E, Kaynig V, Longair M, Pietzsch T, et al. Fiji: an open-source platform for biological-image analysis. *Nat Methods.* (2012) **9**:676–82. doi: 10.1038/nmeth.2019
91. Heiligenstein X, Paul-Gilloteaux P, Raposo G, Salamero J. eC-CLEM: a multidimension, multimodel software to correlate intermodal images with a focus on light and electron microscopy. *Methods Cell Biol.* **140**:335–52. doi: 10.1016/bs.mcb.2017.03.014
92. Miura K, Paul-Gilloteaux P, Tosi S, Colombelli J. Workflows and components of bioimage analysis. In: Miura K, Sladoje N, editors. *Bioimage Data Analysis Workflows. Learning Materials in Biosciences*. Cham: Springer (2020) p. 1–7.
93. Paul Gilloteaux P, Schorb M. Correlating data from imaging modalities. In: Verkade P, Collinson L, editors. *Correlative Imaging, Focusing on the Future.* Wiley (2019) p. 191–210.

94. Sotiras A, Davatzikos C, Paragios N. Deformable medical image registration: a survey. *IEEE Trans Med Imaging.* (2013) **32**:1153–90. doi: 10.1109/TMI.2013.2265603
95. Acosta BMT, Bouthemy P, Kervrann C. A common image representation and a patch-based search for correlative light-electron-microscopy (CLEM) registration. In: *IEEE 13th International Symposium on Biomedical Imaging (ISBI)*. Prague (2016). p. 257–260.
96. Acosta BMT, Heiligenstein X, Malandain G, Bouthemy P. Intensity-based matching and registration for 3D correlative microscopy with large discrepancies. In: *IEEE 15th International Symposium on Biomedical Imaging (ISBI 2018)*. Washington, DC (2018). p. 493–496.
97. Cao T, Zach C, Modla S, Powell D, Czymmek K, Niethammer M. Multi-modal registration for correlative microscopy using image analogies. *Med Image Anal.* (2014) **18**:914–26. doi: 10.1016/j.media.2013.12.005
98. Gutierrez-Becker B, Mateus D, Peter L, Navab N. Guiding multimodal registration with learned optimization updates. *Med Image Anal.* (2017) **41**:2–17. doi: 10.1016/j.media.2017.05.002
99. Blendowski M, Bouteldja N, Heinrich MP. Multimodal 3D medical image registration guided by shape encoder-decoder networks. *Int J Comput Assist Radiol Surg.* (2019) **15**:1–8. doi: 10.1007/s11548-019-02089-8
100. Huang X, Zhang J, Fan L, Wu Q, Yuan C. A systematic approach for cross-source point cloud registration by preserving macro and micro structures. *IEEE Trans Image Process.* (2017) **26**:3261–76. doi: 10.1109/TIP.2017.2695888
101. Hu Y, Modat M, Gibson E, Li W, Ghavami N, Bonmati E, et al. Weakly-supervised convolutional neural networks for multimodal image registration. *Med Image Anal.* (2018) **49**:1–13. doi: 10.1016/j.media.2018.07.002
102. Arganda-Carreras I, Manoliu T, Mazuras N, Schulze F, Iglesias JE, Buhler K, et al. A statistically representative atlas for mapping neuronal circuits in the *Drosophila* adult brain. *Front Neuroinform.* (2018) **12**:13. doi: 10.3389/fninf.2018.00013
103. Muenzing SEA, Strauch M, Truman JW, Buhler K, Thum AS, Merhof D. larvalign: aligning gene expression patterns from the larval brain of *Drosophila* melanogaster. *Neuroinformatics.* (2018) **16**:65–80. doi: 10.1007/s12021-017-9349-6
104. Schlachter M, Fechter T, Adebahr S, Schimek-Jasch T, Nestle U, Bühler K. Visualization of 4D multimodal imaging data and its applications in radiotherapy planning. *J Appl Clin Med Phys.* (2017) **18**:183–93. doi: 10.1002/acm2.12209
105. Schlachter M, Fechter T, Jurisic M, Schimek-Jasch T, Oehlke O, Adebahr S, et al. Visualization of deformable image registration quality using local image dissimilarity. *IEEE Trans Med Imaging.* (2016) **35**:2319–28. doi: 10.1109/TMI.2016.2560942
106. Heiligenstein X, Paul-Gilloteaux P, Belle M, Raposo G, Salamero J. eC-CLEM: flexible multidimensional registration software for correlative microscopies with refined accuracy mapping. *Microsc Microanal.* (2017) **23**:360–1. doi: 10.1017/S1431927617002483
107. Ganglberger F, Swoboda N, Frauenstein L, Kaczanowska J, Haubensak W, Bühler K. BrainTrawler: a visual analytics framework for iterative exploration of heterogeneous big brain data. *Comput Graphics.* (2019) **82**:304–20. doi: 10.1016/j.cag.2019.05.032
108. Pietzsch T, Saalfeld S, Preibisch S, Tomancak P. BigDataViewer: visualization and processing for large image data sets. *Nat Methods.* (2015) **12**:481–3. doi: 10.1038/nmeth.3392
109. Brown E, Verkade P. The use of markers for correlative light electron microscopy. *Protoplasma.* (2010) **244**:91–7. doi: 10.1007/s00709-010-0165-1
110. Kandela IK, Albrecht RM. Fluorescence quenching by colloidal heavy metals nanoparticles: implications for correlative fluorescence and electron microscopy studies. *Scanning.* (2007) **29**:152–61. doi: 10.1002/sca.20055
111. Gorelick S, Buckley G, Gervinskas G, Johnson TK, Handley A, Caggiano MP, et al. PIE-scope, integrated cryo-correlative light and FIB/SEM microscopy. *Elife.* (2019) **8**:e45919. doi: 10.7554/eLife.45919
112. Pfister G, Stroh CM, Perschinka H, Kind M, Knoflach M, Hinterdorfer P, et al. Detection of HSP60 on the membrane surface of stressed human endothelial cells by atomic force and confocal microscopy. *J Cell Sci.* (2005) **118**:1587–94. doi: 10.1242/jcs.02292
113. Prinz F, Schlange T, Asadullah K. Believe it or not: how much can we rely on published data on potential drug targets? *Nat Rev Drug Discov.* (2011) **10**:712. doi: 10.1038/nrd3439-c1
114. Begley CG, Ellis LM. Drug development: raise standards for preclinical cancer research. *Nature.* (2012) **483**:531–3. doi: 10.1038/483531a
115. Begley CG, Ioannidis JP. Reproducibility in science: improving the standard for basic and preclinical research. *Circ Res.* (2015) **116**:116–26. doi: 10.1161/CIRCRESAHA.114.303819
116. Peers IS, Ceuppens PR, Harbron C. In search of preclinical robustness. *Nat Rev Drug Discov.* (2012) **11**:733–4. doi: 10.1038/nrd3849
117. Lieu CH, Tan AC, Leong S, Diamond JR, Eckhardt SG. From bench to bedside: lessons learned in translating preclinical studies in cancer drug development. *J Natl Cancer Inst.* (2013) **105**:1441–56. doi: 10.1093/jnci/djt209
118. Herfert K, Mannheim JG, Kuebler L, Marciano S, Amend M, Parl C, et al. Quantitative rodent brain receptor imaging. *Mol Imaging Biol.* (2020) **22**:223–44. doi: 10.1007/s11307-019-01368-9
119. Roy Choudhury K, Gibson R. Reproducible research in medical imaging. *Mol Imaging Biol.* (2012) **14**:395–6. doi: 10.1007/s11307-012-0569-8
120. Hackam DG, Redelmeier DA. Translation of research evidence from animals to humans. *JAMA.* (2006) **296**:1731–2. doi: 10.1001/jama.296.14.1731
121. Llovera G, Liesz A. The next step in translational research: lessons learned from the first preclinical randomized controlled trial. *J Neurochem.* (2016) **139**(Suppl. 2):271–9. doi: 10.1111/jnc.13516
122. McNutt M. Journals unite for reproducibility. *Science.* (2014) **346**:679. doi: 10.1126/science.aaa1724
123. Zhu Y, Geng C, Huang J, Liu J, Wu N, Xin J, et al. Measurement and evaluation of quantitative performance of PET/CT images before a multicenter clinical trial. *Sci Rep.* 2018. **8**:9035. doi: 10.1038/s41598-018-27143-4
124. Hristova I, Boellaard R, Galette P, Shankar LK, Liu Y, Stroobants S, et al. Guidelines for quality control of PET/CT scans in a multicenter clinical study. *EJNMMI Phys.* (2017) **4**:23. doi: 10.1186/s40658-017-0190-7
125. Aide N, Lasnon C, Veit-Haibach P, Sera T, Sattler B, Boellaard R. EANM/EARL harmonization strategies in PET quantification: from daily practice to multicentre oncological studies. *Eur J Nucl Med Mol Imaging.* (2017) **44(Suppl 1)**:17–31. doi: 10.1007/s00259-017-3740-2
126. Murphy P, Koh DM. Imaging in clinical trials. *Cancer Imaging.* (2010) **10**:S74–82. doi: 10.1102/1470-7330.2010.9027
127. van Horn JD, Toga AW. Multisite neuroimaging trials. *Curr Opin Neurol.* (2009) **22**:370–8. doi: 10.1097/WCO.0b013e32832d92de
128. Stout D, Berr SS, LeBlanc A, Kalen JD, Osborne D, Price J, et al. Guidance for methods descriptions used in preclinical imaging papers. *Mol Imaging.* (2013) **12**:1–15. doi: 10.2310/7290.2013.00055
129. Kilkenny C, Browne WJ, Cuthill IC, Emerson M, Altman DG. Improving bioscience research reporting: the ARRIVE guidelines for reporting animal research. *PLoS Biol.* (2010) **8**:e1000412. doi: 10.1371/journal.pbio.1000412
130. *Data Availability*. (2019). Available online at: https://journals.plos.org/plosone/s/data-availability (accessed November 16, 2019).
131. Data availability statements and data citations policy: guidance for authors. Available online at: https://www.nature.com/documents/nr-data-availability-statements-data-citations.pdf. (accessed November 16, 2019)
132. Wilkinson MD, Dumontier M, Aalbersberg IJ, Appleton G, Axton M, Baak A, et al. The FAIR guiding principles for scientific data management and stewardship. *Sci Data.* (2016) **3**:160018. doi: 10.1038/sdata.2016.18
133. Mannheim JG, Mamach M, Reder S, Traxl A, Mucha N, Disselhorst JA, et al. Reproducibility and comparability of preclinical PET imaging data: a multicenter small-animal PET study. *J Nucl Med.* (2019) **60**:1483–91. doi: 10.2967/jnumed.118.221994
134. Voelkl B, Vogt L, Sena ES, Wurbel H. Reproducibility of preclinical animal research improves with heterogeneity of study samples. *PLoS Biol.* (2018) 16:e2003693. doi: 10.1371/journal.pbio.2003693
135. Bath PM, Macleod MR, Green AR. Emulating multicentre clinical stroke trials: a new paradigm for studying novel interventions in experimental models of stroke. *Int J Stroke.* (2009). **4**:471–9. doi: 10.1111/j.1747-4949.2009.00386.x

136. Dirnagl U, Hakim A, Macleod M, Fisher M, Howells D, Alan SM, et al. A concerted appeal for international cooperation in preclinical stroke research. *Stroke*. (2013) **44**:1754–60. doi: 10.1161/STROKEAHA.113.000734
137. Lefer DJ, Bolli R. Development of an NIH consortium for preclinicAl AssESsment of CARdioprotective therapies (CAESAR): a paradigm shift in studies of infarct size limitation. *J Cardiovasc Pharmacol Ther*. (2011). **16**:332–9. doi: 10.1177/1074248411414155
138. Gueld MO, Kohnen M, Keysers D, Schubert H, Wein BB, Bredno J, et al. Quality of DICOM header information for image categorization. *Proc. SPIE 4685, Medical Imaging 2002: PACS and Integrated Medical Information Systems: Design and Evaluation,* p. 280–7. doi: 10.1117/12.467017
139. Iudin A, Korir PK, Salavert-Torres J, Kleywegt GJ, Patwardhan A. EMPIAR: a public archive for raw electron microscopy image data. *Nat Methods*. (2016) **13**:387–8. doi: 10.1038/nmeth.3806
140. Bourne RM, Bailey C, Johnston EW, Pye H, Heavey S, Whitaker H, et al. Apparatus for histological validation of *in vivo* and *ex vivo* magnetic resonance imaging of the human prostate. *Front Oncol*. (2017) 7:47. doi: 10.3389/fonc.2017.00047
141. Ellenberg J, Swedlow JR, Barlow M, Cook CE, Sarkans U, Patwardhan A, et al. A call for public archives for biological image data. *Nat Methods*. (2018) **15**:849–54. doi: 10.1038/s41592-018-0195-8
142. Schellenberger P, Kaufmann R, Siebert CA, Hagen C, Wodrich H, Grunewald K. High-precision correlative fluorescence and electron cryo microscopy using two independent alignment markers. *Ultramicroscopy*. (2014) **143**:41–51. doi: 10.1016/j.ultramic.2013.10.011
143. Cohen EAK, Ober RJ. Analysis of Point based image registration errors with applications in single molecule microscopy. *IEEE Trans Signal Process*. (2013) **61**:6291–306. doi: 10.1109/TSP.2013.2284154
144. Fitzpatrick JM, West JB. The distribution of target registration error in rigid-body point-based registration. *IEEE Trans Med Imaging*. (2001) **20**:917–27. doi: 10.1109/42.952729
145. Xiao Y, Rivaz H, Chabanas M, Fortin M, Machado I, Ou Y, et al. Evaluation of MRI to ultrasound registration methods for brain shift correction: the CuRIOUS2018 challenge. *IEEE Trans Med Imaging*. (2020) **39**:777–86. doi: 10.1109/TMI.2019.2935060
146. Sartori A, Gatz R, Beck F, Rigort A, Baumeister W, Plitzko JM. Correlative microscopy: bridging the gap between fluorescence light microscopy and cryo-electron tomography. *J Struct Biol*. (2007) **160**:135–45. doi: 10.1016/j.jsb.2007.07.011
147. Schwartz CL, Sarbash VI, Ataullakhanov FI, McIntosh JR, Nicastro D. Cryo-fluorescence microscopy facilitates correlations between light and cryo-electron microscopy and reduces the rate of photobleaching. *J Microsc*. (2007) **227**:98–109. doi: 10.1111/j.1365-2818.2007.01794.x
148. Schorb M, Briggs JA. Correlated cryo-fluorescence and cryo-electron microscopy with high spatial precision and improved sensitivity. *Ultramicroscopy*. (2014) **143**:24–32. doi: 10.1016/j.ultramic.2013.10.015
149. Tuijtel MW, Koster AJ, Jakobs S, Faas FGA, Sharp TH. Correlative cryo super-resolution light and electron microscopy on mammalian cells using fluorescent proteins. *Sci Rep*. (2019) **9**:1369. doi: 10.1038/s41598-018-37728-8
150. Arnold J, Mahamid J, Lucic V, de Marco A, Fernandez JJ, Laugks T, et al. Site-specific Cryo-focused ion beam sample preparation guided by 3D correlative microscopy. *Biophys J*. (2016) **110**:860–9. doi: 10.1016/j.bpj.2015.10.053
151. Agronskaia AV, Valentijn JA, van Driel LF, Schneijdenberg CT, Humbel BM, van Bergen en Henegouwen PM, et al. Integrated fluorescence and transmission electron microscopy. *J Struct Biol*. (2008) **164**:183–9. doi: 10.1016/j.jsb.2008.07.003
152. Peddie CJ, Liv N, Hoogenboom JP, Collinson LM. Integrated light and scanning electron microscopy of GFP-expressing cells. *Methods Cell Biol*. (2014) **124**:363–89. doi: 10.1016/B978-0-12-801075-4.00017-3
153. Fabritius G, Brix G, Nekolla E, Klein S, Popp HD, Meyer M, et al. Cumulative radiation exposure from imaging procedures and associated lifetime cancer risk for patients with lymphoma. *Sci Rep*. (2016) 6:35181. doi: 10.1038/srep35181
154. Salminen E, Niiniviita H, Jarvinen H, Heinavaara S. Cancer death risk related to radiation exposure from computed tomography scanning among testicular cancer patients. *Anticancer Res*. (2017) **37**:831–4. doi: 10.21873/anticanres.11385
155. Clark DP, Badea CT. Hybrid spectral CT reconstruction. *PLoS ONE*. (2017) **12**:e0180324. doi: 10.1371/journal.pone.0180324
156. Trojanova E, Schyns L, Ludwig D, Jakubek J, Le Pape A, Sefc L, et al. Tissue sensitive imaging and tomography without contrast agents for small animals with Timepix based detectors. *J Instrum*. (2017) **12**:C01056. doi: 10.1088/1748-0221/12/01/C01056
157. Turecek D, Jakubek J, Trojanova E, Sefc L, Kolarova V. Application of timepix3 based CdTe spectral sensitive photon counting detector for PET imaging. *Nucl Instrum Methods Phys Res A*. (2018) **895**:84–9. doi: 10.1016/j.nima.2018.04.007
158. Trojanova E, Jakubek J, Turecek D, Sykora V, Francova P, Kolarova V, et al. Evaluation of Timepix3 based CdTe photon counting detector for fully spectroscopic small animal SPECT imaging. *J Instrum*. (2018) **13**:C01001. doi: 10.1088/1748-0221/13/01/C01001
159. Turecek D, Jakubek J, Trojanova E, Sefc L. Compton camera based on Timepix3 technology. *J Instrum*. (2018) **13**:C11022. doi: 10.1088/1748-0221/13/11/C11022
160. Sakai M, Yamaguchi M, Nagao Y, Kawachi N, Kikuchi M, Torikai K, et al. *In vivo* simultaneous imaging with (99m)Tc and (18)F using a Compton camera. *Phys Med Biol*. (2018) **63**:205006. doi: 10.1088/1361-6560/aae1d1
161. Bruns OT, Bischof TS, Harris DK, Franke D, Shi Y, Riedemann L, et al. Next-generation *in vivo* optical imaging with short-wave infrared quantum dots. *Nat Biomed Eng*. (2017) **1**:0056. doi: 10.1038/s41551-017-0056
162. George J, Van Wettere AJ, Michaels BB, Crain D, Lewbart GA. Histopathologic evaluation of postmortem autolytic changes in bluegill (*Lepomis macrohirus*) and crappie (*Pomoxis anularis*) at varied time intervals and storage temperatures. *PeerJ*. (2016) **4**:e1943. doi: 10.7717/peerj.1943
163. Copper JE, Budgeon LR, Foutz CA, van Rossum DB, Vanselow DJ, Hubley MJ, et al. Comparative analysis of fixation and embedding techniques for optimized histological preparation of zebrafish. *Comp Biochem Physiol C Toxicol Pharmacol*. (2018) **208**:38–46. doi: 10.1016/j.cbpc.2017.11.003
164. Kaufmann R, Hagen C, Grunewald K. Fluorescence cryo-microscopy: current challenges and prospects. *Curr Opin Chem Biol*. (2014) **20**:86–91. doi: 10.1016/j.cbpa.2014.05.007
165. Heimel P, Swiadek NV, Slezak P, Kerbl M, Schneider C, Nurnberger S, et al. Iodine-enhanced micro-CT imaging of soft tissue on the example of peripheral nerve regeneration. *Contrast Media Mol Imaging*. (2019) **2019**:7483745. doi: 10.1155/2019/7483745
166. Ouzounov DG, Wang T, Wang M, Feng DD, Horton NG, Cruz-Hernandez JC, et al. *In vivo* three-photon imaging of activity of GCaMP6-labeled neurons deep in intact mouse brain. *Nat Methods*. (2017) **14**:388–90. doi: 10.1038/nmeth.4183
167. Ding F, Zhan Y, Lu X, Sun Y. Recent advances in near-infrared II fluorophores for multifunctional biomedical imaging. *Chem Sci*. (2018) **9**:4370–80. doi: 10.1039/C8SC01153B
168. van den Berg PJ, Daoudi K, Steenbergen W. Review of photoacoustic flow imaging: its current state and its promises. *Photoacoustics*. (2015) **3**:89–99. doi: 10.1016/j.pacs.2015.08.001
169. Schorb M, Gaechter L, Avinoam O, Sieckmann F, Clarke M, Bebeacua C, et al. New hardware and workflows for semi-automated correlative cryo-fluorescence and cryo-electron microscopy/tomography. *J Struct Biol*. (2017) **197**:83–93. doi: 10.1016/j.jsb.2016.06.020
170. Lo YH, Liao C-T, Zhou J, Rana A, Bennett C, Murnane M, et al. Multimodal x-ray and electron microscopy of the Allende meteorite. *Sci Adv*. (2019) **5**:eaax3009. doi: 10.1126/sciadv.aax3009
171. Colom A, Casuso I, Rico F, Scheuring S. A hybrid high-speed atomic force-optical microscope for visualizing single membrane proteins on eukaryotic cells. *Nat Commun*. (2013) **4**:2155. doi: 10.1038/ncomms3155
172. Handschuh-Wang S, Wang T, Zhou X. Recent advances in hybrid measurement methods based on atomic force microscopy and surface sensitive measurement techniques. *RSC Adv*. (2017) **7**:47464–47499. doi: 10.1039/C7RA08515J

173. Haring MT, Liv N, Zonnevylle AC, Narvaez AC, Voortman LM, Kruit P, et al. Automated sub-5 nm image registration in integrated correlative fluorescence and electron microscopy using cathodoluminescence pointers. *Sci Rep.* (2017) **7**:43621. doi: 10.1038/srep43621
174. Leitgeb RA, Baumann B. Multimodal optical medical imaging concepts based on optical coherence tomography. *Front Phys.* (2018) **6**:00114. doi: 10.3389/fphy.2018.00114
175. Stuker F, Ripoll J, Rudin M. Fluorescence molecular tomography: principles and potential for pharmaceutical research. *Pharmaceutics.* (2011) **3**:229–74. doi: 10.3390/pharmaceutics3020229
176. Prabhakar N, Belevich I, Peurla M, Heiligenstein X, Chang H-C, Sahlgren C, et al. Dynamic-ultrastructural cell volume (3D) correlative microscopy facilitated by intracellular fluorescent nanodiamonds as multi-modal probes. *bioRxiv.* (2019) 823278. doi: 10.1101/823278
177. Louie A. Multimodality imaging probes: design and challenges. *Chem Rev.* (2010) **110**:3146–95. doi: 10.1021/cr9003538
178. Ose T, Autio JA, Ohno M, Nishigori K, Tanki N, Igesaka A, et al. A novel Tungsten-based fiducial marker for multi-modal brain imaging. *J Neurosci Methods.* (2019) **323**:22–31. doi: 10.1016/j.jneumeth.2019.04.014
179. An FF, Chan M, Kommidi H, Ting R. Dual PET and near-infrared fluorescence imaging probes as tools for imaging in oncology. *AJR Am J Roentgenol.* (2016) **207**:266–73. doi: 10.2214/AJR.16.16181
180. Bushong EA, Johnson DD, Jr, Kim KY, Terada M, Hatori M, et al. X-ray microscopy as an approach to increasing accuracy and efficiency of serial block-face imaging for correlated light and electron microscopy of biological specimens. *Microsc Microanal.* (2015) **21**:231–8. doi: 10.1017/S1431927614013579
181. Shu X, Lev-Ram V, Deerinck TJ, Qi Y, Ramko EB, Davidson MW, et al. A genetically encoded tag for correlated light and electron microscopy of intact cells, tissues, and organisms. *PLoS Biol.* (2011) **9**:e1001041. doi: 10.1371/journal.pbio.1001041
182. Ariotti N, Hall TE, Parton RG. Correlative light and electron microscopic detection of GFP-labeled proteins using modular APEX. *Methods Cell Biol.* (2017) **140**:105–21. doi: 10.1016/bs.mcb.2017.03.002
183. Rijnsoever Cv, Oorschot V, Klumperman J. Correlative light-electron microscopy (CLEM) combining live-cell imaging and immunolabeling of ultrathin cryosections. *Nature Methods.* (2008) **5**:973–80. doi: 10.1038/nmeth.1263
184. Eberle AL, Mikula S, Schalek R, Lichtman J, Tate MLK, Zeidler D. High-resolution, high-throughput imaging with a multibeam scanning electron microscope. *J Microsc.* (2015) **259**:114–20. doi: 10.1111/jmi.12224
185. Collinson LM, Carroll EC, Hoogenboom JP. Correlating 3D light to 3D electron microscopy for systems biology. *Curr Opin Biomed Eng.* (2017) **3**:49–55. doi: 10.1016/j.cobme.2017.10.006
186. Hoehndorf R, Schofield PN, Gkoutos GV. The role of ontologies in biological and biomedical research: a functional perspective. *Brief Bioinform.* (2015) **16**:1069–80. doi: 10.1093/bib/bbv011
187. Smith B, Arabandi S, Brochhausen M, Calhoun M, Ciccarese P, Doyle S, et al. Biomedical imaging ontologies: a survey and proposal for future work. *J Pathol Inform.* (2015) **6**:37. doi: 10.4103/2153-3539.159214
188. Caicedo JC, Goodman A, Karhohs KW, Cimini BA, Ackerman J, Haghighi M, et al. Nucleus segmentation across imaging experiments: the 2018 data science bowl. *Nat Methods.* (2019) **16**:1247–53. doi: 10.1038/s41592-020-0733-z
189. Li R, Zhang W, Suk H-I, Wang L, Li J, Shen D, et al. Deep learning based imaging data completion for improved brain disease diagnosis. *Med Image Comput Comput Assist Interv.* (2014) **17**(Pt. 3):305–12. doi: 10.1007/978-3-319-10443-0_39
190. Weigert M, Schmidt U, Boothe T, Müller A, Dibrov A, Jain A, et al. Content-aware image restoration: pushing the limits of fluorescence microscopy. *Nat Methods.* (2018) **15**:1090–7. doi: 10.1038/s41592-018-0216-7
191. Christiansen EM, Yang SJ, Ando DM, Javaherian A, Skibinski G, Lipnick S, et al. *In silico* labeling: predicting fluorescent labels in unlabeled images. *Cell.* (2018) **173**:792–803.e19. doi: 10.1016/j.cell.2018.03.040

**Conflict of Interest:** The authors declare that the research was conducted in the absence of any commercial or financial relationships that could be construed as a potential conflict of interest.

frontiers in Physics

ORIGINAL RESEARCH
published: 21 April 2020
doi: 10.3389/fphy.2020.00088

# Optimizing Diffusion Imaging Protocols for Structural Connectomics in Mouse Models of Neurological Conditions

*Robert J. Anderson[1], Christopher M. Long[1], Evan D. Calabrese[2], Scott H. Robertson[1], G. Allan Johnson[1], Gary P. Cofer[1], Richard J. O'Brien[3] and Alexandra Badea[1,3]**

[1] Department of Radiology, Duke University, Durham, CA, United States, [2] Department of Radiology and Biomedical Imaging, University of California, San Francisco, CA, United States, [3] Department of Neurology, School of Medicine, Duke University, Durham, CA, United States

Network approaches provide sensitive biomarkers for neurological conditions, such as Alzheimer's disease (AD). Mouse models can help advance our understanding of underlying pathologies, by dissecting vulnerable circuits. While the mouse brain contains less white matter compared to the human brain, axonal diameters compare relatively well (e.g., ∼0.6 μm in the mouse and ∼0.65–1.05 μm in the human corpus callosum). This makes the mouse an attractive test bed for novel diffusion models and imaging protocols. Remaining questions on the accuracy and uncertainty of connectomes have prompted us to evaluate diffusion imaging protocols with various spatial and angular resolutions. We have derived structural connectomes by extracting gradient subsets from a high-spatial, high-angular resolution diffusion acquisition (120 directions, 43-μm-size voxels). We have simulated protocols with 12, 15, 20, 30, 45, 60, 80, 100, and 120 angles and at 43, 86, or 172-μm voxel sizes. The rotational stability of these schemes increased with angular resolution. The minimum condition number was achieved for 120 directions, followed by 60 and 45 directions. The percentage of voxels containing one dyad was exceeded by those with two dyads after 45 directions, and for the highest spatial resolution protocols. For the 86- or 172-μm resolutions, these ratios converged toward 55% for one and 39% for two dyads, respectively, with $<$7% from voxels with three dyads. Tractography errors, estimated through dyad dispersion, decreased most with angular resolution. Spatial resolution effects became noticeable at 172 μm. Smaller tracts, e.g., the fornix, were affected more than larger ones, e.g., the fimbria. We observed an inflection point for 45 directions, and an asymptotic behavior after 60 directions, corresponding to similar projection density maps. Spatially downsampling to 86 μm, while maintaining the angular resolution, achieved a subgraph similarity of 96% relative to the reference. Using 60 directions with 86- or 172-μm voxels resulted in 94% similarity. Node similarity metrics indicated that major white matter tracts were more robust to downsampling relative to cortical regions. Our study provides guidelines for new protocols in mouse models of neurological conditions, so as to achieve similar connectomes, while increasing efficiency.

**Keywords: diffusion imaging, MRI, connectivity (graph theory), mouse model, brain, neurodegenerative diseases**

OPEN ACCESS

**Edited by:**
*Andreas Hess, University of Erlangen-Nuremberg, Germany*

**Reviewed by:**
*Boran Han, Harvard University, United States*
*Silvia Capuani, Italian National Research Council, Italy*

***Correspondence:**
*Alexandra Badea*
*alexandra.badea@duke.edu*

**Specialty section:**
*This article was submitted to Medical Physics and Imaging, a section of the journal Frontiers in Physics*

***Received:** 07 December 2019*
***Accepted:** 11 March 2020*
***Published:** 21 April 2020*

**Citation:**
*Anderson RJ, Long CM, Calabrese ED, Robertson SH, Johnson GA, Cofer GP, O'Brien RJ and Badea A (2020) Optimizing Diffusion Imaging Protocols for Structural Connectomics in Mouse Models of Neurological Conditions. Front. Phys. 8:88. doi: 10.3389/fphy.2020.00088*

## INTRODUCTION

A growing body of evidence suggests that altered brain connectivity is present in a variety of neurologic and psychiatric diseases. For example neurological conditions such as AD [1, 2], autism spectrum disorders [3], and psychiatric conditions such as schizophrenia [4] can be viewed as connectopathies. Multimodal network analyses can help identify early alterations associated with pathological processes both at the functional and structural levels. Structural connectomes based on diffusion MRI may produce sensitive biomarkers to monitor these conditions since they integrate the effects of multiple pathologies (atrophy, myelination, toxicity of the environment due to, e.g., oligomers, microstructural changes) [5].

While studies on diffusion imaging in the human brain have previously addressed the tradeoffs associated with spatial vs. angular resolution, the mouse brain provides insight into white matter connectivity at a vastly different scale and, thus, deserves special attention. We need to compare 2-mm linear dimension voxel sizes in humans (corresponding to 8-$mm^3$ voxel volumes), vs. 0.2–0.043-mm linear dimension voxel sizes (corresponding to $\sim 8 \times 10^{-2}$- $8 \times 10^{-5}$-$mm^3$ voxel volumes) required to distinguish similar levels of anatomical detail in mouse brains [6–11]. This increased resolution enables the observation of brain architecture at the level of cellular layers, which, therefore, can help us gain insight into the mechanistic drivers behind the etiology and progression of disease, using animal models where axonal dimensions are relatively similar to humans [12, 13].

Yet, using sensitive methods for identifying pathways affected early on in animal models remains difficult. Difficulties in optimizing diffusion imaging protocols arise from the need for long acquisition times, to achieve sufficient signal to noise for smaller voxels. These are required for dissecting vulnerable pathways and networks, early on in the disease process, or subtle changes in time or following interventions. The mouse brain architecture, in contrast with the human brain, presents with thin, relatively sparse white matter tracts. The imaging protocols required for resolving small tract-based connections are, thus, demanding a high spatial resolution. In addition, increasing the angular sampling and the number of b values may reduce biases and produce more accurate models. This translates into long protocols, and subsequently costs in terms of time and money, which need to be balanced against the desired increases in spatial and angular resolution.

In this work, we have examined the balance between spatial and angular resolutions and inferred suggestions for recommended future protocols. In particular, we examined a set of nodes/brain regions that are relevant for neurodegenerative conditions such as AD. We used simulations based on downsampling a high-spatial, high-angular data set, and assessed the effect of relaxing these requirements/parameters on the accuracy of the reconstructed tracts and connectome, when compared against our reference protocol. We have focused our analyses on regions expected to be affected in AD, such as fimbria, fornix, and hippocampus, septum, hypothalamus, and also the lateral geniculate nucleus. We evaluated how different protocols led to increasingly more robust results and how fast errors change with spatial and angular sampling resolution. Our results can inform future population studies, in particular, for models of neurodegenerative disease.

## METHODS

Imaging was performed, as previously reported [14] on a 9.4-Tesla small-animal imaging system controlled by an Agilent VnmrJ 4 console. Diffusion imaging was accomplished using a 3D diffusion-weighted spin-echo pulse sequence with repetition time (TR) = 100 ms, echo time (TE) = 15 ms, and b value = 4,000 s/$mm^2$. The acquisition matrix was $568 \times 284 \times 228$ over a $24.4 \times 12.2 \times 9.8$ mm field of view, resulting in isotropic $43 \times 43 \times 43$ μm voxels (referred from now on as 43-μm linear voxel dimension). The diffusion protocol included 120 diffusion directions [15, 16] and 11 non-diffusion-weighted (b0) measurements (i.e., one b0 every 12 diffusion measurements).

Angular downsampling of the original diffusion data set was performed by obtaining the optimal diffusion directions for each angular subset [15, 16] and extracting the closest gradient vector from the 120 unique diffusion directions. The closest gradient orientation was chosen by maximizing the dot product between the optimal gradient vector and the possible vectors found in the original gradient table.

Spatial downsampling of the original diffusion data set was performed by cropping the data in k space, resulting in three levels of isotropic spatial resolution: 43-, 86-, 172-μm linear voxel dimension.

The condition numbers for the gradient subset matrices, defining angular sampling, were calculated in MATLAB (Natick, MA), based on the ratio between the largest and smallest singular values for each matrix. The stability of the condition numbers was evaluated for each of the gradient subsets following 50,000 simulated rotations of these matrices.

Diffusion data processing was done on a high-performance computing cluster with 96 physical cores and 1.5 TB of RAM. All 131 image volumes were registered to the first b0 image using advanced normalization tools (ANTs) affine transformation [17] to correct for eddy current distortions. Scalar image volumes were reconstructed using FSL's DTIFIT [18]. Fiber data for probabilistic tractography were reconstructed using FSL's BEDPOSTX [19] with a maximum of four fiber orientations per voxel. In-home written scripts and FSL were used to estimate the numbers of tracts with one, two, three, or four dyads and to estimate errors/uncertainty based on dyad dispersion.

Automated atlas-based segmentation was performed [20] using an atlas, which combines the Waxholm Space atlas [21] for subcortical labels, and the Ullmann atlas of the neocortex [22], with a total of 332 regions—symmetrized relative to the midsagittal plane. Connectomes were constructed using SAMBA [23], and DSI Studio [24] for a subset of brain regions. These include for simplicity, the connectivity matrices generated pertaining solely to left-sided seed regions connecting to left-sided targets. We next evaluated the similarity of connectomes based on global Spearman correlation coefficients among 12 representative acquisition schemes (four angular sampling

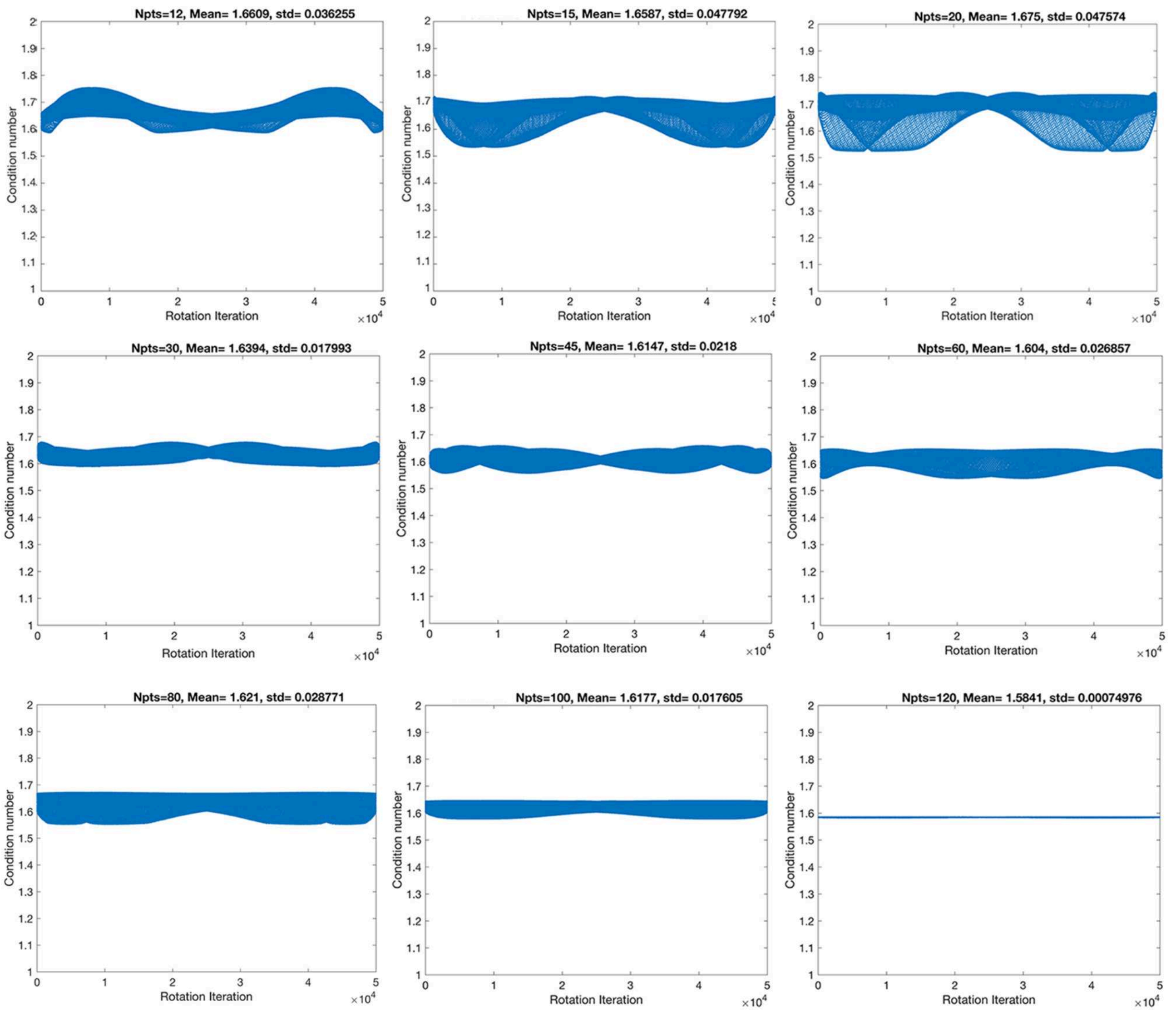


**FIGURE 1 |** The stability of the condition numbers increased, and the standard deviation decreased with angular resolution, although not monotonically, denoting that some sampling schemes are more robust to rotational variance, due to their geometrical symmetry properties.

**TABLE 1 |** The smallest mean condition numbers (CN) ranked the 120-direction scheme as optimal, followed by the 60, then 45-direction schemes.

| Angles | CN | CN (mean) | STD | STD (CN)/SQRT (Angles) | Rank CN (mean) | Rank STD |
|---|---|---|---|---|---|---|
| 12 | 1.647 | 1.661 | 3.626E−02 | 1.047E−02 | 8 | 7 |
| 15 | 1.709 | 1.659 | 4.779E−02 | 1.234E−02 | 7 | 9 |
| 20 | 1.696 | 1.675 | 4.758E−02 | 1.064E−02 | 9 | 8 |
| 30 | 1.633 | 1.639 | 1.799E−02 | 3.285E−03 | 6 | 3 |
| 45 | 1.610 | 1.615 | 2.180E−02 | 3.250E−03 | 3 | 4 |
| 60 | 1.561 | 1.604 | 2.685E−02 | 3.467E−03 | 2 | 5 |
| 80 | 1.645 | 1.621 | 2.877E−02 | 3.217E−03 | 5 | 6 |
| 100 | 1.643 | 1.618 | 1.761E−02 | 1.761E−03 | 4 | 2 |
| 120 | 1.585 | 1.584 | 7.494E−04 | 6.841E−05 | 1 | 1 |

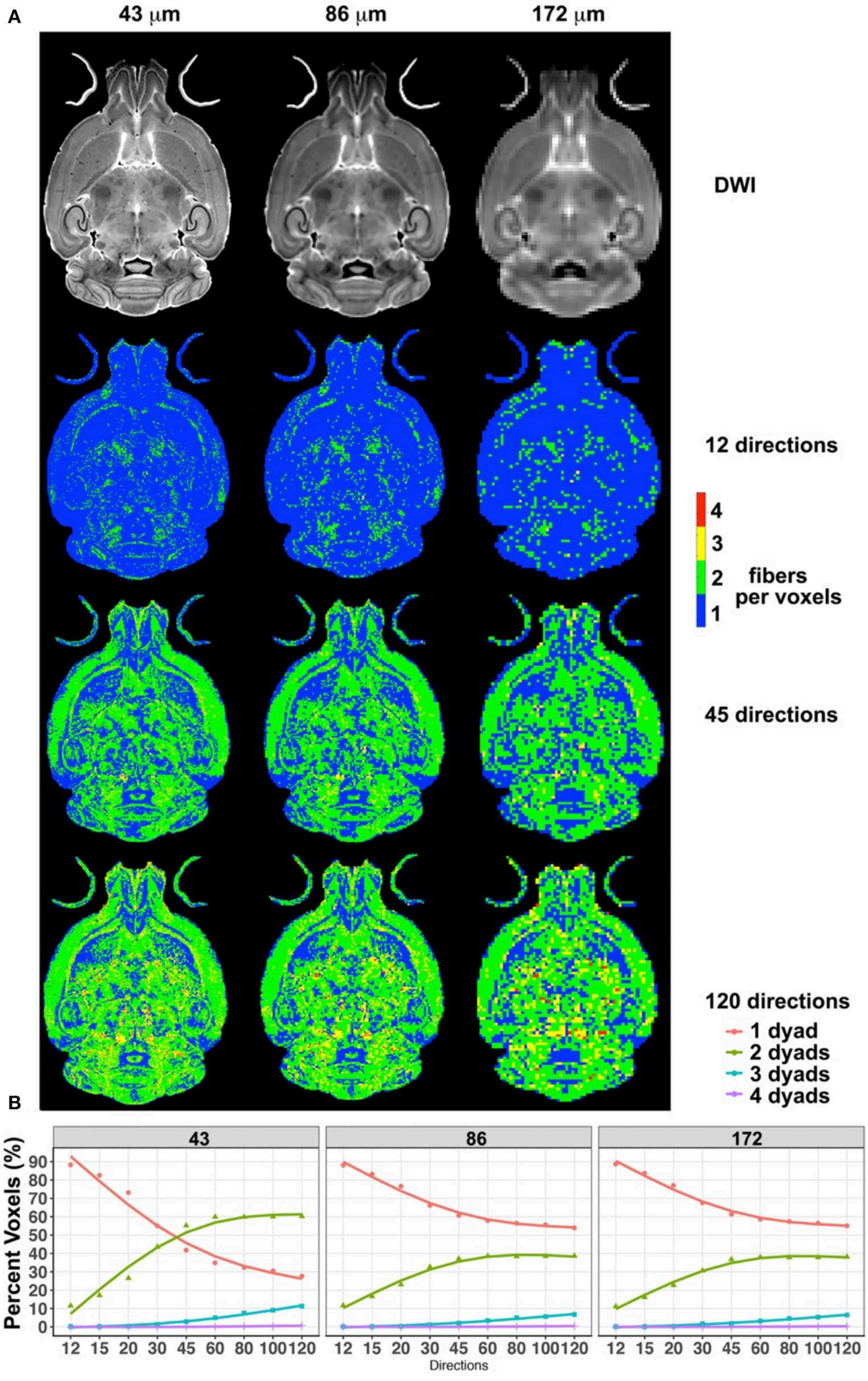


**FIGURE 2 |** The effect of spatial resolution (horizontal axis) and angular resolution (vertical axis) on the number of voxels with one, two, three, or four fibers (dyads) per voxels **(A)**. **(A)** Effects for 12, 45, and 120 directions, chosen as examples for low-, medium-, and high-angular sampling. **(B)** Effects for sampling schemes between 12 and 120 at three spatial resolutions (43, 86, and 172 μm). These results illustrated the advantages of high-angular and spatial-resolution protocols in terms of sensitivity and stability.

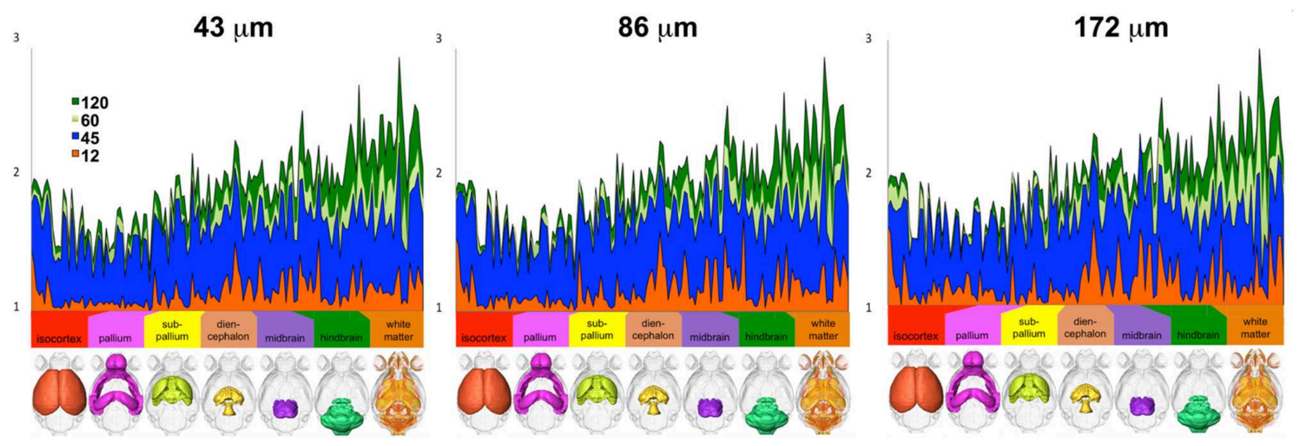


**FIGURE 3 |** The number of voxels with one, two, and three dyads varied per region, but differences relative to the reference protocol (high-spatial, high-angular resolution) consistently decreased with increasing number of angular directions (only 12, 45, 60, and 120 directions are shown for simplicity) and with increasing spatial resolution (i.e., smaller voxels; ranging from 43-μm linear dimension for the reference to 86 and 172 μm).

schemes and three spatial resolution levels). Node wise similarity was evaluated as in Blondel et al. [25]. Specifically, the similarity matrices were obtained as the limit of the normalized even iterates of $S_k + 1 = BS_kA^T + B^TS_kA$, where $A$ and $B$ are the two graph adjacency matrices, and $S_0$ is a matrix whose entries are equal to 1.

## RESULTS

We have evaluated the effect of different angular diffusion sampling schemes and spatial resolutions on mouse brain connectivity, from the point of view of stability, with reference to a published data set, and with the aim to identify balanced acquisition schemes in terms of cost and accuracy.

First, we have evaluated nine angular sampling schemes from the point of view of their stability, through their condition numbers, as well as their standard deviations (**Figure 1**). The condition numbers define the asymptotic worst-case relative change in output for a relative change in input.

The highest spatial and angular resolution scheme had the smallest condition numbers (1.58) and standard deviation ($7.5 \times 10^{-4}$). The ranking in terms of condition number was followed by the 60- and 45-direction angular sampling schemes, while the standard deviation followed the ranking 100, 45, and 60 (**Table 1**).

We focused the rest of our analyses on the 45- and 60-direction schemes and compared the results against the reference 120-direction scheme, at three different spatial resolution levels throughout.

Downsampled diffusion data sets were used to estimate the total number of fibers per voxel in each set (**Figure 2**). The total fiber count increased from $7.4 \times 10^6$ for 12 directions to $1.07 \times 10^7$ for 45 and $1.13 \times 10^7$ for 60 directions and $1.23 \times 10^7$ for 120 directions. The steepest changes occurred below 45 directions.

Interestingly, while the number of voxels detected to have one fiber direction was dominant for small angular sampling schemes, this number was exceeded by the number of voxels identified to have two fiber directions, if the sampling schemes had more than 45 angular directions and at a spatial resolution of 43 μm. The number of voxels with one dyad reached 42% for 45 directions, and 35% for 60 directions. The number of voxels with two dyads increased with increasing angular sampling, reaching 55% for 45 directions and 60% for 60 directions. Thus, these two curves intersected, and the ratio of one- to two-dyad voxels changed after ∼45 directions. However, the two curves did not intersect for the 86- and 172-μm spatial resolution scenarios. The number of voxels with one fiber direction plateaued at ∼55%, and the number of voxels with two fiber directions at ∼38% for 86- and 172-μm spatial resolutions, with modest increases between 45 and 60 angular samples, and <7% contribution from voxels with three directions. These two data sets had very similar behaviors in terms of the number of voxels with one or two dyads.

These effects were found to be region dependent, although we noted a consistent trend in the ratios between one, two, and three dyads across all three resolution samples (**Figure 3**).

We next focused our analysis on the fimbria and fornix because these tracts have been reported to be relevant in neurodegenerative conditions such as Alzheimer's disease. Our qualitative evaluation showed that tract density maps reconstructed from 12 directions did not capture the cortical–cortical connectivity with the same sensitivity as the 45-, 60-, or 120-direction schemes (**Figure 4**). While less striking, the loss of spatial resolution also resulted in a change in the anatomical definition for the projections, and loss of connectivity through smaller regions (e.g., alveus).

The connectivity of the left hippocampus (**Figure 5**) illustrated a striking similarity between the 120- and 60-directions schemes and loss of similarity for lower angular resolution schemes. In particular, cortical projections occupied

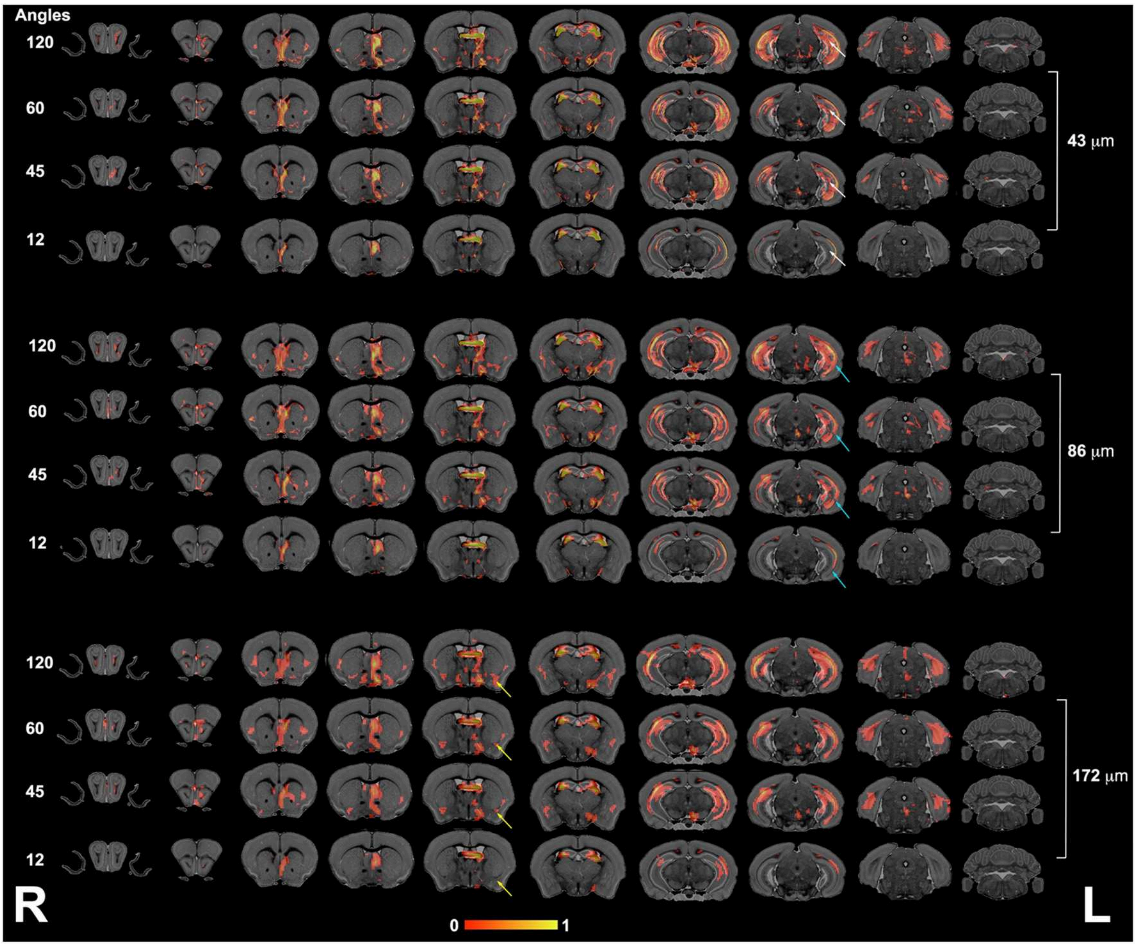


**FIGURE 4 |** The fimbria connectivity mapped as a function of spatial and angular resolution. The connectivity of the left fimbria was reconstructed for protocols with 12, 45, 60, and 120 directions, at the full 43-μm resolution, clearly illustrating limitations of smaller angular sampling protocols at capturing projections though the hippocampus (white arrows) and amygdala (yellow arrows). Less clear were the effects of spatial resolution in the range 43–172 μm where SNR and partial volume effects both played a role. However, the projections through the hippocampus covered reduced areas, and projections into the alveus were partially lost in the lower resolution protocol (blue arrows). L, left; R, right.

smaller areas, especially those requiring interhemispheric connections. The loss of spatial resolution resulted in some clusters appearing larger (e.g., in the amygdala), or conversely, some of the connections were lost (e.g., hindbrain, cerebellum).

We based our quantitative error analysis on the dyad dispersion for the first- (**Figure 6A**) and second-order dyads (**Figure 6B**). Our results showed that errors decayed as the number of angular samples increased both for white matter and for gray matter regions, and the errors increased as we relaxed the spatial resolution. This effect toward increased dispersion was particularly important for thin regions such as the fornix in dyad one (**Figure 6A**). An inflection point was noticed in particular for gray mater regions for 45 directions, and the curves tended to converge toward an asymptotic behavior starting with 60 directions. The dispersion values were larger for the second-order dyad (**Figure 6B**), but the trends were consistent with those observed for dyad one, with an asymptotic behavior predominantly observed in gray matter regions for schemes with more than 60 directions.

Probabilistic tractography was used to generate connectivity matrices, based on the number of streamlines connecting selected regions that are likely to play a role in neurodegenerative disease models. In general, the connectivity differences between our reference and those of the 45- or 60-direction data sets were considerably smaller relative to those involving 12 directions (**Figure 7**). The sensitivity to capturing connectivity of smaller, and in particular, cortical gray matter regions was evident in the chord diagrams (**Figure 7**), which appeared sparser for 12 directions relative to 45, 60, and 120 directions. The sparsity was evident for gray matter-to-gray matter connections, in particular, for cortical domains. For small angular resolutions, the connectomes were dominated by wide bands involving myelinated white matter tract regions connecting to the hippocampus or septum. Gray matter-to-gray matter connections appeared more prominent with higher angular

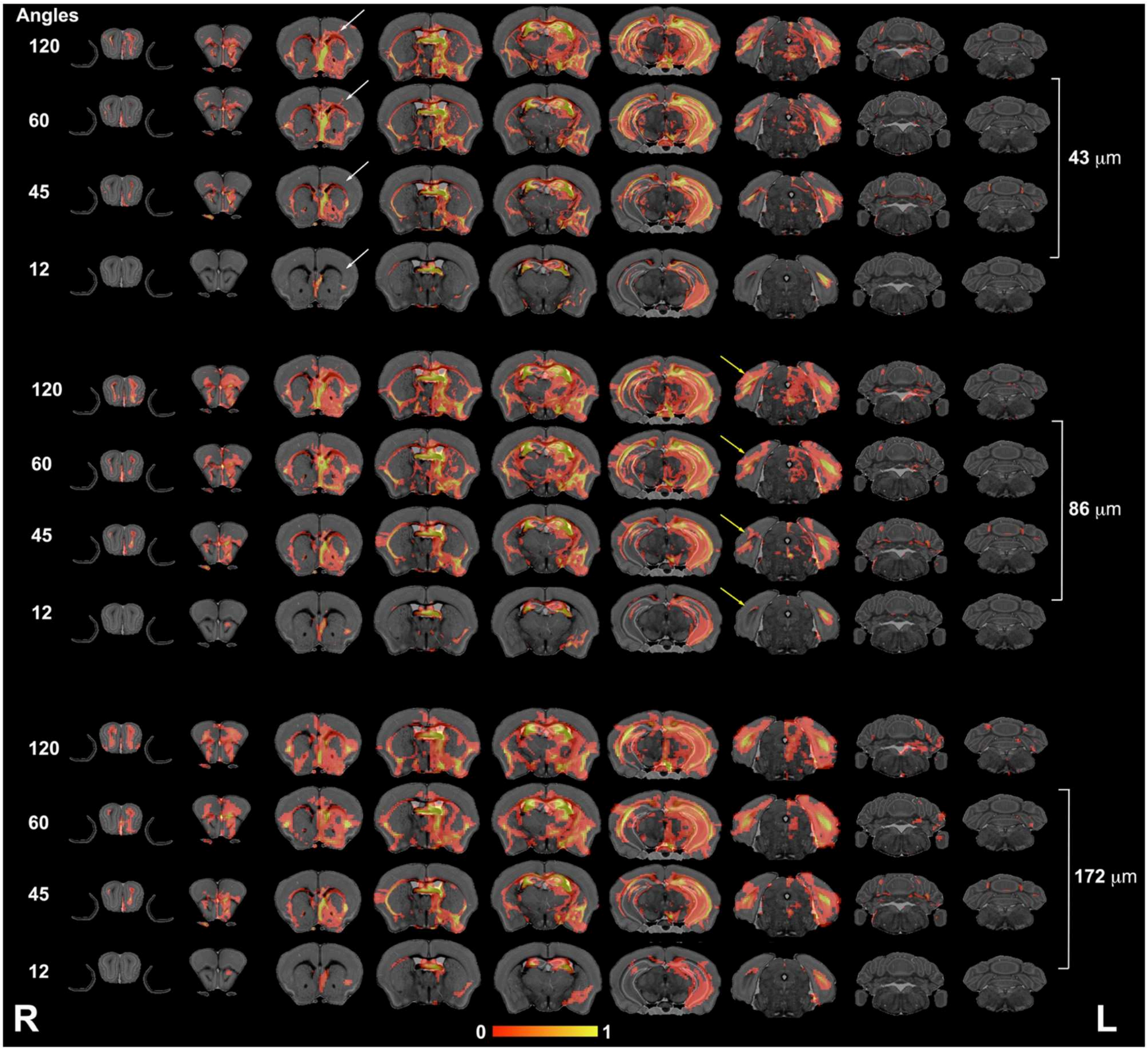


**FIGURE 5 |** The hippocampus connectivity mapped as a function of spatial and angular resolution. Hippocampal connectivity (the left hemisphere was seeded) was affected more by angular resolution, especially for cortical regions (white arrows), but also in the ability to retrieve cross hemispheric projections (yellow arrows). L, left; R, right.

sampling, in particular for schemes with more than 45 directions, with a noticeable qualitative similarity between 60 and 120 angles.

To quantify the similarity between connectomes, we used non-parametric correlation analysis. The Spearman correlation among the connectivity matrices was significant ($p < 0.001$) for all comparisons tested.

The highest global correlation overall was found among the 86-μm spatial resolution connectomes acquired with 60 and 120 directions, 0.97, while the correlation between connectomes acquired at the same 86-μm spatial resolution with 45 and 120 directions was 0.92. When compared against the reference high-spatial, high-angular resolution protocol (S1, A120), the highest correlations were with (S2, A120) at 0.96, followed by (S1, A60) and (S2, A60) at 0.94, then (S4, A120) at 0.93 (**Figure 8,** left). When comparing the 45-direction protocols against the reference (high-spatial, high-angular resolution) protocol (S1, A120), the highest correlation was obtained with (S2, A45) at 0.91 followed by (S1, A45) at 0.90 (**Figure 8,** right).

In our experiments (S1, A120) was robust to downsampling, achieving a correlation of 0.96 with (S2, A120) and 0.93 with (S4, A120). The angular resolution had a strong effect, with the similarity dropping to 0.7 with (S1, A12), 0.9 with (S1, A45), and 0.94 with (S1, A60). The lowest similarity from our subgraph comparison was between (S2, A120) and (S2, A12) at 0.64,

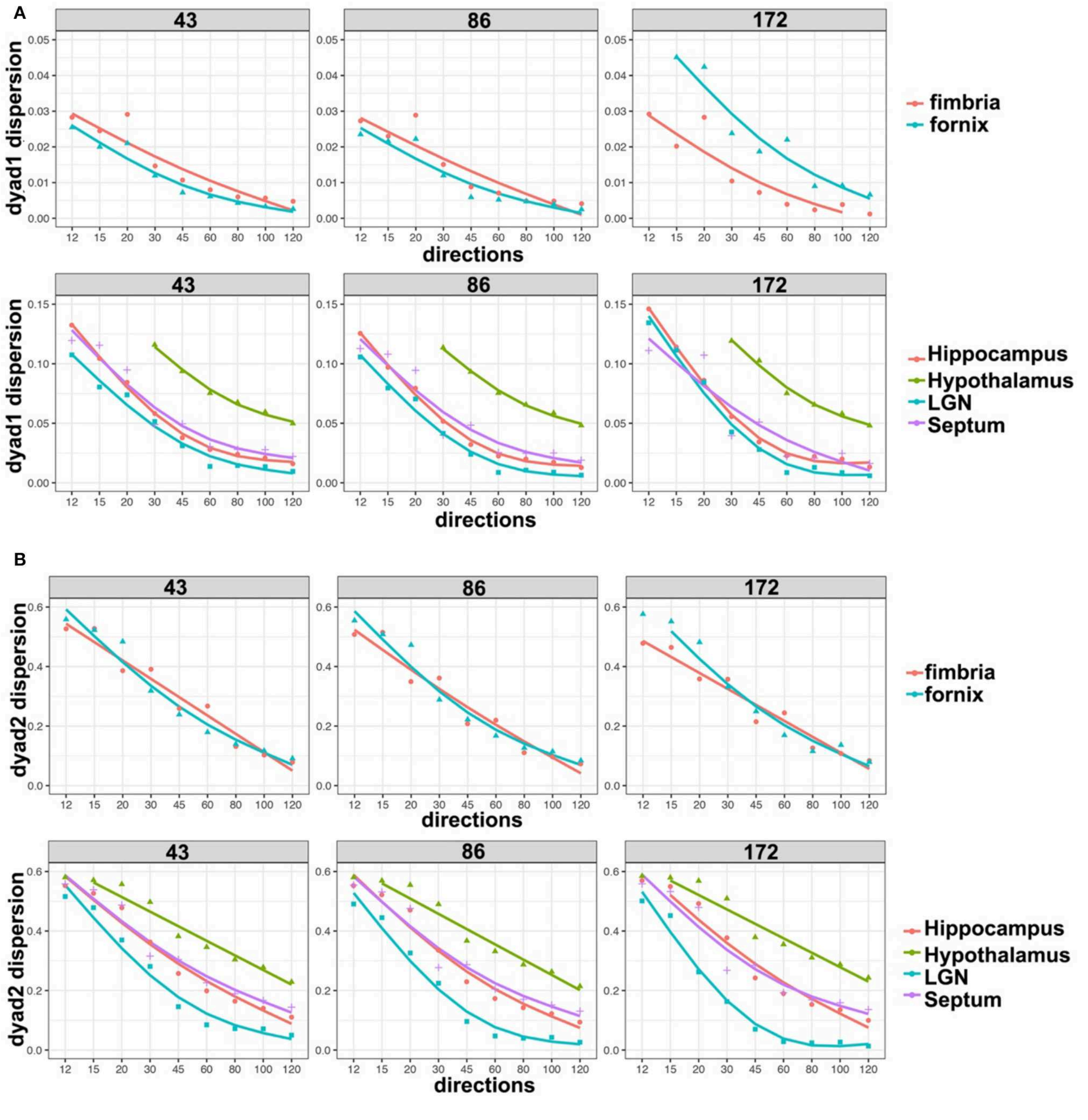


**FIGURE 6 |** Dyad dispersion as a measure of error. The dyad one dispersion shows decreasing errors for higher angular samples, with an inflection point at 45° and increasing stability after 60° **(A)**. Similar errors were apparent for 43 and 86 μm, but the errors were larger for 172 μm. Dyad two showed a stronger effect of resolution, and larger errors, which also tapered off after more than 60 directions were acquired **(B)**. LGN, lateral geniculate nucleus.

followed by (S2, A120) with (S1, A12) and (S2, A12) with (S4, A120) at 0.65. Our results suggest that higher-angular resolution schemes are generally more robust to detecting changes in animal models of neurological conditions.

Furthermore, we computed measures of similarity between individual graph vertices. The vertex-wise graph similarity pairwise for these subgraphs, shown in **Figure 9** after thresholding at a 0.1 level, illustrated differences in sparsity. Graphs were less sparse as the numbers of angular samples/directions increased above 45 to 60 and 120 directions. Based on the vertex score, the robustness of some nodes relative to others became evident when undergoing downsampling, first for fimbria, followed by the fornix. The similarity between the hippocampus (Hc) and fimbria (fi) and fornix (fx) was 0.1 and 0.07. For the 45-direction scheme, the similarity between full resolution and 86-μm resolution for fimbria was 0.45, while for

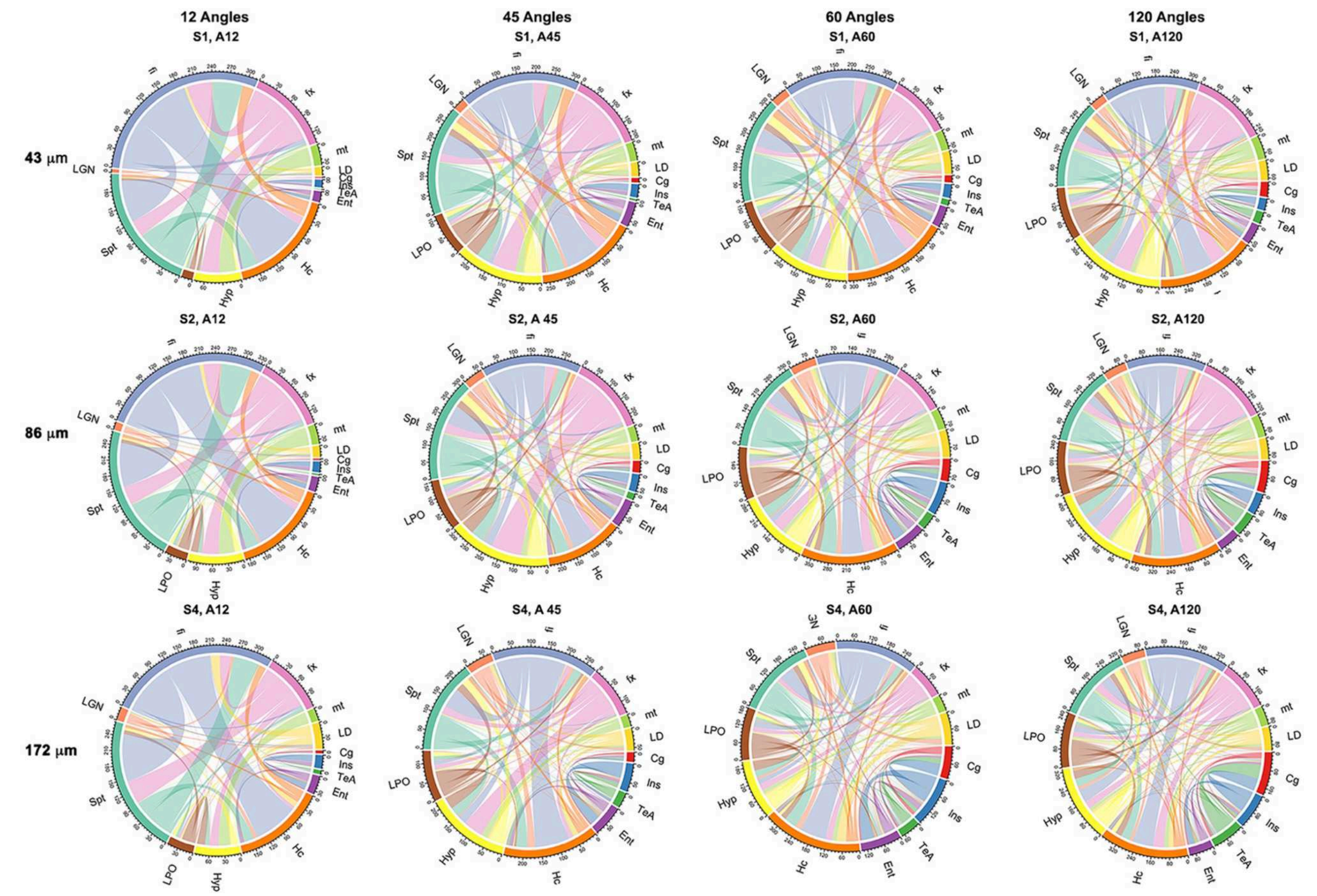


**FIGURE 7 |** Adjacency matrices shown as chord diagrams for a subset of 13 regions relevant to neurodegenerative diseases showed qualitatively greater similarity to the reference connectome of 120 directions (A120) for 45 (A45) and 60 directions (A60) when compared to the similarity between 120 (A120) and 12 directions (A12). Spatial resolution also had an effect on the chord diagrams, in particular, at the level four times downsampling (S4; 172 μm), but this was less pronounced when comparing two times downsampling (S2; 86 μm) with fully sampled (S1; 43 μm) protocols. The chord diagrams showed that all protocols can capture the connectivity of the hippocampus (Hc) and its connecting fibers (fx, fornix; fi, fimbria), but shorter protocols have reduced sensitivity for smaller nuclei (LD, laterodorsal thalamic nuclei; LGN, lateral geniculate nuclei; LPO, lateral preoptic nucleus) and lack sensitivity required for cortical connectivity, e.g., for the cingulate (Cg) and entorhinal cortices (Ent).

the fx, it was 0.18, and for the hippocampus and septum, it was 0.16 indicating more robustness for larger regions. Hc with fi and fx was 0.21 and 0.11, respectively. The similarity for fi (0.27) and fx (0.24) decreased with downsampling spatial resolution for the 120-direction schemes; however, more regions picked up more similar connections across these two graphs. For example, the hippocampus score was 0.21, and for septum, 0.15, with Hc to fi and fx being 0.17 and 0.12, respectively. These results suggest that while major white matter tracts were robust with respect to changes in spatial and angular resolution, this needs to be balanced against the vulnerability of smaller white matter tracts and cortical domains to such changes, and sparsity of the connectome and graph similarity matrices are important factors to consider.

In conclusion, our results support that angular and spatial resolution need to be balanced with respect to time- and cost-imposed demands to enable population studies, and parameters for efficient protocols with minimum loss of sensitivity should be recommended, suggesting that an acquisition with 60 angular samples provides a good compromise in terms of minimizing errors relative to a reference high-spatial, high-angular resolution protocol. Halving both spatial and angular resolutions yields an eight-time speed factor. When time is a constraint, compromises in terms of spatial resolution may need to be made. Importantly, more efficient acquisitions are amenable to future population studies.

## DISCUSSION

Several studies using tractography-based connectomics have reported abnormal network organization associated with morphometric changes and AD pathologies [26, 27]. Still, to understand the etiology of human neurodegenerative diseases such as AD has proven difficult. This is due to AD's complex nature, multiple pathologies, and various associated comorbidities. In spite of their limitations and simplicity,

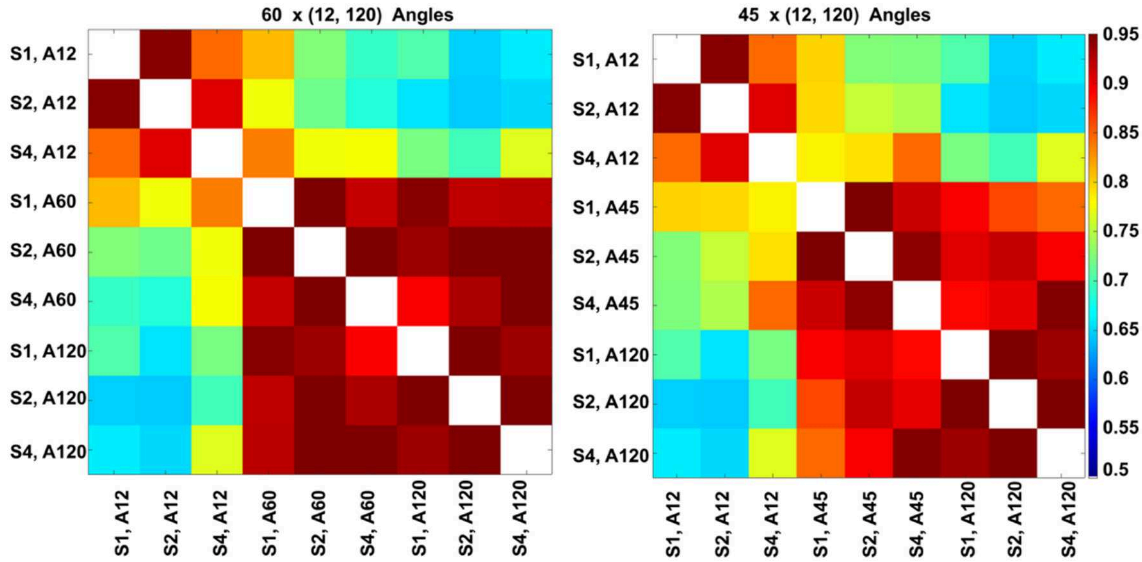


**FIGURE 8 |** Global connectome similarity. Spearman correlations among the connectomes obtained for three resolution levels (S1, fully sampled at 43-μm linear voxel dimension; S2, downsampled by a factor of 2–86 μm; S4, downsampled by a factor of 4–172 μm; and each of the 12, 45, 60, and 120 angular resolution schemes (A12, A45, A60, A120) indicated that the highest similarities were obtained between the 60 and 120 angular samples schemes for all spatial resolutions. While the patterns were similar, similarities were lower for the 45 and 120 angular sample schemes for all resolutions relative to 60- and 120-direction schemes. When comparing against the reference set, the median was 0.89 for sets with 45 directions, but 0.92 for sets with 60 directions; and the maximum for 45 directions was 0.91, but 0.94 for 60 directions. The global maximum 0.97 was obtained when comparing (S2, A60) vs. (S2, A120); or (S1, A45) vs. (S2, A45).

mouse models provide tools to examine the effect of singular pathologies, and the interaction of multiple factors in a well-controlled environment and, importantly, from early on.

Given the challenges in phenotyping mouse models of neurological conditions, imaging protocols are required to provide sensitive quantitative biomarkers with good spatial mapping abilities. In a previous study, we have defined a diffusion MRI data reference set with the highest reported resolution for the whole mouse brain [11]. This data set was acquired using 120 angular samples and 43-μm spatial resolution, requiring a scan time of 235 h. Replicating this acquisition for population studies is prohibitive in terms of both time and cost. To address this problem, we must define reduced protocols that ensure sufficient fidelity and compare well with the reference data set, but that can be acquired in a greatly reduced time. This will enable population studies and give insight into vulnerable networks that may provide early biomarkers and enable us to quantify disease progression or response to interventions. We, thus, performed a simulation study, examining subsets of angular samples from the reference set, and the effect of reducing spatial resolution.

We have focused on evaluating regions of interest in Alzheimer's research, from hippocampus, which represents 5% of the mouse brain volume, to fimbria and fornix, which represents only 0.05% of the mouse brain volume [13]. In our simulations, we have extracted nine gradient subsets to evaluate subsequent changes in several metrics. Our metrics evaluated the stability/noise of the diffusion schemes through the condition number; the relative number of detected voxels with one, two, three, and four directions or dyads, globally and on a per-region basis; the extent of projections for the fimbria and hippocampus; the dyad dispersion and connectome similarity globally, and on a per-node basis. Our results corroborated to support that schemes with 45 angular samples started to approximate well the reference connectome and that errors were substantially reduced and started plateauing for 60 angular samples acquired with 43- or 86-μm spatial resolution.

The performance of the 60-direction protocols was very similar to the reference set, both qualitatively and quantitatively, and executing such protocols would lead to substantial reductions in acquisition time (eight times when combined with a downsampled spatial resolution), providing a connectome with 0.94 correlation with the reference set. Further reductions in acquisition times come from compressed sensing [28], which several groups have implemented for mouse MRI [29–31]. Such advances can help translate diffusion protocols into population studies [32] incorporating multiple biomarkers from morphometry [33], microstructural properties based on diffusion [13] or magnetic susceptibility [34], or network properties [35]. Such integrative studies may better predict changes in behaviors, modeling those observed in humans with neurodegenerative conditions [34].

Optimization studies are important when it comes to assess newly proposed diffusion models, acquisition schemes, various pathologies, and different animal models—to help understand the human brain [36, 37]. In this study, we were limited to a single specimen meta-analysis using extracted gradient subsets, but this approach provided useful information to help

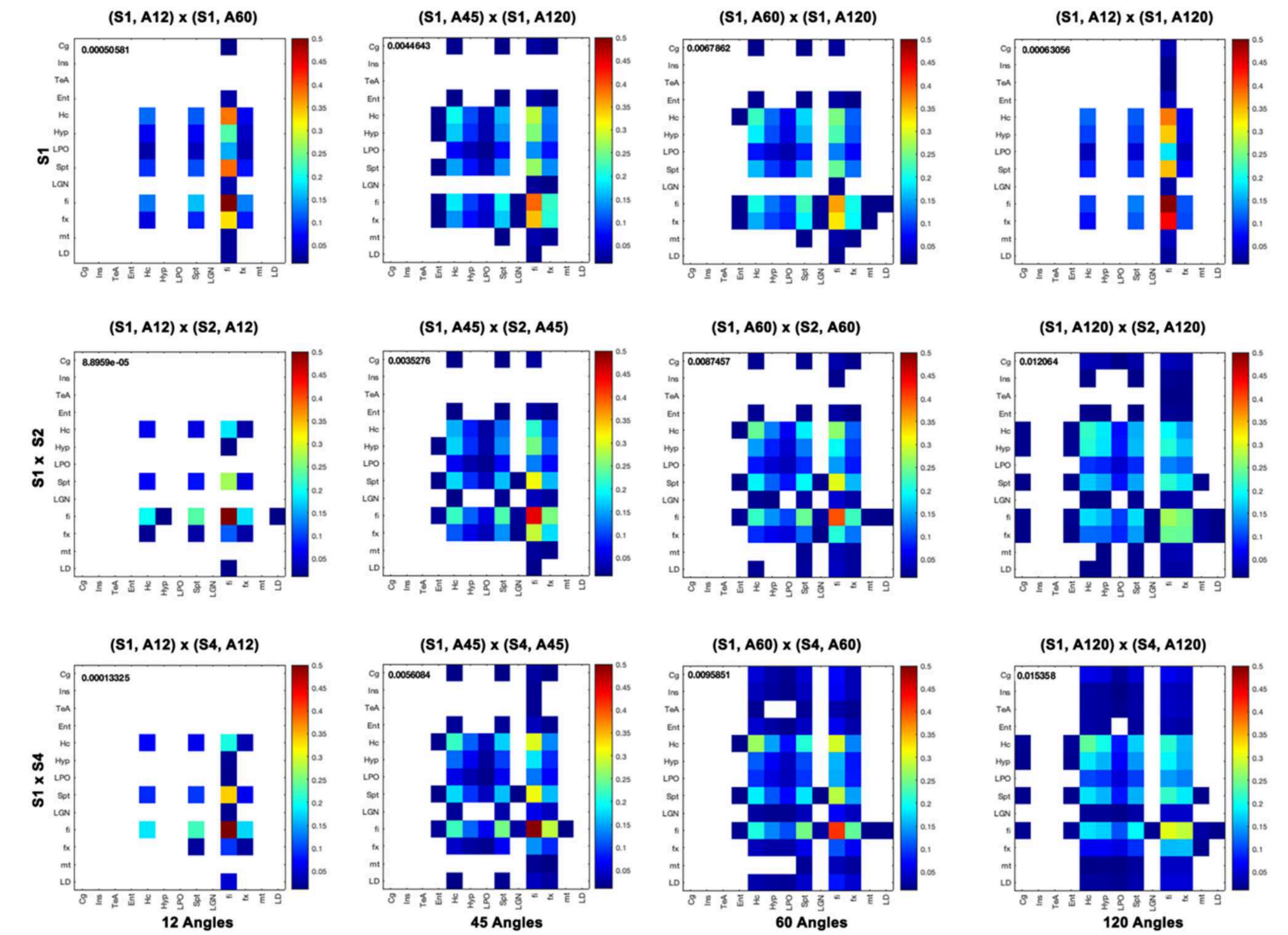


**FIGURE 9 |** Vertex-based graph similarity showed that white matter tracts were more robust to downsampling relative to nodes representing gray matter and, in particular, cortical domains. Our subgraph's regions of interest include the cingulate cortex (Cg), insular cortex (Ins), temporal association areas (TeA), entorhinal cortex (Ent), hippocampus (Hc), hypothalamus (Hyp), preoptic telencephalon (LPO), septum (Spt), lateral geniculate nucleus (LGN), fimbria (fi), fornix (fx), mamilothalamic tract (mt), and laterodorsal thalamic nuclei (LD). When comparing graphs for different spatial resolutions, the fi was most similar between 43- and 86-$\mu$m resolutions with a score of 0.85, and also relative to 172 $\mu$m with a score of 0.82, but most other graph nodes were not. Among angular sampling schemes, the fimbria was also robust, with a similarity score between the 12 and 120 directions of 0.5, followed by the fornix, hippocampus, and septum with 0.1. The cortical regions were most likely to be dissimilar when changing spatial or angular sampling schemes. Median similarity scores are shown for each graph comparison.

devise future group-based analyses. We have used the condition number for our acquisition schemes as a measure of noise performance [38], but better schemes may be designed in the future to increase rotational stability. Our recommendations are based on a finite set of metrics for a subgraph selected based on relevance to AD and a single b value acquisition. More regions would need to be included to generalize the recommendations; however, our results point to robustness of major white matter tracts, in contrast to thin, small white matter tracts and cortical–cortical connections, which are particularly vulnerable to reduced acquisition schemes. Moreover, future studies may be improved by the addition of multiple diffusion shells and more complex diffusion models. A reduction by a factor of eight in acquisition time for half the resolution and 60 directions provided an attractive avenue. However, the number of voxels with more than one dyad could not be retrieved to the same extent at lower spatial resolution. Still the similarity of the subgraphs based on anatomical regions known to be involved in pathological aging approached 0.94. Our study benefitted from the use of high-performance computing, which enhances the speed of optimization and quality control studies required before establishing new protocols in both mice and humans [39].

Our methods are applicable to other DWI studies in rodent models, and we expect that the conclusions will remain valid in the same range of spatial resolutions and may change as we approach resolutions used in human brain imaging. Still, our results align with recommendations for human brain studies, where angular sampling schemes with more than 30 directions [40] are recommended for a robust estimation of the diffusion tensor orientations and mean diffusivity. More than 45 directions are required for spherical deconvolution using spherical harmonics of order eight [41, 42]. Acquiring more than 45 directions helps with fitting and avoiding issues with imperfections in the uniformity of the diffusion gradient directions and meet signal-to-noise requirements. Therefore, 40 directions or more are widely used for the human brain [26, 27], and state of the art protocols employ multiple diffusion shells/b values, e.g., $n = 3$, and with 60 directions per shell [43]. Harmonization efforts [44] are currently under way to establish diffusion imaging guidelines and/or translate among protocols, such as those used for ADNI3 [45].

While the field of mouse imaging is much smaller, and efforts for standardization are not yet widespread, we hope that our study can inform the design of future experiments using statistical connectomics in models of neurological conditions, such as Alzheimer's disease, and that network biomarkers will provide enhanced sensitivity to early and subtle changes arising due to multiple, interacting pathologies.

## DATA AVAILABILITY STATEMENT

All datasets generated for this study are included in the article/supplementary material.

## AUTHOR CONTRIBUTIONS

RA, CL, GC, and AB designed simulation experiments and wrote code. SR and EC contributed code. GJ is the director of CIVM, oversees resources, and provided input in the initial phases of the project. RO'B contributed insight into the brain networks to be evaluated. RA, CL, and AB wrote the manuscript, which the other authors reviewed and edited.

## FUNDING

This work was supported by the National Institutes of Health through K01 AG041211, R01 AG045422, R56 AG051765, R56 AG057895, RF1 AG057895, and R01 AG066184. CIVM was supported by P41 EB015897 until 2018 and since then by U24CA220245.

## ACKNOWLEDGMENTS

We thank Dr. Tobias Wood, and Jacques Stout for helpful discussions. We thank all CIVM-ers for their efforts to build and maintain this small animal imaging resource and a collaborative learning environment.

## REFERENCES

1. Lim HK, Nebes R, Snitz B, Cohen A, Mathis C, Price J, et al. Regional amyloid burden and intrinsic connectivity networks in cognitively normal elderly subjects. *Brain.* (2014) **137**:3327–38. doi: 10.1093/brain/awu271
2. Toga AW, Thompson PM. Connectopathy in ageing and dementia. *Brain.* (2014) **137**:3104–6. doi: 10.1093/brain/awu276
3. Yamasaki T, Maekawa T, Fujita T, Tobimatsu S. Connectopathy in autism spectrum disorders: a review of evidence from visual evoked potentials and diffusion magnetic resonance imaging. *Front Neurosci.* (2017) **11**:627. doi: 10.3389/fnins.2017.00627
4. Collin G, Turk E, van den Heuvel MP. Connectomics in schizophrenia: from early pioneers to recent brain network findings. *Biol Psychiat.* (2016) **1**:199–208. doi: 10.1016/j.bpsc.2016.01.002
5. Ye C, Albert M, Brown T, Bilgel M, Hsu J, Ma T, et al. Extended multimodal whole-brain anatomical covariance analysis: detection of disrupted correlation networks related to amyloid deposition. *Heliyon.* (2019) **5**:e02074. doi: 10.1016/j.heliyon.2019.e02074
6. Harsan L-A, Dávid C, Reisert M, Schnell S, Hennig J, von Elverfeldt D, et al. Mapping remodeling of thalamocortical projections in the living reeler mouse brain by diffusion tractography. *Proc Natl Acad Sci USA.* (2013) **110**:E1797. doi: 10.1073/pnas.1218330110
7. Wu D, Xu J, McMahon MT, van Zijl PCM, Mori S, Northington FJ, et al. *In vivo* high-resolution diffusion tensor imaging of the mouse brain. *Neuroimage.* (2013) **83**:18–26. doi: 10.1016/j.neuroimage.2013.06.012
8. Alomair OI, Brereton IM, Smith MT, Galloway GJ, Kurniawan ND. *In vivo* high angular resolution diffusion-weighted imaging of mouse brain at 16.4 Tesla. *PLoS ONE.* (2015) **10**:e0130133. doi: 10.1371/journal.pone.0130133
9. Aydogan DB, Jacobs R, Dulawa S, Thompson SL, Francois MC, Toga AW, et al. When tractography meets tracer injections: a systematic study of trends and variation sources of diffusion-based connectivity. *Brain Struct Funct.* (2018) **223**:2841–58. doi: 10.1007/s00429-018-1663-8
10. Pervolaraki E, Tyson AL, Pibiri F, Poulter SL, Reichelt AC, Rodgers RJ, et al. The within-subject application of diffusion tensor MRI and CLARITY reveals brain structural changes in Nrxn2 deletion mice. *Mol Autism.* (2019) **10**:8. doi: 10.1186/s13229-019-0261-9
11. Calabrese E, Badea A, Cofer G, Qi Y, Johnson GA. A diffusion MRI tractography connectome of the mouse brain and comparison with neuronal tracer data. *Cereb Cortex.* (2015) **25**:4628–37. doi: 10.1093/cercor/bhv121
12. Barazany D, Basser PJ, Assaf Y. *In vivo* measurement of axon diameter distribution in the corpus callosum of rat brain. *Brain.* (2009) **132**:1210–20. doi: 10.1093/brain/awp042
13. Badea A, Kane L, Anderson RJ, Qi Y, Foster M, Cofer GP, et al. The fornix provides multiple biomarkers to characterize circuit disruption in a mouse model of Alzheimer's disease. *Neuroimage.* (2016) **142**:498–511. doi: 10.1016/j.neuroimage.2016.08.014
14. Calabrese E, Badea A, Coe CL, Lubach GR, Shi Y, Styner MA, et al. A diffusion tensor MRI atlas of the postmortem rhesus macaque brain. *Neuroimage.* (2015) **117**:408–16. doi: 10.1016/j.neuroimage.2015.05.072
15. Koay CG. A simple scheme for generating nearly uniform distribution of antipodally symmetric points on the unit sphere. *J Comput Sci.* (2011) **2**:377–81. doi: 10.1016/j.jocs.2011.06.007
16. Koay CG, Hurley SA, Meyerand ME. Extremely efficient and deterministic approach to generating optimal ordering of diffusion MRI measurements. *Med Phys.* (2011) **38**:4795–801. doi: 10.1118/1.3615163
17. Avants BB, Tustison NJ, Song G, Cook PA, Klein A, Gee JC. A reproducible evaluation of ANTs similarity metric performance in brain image registration. *Neuroimage.* (2011) **54**:2033–44. doi: 10.1016/j.neuroimage.2010.09.025
18. Behrens TE, Woolrich MW, Jenkinson M, Johansen-Berg H, Nunes RG, Clare S, et al. Characterization and propagation of uncertainty in diffusion-weighted MR imaging. *Magn Reson Med.* (2003) **50**:1077–88. doi: 10.1002/mrm.10609
19. Behrens TE, Berg HJ, Jbabdi S, Rushworth MF, Woolrich MW. Probabilistic diffusion tractography with multiple fibre orientations: what can we gain? *Neuroimage.* (2007) **34**:144–55. doi: 10.1016/j.neuroimage.2006.09.018
20. Sharief AA, Badea A, Dale AM, Johnson GA. Automated segmentation of the actively stained mouse brain using multi-spectral MR microscopy. *Neuroimage.* (2008) **39**:136–45. doi: 10.1016/j.neuroimage.2007.08.028
21. Johnson GA, Badea A, Brandenburg J, Cofer G, Fubara B, Liu S, et al. Waxholm space: an image-based reference for coordinating mouse brain research. *Neuroimage.* (2010) **53**:365–72. doi: 10.1016/j.neuroimage.2010.06.067

22. Ullmann JF, Watson C, Janke AL, Kurniawan ND, Reutens DC. A segmentation protocol and MRI atlas of the C57BL/6J mouse neocortex. *Neuroimage.* (2013) **78**:196–203. doi: 10.1016/j.neuroimage.2013.04.008
23. Anderson RJ, Cook JJ, Delpratt NA, Nouls JC, Gu B, McNamara JO, et al. Small Animal Multivariate Brain Analysis (SAMBA): a high throughput pipeline with a validation framework. (2017) *eprint arXiv:1*709.10483. doi: 10.1007/s12021-018-9410-0
24. Yeh FC, Verstynen TD, Wang Y, Fernandez-Miranda JC, Tseng WY. Deterministic diffusion fiber tracking improved by quantitative anisotropy. *PLoS ONE.* (2013) **8**:e80713. doi: 10.1371/journal.pone.0080713
25. Blondel VD, Gajardo A, Heymans M, Senellart P, Van Dooren P. A measure of similarity between graph vertices: applications to synonym extraction and web searching. *SIAM Rev.* (2004) **46**:647–66. doi: 10.1137/S0036144502415960
26. Kim WH, Racine AM, Adluru N, Hwang SJ, Blennow K, Zetterberg H, et al. Cerebrospinal fluid biomarkers of neurofibrillary tangles and synaptic dysfunction are associated with longitudinal decline in white matter connectivity: a multi-resolution graph analysis. *NeuroImage Clin.* (2019) **21**:101586. doi: 10.1016/j.nicl.2018.10.024
27. Wang Y, Xu CJ, Park H, Lee S, Stern Y, Yoo S, et al. Diagnosis and prognosis of Alzheimer's disease using brain morphometry and white matter connectomes. *NeuroImage.* (2019) **23**:101859. doi: 10.1016/j.nicl.2019.101859
28. Lustig M, Donoho D, Pauly JM. Sparse MRI: the application of compressed sensing for rapid MR imaging. *Magn Reson Med.* (2007) **58**:1182–95. doi: 10.1002/mrm.21391
29. Smith DS, Welch EB, Li X, Arlinghaus LR, Loveless ME, Koyama T, et al. Quantitative effects of using compressed sensing in dynamic contrast enhanced MRI. *Phys Med Biol.* (2011) **56**:4933–46. doi: 10.1088/0031-9155/56/15/018
30. Nguyen KV, Li JR, Radecki G, Ciobanu L. DLA based compressed sensing for high resolution MR microscopy of neuronal tissue. *J Magn Reson.* (2015) **259**:186–91. doi: 10.1016/j.jmr.2015.08.012
31. Wang N, Anderson RJ, Badea A, Cofer G, Dibb R, Qi Y, et al. Whole mouse brain structural connectomics using magnetic resonance histology. *Brain Struct Funct.* (2018) **223**:4323–35. doi: 10.1007/s00429-018-1750-x
32. Anderson RJ, Wang N, Cook JJ, Cofer GP, Dibb R, Johnson GA, et al. A high performance computing cluster implementation of compressed sensing reconstruction for MR histology. *Proc Intl Soc Mag Reson Med*. (2018) **26**.
33. Anderson RJ, Cook JJ, Delpratt N, Nouls JC, Gu B, McNamara JO, et al. Small Animal Multivariate Brain Analysis (SAMBA) - a high throughput pipeline with a validation framework. *Neuroinformatics*. (2018) **17**:451–72. doi: 10.1007/s12021-018-9410-0
34. Badea A, Delpratt NA, Anderson RJ, Dibb R, Qi Y, Wei H, et al. Multivariate MR biomarkers better predict cognitive dysfunction in mouse models of Alzheimer's disease. *Magn Reson Imaging.* (2019) **60**:52–67. doi: 10.1016/j.mri.2019.03.022
35. Badea A, Wu W, Shuff JM, Wang M, Anderson RJ, Qi Y, et al. Identifying vulnerable brain networks in mouse models of genetic risk factors for late onset Alzheimer's disease. *Front Neuroinform*. (2019) **13**:72. doi: 10.3389/fninf.2019.00072
36. Fujiyoshi K, Hikishima K, Nakahara J, Tsuji O, Hata J, Konomi T, et al. Application of q-Space diffusion MRI for the visualization of white matter. *J Neurosci.* (2016) **36**:2796–808. doi: 10.1523/JNEUROSCI.1770-15.2016
37. Fan Q, Nummenmaa A, Wichtmann B, Witzel T, Mekkaoui C, Schneider W, et al. Validation of diffusion MRI estimates of compartment size and volume fraction in a biomimetic brain phantom using a human MRI scanner with 300mT/m maximum gradient strength. *Neuroimage.* (2018) **182**:469–78. doi: 10.1016/j.neuroimage.2018.01.004
38. Skare S, Hedehus M, Moseley ME, Li TQ. Condition number as a measure of noise performance of diffusion tensor data acquisition schemes with MRI. *J Magn Reson.* (2000) **147**:340–52. doi: 10.1006/jmre.2000.2209
39. Kim H, Irimia A, Hobel SM, Pogosyan M, Tang H, Petrosyan P, et al. "The LONI QC system: a semi-automated, web-based and freely-available environment for the comprehensive quality control of neuroimaging data. *Front Neuroinform.* (2019) **13**:60. doi: 10.3389/fninf.2019.00060
40. Jones DK. The effect of gradient sampling schemes on measures derived from diffusion tensor MRI: a Monte Carlo study. *Magn Reson Med.* (2004) **51**:807–15. doi: 10.1002/mrm.20033
41. Jones DK, Knösche TR, Turner R. White matter integrity, fiber count, and other fallacies: the do's and don'ts of diffusion MRI. *Neuroimage.* (2013) **73**:239–54. doi: 10.1016/j.neuroimage.2012.06.081
42. Tournier JD, Calamante F, Connelly A. Determination of the appropriate b value and number of gradient directions for high-angular-resolution diffusion-weighted imaging. *NMR Biomed.* (2013) **26**:1775–86. doi: 10.1002/nbm.3017
43. Tax CM, Grussu F, Kaden E, Ning L, Rudrapatna U, John Evans C, et al. Cross-scanner and cross-protocol diffusion MRI data harmonisation: a benchmark database and evaluation of algorithms. *Neuroimage.* (2019) **195**:285–99. doi: 10.1016/j.neuroimage.2019.01.077
44. Fortin JP, Parker D, Tunc B, Watanabe T, Elliott MA, Ruparel K, et al. Harmonization of multi-site diffusion tensor imaging data. *Neuroimage.* (2017) **161**:149–70. doi: 10.1016/j.neuroimage.2017.08.047
45. Zavaliangos-Petropulu A, Nir TM, Thomopoulos SI, Reid RI, Bernstein MA, Borowski B, et al. Diffusion MRI indices and their relation to cognitive impairment in brain aging: the updated multi-protocol approach in ADNI3. *Front Neuroinform.* (2019) **13**:2. doi: 10.3389/fninf.2019.00002


**Conflict of Interest:** The authors declare that the research was conducted in the absence of any commercial or financial relationships that could be construed as a potential conflict of interest.

frontiers in Physics

BRIEF RESEARCH REPORT
published: 24 April 2020
doi: 10.3389/fphy.2020.00123

Check for updates

# Impact of Attenuation Correction on Quantification Accuracy in Preclinical Whole-Body PET Images

*Thomas Wanek, Lara Schöllbauer, Thomas Filip, Severin Mairinger, Michael Sauberer, Matthias Blaickner and Claudia Kuntner**

*Preclinical Molecular Imaging, AIT Austrian Institute of Technology GmbH, Seibersdorf, Austria*

**Background:** Whole-body PET images can be obtained by using the "step-and-shoot" (SaS) method (using multiple bed positions) or continuous bed motion (CBM). As transmission scans are not always feasible, an alternative method where attenuation data can be generated via emission-based attenuation correction (AC) maps is of interest. The aim of this preclinical study was to investigate the influence of the acquisition method and AC on the quantitation accuracy of [$^{18}$F]FDG-PET.

**Methods:** [$^{18}$F]FDG-PET phantom images were acquired using either SaS or CBM. Transmission scans were recorded for the SaS method using a $^{57}$Co-point source. Emission-based attenuation sinograms were obtained from the images after segmentation and inverse Fourier rebinning. PET images were reconstructed without AC, transmission based (TX-AC) and emission-based (EM-AC) attenuation correction. Moreover, [$^{18}$F]FDG-PET scans of rats bearing mammary carcinomas acquired using either SaS or CBM were analyzed retrospectively and quantification in tissues was compared.

**Results:** Phantom recovery coefficients ($R_C$) varied greatly, ranging from 0.49 ± 0.01 to 1.15 ± 0.07, dependent on acquisition method, reconstruction algorithm and AC method. In CBM acquired images, EM-AC improved quantification accuracy when compared to no-AC images in the phantom studies ($R_C$ 0.79 ± 0.02 vs. 0.49 ± 0.01, respectively) and in tumors of rats (DMBA model: 1.16±0.42 SUV vs. 0.86±0.28 SUV, respectively).

**Conclusion:** The method of AC has a strong influence on the quantification of [$^{18}$F]FDG. Our data indicates that EM-AC improves quantification in images obtained by CBM and SaS. However, the obtained values were still underestimated when compared to TX-AC corrected images.

**Keywords: positron emission tomography, attenuation correction, quantification, FDG, emission-based attenuation**

OPEN ACCESS

***Edited by:***
*Kris Thielemans,*
*University College London,*
*United Kingdom*

***Reviewed by:***
*Daniele Panetta,*
*Italian National Research Council, Italy*
*Francesca Leek,*
*University College London,*
*United Kingdom*

***Correspondence:***
*Claudia Kuntner*
*claudia.kuntner@ait.ac.at*

***Specialty section:***
*This article was submitted to Medical Physics and Imaging, a section of the journal Frontiers in Physics*

***Received:*** *13 December 2019*
***Accepted:*** *30 March 2020*
***Published:*** *24 April 2020*

***Citation:***
*Wanek T, Schöllbauer L, Filip T, Mairinger S, Sauberer M, Blaickner M and Kuntner C (2020) Impact of Attenuation Correction on Quantification Accuracy in Preclinical Whole-Body PET Images. Front. Phys. 8:123. doi: 10.3389/fphy.2020.00123*

## INTRODUCTION

Quantitative whole-body examinations are one of the key strengths of preclinical positron emission tomography (PET) and computed tomography (CT) systems. However, due to the restricted axial field of view (FOV) of several centimeters both in clinical and preclinical PET scanners, a whole-body scan in humans or larger animals such as rats or rabbits cannot be recorded in one single scan acquisition. Therefore, for obtaining a whole-body scan, two different scanning methods are commonly applied.

In the first method, the "step-and-shoot" (SaS) method, several emission scans are recorded using multiple bed positions to cover the whole body [1]. For this, the subject is positioned on the bed, moved to the first bed position and coincidences are recorded for a predefined time (e.g., 10–15 min). Then the bed is moved to the next position and the procedure is repeated. Typically, the bed positions overlap each other for several cm in order to facilitate subsequent processing of the images. To correct for photon attenuation in the scanned subject, a separate attenuation correction (AC) scan is recorded for each single bed position in singles mode using either a transmission source such as $^{57}$Co (TX-AC) or a CT-based attenuation map [2]. Finally, the reconstructed and TX-AC corrected images are stitched, and decay corrected using algorithms usually implemented in the scanner software. The advantage of this method is that it usually follows established laboratory procedures for emission scans as this type of scanning is routinely performed and it provides a higher slice sensitivity [3]. However, scanning time is increased for each scanned individual which significantly decreases the daily imaging throughput.

An alternative method to the SaS-method is the continuous bed motion (CBM) method. Here, the bed is continuously moved horizontally back and forth through the axial FOV between a specified start- and end-position and coincidences are recorded. The main advantage of this method is that it provides a more uniform sensitivity over the entire image and offers better image quality due to over sampling [4], which often aids in the identification of smaller tumors or affected lymph nodes. Preclinical PET systems have implemented CBM since 2009 [5, 6], whereas the clinical implementation just started more recently [7–10]. The main disadvantage of CBM in preclinical imaging is that it usually does not offer the possibility to perform a transmission scan required for AC. This is of special relevance for stand-alone preclinical PET scanners, which are not combined with a CT and can thus not use the CT image to generate a μ-map for attenuation correction. Consequently, the improved image quality provided by CBM comes at the cost of a decreased quantification accuracy. One way to overcome this issue is the generation of emission-based attenuation correction (EM-AC) factors or maps [11]. Here, image data is first segmented assuming a uniform attenuation in manually delineated regions and then forward projected to generate an attenuation sinogram, which is then used for attenuation correction during image reconstruction [12]. This method is relatively fast, easy to use and implemented in most preclinical PET systems. In addition, EM-AC eliminates the time required for an extra attenuation measurement, resulting in a significant reduction in overall scanning time.

In this study we compared No-AC, TX-AC, and EM-AC and their influence on image quantification by phantom measurements acquired using the SaS and CBM method. We furthermore investigated the biological relevance of our findings by performing a retrospective analysis of a dataset of [$^{18}$F]FDG-PET scans in rats bearing chemically induced breast cancer tumors. We first evaluated brain and liver uptake in whole-body scans of rats acquired using the SaS method and applied no-AC, TX-AC, or EM-AC during reconstruction of the images. Secondly, we assessed whole-body scans of rats acquired using the CBM method and compared the quantification in tumors in reconstructed images using either filtered back projection (FBP) or ordered subset expectation maximization (OSEM) with or without EM-AC.

# METHODS

## Phantom Study

A cylindrical hollow phantom made from polyethylene with a diameter of 7 cm, a length of 16.5 cm and a wall thickness of 0.2 cm was filled with 36.1 ± 8.0 MBq aqueous [$^{18}$F]FDG solution and placed on the scanner bed of a preclinical PET scanner (micro PET Focus 220, Siemens Healthineers, Knoxville, TN, USA), which provides 7.6 cm axial and 22 cm transaxial FOV [13]. After moving the phantom to the center FOV, PET emission scans at 3 consecutive bed positions were acquired for 10 min/bed position with an energy window of 350–750 keV and a coincidence time window of 6 ns. The horizontal bed position was moved between the measurements in axial direction for ∼6.6 cm to cover a total axial FOV of 20.8 cm. A horizontal overlap of 1 cm was applied to the images to facilitate further stitching of the images. Afterwards, a 10-min transmission scan using a rotating $^{57}$Co point source (120–125 keV energy window) was recorded in singles mode for each bed position. CBM measurements were performed by placing the phantom on the scanner bed and a subsequent emission recording for a time of 20 min (350–750 keV energy window, 6 ns timing window). The phantom was moved through the field of view for four times back and forth (8 passes) to cover the same region of interest multiple times during data acquisition spanning an axial FOV of 27.1 cm.

## Animal Studies

### Chemicals

Radiosynthesis and quality control of [$^{18}$F]FDG was performed using standard methods [14]. 1-Methyl-1-nitrosourea (MNU) and 1-methyl-1 nitrosourea (DMBA) were obtained by Sigma-Aldrich (Schnelldorf, Germany). For *in vivo* application, MNU was dissolved in sterile saline solution and acidified to pH 5.0 with acetic acid. DMBA was dissolved in sesame oil.

### Research Animals and Tumor Induction

Female 5–6 weeks old Sprague-Dawley rats (Crl:CD, Charles River, Sulzfeld, Germany) were initially used in the study. Animals were housed in groups in a temperature and humidity-controlled facility on a 12 h light/ dark cycle and fed a standard laboratory diet. Food and water were available *ad libitum* and animals were weighed weekly during the experiment. Tumors were generated following published procedures by the administration of the carcinogens MNU [15, 16] or DMBA as follows [17, 18]. MNU was injected intraperitoneally at a dose of 50 mg/kg and a volume of 5 mL/kg body weight ($n$ = 12). If animals did not exhibit tumors within 3 weeks, MNU injection was repeated on day 29 and day 57 after initiation of the study. DMBA was administered by oral gavage at a dose of 20 mg/kg ($n = 8$) or 50 mg/kg BW ($n = 12$) at a volume of 5 mL/kg. Animals were observed regularly to determine the development and localization of tumors. All experiments involving laboratory animals were approved by the respective authorities and the study procedures were in full accordance with the European Communities Council Directive of September 22, 2010 (2010/63/EU). All procedures were in compliance with the institutional biosecurity and radiation safety regulations.

### PET Imaging Procedure

At the time point of PET imaging, mean body weight of rats were 236 ± 33 g. The following standardized imaging setup was applied for all [$^{18}$F]FDG scans [19–21]. In brief, rats were deprived of food for 18 ± 4 h prior [$^{18}$F]FDG administration. Rats had access to drinking water at all times. Body warming was achieved by placing the entire cage on a heating pad kept at 38°C. Warming was initiated ~30 min before tracer injection and continued throughout the uptake and image acquisition period. Rats were pre-anesthetized by inhalation anesthesia (1–4% isoflurane in oxygen) in an induction box. Subsequently, 0.1 mL containing 30.0 ± 12.5 MBq [$^{18}$F]FDG solution diluted with saline was administered intravenously via tail vein injection under isoflurane anesthesia. Rats were kept anesthetized throughout the whole uptake and imaging period and the isoflurane concentration level was adjusted to obtain a breathing rate of 20–60 breath/min during the PET acquisition, indicating a comparable level of anesthesia.

PET emission data with an energy window of 350–750 keV and a coincidence time window of 6 ns were acquired at 1 h after [$^{18}$F]FDG injection into rats ($n = 9$) using the SaS method for 10 min/bed position with three bed positions to cover the whole body of the animal. The bed was moved from one position to the next by 6.6 cm covering in total an axial FOV of 20.8 cm. Overlap in the resulting images between the positions was 1 cm. Before the emission scan, an attenuation measurement was done with the rotating $^{57}$Co point source for 10 min at each position. Total scan time per animal was 60 min.

In a second cohort of rats ($n = 20$) a 20 min scan (350–750 keV energy window, 6 ns timing window) was acquired at 1 h after [$^{18}$F]FDG injection using the CBM tool to cover the whole body of the rats. Thereby, the bed was slowly moved through the FOV for four times back and forth (8 passes) covering an axial FOV of 27.1 cm.

## Image Data Generation and Analysis

As the rat images were analyzed retrospectively, some of the original raw data (list mode files and sinograms) were no longer available. Thus, all emission sinograms used for comparing different AC methods were generated by inverse Fourier rebinning from the available image files, which were originally reconstructed using Fourier rebinning (FORE) followed by filtered back projection (FBP), using the forward projection tool implemented in the image analysis software ASIPro VM 6.0 (Siemens Healthineers). To be consistent, we applied the same procedure to the acquired phantom images. The thus generated emission sinograms were further used for image reconstruction as described below. To validate this approach, we also compared image files reconstructed from the generated emission sinograms with image files from the original emission sinograms (when available).

The generated emission sinograms were reconstructed using FORE followed by FBP algorithm with ramp filter or OSEM at an image zoom of 3.163 and an image matrix of 128 × 128 × 95 (SaS) or 128 × 128 × 351 (CBM) resulting in a voxel size of 0.6 × 0.6 × 0.796 mm$^3$. The standard data correction protocol (normalization, decay correction, and injection decay correction) was applied to the data. Scatter correction was not applied to the emission data as the used reconstruction software does not permit scatter correction of non-AC data to allow for a comparable ratio between the AC and non-AC corrected images.

For calculation of the EM-AC file, the emission calibration and segmentation tool implemented in ASIPro VM 6.0 was used. PET emission images were segmented to obtain the outer border of the phantom or the rat. The area inside the segmented phantom or rat was assumed to be water and assigned an attenuation coefficient of 0.095 cm$^{-1}$ (511 keV), the area outside was assumed to be background and assigned an attenuation coefficient of 0 cm$^{-1}$. After segmentation was completed, a 2D sinogram was projected and inverse Fourier rebinning with a span of 47 and a ring difference of 23 was performed. The obtained sinogram was defined as emission-based sinogram (EM-AC sinogram) for attenuation correction. The flow chart of the processed image data, calculated sinograms and reconstructed image files is depicted in **Figure 1**. Images were reconstructed without (No-AC), with transmission-based (TX-AC) and with emission-based (EM-AC) attenuation correction. Images obtained with the SaS technique were stitched together using the stitching tool implemented in ASIPro VM 6.0.

A calibration factor for converting units of PET images into absolute radioactivity concentration units was generated by imaging a phantom filled with a known concentration of [$^{18}$F]FDG at identical measurements parameters and reconstructed using FBP including TX-AC. The activity concentration in the phantom was calculated from the activity measured in a dose calibrator (CRC-25R, Capintec Pittsburgh, PA, USA) and the fill volume of the phantom.

Three cylindrical volumes of interest (VOI) with a diameter of 55 mm and 10 mm height were outlined on multiple planes of the PET images from the phantom study using the image analysis software Amide [22]. For evaluation of the effects of different AC methods the recovery coefficients ($R_C$) as the ratio of measured activity concentration to known activity concentration for each AC method were calculated with the following equations:

$$R_C = \frac{C_T}{C_{known}}$$

where $C_T$ is the radioactivity concentration derived from the target VOI in kBq/cc in the uncorrected image (No-AC), TX-AC, and the EM-AC corrected image, respectively. $C_{known}$ is the known radioactivity concentration calculated from the administered radioactivity (kBq) measured in a dose calibrator

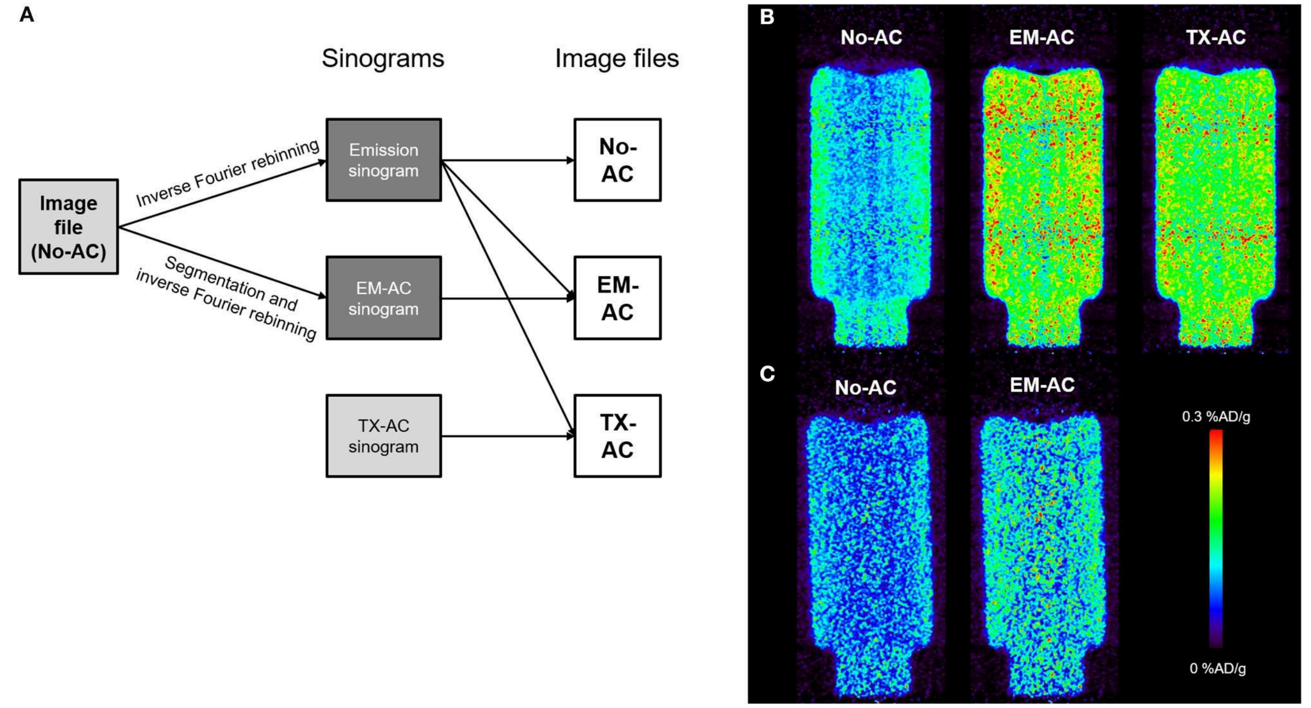


**FIGURE 1 | (A)** Flow chart of the steps involved in the emission-based (EM-AC) and transmission-based (TX-AC) attenuation correction in the current study. Data files in light gray are original data (images or sinograms), data files in dark gray were calculated from the image files and final image files reconstructed using the 3 different AC methods (No-AC, EM-AC and TX-AC). **(B)** Phantom FDG-PET images acquired using the SaS method with 3 bed positions and C) phantom FDG-PET images acquired using the CBM method. The applied AC method is indicated in the images and PET images are displayed in percent applied dose per gram (%AD/g).

and the fill volume of the phantom (mL) under the assumption of a density of water of 1 g*mL$^{-1}$.

In the animal studies, predefined ellipsoidal or spherical VOIs were applied for whole brain (12 × 20 × 8 mm$^3$) and liver (10 mm diameter) whereas the tumor was manually delineated on multiple planes of the PET images. The derived [$^{18}$F]FDG concentration values were calculated from the mean and max value of the VOI and quantified in terms of standardized uptake value (SUV$_{mean}$ and SUV$_{max}$) using the following equation:

$$SUV = \frac{C_T}{D_{Inj}} \times W_S$$

where $C_T$ is the mean or maximum radioactivity concentration in the target VOI in kBq/cc, $D_{Inj}$ the administered dose in kBq and $W_S$ the body weight of the animal in gram.

For comparing the effect of the different AC methods on tumor quantification, individual tumor values are derived either from one animal with one or multiple tumors or from animals, which were scanned multiple times.

## Statistics

All values are given as mean values (± standard deviation). The obtained AC-corrected values were compared to No-AC corrected values using a paired *t*-test in GraphPad Prism 8.3.0.; $p < 0.05$ was considered statistically significant.

## RESULTS

As not all emission sinograms were available at the time of analysis, the emission sinograms used for all AC techniques (phantom and rats, No-AC, EM-AC, and TX-AC) were generated from the original images by applying inverse Fourier rebinning. In order to validate this approach images reconstructed from the generated sinograms were compared to images reconstructed from the original sinograms (phantom and rat SaS). Quantitative analysis of phantom images based on the generated or original sinograms were in good agreement (SUV$_{mean}$ < 1%). In rats, similar differences of liver and brain activity (SUV$_{mean}$ < 1%) between images based on the generated or original sinogram were observed. In contrast, maximum activity concentration (SUV$_{max}$) were significantly lower using the inverse Fourier rebinning approach compared to the original sinograms on both, phantom and rat images.

The recovery coefficients (R$_C$) calculated from the set of reconstructed images, applying No-AC, TX-AC or EM-AC of the cylindrical phantom filled with [$^{18}$F]FDG solution scanned with the SaS method and CBM are summarized in **Table 1**. Moreover, phantom images acquired using the SaS and the CBM method and reconstructed using No-AC, EM-AC, and TX-AC (only SaS method) are shown in **Figures 1B,C**. As shown in the phantom images, axial image uniformity is superior in the phantom images acquired using CBM as compared to phantom images acquired using SaS. In the later, the overlapping bed position are clearly

**TABLE 1** | Recovery coefficients ($R_C$) for mean radioactivity concentrations of the phantom studies which were acquired either with the SaS method or continuous bed motion (CBM) and the images reconstructed using different method of attenuation correction (AC).

| | | SaS | CBM |
|---|---|---|---|
| **FBP** | | $R_C$ | $R_C$ |
| | *No-AC* | 0.63 ± 0.01 | 0.49 ± 0.01 |
| | *TX-AC* | 1.02 ± 0.08 | n.a. |
| | *EM-AC* | 1.15 ± 0.07 | 0.79 ± 0.02 |
| **OSEM** | | $R_C$ | $R_C$ |
| | *No-AC* | 0.63 ± 0.01 | 0.50 ± 0.01 |
| | *TX-AC* | 1.07 ± 0.01 | n.a. |
| | *EM-AC* | 1.15 ± 0.07 | 0.80 ± 0.02 |

*For calculation of the $R_C$ please refer to the materials and method section.*
*n.a., not assessed.*

visible in the images. Applying no attenuation correction during image reconstruction leads to an underestimation of mean radioactivity concentrations in the investigated VOI of 50 or 37% in CBM and SaS acquired emission scans, independent from the applied image reconstruction algorithm (FBP or OSEM). Implementing transmission-based attenuation correction (TX-AC) to the identical images acquired in SaS mode increased the quantification accuracy as assessed by the $R_C$ value to 1.02 ± 0.08 and 1.07 ± 0.01 for FBP and OSEM reconstructed images, respectively. Emission-based AC showed comparable improvements in quantification accuracy in SAS acquired images ($R_C$ of 1.15 ± 0.07 and 1.15 ± 0.07) for FBP and OSEM. In phantom images acquired with CBM, EM-AC increased the quantification accuracy in FBP ($R_C$ of 0.79 ± 0.02) and OSEM ($R_C$ of 0.80 ± 0.02) reconstructed images compared to No-AC images.

The results from the retrospective analysis using No-AC, EM-AC, or TX-AC for quantification of brain and liver [$^{18}$F]FDG uptake in rat images acquired with the SaS method (n=9) are shown in **Figures 2A,B**. Rat FDG images are shown in **Figure 2C**. Mean brain uptake ($SUV_{mean}$) was increased by 40% ($p < 0.0001$) and 18% ($p < 0.0001$) when applying the TX-AC and EM-AC method, respectively, compared to No-AC (**Figure 2A**). In the liver VOI the effect of AC was even more pronounced with increases of 60% ($p < 0.0001$) and 32% ($p = 0.008$) in mean liver uptake ($SUV_{mean}$) values after TX-AC and EM-AC, respectively (**Figure 2B**). Overall in both analyzed VOIs, [$^{18}$F]FDG uptake values ($SUV_{mean}$) were significantly lower in the EM-AC images as compared to the TX-AC images.

Whole-body rat images acquired using the CBM method are shown in **Figure 3B**. The obtained uptake values in tumors, calculated from whole-body rat images acquired using CBM and reconstructed using either No-AC or EM-AC are shown in **Figure 3A**. In parallel to the phantom study, EM-AC generally increased the mean uptake values irrespective of the image reconstruction algorithm used. For example, [$^{18}$F]FDG $SUV_{mean}$ tumor uptake values in FBP reconstructed images were increased by 33 ± 10% ($p = 0.0034$) in the DMBA group ($n = 14$) and by 36 ± 8% ($p = 0.001$) in the MNU group ($n = 6$) after EM-AC. When performing OSEM reconstruction, EM-AC led to an increase in $SUV_{mean}$ tumor uptake values by 68% ($p < 0.0001$) and 78% ($p = 0.001$) in the DMBA and MNU group, respectively. Interestingly, EM-AC had an effect in the same order of magnitude on the $SUV_{max}$ tumor values (∼38% increase) when using FBP reconstruction, whereas in the OSEM reconstructed images, $SUV_{max}$ tumor values exhibited an increase of ∼100% after applying EM-AC.

## DISCUSSION

In contrast to human PET studies, where the CBM acquisition method was just recently introduced and is now used for diagnostic [$^{18}$F]FDG-PET [9, 23], this method is rarely applied in preclinical whole-body imaging. The main reason for this is that in preclinical imaging either the transaxial FOV of the preclinical PET scanner is large enough for a whole-body scan of the scanned subject (e.g., mouse), the exact imaging region is known to the examiner (e.g., in subcutaneous tumor studies) or the quantitative properties of PET imaging are prioritized over data on whole-body distribution, which might be the case in imaging of larger animals such as rats or rabbits. However, CBM offers the opportunity to increase image throughput, as the total measurement time required for a CBM acquisition is significantly lower than the cumulative effort for emission and transmission acquisitions at multiple bed positions. Compared to SaS, imaging time in CBM could be reduced by a factor of two, therefore doubling the putative imaging output per day which consequently effects the study statistics and allows for higher group numbers—factors that are of high importance in oncology studies. Additionally, the anesthesia duration for the scanned subjects can be shortened in CBM, which decreases the overall burden for the laboratory animals under investigation, again an important factor in oncology studies where repeated measurements over study days (e.g., therapy monitoring studies) are required. Moreover, it has been reported and demonstrated in the phantom study that CBM offers the advantage of a more uniform sensitivity over the entire image and therefore results in a better image quality when compared to SaS-acquired images.

In this study we investigated alternative approaches for AC to achieve accurate estimates of radiotracer concentration in different regions of interest in images acquired with CBM. Initially, phantom studies using a rat-sized hollow cylinder filled with a known activity concentration of [$^{18}$F]FDG in aqueous solution were performed. PET emission images were recorded using both acquisition methods, SaS and CBM, and corresponding transmission scans were performed for the SaS images. Furthermore, the originally FBP-reconstructed images were segmented, and attenuation coefficients were manually assigned to the corresponding parts of the image which was subsequently inverse Fourier rebinned into an emission-based attenuation sinogram. This EM-AC sinogram was then used for AC in the reconstruction of the phantom images using FBP and OSEM algorithm.

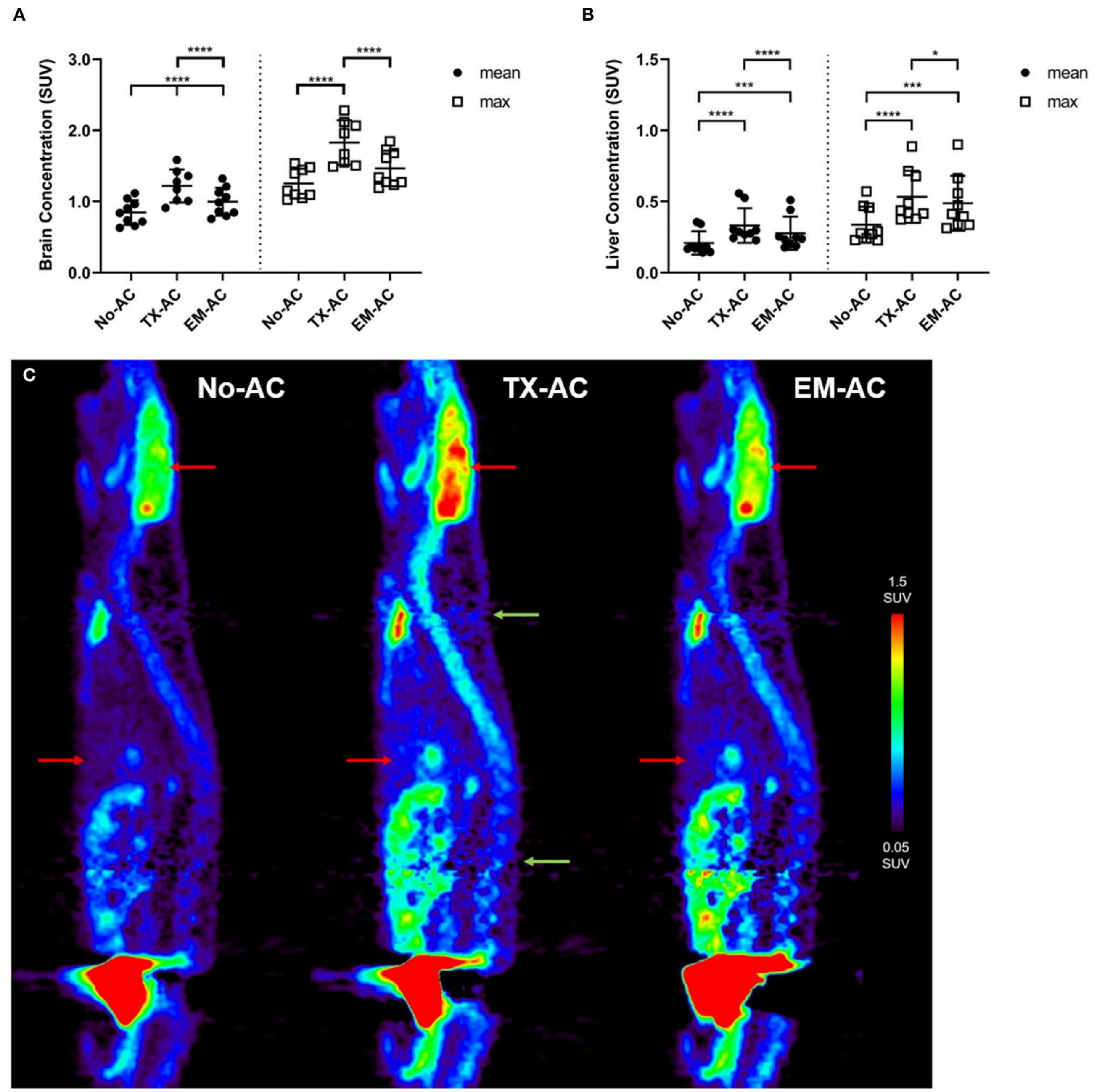


**FIGURE 2 | (A)** Brain and **(B)** liver mean (filled circle) and max (open square) [$^{18}$F]FDG activity concentration values (SUV) obtained in rats ($n = 9$). Images were recorded using the SaS method and reconstructed with FBP without (No-AC), with transmission-based (TX-AC) and with emission-based (EM-AC) attenuation correction ($^{*}p < 0.05$, $^{***}p < 0.001$, $^{****}p < 0.0001$). **(C)** Sagittal rat FDG-PET images acquired using the SaS method and reconstructed with FBP. Brain and liver are indicated with red arrows and overlapping bed positions are indicated with green arrows.

During data search for “real” rat imaging data to compare phantom data with, it was recognized that not all original raw data were still available for retrospective analysis. Therefore, the possibility to generate emission sinograms out of the original image files by inverse Fourier rebinning was investigated, initially in the phantom dataset, as well as subsequently in the rat images. Comparison of the quantification result of the inverse Fourier rebinned sinograms (and further reconstructed images) with the original image files showed an excellent agreement. Consequently, the generation of the emission sinograms out of the image files can be a feasible approach if the original listmode or sinogram raw data is missing and images need to be reconstructed with a different reconstruction algorithm or parameters.

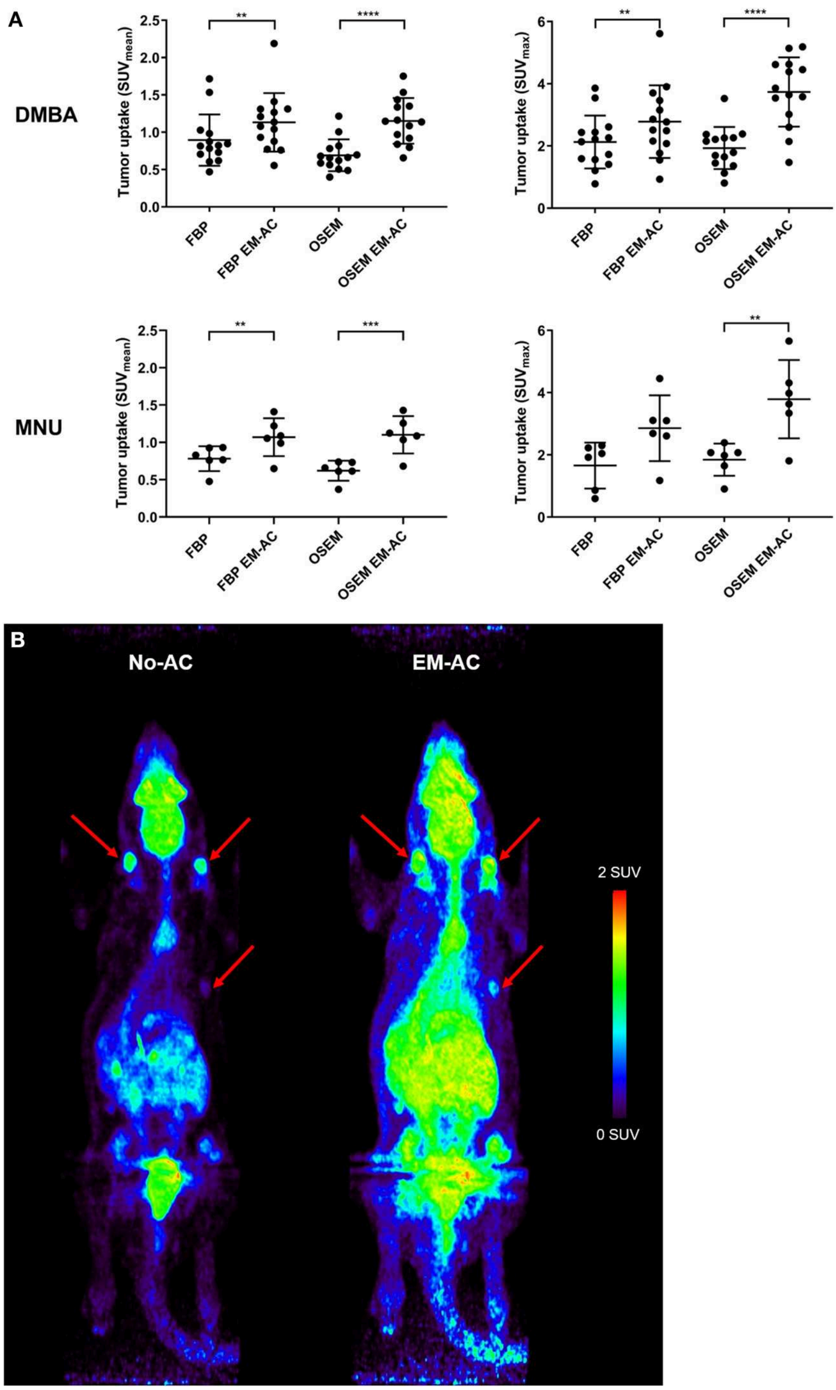


**FIGURE 3 | (A)** Quantification in tumors ($SUV_{mean}$ and $SUV_{max}$) induced by DMBA ($n = 14$) or MNU ($n = 6$) in rat whole body images acquired with continuous bed motion (CBM). Images were reconstructed using FBP or OSEM without attenuation correction and with emission-based attenuation correction (EM-AC) ($^{**}p < 0.01$, $^{***}p < 0.001$, $^{****}p < 0.0001$). **(B)** Maximum intensity projection of a whole-body PET image showing [$^{18}$F]FDG distribution in a tumor bearing rat (MNU) acquired with CBM without AC (left side) and with EM-AC (right side). Tumors are indicated with red arrows. Images were reconstructed with OSEM.

Quantitative evaluation of the phantom data and comparison of the derived concentration values to the expected values revealed the influence of the acquisition mode (SAS vs. CBM) and attenuation correction on those data. Applying no attenuation correction to the phantom data showed a reduction in quantitative accuracy by −37% in SaS acquired images reconstructed using FBP or OSEM. These values are quite in line with literature data where it was reported that the accuracy of the activity concentration is reduced by −38% in the uncorrected vs. the attenuation corrected image [24]. Moreover, a simulation study using the Moby phantom with increasing diameters from 2.1 cm to 6.4 cm also showed a 30–40% error in soft tissue quantification starting from 4.7 cm diameter, which is roughly the diameter of a rat [25]. The reduction was even more pronounced in the phantom CBM data, were a decrease of −50% in quantitation accuracy was observed. Applying TX-AC to SaS acquired data increased quantification accuracy to acceptable levels of <10% for all reconstruction algorithms. Interestingly, EM-AC overestimated the activity concentration by 15% in SaS acquired images. However, the such derived values are well within the tolerance range for PET measurements keeping in mind that especially FDG-PET scans in rodents are heavily influenced by animal handling of up to a factor of 2 as shown in a recent study [21]. In CBM data, EM-AC greatly improved image quantitation for both reconstruction algorithms, even though these values are still below the expected concentrations or compared to TX-AC data.

As a next step, the effect of transmission-based (TX-AC) vs. emission-based (EM-AC) attenuation correction in SaS acquisitions of whole-body rat PET images were assessed. In brain and liver VOIs the activity concentration without AC and with TX-AC reflected the results of the phantom studies as such, that mean brain and liver [$^{18}$F]FDG uptake values were increased by 40 and 60%, respectively, after applying TX-AC. Application of EM-AC to the same data increased the $SUV_{mean}$ in brain and liver by 18 and 32%, respectively. This is in contrast to the phantom study were both AC methods achieved a comparable result in terms of quantification accuracy. A possible explanation for this observation might be an incorrect segmentation. As the skull itself was not visible in the FDG rat images, it was not feasible to include bone material into the segmented images and thus leading to an underestimation of brain FDG uptake. A previous study suggests a careful evaluation of EM-AC in applications where a uniform structure cannot be assumed [26].

When using CBM for tumor-bearing rats this study found that the [$^{18}$F]FDG uptake after EM-AC was increased with respect to uncorrected images by 34% in the tumors VOI's. Similar results were also obtained by other groups in subcutaneous tumor mouse models [27], where they reported an attenuation recovery of ∼13% in tumors. This value is slightly lower as the results from this study, but as mice were used in contrast to rats, a lower attenuation recovery might be expected. D'Ambrosio et al. [28] compared two attenuation correction methods based on CT and segmentation of emission images in phantom, mice and rat images. In line with this study, it was reported that EM-AC leads to lower uptake values (lower ROI counts) as compared to TX-AC. For example, differences between the EM-AC and CT-AC method of <9% for the myocardium and left ventricle VOI in rats were reported. This difference is much lower as the difference found in the liver and brain VOI in this study (∼17%). However, this might be due to the different position of the VOI inside the body and the attenuation effect of the surrounding tissue.

However, even with this underestimation in [$^{18}$F]FDG organ and tumor uptake, EM-AC did improve tumor identification and tumor delineation in CBM acquired images. Especially small tumors with lower [$^{18}$F]FDG uptake can be easily overlooked without AC (see **Figure 3B**). This is of special relevance in chemically induced tumor models, where tumors can develop spontaneously, and the exact tumor locations are unknown. More importantly, the EM-AC method could be an important alternative in preclinical PET/MR scanners where no attenuation correction is available.

## CONCLUSION

Attenuation correction had a strong influence on the quantification accuracy of PET images. The present study revealed, that EM-AC can improve quantitative accuracy in PET scans acquired with continuous bed motion. Moreover, tumor identification and tumor delineation in the final images especially for small tumors could be improved by EM-AC in CBM and SaS acquired images even if the obtained values were still underestimated as compared to TX-AC reconstructed images.

## DATA AVAILABILITY STATEMENT

The datasets generated for this study are available on request to the corresponding author.

## ETHICS STATEMENT

All applicable institutional and/or national guidelines for the care and use of laboratory animals were followed and the study was reviewed and approved by the responsible national authorities (Amt der Niederösterreichischen Landesregierung).

## AUTHOR CONTRIBUTIONS

TW initiated and designed the study, coordinated, and participated in the experiments. LS performed data reconstructions and image data analysis. TF was responsible for preparing the animal model. SM and MS performed the microPET measurements. TW, MB, and CK summarized the data and drafted the manuscript. All authors read and approved the final manuscript.

## FUNDING

We acknowledge funding support from the Austrian Research Promotion Agency (FFG) (FEMtech studentship for LS).

## ACKNOWLEDGMENTS

The authors wish to thank Maria Zsebedics for help in conducting the PET experiments and the radiochemistry staff (Seibersdorf Labor GmbH) for their continuous support.

## REFERENCES


1. Dahlbom M, Hoffman EJ, Hoh CK, Schiepers C, Rosenqvist G, Hawkins RA, et al. Whole-body positron emission tomography: Part I. Methods and performance characteristics. *J Nucl Med.* (1992) **33**:1191–9.
2. Lehnert W, Meikle SR, Siegel S, Newport D, Banati RB, Rosenfeld AB. Evaluation of transmission methodology and attenuation correction for the microPET Focus 220 animal scanner. *Phys Med Biol.* (2006) **51**:4003–16. doi: 10.1088/0031-9155/51/16/008
3. Siman W, Kappadath SC. Comparison of step-and-shoot and continuous-bed-motion PET modes of acquisition for limited-view organ scans. *J Nucl Med Technol.* (2017) **45**:290–6. doi: 10.2967/jnmt.117.195438
4. Del Guerra A, Belcari N. Dual-modality preclinical SPECT/PET instrumentation. In: Zaidi H, editor. *Molecular Imaging of Small Animals: Instrumentation and Applications.* New York, NY: Springer (2014). p. 337–50. doi: 10.1007/978-1-4939-0894-3_11
5. Marik J, Tartis MS, Zhang H, Fung JY, Kheirolomoom A, Sutcliffe JL, et al. Long-circulating liposomes radiolabeled with [(18)F]fluorodipalmitin ([(18)F]FDP). *Nucl Med Biol.* (2007) **34**:165–71. doi: 10.1016/j.nucmedbio.2006.12.004
6. Ceccarini G, Flavell RR, Butelman ER, Synan M, Willnow TE, Bar-Dagan M, et al. PET imaging of leptin biodistribution and metabolism in rodents and primates. *Cell Metab.* (2009) **10**:148–59. doi: 10.1016/j.cmet.2009.07.001
7. Osborne DR, Acuff S, Cruise S, Syed M, Neveu M, Stuckey A, et al. Quantitative and qualitative comparison of continuous bed motion and traditional step and shoot PET/CT. *Am J Nuclear Med Mol Imaging.* (2015) **5**:56–64.
8. Acuff SN, Osborne D. Clinical workflow considerations for implementation of continuous-bed-motion PET/CT. *J Nucl Med Technol.* (2016) **44**:55–8. doi: 10.2967/jnmt.116.172171
9. Yamashita S, Yamamoto H, Nakaichi T, Yoneyama T, Yokoyama K. Comparison of image quality between step-and-shoot and continuous bed motion techniques in whole-body (18)F-fluorodeoxyglucose positron emission tomography with the same acquisition duration. *Ann Nucl Med.* (2017) **31**:686–95. doi: 10.1007/s12149-017-1200-5
10. Lu YH, Fontaine K, Gallezot JD, Mulnix T, Panin V, Jones J, et al. Whole-body continuous-bed-motion PET list-mode reconstruction with non-rigid event-by-event respiratory motion correction. *J Nucl Med.* (2019) **60**:105.
11. Berker Y, Li Y. Attenuation correction in emission tomography using the emission data–A review. *Med Phys.* (2016) **43**:807–32. doi: 10.1118/1.4938264
12. Zaidi H, Hasegawa B. Determination of the attenuation map in emission tomography. *J Nucl Med.* (2003) **44**:291–315.
13. Tai YC, Ruangma A, Rowland D, Siegel S, Newport DF, Chow PL, et al. Performance evaluation of the microPET focus: a third-generation microPET scanner dedicated to animal imaging. *J Nucl Med.* (2005) **46**:455–63.
14. Hamacher K, Coenen HH, Stocklin G. Efficient stereospecific synthesis of no-carrier-added 2-[18F]-fluoro-2-deoxy-D-glucose using aminopolyether supported nucleophilic substitution. *J Nucl Med.* (1986) **27**:235–8.
15. Tsubura A, Lai YC, Miki H, Sasaki T, Uehara N, Yuri T, et al. Animal models of N-Methyl-N-nitrosourea-induced mammary cancer and retinal degeneration with special emphasis on therapeutic trials. *In vivo.* (2011) **25**:11–22. Available online at: http://iv.iiarjournals.org/content/25/1/11.abstract
16. Saminathan M, Rai RB, Dhama K, Ranganath GJ, Murugesan V, Kannan K, et al. Histopathology and immunohistochemical expression of N-Methyl-N-Nitrosourea (NMU) induced mammary tumours inague-dawley rats. *Asian J Anim Vet Adv.* (2014) **9**:621–40. doi: 10.3923/ajava.2014.621.640
17. Dias M, Cabrita S, Sousa E, Franca B, Patricio J, Oliveira C. Benign and malignant mammary tumors induced by DMBA in female wistar rats. *Eur J Gynaecol Oncol.* (1999) **20**:285–8.
18. Barros AC, Muranaka EN, Mori LJ, Pelizon CH, Iriya K, Giocondo G, et al. Induction of experimental mammary carcinogenesis in rats with 7,12-dimethylbenz(a)anthracene. *Revista do Hospital das Clinicas.* (2004) **59**:257–61. doi: 10.1590/S0041-87812004000500006
19. Fueger BJ, Czernin J, Hildebrandt I, Tran C, Halpern BS, Stout D, et al. Impact of animal handling on the results of $^{18}$F-FDG PET studies in mice. *J Nucl Med.* (2006) **47**:999–1006.
20. Wong KP, Sha W, Zhang X, Huang SC. Effects of administration route, dietary condition, and blood glucose level on kinetics and uptake of 18F-FDG in mice. *J Nucl Med.* (2011) **52**:800–7. doi: 10.2967/jnumed.110.085092
21. Mannheim JG, Mamach M, Reder S, Traxl A, Mucha N, Disselhorst JA, et al. Reproducibility and comparability of preclinical PET imaging data: a multicenter small-animal PET study. *J Nucl Med.* (2019) **60**:1483–91. doi: 10.2967/jnumed.118.221994
22. Loening AM, Gambhir SS. AMIDE: a free software tool for multimodality medical image analysis. *Mol Imaging.* (2003) **2**:131–7. doi: 10.1162/153535003322556877
23. van der Vos CS, Koopman D, Rijnsdorp S, Arends AJ, Boellaard R, van Dalen JA, et al. Quantification, improvement, and harmonization of small lesion detection with state-of-the-art PET. *Eur J Nucl Med Mol Imaging.* (2017) **44**(Suppl. 1):4–16. doi: 10.1007/s00259-017-3727-z
24. Chow PL, Rannou FR, Chatziioannou AF. Attenuation correction for small animal PET tomographs. *Phys Med Biol.* (2005) **50**:1837–50. doi: 10.1088/0031-9155/50/8/014
25. Konik A, Koesters T, Madsen MT, Sunderland JJ. Evaluation of attenuation and scatter correction requirements as a function of object size in small animal PET imaging. *IEEE Trans Nucl Sci.* (2011) **58**:2308–14. doi: 10.1109/TNS.2011.2160998
26. Maeda Y, Kudomi N, Sasakawa Y, Monden T, Kato K, Yamamoto Y, et al. Applicability of emission-based attenuation map for rapid CBF, OEF, and CMRO2 measurements using gaseous (15)O-labeled compounds. *EJNMMI Phys.* (2015) **2**:12. doi: 10.1186/s40658-015-0115-2
27. El Ali HH, Bodholdt RP, Jorgensen JT, Myschetzky R, Kjaer A. Importance of attenuation correction (AC) for small animal PET imaging. *Diagnostics.* (2012) **2**:42–51. doi: 10.3390/diagnostics2040042
28. D'Ambrosio D, Zagni F, Spinelli AE, Marengo M. Attenuation correction for small animal PET images: a comparison of two methods. *Comput Math Methods Med.* (2013) **2013**:103476. doi: 10.1155/2013/103476


**Conflict of Interest:** The authors declare that the research was conducted in the absence of any commercial or financial relationships that could be construed as a potential conflict of interest.

frontiers in Physics

REVIEW
published: 05 May 2020
doi: 10.3389/fphy.2020.00124

# Preclinical Ultrasound Imaging—A Review of Techniques and Imaging Applications

*Carmel M. Moran* and Adrian J. W. Thomson*

*Centre for Cardiovascular Science, University of Edinburgh, Edinburgh, United Kingdom*

Ultrasound imaging is a well-established clinical imaging technique providing real-time, quantitative anatomical and physiological information in humans. The lack of ionizing radiation and relative low purchase and maintenance costs results in it being one of the most frequently used clinical imaging techniques with increasing use for guiding interventional clinical procedures. Until 20 years ago, translation of clinical ultrasound practices to preclinical applications proved a significant technological challenge due to the smaller size (25 g vs. 70 kg) and rapid conscious heart-rate (500–700 bpm vs. 60 bpm) of the mouse requiring an increase in both spatial and temporal resolution of 10–20-fold in order to achieve diagnostic information comparable to that achieved clinically. Since 2000 [1], these technological challenges have been overcome and commercial high frequency ultrasound scanners have enabled longitudinal studies of disease progression in small animal models to be undertaken. Adult, neonatal and embryonic rats, mice and zebrafish can now be scanned with resolutions down to 30 microns and with sufficient temporal resolution to enable cardiac abnormalities in all these species to be identified. In mice and rats, quantification of blood flow in cardiac chambers, renal, liver and uterine vessels, and intra-mural tissue movements can be obtained using the Doppler technique. Ultrasonic contrast microbubbles used routinely for clinical applications are now being further developed to include targeting mechanisms and drug-loading capabilities and the results in animal models bode well for translation for targeted drug delivery in humans.

**Keywords: ultrasound, preclinical, mouse model, rat model, zebrafish**



***Edited by:***
*Andreas Hess,*
*University of Erlangen Nuremberg, Germany*

***Reviewed by:***
*David B. Stout,*
*Independent Researcher, Culver City, United States*
*Boran Han,*
*Harvard University, United States*

****Correspondence:***
*Carmel M. Moran*
*carmel.moran@ed.ac.uk*

***Specialty section:***
*This article was submitted to Medical Physics and Imaging, a section of the journal Frontiers in Physics*

***Received:*** *29 November 2019*
***Accepted:*** *30 March 2020*
***Published:*** *05 May 2020*

***Citation:***
*Moran CM and Thomson AJW (2020) Preclinical Ultrasound Imaging—A Review of Techniques and Imaging Applications. Front. Phys. 8:124. doi: 10.3389/fphy.2020.00124*

## INTRODUCTION

Although ultrasound has been used extensively since its development to study preclinical animal models much of the early work in this field was undertaken using transducers designed for ultrasound scanning of clinical small-parts or intra-operative imaging and operating in the frequency range between 10 and 20 MHz. Such frequencies enable images with spatial resolutions of the order of hundreds of microns to be acquired thus limiting their effectiveness in detecting abnormalities in smaller preclinical models. Additionally, clinical scanners designed to image the human heart with 60–100 beats per minute (bpm) had insufficient temporal resolution to image the rapid heart movement of preclinical models (400–600 bpm). The technological challenges of designing and manufacturing a commercial ultrasound scanner capable of resolving structures smaller than 100 microns and with sufficient temporal resolution to resolve cardiac motion within a mouse heart was overcome with the launch of the first commercially available preclinical ultrasound scanner in year 2000. Since then there has been a meteoric rise in the number of biology research publications using preclinical ultrasound imaging to assess adult, neonatal and embryonic rats, mice, and zebrafish with spatial resolutions approaching 30 micron and with frame-rates of up to 350 Hz achievable when imaging adult murine hearts enabling cardiac abnormalities to be identified. In addition, blood flow within cardiac chambers, renal, liver and uterine vessels can be measured in real-time using the Doppler function on the scanners and elastic properties of tissues can be measured using elastography techniques. New and exciting applications using ultrasonic contrast microbubbles designed to target specific biological markers and with drug-loading capabilities are being developed and tested in animal models. Technological advances in transducer manufacture has resulted in linear array transducers now replacing the first generation of mechanically-driven single-element transducers.

In this manuscript we will review the different imaging modes available on preclinical ultrasound scanners and highlight their utility for imaging of preclinical models. For clarity, the words preclinical animal model are used to describe small non-companion animals for which the genetic footprint can be modified and refers predominantly to mice, rats and zebrafish. All images and experiments described were performed under a UK Home Office Licence following ethical review by the University of Edinburgh.

## TECHNIQUES OF ULTRASOUND IMAGING

Ultrasound waves are emitted from an ultrasound transducer. The choice of frequency of the transducer is important as higher frequencies give increased spatial resolution (i.e., smaller objects can be resolved) but the depth over which useful information can be obtained is reduced. For preclinical imaging, frequencies between 20 and 55 MHz are generally used with 15–20 MHz (image depth 3–4 cm) being used for adult rats, 30–40 MHz (image depth 10–20 mm) for adult mice and higher frequencies (up to 50 MHz, image depth 9 mm) used for neonatal mouse studies and embryonic and adult zebrafish imaging. When the transducer is coupled to the surface of the body using warmed ultrasound coupling gel, ultrasound images can be acquired in real-time. Ultrasound images are essentially two-dimensional (2D) cross-sectional slices through the body with the portion of anatomy closest to the transducer (generally the skin) displayed at the top of the screen and organs more distal displayed at depth. The depth at which organs are displayed on the screen is determined by the length of time the emitted ultrasound beam takes to return to the surface of transducer assuming a standard speed of sound in soft tissue of 1,540 $ms^{-1}$ and assuming no multiple scattering has taken place. Unlike clinical ultrasound imaging in which scans are undertaken with the sonographer moving the transducer in real-time over the skin surface, for preclinical ultrasound scanning, the transducer is mounted in a probe-holder with 3D versatile movement enabling the probe to be oriented to any desired angle whilst avoiding small, but at high resolution, significant human movement compromising the quality of image acquisition. For almost all ultrasound imaging of preclinical models, the models are anesthetized prior to ultrasound scanning. With rats and mice, prior to ultrasound scanning, thick animal hair can be removed using electric hair clippers followed by the application of a depilatory cream to the scanning area. The use of the cream ensures that air bubbles are not trapped under any remaining hair stubble. Once the hair is removed, warmed coupling gel is placed on the body of the animal. Meanwhile, the temperature of the animal is recorded continuously especially in experiments where large amounts of the mouse hair has been removed. The probe is then lowered into the coupling gel. Due to the small size of preclinical models and their physical fragility, when scanning most organs, the ultrasound transducer does not touch the animal but scans through a thin layer of gel between the transducer head and the animal skin.

### 2D B-Mode Imaging

B-mode imaging or brightness-mode is the most commonly used mode in ultrasound imaging. In B-mode imaging 2D cross-sectional images of the animal are displayed in real-time on the screen. Images are acquired in transmit-receive mode where the transducer emits an ultrasound pulse, then pauses to receive signals back at the transducer which have been reflected and scattered from organ boundaries and parenchyma. This received signal is rapidly processed to form the gray-scale image displayed on the screen with highly reflective structures such as organ boundaries giving brighter (whiter) echoes and structures which scatter less ultrasound (e.g., blood) being darker. The focal position (highlighted as a yellow arrow in **Figure 1**) is the depth of optimal spatial resolution within the image. Using array probes, multiple focal zones can be selected but this will have a detrimental effect on the maximum frame-rate obtained. This may not be important for the more static abdominal organs but for cardiac imaging generally only one focal zone is used.

Due to the rapid generation of ultrasound images, all scanners have the capability to freeze image acquisition and scroll (cine) through a pre-defined number of images in order to review the most recent acquisitions. Single images and short video clips can be saved on the scanner—the length of video clip is usually pre-set and tends to be longer for video clips acquired during echocardiographic studies and contrast imaging studies than for abdominal scans (see below).

### M-Mode Imaging

M-mode imaging or motion-imaging is used principally to study fast moving structures such as heart-wall movement or valvular movement. A single line is selected in the B-mode image intersecting the chamber walls or valves of interest and ultrasound data is acquired only along the pre-selected M-mode line. Consequently data is acquired with high temporal resolution, as only one line of data is acquired rather than 128 lines of data in a full B-mode image. The M-mode data is displayed as a continuous function of time scrolling across the screen with depth on the y-axis and time on the x-axis (**Figure 2**).

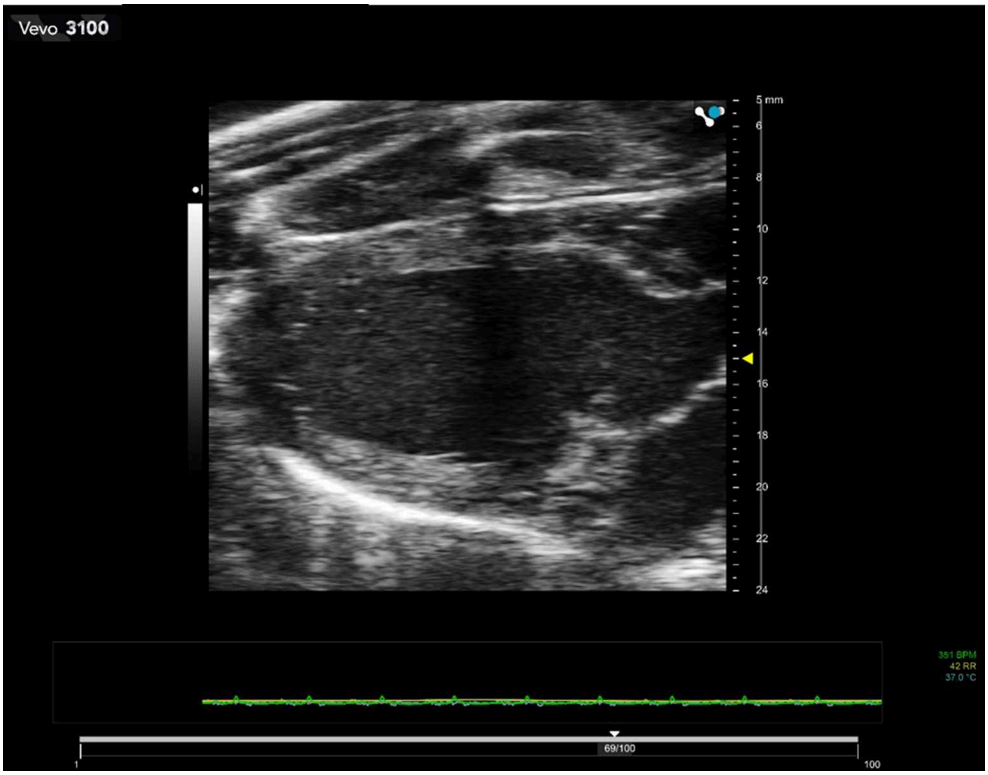


**FIGURE 1 |** 2D B-mode image of a rat heart in diastole. Transducer used is 21 MHz center-frequency and focus of the beam is set at 15 mm depth. The dark zone running through the center of the image is caused by shadowing from the ribs.

## Three-Dimensional (3D) and 4-Dimensional (4D) Imaging

Currently, three-dimensional preclinical ultrasound images are generated by the acquisition of consecutive B-mode ultrasound images acquired at discrete step sizes along a pre-determined path. Commercial software then reconstructs the 3D volume with elevational resolution dependent on the step size between consecutive B-mode image acquisitions (**Figure 3**). For cardiac applications, images tend to be ECG and respiration-gated enabling accurate volumes of left ventricles to be determined which are not dependent on assumptions of the shape of the organs. In newer preclinical ultrasound scanners, complete 3D acquisitions are possible over a cardiac cycle (4D) enabling the dynamic movement of the heart to be viewed from any orientation. Acquisition times can be several minutes, dependent on the step-size between acquisition slices and relies upon good ECG and respiratory gating and high frame-rates. 3D imaging is also used to good effect in acquiring tumor volume data-sets, avoiding the need to make assumptions about the shape of tumor from a 2D image or the use of measurement calipers for superficial tumor volume assessment.

## Doppler Techniques

Measurement of blood flow relies upon the use of the Doppler principle such that the measured change in frequency between a transmitted and received ultrasound beam is related to the velocity of the scatterers (red blood cells) from which the ultrasound beam is reflected.

### Spectral Doppler

Spectral Doppler enables the Doppler frequency shift within a pre-selected region-of-interest (Doppler sample volume) to be displayed as a function of time. Most accurate measurements are made when the Doppler scatterers (red blood cells) are moving in the direction of the transmitted ultrasound beam. If the ultrasound beam cannot be aligned with the direction of blood flow, an angle correction can be made which attempts to compensate for this lack of alignment (**Figure 4**).

### Color Doppler

In Color Doppler mode, the mean velocity of scatterers (red blood cells) within a pre-selected region-of-interest are color-encoded and superimposed on the gray-scale B-mode image. In clinical applications blood moving away from the transducer tends to be encoded in shades of blue and blood moving toward the transducer in shades of red. For preclinical applications, color Doppler is especially useful for the rapid location of vessels (**Figure 5**).

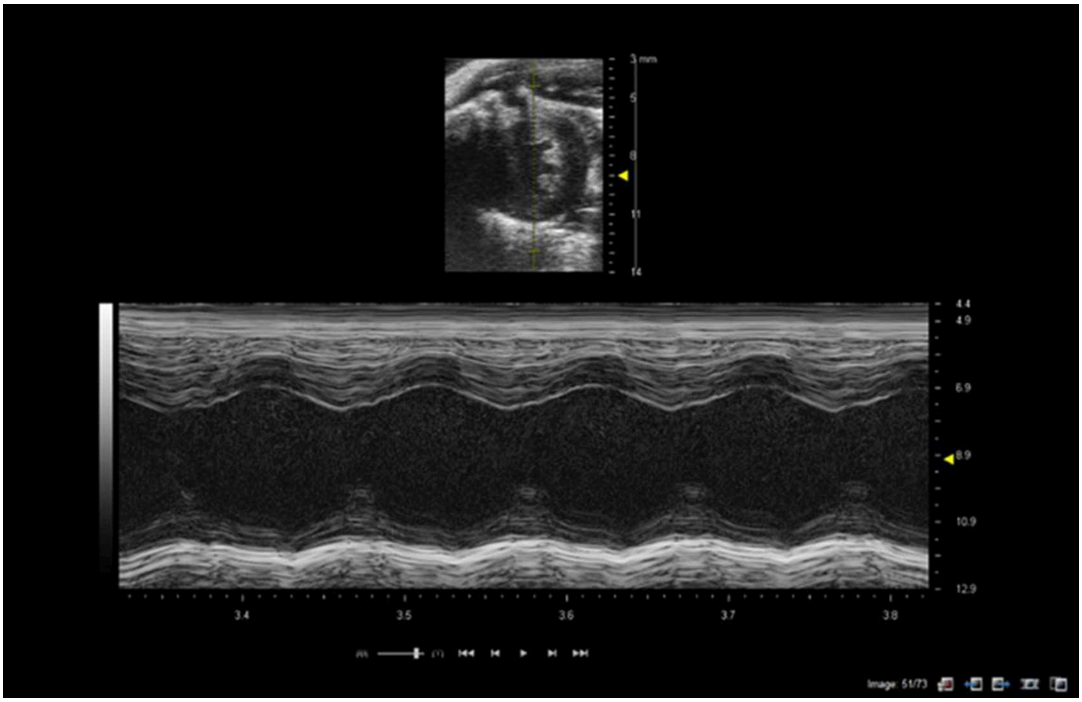


**FIGURE 2 |** M-mode of mouse heart showing short-axis B-mode image in top half of image with M-mode line selected (yellow line in image). Lower image shows M-mode trace through the left ventricle at level of papillary muscles. Images acquired using a 40 MHz probe focussed at 9 mm depth.

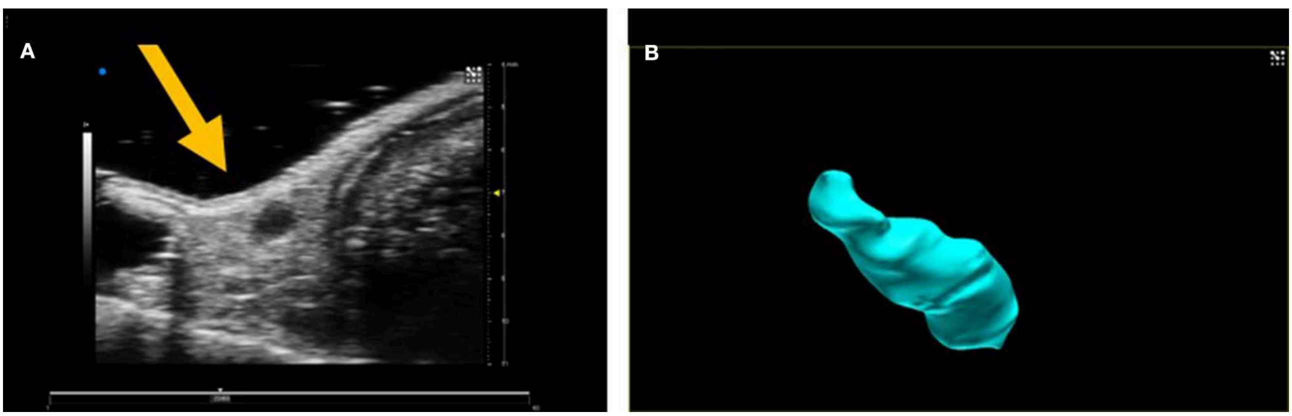


**FIGURE 3 | (A)** 2D B-mode image of an inguinal lymph node and **(B)** 3D volume of lymph node after 3D acquisition.

## Power Doppler

In Power Doppler mode the power of the Doppler signal backscattered from red blood cells is displayed as a function of time within a pre-selected region of interest. The color is superimposed onto the gray-scale B-mode image. However, no directional information on blood flow is obtained but power Doppler is a more sensitive indicator of vascularity and thus useful in the detection of small vessels containing slower blood flow (**Figure 6**).

## Doppler Tissue Tracking

The Doppler principle can also be applied to quantify both inter- and intra- regional soft tissue movement in a technique known as *tissue Doppler imaging*. In this technique, the sample volume is placed within the moving tissue of interest, and the amplitude of the high-pass filter is reduced to enable slow, high-amplitude signals corresponding to tissue to be tracked [2]. By measuring the velocities between tissues regions, velocity gradients (rate of change of velocity with distance) and strain rate information

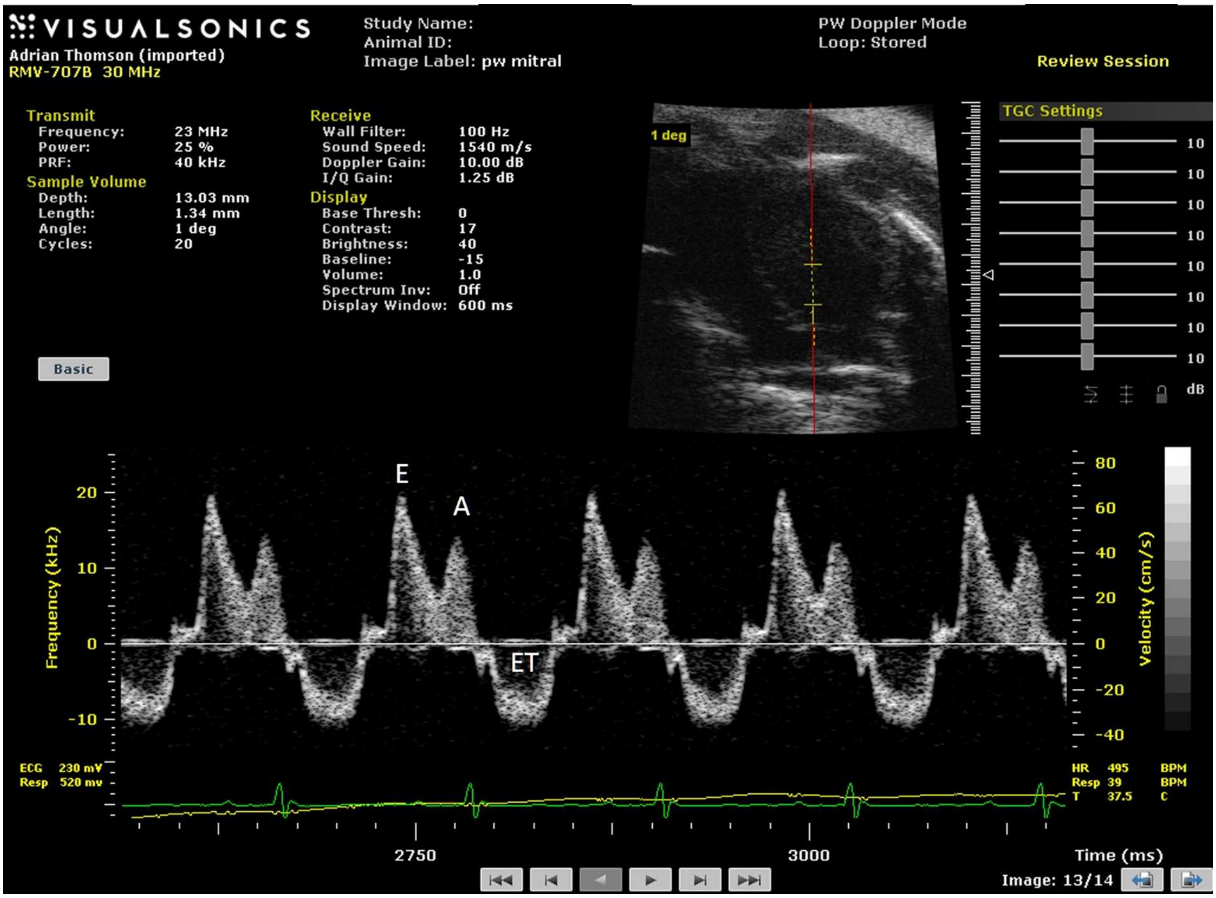


**FIGURE 4 |** Spectral Doppler trace with Doppler sample volume situated in center of left ventricle enables both inflow and outflow from the left ventricle to be measured with early (E) and late (atrial—A) waves and ejection time (ET) highlighted in the spectral Doppler trace. In addition isovolumic relaxation time (IVRT) and isovolumic contraction time (IVCT) may be measured where IVRT is equal to the time from the closure of the aortic valve to opening of mitral value and IVCT is the time of closure of mitral valve to opening of aortic valve.

can be calculated. However, tissue Doppler is only useful when the tissue motion is aligned with the direction of the ultrasound beam which has limitations in the assessment of cardiac radial function but has been used to good effect in studying mitral valve annulus movement.

## Newer Imaging Techniques

### Speckle Tracking

Alternative non-Doppler techniques such as *speckle tracking* can also be used to track tissue motion and as such are not reliant on alignment between beam and direction of movement. Speckle is effectively the fine background noise on ultrasound images. It is formed by the interference between echoes from structures which are smaller than the resolution of the ultrasound system. This interference pattern (speckle) is random and unique for any volume of tissue and although it may change with movement of the tissue, image processing techniques can be used to recognize and track the movement in 2D and 3D [3]. In order to use speckle tracking techniques, high frame-rates are required (>250 frames/s) with faster heart rates requiring higher frame-rates to ensure points of maximal and minimum strain and rate are captured. Using speckle tracking a range of parameters can be measured including displacement, velocity and strain and strain-rate.

### Elastography Techniques

*Ultrasound Elastography* techniques are used to obtain information on the stiffness of tissue and can essentially be divided into those techniques which measure strain and those which measure shear wave velocity and from that directly measure Young's modulus (stress/strain). *Strain elastography* involves deformation of the tissue by application of a force (stress) and measuring the resulting degree of compression or extension of the tissue (strain) and comparing this to a reference soft tissue yielding a parameter known as the strain ratio. Since the magnitude of the stress applied is difficult to measure, strain elastography is not an intrinsic measure of tissue stiffness *per se* but the strain ratio can be used to infer tissue stiffness. Strain-rate is the change of tissue deformation with time. Both strain and strain-rate are routinely used in cardiac

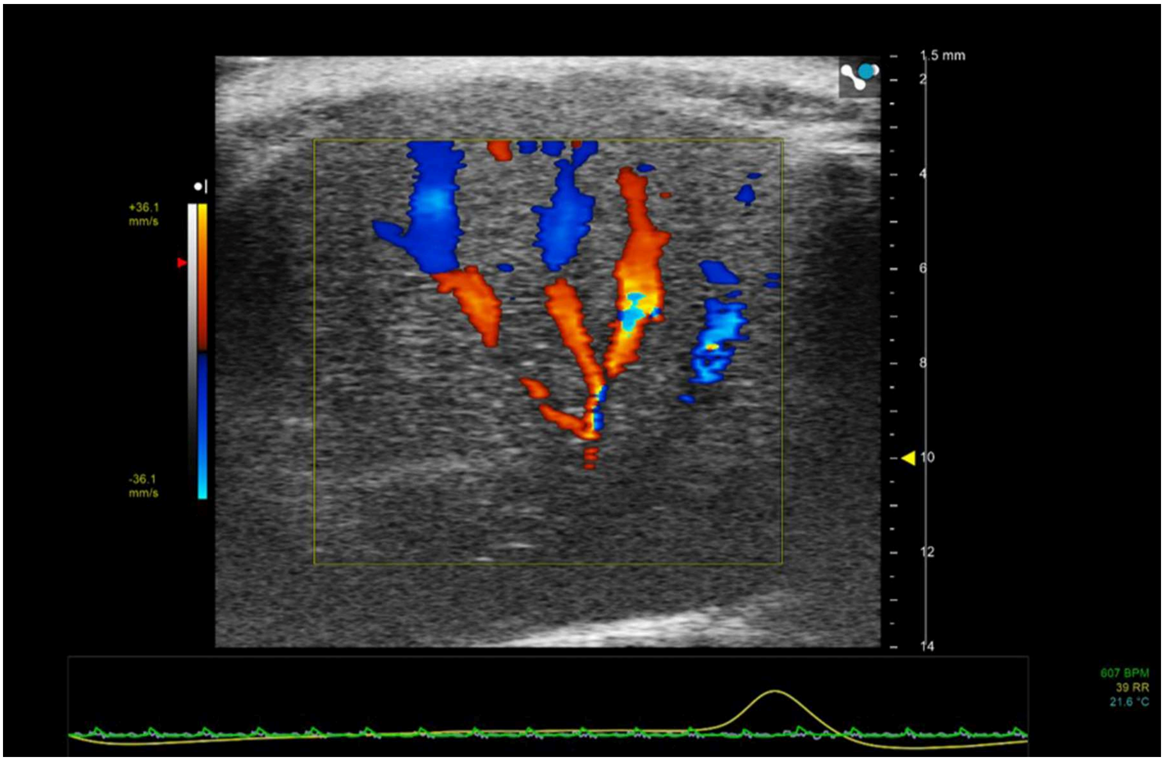


**FIGURE 5 |** Color Doppler region of interest superimposed on 2D B-mode image of mouse liver. Color Doppler shows the vessel network—blue indicating movement of blood away from the transducer and red toward the transducer.

applications, where strain and strain-rate values from different regions of the myocardium can be compared. Strain analysis using ultrasound is generally performed using speckle tracking techniques whereby the speckle within different pre-selected ROIs (kernals) is tracked and the relative displacement between the two kernals can be measured. The distance between the two kernals, enables strain to be calculated and the variation of strain over time is *strain-rate* ($s^{-1}$) [4] (**Figure 7**).

Alternatively, the measurement of *shear wave velocity* enables a quantitative measurement of Young's modulus of elasticity, E, provided that the tissue can be assumed to be incompressible (no change in density) and uniformly elastic (**Figure 8**). The shear modulus G is related to the Young's modulus of elasticity E, by the following equation. $E = 3G$. Shear wave velocity, $c_{s,}$ generated as a result of a shearing force is given by, $c_s = \sqrt{(G/\rho)}$. By measuring the shear speed (usually between 1 and 10 $m.s^{-1}$) and knowing the density, ρ, of the soft tissue (estimated at 1,000 $kg.m^{-3}$), Young's modulus of elasticity can be calculated from the equation $E = 3\rho c_s^2$. Hence measuring the shear speed can provide quantitative information on the elastic modulus. More detailed information on elastography techniques can be found in Hoskins [5] and Bamber et al. [6].

### Non-linear Imaging Techniques

Non-linear imaging techniques are utilized principally in the detection of ultrasonic contrast microbubbles (encapsulated gas bubbles). Contrast microbubbles when insonated with an ultrasound beam will begin to oscillate, expanding during the negative phase of the cycle and contracting during the positive phase. Dependent on the frequency and amplitude of the transmitted ultrasound the microbubbles can produce a significant non-linear backscattered signal without being destroyed. Since soft tissues predominantly scatter ultrasound in a linear manner by removing or canceling the linear component of the backscattered signal the kinetics and dynamic enhancement of organs can be visualized and quantified by measuring the increase in non-linear signal as a function of time. This can then be displayed in a variety of ways such as a maximum intensity projection sequence which will enable the dynamic filling patterns to be established within a region or as a graph illustrating the backscattered intensity kinetics within a region-of-interest (**Figure 9**).

### Ultrafast Doppler

Novel imaging techniques such as ultrafast imaging and ultrafast Doppler techniques enable exquisitely detailed images and volumes of tumor vascularity to be built up even from vessels with very slow flow which are difficult to locate with standard Doppler techniques [7].

## PRECLINICAL ULTRASOUND—CARDIAC APPLICATIONS

The heart is probably the most challenging organ to image within the rodent due to its small size and rapid and

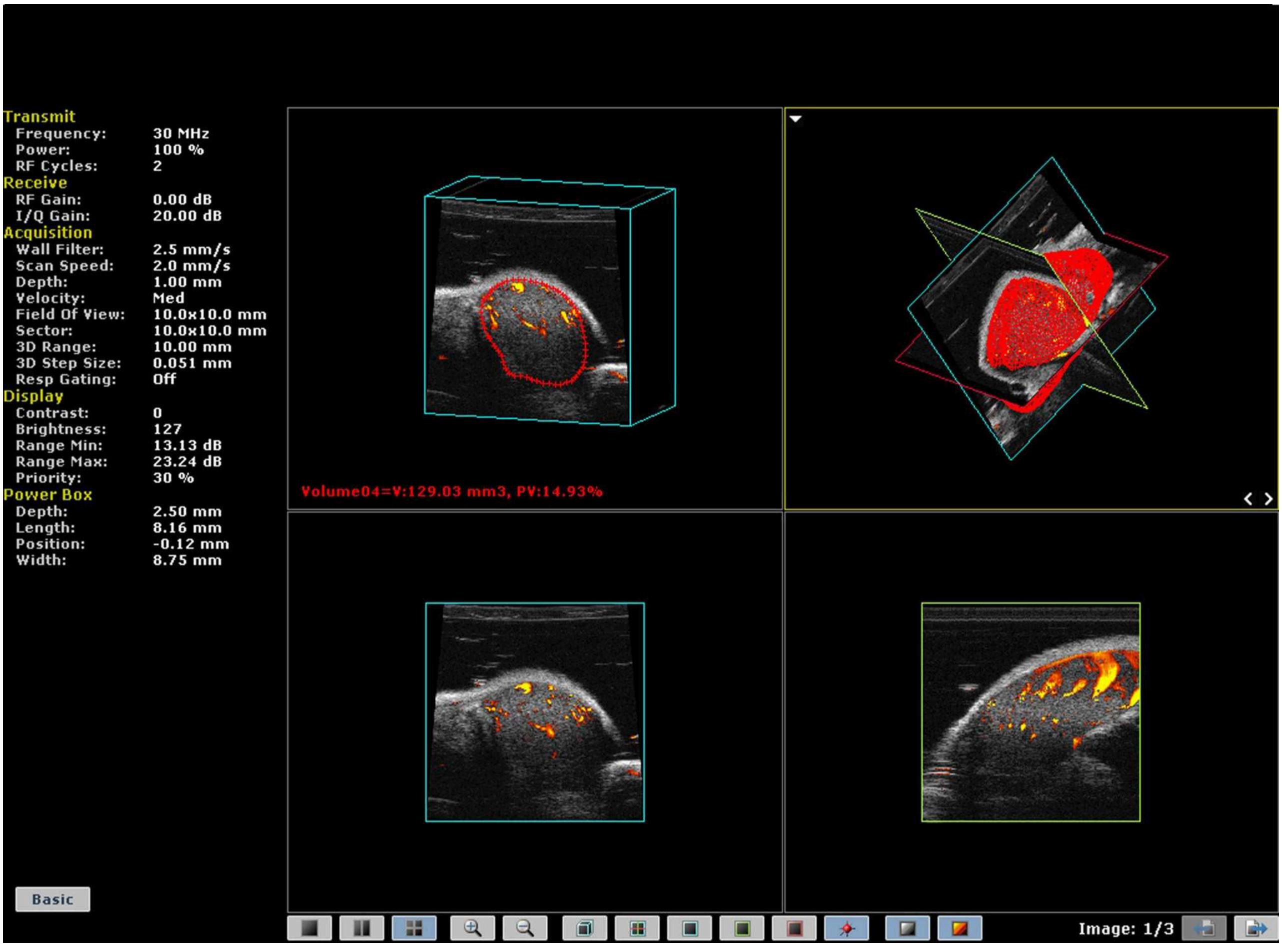


**FIGURE 6 |** 3D Power Doppler image of mouse testes. Imaged using 40 MHz probe.

complex motion. However, rodent models of cardiac diseases and myocardial infarction (MI) give valuable insights into anatomic and physiologic changes which are often directly aligned with changes observed in human cardiac disease and thus provide opportunities to assess novel therapeutic approaches and interventions.

Adult and neonatal cardiac scanning in mice, is routinely undertaken with the mouse in the supine position, hence the standard views obtained from mouse models are not exactly comparable to images acquired from clinical subjects who are scanned while lying in the left decubitus position. The ECG, respiration and temperature of the mouse are continuously recorded and monitored to ensure minimal variation throughout the scan-time. However, due to the range of mouse strains, anesthetic choice and depth there is a wide variation in accepted normal ranges of rodent cardiac indices. A recent review recommended standardized methods of measuring and reporting cardiac physiology in the adult murine model [8] and forms a useful step toward the introduction of standardized scanning procedures similar to those introduced by the American Society of Echocardiography and the European Association of Cardiovascular Imaging for clinical practice [9].

Similarly to clinical studies, all of the ultrasound imaging modalities: B-mode, M-mode, Doppler ultrasound and strain imaging can be used to assess cardiac function in mice.

## Measurement of Cardiac Function in Adult Rodents

For adult mice scanning, transducer frequencies of 30–40 MHz are used, while for rats, ultrasound transducers operating between 10 and 25 MHz may be used—the higher frequencies for applications in smaller rats. To achieve high temporal resolution, only one focal position should be selected and placed at a depth commensurate with the region-of-interest.

There are two standard views used for initial assessment of the heart using parasternal 2D *B-mode imaging*—long-axis and short-axis views. Using these views initially provides a gross overview of the movement of left ventricular myocardial walls and mitral and aortic valve movements enabling areas of hyper-, hypo- or dyskinetic regions to be identified for further investigation. Due to the rapid heart-rate, cine-loops

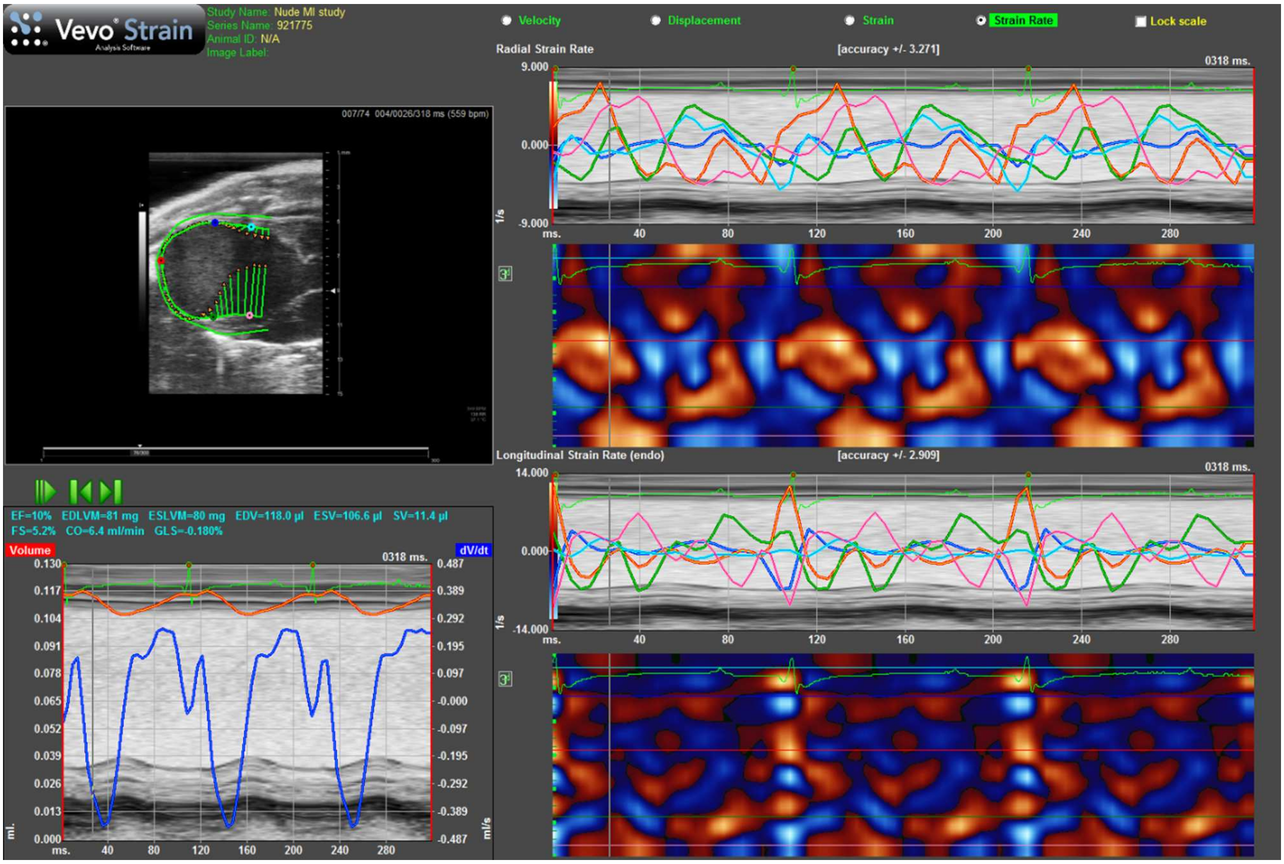


FIGURE 7 | Strain rate imaging of a nude mouse with MI as the result of ligation of left coronary artery. Top lhs is long-axis view of heart with arrows indicating direction and magnitude of movement of endocardial border. Bottom lhs shows change in volume of cavity over consecutive cardiac cycles alongside ECG and respiration. Top rhs shows radial strain-rate curves from five points selected on endocardial border while lower rhs shows longitudinal strain-rate curves from the same five points.

are generally acquired and can be reviewed at a much slower rate enabling key-points in the cardiac cycle such as systole and diastole to be identified. Alternatively a technique known as electrocardiogram-gated kilohertz visualization (EKV) can be used to investigate motion over one cardiac cycle with very high temporal resolution (1,000 frames/s). EKV scanning acquisition times are of the order of 30–60 s with the acquisition gated on the ECG and respiration cycles. Effectively sequential M-modes are acquired across the heart and temporally interleaved into a high temporal resolution 2D B-mode image data set of a cardiac cycle. Using this technique enables easier tracking of myocardial borders. Parameters that can be measured from B-mode or EKV images include stroke volume, ejection fraction, cardiac output, endocardial area, epicardial area, and percentage fractional myocardial area change. The formula and techniques used to measure these are beyond the scope of this review but can be found in Lang et al. [10].

*M-mode* is especially useful for the measurement of the maximum and minimum dimensions of the ventricles for calculation of cardiac indices such as fractional shortening and for the assessment of myocardial wall abnormalities (**Figure 2**). However, M-mode measurements of chamber size should not be used for measurement of cardiac indices derived from volume measurements (e.g., ejection fraction) as these make assumptions re the shape of ventricles which are prone to error especially for animal models which have suffered myocardial infarctions and for which the shape of the ventricle can undergo deformation and remodeling. M-mode imaging can also provide information about valve movements with the M-mode line aligned with the tip of the mitral valve leaflets to study the thickness of the leaflets and valvular dynamics. Likewise for the aortic valve M-mode can be used to assess aortic valve cusp separation.

*Four–dimensional imaging* of the rodent heart is undertaken by acquiring multiple 2D EKV cineloops over a cardiac cycle. Gating on the ECG and respiration can be done either during acquisition or reconstruction of the 3D data-set. These cineloops are acquired at discrete, user-determined distances in either long- or short- axis views yielding a full 4D dataset. The cineloops are then temporally interleaved and reconstructed to allow the heart to be dynamically visualized over one cardiac cycle. 4D imaging enables the volume of cardiac chambers to be established with fewer inherent assumptions re the shape and dynamics of the chambers compared to calculations using 2D images (**Figure 10**). As such calculation of indices requiring volume

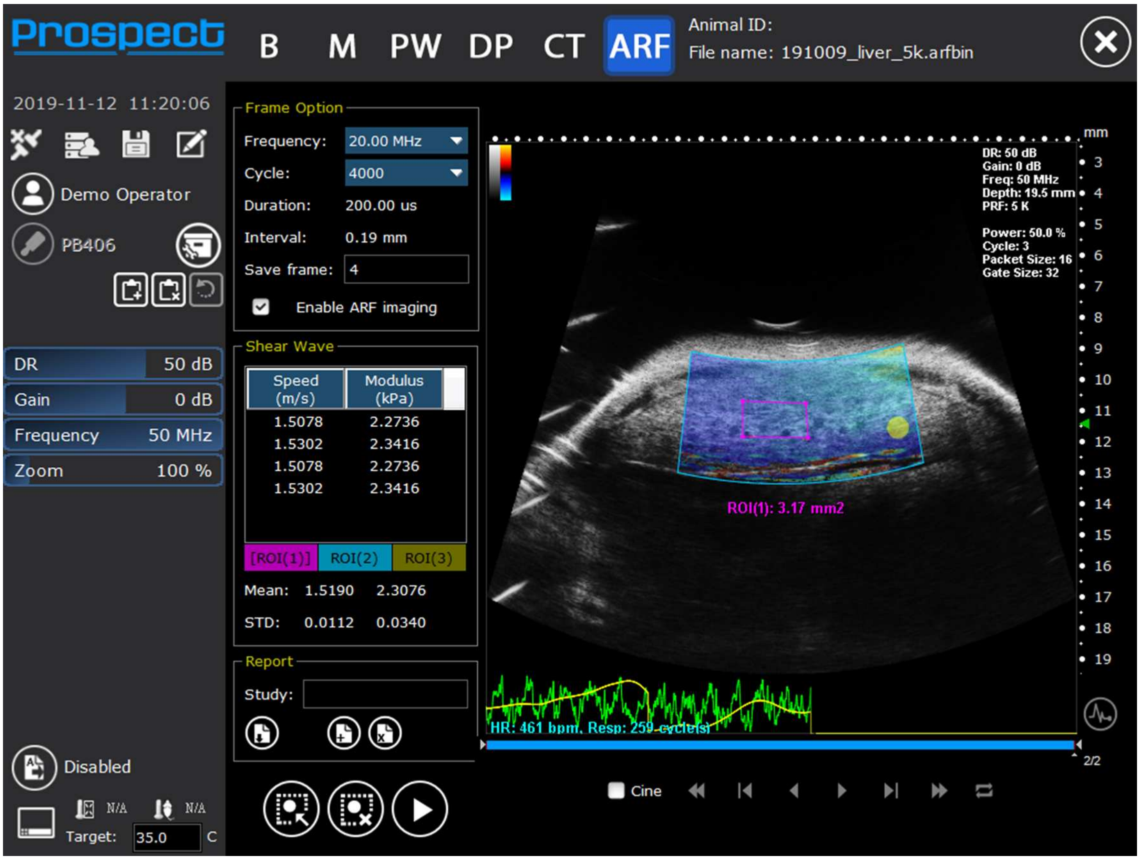


**FIGURE 8 |** Shear wave elastography image of liver showing mean shear wave velocities and Young's modulus from a mouse liver (Reproduced with permission from S-Sharp Corporation).

calculations, e.g., ejection fraction are more accurate and precise than measurements undertaken using 2D acquisitions [11].

*Doppler measurements* are used in echocardiography to measure blood flow across the mitral and aortic valves within the heart. With the Doppler sample volume sited at mid-ventricular level, in the apical 4-chamber view, mitral valve early (E) and late [atrial (A)] inflow velocities can be seen in the mitral spectral Doppler trace—the ratio of E/A and the deceleration time of the E-wave are indicators used in the assessment of diastolic function (**Figure 4**). For some animals, separation of the E and A waves can be difficult to achieve due to the high heart-rates displayed by adult mice. However, isovolumic relaxation time can be measured along with systolic parameters such as ejection time and isovolumic contraction time enabling the calculation of myocardial performance index, an indicator of cardiac performance (see section on embryonic imaging).

*Color Doppler* is used in adult rodent echocardiography for the rapid assessment of blood flow within the chambers and specifically across valves. Constriction of valves can result in jetting which can be visualized as rapid flashes of color across the valves during contraction of chambers. This enables easier localization of the spectral Doppler sample volume within the jet to measure maximal velocities for assessment of constriction of valves. Color Doppler can also be used to localize small vessels. **Figure 11** shows a duplex image (color and spectral Doppler) where color Doppler has being used to localize and identify the left anterior coronary artery and spectral Doppler enabling measurement of the velocities within the artery.

## Strain and Strain-Rate Imaging

Strain and strain-rate imaging are of specific value in rodent cardiac imaging providing information on regional myocardial deformation. Most commercial scanners use speckle tracking to determine strain (deformation)—by measuring the relative displacement of two kernals to determine strain and its variation over time to give strain-rate. In addition to a global strain parameter, radial, circumferential and longitudinal strain can be obtained providing information on regional segmental myocardial motion and systolic function. The timing of maximum and minimum strain and strain-rate values relative to systole and diastole can provide data on desynchronises between different myocardial regions especially relevant in infarct models (**Figure 7**) [12–14].

## Contrast Agents

Ultrasonic contrast agents used in preclinical studies for ultrasonic enhancement are composed of lipid-encapsulated gas-filled microbubbles which are injected via the tail-vein into the rodent. The agents are purely vascular agents, mixing freely with the blood. Limited enhancement is achieved using

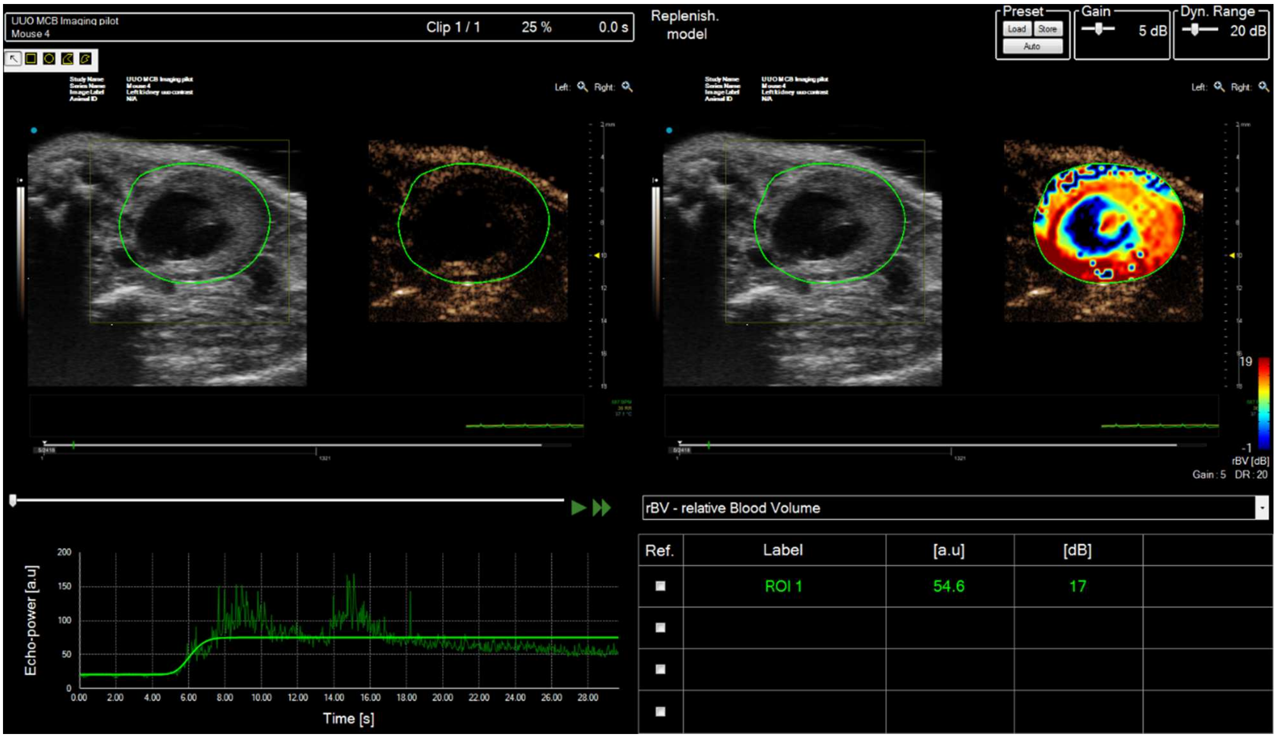


**FIGURE 9 |** Contrast analysis of data-set acquired from right mouse kidney post ischemia-reperfusion (IRI) injury after tail-vein bolus injection of SonoVue. Mouse scanned in prone position. Multiple regions of interest (ROIs) can be drawn onto the image and the enhancement can be tracked as a function of time (bottom LHS). The relative enhancement of each ROI relative to pre-contrast image can be calculated and color-encoded (Top RHS).

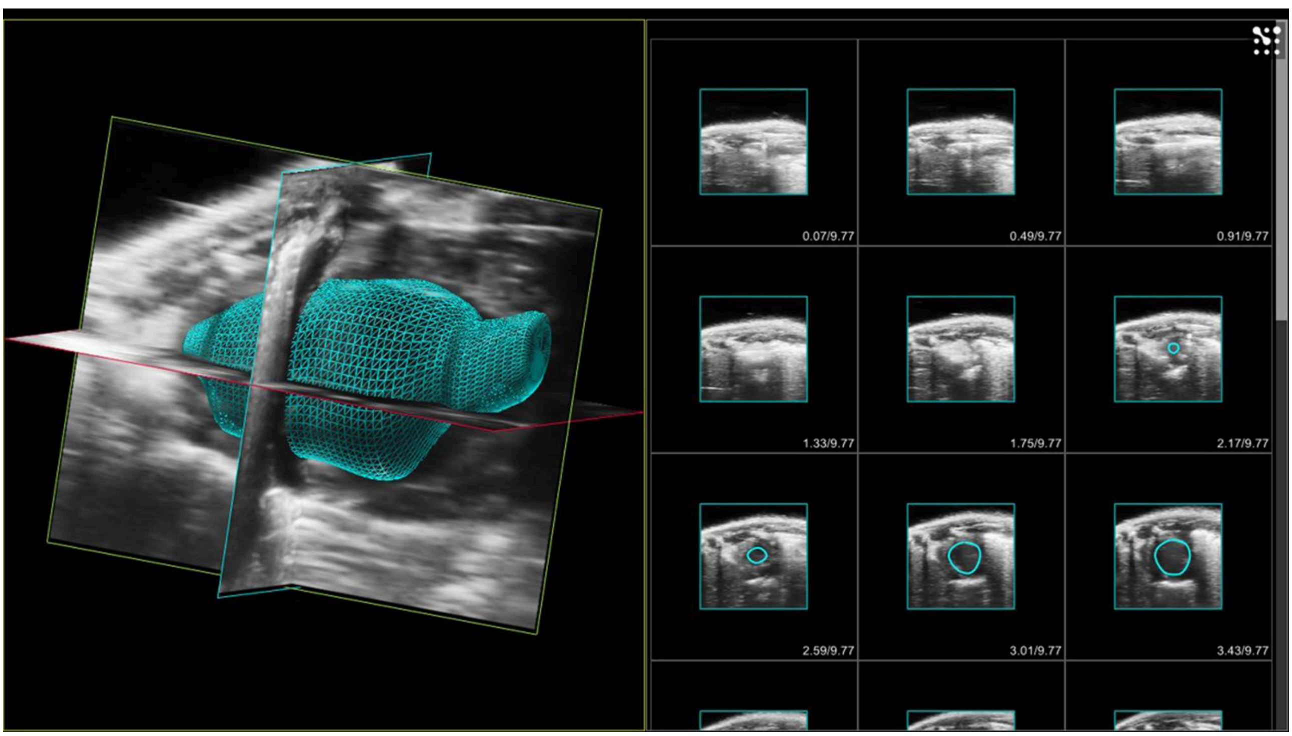


**FIGURE 10 |** LHS - 3D volume of murine left ventricle with aortic root. Images acquired at end-diastole. RHS 2D acquired images with endocardial borders of left ventricle highlighted in each slice.

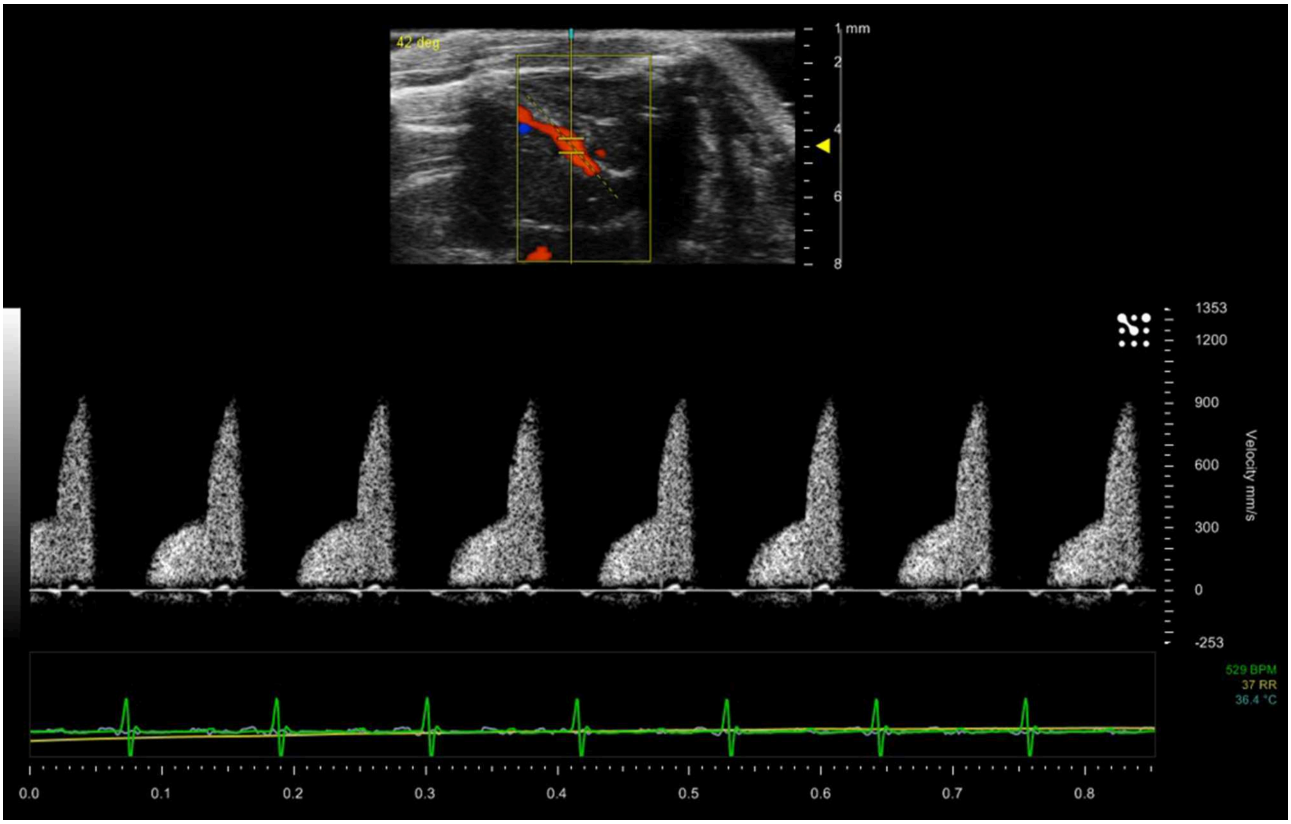


**FIGURE 11** | Blood flow within the left anterior descending coronary artery of a mouse model. Maximum velocity within the artery is 900 mm/sec.

B-mode imaging, but in many instances this is sufficient to give enhancement of endocardial borders even at these high frequencies far removed from the resonant frequency of the microbubbles. Such enhancement enables better visualization and delineation of chamber volumes. The maximum recommended volume of contrast is 5 µl/g IV for rats but for mice a bolus injection of 50 µl is sufficient to see enhancement within the heart.

## Measurement of Cardiac Function in Embryonic Mice

In embryonic mice and rats, the ultrasound backscattered signal from the circulating red blood cells is much greater than in adults. This is due to the nucleation of the red blood cells within the embryos and this enhancement can persist up to 3 to 4 days post-birth. This enhancement of the cardiac chambers, along with the complexities of determining the direction of blood flow within embryonic hearts and subsequent alignment of the Doppler beam along the direction of blood flow can make measurement of cardiac performance of embryos a challenging technique. In addition, since it is not possible to obtain an ECG from the embryos, the timing of diastole and systole is determined either by measurement of the movement of the myocardial walls or from the spectral Doppler waveform. Finally, the user needs to be mindful of the duration of anesthesia and its effect on both dam and embryos.

Since determination of the orientation of the heart can be challenging, even in older embryos, measurement of ratios calculated from the Doppler spectral trace will negate the angle dependence associated with aligning the Doppler beam with the direction of flow. Hence E/A ratios discussed above are useful indices to obtain although in embryos the A wave tends to be larger than the E wave. Likewise a parameter known as the myocardial performance (Tei) index which is a ratio of timing intervals determined from the spectral Doppler trace [summation of the isovolumic relaxation time (IVRT) and isovolumic contraction time (IVCT) divided by the ejection time (ET)] is useful and is largely unaffected by the angle of insonation. The myocardial performance is an indicator of overall cardiac performance with higher index values corresponding to an increasing dysfunctional heart. Strain rate imaging in embryonic mice is challenging and this may be due to the increased echogenicity of the blood pool, making speckle tracking more difficult.

## Measurement of Cardiac Function in Neonatal Mice

Cardiac scanning of neonatal mice from day 1 post-partum (P1) is also possible. However, due to their small size and reduced hair-cover, care needs to be taken to ensure that they maintain body temperature (monitored using a neonatal rectal probe) throughout the scan. In addition, neonates can present anesthesia challenges and use of an adaptor and nose cone to ensure sufficient depth of anesthesia is recommended. In addition, dependent on the scanning table utilized, it is often necessary to use copper-tape to extend the electrodes to ensure a good ECG signal is obtained [15]. Ultrasound probes operating up to 50 MHz can be used to image early post-partum neonates and EKV scanning can be used to acquire high temporal and spatial resolution images.

## Measurement of Cardiac Function in Zebrafish

The zebrafish (*Danio rerio*) has increasingly become an important tool in medical research [16], with significant application to the investigation of an extensive range of cardiovascular human diseases [17]. Its small size and corresponding small space requirements, relatively rapid sexual maturity (∼3 months), generation of hundreds of embryos every week and external fertilization makes it increasingly one of the accessible animals for study.

The cardiac function of zebrafish can be imaged using preclinical ultrasound. The zebrafish heart is composed of 4 chambers—sinus venosus, atrium, ventricle and bulbus arteriosus. Light anesthesia can be induced for adult fish by injection of MS222 in the tank water. The fish can then be manipulated and placed on their dorsal side and gently restrained using plasticine that is lightly hand-molded around their bodies. Transducers up to 55 MHz can be used to image the hearts in both long and short axis views. Obtaining an ECG signal from adult zebrafish is challenging so the timing of systole and diastole is determined from cardiac chamber size and spectral Doppler traces with adult heart rates ranging from 120 to 180 beats/min. Additionally, the echogenicity of blood within adult zebrafish is similar to the surrounding tissue structures (**Figure 12**) making the differentiation of chamber volumes challenging.

## Measurement of Cardiac Function in Embryonic Zebrafish

Assessment of cardiac function in embryonic zebrafish using ultrasound is also possible although the optical transparency of

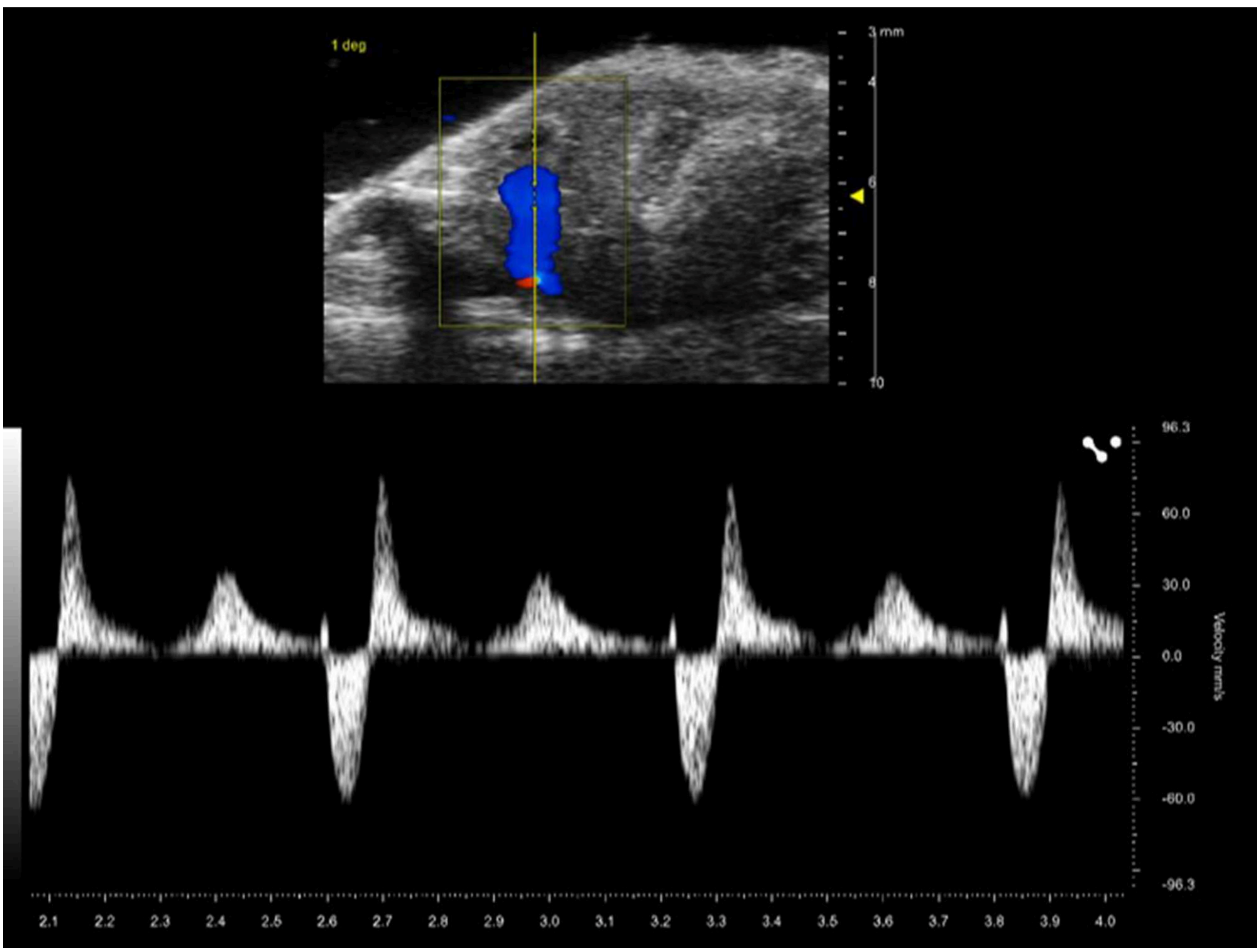


**FIGURE 12 |** Spectral and color Doppler (Duplex) image of adult zebrafish heart.

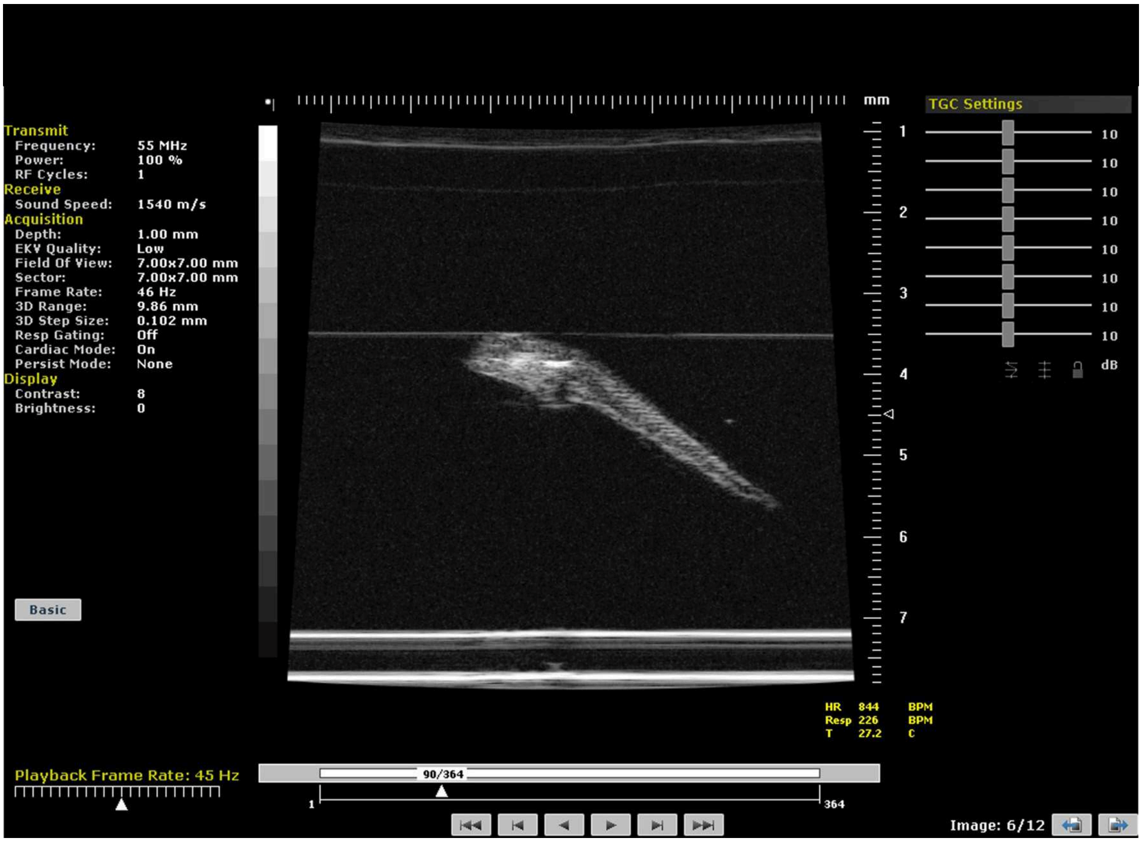


**FIGURE 13 |** B-mode image of a 5 day-post-fertilization zebrafish embryo suspended in agar. Embryo imaged at 55 MHz.

embryos means that cardiac function can also be studied using light microscopy techniques including video edge-detection techniques. Using Doppler ultrasound techniques, a rapid assessment of cardiac function can be undertaken with heart-rates in zebrafish embryos dependent on the temperature but at 28°C are around 200 bpm [18]. Before scanning, embryos are anesthetized in a petri-dish using MS222 and then embedded in agarose. Once the agar has set, fresh aquarium water is added to the dish to limit the effects of anesthesia. Individual embryonic fish can be then identified, and the orientation of their hearts noted using a stereomicroscope. The dish is then placed on top of a heated plate and temperature maintained at 28.5°C whilst scanning is being undertaken with a thermocouple placed adjacent to the embryo to monitor temperature. The ultrasound transducer is then lowered into the water and individual embryos may then be scanned (**Figure 13**).

## PRECLINICAL ULTRASOUND—KIDNEY APPLICATIONS

The kidneys in a mouse can either be scanned with the mouse in supine or prone position. The hair can be removed firstly with electric hair clippers and then with depilatory cream. Unless contrast agents are being used, high temporal resolution is not required for imaging the kidneys so multiple focal positions can be selected across the depth of the kidney. Frequencies used tend be between 30 and 40 MHz dependent on the size of the animal. B-mode imaging is used to locate the kidney with the cortex of the kidney tending to have increased backscatter (brighter) compared to the central medulla. Both kidneys can be scanned in the adult rodent. **Figure 14** shows an image of a mouse kidney and a duplex image using color Doppler to locate the vessel and direction of flow before placing the spectral Doppler sample volume within the vessel. Renal blood flow can be measured and the renal arterial resistive index calculated (peak systolic velocity—the end diastolic velocity) /peak systolic velocity) and its value indicative of the resistance to blood flow in the vascular bed [19].

Vascularity of the kidney can also be studied using ultrasonic contrast agents. When contrast is being used, the mouse is scanned in the prone position avoiding the potential of imaging artifacts caused by intestinal shadowing which can occur when the kidneys are scanned with the mouse in the supine position. Contrast agents are bolus-injected or infused using a syringe pump via the tail-vein. An injection of 50 μl Micromarker (Bracco Research SpA, Geneva, Switzerland) over a 5 second period of a 1:5 dilution is a typical dosing regimen. For acquisition, baseline images are acquired in contrast-specific imaging mode immediately prior to injection of the contrast

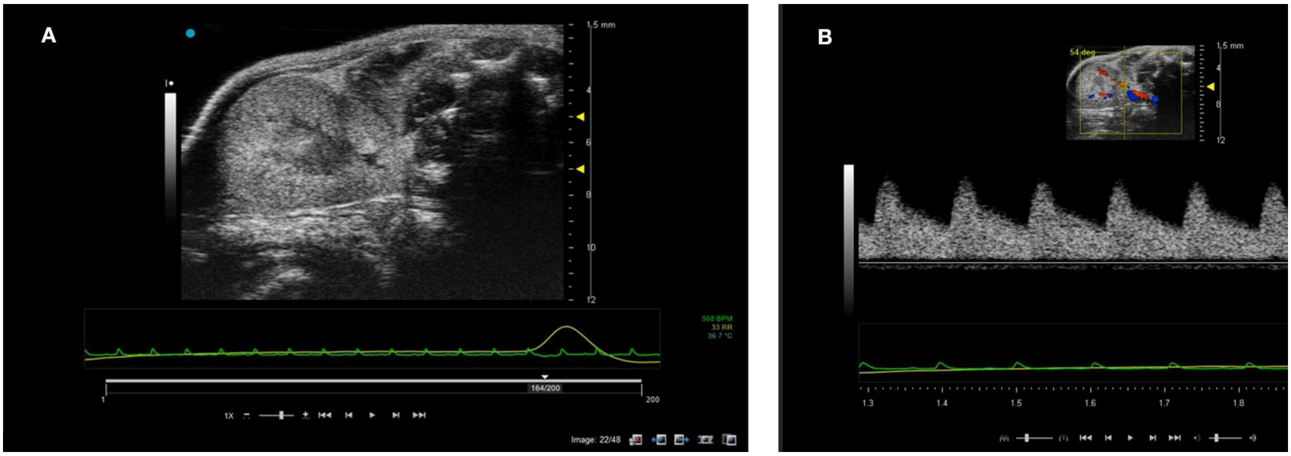


**FIGURE 14 | (A)** B-mode image of kidney. Note the two focal positions on the image. **(B)** Duplex image of mouse kidney. In the Duplex image, the sample volume is localized using the color Doppler box as an indicator to show where the vessel lies and direction of blood flow.

agent and are saved either as a separate data-set or a temporal stamp is placed on the contrast image sequence indicating when contrast is injected and images taken prior to this time-stamp are considered baseline images. An alternative approach is to inject the contrast agent, then destroy the contrast agent within the 2D plane using a short, low-frequency high pressure acoustic pulse. The low-pressure contrast-specific imaging sequence is then reinstated, with the initial frames immediately after these high pressure pulses regarded as baseline images with subsequent frames displaying contrast enhancement. After contrast injection a long sequence of 2D images are obtained, the length of sequence can be pre-set by the user. Once the sequence has been saved, either in-house software or contrast-specific software developed by the manufacturers can be used to map the intensity of the backscattered signal within the regions-of-interest (eg medulla, cortex) to study the perfusion-dynamics. Metrics of interest include area-under-the curve, time-to-peak enhancement, wash-in rate and these can be used as indicators of blood volume and vessel density [20]. In many instances if an ischemic-reperfusion-injury (IRI) mouse model is being studied, one kidney can act as a control and both B-mode and contrast-enhancement data can then be acquired from both kidneys.

## PRECLINICAL ULTRASOUND—LIVER APPLICATIONS

The liver is a large organ within the mouse and consists of four lobes. To image the mouse liver, the mouse is again scanned in the supine position using insonating frequencies between 30 and 40 MHz (**Figure 15**). B-mode ultrasound can be used to image all 4 lobes of the liver while ultrasound enables the portal vein and hepatic artery to be identified and blood velocities measured. Identification and sizing of tumors; staging of non-alcoholic fatty liver disease [21] and determination of fibrosis in the liver can also be achieved at preclinical frequencies. For the assessment of fibrosis in the liver, shear wave imaging techniques can also be used to measure the viscoelastic properties of mouse liver (**Figure 8**) [22]. For preclinical imaging applications, shear waves are generally generated by a lower frequency 20 MHz radiation pulse and a 40 MHz probe used to measure the shear wave propagation within the liver tissue.

## PRECLINICAL—ULTRASOUND: GUIDED INJECTIONS

High-frequency ultrasound can also be used to guide injections into specific areas within the mouse anatomy. For injections into joints, this has recently been shown to have a higher success rate than using traditional anatomic landmarks [23]. Moreover, the less invasive approach of inducing infection within the uterus of a mouse using ultrasound-guided injections of lipopolysaccharide rather than through a mini-laparotomy clearly aligns with the principles of reduction, replacement and refinement which are central considerations for animal research [24]. Injections into fetal brains on externalized embryos, into adult kidneys and pancreas for orthotopic tumor cell injections and into the myocardium can all be undertaken.

## PRECLINICAL ULTRASOUND: LYMPH NODES

Due to their size and location, identification of lymph nodes using high frequency ultrasound can be difficult within the mouse model with many lying deep within the body, encapsulated in fat pads and some, such as the mesenteric lymph node, surrounded by the intestines. However, for cancer models it is important to locate the sentinel lymph node i.e., the node to which the primary tumor drains to first. To this end, both novel contrast agents [25] and novel ultrasound imaging techniques are under development to aid the detection of the location of this node [26].

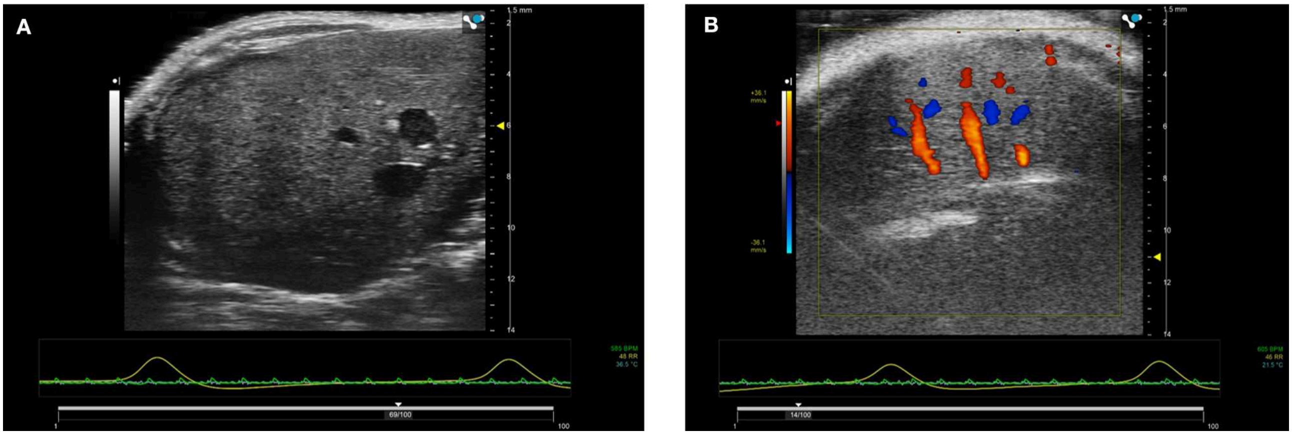


**FIGURE 15 | (A)** B-mode image of right lobe of normal mouse liver. Imaged using 40 MHz probe. **(B)** Color Doppler image of liver showing hepatic blood flow within the liver.

## PRECLINICAL ULTRASOUND: CRANIAL

The use of ultrasound to study the development of the embryonic mouse brain *in utero* is well-established [27, 28] with development of individual embryos tracked throughout gestation. However, the effects of attenuation and resultant aberrations in the ultrasound field caused by the skull in post-natal mice and rats tend to yield poor quality images resulting in the need for either a craniotomy or thinning of the skull to remove or reduce these effects. However in recent years, the use of high frequency *transcranial* ultrasound to study brain vasculature and cortex activation in non-anaethetised mice enabling longitudinal studies on post-natal brain development has been demonstrated [29]. The techniques utilized ultrafast (>500 Hz) compound Doppler techniques where the backscatter from multiple plane-wave emissions acquired at a range of angles are compounded. These early studies show in exquisite detail the future potential of using ultrasound for neuroscience applications.

## DISCUSSION

The real-time nature of ultrasound, its small footprint in the preclinical laboratory and the inexpensive nature of ultrasound imaging compared to MRI and PET/CT, have made it a vital element within the preclinical imaging laboratory. However, the ease of image acquisition using ultrasound by non-specialist researchers has also resulted in a lack of rigor in the reporting of the scanning planes utilized to acquire measurements. This lack of rigor has resulted in a lack of consensus on the "normal" range of physiological values. The effect of heart-rate, temperature, type and depth of anesthesia also influence cardiac measurements and are essential to report in any study [30, 31].

The vast increase in computing power has resulted in reductions in acquisition time of 3D volumes of organs and tumors and 4D acquisitions of the moving heart. Although these extra imaging dimensions will undoubtedly result in more accurate volume measurements it is not yet clear of their potential to provide additional diagnostic information. However, for the non-specialist user of ultrasound acquiring data in 3D enables visualization of structures more easily than from a single 2D imaging plane.

Although widely used within the clinical community, techniques such as strain, strain-rate and shear wave imaging are still gaining traction within the preclinical community. Strain and strain-rate values and the timing of their maximum values within the cardiac cycle may well prove useful as early indicators of myocardial dysfunction similar to that found in clinical studies. The use of shear wave imaging to measure fibrosis in the liver has been developed on one commercial preclinical platform. Certainly, the evidence is encouraging that these techniques can provide useful diagnostic information but more studies are required to validate this for preclinical rodent models and similarly to clinical studies there must be an understanding of the limitations of the technique [4].

Contrast agent development has been ongoing for the last 30 years with initial emphasis on the development of agents to highlight the ultrasound signal from vascular structures. Since contrast-specific imaging techniques rely on generating images based on the non-linear signal scattered from the microbubbles, a transducer of sufficient frequency bandwidth and sensitivity to these signals is required. At the frequencies used in clinical applications this is easily achieved (for a 4 MHz center frequency transducer, second harmonic is at 8 MHz) and transducers used for contrast imaging are usually sensitive up to at least the second harmonic i.e., twice the fundamental transmitted frequency. However, at preclinical frequencies, this is more challenging—in order to capture signals generated at the second harmonic, a much broader bandwidth transducer is required (20 MHz center frequency with second harmonics generated at 40 MHz and sub-harmonics at 10 MHz). Consequently, it tends to be the lower frequency preclinical transducers which have been optimized for contrast-specific imaging and thus, especially in mouse and zebrafish studies, there is an immediate reduction in spatial resolution when undertaking contrast studies. The development of capacitive micromachined ultrasound transducers (CMUTs) may provide a solution for higher resolution contrast microbubble work. CMUTS rely on a change in capacitance for generation of ultrasound rather than piezoelectricity and because they can be micromachined, lightweight 2D arrays are easily manufactured. In addition, they can be operated over a broad bandwidth and hence may be useful in the generation and detection of non-linear signals from contrast agents at higher frequencies necessary for optimal spatial resolution in preclinical animal models.

Super-resolution imaging can be used to generate very high resolution images. Using a sparse distribution of contrast microbubbles whereby single microbubbles are considered as point sources and over multiple ultrafast frame acquisitions composite images can be built up with resolution beyond the diffraction limit of the transmitted ultrasound [32]. Although the images require considerable post-processing, these images are exquisite in the detail. Improved computing power will improve the speed at which these images can be generated.

Although there is only one commercially available contrast agent manufactured for preclinical applications, lipid-encapsulated microbubbles can be made within the lab environment [33]. These microbubbles can be formulated to be used not only as contrast-enhancing agents but also as theranostic agents since targeting ligands can be relatively easily attached to the lipid shells and a drug payload incorporated within or loaded onto the microbubble shells. Although it is known that the drug payload can be released by insonation of the contrast microbubble by a high pressure acoustic pulse the translation of results obtained under highly controlled conditions *in vitro* have not yet been effectively translated to preclinical and clinical studies [34]. However, the development of mono-disperse microbubbles coupled with increasing access to the drive electronics within commercial preclinical scanners is likely to prompt new imaging sequences specifically tailored to these unique microbubble formulations and provide new and exciting theranostic applications.

Finally the use of artificial intelligence (AI) is an exciting area of research undergoing evaluation in the clinical ultrasound workload pipeline. Within clinical ultrasound imaging, AI is currently being evaluated for automatic feature detection, image optimization and quantification. Within the preclinical ultrasound imaging community, AI is now incorporated in one preclinical ultrasound platform to automatically define boundaries and complete left ventricular functional measurements [35]. Although the results suggested that the quality of ultrasound images acquired was a limiting factor for AI quantification, for the non-specialist preclinical ultrasound user AI is likely to make scanners simpler to use, make image analysis easier and more rapid to implement.

## CONCLUSION

In this review article, a range of applications utilizing preclinical ultrasound imaging techniques have been discussed. However, this list is not exhaustive. The range of preclinical applications for which ultrasound imaging is capable of providing meaningful diagnostic information is likely to rapidly increase over the next decade as these scanners become embedded technology within biology laboratories. The increasing use of AI and the use of contrast microbubble formulations allied with unique driving and detection mechanisms will ensure that preclinical ultrasound remains a versatile and cost-effective tool.

## AUTHOR CONTRIBUTIONS

CM wrote the original manuscript. AT reviewed the manuscript and acquired almost all the images.

## FUNDING

This work was supported by The Wellcome Trust - Grant Number 212923/Z/18/Z.

## REFERENCES

1. Foster FS, Pavlin CJ, Harasiewicz KA, Christopher DA, Turnbull DH. Advances in ultrasound biomicroscopy. *Ultrasound Med Biol.* (2000) **26**:1–27. doi: 10.1016/S0301-5629(99)00096-4
2. Polito MV, Stoebe S, Galasso G, De Rosa R, Citro R, Piscione F, et al. Analysis of regional right ventricular function by tissue Doppler imaging in patients with aortic stenosis. *J Cardiovasc Echogr*. (2019) **29**:111–8. doi: 10.4103/jcecho.jcecho_27_19
3. McDicken WN, Thomson A, White A, Toor I, Gray, G, Moran CM, et al. 3D angle-independent Doppler and speckle tracking for the myocardium and blood flow. *Echo Res Pract.* (2019) **6**:105–14. doi: 10.1530/ERP-19-0040
4. Amzulescu MS, de Craene M, Langet H, Pasquet A, Vancraeynest D, Pouleur AC, et al. Myocardial strain imaging: review of general principles, validation, and sources of discrepancies. *European Heart Journal – Cardiovasc Imag.* (2019) **20**:605–19. doi: 10.1093/ehjci/jez041
5. Hoskins PR. Principles of ultrasound elastography. *Ultrasound*. (2012) **20**:8–15. doi: 10.1258/ult.2011.011005
6. Bamber J, Cosgrove D, Dietrich CF, Fromageau J, Bojunga J, Calliada F, et al. EFSUMB guidelines and recommendations on the clinical use of ultrasound elastography. Part 1: Basic principles and technology. *Ultraschall Med*. (2013) **34**:169–84. doi: 10.1055/s-0033-1335205
7. Demene C, Payen T, Dizeux A, Barrois G, Gennisson J-L, Bridal L, et al. 3-D longitudinal imaging of tumor angiogenesis in mice in vivo using ultrafast Doppler tomography. *Ultrasound Med Biol*. (2019) **45**:1284–96. doi: 10.1016/j.ultrasmedbio.2018.12.010
8. Lindsey ML, Kassiri Z, Virag JAI, de Castro Bras LE, Shcerrer-Crosbie M. Guidelines for measuring cardiac physiology in mice. *Am J Physiol Heart Circ Physiol*. (2018) **314**:H733–52. doi: 10.1152/ajpheart.00339.2017
9. Nagueh SF, Smiseth OA, Appleton CP, Byrd IIIBF, Dokainish H, Edvardsen T, et al. Recommendations for the evaluation of left ventricular diastolic function by echocardiography: an update from the American Society of Echocardiography and the European Association of Cardiovascular Imaging. *J Am Soc Echo*. (2016) **29**:277–314. doi: 10.1016/j.echo.2016.01.011
10. Lang RM, Badano LP, Mor-Avi V, Afilalo J, Armstrong A, Ernande L, et al. Recommendations for cardiac chamber quantification by echocardiography in adults: an update from the American Society of Echocardiography and

the European Association of Cardiovascular Imaging. *J Am Soc Echocardiogr*. (2015) **28**:1–39. doi: 10.1016/j.echo.2014.10.003

11. Damen FW, Berman AG, Soepriatna AH, Ellis JM, Buttars SD, Aasa KL, et al. High-frequency 4-Dimensional ultrasound (4DUS): a reliable method for assessing murine cardiac function. *Tomography*. (2017) **3**:180–7. doi: 10.18383/j.tom.2017.00016
12. Bhan A, Sirker A, Zhang J, Protti A, Catibog N, Driver W, et al. High-frequency speckle tracking echocardiography in the assessment of left ventricular function and remodelling after murine myocardial infarction. *Am J Physiol Heart Circ Physiol*. (2014) **306**:H1371–83. doi: 10.1152/ajpheart.00553.2013
13. Boyle JJ, Soepriatna A, Damen F, Rowe RA, Pless RB, Kovacs AGoergen CJ, et al. Regularization-free strain mapping in three dimensions, with applications to cardiac ultrasound. *J Biomed Eng*. (2019) **141**:011010–11. doi: 10.1115/1.4041576
14. Schnelle M, Caitbog N, Zhang M, Nabeebaccus AA, Anderson G, Richards DA, et al. Echocardiographic evaluation of diastolic function in mouse models of heart disease. *J Mol Cell Cardiol*. (2018) **114**:20–8. doi: 10.1016/j.yjmcc.2017.10.006
15. Castellan RFP, Thomson A, Moran CM, Gray GA. Longitudinal assessment of cardiac structural and functional maturation and regeneration following injury in the neonatal mouse using electrocardiogram-gated high-resolution ultrasound. *Ultrasound Med Biol*. (2020) **46**:167–79. doi: 10.1016/j.ultrasmedbio.2019.09.012
16. Lieschke GJ, Currie PD. Animal models of human disease: zebrafish swim into view. *Nat Rev Genet*. (2007) **8**:353–67. doi: 10.1038/nrg2091
17. Wang LW, Hutter IG, Santiago CF, Kesteven SH, Yi Z-Y, Feneley MP, et al. Standardized echocardiographic assessment of cardiac function in normal adult zebrafish and heart disease models. *Dis Model Mech*. (2017) **10**:63–76. doi: 10.1242/dmm.026989
18. Gierten J, Pylatiuk C, Hammouda O, Schock C, Stegmaier J, Wittbrodt J, et al. Automated high-throughput heartbeat quantification in medaka and zebrafish embryos under physiological conditions. *Sci Rep*. (2020) **10**:2046. doi: 10.1038/s41598-020-58563-w
19. Abe M, Akaishi T, Miki T, Miki M, Funamizu Y, Araya K, et al. Influence of renal function and demographic data on intrarenal Doppler ultrasonography. *PLoS ONE*. (2019) **14**:e0221244. doi: 10.1371/journal.pone.0221244
20. Liang S, Gao Y, Liu Y, Qiu C, Chen Y, Zhu S. Contrast-enhanced ultrasound in evaluating of angiogenesis and tumour staging of nasophyryngeal carcinoma in nude mice. *PLoS ONE*. (2019) **14**:e0221638. doi: 10.1371/journal.pone.0221638
21. Fernandez-Dominguez I, Echevarria-Uraga JJ, Gomez N, Luka Z, Wager C, Lu SC, et al. High-frequency ultrasound imaging for longitudinal evaluation of non-alcoholic fatty liver progression in mice. *Ultrasound Med Biol*. (2011) **37**:1161–9. doi: 10.1016/j.ultrasmedbio.2011.04.012
22. Yeh C-Y, Chen B-R, Kuo P-L, Li P-C. *In vivo* measurement of liver elasticity on mice using a single element preclinical ultrasound system. *IEEE Trans Ultrason Ferroelectr Freq Control*. (2015) **62**:1295–307. doi: 10.1109/TUFFC.2014.006953
23. Ruiz A, Bravo D, Duarte A, Adler RS, Raya JG. Accuracy of ultrasound-guided versus landmark-guided intra-articular injection for rat knee joints. *Ultrasound Med Biol*. (2019) **45**:2787–96. doi: 10.1016/j.ultrasmedbio.2019.06.403
24. Rinaldi SF, Makieva S, Frew L, Wade J, Thomson A, Moran CM, et al. Ultrasound-guided intrauterine injection of lipopolysaccharide as a novel model of preterm birth in the mouse. *AM J Pathol*. (2015) **185**:1201–6. doi: 10.1016/j.ajpath.2015.01.009
25. Yoon H, Yarmoska SK, Hannah AS, Yoon C, Hallam KA, Emelianov SY. Contrast-enhanced ultrasound imaging *in vivo* with laser-activated nanodroplets. *Med Phys*. (2017) **44**:3444–9. doi: 10.1002/mp.12269
26. Evertsson M, Kjellmann P, Cinthio M, Andersson R, Tran TA, Zandt R, et al. Combined magnetomotive ultrasound, PET/CT, and MR imaging of 68Ga-labelled superparamagnetic iron oxide nanoparticles in rat sentinel lymph nodes. *Sci Rep*. (2017) **7**:4824. doi: 10.1038/s41598-017-04396-z
27. Aristizabal O, Mamou J, Ketterling JA, Turnbull DH. High-throughput, high-frequency 3-D ultrasound for in utero analysis of embryonic mouse brain development. *Ultrasound Med Biol*. (2013) **39**:2321–32. doi: 10.1016/j.ultrasmedbio.2013.06.015
28. Autuori MC, Pai YJ, Stuckey DJ, Savery D, Marconi AM, Massa V, et al. Use of high-frequency ultrasound to study the prenatal development of cranial neural tube defects and hydrocephalus in Gldc-deficient mice. *Prenat Diagno*. (2017) **37**:273–81. doi: 10.1002/pd.5004
29. Tiran E, Ferrier J, Deffieux T, Gennisson JL, Pezet S, Lenkei Z, et al. Transcranial functional ultrasound imaging in freely moving awake mice and anesthetized young rats without contrast agent. *Ultrasound Med Biol*. (2017) **43**:1679–89. doi: 10.1016/j.ultrasmedbio.2017.03.011
30. Stout D, Berr SS, LeBlanc A, Kalen JD, Osbourne D, Price J, et al. Guidance for methods descriptions used in preclinical imaging papers. *Mol Imag*. (2013) **12**:1–15. doi: 10.2310/7290.2013.00055
31. Pachon RE, Scharf BA, Vatner DE, Vatner SF. Best anesthetics for assessing left ventricular systolic function by echocardiography in mice. *Am J Physiol*. (2015) **308**:H1525–9. doi: 10.1152/ajpheart.00890.2014
32. Errico C, Pierre J, Pezet S, Desailly Y, Lenkei Z, Couture O, et al. Ultrafast ultrasound localization microscopy for deep super-resolution vascular imaging. *Nature*. (2015) **527**:499–502. doi: 10.1038/nature16066
33. Owen J, Kamila S, Shrivastava S, Carugo D, de la Serna JB, Mannaris C, et al. The role of PEG-40-sterate in the production, morphology and stability of microbubbles. *Langmuir*. (2019) **35**:10014–24. doi: 10.1021/acs.langmuir.8b02516
34. Roovers S, Segers T, Lajoinie G, Deprez J, Versluis M, de Smedt SC, et al. The role of ultrasound-driven microbubble dynamics in drug delivery: from microbubble fundaments to clinical translation. *Langmuir*. (2019) **35**:10173–91. doi: 10.1021/acs.langmuir.8b 03779
35. Grune J, Ritter D, Kraker K, Pappritz K, Beyhoff N, Schutte T, et al. Accurate assessment of LV function using the first automated 2D-border detection algorithm for small animals -evaluation and application to models of LV dysfunction. *Cardiovasc Ultrasound*. (2019) **17**:7. doi: 10.1186/s12947-019-0156-0


**Conflict of Interest:** The authors declare that the research was conducted in the absence of any commercial or financial relationships that could be construed as a potential conflict of interest.

frontiers in Physics

ORIGINAL RESEARCH
published: 08 May 2020
doi: 10.3389/fphy.2020.00126

# Protocols for Dual Tracer PET/SPECT Preclinical Imaging

*Julia E. Blower, Jayanta K. Bordoloi, Alex Rigby, Matthew Farleigh, Jana Kim, Hugh O'Brien, Jonathan Jackson, Constantinos Poyiatzis, James Bezer, Kavitha Sunassee, Philip J. Blower and Lefteris Livieratos**

*School of Biomedical Engineering and Imaging Sciences, King's College London, St Thomas' Hospital, London, United Kingdom*

**Background:** Multi-tracer PET/SPECT imaging enables different modality tracers to be present simultaneously, allowing multiple physiological processes to be imaged in the same subject, within a short time-frame. Fluorine-18 and technetium-99m, two commonly used PET and SPECT radionuclides, respectively, possess different emission profiles, offering the potential for imaging one in the presence of the other. However, the impact of the presence of each radionuclide on scanning the other could be significant and lead to confounding results. Here we use combinations of $^{18}$F and $^{99m}$Tc to explore the challenges posed by dual tracer PET/SPECT imaging, and investigate potential practical ways to overcome them.

**Methods:** Mixed-radionuclide $^{18}$F/$^{99m}$Tc phantom PET and SPECT imaging experiments were carried out to determine the crossover effects of each radionuclide on the scans using Mediso nanoScan PET/CT and SPECT/CT small animal scanners.

**Results:** PET scan image quality and quantification were adversely affected by $^{99m}$Tc activities higher than 100 MBq due to a high singles rate increasing dead-time of the detectors. Below 100 MBq $^{99m}$Tc, PET scanner quantification accuracy was preserved. SPECT scan image quality and quantification were adversely affected by the presence of $^{18}$F due to Compton scattering of 511 keV photons leading to over-estimation of $^{99m}$Tc activity and increased noise. However, $^{99m}$Tc:$^{18}$F activity ratios of > 70:1 were found to mitigate this effect completely on the SPECT. A method for correcting for Compton scatter was also explored.

**Conclusion:** Suitable combinations of injection sequence and imaging sequence can be devised to meet specific experimental multi-tracer imaging needs, with only minor or insignificant effects of each radionuclide on the scan of the other.

**Keywords: SPECT, PET, radionuclide, phantom, multi-modality, dual-radionuclide, dead-time, scatter**

OPEN ACCESS

***Edited by:***
*Claudia Kuntner, Austrian Institute of Technology, Austria*

***Reviewed by:***
*Daniele De Paula Faria, University of São Paulo, Brazil*
*Christophe M. Deroose, KU Leuven, Belgium*

****Correspondence:***
*Lefteris Livieratos*
*Lefteris.livieratos@kcl.ac.uk*

***Specialty section:***
*This article was submitted to Medical Physics and Imaging, a section of the journal Frontiers in Physics*

***Received:*** *06 December 2019*
***Accepted:*** *31 March 2020*
***Published:*** *08 May 2020*

***Citation:***
*Blower JE, Bordoloi JK, Rigby A, Farleigh M, Kim J, O'Brien H, Jackson J, Poyiatzis C, Bezer J, Sunassee K, Blower PJ and Livieratos L (2020) Protocols for Dual Tracer PET/SPECT Preclinical Imaging. Front. Phys. 8:126. doi: 10.3389/fphy.2020.00126*

## INTRODUCTION

Individually, PET and SPECT tracers allow us to probe the underlying molecular characteristics of physiological processes, one mechanism at a time. The ability to image one tracer in the presence of another—dual radionuclide PET/SPECT imaging—enables different modality tracers to be present simultaneously, thus allowing multiple processes to be imaged in the same subject, within a much shorter period of time (removing the need to wait for tracer decay). For example, radionuclides fluorine-18 (PET) and technetium-99m (SPECT) each possess different emission profiles and, in theory, can be imaged in the presence of the other, but the impact of each on scanning of the other (i.e. the SPECT and PET scans respectively), could be significant and lead to confounding results.

Acquiring a PET image in the presence of a SPECT radionuclide may introduce additional dead-time (the time after each photon is detected by the scanner during which the system is not able to record another event). Photons emitted from decaying $^{99m}$Tc nuclei are not coincident, and their energy of 140 keV is much lower than the 511 keV PET scanner energy window, so do not contribute to the image data acquired. However, they do interact with the PET detectors, and at high enough flux, can potentially prevent true coincidence events from the positron emitter being recorded. One study in mice showed PET signal loss of 12% due to increased dead-time when $^{99m}$Tc was present in an almost 10-fold higher activity compared to $^{18}$F [1]. It is worth noting that this phenomenon is not specific to mixed radionuclide effects, and dead-time is generally recognized as a performance-limiting factor at high concentrations of PET tracers [2].

Performing a SPECT scan in the presence of a PET radionuclide can also be problematic. If $^{18}$F is present during a $^{99m}$Tc SPECT scan, a proportion of the photons from $^{18}$F positron annihilation will enter the SPECT $^{99m}$Tc energy window (140.5 keV, ±10% i.e. 20% width) due to Compton scattering—the scattering of a photon by a charged particle, resulting in a decrease in energy and change in trajectory of the photon. Previous studies have shown that this down-scatter can generate significant noise and artifacts in the SPECT image [1]. A clinical study showed that the simultaneous use of $^{99m}$Tc-sestamibi and [$^{18}$F]FDG (with a $^{99m}$Tc:$^{18}$F ratio of 3.2:1) resulted in a <6 % increase in the apparent $^{99m}$Tc count rate due to down-scatter from $^{18}$F [3]. This overestimation can be corrected for on clinical scanners by the use of auxiliary energy windows; such methods use the signal in parts of the spectrum outside the photopeak window to estimate an amount of signal to subtract from the imaging window to correct for scatter [4, 5]. However, these methods may be difficult to implement in a preclinical setting due to the low volume of the scatter medium (mice, rats etc.) and hardware and software constraints.

Here, we explore some of the challenges posed by dual tracer PET/SPECT preclinical imaging using radionuclides $^{18}$F and $^{99m}$Tc as examples, and investigate potential practical ways to overcome these obstacles by appropriate experimental design. Mixed-radionuclide $^{18}$F/$^{99m}$Tc phantom experiments were carried out to determine the crossover effects of each radionuclide on the scans, and ultimately, to help design the optimal protocol for *in vivo* dual radionuclide preclinical imaging using $^{18}$F and $^{99m}$Tc.

# METHODS

## PET Scanner Phantoms

Plastic syringes (5 mL) were filled with either $^{18}$F only (5 MBq), $^{99m}$Tc only (5 MBq), or mixtures of $^{18}$F (5 MBq) and increasing amounts of $^{99m}$Tc (5, 50, 100, 150, 200, 250, 350 MBq). Activities of 5 MBq $^{18}$F and < 200 MBq $^{99m}$Tc reflect routine protocols avoiding count-rate limitations of each modality separately. Volumes were made up to 3 mL by addition of water. Radioactivity in each syringe was measured using a dose calibrator (Capintec, Ramsey, NJ, USA), calibrated to the national standard. First the syringe was filled with $^{18}$F only and the activity measured. Then the required activity of $^{99m}$Tc was prepared in a microcentrifuge tube, measured in the dose calibrator, and transferred to the syringe. Residual $^{99m}$Tc activity in the needle and microcentrifuge tube was subtracted from the measured activity. Syringes were inverted several times for uniform distribution of radioactivity. Each syringe was placed in the pre-calibrated nanoPET/CT (Mediso, Budapest, Hungary; system sensitivity 4.67% for a 350–650 keV energy window and 4 ns coincidence window [2]). A 15 min PET scan was acquired with a 5 ns coincidence window in 1–5 coincidence mode. Subsequently, a CT scan was obtained for attenuation correction with a 55 kVp X-ray source, 600 ms exposure time in 180 projections over ∼6 min. PET images were reconstructed in Nucline v.0.21 using Tera-Tomo 3D reconstruction with 4 iterations, 6 subsets, 1–3 coincidence mode, voxel sized 0.4 mm (isotropic), energy window 400–600 keV with attenuation, and scatter correction. Images were analyzed in VivoQuant$^{TM}$ v.3.5, patch 2 software (Invicro LLC., Boston, USA). The activity was determined within a cylindrical ROI slightly larger than the syringe. The same cylindrical ROI was used for each scan and translated or rotated to accommodate variations in the placement of each syringe. The resulting activity from the PET/CT scan was compared to the decay-corrected activity measured in the dose calibrator. Quantitative assessment of image quality was assessed by calculating the coefficient of variation for each image: a small spherical ROI was drawn over the images and the standard deviation within the ROI was divided by the mean within that ROI (**Supplementary Figure 1**).

## SPECT Scanner Phantoms

Plastic microcentrifuge tubes (1.5 mL) were filled with either $^{99m}$Tc only (1 MBq), $^{18}$F only (1 MBq), or mixtures of $^{99m}$Tc (1, 10, 30, 50, 70 MBq) and $^{18}$F (1 MBq) to achieve $^{99m}$Tc:$^{18}$F ratios ranging from 1:1 to 70:1. Volumes were made up to 1 mL by addition of water. Radioactivity in each tube was measured using a dose calibrator (Capintec, Ramsey, NJ, USA), calibrated to the national standard. First the tube was filled with $^{18}$F only and the activity measured. Then the required activity of $^{99m}$Tc was prepared in a second microcentrifuge tube, measured in the dose calibrator, and transferred to the first tube. Residual $^{99m}$Tc activity in the needle and second tube was subtracted from the measured activity. Tubes were inverted several times and vortexed for uniform distribution of radioactivity. Each tube was placed in the pre-calibrated nanoSPECT/CT Silver Upgrade (Mediso Ltd., Budapest, Hungary) and imaged with acquisition time 15 min, frame time of 35 s using a 4-head scanner with 4 × 9 (1 mm) pinhole collimators in helical scanning mode, and CT images with a 55 kVp X-ray source, 1,000 ms exposure time in 180 projections over approximately 9 min. Images were reconstructed in a 256 × 256 matrix, voxel size 0.3 mm (isotropic) using HiSPECT (ScivisGmbH) a reconstruction software package, and images were fused using proprietary VivoQuant™ v.3.5, patch 2 software (Invicro LLC., Boston, USA). The resulting activity from the SPECT/CT scan was compared to the decay-corrected activity measured in the dose calibrator.

## Compton Scatter Data Correction

A method to correct for the effects of 511 keV scattered photons on SPECT image quantification and quality was explored. A set of phantom experiments was performed on the nanoSPECT/CT as proof-of-concept. To obtain an $^{18}$F scatter map, a microcentrifuge tube containing $^{18}$F only (2 MBq, 1 mL) was placed in a 50 mL Falcon tube of water (to mimic preclinical scatter conditions) and a 15 min SPECT scan was acquired, followed by a CT scan. Next, a tube containing a mixture of $^{99m}$Tc (50 MBq) and $^{18}$F (2 MBq) was placed in a 50 mL Falcon tube on the scanner and a 15 min was acquired, followed by a CT scan. Finally, a tube containing $^{99m}$Tc only (50 MBq) was placed on the scanner and a 15 min scan was acquired. The scatter correction was applied by subtracting the $^{18}$F-only SPECT scatter map from the mixed-radionuclide SPECT scan, according to the programming code (Python 3) in **Supplementary Figure 2A**. Automatic scatter correction was applied by scaling the voxel values in both the $^{18}$F-only scan and the mixed-radionuclide scan using their "COUNTS Real World Value Slope" as determined by the SPECT scanner calibration saved in the original dicom files. This allowed a matrix subtraction to be performed where each voxel value corresponded directly with real world counts, as measured by the SPECT. The images were then converted back using the Value Slope for the original mixed-radionuclide image (**Supplementary Figure 2B**). Both the original and scatter-corrected images were analyzed in VivoQuant™ v.3.5, patch 2 software (Invicro LLC., Boston, USA). The activity in each image was determined using the same ROI, within a region slightly larger than the microcentrifuge tube. The activity quantified in both images was compared to the decay-corrected activity measured in the dose calibrator.

It is important to note that the radioactivity quantities used in these experiments reflect the doses appropriate for our scanner system specifications; tested doses may need to be adjusted for other systems.

# RESULTS

## Effect of $^{99m}$Tc on PET Scans

The effect of the presence of SPECT radionuclide $^{99m}$Tc on $^{18}$F PET scans was assessed by the use of phantoms. The PET scanner was calibrated prior to the start of the study following manufacturer procedures; $^{18}$F-only phantoms measured in the dose calibrator and PET scanner showed good agreement (within 2%).

In the presence of up to 100 MBq $^{99m}$Tc, 5 MBq $^{18}$F was accurately quantified by the PET scanner: an over-estimation of < 5% activity was observed in the presence of 50 and 100 MBq $^{99m}$Tc (**Figure 1**). At higher activities of $^{99m}$Tc, PET scanner quantification became less accurate and consistently under-estimated the amount of $^{18}$F present. At 150 MBq of $^{99m}$Tc, $^{18}$F quantification was underestimated by < 10% and became progressively worse with increasing amounts of $^{99m}$Tc: at 350 MBq the scanner was underestimating activity of $^{18}$F by > 80% (**Figure 1**). The live acquisition energy spectrum (**Figure 2**, **Supplementary Figure 3**) showed that at these higher activities of $^{99m}$Tc, photons at 140 keV (attributable to $^{99m}$Tc decay) overwhelmed the detection of 511 keV photons originating from $^{18}$F decay suggesting that the dead-time correction could not cope with the increased singles rate. Note that the true counts decrease considerably when adding $^{99m}$Tc to $^{18}$F (**Supplementary Tables 1**, **2**). However, activity quantification showed low errors up to 100 MBq added $^{99m}$Tc (**Figure 1**) due to the intrinsic dead-time correction of the scanner. Note also that both $^{99m}$Tc only and water have similar numbers of true counts which originate from the intrinsic radiation of the LYSO:Ce crystals.

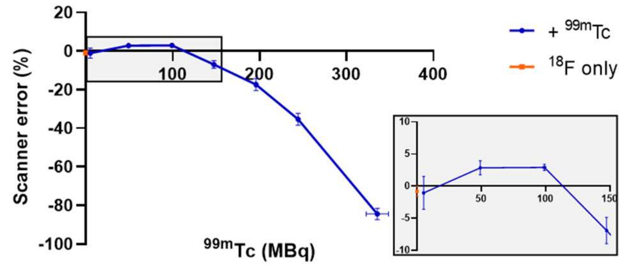


**FIGURE 1 |** Effect of different amounts of $^{99m}$Tc on the accuracy of PET scanner quantification of 5 MBq $^{18}$F. The effect on scanner quantification was assessed by comparing the amount of $^{18}$F measured by the dose calibrator to that measured by the PET scanner; $n = 3$, mean ± SD. Gray box inset provides zoom of 0–150 MBq region.

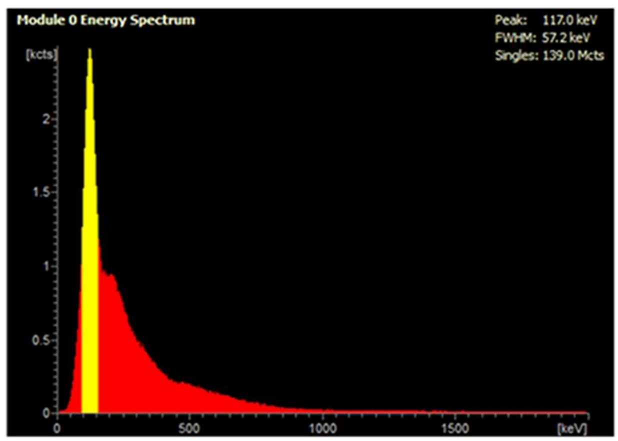


**FIGURE 2 |** Live acquisition energy spectrum obtained during a PET scan of a mixed radionuclide phantom containing 5 MBq $^{18}$F and 250 MBq $^{99m}$Tc. The yellow peak at 140 keV corresponds to the energy of $^{99m}$Tc γ photons, which reduces detection of $^{18}$F coincident photons at 511 keV.

The effect of $^{99m}$Tc on PET image quality was examined (qualitatively) by observing image noise present with increasing $^{99m}$Tc activity in the field-of-view. PET image quality was

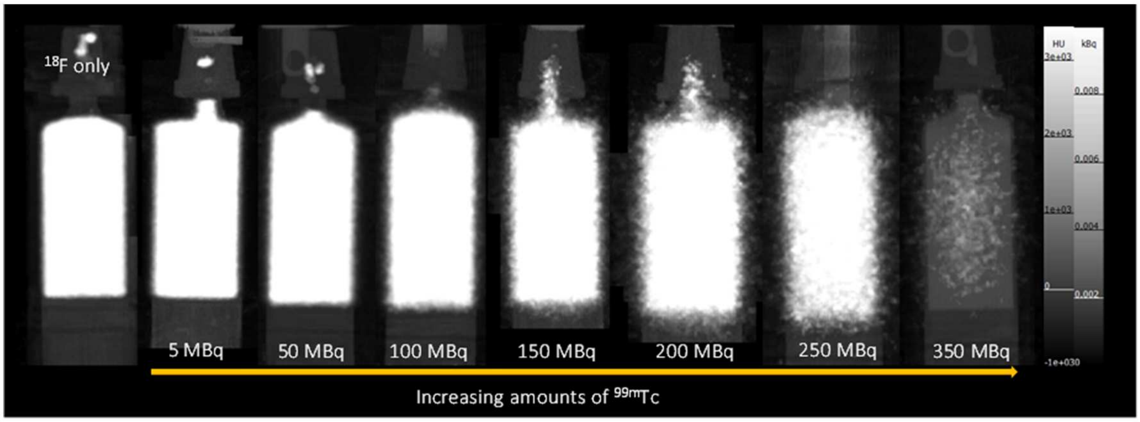


**FIGURE 3 |** PET-CT MIPs of mixed-radionuclide $^{18}$F + $^{99m}$Tc phantoms. Each syringe contains $^{18}$F (5 MBq) mixed with increasing amounts of $^{99m}$Tc (0–350 MBq). An $^{18}$F only (5 MBq) control is included for comparison.

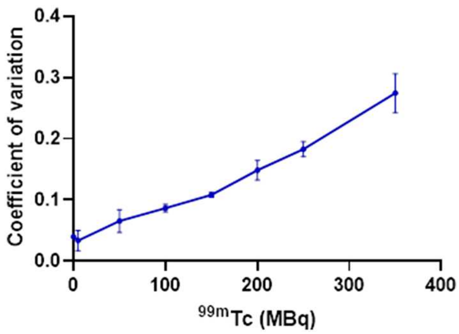


**FIGURE 4 |** Effect of increasing amounts of $^{99m}$Tc on the PET image quality of 5 MBq $^{18}$F, quantified by calculating the coefficient of variation within an ROI for each image (SD/mean); $n = 3$.

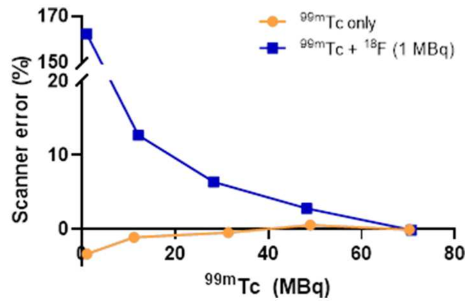


**FIGURE 5 |** Effect of $^{18}$F (1 MBq) on the accuracy of SPECT scanner quantification of increasing amounts of $^{99m}$Tc. The effect on scanner quantification was assessed by comparing the amount of $^{99m}$Tc measured by the dose calibrator to that measured by the SPECT scanner.

maintained in the presence of 5 MBq $^{99m}$Tc when compared to its $^{18}$F-only control (**Figure 3**). Addition of 50 MBq $^{99m}$Tc caused image quality (in terms of signal-to-noise) to deteriorate noticeably, with images becoming more diffuse and lacking in definition. Image quality became progressively worse with increasing amounts of $^{99m}$Tc (**Figure 3**). These qualitative observations were supported by quantitative analysis of the images: the coefficient of variation for each image increased with increasing amounts of $^{99m}$Tc present (**Figure 4**).

## Effect of $^{18}$F on SPECT Scans

The effect of the presence of PET radionuclide $^{18}$F on $^{99m}$Tc SPECT scans was assessed by the use of phantoms. The SPECT scanner calibration was checked prior to the start of the study: $^{99m}$Tc-only phantoms measured in the dose calibrator and SPECT scanner showed good agreement (within 5%).

At equivalent activities of $^{99m}$Tc and $^{18}$F (1:1), quantification of $^{99m}$Tc was poor, with the scanner overestimating $^{99m}$Tc activity by > 150% (1 MBq vs. 2.75 MBq) (**Figure 5**). A 10-fold increase in the activity of $^{99m}$Tc relative to $^{18}$F dramatically improved scanner quantification accuracy, reducing $^{99m}$Tc activity overestimation to 10% (**Figure 5**). Further increases in the quantity of $^{99m}$Tc incrementally improved scanner quantification accuracy in the presence of 1 MBq $^{18}$F. The adverse effects of $^{18}$F on scanner quantification accuracy were mitigated completely when $^{99m}$Tc was in 70-fold excess compared to $^{18}$F (**Figure 5**). SPECT image quality was also affected by the presence of $^{18}$F, with high levels of noise observed at $^{99m}$Tc:$^{18}$F ratios of 1:1 and 10:1 (**Figure 6**). At ratios of 30:1 and above, noise levels observed qualitatively in the images were significantly reduced and images became sharper (**Figure 6**). The acquisition energy spectrum of an $^{18}$F-only phantom on the SPECT scanner showed detection of a range of photon energies, including some in the 140 ± 10% (20% width) keV $^{99m}$Tc energy window (**Figure 7**).

## Compton Scatter Data Correction

The SPECT scanner calibration was checked prior to the start of the study: $^{99m}$Tc-only phantoms measured in the dose calibrator and SPECT scanner showed good agreement (within 1%): a $^{99m}$Tc-only sample measured 50.8 MBq and 51.0 MBq in the

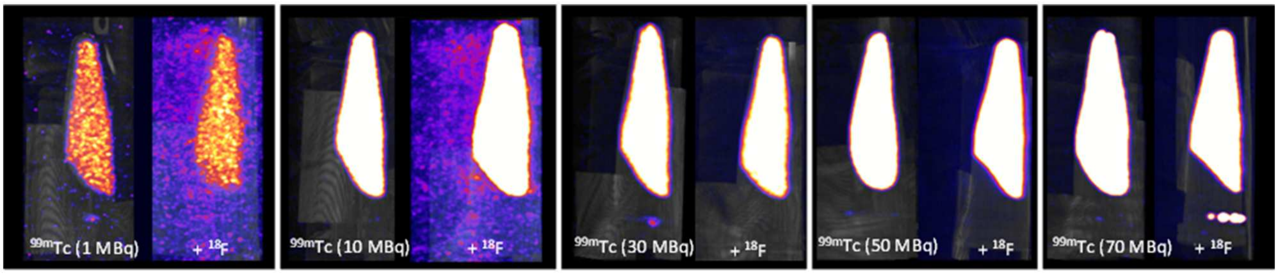


**FIGURE 6 |** SPECT-CT MIPs of $^{99m}$Tc only and mixed-radionuclide $^{99m}$Tc + $^{18}$F phantoms. Each tube contained either $^{99m}$Tc only (1, 10, 30, 50, 70 MBq) or $^{99m}$Tc (1, 10, 30, 50, 70 MBq) mixed with $^{18}$F (1 MBq). All images scaled to the same threshold and intensity.

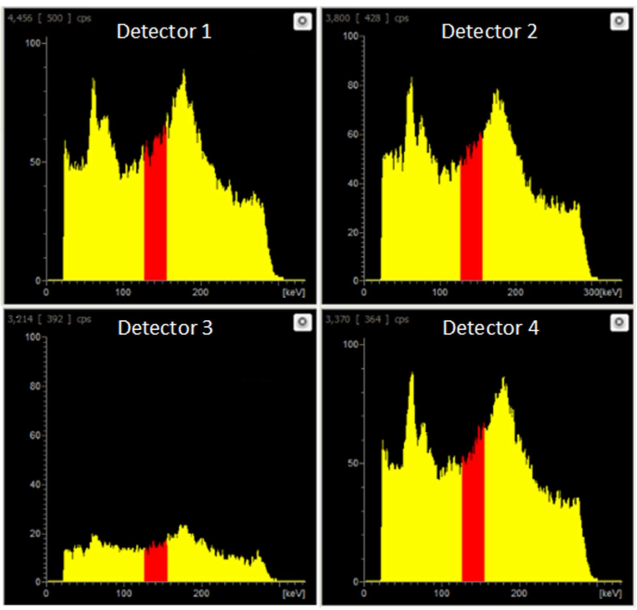


**FIGURE 7 |** Live acquisition energy spectrum obtained during a SPECT scan of an $^{18}$F-only phantom (1 MBq). A range of energies is evident, including energies in the 140.5 keV ±10% (i.e. 20% width) $^{99m}$Tc energy window (red).

dose calibrator and the SPECT scanner, respectively. The mixed-radionuclide sample containing $^{18}$F (2 MBq) plus $^{99m}$Tc (50.7 MBq, measured by dose calibrator) was quantified as 55.84 MBq on the SPECT scanner in the 140 ± 10% keV window, an over-estimate of 10% resulting from the contribution of Compton-scattered 511 keV photons to the 140 keV window. Upon subtraction of the $^{18}$F-only phantom counts from the mixed $^{18}$F+$^{99m}$Tc counts, the resulting "scatter-corrected" data were quantified at 51.89 MBq, an over-estimation of only 2%. The coefficient of variation for the original image and scatter-corrected image was 0.098 and 0.102, respectively. The resulting image was visibly similar to the $^{99m}$Tc-only control image, showing a substantial reduction in noise and comparable activity compared to the mixed-radionuclide image (**Figure 8**). This could be implemented in practice as data correction: initially a SPECT scan of the $^{18}$F present is acquired before injection of $^{99m}$Tc, to establish the $^{18}$F down-scatter contribution; following injection of $^{99m}$Tc and acquisition of the SPECT scan, the $^{18}$F down-scatter component is subtracted to provide an accurate $^{99m}$Tc uptake distribution.

## DISCUSSION

Our specific motivation for this work originated from the need to compare directly two PET tracers for the same biological target, both labeled with $^{18}$F, to understand subtle differences in behavior between the two tracers *in vivo*. Since the two tracers were labeled with the same PET radionuclide, and hence had identical physical emission profiles, they could not be compared *simultaneously* in the same animal. A consecutive imaging protocol (administration and PET imaging of the first tracer, followed by administration and PET imaging of the second tracer in the same animal) was possible, in theory. However, the need to allow the first tracer to decay sufficiently to prevent residual activity interfering with the second scan, combined with limits on animal exposure to anesthesia and recovery time (our specific animal license requires a minimum of 3 h between mouse recovery and being re-anesthetized) means the imposed delay between tracer administration could lead to significant physiological changes (effects of anesthesia, metabolism, tumor size etc.) in the animal between the two scans. Similarly, evaluating each tracer in a different animal introduces inherent variability between mice, thus no longer maintaining a controlled environment for accurate tracer comparison.

Our solution was to adopt a paired-control approach, using a single SPECT ($^{99m}$Tc) tracer (for the same biological target) in conjunction with each PET tracer, where each tracer can be imaged in the presence of the other because $^{18}$F and $^{99m}$Tc possess different emission profiles. Thus, the need to understand the impact of each radionuclide on the scanning of the other presented itself, and mixed-radionuclide $^{18}$F/$^{99m}$Tc phantom experiments were carried out to determine the crossover effects of each radionuclide on the scans. Of course, dual radionuclide PET/SPECT imaging is not only relevant to our niche example; it is of value more generally, to enable evaluation of different, but related, biological systems

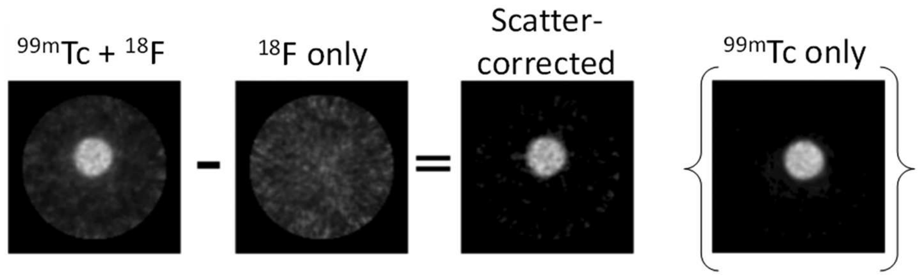


**FIGURE 8 |** Proof-of-concept for SPECT scatter data correction method. The $^{18}$F-only scatter map image was subtracted from the $^{99m}$Tc + $^{18}$F mixed-radionuclide image to achieve the final scatter-corrected image. The $^{99m}$Tc-only image is included for comparison.

at (almost) the same time using different tracers labeled with different radionuclides.

Firstly we examined the effect of $^{99m}$Tc on $^{18}$F PET scans. Dead-time effects are observed on the PET scanner when there is too much of any radionuclide. A previous Noise Equivalent Counting (NEC) study performed on our PET scanner showed count-rate peaks at 430 kcps at 36 MBq and 130 kcps at 27 MBq for $^{18}$F in mouse and rat phantoms, respectively [2]. The injected activity for a mouse in our PET scanner is typically 2–10 MBq; 5 MBq $^{18}$F was used in this phantom experiment, which is well below the NEC peaks, and therefore quantification is not affected by dead-time when this quantity of $^{18}$F alone is used. However, when combined with $^{99m}$Tc, we must assess the contribution of $^{99m}$Tc photons emitted to scanner dead-time, and hence the effects on PET image quality and quantification. We see that when combined with lower amounts of $^{99m}$Tc (<100 MBq), $^{18}$F quantification is unaffected, but 140 keV photon contribution from higher amounts of $^{99m}$Tc (>150 MBq) prevents coincident 511 keV PET photons being recorded, causing the scanner to significantly underestimate $^{18}$F activity. In practice, a typical $^{99m}$Tc SPECT scan requires only 10–40 MBq injection. These results enable us to assess the feasibility of a hypothetical imaging protocol as follows: (i) administration of SPECT tracer ($^{99m}$Tc, 40 MBq) (ii) SPECT image acquisition (1 h) (iii) administration of PET tracer ($^{18}$F, 5 MBq) (iv) PET image acquisition (1 h), in the presence of $^{99m}$Tc. Our phantom studies show that at these levels of activity, $^{18}$F PET quantification is not affected by the presence of $^{99m}$Tc. However, even at levels of $^{99m}$Tc where quantification accuracy is maintained, PET image quality does appear to be compromised. In the presence of 50 MBq $^{99m}$Tc, images becomes a little more diffuse with reduced definition. While this slight decrease in image quality is unlikely to be problematic for the majority of imaging scenarios, it could make identification and visualization of very small biological structures (e.g. tumor metastases) more difficult.

Next we examined the effect of $^{18}$F on $^{99m}$Tc SPECT scans. In the presence of $^{18}$F, $^{99m}$Tc SPECT image quantification and quality were affected by Compton scatter, leading to an over-estimation of $^{99m}$Tc and increase in noise. However, when $^{99m}$Tc activity was 70-fold higher than $^{18}$F this over-estimation could be mitigated completely and image quality preserved.

In practice, a good 1 h dynamic PET scan can be achieved with 3 MBq $^{18}$F alone and, taking into account decay ($t_{1/2}$ = 109.8 min), no more than 2 MBq of $^{18}$F tracer would be residual in the animal after the 1 h scan. Our results enable assessment of the feasibility of an alternative hypothetical imaging protocol, as follows: (i) administration of PET tracer ($^{18}$F, 3 MBq) (ii) PET image acquisition (1 h) (iii) administration of SPECT tracer ($^{99m}$Tc, > 140 MBq, to maintain 70:1 $^{99m}$Tc:$^{18}$F ratio) (iv) SPECT image acquisition (1 h) in the presence of $^{18}$F. Our phantom studies show that at these radionuclide activity ratios, $^{99m}$Tc SPECT image quantification and quality is not affected by the presence of $^{18}$F. However, although we can control this radionuclide activity ratio at the time of SPECT tracer injection, we cannot know if this 70:1 ratio is maintained *in vivo*—the biodistribution of both PET and SPECT tracers would need to be similar for this to be true. This, plus the need for otherwise unnecessarily high levels of radioactivity, makes this protocol an inferior option.

From a biological perspective, it would be preferable to co-administer both tracers at the same time, but based on our findings, there is no combination of imaging sequence and tracer quantity (without waiting several hours for radionuclide decay) that would allow the two radionuclides to be injected *simultaneously* and each scanned in the presence of the other, without having a major effect on image quality and quantification. Furthermore, images of each tracer at the same time after injection could not be obtained with simultaneous injection.

We also explored simple computational methods for correcting for the effects of Compton scatter on the SPECT scanner. One approach involves using the $^{18}$F-only PET scan to identify sources of $^{18}$F, and then subtracting this from the mixed-radionuclide SPECT scan. This process becomes quite complex because we are attempting to combine data collected from two different and essentially unrelated pieces of equipment; differences between the PET and SPECT scanners must be accounted for and this requires additional calibration steps to be done for each set of measurements obtained on the scanners. An additional complication of this method is the need to maintain animal position between the two scanners so that images can be accurately co-registered. Even with the most careful transfer between scanners (the animal bed is compatible with both scanners and could be transferred without removing the mouse), a registration step would be required using the CT scans of the mice to obtain a "best case" match for the scatter map. While it would be possible to produce a warp field for the mouse shift in position, this quickly becomes an overly-complex solution. A more practical approach might therefore be achieved using the SPECT scanner directly to obtain an $^{18}$F scatter map, prior to injection of $^{99m}$Tc. This method would involve incorporating an additional SPECT scan into the scanning protocol and makes the assumption that scatter present in the $^{18}$F-only scatter map is comparable to that obtained when the SPECT tracer is also present (i.e. no change in biodistribution between SPECT scans). The scatter map must also be corrected for radionuclide decay between scans. Our proof-of-concept phantom experiment demonstrated that this scatter-correction method could be used easily and successfully to remove noise caused by Compton scattering of $^{18}$F photons. The proposed preclinical imaging protocol would then be as follows: (i) administration of PET tracer ($^{18}$F) (ii) PET image acquisition (iii) SPECT image acquisition (to obtain $^{18}$F scatter map) (iv) administration of SPECT tracer ($^{99m}$Tc) (v) SPECT image acquisition (in the presence of $^{18}$F) (vi) scatter map image subtraction. This approach builds the scatter map acquisition into the scanning protocol, and would therefore be applicable to any PET/SPECT radionuclide combination, any radionuclide activity, and any scanner model, without requiring calibration for each experiment, making this method an attractive option for dual radionuclide PET/SPECT imaging.

The ability to obtain accurate parallel scans with PET and SPECT tracers would allow the limits of molecular imaging to be extended and would be useful for comparison of different radiotracers or to image multiple related molecular processes simultaneously to obtain a deeper understanding of interlinked processes. Examples could include temporospatial mapping of anti-cancer drug delivery (e.g. via liposomal formulation) and response in relation to the disease site [6], and in advanced cell-based therapies where the trafficking of cells to disease sites has to be quantified alongside mapping of the disease and response to therapy. Similarly, SPECT imaging of the biodistribution of therapeutic radionuclides that emit both imageable gamma photons (e.g. $^{177}$Lu, $^{67}$Cu, $^{188}$Re) could be performed alongside PET imaging (e.g. with [$^{18}$F]FDG or other tracer) of metabolic response to therapy. It would also enable imaging of multiple molecular characteristics of disease in an animal to obtain metabolic and gene expression profiles or characterize diseases such as cancer where heterogeneity is to be expected.

## CONCLUSION

Sequential PET and SPECT data acquisition whilst both positron- and gamma-emitters are present is feasible under certain conditions without substantial influence on image quantification accuracy. Suitable combinations of injection sequence and imaging sequence can be devised to match the biological requirements of a particular experiment, using existing commercial small animal PET and SPECT scanners, with only minor or insignificant effects of each radionuclide on the scan of the other. However, simultaneous tracer injection is not feasible under any combination of imaging sequence and tracer quantity, and does not allow images of each tracer to be obtained at the same time after injection.

## DATA AVAILABILITY STATEMENT

The datasets generated for this study are available on request to the corresponding author.

## AUTHOR CONTRIBUTIONS

LL and PB contributed conception of the study. LL, PB, JEB, JKB, AR, MF, HO'B, JJ, KS, JB, and CP contributed design of the study. JEB, JKB, AR, MF, JK, and CP contributed phantom data acquisition. JKB, JK, JEB, and KS contributed image analysis. HO'B and JJ contributed code development. JEB wrote the first draft of the manuscript. LL, PB, JEB, KS, and JK contributed to manuscript revision. All authors read and approved the submitted version.

## FUNDING

This work was supported by the Wellcome EPSRC Centre for Medical Engineering at KCL [grant number WT 203148/Z/16/Z], the KCL/UCL Comprehensive Cancer Imaging Centre funded by CRUK and EPSRC in association with the MRC and DoH (England), the EPSRC Centre for Doctoral Training in Medical Imaging at King's College London and Imperial College London, Wellcome Multi User Equipment Grant A multiuser radioanalytical facility for molecular imaging and radionuclide therapy research and the National Institute for Health Research (NIHR) Biomedical Research Centre based at Guy's and St Thomas' NHS Foundation Trust and KCL [grant number IS-BRC-1215-20006]. PET and SPECT scanning equipment at KCL was funded by an equipment grant from the Wellcome Trust under grant number WT 084052/Z/07/Z. The views expressed are those of the authors and not necessarily those of the NHS, the NIHR or the Department of Health.

## ACKNOWLEDGMENTS

The authors would like to thank the King's College London & Guy's and St Thomas' PET Centre for the supply of $^{18}$F, and Guy's and St Thomas' NHS Trust Radiopharmacy for the supply of $^{99m}$Tc.

## SUPPLEMENTARY MATERIAL

The Supplementary Material for this article can be found online at: https://www.frontiersin.org/articles/10.3389/fphy.2020.00126/full#supplementary-material

## REFERENCES


1. Chapman SE, Diener JM, Sasser TA, Correcher C, Gonzalez AJ, Avermaete TV, et al. Dual tracer imaging of SPECT and PET probes in living mice using a sequential protocol. *Am J Nucl Med Mol Imaging*. (2012) **2**:405–14.
2. Szanda I, Mackewn J, Patay G, Major P, Sunassee K, Mullen GE, et al. National Electrical Manufacturers Association NU-4 performance evaluation of the PET component of the NanoPET/CT preclinical PET/CT scanner. *J Nucl Med*. (2011) **52**:1741–7. doi: 10.2967/jnumed.111.088260
3. Sandler MP, Videlefsky S, Delbeke D, Patton JA, Meyerowitz C, Martin WH, et al. Evaluation of myocardial-ischemia using a rest metabolism stress perfusion protocol with F-18 deoxyglucose technetium-99m midi and dual-isotope simultaneous-acquisition single-photon emission computed-tomography. *J Am Coll Cardiol*. (1995) **26**:870–8. doi: 10.1016/0735-1097(95)00295-6
4. Ichihara T, Ogawa K, Motomura N, Kubo A, Hashimoto S. Compton scatter compensation using the triple-energy window method for single-isotope and dual-isotope spect. *J Nucl Med*. (1993) **34**:2216–21.
5. Wu J, Ma TY, Liu H, Xia Y, Chen S, Wang S, et al. Feasibility studies of simultaneous PET and SPECT dual-tracer imaging with a stationary multi-pinhole collimator inserted to animal PET detector. *IEEE Nucl Sci Conf R*. (2012) **2012**:2788–91. doi: 10.1109/NSSMIC.2012.6551636
6. Man F, Lim L, Volpe A, Gabizon A, Shmeeda H, Draper B, et al. *In vivo* PET tracking of (89)Zr-labeled Vgamma9Vdelta2 T cells to mouse xenograft breast tumors activated with liposomal alendronate. *Mol Ther*. (2019) **27**:219–29. doi: 10.1016/j.ymthe.2018.10.006


**Conflict of Interest:** The authors declare that the research was conducted in the absence of any commercial or financial relationships that could be construed as a potential conflict of interest.

REVIEW
published: 25 May 2020
doi: 10.3389/fphy.2020.00151

# *In vivo* PET/MRI Imaging of the Chorioallantoic Membrane

Gordon Winter[1], Andrea B. F. Koch[1], Jessica Löffler[1,2], Fedor Jelezko[3], Mika Lindén[4], Hao Li[2,5], Alireza Abaei[2], Zhi Zuo[2,6], Ambros J. Beer[1] and Volker Rasche[2,7]*

[1] Department of Nuclear Medicine, Ulm University Medical Center, Ulm, Germany, [2] Core Facility Small Animal MRI, Medical Faculty, Ulm University, Ulm, Germany, [3] Institute for Quantum Optics, Ulm University, Ulm, Germany, [4] Institute for Inorganic Chemistry II, Ulm University, Ulm, Germany, [5] Department of Cardiology, The Second Hospital of Shandong University, Jinan, China, [6] Department of Cardiology, Zhongda Hospital, Medical School of Southeast University, Nanjing, China, [7] Department of Internal Medicine 2, Ulm University Medical Center, Ulm, Germany

The Hen's Egg Test Chorioallantoic Membrane (HET-CAM) of fertilized chick eggs represents a unique model for biomedical research. With its steadily increasing use, non-invasive *in ovo* imaging for longitudinal direct quantification of the biodistribution of compounds or monitoring of surrogate markers has been introduced. The full range of imaging methods has been applied to the HET-CAM model. From the current perspective, Magnetic Resonance Imaging (MRI) and Positron Emission Tomography (PET) appear promising techniques, providing detailed anatomical and functional information (MRI) and excellent sensitivity (PET). Especially by combining both techniques, the required sensitivity and anatomical localization of the signal source renders feasible. In the following, a review of recent applications of MRI and PET for *in ovo* imaging with a special focus on techniques for imaging *xenotransplanted* tumors on the CAM will be provided.

**Keywords: HET-CAM, MRI, PET, imaging, biodistribution, targeting**

OPEN ACCESS

***Edited by:***
*Claudia Kuntner,*
*Austrian Institute of Technology (AIT), Austria*

***Reviewed by:***
*Violaine See,*
*University of Liverpool, United Kingdom*
*Anne Herrmann,*
*University of Liverpool, United Kingdom*

***Correspondence:***
*Volker Rasche*
*volker.rasche@uni-ulm.de*

***Specialty section:***
*This article was submitted to Medical Physics and Imaging, a section of the journal Frontiers in Physics*

***Received:*** *02 December 2019*
***Accepted:*** *15 April 2020*
***Published:*** *25 May 2020*

***Citation:***
*Winter G, Koch ABF, Löffler J, Jelezko F, Lindén M, Li H, Abaei A, Zuo Z, Beer AJ and Rasche V (2020) In vivo PET/MRI Imaging of the Chorioallantoic Membrane. Front. Phys. 8:151. doi: 10.3389/fphy.2020.00151*

## INTRODUCTION

The Hen's Egg Test Chorioallantoic-Membrane (HET-CAM) of fertilized chicken eggs represents a unique model for biomedical research. During the development, the mesodermal layers of the allantois and chorion form the chorioallantoic membrane (CAM). This structure forms a rich vascular network enabling to study tissue grafts, tumor growth, metastasis formation, wound healing, drug delivery, toxicologic analysis, angiogenic and anti-angiogenic molecules [1].

The HET-CAM represents a relatively simple, quick, and low-cost model that allows screening of a large number of pharmacological samples in a short time. It has been successfully used to study cancer progression and its pharmacological treatment [2–8], angiogenesis [9], pharmacokinetics [10], properties of novel nanomaterials [9, 11], or as a model system to study microsurgical instruments and techniques [12]. Especially for xenotransplantation tumor models, the HET-CAM offers various advantages in comparison to the murine models. Since the development of the lymphoid system starts in the late stage of incubation, the HET-CAM model represents a naturally immunodeficient host, enabling xenotransplantation of many kinds of tumors without species-specific limitations [11]. The blood vessel network of the CAM thereby provides an excellent environment for primary tumor formation and a basis for angiogenic blood vessel formation [12]. Human cell line derived [13] xenografts are considered an increasingly valuable tool in oncology potentially providing biologically models of many different cancer types. Where immunodeficient rodent models pose barriers to widespread application due to cost and efficiency constraints, the HET-CAM model renders as efficient model especially for initial testing of tumor progression [10, 14–16], in many countries not requiring any approval for animal experiments, if sacrificed before hatching.

Due to its simplicity, the HET-CAM model appears as ideal platform for initial testing of pharmacological compounds and tissue properties, including biodistribution assessment or efficacy assessment of new compounds [1, 8, 13–19].

With the increasing use of the HET-CAM model and the need for longitudinal monitoring, non-invasive *in ovo* imaging of the chick embryo and especially the CAM has gained interest over recent years. Optical methods like optical coherence tomography (OCT) and Doppler techniques have successfully been applied for deriving functional and physiological properties of the embryo [20–38]. Three-dimensional microcomputed tomography (μCT) has been applied *in ovo*, especially in the field of bone volume and mineral density assessment [39–46]. With the recent advances in magnetic resonance tomography (MRI) its application to *in ovo* imaging has rendered feasible and many applications of the technique in the live embryo as well as after sacrification have been reported for different scientific fields, including embryonal development [47–54], ophthalmology [48–57], oncology [58–63], metabolic assessment [54, 64], and initial testing of the biodistribution of new compounds [65–67]. Further, nuclear imaging methods have been translated to *in ovo* imaging, mainly for initial testing of new labeling strategies [19, 68–71].

Considering the capability of the HET-CAM model for monitoring the growth and progression of xenotransplanted tumors rises a huge potential for its use in the evaluation of the biodistribution of new compounds, especially in combination with specific targeting strategies. In this context the combination of the multi-contrast capabilities of MRI with the outstanding sensitivity of positron emission tomography (PET) appears promising. In the following a review of recent applications of MRI and PET for *in ovo* imaging with a special focus on techniques for imaging xenotransplanted tumors on the CAM will be provided.

## THE HET-CAM MODEL

In preclinical research and drug development can-cer cell lines (CCL) are frequently used. However, in culture, CCLs often fail to retain morphology, cellular heterogeneity, and molecular profiles of the donor tissue [72, 73], and drug performance in xenografts may not perfectly reflect clinical efficacy [74]. The success of new drugs in oncology requires preclinical models that render the full heterogeneity and pathophysiology of patient tumors, and CCL or patient-derived xenografts (PDX) may mimic physiological drug effects [75, 76].

A broad range of applications for CCL and PDX have been reported using rodent models as host and their efficient use in prediction of response, development of biomarkers, and monitoring and identification of efficient treatment regimens has been proven [77]. Despite their frequent use, rodent models have practical and scientific limitations. In many applications, rodent models have shown a very limited success rate in engraftment. Successful engraftment often takes several months. Further high, often prohibitive costs and resources are required for keeping rodents in an appropriate facility under proper hygienic conditions. They are labor-intensive, time-consuming, and require ethical approval by the regulatory authorities.

The HET-CAM model represents a well-established alternative *in vivo* assay. It presents a highly vascularized extra-embryonic membrane, which is connected to the embryo through a continuous circulatory system. Even though T and B cells can be detected in the chick embryo immune system by embryo development day (EDD) 11 and 12, full immune competence is not developed until EDD 18 [16]. The HET-CAM is a low-cost model with the limita-tion of developing a nonspecific inflammatory response after EDD 15 [1]. Xenotransplantation and growth of cancer cell lines on the CAM is well-established (**Figure 1**) and has amongst others been applied for initial assessment of the efficacy of anticancer drugs [78]. Compared to the rodent models, tumor formation on the CAM is fast, with graft vascularization and thus interface to the chick embryo vascular system normally established already after 2-5 days [79].

For xenotransplantation, fertilized chicken eggs e.g., White Leghorn (*Gallus domesticus*) are purchased from a hatchery and maintained at 37.8°C and a 60% relative humidity atmosphere for the whole incubation period. Upon arrival the eggs are carefully cleaned (e.g., by 70% ethanol solution) and incubation is started (EDD 0). After 4 days (EDD 4) of incubation the eggs are fenestrated and analyzed for fertilization by visual assessment of the CAM vascularization and heartbeat of the embryo. The shell access window is sealed to prevent contamination and the egg placed back into the incubator. Cancer cells are seeded on the CAM and a solid tumor, well interfaced to the extra-embryonic vascular system, forms within few days [1, 16]. The viability of the embryos needs to be monitored daily by checking the CAM vasculature for blood flow, physiological embryo movement, and the growth of the chick embryo according to Hamburger and Hamilton [80].

## MAGNETIC RESONANCE IMAGING (MRI)

With its versatile image contrast, MRI raised interest in imaging of chick embryos already in the 80s. In 1986, Bone et al. [81, 82] reported first three-dimensional MR microscopy on the live chick embryo. At a 1.5T prototype system with dedicated gradient system and receive coil, they achieved a spatial resolution of 200 x 200 x 1200 $\mu m^3$ with T1 and T2 weighting, applying partial saturation (PS) and spin echo (SE) 3D-Fourier imaging techniques (3D-FT). To minimize motion-induced image artifacts, the chick embryo was immobilized by placing the egg in ice chips between 20 (EDD 11) and 90 (EDD 15) minutes. Imaging was performed at room temperature. Even though the spatial resolution and hence the fidelity of the anatomical details was still limited, Bone et al. clearly showed the potential combination of *in ovo* imaging and MRI as basis for further MRI studies. Improvements in spatial resolution were

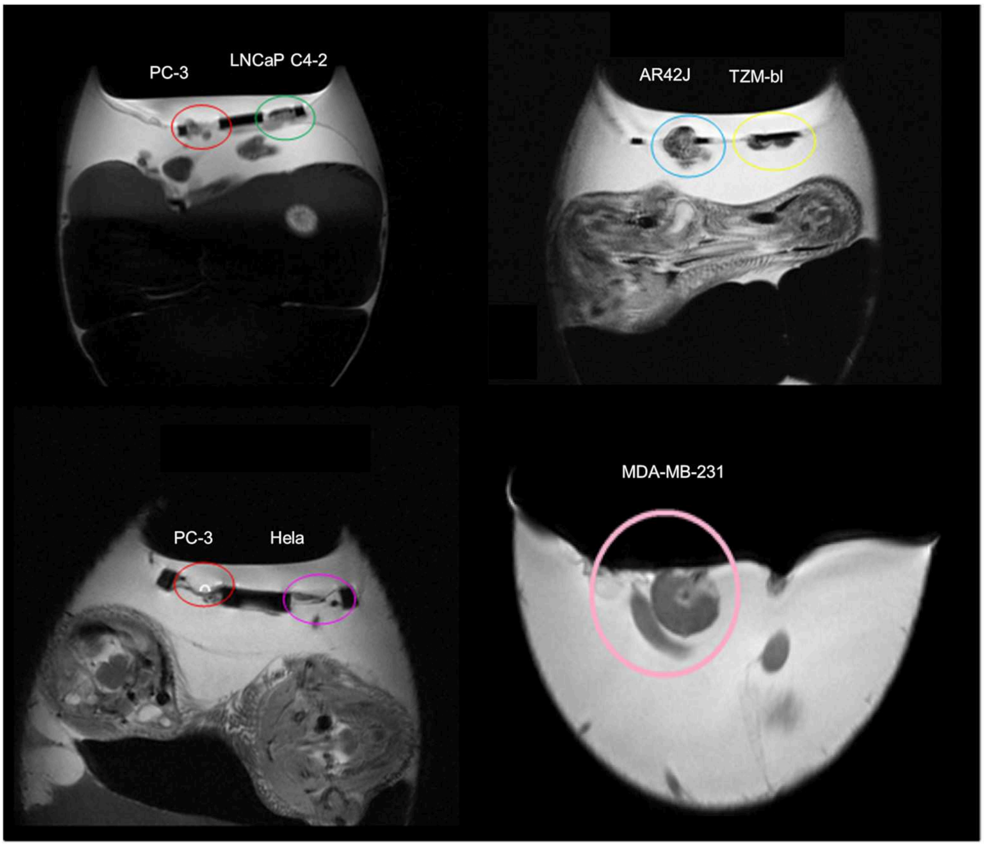


**FIGURE 1 |** Magnetic resonance images (MRI) of xenotransplanted tumors grown on the chorioallantoic membrane (CAM) from different cell lines (prostate cancer: PC-3, LNCaP C4-2; pancreas cancer: AR42J; adenocarcinoma: TZM-bl; cervical cancer: HELA; breast cancer: MDA-MB-231). Unpublished imaging material provided by Winter and Li.

reported by Effmann et al. [83], who used an implantable 18 mm diameter RF coil wrapped around the chick embryo, inductively coupled to an outside MR receiver [84]. With the resulting gain in signal-to-noise ratio (SNR), the PS 3D-FT could provide images with spatial resolutions of up to 50 x 50 x 600 $\mu m^3$ within 1-2 h scan times.

Assessment of metabolic developments by phosphorus $^{31}P$ MR spectroscopy (MRS) in correlation with anatomic developments were first reported by Moseley et al. in 1989 [54], who could clearly demonstrate the decrease of the observable $^{31}P$ volume by 80% indicating the respective tissue uptake. Further spectroscopy work was performed by Lirette et al. [85] for longitudinal quantification of the fat/water ratio ($^{1}H$ MRS) and the phosphormono-/phosphordiester ratio ($^{31}P$ MRS). Data were acquired with a 5 cm—diameter surface coil, in which the eggs were placed centrally. Acquisition times were below 1 h. Embryo motion was controlled by applying 1–2% halothane during scanning. Peebles et al. [86] applied $^{1}H$ MRS for monitoring of brain metabolites and diffusion MRI for assessment of changes in the apparent diffusion coefficient (ADC) in the brain during hypoxia. Immobilization of the chick embryo was achieved by dropping 5.0 mg Ketamine onto the CAM. Single voxel MRS of 6 x 6 x 6 $mm^3$ volumes of interest were acquired in about 30 minutes acquisition time, with subsequent acquisition of the diffusion MRI by a two-point method with 230 x 230 x 2000 $\mu m^3$ resolution.

Falen et al. [53] and Hutchison et al. [87] applied MRI with T1 and T2—weighted imaging techniques to the assessment of the yolk structure. Both reported the applicability of MRI for the assessment of the morphology of yolk, albumen, air space, and eggshell. The inner structure of the yolk, including concentric yolk rings, could be clearly visualized by this non-destructive imaging technique. In 2000, Donoghue et al. [88] reported the application of MRI for monitoring residue transfer into egg yolk. After injection of Gd-DTPA, the transfer of the drug into the yolk was monitored by scanning the egg applying a T1-weighted (MP-RAGE) sequence. It could be shown that Gd-DTPA residues were incorporated into the yolk ring structure.

Assessment of the chick embryo vasculature by MRI was reported by Smith et al. in 1992 [89]. They performed *ex vivo* high-resolution MRI of the embryonic vasculature after perfusion fixation of the vasculature structure with gadolinium-doped gelatin. A similar approach was chosen by Hogers et al. [52] to demonstrate the benefit of ultra-highfield imaging by

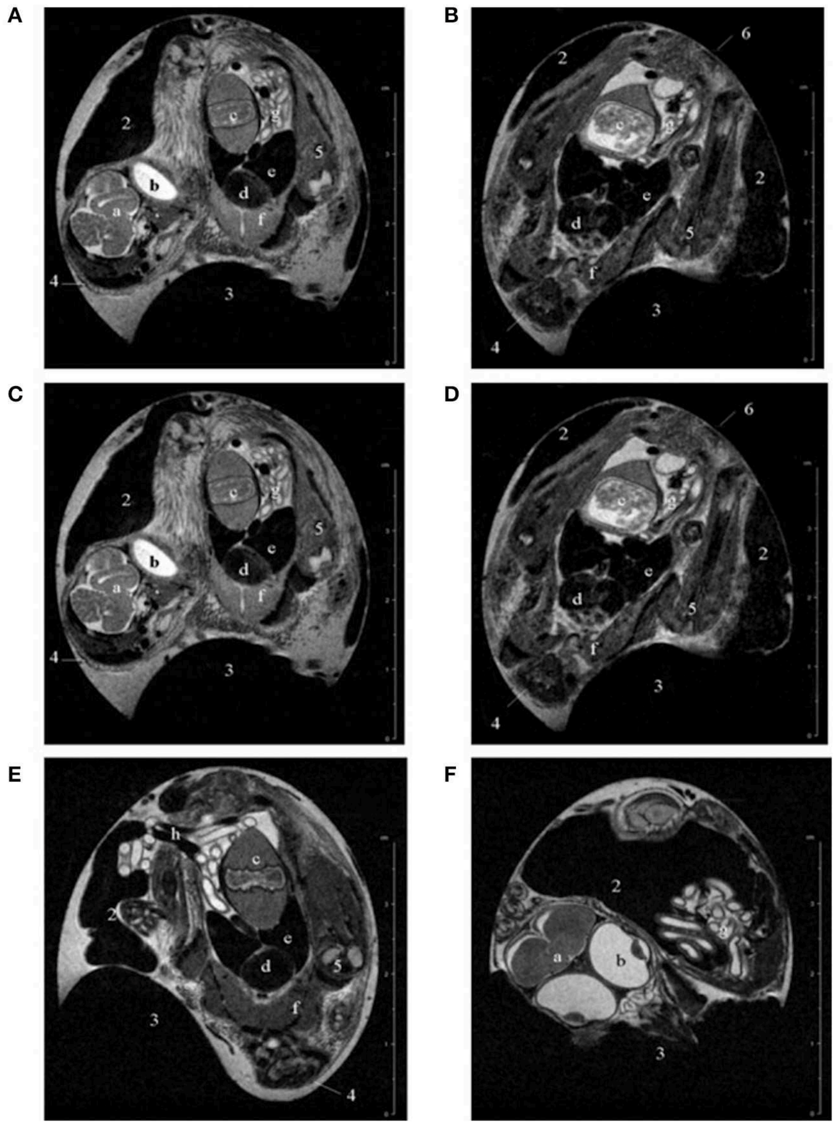


**FIGURE 2 |** Representative examples of T2-weighted multislice scans of chick embryos in ovo at **(A)** 12, **(B)** 15, **(C)** 17, **(D)** 18, **(E)** 19, and **(F)** 20 days of incubation. 1, albumen; 2, yolk; 3, air sac; 4, head; 5, limb; 6, rump; a, brain; b, eye; c, gizzard; d, heart; e, liver; f, pectoral muscles; g, intestine; h, umbilical vessels. The complete scans can be viewed at www.gla.ac.uk/7tmr/chickegg.htm. This research was originally published in JMRI: Noninvasive Monitoring of Chick Development In Ovo Using a 7T MRI System From Day 12 of Incubation Through to Hatching. Bain et al. [51].

comparing MRI *in vitro* microscopy between 7T and 17.6T field strength. A similar *ex vivo* technique was applied by Zhang et al. [90] and Yelbuz et al. [91, 92], who used the combination of perfusion with immersion fixation and a small molecular gadolinium agent to improve image contrast between the myocardial wall and heart lumen. Isotropic three-dimensional images with up to $25^3$ $\mu m^3$ spatial resolution were acquired with a T1-weighted spin warp technique in about 29 h scan time at 9.4T field strength. *In ovo* quantification of the cardiac function was reported by Holmes et al. [93, 94] applying a self-gating technique for cardiac synchronization of the data. Even though adequate image quality could be obtained, the authors identified the bulk embryo motion at earlier stages as main limiting factor for reproducible image quality.

Noninvasive monitoring of chick embryo development was reported by Bain et al. [51] in 2007. For optimal image contrast a T2-weighted spin echo technique (RARE) was applied yielding 195 x 195 x 500 $\mu m^3$ spatial resolution within 25 minutes scan time at 7T (**Figure 2**). Rapid three-dimensional T1-weighted techniques provided higher spatial resolution, but organ contrast was not sufficient. For chick embryo immobilization, Bain et al. [51] used a precooling protocol, keeping the chicken eggs at

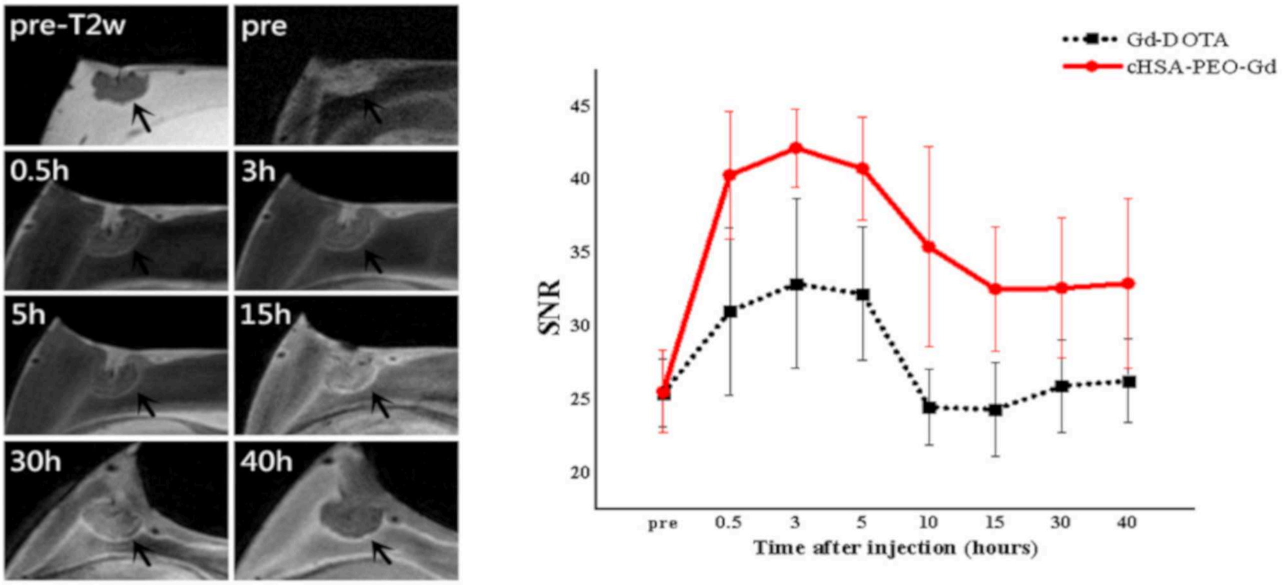


**FIGURE 3 |** Representative MR images of cHSA-PEO(2000)16-Gd biodistribution in solid tumor (left) and comparison of the SNR (Signal-to-Noise Ratio) of the tumor (right) over the first 40 h after systemic injection of cHSA-PEO(2000)16-Gd and Gd-DOTA. This research was originally published under the terms of the CC BY license (Creative Commons Attribution 4.0 International License) in Sci Rep: The CAM cancer xenograft as a model for initial evaluation of MR labeled compounds. Zuo et al. [65].

4°C for 60 min prior to data acquisition with subsequent data acquisition at room temperature. No slowdown or arrest of the chick embryo development was observed by the cooling or the MRI examinations. As alternative cooling protocol, Li et al. [95] suggested data acquisition at 19°C thus enabling scan times of up to 4 hours in quail embryos. More advanced imaging techniques including T1 and T2 mapping as well as magnetization transfer ratio (MTR) quantification were reported by Boss et al. [50]. Motion reduction was achieved by application of 0.5 mL Ketamine onto the CAM. Images were acquired with two-dimensional multi-slice techniques at a spatial resolution of 180 x 180 x 1000 $\mu m^3$ (T1), 260 x 260 x 1000 $\mu m^3$ (T2), and 230 x 230 x 1000 $\mu m^3$ (MTR). In 2015, Zhou et al. [49] translated developmental imaging of the brain to a 3T clinical scanner equipped with a dedicated small animal coil. T2 weighted RARE images as well as DTI data could be acquired at reasonable spatial resolution (T2w: 170 x 170 x 1000 $\mu m^3$ in 8 minutes, DTI: 1.25 x 1.25 x 1 $mm^3$ in 6 minutes), enabling noninvasive analysis of brain development including structural information. Imaging of the chick embryo brain development after Zika virus infection was reported by Goodfellow et al. [96], who could clearly demonstrate Zika virus induced microcephaly. High-resolution MRI at 7T were presented by Lindner et al. [48] for monitoring the chick embryo eye development. Immobilization of the embryo was achieved by bedding the egg on crushed ice ten minutes before scanning.

A first application of *in ovo* MRI for the assessment of the biodistribution of new compounds was reported by Dingman et al. [97] in 2003. They longitudinally investigated the distribution of a 19F-labeled L-6-heptafluorobutyryl-5-hydroxytryptophan including uptake dynamics and crossing of the blood-brain barrier. In 2007, Oppitz et al. [98] suggested the use of chick embryo model for evaluation of the advantages and limitations of MRI to monitor the migration of superparamagnetic iron oxide (SPIO) labeled cells. A similar approach was presented by Pereira et al. [99] who showed in the chick embryo model an improved sensitivity for *in vivo* cell tracking after implantation by supplementing the culture medium with adequate iron sources as compared to the use of reporter genes. Faucher et al. [100] used the HET-CAM model for initial investigation of ultra-small gadolinium oxide nanoparticles for labeling of glioblastoma cells, seeded on the CAM. Taylor et al. [101] used the chick embryo model for initial evaluation of new nano- and micro-sized magnetic particles for cell tracking. All imaging was performed *ex vivo*. In 2017, Zuo et al. [65] reported the use of human cancer cell lines xenotransplanted onto the CAM for initial assessment of the biodistribution of MR labeled drugs. After injection of Gd-DOTA, the biodistribution of the compound in the chick embryo as well as in the xenotransplanted tumor was observed. By longitudinal imaging studies over 40 h, the accumulation and clearance of the contrast agent could be monitored. The technique was applied for demonstrating the feasibility of the HET-CAM tumor model for monitoring the fate of new MR labeled drugs by following the image contrast after intravenous administration of a gadolinium-labelled polymeric nanoparticle at high spatial resolution, applying an immobilization protocol as suggested earlier [61]. In direct comparison with conventional contrast agents, a significantly prolonged retention time of the polymeric nanoparticle in the tumor could be shown (**Figure 3**). For assessment of the intra-tumor distribution, 3D T1 weighted data were acquired at high spatial resolution of 100 x 100

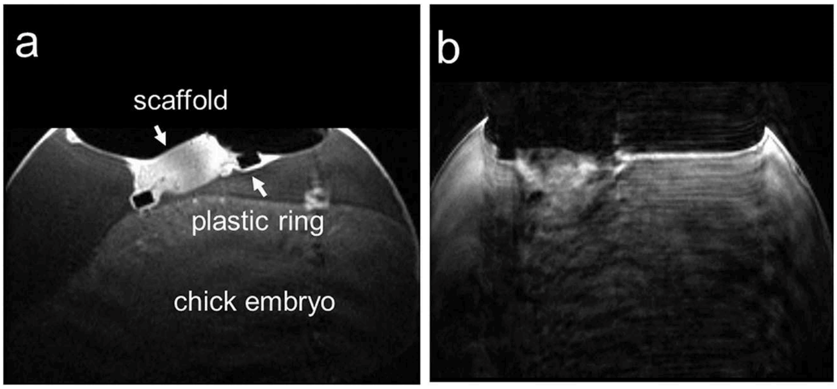


**FIGURE 4 |** Two in ovo T1-weighted MR images of the chick embryo on ID 14, seven days post-implantation on the CAM acquired in an axial slice through the biomaterial scaffold; **(a)** image without motion artifact and **(b)** image with motion artifacts that was excluded from further analysis. This research was originally published under the terms of the CC BY license (Creative Commons Attribution 4.0 International License) in Sci Rep: Comparison of medetomidine, thiopental and ketamine/midazolam anesthesia in chick embryos for in ovo Magnetic Resonance Imaging free of motion artifacts. Waschkies et al. [106].

x 560 μm$^3$. Hafner et al. [102] used a similar approach for initial evaluation of the biodistribution of a multifunctional drug carrier.

Buschmann et al. [103] reported implantation of human osteoblasts-seeded scaffolds onto the CAM. One week after xenotransplantation, MRI (T1, T2 quantification) analysis was performed *ex vivo*, after intravenous injection or dripping of gadolinium onto the scaffold before sacrificing the embryo allowing for the analysis of the formation of new capillaries. The published *ex vivo* data clearly indicated the potential of the HET-CAM model as cheap reliable model for monitoring the angiogenesis in tissue-engineering. This work was further developed by Chesnick et al. [104] by initial testing of a new adrenolate labeled gadolinium complex for specific targeting to bone mineral. In 2015, Pfiffner et al. [105] presented *in vivo* MRI at 4.7T to noninvasively quantify and monitor the perfusion capacity in the HET-CAM model. After placing a biomaterial on the CAM, its perfusion capacity was quantified by relaxation rate changes after intravenous injection of the gadolinium-based contrast agent. Immobilization of the chick embryo was achieved by 5 drops of ketamine 1:100 (Ketasol-100, Graeub, Switzerland) dripped onto the CAM surface. Anatomical reference images were obtained applying a FLASH sequence at measured spatial resolution of roughly 500$^2$ μm$^2$. T1 and T2 maps were derived applying RARE sequences with multiple repetition times (TR) and echo times (TE) at spatial resolution of 200 x 200 x 1000 μm$^3$ before and at different time points after intravenous injection of 100 μL Gd-DOTA (0.5M) MRI contrast agent. Relaxation rate changes over the scaffold could be clearly assessed indicating different vascular density, which was confirmed by histology.

Motion artifacts introduced by bulk motion of the chick embryo is a major limiting factor for high-resolution imaging of the CAM (**Figure 4**). In 2015, Waschkies et al. [106] investigated the use of different anesthesia drugs for immobilization, whereas Zuo et al. [61] evaluated an age-adjusted precooling protocol for high-resolution imaging of the CAM. In Waschkies *et al*, medetomidine at a dosage of 0.3 mg/kg, was compared to thiopental at 100 mg/kg and ketamine/midazolam at 50 and 1 mg/kg. The soluble anesthetics were applied by dropping a total volume of 0.3 mL onto the surface of the CAM. It was demonstrated that medetomidine performed best, enabling motion-free MRI for a period of about 30 min starting 10 min after application. Ketamine/midazolam yielded insufficient depth of anesthesia and thiopental anesthesia did not immobilize the chick embryo sufficiently long. In contrast, Zuo et al. investigated the use of an anesthesia-free immobilization approach. As extension to earlier published work [51], they suggested adaptation of the precooling time according to the age of the chick embryo, thereby achieving almost complete immobilization of the chick embryo for at least 60 min thus allowing multi-contrast high-resolution imaging of the chick embryo and xenotransplanted tumors on the CAM (**Figures 5**, **6**). The suggested cooling protocol allowed *in vivo* imaging at high spatial resolution as 77 x 91 x 500 μm$^3$ (T2 weighted anatomic, 2D), 200 x 200 x 500 μm$^3$ (diffusion weighted, 2D), 104 x 98 x 500 μm$^3$ (T2 mapping, 2D), and 100 x 100 x 560 μm$^3$ (T1 weighted, 3D). Tumor volume and growth could be monitored longitudinally from day 4 to day 9 after xenotransplantation. The tumor progression could be monitored for each individual case (**Figure 7**) and the volumes derived from MRI at day 9 excellently correlated with the respective volumes derived after resection of the tumors. In 2018, Herrmann et al. [58] reported the application of MRI to measure primary neuroblastoma tumor size and metastasis in a chick embryo model. Human neuroblastoma cells labeled with green fluorescent protein (GFP) and micron-sized iron particles were xenotransplanted on the CAM at EDD 7. At EDD 14, T2 RARE and T2-weighted fast low angle shot (FLASH) data were acquired (**Figure 8**) using the cooling protocol as suggested by Zuo et al. [61]. Additionally, Herrmann et al. performed time-of-flight (ToF) MR angiography (MRA) and reported a reduced blood flow if using the cooling protocol, making successful ToF acquisition unfeasible. Instead, ketamine anesthesia (3.6 mM ketamine in 500 μL PBS) was applied resulting in MRI data free

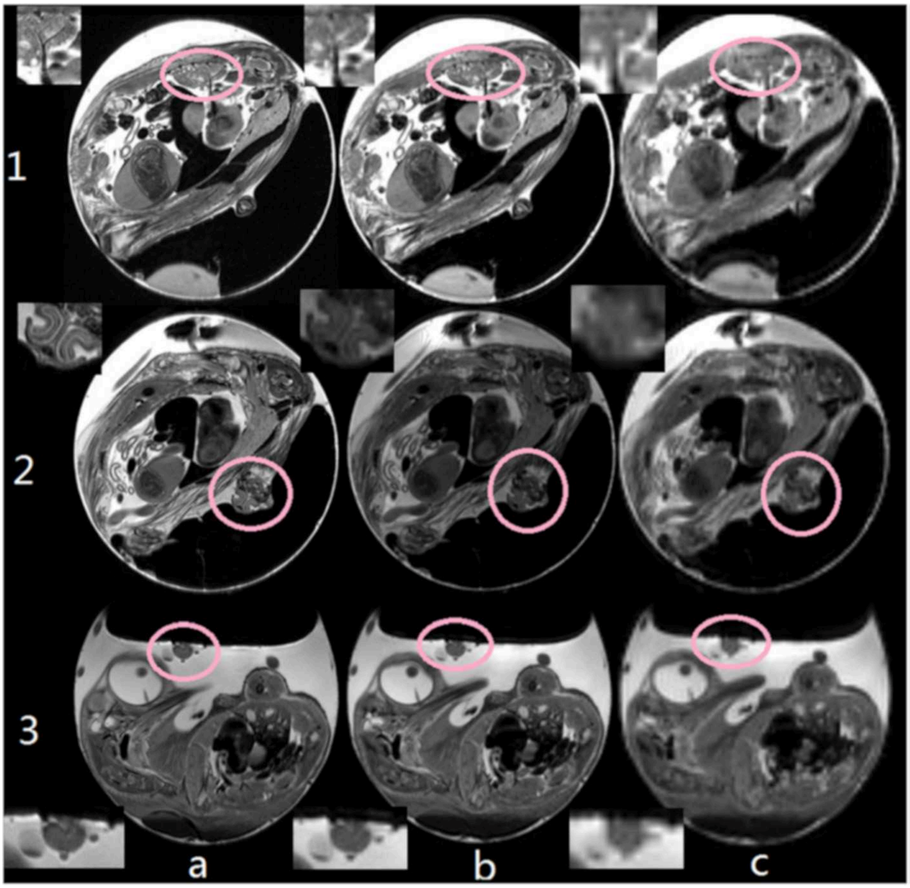


**FIGURE 5 |** Comparison between different image resolution: **(a)** 77 × 91 μm², **(b)** 200 × 200 μm², and **(c)** 500 × 500. With increasing resolution, details of e.g., the pulmonary veins (1), the beak (2, axial orientation), and tumor tissues (3) could be clearly resolved. Insets show details of the respective target structures. This research was originally published in NMR Biomed: High-resolution MRI analysis of breast cancer xenograft on the chick chorioallantoic membrane. Zuo et al. [61].

of motion artifacts for a period of 30 min. The micron-sized iron labeling of the cells allowed *in ovo* assessment of the primary tumor and detection of metastatic deposits.

## POSITRON EMISSION TOMOGRAPHY (PET)

Most anatomic and functional imaging of the HET-CAM model has been performed by MRI so far. The main limitation of PET results from its rather low spatial resolution, which does not fit the high spatial resolution demands for imaging of the CAM. To gain from the outstanding sensitivity of PET, thus in almost all work published, PET (or SPECT) imaging was complimented by Computer Tomography (CT), x-ray, or MRI for providing additional anatomic details.

In 2012, Würbach et al. [71] introduced using $^{18}$F-fluoride PET for assessment of bone metabolism. For radionuclide injection, a self-built catheter made of a 30G needle and a polythene tube with 0.28 mm inner diameter was introduced into one of the CAM vessels. Imaging was performed for a period of roughly 75 minutes yielding dynamic images (55 time frames) as well as high-quality static data. Applying an iterative ordinary Poisson maximum *a posteriori* reconstruction yield voxel sizes of roughly 400 x 400 x 800 $\mu m^3$. The results proved the quantitative and reproducible assessment of bone metabolism in anesthetized chick embryos. Immobilization of the chick embryo during scanning was achieved by exposing the CAM to isoflurane at 1.5% concentration as suggested by Heidrich et al. [107], who investigated different anesthesia schemes for *in vivo* imaging of avian embryos, including isoflurane, 2,2,2-tribromoethanol (Avertin), and urethane/α-chloralose (UC). UC and Avertin were directly applied as liquids onto the CAM. For isoflurane anesthesia, the egg was exposed to an isoflurane concentration of 5% in oxygen. For induction, the eggs were placed into a narcosis induction chamber. Toxic side effects and only poor correlation between narcosis depth and dose limited the application of UC and Avertin and the authors clearly favored the use of Isoflurane due to its high tolerability enabling repeated imaging of the avian embryos at a daily basis. In 2013, Gebhardt et al. [70] applied a similar approach as Würbach et al. [71] to initially

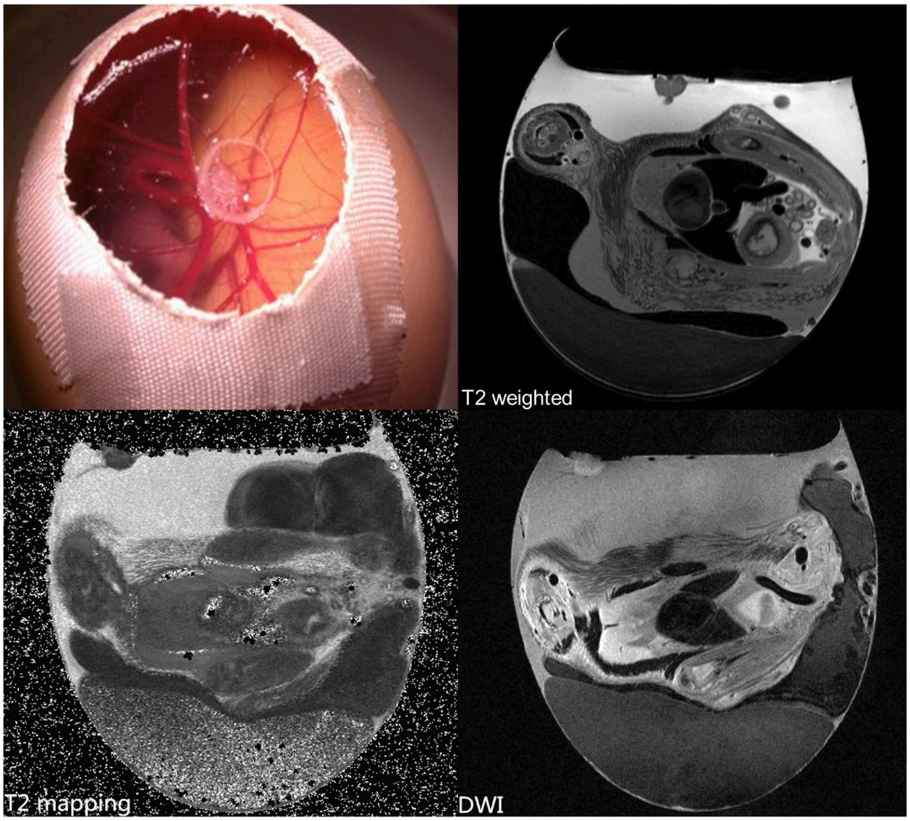


**FIGURE 6 |** *In vivo* high-resolution MRI with T2 and diffusion weighting (DWI), and T2 quantification of a Human breast tumor (carcinoma cell line MDA-MB-231) xenotransplanted on the CAM. Unpublished imaging material provided by Zuo obtained with precooling and MR protocols as described in [61].

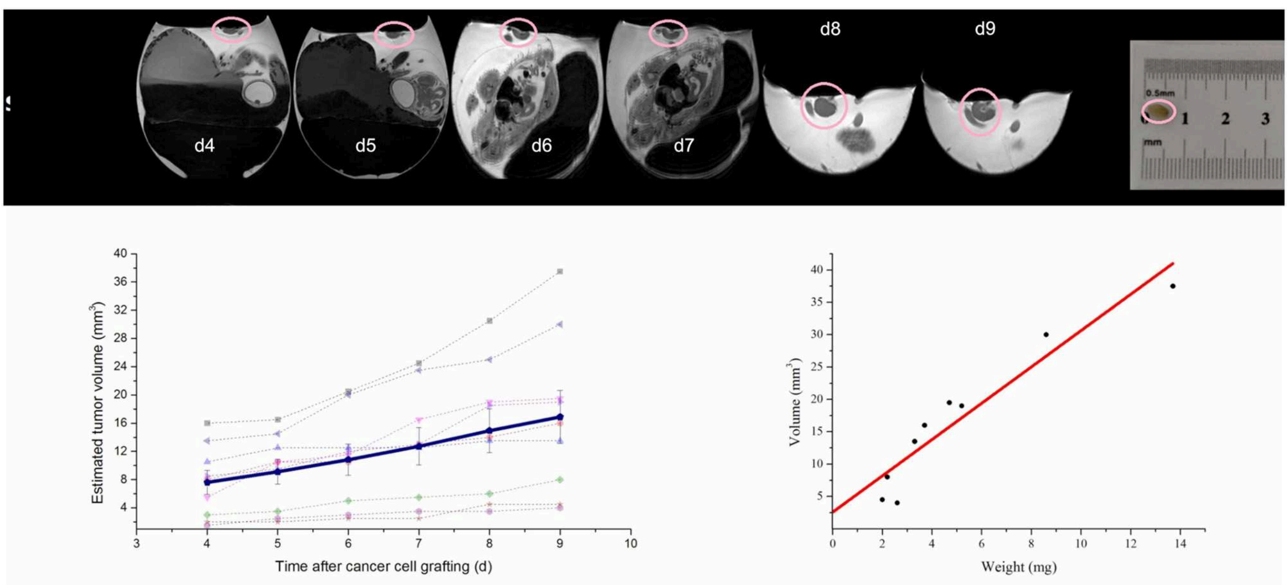


**FIGURE 7 |** Monitoring the progression of xenotransplanted tumor (circle) from day 4 to day 9 after cell seeding on the CAM. (Top) High-resolution T2 weighted MR images; (lower left) individual tumor volumes ($n = 9$) and mean volume progression (solid line); (lower right) correlation of tumor volume ($n = 9$) and weight after tumor resection at day 9. Modified from original research published in NMR Biomed: High-resolution MRI analysis of breast cancer xenograft on the chick chorioallantoic membrane. Zuo et al. [61].

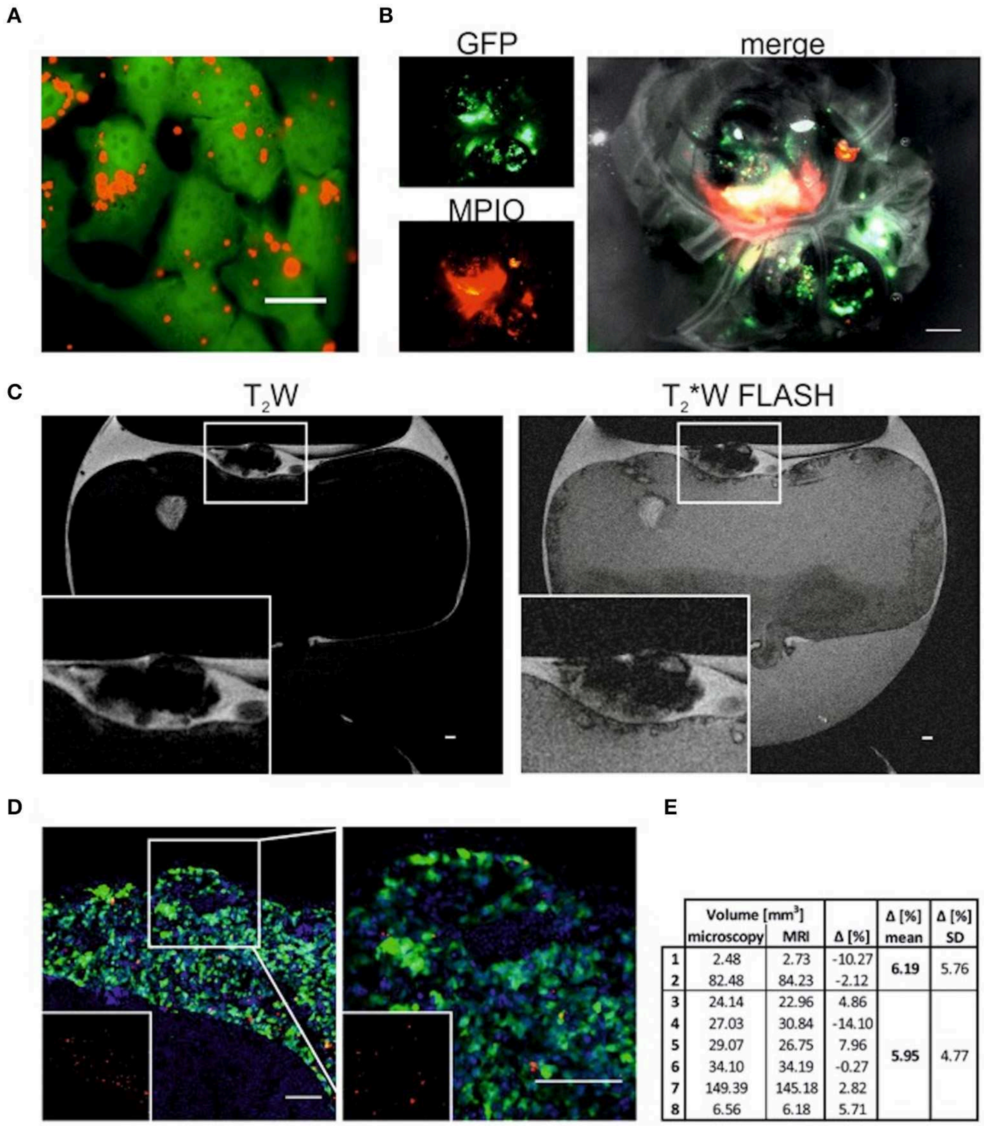


| | Volume [mm³] microscopy | Volume [mm³] MRI | Δ [%] | Δ [%] mean | Δ [%] SD |
|---|---|---|---|---|---|
| 1 | 2.48 | 2.73 | -10.27 | 6.19 | 5.76 |
| 2 | 82.48 | 84.23 | -2.12 | | |
| 3 | 24.14 | 22.96 | 4.86 | 5.95 | 4.77 |
| 4 | 27.03 | 30.84 | -14.10 | | |
| 5 | 29.07 | 26.75 | 7.96 | | |
| 6 | 34.10 | 34.19 | -0.27 | | |
| 7 | 149.39 | 145.18 | 2.82 | | |
| 8 | 6.56 | 6.18 | 5.71 | | |

**FIGURE 8 |** T2W and T2*W FLASH images of tumors labeled with MPIO **(A)** GFP-expressing SK-N-AS cells (green) 24 h -postlabeling with 20 mM MPIO (Suncoast Yellow Encapsulated Magnetic Polymers—Bangs Beads, Red). Scale bar is 20 mm. **(B)** Single channel and overlay image of neuroblastoma tumor postdissection formed by GFP-expressing SK-N-AS cells (green) which were labeled with MPIO (red) 48 h prior CAM implantation. Scale bar is 1000 mm. **(C)** Representative sagittal T2Wand T2*W FLASH MRI images of embryonated chicken egg at E14 **(A)**. Tumor formed by cells labeled with MPIO can be identified on top of the CAM (zoom in inset). Scale bar is 1000 mm. **(D)** Representative image of tumor formed on the CAM by GFP-expressing SK-N-AS cells (green) labeled with MPIO (red). Nuclei are stained with Hoechst (blue). Inset shows MPIO only (red). Right image is 2.5_ zoom. Scale bar is 100 mm. **(E)** Comparison of tumor volume (mm3) measured by microscopy or MRI. Tumors 1 to 2 were formed by cells without MPIO, tumors 3 to 8. This research was originally published under the terms of the CC BY license (Creative Commons Attribution 4.0 International License) in Mol Imaging: Magnetic Resonance Imaging for Characterization of a Chick Embryo Model of Cancer Cell Metastases. Herrmann et al. [58].

evaluate the dynamic behavior of new PET tracers in the chick embryo model as an *in vivo* assay. Various $^{18}F$, $^{64}Cu$, and $^{68}Ga$-labeled compounds were investigated and the potential of the chick embryo model as efficient *in vivo* model could be shown.

Warnock et al. [69] demonstrated the use of the CAM for screening of novel PET tracers. At EDD 11, the eggs were opened and 5 x $10^6$ human U87 glioblastoma cells in 20 μL of culture medium xenotransplanted onto the CAM. At EDD 18 PET/CT imaging of the tumors was performed. During scanning the egg was reproducible positioned in both systems in a small animal imaging cell (Minerve equipment veterenaire) allowing temperature control and isoflurane anesthesia (2% in air). Uptake of the radiotracer was clearly demonstrated by time-activity curves and in the PET images (**Figure 9**). Contrast-agent enhanced μCT data provided accurate anatomic correlation,

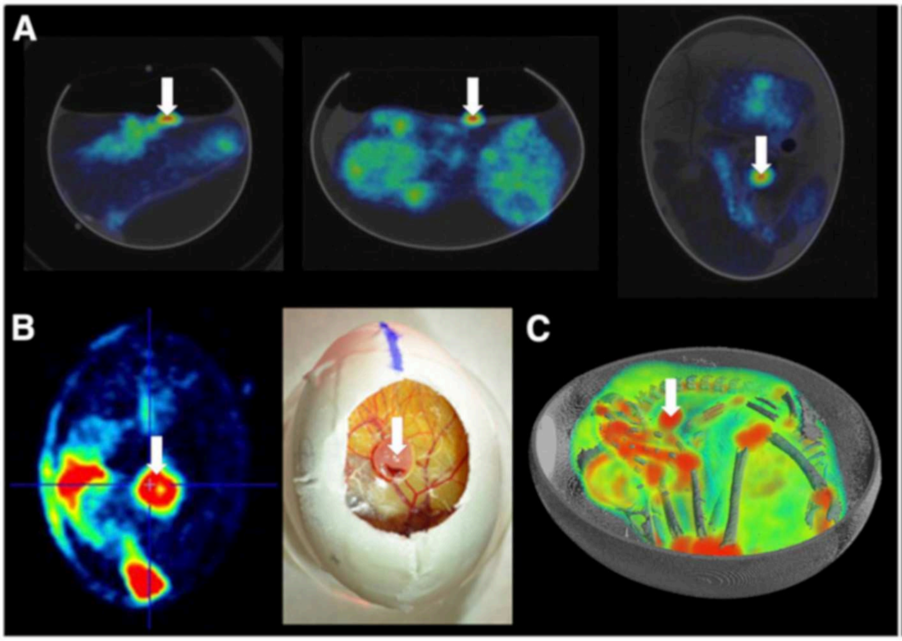


**FIGURE 9 | (A)** Two-dimensional coregistered PET and CT images of the chicken egg after [$^{18}$F]-FDG injection and 45 min tracer uptake. **(B)** Visual comparison of 18F-FDG uptake in glioblastoma at level of CAM to photograph illustrating tumor localization. **(C)** 3D visualization of overlaid PET and CT images for [$^{18}$F]-FDG uptake in embryo and U87 human glioblastoma tumor (white arrow). This research was originally published in JNM: *in vivo* PET/CT in a human glioblastoma chicken chorioallantoic membrane model: a new tool for oncology and radiotracer development. Warnock et al. © by the Society of Nuclear Medicine and Molecular Imaging, Inc. [69].

enabling distinction of the uptake in the joints and the tumor. Their outcome clearly indicated the potential of the suggested HET-CAM model for initial assessment of the pharmacokinetics of new compounds.

Haller et al. [19] investigated the tissue distribution and stability of different $^{18}$F, $^{125}$I, $^{99m}$Tc, and $^{177}$Lu—labeled radiopharmaceuticals. For imaging purposes the chick embryos were euthanized by shock-freezing in liquid nitrogen at different time points after administration of the radioactivity. In comparison with the established mouse models, they concluded a similar tissue distribution and stability of radiopharmaceuticals in the chick embryo. The very similar behavior in the two *in vivo* models indicate the potential of using the chick embryo as an inexpensive and simple test model for preclinical screening of novel radiopharmaceuticals. To overcome the limitations of the small anatomies with respective requirement of dedicated high-resolution imaging equipment, Freesmeyer et al. [108] suggested the translation of the work into ostrich eggs and demonstrated the potential use for different radiotracers even on conventional PET/CT systems. Even though overcoming the issues with small anatomy and high-spatial resolution requirements, ostrich eggs cannot be seen as a real alternative to chick embryos, since they are not readily available, hardly established in science, expensive and often do not fit into conventional small animal imaging equipment.

In a recent work of Zlatopolskiy et al. [68] the HET-CAM model was used for evaluation of radiotracers addressing the tryptophan metabolic pathway. An efficient method for the synthesis of fluorotryptophans, labeled in different positions with $^{18}$F is presented and their biological evaluation regarding tumor targeting evaluated in the HET-CAM model. Therefor MCF7, PC-3, and NCI-H69 xenografts were cultivated on the CAM. The tissue distribution of the new agent 7-[$^{18}$F]FTrp in comparison to conventional $^{18}F^{-}$ was assessed after systemic injection. While in the $^{18}$F-scans tracer uptake was mainly observed in bones, joints, and beak of the chick embryos, 7-[$^{18}$F]FTrp clearly delineated the tumor.

Even though CT represents an important imaging tool providing relevant anatomic information and has proven clinical success in combination with PET, its only limited soft tissue contrast is often insufficient. To that respect in 2019 Steinemann et al. [109] and Winter et al. [110] combined *in ovo* PET with MRI to make full advantage from the high sensitivity of PET and the excellent soft tissue contrast in MRI. Steinemann et al. used the imaging approach for monitoring the effectiveness of a new chimeric inhibitor (animacroxam, which combines histone deacetylase (HDAC) inhibitory and cytoskeleton-interfering pharmacophores) to the clinical approved HDAC in testicular germ cell tumor. Tumor plaques were grown from $10 \times 10^6$ 2102EP cells mixed with 150 μl matrigel and transplanted onto the CAM. Imaging was performed three days after xenotransplantation to allow angiogenic connection of the xenograft to the CAM. Injection

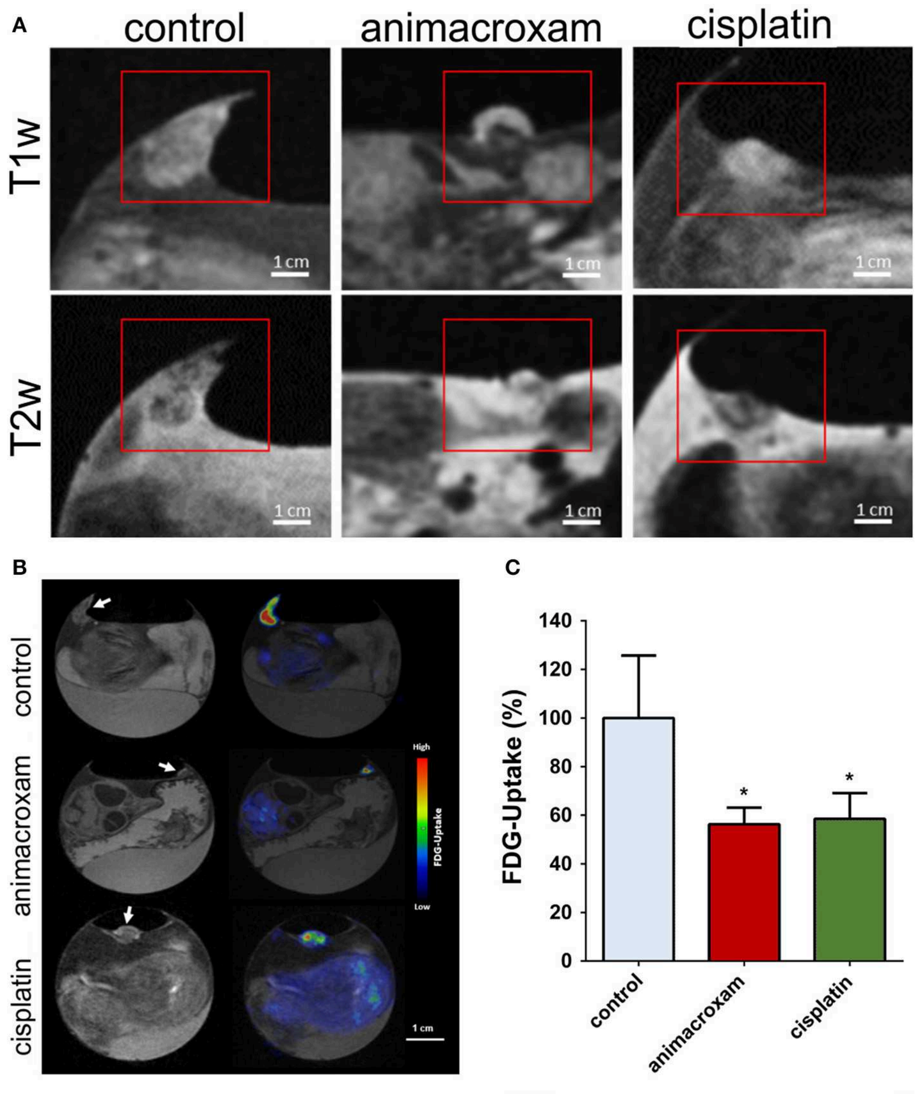


**FIGURE 10 |** Animacroxam induces 'cap formation' and suppresses glucose uptake in inoculated TGCT plaques. **(A)** T1w and T2w images of control-, animacroxam-, and cisplatin-treated tumor plaques. Animacroxam-treated tumors show a distinct viable tumor core (dark in T1w-/bright in T2w images) and a necrotic cap (bright in T1w-/dark in T2w images). **(B)** T1w and corresponding PET-MR images of [$^{18}$F]-FDG uptake in tumor plaques treated with NaCl, animacroxam, or cisplatin. **(C)** Animacroxam (5.0 $\mu$m)- and cisplatin (2.5 $\mu$m)-treated tumor plaques showed a reduced uptake of [$^{18}$F]-FDG. Results are shown as means ± SEM of at least $n = 3$ independent experiments. Scale bar = 1 cm. *$P$-values of $\leq 0.05$, unpaired $t$-test. This research was originally published under the terms of the Creative Commons Attribution License (CC BY) in Molecular Oncology: Antitumor and antiangiogenic activity of the novel chimeric inhibitor animacroxam in testicular germ cell cancer, Steinemann et al. [109].

of the compounds [concentrations calculated assuming 1 mL blood volume: 5 $\mu$M animacroxam, 2.5 $\mu$M cisplatin, or NaCl (0.9%)], was done intravenously via a 30G syringe. The tumor volume was derived from MRI measurements (3D T1w-GRE, 290 x 290 x 500 $\mu m^3$, TR/TE = 50 ms/2.7 ms; 2D RARE, 290 x 290 x 700 $\mu m^3$, TR/TE = 8885 ms/100 ms) prior and 7 days after treatment. Immobilization of the chick embryos was obtained by 1 h precooling. Tumors could be clearly delineated in the MRI data and respective volumes quantified. Respective glucose uptake of the tumors was assessed by [$^{18}$F]-FDG PET imaging (0.1 mL of 12 MBq). Fusion of the PET and MRI data showed excellent agreement between tumor extend and FDG uptake (**Figure 10**). The observed reduction in tumor volume under treatment correlated well with the observed reduced glucose uptake. Winter et al. evaluated the HET-CAM for initial testing of the binding specificity of targeted compounds. They used the well-characterized PSMA-specific PET radiotracer [$^{68}$Ga]-PSMA-11 to demonstrate the principle of the HET-CAM model for evaluation of specific radioligand accumulation in prostate cancer xenografts (**Figure 11**). At EDD 6, tumor cells of the PSMA-positive cell line LNCaP C4-2 (1 x $10^6$ cells) and the PSMA-negative control PC-3 (7.5 x $10^5$

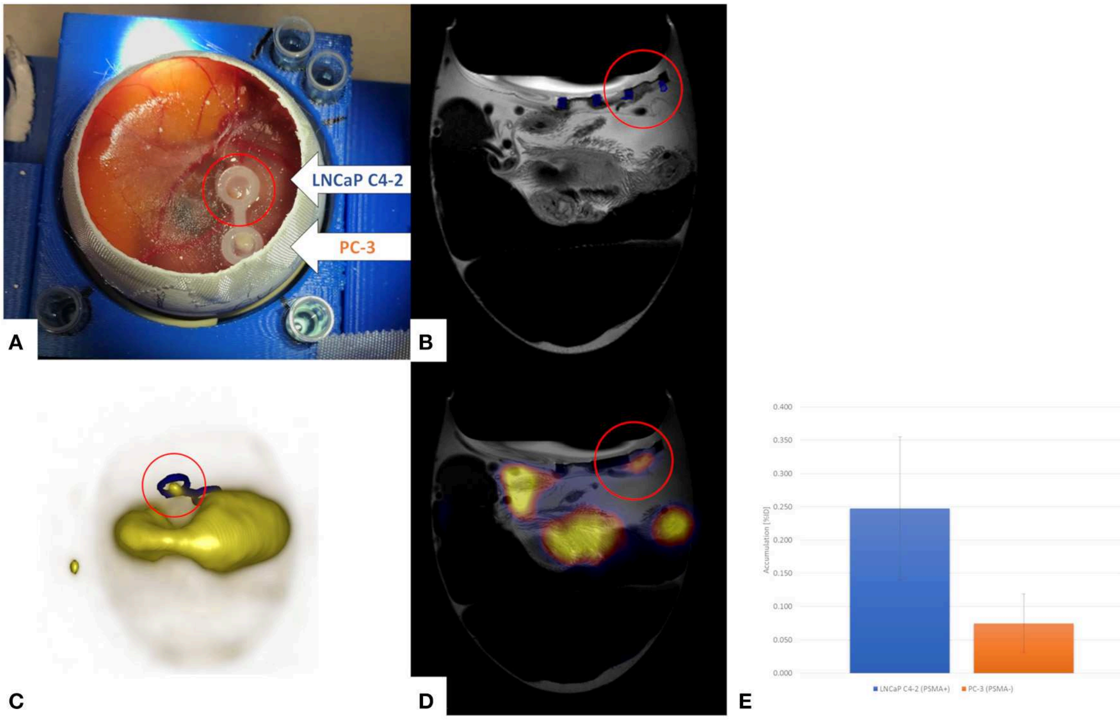


**FIGURE 11 |** PET/MRI for quantification of the PSMA-specific PET radiotracer [$^{68}$Ga]-PSMA-11 in the HET-CAM model with dual tumor seeding (LNCaP C4-2, PSMAQ17 positive; PC-3, PSMA negative) **(A)**. The tumors can be nicely visualized by high-resolution MRI (**B**, red circle). Distribution of the [$^{68}$Ga]-PSMA-11 by PET reveals strong signal at one location of the CAM and some general accumulation in the chick embryo **(C)**. Fusion of the PET and MRI data **(D)** reveals tracer accumulation in the PSMA positive tumor (red circle), which is proven by gamma counting after resection of the tumors **(E)**. Unpublished imaging material provided by Winter G. and Li H.

cells) mixed in Matrigel (40%, v/v) were grafted on the CAM in two silicon rings. MR and PET imaging was performed starting on EDD 12. Anatomical information was provided by high-resolution imaging using a small animal MR based on the protocol of Zuo et al. [61, 65]. For PET, 150 μl of [$^{68}$Ga]-PSMA-11 solution was injected into a chorioallantoic membrane vessel followed by a dynamic 60 minutes PET scan. Registration between both imaging modalities was achieved by a self-built animal holder with PET and MRI visible fiducial markers. Tumor growth could be quantified by MR imaging. In addition to PET imaging the tumor entities were excised from the membrane after measurement and the accumulated activity was separately quantified by γ-counter (COBRA II, Perkin Elmer) detection. As expected, in comparison to the PC-3 tumors, higher accumulation of [$^{68}$Ga]-PSMA-11 was observed in the LNCaP C4-2 tumors, indicating the applicability of the HET-CAM model for initial testing of binding specificity of targeted compounds.

## DISCUSSION

The HET-CAM model has been exerted to numerous applications. It represents a simple, quick, and low-cost model, not rising any regulatory concerns in many countries if sacrificed before hatching. However, there is a consensus in the scientific community that it is illogical to conclude that the neural capacity to experience pain is not fully developed prior to hatching and that beyond a critical point in development avian embryos are capable of experiencing pain. The exact stage of development at which this capacity is sufficiently developed to warrant concern has not yet been determined. Society recognizes that a critical period in chick embryo development occurs 72 h prior to hatching and from an ethical point of view embryos should be sacrificed prior to EDD 18.

Since the HET-CAM model represents a naturally immunodeficient host, xenotransplantation of many kinds of tumors without species-specific limitations are possible. Even considering the fact that not all organs are fully developed, the established circulation and the highly vascularized CAM, which is connected to the embryo through a continuous circulatory system make it a natural candidate in-between cell culture and animal experiments, especially for initial testing of new compounds. Even though not finally established, it will likely play an important role in early drug development as pointed out in **Figure 12**. Compounds without detectable toxicity in cell and eventually zebra fish assays, may be initially evaluated regarding efficacy and biodistribution in the HET-CAM model, thereby reinforcing the potential of this convenient, 3R compliant, *in vivo*

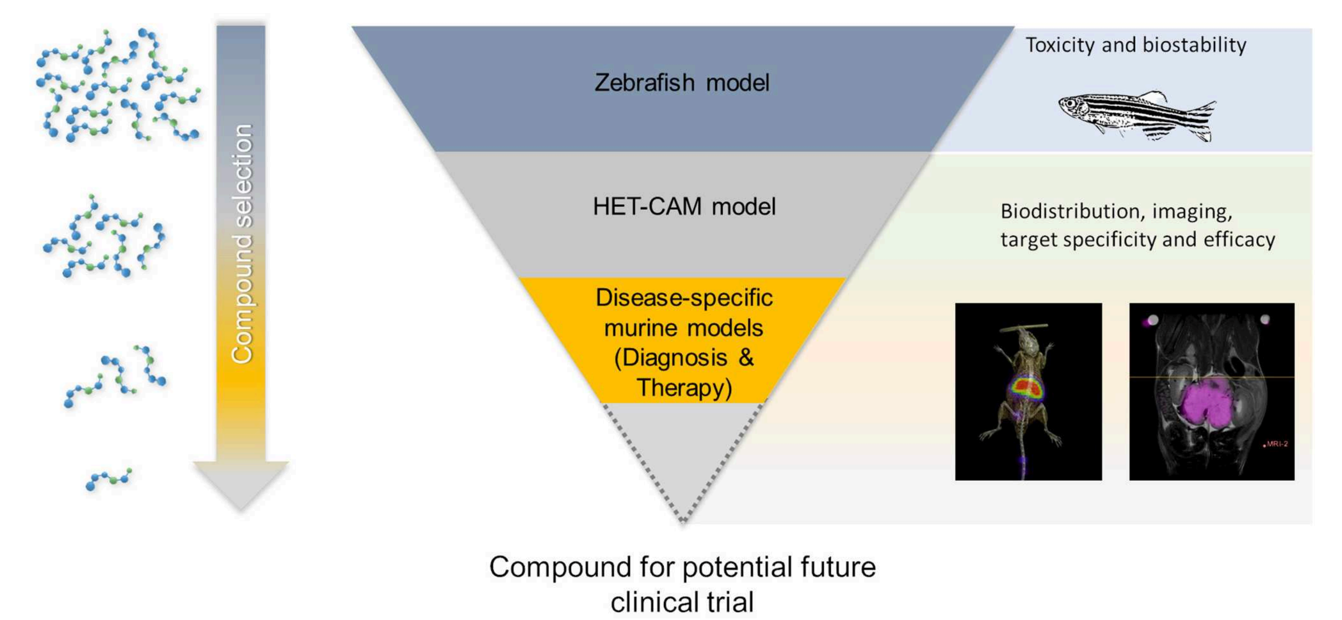


**FIGURE 12 |** Potential role of PET-MRI imaging in the HET-CAM model within new drug developments.

model for cancer research. Only compounds showing promising properties will then further be evaluated in animal models, thus reducing the need for animal studies and related costs.

Non-invasive imaging will likely play an increasingly important role for direct visualization of the biodistribution of respectively labeled compounds and longitudinal monitoring of surrogate markers such as tumor progression and metabolism. MRI appears as an attractive imaging approach providing flexible image contrast and assessment to different tissue-specific parameters like MR relaxation times, diffusion and perfusion. Even though it offers the possibility of tailoring image contrast to the specific application, its intrinsic low sensitivity often limits its application in identification of small amounts or only traces of compounds. This limitation raises the increasing interest in using PET in the context of HET-CAM imaging. The excellent sensitivity of PET combined with the excellent anatomic detail of MRI appears as an ideal combination for anatomic, metabolic, and molecular imaging in the HET-CAM model.

Even though in PET motion compensation of the embryo may not be of paramount importance due to its only limited spatial resolution, in MRI coping with embryo motion is one of the major challenges to finally achieve the required high-spatial resolution. Over the last years efficient immobilization approaches of the chick embryo have successfully been evaluated *in ovo* (**Table 1**). Promising approaches include the precooling of the egg prior to scanning, the application of halothane and isoflurane, and the use of anesthesia agents dropped directly onto the CAM. Good to excellent immobilization could be achieved with almost all approaches. Major differences were reported regarding immobilization duration and resulting possible image acquisition times, tolerability by the chick embryo, side effects, and easiness to use. For high-resolution anatomic imaging, precooling appears as an excellent approach, allowing long scan times of up to one hour and being easy-to-use. However, the related slowdown in metabolism [113] and blood flow [58] may limit its application in cases where physiological properties are under investigation. Here, in contrast to halothane, isoflurane was reported to not impact aortic blood flow and cardiac performance [114] and may be a good alternative with the limitation of a quite complex imaging setup. Both approaches are well tolerated by the chick embryo allowing for repeated measurements in longitudinal studies. Liquid anesthetics applied by directly dropping onto the CAM are easy to use and a variety of agents have been reported with widely varying anesthesia efficiency and often toxic side effects [58, 106, 107]. Even though, ketamine was reported to reduce cardiac contraction force in isolated chick embryo heart at EDD 4 and EDD 7 [115], Herrmann et al. reported the advantage of ketamine over precooling for time-of-flight MRI [58] and showed its possible use in applications being sensitive compromised circulation or metabolism in cases of rather short acquisition times.

This review specifically addresses MRI/PET imaging techniques for HET-CAM applications. Even though highly attractive for high-quality multi-contrast morphological and functional imaging in combination with high-sensitive imaging of radio-labeled compounds, both represent high-cost imaging techniques requiring long acquisition times with only limited applicability to high-throughput applications. A wide range of alternative somehow competing techniques have been proposed over recent years. Most prominent to mention at this point are

**TABLE 1** | Overview of reported *in vivo* in ovo imaging and spectroscopy studies.

| References | Modality | Application | Imaging technique | Dimension | Spatial resolution | Immobilization | EDD | Scan time |
|---|---|---|---|---|---|---|---|---|
| Bone et al. [81] | MRI (1H, 1.5T) | Embryonic anatomy | T1-/T2-weighted SE | 3D | 200 × 200 × 1200 μm$^3$ | Precooling (EDD 11 20 minutes, EDD15 90 minutes) on ice chips | 11, 15 | Not reported |
| Effmann et al. [83] | MRI (1H, 2T) | Embryonic anatomy | T1-weighted SE | 2D | 50 × 50 × 600 μm$^3$ | Not reported | 4,6,9 | 1–2 h |
| Moseley et al. [54] | MRS (31P, 2T), MRI (1H, 2T) | Metabolic (MRS) and anatomic (MRI) development | T1/T2-weighted SE | Single voxel (MRS), 2D (MRI) | Whole egg (MRS) 270 × 270 × 2000 μm$^3$ to 350 × 700 × 3000 μm$^3$ (MRI) | Not reported | 4, 9, 12, 15, 17, 18, 19, 20, 21 (MRS), 5, 9, 15, 23 (MRI) | 20 min (512 NSA, MRS), not reported (MRI) |
| Lirette et al. [85] | MRS (31P, 1H, 2T) | Metabolic development, fat-water fraction | | Single voxel | Whole egg | Halothane | 0, 2, 4, 6, 8, 10, 12, 14, 16, 17, 19, 20 | |
| Peebles et al. [86] | MRS (1H, 7T), MRI (1H, 7T) | Metabolic (MRS) and diffusion (MRI) response to hypoxia and recovery | PRESS, 2pt diffusion | Single voxel (MRS), 2D (MRI) | 6 × 6 × 6 mm$^3$ (MRS), 230 × 460 × 2000 μm$^3$ (MRI) | Ketamine | 19 | 21.3 min (MRS), not reported (MRI) |
| Falen et al. [53] | MRI (1H, 2T) | Yolk structure | SE | 2D | 250 × 250 × 1250 μm$^3$ to 500 × 500 × 1250 μm$^3$ | Not reported | daily | 1 h |
| Hutchison et al. [87] | MRI (1H, 2T) | Yolk structure | T1-/T2-weighted SE | 2D | 235 × 310 μm$^2$ | Not reported | 1 | Not reported |
| Donoghue et al. [88] | MRI (1H, 1.5T) | Residue transfer | IR-FLASH (MP-RAGE) | 3D | 1000 × 780 × 1250 μm$^3$ | Precooling | not reported | Not reported |
| Holmes et al. [93] | MRI (1H, 7T) | Cardiac function | T1–weighted GE | 2D | 300 × 300 × 1500 μm$^3$ | Self-gated | 8, 13, 16, 20 | Not reported |
| Bain et al. [51] | MRI (1H, 7T) | Chick embryo development | T2–weighted SE | 2D | 192 × 195 × 500 μm$^3$ | Precooling | 12, 15, 17, 18, 19, 20 | 25 min |
| Boss et al. [50] | MRI (1H, 7T) | MR relaxation parameter changes during embryonic development | IR–TSE (T1–mapping), HASTE (T2–mapping), MT- prepared GE | 2D (T1/T2– mapping), 3D (MTR) | 180 × 180 × 1000 μm$^3$ (T1–mapping), 260 × 260 × 1000 μm$^3$(HASTE), 230 × 230 × 1000 μm$^3$ (MTR) | Ketamine | 5, 8, 11, 16 | Not reported |
| Zhou et al. [111] | MRI (1H, 3T) | Muscle fiber tracking during embryonic development | T1- / T2- weighted TSE, DTI | 2D | 200 × 200 × 2000 μm$^3$ (T1w), 200 × 200 × 1200 μm$^3$ (T2w), 600 × 600 × 1200 μm$^3$ (dti) | No, single- and double-precooling | 4, 5, 6,7, 8, 9, 10, 11, 12, 13, 18, 19 | 2 min 17 s (T1w), 12 min 23 s (t2w), 31 min 14 s (DTI) |
| Lindner et al. [48] | MRI (1H, 7T) | Embryonic development of the eye | T2–weighted TSE | 2D | 74 × 74 × 700 μm$^3$ | Bedding on crushed ice for EDD > 10 | 1–20 daily | |
| Dingman et al. [112] | MRI (19F, not reported) | Biodistribution of 19F-labeled compound | Not-reported | Not-reported | Not-reported | Not-reported | 15, 16, 17, 18 | |
| Oppitz et al. [98] | MRI (1H, 3T) | Migration of iron labeled melanoma cells | T2*-weighted | 3D | $300^3$–$1000^3$ μm$^3$ | Not reported | 6, 9, 18, 20 | 12 s / slice |

*(Continued)*

**TABLE 1** | Continued

| References | Modality | Application | Imaging technique | Dimension | Spatial resolution | Immobilization | EDD | Scan time |
|---|---|---|---|---|---|---|---|---|
| Faucher et al. [100] | MRI (1H, 1.5T) | Localization of Gd−labeled GL-261 glioblastoma cells | T1–weighted GR | 3D | 350 × 350 × 500 μm$^3$ | Precooling | 10, 11, 13 | 6–7 min |
| Zuo et al. [61] | MRI (1H, 11.7T) | CAM tumor morphology | T2–weighted TSE, T2 mapping, diffusion weighted, T1–weighted GE | 2D (T2, T2–mapping, DWI) 3D (T1 weighted GE) | 77 × 91 × 500 μm$^3$ (t2w), 200 × 200 × 500 μm$^3$ (DWI), 104 × 98 × 500 μm$^3$ (T2 mapping), 100 × 100 × 560 μm$^3$ | Precooling | 11–16, daily | 15 min 32s (t2w), 60 min (DWI), 34 min (T2 mapping), 4 min 9 s (t1w) |
| Zuo et al. [65] | MRI (1H, 11.7T) | Biodistribution of Gd–labeled compounds | T1-weighted GE, T2-weighted SE | 3D (T1w), 2D (T1w) | 100 × 100 × 560 μm (T1w), 77 × 91 × 500 μm$^3$ (t2w) | Precooling | 16 (injection), pre- and 30 min, 3 h, 20 h, 40 h after injection | 4 min 9 s (T1w), 15 min 32 s (t2w) |
| Pfiffner et al. [105] | MRI (1H, 4.7T) | Perfusion capacity of 3D biomaterials | T1-weighted GE, T1-/ T2-mapping | 2D | 500 × 500 × 1000 μm$^3$ | Ketamine | 14 | 25 s (GE), 9 min 40 s (mapping) |
| Waschkies et al. [106] | see Pfiffner et al. [105] | See Pfiffner et al. [105] | See Pfiffner et al. [105] | See Pfiffner et al. [105] | See Pfiffner et al. [105] | Metetomidone, thiopental, ketamine/midazolam | see Pfiffner et al. [105] | See Pfiffner et al. [105] |
| Herrmann et al. [58] | MRI(1H, 9.4T) | Tracking of magnetic particle labeled tumor cells | T2-weighted TSE, T2*-weighted GE, Time of flight (TOF) | 2D | 88/166 × 88/166 × 400/500 mm3 (t2w), 88 × 88 × 400 μm$^3$ (t2*, tof) | Precooling (T2-/T2*w), ketamine (Tof) | 14 | 13 min 24 s−31 min 56 s (t2w), 22 min 35s (T2*), 12 min 4 s (Tof) |
| Würbach et al. [71] | PET ($^{18}$F) | Bone metabolism | Static, dynamic | 3D | 400 × 400 × 800 μm$^3$ | Isoflurane | 13–18 | 75 min |
| Heidrich et al. [107] | PET/μCT | Immobilization | Static | 3D | Not reported | Isoflurane, 2,2,2-tribromoethanol, urethane/α-chloralose | 11–18 | 6 min |
| Warnock et al. [69] | PET ($^{18}$F) / μCT | Screening of novel PET tracer | Dynamic, static | 3D | 433 × 433 × 796 μm$^3$ (PET), 100$^3$ μm$^3$ (μct) | Isoflurane | 18 | 45 min (PET), not-reported (μct) |
| Zlatopolskiy et al. [68] | PET ($^{18}$F) | Tracer accumulation in CAM tumor | Static | 3D | 1.4$^3$ mm$^3$ (PET) | Isoflurane | 7 | 30 min |
| Steinemann et al. [109] | PET ($^{18}$F) / MRI (1H, 1T) | Tumor growth and metabolism | T1-weighted GE, T2-weighted TSE, static (PET) | 3D (GE, PET), 2D (TSE) | 290 × 290 × 500 μm$^3$ (GE), 290 × 290 × 700 μm$^3$ (TSE), not reported (PET) | Precooling | 10, 17 | Not reported |
| Winter et al. [110] | PET ($^{68}$Ga), MRI (1H, 11.7T) | Binding specificity of target-specific radioligands | Dynamic (PET), T2-/T1–weighted SE (MRI) | 3D (PET), 2D (MRI) | 1.4$^3$ mm$^3$ (PET), 100 × 100 × 560 μm (T1w), 77 × 91 × 500 μm$^3$ (t2w) | Precooling (MRI), none (PET) | 12 | |

*MRI, magnetic resonance imaging; MRS, magnetic resonance spectroscopy; PET, positron emission tomography; μCT, microscopy computer tomography; SE, spin echo; TSE, turbo spin echo; GE, gradient echo; IR, inversion recovery; MT, magnetization transfer; FLASH, fast low angle shot; HASTE, half-Fourier single-shot turbo spin echo.*

optical methods [116, 117] including bioluminescence [118], fluorescence [119], and tomographic [120, 121] techniques. Furthermore, ultrasonographic imaging [122], x-ray based tomographic [45] and even photoacoustic techniques [123] have been introduced, the latter of which with the potential for label-free imaging. In combination with single photon emission tomography (SPECT), tomographic x-ray techniques have been applied to initial evaluation of radiopharmaceuticals in chick embryos [19].

In conclusion, the expected increasing interest in the HET-CAM model as an intermediate step between cell culture and animal model for initial testing of new compounds makes *in ovo* imaging an important tool for monitoring the fate of compounds after systemic injection or surrogate markers. The combination of MRI and PET appears promising by combining the sensitivity of PET with detailed anatomic and functional information provided by MRI.

## AUTHOR CONTRIBUTIONS

GW, AK, JL, AA, AB, HL, and ZZ performed measurements in the context of the presented work. FJ and ML provided in-depth knowledge on nano-particles. GW and VR wrote the manuscript, and are responsible for the in ovo experiments.

## ACKNOWLEDGMENTS

The authors received funding from the European Union's Horizon 2020 research and innovation programme under grant agreement No. 667192, and by the Deutsche Forschungsgemeinschaft (DFG) through the Collaborative Research Center 1279—The exploration of the Human Peptidome. Further the general support of the MoMAN imaging center of Ulm University is acknowledged.

## REFERENCES

1. Ribatti D. The chick embryo chorioallantoic membrane (CAM). A multifaceted experimental model. *Mech Dev.* (2016) **141**:70–7. doi: 10.1016/j.mod.2016.05.003
2. Buchele B, Zugmaier W, Genze F, Simmet T. High-performance liquid chromatographic determination of acetyl-11-keto-alpha-boswellic acid, a novel pentacyclic triterpenoid, in plasma using a fluorinated stationary phase and photodiode array detection: application in pharmacokinetic studies. *J Chromatogr B Analyt Technol Biomed Life Sci.* (2005) **829**:144–8. doi: 10.1016/j.jchromb.2005.09.043
3. Syrovets T, Gschwend JE, Buchele B, Laumonnier Y, Zugmaier W, Genze F, et al. Inhibition of IkappaB kinase activity by acetyl-boswellic acids promotes apoptosis in androgen-independent PC-3 prostate cancer cells in vitro and in vivo. *J Biol Chem.* (2005) **280**:6170–80. doi: 10.1074/jbc.M409477200
4. Estrada AC, Syrovets T, Pitterle K, Lunov O, Buchele B, Schimana-Pfeifer J, et al. Tirucallic acids are novel pleckstrin homology domain-dependent Akt inhibitors inducing apoptosis in prostate cancer cells. *Mol Pharmacol.* (2010) **77**:378–87. doi: 10.1124/mol.109.060475
5. Morad SA, Schmidt C, Buchele B, Schneider B, Wenzler M, Syrovets T, et al. (8R)-3beta,8-dihydroxypolypoda-13E,17E,21-triene induces cell cycle arrest and apoptosis in treatment-resistant prostate cancer cells. *J Nat Prod.* (2011) **74**:1731–6. doi: 10.1021/np200161a
6. Morad SA, Schmid M, Buchele B, Siehl HU, El Gafaary M, Lunov O, et al. A novel semisynthetic inhibitor of the FRB domain of mammalian target of rapamycin blocks proliferation and triggers apoptosis in chemoresistant prostate cancer cells. *Mol Pharmacol.* (2013) **83**:531–41. doi: 10.1124/mol.112.081349
7. Vogler M, Walczak H, Stadel D, Haas TL, Genze F, Jovanovic M, et al. Targeting XIAP bypasses Bcl-2-mediated resistance to TRAIL and cooperates with TRAIL to suppress pancreatic cancer growth in vitro and in vivo. *Cancer Res.* (2008) **68**:7956–65. doi: 10.1158/0008-5472.CAN-08-1296
8. Swadi RR, Sampat K, Herrmann A, Losty PD, See V, Moss DJ. CDK inhibitors reduce cell proliferation and reverse hypoxia-induced metastasis of neuroblastoma tumours in a chick embryo model. *Sci Rep.* (2019) **9**:9136. doi: 10.1038/s41598-019-45571-8
9. Loos C, Syrovets T, Musyanovych A, Mailander V, Landfester K, Simmet T. Amino-functionalized nanoparticles as inhibitors of mTOR and inducers of cell cycle arrest in leukemia cells. *Biomaterials.* (2014) **35**:1944–53. doi: 10.1016/j.biomaterials.2013.11.056
10. Vargas A, Zeisser-Labouebe M, Lange N, Gurny R, Delie F. The chick embryo and its chorioallantoic membrane (CAM) for the in vivo evaluation of drug delivery systems. *Adv Drug Deliv Rev.* (2007) **59**:1162–76. doi: 10.1016/j.addr.2007.04.019
11. Lunov O, Syrovets T, Loos C, Beil J, Delacher M, Tron K, et al. Differential uptake of functionalized polystyrene nanoparticles by human macrophages and a monocytic cell line. *ACS Nano.* (2011) **5**:1657–69. doi: 10.1021/nn2000756
12. Leng T, Miller JM, Bilbao KV, Palanker DV, Huie P, Blumenkranz MS. The chick chorioallantoic membrane as a model tissue for surgical retinal research and simulation. *Retina.* (2004) **24**:427–34. doi: 10.1097/00006982-200406000-00014
13. DeBord LC, Pathak RR, Villaneuva M, Liu HC, Harrington DA, Yu W, et al. The chick chorioallantoic membrane (CAM) as a versatile patient-derived xenograft (PDX) platform for precision medicine and preclinical research. *Am J Cancer Res.* (2018) **8**:1642–60.
14. Vu BT, Shahin SA, Croissant J, Fatieiev Y, Matsumoto K, Le-Hoang Doan T, et al. Chick chorioallantoic membrane assay as an in vivo model to study the effect of nanoparticle-based anticancer drugs in ovarian cancer. *Sci Rep.* (2018) **8**:8524. doi: 10.1038/s41598-018-25573-8
15. Ribatti D, Tamma R. The chick embryo chorioallantoic membrane as an in vivo experimental model to study human neuroblastoma. *J Cell Physiol.* (2018) **234**:152–7. doi: 10.1002/jcp.26773
16. Ribatti D. The chick embryo chorioallantoic membrane as a model for tumor biology. *Exp Cell Res.* (2014) **328**:314–24. doi: 10.1016/j.yexcr.2014.06.010
17. Gabrielli MG, Accili D. The chick chorioallantoic membrane: a model of molecular, structural, and functional adaptation to transepithelial ion transport and barrier function during embryonic development. *J Biomed Biotechnol.* (2010) 2010:940741. doi: 10.1155/2010/940741
18. Nowak-Sliwinska P, Segura T, Iruela-Arispe ML. The chicken chorioallantoic membrane model in biology, medicine and bioengineering. *Angiogenesis.* (2014) **17**:779–804. doi: 10.1007/s10456-014-9440-7
19. Haller S, Ametamey SM, Schibli R, Muller C. Investigation of the chick embryo as a potential alternative to the mouse for evaluation of radiopharmaceuticals. *Nucl Med Biol.* (2015) **42**:226–33. doi: 10.1016/j.nucmedbio.2014.10.010
20. Duman R, Ertekin T, Duman R, Aslan E, Sabaner MC, Cetinkaya E. The novel model: Experimental optical coherence tomography-guided anterior segment imaging chick embryo model. *Indian J Ophthalmol.* (2019) **67**:54–8. doi: 10.4103/ijo.IJO_263_18
21. Ko ZY, Mehta K, Jamil M, Yap CH, Chen N. A method to study the hemodynamics of chicken embryo's aortic arches using optical coherence tomography. *J Biophotonics.* (2017) **10**:353–9. doi: 10.1002/jbio.201600119
22. Goenezen S, Chivukula VK, Midgett M, Phan L, Rugonyi S. 4D subject-specific inverse modeling of the chick embryonic heart outflow tract hemodynamics. *Biomech Model Mechanobiol.* (2016) **15**:723–43. doi: 10.1007/s10237-015-0720-y

23. Midgett M, Chivukula VK, Dorn C, Wallace S, Rugonyi S. Blood flow through the embryonic heart outflow tract during cardiac looping in HH13-HH18 chicken embryos. *J R Soc Interface.* (2015) **12**:20150652. doi: 10.1098/rsif.2015.0652
24. Ma Z, Dou S, Zhao Y, Guo C, Liu J, Wang Q, et al. In vivo assessment of wall strain in embryonic chick heart by spectral domain optical coherence tomography. *Appl Opt.* (2015) **54**:9253–7. doi: 10.1364/AO.54.009253
25. Filas BA, Xu G, Taber LA. Probing regional mechanical properties of embryonic tissue using microindentation and optical coherence tomography. *Methods Mol Biol.* (2015) **1189**:3–16. doi: 10.1007/978-1-4939-1164-6_1
26. Yin X, Liu A, Thornburg KL, Wang RK, Rugonyi S. Extracting cardiac shapes and motion of the chick embryo heart outflow tract from four-dimensional optical coherence tomography images. *J Biomed Opt.* (2012) **17**:96005–1. doi: 10.1117/1.JBO.17.9.096005
27. Liu A, Yin X, Shi L, Li P, Thornburg KL, Wang R, et al. Biomechanics of the chick embryonic heart outflow tract at HH18 using 4D optical coherence tomography imaging and computational modeling. *PLoS ONE.* (2012) **7**:e40869. doi: 10.1371/journal.pone.0040869
28. Li P, Wang RK. Optical coherence tomography provides an ability to assess mechanical property of cardiac wall of developing outflow tract in embryonic heart in vivo. *J Biomed Opt.* (2012) **17**:120502. doi: 10.1117/1.JBO.17.12.120502
29. Li P, Yin X, Shi L, Rugonyi S, Wang RK. In vivo functional imaging of blood flow and wall strain rate in outflow tract of embryonic chick heart using ultrafast spectral domain optical coherence tomography. *J Biomed Opt.* (2012) **17**:96006–1. doi: 10.1117/1.JBO.17.9.096006
30. Happel CM, Thommes J, Thrane L, Manner J, Ortmaier T, Heimann B, et al. Rotationally acquired four-dimensional optical coherence tomography of embryonic chick hearts using retrospective gating on the common central A-scan. *J Biomed Opt.* (2011) **16**:096007. doi: 10.1117/1.3622491
31. Liu X, Zhang K, Huang Y, Kang JU. Spectroscopic-speckle variance OCT for microvasculature detection and analysis. *Biomed Opt Express.* (2011) **2**:2995–3009. doi: 10.1364/BOE.2.002995
32. Li P, Yin X, Shi L, Liu A, Rugonyi S, Wang R. Measurement of strain and strain rate in embryonic chick heart in vivo using spectral domain optical coherence tomography. *IEEE Trans Biomed Eng.* (2011) **58**:51. doi: 10.1109/TBME.2011.2153851
33. Osiac E, Saftoiu A, Gheonea DI, Mandrila I, Angelescu R. Optical coherence tomography and Doppler optical coherence tomography in the gastrointestinal tract. *World J Gastroenterol.* (2011) **17**:15–20. doi: 10.3748/wjg.v17.i1.15
34. Manner J, Thrane L, Norozi K, Yelbuz TM. In vivo imaging of the cyclic changes in cross-sectional shape of the ventricular segment of pulsating embryonic chick hearts at stages 14 to 17: a contribution to the understanding of the ontogenesis of cardiac pumping function. *Dev Dyn.* (2009) **238**:3273–84. doi: 10.1002/dvdy.22159
35. Liu A, Wang R, Thornburg KL, Rugonyi S. Efficient postacquisition synchronization of 4-D nongated cardiac images obtained from optical coherence tomography: application to 4-D reconstruction of the chick embryonic heart. *J Biomed Opt.* (2009) **14**:044020. doi: 10.1117/1.3184462
36. Rugonyi S, Shaut C, Liu A, Thornburg K, Wang RK. Changes in wall motion and blood flow in the outflow tract of chick embryonic hearts observed with optical coherence tomography after outflow tract banding and vitelline-vein ligation. *Phys Med Biol.* (2008) **53**:5077–91. doi: 10.1088/0031-9155/53/18/015
37. Filas BA, Knutsen AK, Bayly PV, Taber LA. A new method for measuring deformation of folding surfaces during morphogenesis. *J Biomech Eng.* (2008) **130**:061010. doi: 10.1115/1.2979866
38. Chen Z, Milner TE, Srinivas S, Wang X, Malekafzali A, van Gemert MJ, et al. Noninvasive imaging of in vivo blood flow velocity using optical Doppler tomography. *Opt Lett.* (1997) **22**:1119–21. doi: 10.1364/OL.22.001119
39. Seal HE, Lilian SJ, Popratiloff A, Hirsch JC, Peusner KD. Implementing the chick embryo model to study vestibular developmental disorders. *J Neurophysiol.* (2019) **122**:2272–83. doi: 10.1152/jn.00434.2019
40. Shigeta Y, Fujiwara N, Koike M, Yamataka A, Doi T. Bone mineral density is increased in the cadmium-induced omphalocele chick model by using three-dimensional micro-computed tomography. *Pediatr Surg Int.* (2019) **35**:911–4. doi: 10.1007/s00383-019-04501-5
41. Moreno-Jimenez I, Hulsart-Billstrom G, Lanham SA, Janeczek AA, Kontouli N, Kanczler JM, et al. The chorioallantoic membrane (CAM) assay for the study of human bone regeneration: a refinement animal model for tissue engineering. *Sci Rep.* (2016) **6**:32168. doi: 10.1038/srep32168
42. Yair R, Shahar R, Uni Z. In ovo feeding with minerals and vitamin D3 improves bone properties in hatchlings and mature broilers. *Poult Sci.* (2015) **94**:2695–707. doi: 10.3382/ps/pev252
43. Milisits G, Donko T, Dalle Zotte A, Sartori A, Szentirmai E, Emri M, et al. Application of computed tomography to assess the effect of egg yolk ratio on body composition in chickens of different genotype and gender at hatch and during the rearing period. *Br Poult Sci.* (2013) **54**:611–9. doi: 10.1080/00071668.2013.811714
44. Henning AL, Jiang MX, Yalcin HC, Butcher JT. Quantitative three-dimensional imaging of live avian embryonic morphogenesis via micro-computed tomography. *Dev Dyn.* (2011) **240**:1949–57. doi: 10.1002/dvdy.22694
45. Kim JS, Min J, Recknagel AK, Riccio M, Butcher JT. Quantitative three-dimensional analysis of embryonic chick morphogenesis via microcomputed tomography. *Anat Rec (Hoboken).* (2011) :1–10. doi: 10.1002/ar.21276
46. Metscher BD. MicroCT for developmental biology: a versatile tool for high-contrast 3D imaging at histological resolutions. *Dev Dyn.* (2009) **238**:632–40. doi: 10.1002/dvdy.21857
47. Chevalier NR, Dacher N, Jacques C, Langlois L, Guedj C, Faklaris O. Embryogenesis of the peristaltic reflex. *J Physiol.* (2019) **597**:2785–801. doi: 10.1113/JP277746
48. Lindner T, Klose R, Streckenbach F, Stahnke T, Hadlich S, Kuhn JP, et al. Morphologic and biometric evaluation of chick embryo eyes in ovo using 7 Tesla MRI. *Sci Rep.* (2017) **7**:2647. doi: 10.1038/s41598-017-02755-4
49. Zhou Z, Chen Z, Shan J, Ma W, Li L, Zu J, et al. Monitoring brain development of chick embryos in vivo using 3.0 T MRI: subdivision volume change and preliminary structural quantification using DTI. *BMC Dev Biol.* (2015) **15**:29. doi: 10.1186/s12861-015-0077-6
50. Boss A, Oppitz M, Wehrl HF, Rossi C, Feuerstein M, Claussen CD, et al. Measurement of T1, T2, and magnetization transfer properties during embryonic development at 7 Tesla using the chicken model. *J Magn Reson Imaging.* (2008) **28**:1510–4. doi: 10.1002/jmri.21601
51. Bain MM, Fagan AJ, Mullin JM, McNaught I, McLean J, Condon B. Noninvasive monitoring of chick development in ovo using a 7T MRI system from day 12 of incubation through to hatching. *J Magn Reson Imaging.* (2007) **26**:198–201. doi: 10.1002/jmri.20963
52. Hogers B, Gross D, Lehmann V, de Groot HJ, de Roos A, Gittenberger-de Groot AC, et al. Magnetic resonance microscopy at 17.6-Tesla on chicken embryos in vitro. *J Magn Reson Imaging.* (2001) **14**:83–6. doi: 10.1002/jmri.1155
53. Falen SW, Szeverenyi NM, Packard DS, Jr., Ruocco MJ. Magnetic resonance imaging study of the **structure** of the yolk in the developing avian egg. *J Morphol.* (1991) 209:331–42. doi: 10.1002/jmor.1052090308
54. Moseley ME, Wendland MF, Darnell DK, Gooding CA. Metabolic and anatomic development of the chick embryo as studied by phosphorus-31 magnetic resonance spectroscopy and proton MRI. *Pediatr Radiol.* (1989) **19**:400–5. doi: 10.1007/BF02387637
55. Streckenbach F, Klose R, Langner S, Langner I, Frank M, Wree A, et al. Ultrahigh-field quantitative mr microscopy of the chicken eye in vivo throughout the in ovo period. *Mol Imaging Biol.* (2019) **21**:78–85. doi: 10.1007/s11307-018-1208-9
56. Klose R, Streckenbach F, Hadlich S, Stahnke T, Guthoff R, Wree A, et al. [Ultra-high-field MRI in the Chicken Embryo in Ovo - a Model for Experimental Ophthalmology]. *Klin Monbl Augenheilkd.* (2017) **234**:1458–62. doi: 10.1055/s-0043-120675
57. Goodall N, Kisiswa L, Prashar A, Faulkner S, Tokarczuk P, Singh K, et al. 3-Dimensional modelling of chick embryo eye development and growth using high resolution magnetic resonance imaging. *Exp Eye Res.* (2009) **89**:511–21. doi: 10.1016/j.exer.2009.05.014
58. Herrmann A, Taylor A, Murray P, Poptani H, See V. Magnetic resonance imaging for characterization of a chick

embryo model of cancer cell metastases. *Mol Imaging.* (2018) **17**:1536012118809585. doi: 10.1177/1536012118809585

59. Shrivastava S, Barmon D, Kataki AC, Deka P, Sharma JD, Choudhary BK, et al. Magnetic resonance imaging in pre-operative staging of endometrial cancer. *Indian J Cancer.* (2016) **53**:181–5. doi: 10.4103/0019-509X.180859
60. Tung YT, Huang PW, Chou YC, Lai CW, Wang HP, Ho HC, et al. Lung tumorigenesis induced by human vascular endothelial growth factor (hVEGF)-A165 overexpression in transgenic mice and amelioration of tumor formation by miR-16. *Oncotarget.* (2015) **6**:10222–38. doi: 10.18632/oncotarget.3390
61. Zuo Z, Syrovets T, Genze F, Abaei A, Ma G, Simmet T, et al. High-resolution MRI analysis of breast cancer xenograft on the chick chorioallantoic membrane. *NMR Biomed.* (2015) **28**:440–7. doi: 10.1002/nbm.3270
62. Al-Mutawa YK, Herrmann A, Corbishley C, Losty PD, Phelan M, See V. Effects of hypoxic preconditioning on neuroblastoma tumour oxygenation and metabolic signature in a chick embryo model. *Biosci Rep.* (2018) **38**:185. doi: 10.1042/BSR20180185
63. Herrmann A, Rice M, Levy R, Pizer BL, Losty PD, Moss D, et al. Cellular memory of hypoxia elicits neuroblastoma metastasis and enables invasion by non-aggressive neighbouring cells. *Oncogenesis.* (2015) **4**:e138. doi: 10.1038/oncsis.2014.52
64. Kumar V, Nag TC, Sharma U, Mewar S, Jagannathan NR, Wadhwa S. High resolution 1H NMR-based metabonomic study of the auditory cortex analogue of developing chick (Gallus gallus domesticus) following prenatal chronic loud music and noise exposure. *Neurochem Int.* (2014) **76**:99–108. doi: 10.1016/j.neuint.2014.07.002
65. Zuo Z, Syrovets T, Wu Y, Hafner S, Vernikouskaya I, Liu W, et al. The CAM cancer xenograft as a model for initial evaluation of MR labelled compounds. *Sci Rep.* (2017) **7**:46690. doi: 10.1038/srep46690
66. Goodfellow F, Simchick GA, Mortensen LJ, Stice SL, Zhao Q. Tracking and quantification of magnetically labeled stem cells using magnetic resonance imaging. *Adv Funct Mater.* (2016) **26**:3899–915. doi: 10.1002/adfm.201504444
67. Pereira SM, Herrmann A, Moss D, Poptani H, Williams SR, Murray P, et al. Evaluating the effectiveness of transferrin receptor-1 (TfR1) as a magnetic resonance reporter gene. *Contrast Media Mol Imaging.* (2016) **11**:236–44. doi: 10.1002/cmmi.1686
68. Zlatopolskiy BD, Zischler J, Schafer D, Urusova EA, Guliyev M, Bannykh O, et al. Discovery of 7-[(18)F]Fluorotryptophan as a novel positron emission tomography (PET) probe for the visualization of tryptophan metabolism *in vivo*. *J Med Chem.* (2018) **61**:189–206. doi: 10.1021/acs.jmedchem.7b01245
69. Warnock G, Turtoi A, Blomme A, Bretin F, Bahri MA, Lemaire C, et al. In vivo PET/CT in a human glioblastoma chicken chorioallantoic membrane model: a new tool for oncology and radiotracer development. *J Nucl Med.* (2013) **54**:1782–8. doi: 10.2967/jnumed.112.117150
70. Gebhardt P, Wurbach L, Heidrich A, Heinrich L, Walther M, Opfermann T, et al. Dynamic behaviour of selected PET tracers in embryonated chicken eggs. *Rev Esp Med Nucl Imagen Mol.* (2013) **32**:371–7. doi: 10.1016/j.remnie.2013.09.013
71. Wurbach L, Heidrich A, Opfermann T, Gebhardt P, Saluz HP. Insights into bone metabolism of avian embryos in ovo via 3D and 4D 18F-fluoride positron emission tomography. *Mol Imaging Biol.* (2012) **14**:688–98. doi: 10.1007/s11307-012-0550-6
72. Fiebig HH, Maier A, Burger AM. Clonogenic assay with established human tumour xenografts: correlation of in vitro to in vivo activity as a basis for anticancer drug discovery. *Eur J Cancer.* (2004) **40**:802–20. doi: 10.1016/j.ejca.2004.01.009
73. Landis MD, Lehmann BD, Pietenpol JA, Chang JC. Patient-derived breast tumor xenografts facilitating personalized cancer therapy. *Breast Cancer Res.* (2013) **15**:201. doi: 10.1186/bcr3355
74. de Bono JS, Ashworth A. Translating cancer research into targeted therapeutics. *Nature.* (2010) **467**:543–9. doi: 10.1038/nature09339
75. Tentler JJ, Tan AC, Weekes CD, Jimeno A, Leong S, Pitts TM, et al. Patient-derived tumour xenografts as models for oncology drug development. *Nat Rev Clin Oncol.* (2012) **9**:338–50. doi: 10.1038/nrclinonc.2012.61
76. Rosfjord E, Lucas J, Li G, Gerber HP. Advances in patient-derived tumor xenografts: from target identification to predicting clinical response rates in oncology. *Biochem Pharmacol.* (2014) **91**:135–43. doi: 10.1016/j.bcp.2014.06.008
77. Galuschka C, Proynova R, Roth B, Augustin HG, Muller-Decker K. Models in translational oncology: a public resource database for preclinical cancer research. *Cancer Res.* (2017) **77**:2557–63. doi: 10.1158/0008-5472.CAN-16-3099
78. Lokman NA, Elder AS, Ricciardelli C, Oehler MK. Chick chorioallantoic membrane (CAM) assay as an in vivo model to study the effect of newly identified molecules on ovarian cancer invasion and metastasis. *Int J Mol Sci.* (2012) **13**:9959–70. doi: 10.3390/ijms13089959
79. Ribatti D. The chick embryo chorioallantoic membrane (CAM) assay. *Reprod Toxicol.* (2017) **70**:97–101. doi: 10.1016/j.reprotox.2016.11.004
80. Hamburger V, Hamilton HL. A series of normal stages in the development of the chick embryo. *J Morphol.* (1951) **88**:49–92. doi: 10.1002/jmor.1050880104
81. Bone SN, Johnson GA, Thompson MB. Three-dimensional magnetic resonance microscopy of the developing chick embryo. *Invest Radiol.* (1986) **21**:782–7. doi: 10.1097/00004424-198610000-00003
82. Johnson GA, Thompson MB, Drayer BP, Bone SN. Magnetic resonance microscopy in neurologic models. *Acta Radiol Suppl.* (1986) **369**:267–8.
83. Effmann EL, Johnson GA, Smith BR, Talbott GA, Cofer G. Magnetic resonance microscopy of chick embryos in ovo. *Teratology.* (1988) **38**:59–65. doi: 10.1002/tera.1420380109
84. Hollett MD, Cofer GP, Johnson GA. In situ magnetic resonance microscopy. *Invest Radiol.* (1987) **22**:965–8. doi: 10.1097/00004424-198712000-00009
85. Lirette A, Towner RA, Liu Z EG, Janzen. Chambers JR, Fairfull RW, Milligan LP, et al. In vivo nuclear magnetic resonance spectroscopy of chicken embryos from two broiler strains of varying fat content. *Poult Sci.* (1993) **72**:1411–20. doi: 10.3382/ps.0721411
86. Peebles DM, Dixon JC, Thornton JS, Cady EB, Priest A, Miller SL, et al. Magnetic resonance proton spectroscopy and diffusion weighted imaging of chick embryo brain in ovo. *Brain Res Dev Brain Res.* (2003) **141**:101–7. doi: 10.1016/S0165-3806(03)00002-6
87. Hutchison MJ, Lirette A, Etches RJ, Towner RA, Janzen EG. Research note: an assessment of egg yolk structure using magnetic resonance imaging. *Poult Sci.* (1992) **71**:2117–21. doi: 10.3382/ps.0712117
88. Donoghue DJ, Myers K. Imaging residue transfer into egg yolks. *J Agric Food Chem.* (2000) **48**:6428–30. doi: 10.1021/jf000146h
89. Smith BR, Effmann EL, Johnson GA. MR microscopy of chick embryo vasculature. *J Magn Reson Imaging.* (1992) **2**:237–40. doi: 10.1002/jmri.1880020220
90. Zhang X, Yelbuz TM, Cofer GP, Choma MA, Kirby ML, Johnson GA. Improved preparation of chick embryonic samples for magnetic resonance microscopy. *Magn Reson Med.* (2003) **49**:1192–5. doi: 10.1002/mrm.10460
91. Yelbuz TM, Zhang X, Choma MA, Stadt HA, Zdanowicz M, Johnson GA, et al. Images in cardiovascular medicine. Approaching cardiac development in three dimensions by magnetic resonance microscopy. *Circulation.* (2003) **108**:e154–5. doi: 10.1161/01.CIR.0000102940.17908.CA
92. Yelbuz TM, Waldo KL, Zhang X, Zdanowicz M, Parker J, Creazzo TL, et al. Myocardial volume and organization are changed by failure of addition of secondary heart field myocardium to the cardiac outflow tract. *Dev Dyn.* (2003) **228**:152–60. doi: 10.1002/dvdy.10364
93. Holmes WM, McCabe C, Mullin JM, Condon B, Bain MM. Images in cardiovascular medicine. Noninvasive self-gated magnetic resonance cardiac imaging of developing chick embryos in ovo. *Circulation.* (2008) **117**:e346–7. doi: 10.1161/CIRCULATIONAHA.107.747154
94. Holmes WM, McCabe C, Mullin JM, Condon B, Bain MM. In ovo non-invasive quantification of the myocardial function and mass of chick embryos using magnetic resonance imaging. *NMR Biomed.* (2009) **22**:745–52. doi: 10.1002/nbm.1386
95. Li X, Liu J, Davey M, Duce S, Jaberi N, Liu G, et al. Micro-magnetic resonance imaging of avian embryos. *J Anat.* (2007) **211**:798–809. doi: 10.1111/j.1469-7580.2007.00825.x
96. Goodfellow FT, Tesla B, Simchick G, Zhao Q, Hodge T, Brindley MA, et al. Zika virus induced mortality and microcephaly in chicken embryos. *Stem Cells Dev.* (2016) **25**:1691–7. doi: 10.1089/scd.2016.0231

97. Dingman S, Hurlburt L, Thomas R, Guo C. Tissue immunoassay for 19F-tagged 5-hydroxytryptophan. *J Immunoassay Immunochem.* (2003) 24:325–44. doi: 10.1081/IAS-120025771
98. Oppitz M, Pintaske J, Kehlbach R, Schick F, Schriek G, Busch C. Magnetic resonance imaging of iron-oxide labeled SK-Mel 28 human melanoma cells in the chick embryo using a clinical whole body MRI scanner. *MAGMA.* (2007) **20**:1–9. doi: 10.1007/s10334-006-0062-y
99. Pereira SM, Moss D, Williams SR, Murray P, Taylor A. Overexpression of the MRI reporter genes ferritin and transferrin receptor affect iron homeostasis and produce limited contrast in mesenchymal stem cells. *Int J Mol Sci.* (2015) **16**:15481–96. doi: 10.3390/ijms160715481
100. Faucher L, Guay-Begin AA, Lagueux J, Cote MF, Petitclerc E, Fortin MA. Ultra-small gadolinium oxide nanoparticles to image brain cancer cells in vivo with MRI. *Contrast Media Mol Imaging.* (2011) **6**:209–18. doi: 10.1002/cmmi.420
101. Taylor A, Herrmann A, Moss D, See V, Davies K, Williams SR, et al. Assessing the efficacy of nano- and micro-sized magnetic particles as contrast agents for MRI cell tracking. *PLoS ONE.* (2014) **9**:e100259. doi: 10.1371/journal.pone.0100259
102. Hafner S, Raabe M, Wu Y, Wang T, Zuo Z, Rasche V, et al. High-contrast magnetic resonance imaging and efficientdelivery of an albumin nanotheranostic in triple-negativebreast cancer xenografts. *Adv Therap.* (2019) **2**:1900084. doi: 10.1002/adtp.201900084
103. Buschmann J, Welti M, Hemmi S, Neuenschwander P, Baltes C, Giovanoli P, et al. Three-dimensional co-cultures of osteoblasts and endothelial cells in DegraPol foam: histological and high-field magnetic resonance imaging analyses of pre-engineered capillary networks in bone grafts. *Tissue Eng Part A.* (2011) **17**:291–9. doi: 10.1089/ten.tea.2010.0278
104. Chesnick IE, Fowler CB, Mason JT, Potter K. Novel mineral contrast agent for magnetic resonance studies of bone implants grown on a chick chorioallantoic membrane. *Magn Reson Imaging.* (2011) **29**:1244–54. doi: 10.1016/j.mri.2011.07.022
105. Kivrak Pfiffner F, Waschkies C, Tian Y, Woloszyk A, Calcagni M, Giovanoli P, et al. A new in vivo magnetic resonance imaging method to noninvasively monitor and quantify the perfusion capacity of three-dimensional biomaterials grown on the chorioallantoic membrane of chick embryos. *Tissue Eng Part C Methods.* (2015) **21**:339–46. doi: 10.1089/ten.tec.2014.0212
106. Waschkies C, Nicholls F, Buschmann J. Comparison of medetomidine, thiopental and ketamine/midazolam anesthesia in chick embryos for in ovo Magnetic Resonance Imaging free of motion artifacts. *Sci Rep.* (2015) **5**:15536. doi: 10.1038/srep15536
107. Heidrich A, Wurbach L, Opfermann T, Saluz HP. Motion-artifact-free in vivo imaging utilizing narcotized avian embryos in ovo. *Mol Imaging Biol.* (2011) **13**:208–14. doi: 10.1007/s11307-010-0355-4
108. Freesmeyer M, Kuehnel C, Opfermann T, Niksch T, Wiegand S, Stolz R, et al. The use of ostrich eggs for in ovo research: making preclinical imaging research affordable and available. *J Nucl Med.* (2018) **59**:1901–6. doi: 10.2967/jnumed.118.210310
109. Steinemann G, Dittmer A, Schmidt J, Josuttis D, Fahling M, Biersack B, et al. Antitumor and antiangiogenic activity of the novel chimeric inhibitor animacroxam in testicular germ cell cancer. *Mol Oncol.* (2019) **13**:2679–96. doi: 10.1002/1878-0261.12582
110. Winter G, Koch A, Subgang A, Solbach C, Glatting G, Rasche V, et al. Evaluation of binding specificity of target-specific radioligands in xenografts by multi-modal PET and MR imaging using the Hen's egg test chorioallantoic membrane (HET-CAM) model. *J Nucl Med.* (2019) **16**:1003.
111. Zhou Z, Xu J, Delproposto ZS, Hua J, Fan Y, Zhang Z, et al. Feasibility of in ovo diffusion tractography in the chick embryo using a dual-cooling technique. *J Magn Reson Imaging.* (2012) **36**:993–1001. doi: 10.1002/jmri.23684
112. Dingman S, Hurlburt L, Branch C. Acute no-effect dose for in ova exposure to C3F7 tagged 5-hydroxytryptophan, a novel probe for investigating neural development. *Mol Imaging Biol.* (2004) **6**:12–6. doi: 10.1016/j.mibio.2003.11.001
113. Tazawa H, Rahn H. Temperature and metabolism of chick embryos and hatchlings after prolonged cooling. *J Exp Zool Suppl.* (1987) **1**:105–9.
114. Wojtczak JA. The hemodynamic effects of halothane and isoflurane in chick embryo. *Anesth Analg.* (2000) **90**:1331–5. doi: 10.1097/00000539-200006000-00012
115. Berry DG. Effect of ketamine on the isolated chick embryo heart. *Anesth Analg.* (1974) **53**:919–23. doi: 10.1213/00000539-197453060-00021
116. Kulesa PM, Bailey CM, Cooper C, Fraser SE. In ovo live imaging of avian embryos. *Cold Spring Harb Protoc.* (2010) **2010**:pdb prot5446. doi: 10.1101/pdb.prot5446
117. Canaria CA, Lansford R. Advanced optical imaging in living embryos. *Cell Mol Life Sci.* (2010) **67**:3489–97. doi: 10.1007/s00018-010-0440-5
118. Jefferies B, Tong Z, Nawroth R. Bioluminescence imaging in the chick chorioallantoic membrane assay. *Methods Mol Biol.* (2020) **2081**:211–7. doi: 10.1007/978-1-4939-9940-8_15
119. Jefferies B, Lenze F, Sathe A, Truong N, Anton M, von Eisenhart-Rothe R, et al. Non-invasive imaging of engineered human tumors in the living chicken embryo. *Sci Rep.* (2017) **7**:4991. doi: 10.1038/s41598-017-04572-1
120. Raghunathan R, Singh M, Dickinson ME, Larin KV. Optical coherence tomography for embryonic imaging: a review. *J Biomed Opt.* (2016) **21**:50902. doi: 10.1117/1.JBO.21.5.050902
121. Teddy JM, Lansford R, Kulesa P. Four-color M, 4-D time-lapse confocal imaging of chick embryos. *Biotechniques.* (2005) **39**:703–10. doi: 10.2144/000112017
122. McQuinn TC, Bratoeva M, Dealmeida A, Remond M, Thompson RP, Sedmera D. High-frequency ultrasonographic imaging of avian cardiovascular development. *Dev Dyn.* (2007) **236**:3503–13. doi: 10.1002/dvdy.21357
123. Sharma A, Ishak N, Swee-Hin T, Pramanik M. High resolution, label-free photoacoustic imaging of live chicken embryo developing in bioengineered eggshell. *J Biophotonics.* (2020) **13**:e201960108. doi: 10.1002/jbio.201960108


**Conflict of Interest:** The authors declare that the research was conducted in the absence of any commercial or financial relationships that could be construed as a potential conflict of interest.

frontiers in Physics

REVIEW
published: 10 June 2020
doi: 10.3389/fphy.2020.00183

# Technical Aspects of *in vivo* Small Animal CMR Imaging

**Hao Li[1,2], Alireza Abaei[1], Patrick Metze[3], Steffen Just[3], Qinghua Lu[2] and Volker Rasche[1,3]***

[1] Ulm University, Core Facility Small Animal Imaging, Ulm, Germany, [2] Department of Cardiology, The Second Hospital of Shandong University, Jinan, China, [3] Department of Internal Medicine II, Ulm University Medical Center, Ulm, Germany

Cardiovascular magnetic resonance (CMR) imaging has become an accurate and versatile imaging modality to visualize the cardiovascular system in normal or abnormal conditions. In preclinical research, small rodent animal models of human cardiovascular diseases are frequently used to investigate the basic underlying mechanism of normal and abnormal cardiac function and for monitoring the disease progression under therapy. Technical improvements have enabled the transfer of CMR to small animal research, and as such made this non-invasive technique available to provide insights into cardiac morphology, function, perfusion, and pathophysiology in small animal cardiac disease models. This article reviews the basic technical approaches to *in vivo* small animal magnetic resonance imaging and its variants for the most promising applications.

**Keywords: cardiac MRI, cardiac MRS, imaging techniques, small animals, cardiovascular diseases, cardiac function**

OPEN ACCESS

***Edited by:***
*Andreas Hess, University of Erlangen Nuremberg, Germany*

***Reviewed by:***
*Yu-chung Norman Cheng, Wayne State University, United States*
*Albrecht Ingo Schmid, Medical University of Vienna, Austria*

***Correspondence:**
*Volker Rasche*
*volker.rasche@uni-ulm.de*

***Specialty section:***
*This article was submitted to Medical Physics and Imaging, a section of the journal Frontiers in Physics*

***Received:*** *13 December 2019*
***Accepted:*** *27 April 2020*
***Published:*** *10 June 2020*

***Citation:***
*Li H, Abaei A, Metze P, Just S, Lu Q and Rasche V (2020) Technical Aspects of in vivo Small Animal CMR Imaging. Front. Phys. 8:183. doi: 10.3389/fphy.2020.00183*

## INTRODUCTION

Cardiovascular disease is considered the leading cause of death in the developed world, with high morbidity and mortality [1, 2]. In preclinical research, small rodent animal models of human cardiovascular disease are frequently used to investigate the basic underlying mechanism of normal and abnormal cardiac functions and for monitoring the disease progression under therapy [3]. Over the past decades, the use of small animal models has provided improved understanding of cardiac diseases [4, 5].

Translational research accounts for a large proportion of animal studies performed each year. Since the implementation of the 3 Rs principles (replacement, refinement, reduction) into the European Directive 2010/63/EU, medical imaging is highly recommended in translational research, because it can visualize the progression of the disease longitudinally often in a quantitative and non-invasive way. It thus has the potential to significantly reduce the number of experimental animals. Due to the high spatial and temporal resolutions, a versatile image contrast, and access to metabolic information, magnetic resonance imaging (MRI), and spectroscopy (MRS) have been proven to be promising diagnostic tools to monitor disease progression and response to treatment in small animal models. Its versatility, accuracy and high reproducibility has made cardiovascular magnetic resonance (CMR) imaging the non-invasive reference modality in preclinical research. MRI offers exceptional accuracy in the investigation of cardiac anatomy, perfusion, wall motion, and contractility, and its excellent soft-tissue contrast enables advanced myocardial tissue characterization [6–9].

However, the small size of the mouse heart [5–6 mm left ventricle (LV) diameter, ∼0.2 g of heart weight] [10], high heart (about 250–600 beats per minute [bpm]), respiratory (about 60–160 cycles per minute [cpm]) rates, and fast systemic blood circulation times (4–5 heartbeats) impose substantial challenges for functional assessment by MRI. Over the past decades, major improvements in MRI methodology and instrumentation have been achieved, including rapidly switching high-performance gradient systems, ultra-high magnetic fields (>7 T), and non-Cartesian k-space encoding strategies such as spiral [11, 12] and radial trajectories [13, 14]. In combination with advanced mathematical concepts for image reconstruction [15–17] rapid data acquisition techniques, providing a high temporal resolution while preserving adequate spatial resolution and sufficient volume coverage, have been realized.

The main objective of this manuscript is to summarize the most important technical aspects of *in vivo* small animal CMR imaging and the required variants for specific applications. For the physiological, biological and pharmacological applications and perspective, please refer to comprehensive recent reviews [18–22]. With the included brief description of hardware demands and animal handling strategies, the reader will get familiar with the basic principle and challenges of small animal CMR imaging.

## TECHNICAL CONSIDERATIONS AND METHODOLOGIES

### Hardware

Small animal MRI systems usually possess high field strength ranging from 4.7 up to 21 Tesla and strong gradient systems with bore diameters typically ranging between 10 and 40 cm. Higher field strengths provide an increased signal-to-noise ratio (SNR), thus enabling a higher spatial resolution. Disadvantages arise from changes in relaxation parameters, a higher chemical shift, a higher magnetic field inhomogeneity, susceptibility to artifacts, and increased specific absorption rate (SAR) [23], which often limits the translation of the results to clinical settings. Even though the lower SNR can partly be compensated with dedicated coils at 1.5T and 3T scanner [24, 25], and high-resolution mouse embryonic cardiac images were acquired at 17.6T [26], due to the high costs of ultra-high field instruments, field strengths between 7 and 11.7 T are most commonly used in small animal CMR imaging [7, 27, 28].

Further SNR improvement is achieved with dedicated radio frequency (RF) coils [29, 30]. Especially phased-array coils, additionally enabling parallel imaging [31, 32], have become standard in small animal CMR imaging. Further improvements have been reported by Wagenhaus et al. [33] and Dieringer et al. [34], who showed a 3–5-fold gain in SNR when comparing a 4-element room-temperature heart coil with a cryogenic coil.

As a further major progress, gradient systems that, depending on their inner diameters, provide amplitudes of up to 1,000 mT/m with slew rates of up to 9,000 T/m/s, have been introduced. In combination with efficient water-cooling high-duty cycles have been achieved, thus enabling rapid imaging at a high spatial resolution and a large field-of-view (FOV).

### Animal Handling

Motion is one of the main challenges for *in vivo* imaging. In contrast to human studies, suitable anesthesia is generally required in small animal imaging to prevent animal motion. During scanning, the physiological status of the animal needs to be carefully monitored (e.g., ECG, respiration sensor, rectal temperature probe) and heating blankets are required to avoid temperature loss of the animal during anesthesia. General anesthesia is achieved using injectable or inhalational agents, or a combination of the two methods, to achieve the loss of consciousness, analgesia, suppression of reflex activity, and muscle relaxation [35]. An ideal anesthetic agent for animal CMR imaging should be easy to administer, and provide adequate and reproducible immobilization, preferably without changes in cardiac function and heart rate. However, since such agents are not available, the impact of the agent on cardiovascular physiology, especially depression of cardiac function and heart rate, respiratory function and induced hypothermia [36], has to be carefully considered.

Compared with inhalant agents, injectable anesthetics have several advantages. Their administration is more convenient to perform, and complex and expensive equipment such as precision vaporizers and specific breathing systems are not required. Due to its large safety threshold and compatibility with other drugs, ketamine is one of the most widely used anesthetics in animal research [37]. However, because of muscle rigidity, it is usually combined with xylazine, resulting in cardiac and respiratory depression. Berry et al. [38] reported deep sedation by subcutaneous injection of morphine and midazolam causing significantly less depression of heart rate and ejection fraction than imaging during general anesthesia with isoflurane in mice with normal cardiac function. Pachon et al. [39] suggested that ketamine was the least effective on the LV function and the heart rate, followed by Avertin, isoflurane (see below), and ketamine-xylazine combination. Other agents such as pentobarbitone, fentanyl/fluanisone, and urethane were shown to result in profound cardiovascular depression or prolonged recovery time and are not recommended in cardiac imaging. A general major drawback of injectable agents results from the limited anesthesia duration and adjustment possibilities during scanning.

Even though more complicated, in most cases inhalation anesthesia by halothanes is suggested. Here, the preferred approach is isoflurane inhalation [40]. Major advantages comprise short induction and fast recovery times, convenient adjustment during scanning, rather low hemodynamic depression, and flexible maintenance. In order to achieve high reproducible experiments, isoflurane (5% for induction, 1–1.5% for maintenance) in medical air (0.1 L/min) [7] is normally used.

### Cine Imaging

For the quantification of cardiac function by CMR, rapid data acquisition techniques are required. Where for clinical applications mainly steady-state-free-procession (SSFP) sequences are applied for improving myocardium-blood contrast. In small animal CMR, fast low-angle shot (FLASH) gradient-echo [41] techniques are applied to avoid banding artifacts caused by off-resonances. Because of high heart and respiratory rates, real-time imaging of cardiac function is normally not possible and CMR imaging generally requires synchronization of the data acquisition to the cardiac and respiratory motion. In current practice, prospective triggering and retrospective/self-gated gating are used.

### Prospective Trigger

For the prospective triggering, the ECG signals are simultaneously recorded for synchronization [42, 43]. ECG signals are normally drawn from two electrodes attached to one front and rear paw. After detecting the R wave, data acquisition is performed either at a specific phase of the heart (single-phase imaging) or continuously over multiple consecutive phases of the cardiac cycle (multi-phase or cine imaging, **Figure 1A**). Simultaneously, the respiration phase is measured with a balloon pressure sensor, and respiratory gating is additionally applied to avoid respiratory motion artifacts.

However, radiofrequency pulses and gradient switching induce interferences in the ECG signal and may cause false triggers, which are more prominent at ultra-high magnetic fields. Further, the magneto-hydrodynamic effect is more prominent at higher field-strengths, often limiting the detectability of the R-peak. To avoid severe susceptibility artifacts, non-metallic materials like carbon wires have been introduced almost 30 years ago [44]. Recently, Choquet et al. [45] tested carbon wire electrodes in an 11.7 T magnetic field. Even though R-peaks were usually detectable, a clear distortion in the ECG signal still persisted. Other types of trigger devices such as optical fiber-based gating were developed, and excellent ECG signal quality has been reported [46]. Meanwhile, different filter techniques were developed to reduce ECG distortion during MRI examinations [47–49]. In principle, these filter techniques allow electrical ECG recordings for scan synchronization even at high field strengths. However, a principal limitation of prospective triggering is the required gap prior to the R-peak to ensure its proper detection. This causes loss of the end-diastolic phase or, in case only every second heartbeat is used for triggering, doubling of the scan times.

### Retrospective Gating

In the clinical setting retrospective gating refers to simultaneous recording of the ECG signal with the data acquisition and subsequent reordering of the data into different cardiac phases according to the recorded ECG (**Figure 1B**). In small animal research, the term is related to self-gating techniques. Here, data synchronization is not based on physiological signals and no ECG recording is required. Instead, an additional navigator signal is acquired prior to each data acquisition (echo). After the scan, this navigator signal is analyzed and used to assign each echo to its correct position in the cardiac and respiratory cycles (**Figure 1C**).

Two of the most widely used retrospective gating sequences are self-gated FLASH (IgFLASH) and ultra-short echo time (IgUTE). The advantage of IgUTE compared to its Cartesian counterpart IgFLASH is the shorter achievable echo time (TE), which helps to reduce flow artifacts. Hoerr et al. [50] reported an IgUTE sequence with a minimal TE of 314 μs, clearly showing superior image quality especially for the delineation of small morphological structures like valves or papillary muscles. When compared with igFLASH, a substantial reduction of flow artifacts but maintained functional parameters were reported for IgUTE by Motaal et al. [13].

Compared with prospective triggering, retrospective approaches yielded similar global cardiac function data [43, 51]. As the data are acquired continuously, a flexible number of reconstructed cardiac phases and different temporal resolution can be achieved. However, the data acquired during certain periods of motion are not used for reconstruction. Thence, data oversampling is required to compensate for excluded data [52]. More importantly, the retrospective gating allows for steady-state acquisition, which is essential for mapping myocardial relaxation times [53, 54] or for quantifying image contrast as required in molecular CMR imaging with contrast agents [53, 55].

## Real-Time Imaging

The self-gating techniques enable high-quality cardiac MRI with high reproducibilities [7]. However, the acquisition times in the minute range for a single slice still limit their applications in time critical settings such as pharmacological stress or first-pass perfusion imaging. Recently, based on technical progress in hardware and software, real-time concepts have been introduced and applied in CMR imaging. Real-time imaging refers to the rapid and continuous data acquisition followed by image reconstruction and visualization. To reduce acquisition times, dedicated real-time methods, including parallel imaging [56–58], k-t acceleration methods [59–61], and compressed sensing (CS) [15, 62, 63], have been suggested and initially evaluated [64] for the rapid and continuous acquisition of image series. Real-time methods utilize undersampling techniques, thus reducing the amount of acquired data for a single frame of an image series. Iterative reconstruction algorithms ensure image fidelity, e.g., by adding spatial and temporal regularization. Recent progress in real-time MRI results in high-quality images with high SNR, adequate spatial resolution and unsurpassed temporal resolution [65–68].

Dai et al. [69] first reported real-time cine MRI in mice with a single-shot echo-planar sequence with the Karhunen-Loeve transform (KLT) filter. Radial trajectories have shown favorable properties for real-time imaging by their intrinsic low motion artifact level. Further, due to the continuous recording of all spatial frequencies with every single spoke, undersampling results in almost incoherent artifacts, often showing no noticeable effect on the reconstructed images [70]. Winkelmann et al. [71] showed that a uniform profile distribution is guaranteed with a constant golden angle (111.246°) increment. The concept of Golden Angle (GA) angular spacing enabled data acquisition with optimal k-space coverage almost independent on the number of projections (Fibonacci sequence) and ensured incoherent undersampling artifacts [72]. Wech et al. [64] investigated the application of radial generalized autocalibrating partially parallel acquisitions (GRAPPA) with large golden angle (111.25°) real-time imaging in mice. However, only mid-ventricular slices were reported, and fully left-ventricular functions were not assessed. Its extension to the tiny golden angle (tyGA) [72] enabled the translation of the GA principle to higher field strength and provided even larger flexibility in the selection of the number of projections used for reconstruction of a single frame (generalized Fibonacci

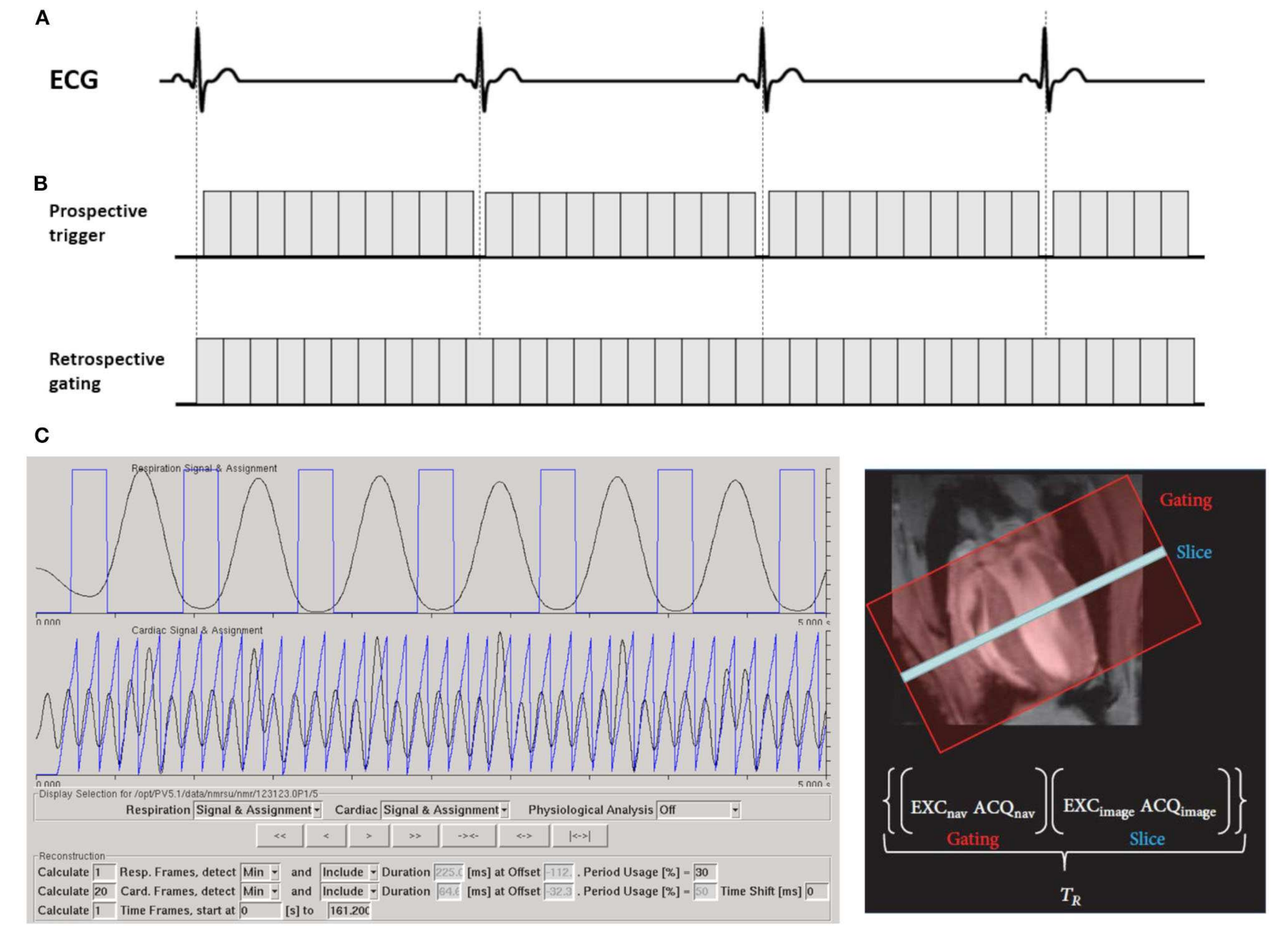


**FIGURE 1 |** Strategies for the synchronization of cardiac cine MRI with the cardiac cycle. **(A)** In the prospective triggering scheme, the acquisition is synchronized with the ECG signal. After detecting the R wave, a suitable trigger delay is set due to application, then cardiac acquisitions can be performed at a specific phase of the heartbeat or to acquire multiple consecutive cardiac phases of the cardiac cycle. **(B)** In the retrospective gating scheme, data are acquired continuously while simultaneously recording the ECG and respiratory signals. **(C)** As an alternative, an additional navigator signal is acquired prior to each echo. Primary signals are calculated from navigator scans. The navigator signals are automatically analyzed and weighted according to their contribution to respiration and cardiac signals. The weighted physiological signals are retrieved (with demerging) and/or frequency filtered (with Fourier Filter) to create respiration and cardiac signal, which are used to assign each echo to its correct position in the cardiac and respiratory cycles. Retrospective gating signal is acquired with ParaVision 5.1 (IntraGate©, Bruker Biospin, Ettlingen, Germany). The partial figure is reproduced with permission from Zuo et al. [7].

sequence). Our group investigates the feasibility of tyGA radial sparse MRI for real-time imaging of cardiac function in healthy mice [73] and a nexilin induced heart failure model [74]. Real-time cardiac tyGA radial sparse sense (tyGRASP) MRI in mice appears feasible with sufficient image quality for the quantification of global functional parameters. It enables a flexible number of projections for image reconstruction and thus offers the possibility for cardiac-phase dependent adjustment of the temporal resolution.

## Accelerated Methods for CMR Imaging

MRI is an essential medical imaging tool with inherently slow data acquisition (**Figure 2A**), which imposes limitations to spatial and temporal resolution and volumetric coverage for dynamic cardiac imaging. The reduction of acquisition times can be achieved by incomplete sampling of *k*-space data. However, related aliasing artifacts often cause degrading of the diagnostic quality. During recent years, various techniques have been developed and applied to increased undersampling, while maintaining diagnostic image quality by advanced reconstruction techniques.

### Compressed Sensing

The mathematical foundation of compressed sensing (CS) was first introduced by Donoho [75] and Candès et al. [76] and translated to MRI by Lustig et al. [15]. CS aims to reconstruct signals and images from a reduced number of *k*-space samples not following the Nyquist criterion. As the MRI data are redundant and naturally compressible by sparse coding in some appropriate transform domain, CS has the potential to significantly reduce scan time.

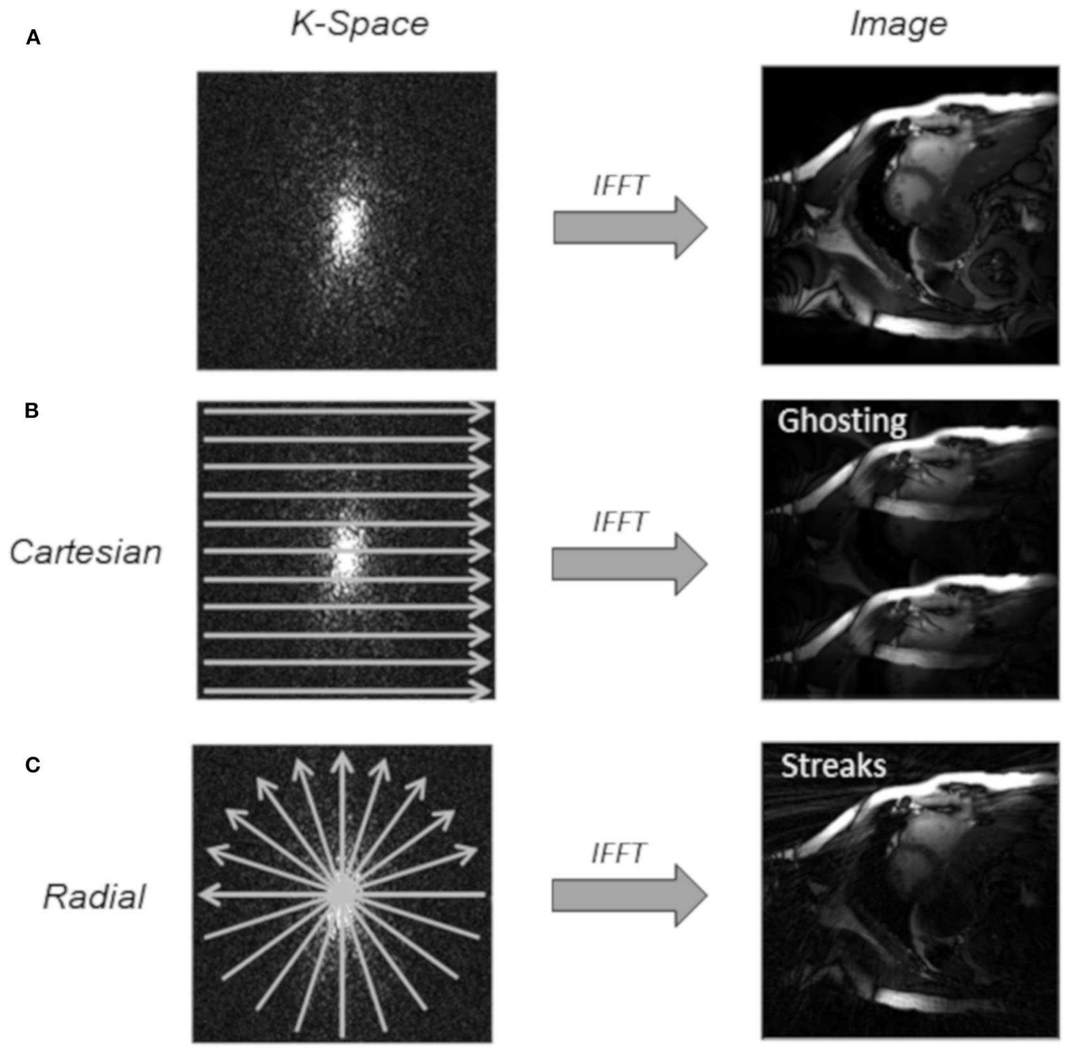


**FIGURE 2 |** Undersampling techniques used for cardiac imaging. **(A)** Fully sampled k-space. **(B)** Regular Cartesian undersampling (2-fold), which results in discrete aliasing artifacts in the reconstructed image with an inverse fast Fourier transform (IFFT). **(C)** Uniform radial undersampling (2-fold) leads to low-intensity streaking artifacts.

A successful application of CS has three basic requirements [16]. First, the desired images have a sparse representation in a known transform domain, and they can be characterized by only a small number of non-zero coefficients. Especially for dynamic CMR imaging, the quasi-periodicity of the heartbeat causes a sparse temporal Fourier transform, and data are as such highly compressible. This enables higher acceleration for dynamic imaging than static imaging [77]. Second, the aliasing artifacts should be incoherent, i.e., that they must manifest as noise-like patterns. Regular undersampling patterns lead to fold over artifacts, known as coherent aliasing (**Figure 2B**). In the Cartesian sampling, some *k*-space lines can be pseudo-randomly omitted, resulting in more incoherent artifacts. Alternatively, due to its highly incoherent undersampling property, many non-Cartesian trajectories, such as radial trajectories [64, 73] (**Figure 2C**), are widely used in CS applications. Especially radial trajectories with golden or tiny golden angle angular increments have proven to be beneficial undersampling properties since almost any arbitrary number of projections provides uniform k-space coverage [78]. Motaal et al. [13] reported UTE Cine images in the rat model, and successfully reconstructed from up to 5-fold undersampled *kt*-space data utilizing a CS algorithm. Wech et al. [64] and Li et al. [73] investigated CS with golden angle radial real-time imaging in the mouse model. Third, a non-linear reconstruction algorithm should be applied to enforce sparsity constrains and data consistency, to suppress incoherent aliasing artifacts [64, 72].

Several studies have shown the feasibility and accuracy of CS to accelerate CMR imaging [79–81]. Further acceleration was reported by combining CS and parallel imaging [64, 82].

## Parallel Imaging

Parallel imaging is a robust method to accelerate the acquisition of MRI data using a reduced number of *k*-space data simultaneously acquired with multiple receive coils. However, simply reducing the number of measured *k*-space data results in aliasing artifacts, mainly represented as well-known ghosting artifacts in Cartesian sampling and streaks in radial sampling [83]. The sensitivity encoding (SENSE) and GRAPPA are two principal methods in parallel imaging to correct for aliasing artifacts. The separate images reconstructed from the signals acquired with the different receive coil elements will have different relative intensities of the aliased component of the image. SENSE makes use of this property to separate the aliased components from the true structures in the image [84]. GRAPPA uses autocalibration signals and neighboring points in k-space to perform reconstruction of the missing portion in the *k*-space [85]. For the proper application of SENSE and GRAPPA, the signal at each point in the FOV has to be simultaneously recorded by several independent receive coil elements and careful alignment of the coil-array with the FOV is required. Theoretically, the maximum acceleration is only limited by the number of independent coils, but SNR limitations normally restrict the possible acceleration [83]. Wagenhaus et al. [33] investigated cardiac functional imaging of mice using a cryogenic quadrature RF coil with parallel imaging of an acceleration factor of 2. Ratering et al. [86] reported accelerated CMR of the mouse heart using self-gated parallel imaging strategies with a high acceleration factor up to 3.

### k-t Acceleration

Cardiac dynamic images are sparse in an appropriate transform domain and exhibit correlations in *k*-space and time, enabling the recovery of missing data in undersampled data acquisitions. Based on this hypothesis, the k-t broad-use linear acquisition speed-up technique (k-t BLAST) and k-t sensitivity encoding (k-t SENSE) were developed to improve the performance of dynamic cardiac imaging. As a further generalization of the original method, k-t principal component analysis (k-t PCA) constrains the reconstruction using a standard data compression technique, thus enabling higher acceleration [87]. Signal correlations are learned from a small set of training data with low spatial but high temporal resolution, with subsequent reconstruction using temporal correlations [88].

Marshall et al. [89] investigated the k-t BLAST with an acceleration factor of three in healthy and myocardial infarction mice. Compared with the gradient echo cine sequence, the k-t BLAST scanning showed no significant differences. Makowski et al. [90] reported first-pass perfusion imaging with 10-fold undersampling in mice on a clinical 3 Tesla MR scanner using the k-t PCA technique.

# PRECLINICAL CMR IMAGING APPLICATION

## Cardiac Function

The heart can be considered as a central circulatory pump, generating the driving force to pump the blood through the vascular system. The visualization and quantification of the cardiac function are crucial, as many diseases have an impact on the performance of the heart.

Global ventricular performance parameters such as end diastolic/systolic volume (EDV/ESV), stroke volume (SV), ejection fraction (EF), and left ventricle mass (LVM) are widely used to evaluate cardiac function, which means the capability of the ventricles to eject blood into the great vessels. To derive accurate and reproducible volumetric quantification from a stack of parallel slices entirely covering the whole ventricle, the Simpson's rule is applied (**Figure 3**). The CMR assessment of the biventricular function is normally acquired with ECG-triggered or self-gated bright-blood contrast gradient-echo techniques [7, 43, 50]. Recently, the concept of real-time imaging was translated to preclinical research [64, 73, 91].

The assessment of systolic function in different mouse models has been investigated and the impact on, e.g., the EF, has been validated [92–94]. In contrast, the assessment of diastolic function in rodents is challenging. Normally the quantification is based on the filling rates at early left ventricular relaxation and late atrial contraction derived from time-volume curves of the left ventricle. Thus, a high temporal resolution acquisition (>60 frames per cardiac cycle) is highly recommended for reliable assessment. Coolen et al. [52] investigated diastolic dysfunction in diabetic mice with frame rates up to 80 frames per cardiac cycle. Later, a temporal resolution of 1 ms was reported by Roberts et al. [95] and the diastolic function was comparable to ultrasound analysis in normal mice.

## Pharmacological Stress Imaging

Assessment of the left ventricular function under pharmacological stress is widely used in cardiovascular research to detect myocardial viability, ischemia or cardiac reserve and to determine the risk of subsequent cardiovascular event. However, due to the fast half-life and rapid metabolism of special drugs, a rapid quantification technique is highly required to visualize acute changes of cardiac morphology and function during pharmacological stress in the preclinical research.

Vasodilator and dobutamine are the main pharmacological agents used in stress CMR imaging [96]. By activating the adenosine receptors, the vasodilator agents can trigger coronary vasodilation and directly increase coronary flow [97]. Dobutamine is a synthetic catecholamine that primarily stimulates $\beta_1$-adrenergic receptor and mildly stimulates $\alpha_1$, $\beta_2$-adrenergic receptor, and augments myocardial contractility [98]. Wiesmann et al. [99] firstly used dobutamine stress MRI to reveal the loss of inotropic and lusitropic response in transgenic heart failure mice with myocardial infarction and diastolic dysfunction as an early sign of cardiac dysfunction. Since then, more and more studies using the dobutamine stress MRI to investigate cardiac function in the mouse model have been reported [93, 100, 101]. Different dobutamine doses and ways of administration were reported (4 to 40 μg/min/kg intravenous infusion [i.v.] or 1.5 μg/g body weight, intra-peritoneal bolus injection [i.p.]). To comply with the rapid imaging demands, real-time techniques combined with tyGA radial sparse MRI have been reported to characterize the acute changes of murine cardiac function from baseline to physiologically stress conditions *in vivo* without ECG and respiration synchronization [102].

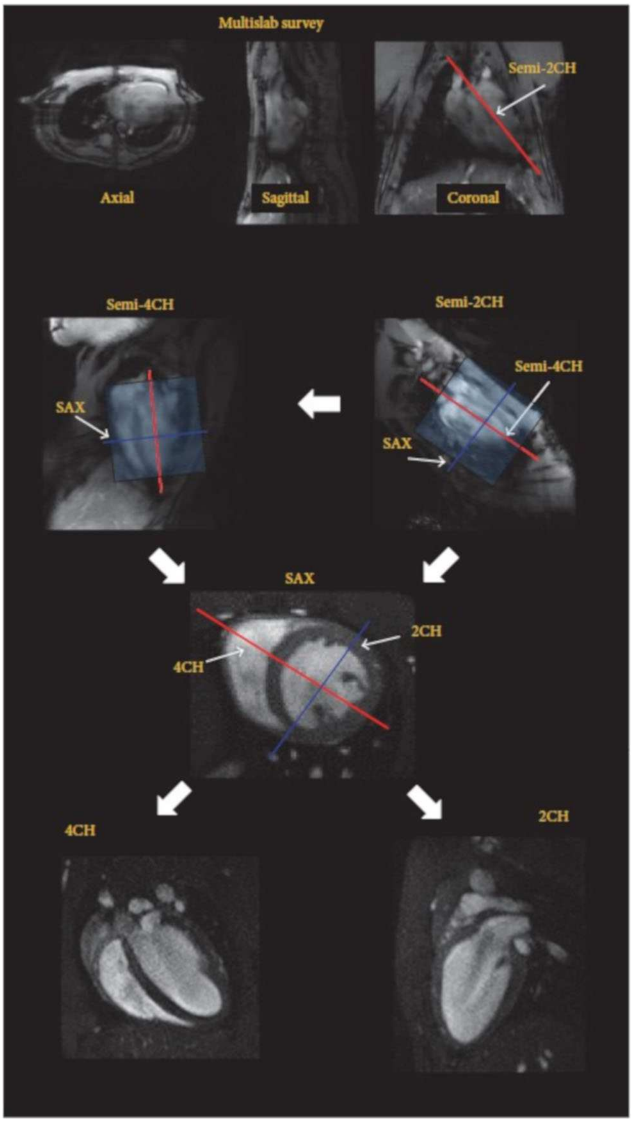


**FIGURE 3 |** Imaging protocol for highly reproducible imaging of cardiac function and anatomy (2/4CH: 2/4-chamber, SAX: short axes orientations). After the acquisition of a fast survey in axial, sagittal, and coronal orientation a long axis (LAX) scans are acquired in semi-2 chamber (2CH) and semi-4 chamber (4CH) orientation, which are used for accurate planning of the short axis stack (SAX). The final 2CH and 4CH orientations are planned on the SAX stack. Reproduced with permission from Zuo et al. [7].

## Myocardial Strain

Myocardial strain is defined as the percentage change of myocardial length compared with the initial state in a certain direction by an internal or external force, and it is a well-validated parameter for evaluating myocardial performance. Several approaches are currently available for myocardial strain assessments.

### Tagging

With the introduction of myocardial tagging in the late 1980s [103, 104], quantification of myocardial strain by CMR imaging became possible. Later, it was introduced by de Crespigny et al. [105] into rodent research. Tagging MRI applies a series of short RF saturation pulses to spatially modulate the longitudinal magnetization prior to the conventional image acquisition, which generates regional tags with stripes or grids on the myocardium (**Figure 4**). The measurement of myocardial strain is derived from the tag deformation over the cardiac cycle.

Initially, spatial modulation of the magnetization (SPAMM) was used to generate a one- or two-dimensional grid of saturated spins [104]. However, due to longitudinal relaxation, tagging contrast is weakened in later cardiac phases. A complementary SPAMM technique (CSPAMM) was introduced by Fischer et al. [107] to improve the grid contrast by using the difference image of two acquisitions with inverted tagging grid phase.

After the tagged image acquisition, quantitative analysis of the strain is achieved by a variety of fast and accurate analysis methods, such as detecting and tracking the tag lines in the images [108], assessing temporal and spatial changes in image intensities by optical flow [109] and harmonic phase (HARP) analysis [110].

Even though tagging MRI is the most validated CMR technique to assess myocardial strain, the requirement for extra image acquisition sequences, influence of tags fading (less relevant for high field-strength and heart rates), and time-consuming post-processing limits its application.

### Tissue Phase Mapping

Velocity encoded tissue phase mapping (TPM) is a valuable technique to evaluate myocardial strain, strain rate and displacement with high spatial and temporal resolutions [111–113]. TPM is based on bipolar gradients to encode myocardial velocity and enables quantitative assessments of the myocardial velocity in three directions over the whole cardiac cycle. TPM is susceptible to eddy-currents and phase distortion induced by concomitant gradient fields [114, 115], and several approaches have been developed to minimize these errors [115–117]. However, TPM-encoded acquisitions are sensitive to flow- and motion-related artifacts and require long acquisition times. Several feasible methods have been developed to accelerate image acquisition and compensate for motion artifacts. Espe et al. [112] introduced in-plane rotation of the FOV in rats to reduce directional-dependent artifacts by acquiring each slice twice. Recently, McGinley et al. [118] investigated accelerated TPM imaging by applying compressed sensing in the myocardial infarction rat model.

### Displacement Encoding With Stimulated Echoes

Displacement encoding with stimulated echoes (DENSE) was introduced for high-resolution myocardial displacement mapping via stimulated echoes with a bipolar gradient by Aletras et al. [119]. It has the distinct advantage of encoding tissue displacements into the pixel phase, thus encoding motion over long periods while maintaining high spatial resolution. However, due to the stimulated echoes, DENSE has the disadvantage of a relatively low SNR. Kim et al. [120] increased SNR of 15–34% by extracting a pair of subsampled DENSE images with uncorrelated noise from the CSPAMM

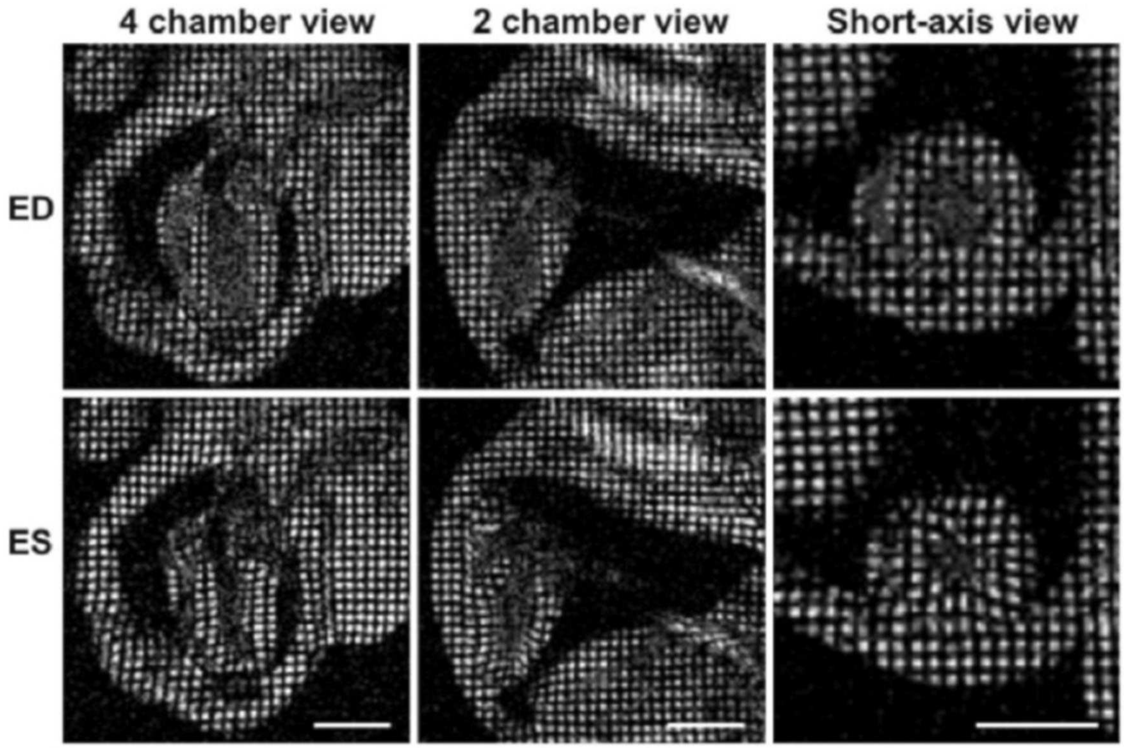


**FIGURE 4 |** Myocardial tagging in the mouse. Four-chamber, two-chamber, and short-axis views of a mouse heart at the end-diastole are shown in the top row, and the end-systolic frames are depicted in the lower row. The movement of the tagged myocardial tissue can be tracked to calculate myocardial strain. Reproduced with permission from Price [106].

image, and combined them during image reconstruction. After initially being implemented as single-frame imaging, DENSE was subsequently extended to cine imaging. In diet-induced obesity mice, high reproducibility was reported in the quantification of the LV function, including strain, torsion, and measures of synchrony [121]. Zhong et al. [122] investigated a 3D cine DENSE sequence with a spiral k-space trajectory in mice. Vandsburger et al. [123] combined DENSE with pharmacological stimulation to investigate the mechanics of endothelial nitric oxide synthase and neuronal nitric oxide synthase in modulating contractions and calcium influx in mice. DENSE has also been shown to be benefited from acceleration techniques, such as parallel imaging and compressed sensing [124, 125]. However, the feasibility of acceleration techniques in preclinical research needs further investigation.

### Feature Tracking

Recently, CMR feature tracking (CMR-FT) was introduced for deriving global and regional myocardial strain [126]. It is mainly based on a block-matching approach. After manual defining endocardial and epicardial borders at end-diastole, in CMR-FT the borders are automatically tracked over the cardiac cycle by correlation of similar regions in the subsequent images (**Figure 5**). As CMR-FT is a promising novel method for the quantification of myocardial strain from routinely acquired cine CMR images without excessive post-processing times, it has the potential for a fast assessment of myocardial mechanics. Its clinical potential has recently been described [128–130], and excellent inter- and intra-observer agreement and high inter-study reproducibility were reported. However, to the best of our knowledge, only one preliminary study with limited temporal resolution of 15 phases per cardiac cycle has been reported in preclinical research [131]. There, feature tracking showed high reproducibility in left ventricle global circumferential and longitudinal strain in healthy mice, whereas reproducibility of radial strain was limited.

## Perfusion

Assessment of myocardial perfusion is considered to be a key parameter in the characterization of cardiac pathology, especially in ischemic heart disease or microvascular dysfunction. In normal conditions, a myocardial oxygen supply is balanced to the continuously changing myocardial oxygen demand. The imbalance of supply and consumption may result in myocardial ischemia. Currently, myocardial perfusion in rodents is typically assessed using arterial spin labeling (ASL) or first-pass perfusion imaging.

### Arterial Spin Labeling

ASL is a valuable CMR technique utilizing arterial blood water protons as an endogenous diffusible tracer to non-invasively quantify regional myocardial blood flow without contrast agents

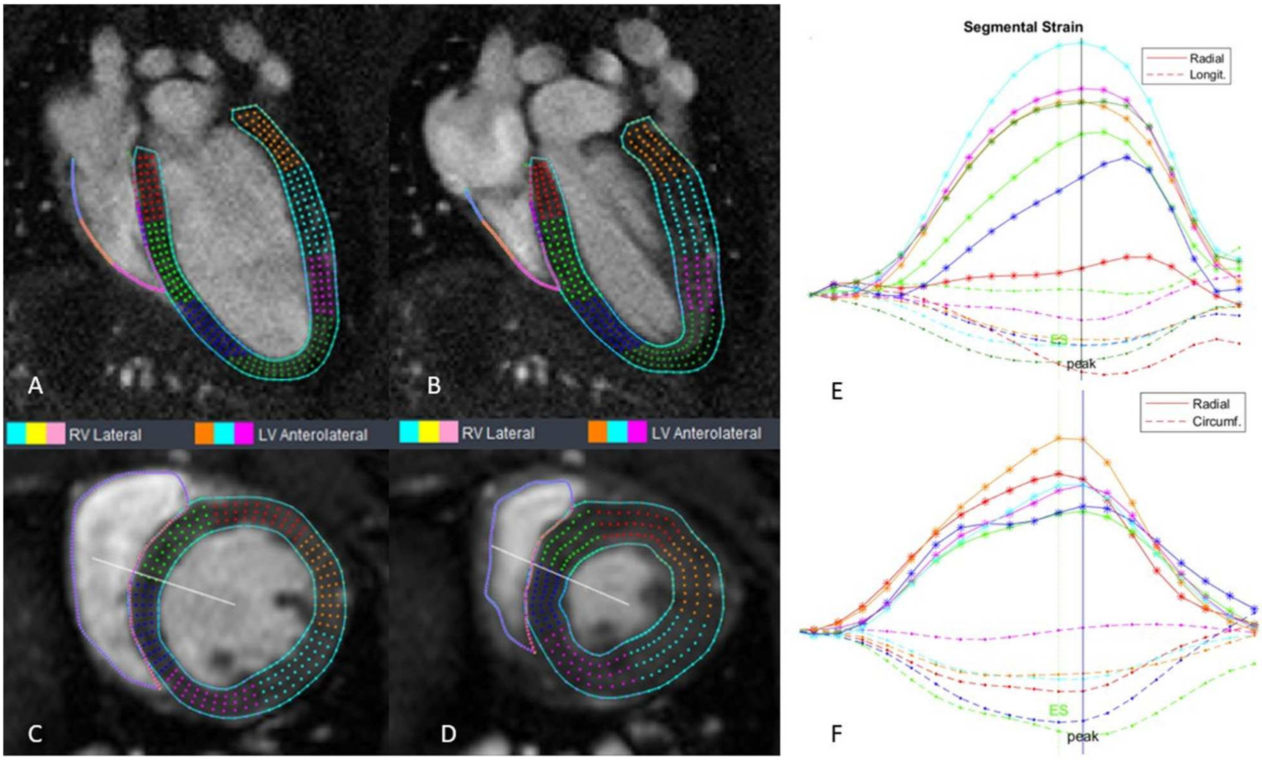


**FIGURE 5 |** Cine CMR images with CMR-FT myocardial strain curves in mouse. **(A)** 4-chamber at end-diastole; **(B)** 4-chamber at end-systole; **(C)** short axis at the end-diastole; **(D)** short axis at the end-systole; **(E)** segmental strain for 4-chamber; **(F)** segmental strain for short axis. Stain analysis was done using Segment v3.0 R7732 [127].

[132]. RF pulses are applied to label arterial blood which then acts as endogenous tracer. ASL requires the subtraction of two images. One image is acquired after the labeled blood flow into the target tissue and the other one is acquired without labeling. The difference between both images can be utilized to calculate the tissue's blood perfusion. The signal difference depends on labeling decays with the time-constant equal to the blood T1 relaxation time. It can be made directly proportional to myocardial blood flow in units of ml-blood per *g*-tissue per minute. However, the contrast differences created by magnetic labeling of blood are inherently limited, which results in relatively low SNR. To compensate for low SNR, high field strength is beneficial.

ASL was firstly demonstrated in the rodent brain by Detre et al. [133]. Later, it was applied to the perfused excised rat heart by Williams et al. [134]. However, ASL suffers from relatively long acquisition times and it is sensitive to variations in heart and respiratory rates [135].

The flow-sensitive alternating inversion recovery (FAIR) combined with the Look-Locker readout scheme is the most widely used technique in ASL (**Figure 6**). Belle et al. [136] employed an LLFAIR-FLASH sequence to quantify myocardial blood flow (MBF) in rats. Due to blood flow, non-excited spins enter the detection slice, which leads to an increase in the relaxation rate. The relative difference in the apparent T1 relaxation times corresponding to selective and non-selective inversion is related to perfusion via a two-compartment tissue model. Kober et al. [137] improved MBF quantification using a respiration and ECG gated LLFAIR single-gradient echo technique in a mouse model. A nearly 10-fold increase in spatial resolution was achieved with respect to previous study in rats [138]. However, this led to a significantly increased acquisition time of about 25 min. Vandsburger et al. [139] investigated a cardio-respiratory gated ASL sequence using a fuzzy C-means algorithm to better cope with respiratory motion and heart rate variations in a myocardial infarction mice model. Abeykoon et al. [140] introduced an ASL method based on the signal intensity of flow sensitized CMR to shorten scan time to 2–4 min. In order to benefit from sensitivity advantages of continuous ASL, Troalen et al. [141] proposed cine-ASL, which is based on an ECG-gated steady-pulsed labeling approach combined with simultaneous readout over the cardia cycle. The cine-ASL led to shorter acquisition time than the LLFAIR technique while preserving spatial resolution and robustness with respect to cardiac motion.

## First-Pass Perfusion

The basic principle of first-pass perfusion imaging involves intravenous injection of a bolus of a suitable contrast agent (CA), with subsequent monitoring of the passage of the CA through the heart. However, the high heart rate (400–600 bpm) and fast systemic blood circulation time limit its application in rodents.

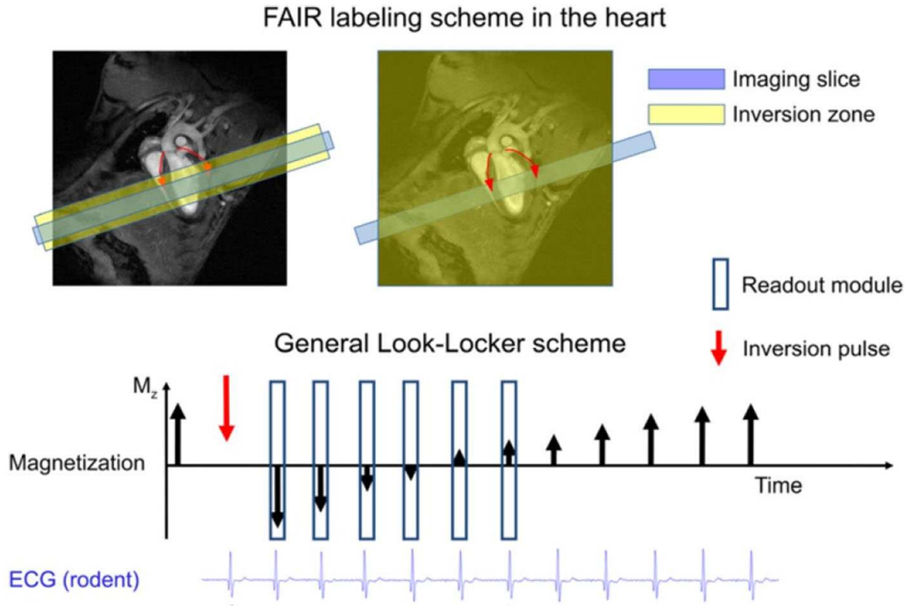


**FIGURE 6 |** The FAIR labeling scheme (**upper** part) consists of two inversion recovery measurements. In the first measurement the labeled zone is only around the imaging slice, and in the second measurement the inversion is global. FAIR is the most commonly used ASL technique in the heart. The timing of the inversion and that of the readout modules should be ECG-gated and occur in the same cardiac phase. The Look-Locker inversion-recovery readout (**lower** part) has been used mainly in the rodent heart, where the rapid heart rate permits dense sampling of the magnetization recovery curve. Reproduced with permission from Kober et al. [132].

Recently, the major progress in data acquisition acceleration has rendered small animal first-pass perfusion imaging feasible.

Makowski et al. [90] firstly proposed first-pass perfusion imaging in mice using a k-t SENSE technique with an acceleration factor of 10 on a clinical 3T scanner. Later, Coolen et al. [142] introduced a segmented ECG-triggered acquisition combined with parallel imaging acceleration to capture the first pass of contrast agent in healthy and myocardial infarction mice. A temporal resolution of one image per three heartbeats was reached. The same group further investigated the quantification of regional perfusion values using a dual-bolus approach in combination with a Fermi-constrained deconvolution model [143]. Later they applied this dual-bolus approach to test the feasibility of first-pass perfusion in pressure overload induced hypertrophy and heart failure mouse models after transverse aortic constriction [144]. The hypertrophic mice revealed reduced myocardial perfusion proportional to LV volume and mass, and a related decrease in LV ejection fraction. Naresh et al. [28] used k-t undersampled dual-contrast first-pass MRI with motion-compensated compressed sensing reconstruction to study myocardial blood flow in a high-fat diet mouse model. They also investigated the repeatability and variability of first-pass perfusion imaging and ASL. They concluded that first-pass MRI shows better repeatability and variability in low MBF conditions such as myocardial infarction. Due to better image quality and lower user variability, ASL is more suitable at high MBF. Recently, the tyGRASP sequence with block-wise cardiac synchronization was reported for first-pass perfusion imaging in nexilin knock-out mice [74]. During each cardiac cycle, a single block of $G_4^7 = 15$ projections with acquisition duration of $t = 31.5ms$ was acquired. For suppression of the background signal and coping with arrhythmic cycles, a non-selective saturation pulse was additionally applied prior to each acquisition block with a saturation recovery time $T_{SAT}$ of 60 ms. The trigger delay was chosen so that the acquisition was performed during end-diastole to further minimize the motion artifacts (**Figure 7**). A temporal resolution of one image per cardiac cycle was achieved. Thus, an improved temporal fidelity of the inflow and washout curves was shown.

## Tissue Characterization

Because of its ability to provide superior soft tissues contrast in exquisite detail, MRI has exceeded other imaging modalities in its multi-parametric capabilities for a comprehensive myocardial tissue characterization. It can provide superior and well-validated biomarkers of important pathophysiological processes in cardiac diseases based on intrinsic relaxation properties T1, T2, and T2* with or without contrast agent. Tissue contrast is tailored by adjusting acquisition parameters such as flip angle, TE, repetition time (TR), and inversion delay (TI). Mapping techniques can further provide direct pixel-by-pixel quantitative myocardial tissue characterization to depict small variations of relaxation properties and to highlight tissue pathology.

### T1 Mapping

The T1 relaxation time is the longitudinal relaxation time, describing the return of the magnetization to thermodynamic equilibrium after excitation. The native T1 value is a tissue specific constant which changes in some pathologic conditions, such as diffuse myocardial fibrosis, hemorrhage, edema,

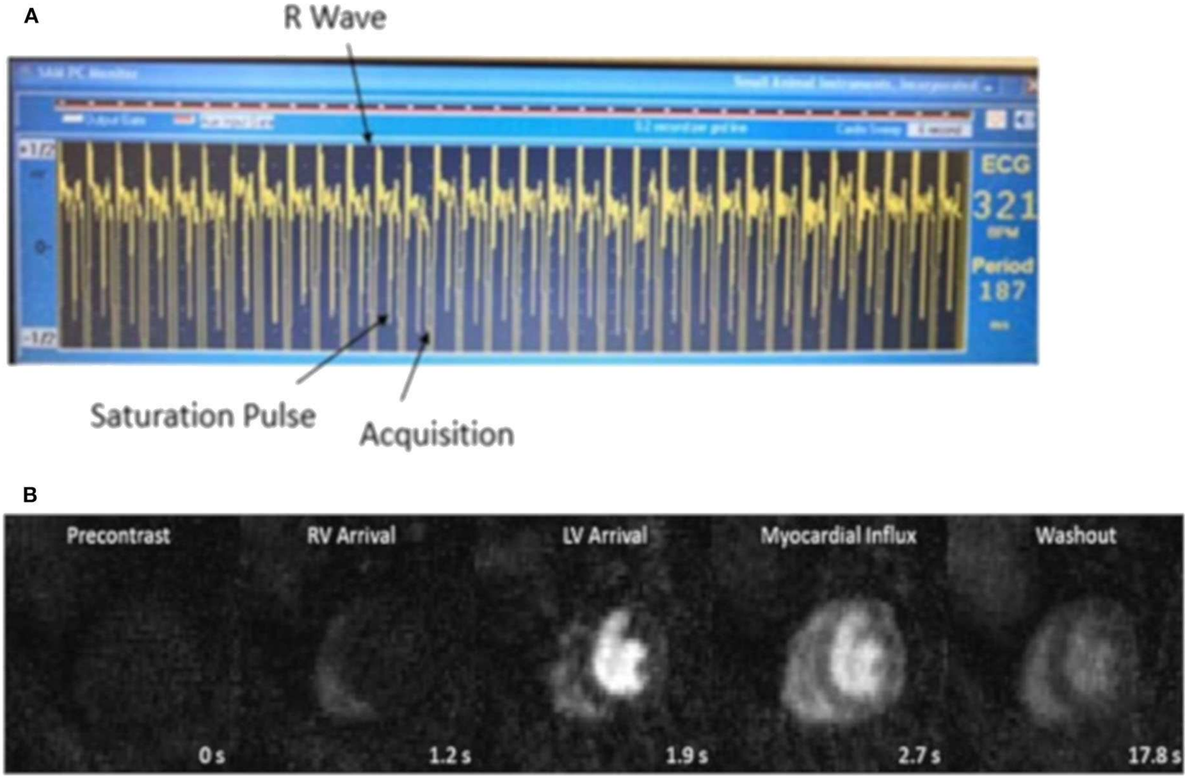


**FIGURE 7 | (A)** ECG signal during scan. According to the heart rate, a trigger delay was set after the detection of the R wave, then the blood and myocardial signal were approximately nulled by a non-selective saturation pulse. The acquisition was performed during end-diastole. **(B)** Time series of myocardial first-pass perfusion images of a nexilin wild-type mouse. From left to right: precontrast, RV arrival, LV arrival, myocardial influx, and washout.

inflammation, and acute infarction [145]. Thus, the quantitation of T1 value can be used to distinguish different soft tissues and pathologies. The general principle for T1 mapping is to acquire multiple images at different inversion times in order to assess the T1 recovery curve.

Several T1 mapping methods have been proposed in preclinical research. One of the most widely used methods for measuring myocardial T1 is a single slice inversion recovery Look-Locker technique [146–148]. With this technique, image datasets are acquired repeatedly after an inversion pulse to create multiple images along the recovery curve. However, this method has several drawbacks. The long TR results in relatively long total acquisition times. Poor ECG signals and variations in the heart rate cause inversion times to differ for subsequent acquisition thus causing k-space inconsistencies. In-plane and through-plane motion between excitations reduce accuracy [54]. An ECG-triggered saturation-recovery Look-Locker (SRLL) method has been proposed by Li et al. [149] to acquire a single-slice T1 map in about 3 min. By combining the SRLL method with a modified model-based compressed sensing method, a 50% reduction in imaging time was achieved for the *in vivo* T1 mapping of the mouse heart [150]. Later, Jiang et al. [151] further extended the method to multi-slice T1 mapping (MRLL) allowing for more coverage without increasing scan time. However, the SRLL sequence yields relatively low SNR and a lower accuracy compared with the inversion recovery. The single shot 2D modified Look-Locker (MOLLI) technique has shown high reproducibility and high SNR in humans [152]. However, it is challenging in mice due to the high heart rates and requirements on spatial resolution. Recently, Nezafat et al. [153] proposed a multi-shot 2D modified Look-Locker sequence for high-resolution T1 mapping in mice at a 3T MRI clinical scanner. A further method for myocardial T1 mapping in mice has been proposed by Coolen et al. [54] using a 3D intra-gate FLASH sequence in combination with a variable flip angle DESPOT1 (driven equilibrium single-pulse observation of T1) analysis. With this protocol, 3D T1 maps of the heart ventricles could be obtained in 20 min with a sufficient spatial resolution (**Figure 8**). Castets et al. [154] accelerated 3D T1 mapping measurements using spiral encoding with a higher spatial resolution ($208 \times 208 \times 315\ \mu m^3$) in a 10–12 min acquisition time.

A promising application for T1 mapping is the quantification of myocardial extracellular volume (ECV) fraction. ECV contains the interstitial and intravascular spaces. Many disease processes affecting the myocardium can be understood through ECV changes, such as diffuse or interstitial myocardial fibrosis. ECV can be measured by combining native and post-contrast T1 mapping of blood and myocardium. Neilan et al. [155] applied and validated a Look-Locker FLASH sequence to quantify ECV in juvenile and aged mice.

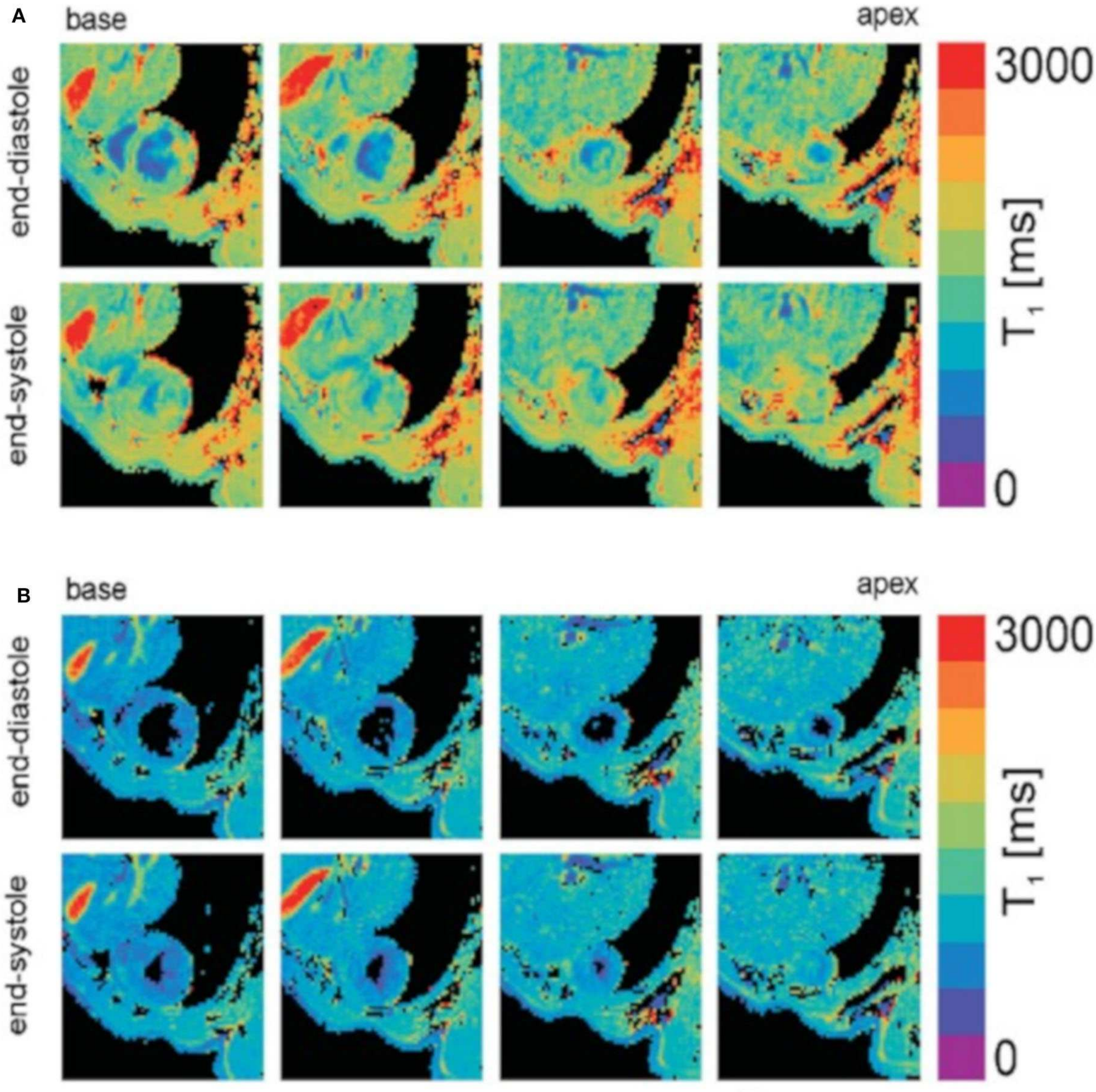


**FIGURE 8 |** T1 mapping of the mouse heart resulting from DESPOT1 analysis of both black-blood **(A)** and bright-blood **(B)** data. T1 maps are shown for four different slices covering the base to apex and for both the end-diastolic and end-systolic cardiac phases. Reproduced with permission from Coolen et al. [54].

## T2 and T2* Mapping

The T2 relaxation time, also referred to as spin-spin or transverse relaxation time, is describing the tissue-specific decay of the transversal magnetization after excitation. Myocardial edema is the main pathology responsible for changes in the T2 value, and it was first demonstrated in a canine model of acute myocardial infarction (AMI) by Higgins et al. [156].

Two variants of T2 mapping techniques are usually used in CMR imaging: dark blood turbo spin-echo (TSE), and bright blood T2 preparation. Schneider et al. [147] mapped T2 in mice by acquiring the spin echo data with echo times ranging from 3.7 to 24 ms. Later, Bun et al. [157] performed T2 measurements with a similar sequence to quantify myocardial fibrosis in diabetic mice at 11.75 T. However, the TSE-based T2 mapping suffered from ghosting artifacts caused by blood flow and signal loss due to through-plane motion [158]. The T2 preparation-based method is less prone to TSE-associated artifacts [159]. It mainly contains a T2 preparation module and a rapid imaging sequence such as FLASH. The T2-preparation module contains non-selective 90 and 180° pulses to create spin-spin relaxation followed by a −90° restore pulse. After the restore pulse, the longitudinal magnetization depends on the tissue T2 value. Beyers et al. [55] proposed a T2 preparation module containing a Carr-Purcell-Meiboom-Grill and Malcolm Levitt (CPMG-MLEV) weighted series of composite 180° pulses, followed by a multi-slice gradient echo readout. In this way, the resulting T2 values are less sensitive to effects of B0 and B1 inhomogeneities. Coolen et al. [160] extended this preparation module with fast steady-state-free-precession (SSFP, FISP) readout. However, the total acquisition time for one T2 measurement with three slices was about 30 min, which limited its application in fast dynamic contrast agent enhanced MRI studies. Chen et al. [161] performed rapid T2 mapping of the mouse heart using the CPMG sequence and compressed sensing reconstruction, which allowed T2 quantification at a temporal resolution of 1 min per slice (**Figure 9**).

T2* relaxation refers to decay of transverse magnetization caused by a combination of spin-spin relaxation and magnetic field inhomogeneity. Gradient-echo MRI with T2*-based contrast can be used to depict different lesions in diseased mouse heart. T2* cardiac MRI has been utilized to evaluate myocardial iron overload and collagen deposits. T2* is reduced in iron- and collagen-laden tissues due to increased magnetic field inhomogeneity. Jackson et al. [162] measured T2* relaxation using two multi-echo gradient echo sequences with 15 echo times in the range of 0.9–14.9 ms at 1 ms intervals in a mouse model of β-thalassemia. Over 10-fold decreased myocardial T2* ($0.7 \pm 0.2$ ms) was observed in the iron-loaded thalassemia group, which was consistent with histological results. van Nierop et al. [163] reported reduced T2* value in myocardial infarction (MI) and transverse aortic constriction (TAC) mice using an ECG-triggered T2*-weighted 3D center-out radial sequence with TE ranging from 21 μs to 4 ms. T2*-shortening contrast agents, such as iron oxide nanoparticles (IONPs), have been used to exploit T2* contrast in mouse cardiovascular system [164, 165]. Sosnovik et al. [164] reported an iron oxide–based particle targeted at apoptotic cells in an ischemia/reperfusion injury mice model. Significantly decreased signal intensity was observed in T2*-weighted FLASH images. Zhou et al. [166] used the Sweep Imaging with Fourier Transformation (SWIFT) technique to visualize iron oxide particle labeled stem cells in the rat heart. Due to its zero echo-time properties, SWIFT images showed reduced blooming artifacts compared to gradient-echo images, and enhancement of off-resonance signals relative to the background. However, a major remaining challenge for IONPs application is to distinguish regions of signal void due to IONPs from those due to low signal tissues or susceptibility artifacts. Even though several bright-iron methods such as off-resonance techniques [167], gradient-compensation techniques [168], and post-processing methods to identify IONP-introduced magnetic field inhomogeneities [169] have been introduced, IONP-induced off-resonances can hardly be distinguished from other sources. This yields a rather low specificity of the IONP approach. Similar to SWIFT, ultrashort echo time (UTE) techniques have been used for providing endogenous T2* contrast [163, 170].

## Contrast Enhanced MRI

Contrast enhanced MRI (CE-MRI) is a widely used imaging technique to investigate microvascular structure and function by injecting a contrast agent. MR contrast agents work by modifying the tissue relaxation properties and thus directly affect the image contrast. This effect is known as relaxivity and enables better visualization of tissues in which the agent accumulates. The contrast agents can be classified as T1-weighted (i.e., gadolinium chelates, manganese chelates) or T2*-weighted (i.e., iron oxide particles). Here, we mainly discuss T1-weighted CE-MRI.

### Late Gadolinium Enhancement MRI

Late gadolinium enhancement (LGE) CMR is a non-invasive reference standard for investigating myocardial viability. In AMI, cellular necrosis, lysis, and edema are the main pathological changes. In chronic infarcted tissues, fibrous scar tissues with increased extracellular space form. Compared with healthy tissues, the Gd-agent was slowly washed in and washed out in pathological tissues with expanded extracellular space. Analysis of the CA dynamics allows to distinguish between healthy and high-risk tissues and myocardial scars [171].

Kim et al. [172] initially applied LGE to study myocardial viability in a rabbit model. A clear difference in contrast kinetics between normal tissue, infarct rim, and infarct core regions could be observed. Yang et al. [173] validated the LGE technique for accurate assessment of infarct size in MI mice. After intravenously injecting a 0.3–0.6 mmol/kg bolus of Gd-DTPA, CA-enhanced images of the entire heart were acquired in 15 to 30 min. Great agreements were achieved for infarct size between LGE images and 2,3,5-triphenyl tetrazolium chloride (TTC) staining. The results were in excellent concordance with many other studies [174–176], which clearly demonstrated LGE cardiac imaging to be a reference standard to follow up myocardial viability *in vivo*.

Two main methods for LGE imaging are the inversion recovery (IR) fast gradient echo sequence and the T1-weighted cine FLASH sequence. Due to the ability to null the signal of remote myocardium, IR shows better contrast between the infarcted and non-infarcted myocardium and is widely used in humans. In preclinical research, Price et al. [177] applied LGE in small animals using a multi-slice IR gradient-echo sequence in combination with a Look-Locker sequence for assessing the optimal inversion point to null the signal from healthy myocardium (300–450 ms for rats, around 330 ms for mice, **Figure 10**). Thomas et al. [174] and Protti et al. [178] compared IR LGE and T1-weighted cine FLASH LGE imaging at 4.7 and 7 T. Both protocols produced reliable results for the assessment of infarction size. Cine FLASH was found to be a more robust, faster and less user dependent method for visualizing infarct size and recommended as the more promising technique in small rodents.

### Manganese-Enhanced MRI (MEMRI)

Unlike gadolinium, which only allows extracellular space imaging for assessment of myocardial viability, manganese provides T1-weighted intracellular contrast through calcium handling. During myocardial contraction, $Ca^{2+}$ enters cardiomyocytes primarily by conduction through voltage-gated L-type calcium channel that causes increase in cytosolic $Ca^{2+}$ concentration, which then binds to troponin C and activates myocardial contraction (excitation-contraction coupling) [179]. After systolic contraction, $Ca^{2+}$ is actively transported into the sarcoendoplasmic reticulum (SR) by Ca-ATPase and excreted from the cell through the sarcolemmal $Na^{+}$-$Ca^{2+}$ exchanger

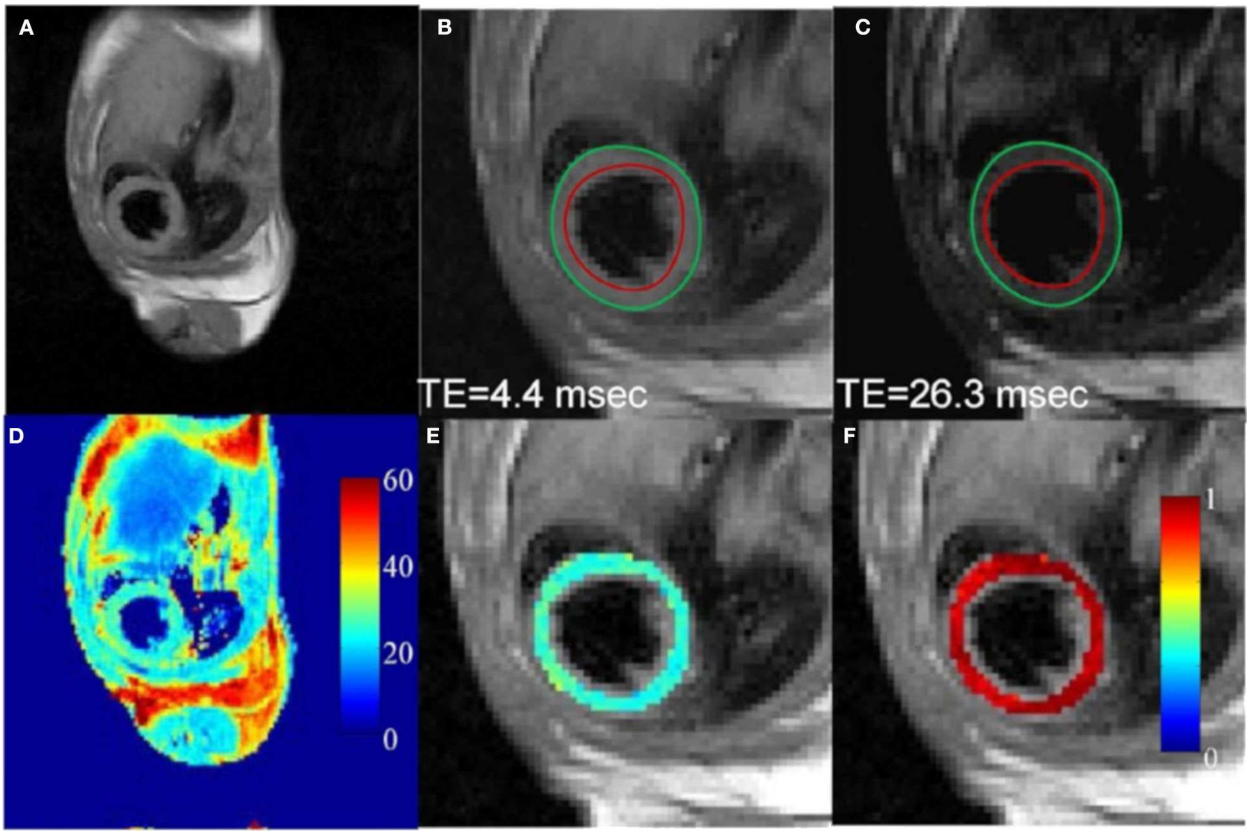


**FIGURE 9 |** *In vivo* T2 mapping of a mouse heart using a fully-sampled dataset. **(A)** Full FOV image of the first echo (TE: 4.4 msec). **(B,C)** Enlarged images of the heart from the first and sixth echo, respectively. Red and green circles represent endocardial and epicardial contours drawn from the first echo image, respectively. **(D)** The corresponding T2 map for the whole image. **(E)** Enlarged T2 map for the mouse heart. **(F)** Map of squared correlation coefficient for the exponential T2 fitting. Reproduced with permission from Chen et al. [161].

[179]. Alterations in calcium handling may impair the $Ca^{2+}$ cycling between the extracellular space, cytosol, and SR, resulting in systolic or diastolic dysfunction. Manganese is a T1 shortening compound taken up through voltage-gated calcium channels into cells with active calcium handling. It has the ability to measure $Ca^{2+}$ channel activity and myocardial viability, and has been validated in various clinical [180–182] and preclinical [183–185] studies. However, its application in clinical routine was limited by its potential toxicity causing myocardial depression. Manganese formulations using chelation or linkage to a calcium compound [186] were developed. Spath et al. [184] investigated manganese-based contrast media in healthy and infarcted rat models (**Figure 11**). The investigated manganese agents resulted in calcium channel-dependent myocardial T1 shortening. A good agreement between infarct size on MEMRI T1 mapping and Masson's trichrome (MTC) staining (bias 1.4, 95% CI −14.8 to 17.1, $p > 0.05$) was reported. In contrast, standard gadolinium delayed enhancement MRI (DEMRI) with the inversion recovery technique overestimated the infarct size (bias 11.4, 95% CI −9.1 to 31.8, $p = 0.0002$), as did DEMRI T1 mapping (bias 8.2, 95% CI −10.7 to 27.2, $p = 0.008$). Recently, Toma et al. [183] proposed a dual contrast MEMRI and DEMRI technique to evaluate the physiologically unstable peri-infarct region and to track the therapeutic effects of telmisartan on the injured myocardium longitudinally with attenuation of the peri-infarct region.

## Diffusion Tensor Imaging

The myocardial fiber anatomy underlies the mechanical and electrical properties of the heart [187]. Within the normal LV, the myofibers follow left-handed helices in the epicardium, and transit smoothly through a circumferential orientation at the mesocardium to right-handed helices in the endocardium. A feasible and accurate technique to characterize and identify fiber structure changes can contribute to elucidating the complex cardiac structure-function relationships. MR diffusion tensor imaging (DTI) has been validated as a valuable tool to obtain non-invasive measures of myocardial microstructure in both clinical and preclinical studies [187–189]. Several quantitative parameters derived from DTI, such as mean diffusivity (MD) and fractional anisotropy (FA), helix angle (HA) and second eigenvector angulation (E2A), can be used to describe myocardial microstructural organization.

After first developed in 1990s [190], DTI has been widely used in brain imaging to study the spatial organization of white matter fiber tracts [191, 192]. The preclinical application of cardiac DTI is more challenging, due to cardiac and respiratory motion,

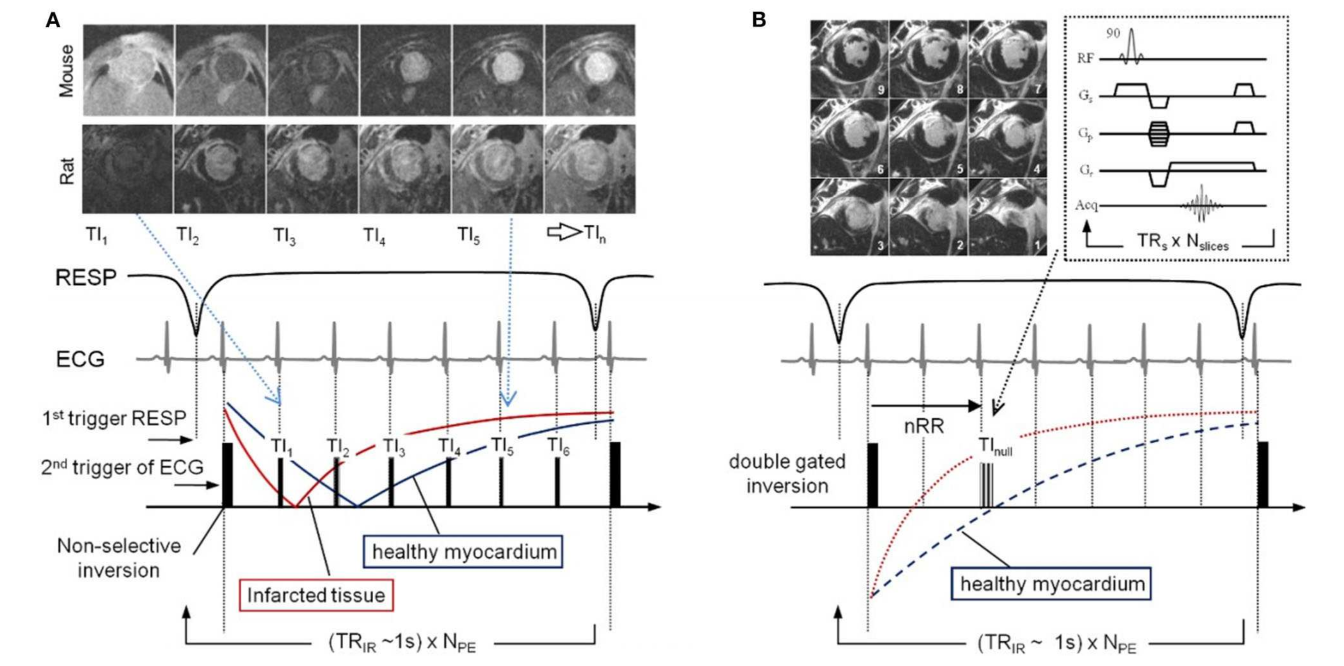


**FIGURE 10 |** Pulse sequence diagrams for LGE imaging. **(A)** Look-Locker pulse sequence and gating strategy used to acquire multiple inversion time (TI). Images from TI1–TI6 time points are shown for both mouse and rat, where the indices are related to the number of R-wave triggers given the double gated inversion pulse. **(B)** The LGE IR sequence diagram follows the same gating and acquisition scheme but acquires a 90° flip angle multislice GRE stack at the nearest TI value to null healthy myocardium. $TR_s$ is the time between slice acquisition pulses, $TR_{IR}$ is the time between inversion pulses, $N_{PE}$ is the number of phase-encoding steps, and $N_{slices}$ is the number of slices. Reproduced with permission from Price et al. [177].

the diffusion signal attenuation, and a short T2 relaxation time causing low SNR condition. Further, high-resolution DTI of the mouse heart is more complicated due to a low degree of diffusion anisotropy in the tissue [188]. With the developments of pulse sequence design and gradient systems, cardiac DTI has become feasible for *in vitro* and *in vivo* applications.

In the beginning, cardiac DTI was mainly performed on isolated hearts. Scollan et al. [193] introduced two-dimensional stimulated echo acquisition mode (STEAM) in perfused rabbit hearts using standard and fast spin-echo pulse sequence with half-sine diffusion gradients in six non-collinear directions. The inclination angle derived from both protocols showed high agreement with histological results. Jiang et al. [188] firstly extended a similar protocol to acquire 3D diffusion-weighted images of 12 directions in a fixed mouse heart. High spatial resolution (isotropic 100 µm) images were acquired in 9.1 h and allowed the quantification of the myocardial structure at more than 170,000 locations throughout the mouse heart, which is about 10 times better than histological studies. The FA value of 0.27 ± 0.06 and the mean diffusion tensor eigenvalues of 0.75 ± 0.13, 0.60 ± 0.13, and 0.51 ± 0.13 x $10^{-3}$ $mm^2/s$ are in good agreement with other studies [193, 194]. Huang et al. [195] firstly investigated *in vivo* DTI-tractography of the mouse heart to follow myocardial microstructural changes in ischemia/reperfusion mouse models. It showed increased MD and FA in acute ischemia (24 h after injury), but decreased values during myocardial healing (2–3 weeks after reperfusion) (**Figure 12**). Later, the same group applied 3D DTI-tractography *in vivo* to study ischemic myocardium and assessed the cell therapy effect [196]. With the velocity-compensated Stejskal-Tanner diffusion sequence, they were able to obtain high-resolution 3D reconstructions of the myofibrillar tracts in the mouse heart. The derived parameters clearly showed that DTI could non-invasively reveal the microstructural features of the myocardium.

## Magnetic Resonance Spectroscopy and Multi-Nuclei Imaging

CMR spectroscopy (CMRS) is a non-invasive technique to investigate the myocardial metabolism. It can use the signal from different endogenous nuclei, including $^{31}$phosphorus ($^{31}P$), $^{1}$Hydrogen ($^{1}H$), $^{23}$Sodium ($^{23}Na$), and $^{13}$Carbon ($^{13}C$), to quantify myocardial metabolism *in vivo* [197]. As the resonance frequency of nuclei is dependent on its molecular environment, different metabolites exhibit slightly different frequencies (chemical shift), thus leading to MR frequency spectra according to the chemical composition of the investigated voxel. An analysis of the frequency response (the MR spectrum) allows quantification of different metabolites [198].

$^{31}P$-MRS is most widely used to quantify high-energy phosphates in the heart, including adenosine triphosphate (ATP) and phosphocreatine (PCr). The mutual transformation of ATP and PCr are necessary to meet the energy consumption required to maintain normal cardiac function. The impairments in energy

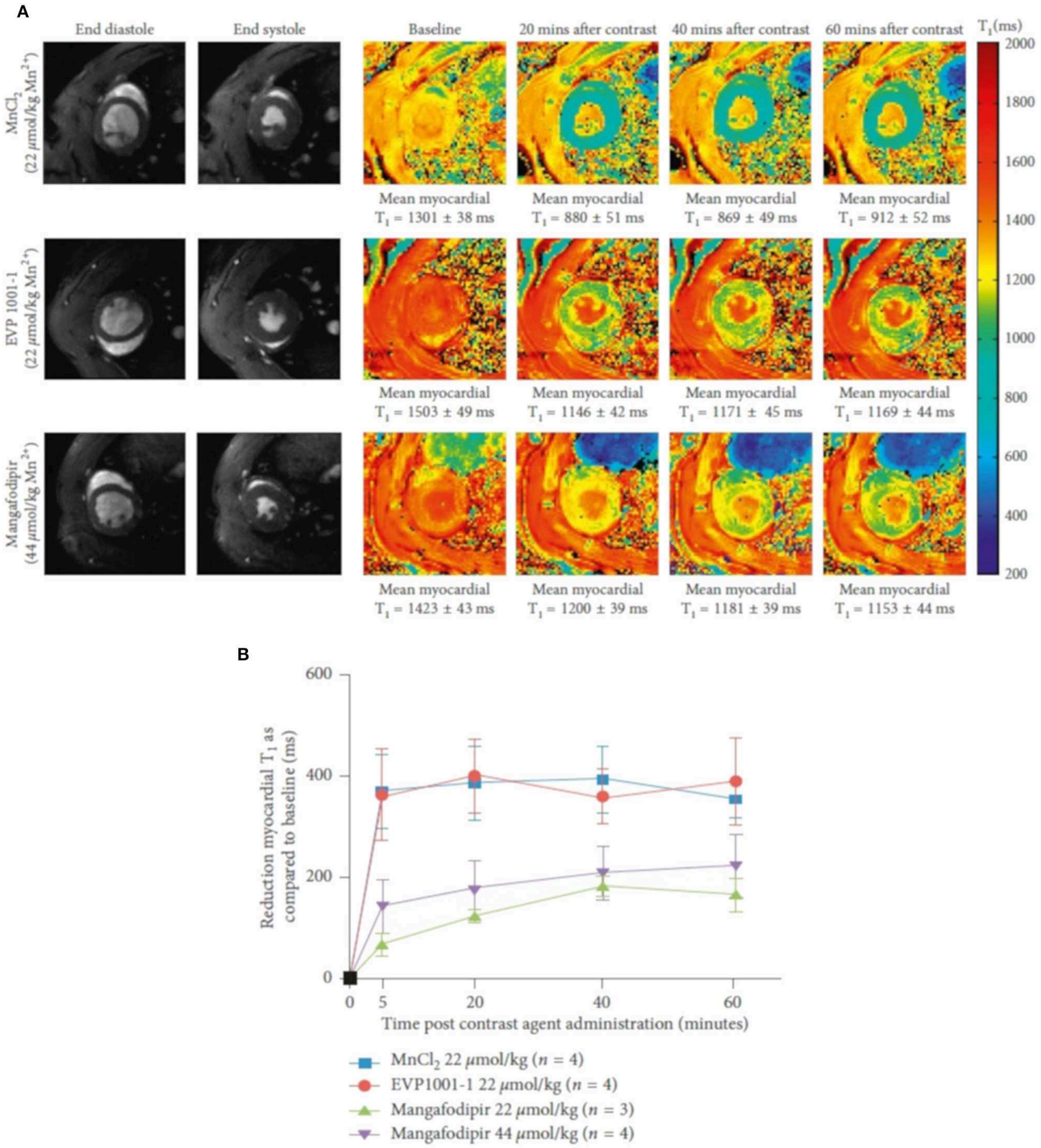


**FIGURE 11 |** T1 shortening with different manganese contrast media over time. **(A)** Normalized T1 maps acquired subsequent to infusion of $MnCl_2$, EVP1001-1, and mangafodipir at 20 min intervals up to 60 min. A clear decreased myocardial T1 value could be observed in all groups. **(B)** Reduction in mean left ventricular T1 values over 60 min with $MnCl_2$, EVP1001-1 and different concentrations of mangafodipir. Two-way ANOVA confirmed a dependence of mean myocardial T1 shortening between each of the contrast agents ($P < 0.0001$). Reproduced with permission from Spath et al. [184].

metabolism reveal pathological processes in cardiac disease. Various preclinical studies showed reduced concentrations of ATP, PCr, and PCr/ATP ratios in cardiomyopathy or heart failure [199–201]. CMRS needs to localize signal to a certain voxel and to exclude signal from nearby structures (e.g., liver, chest skeletal muscle). Localization methods for cardiac MRS

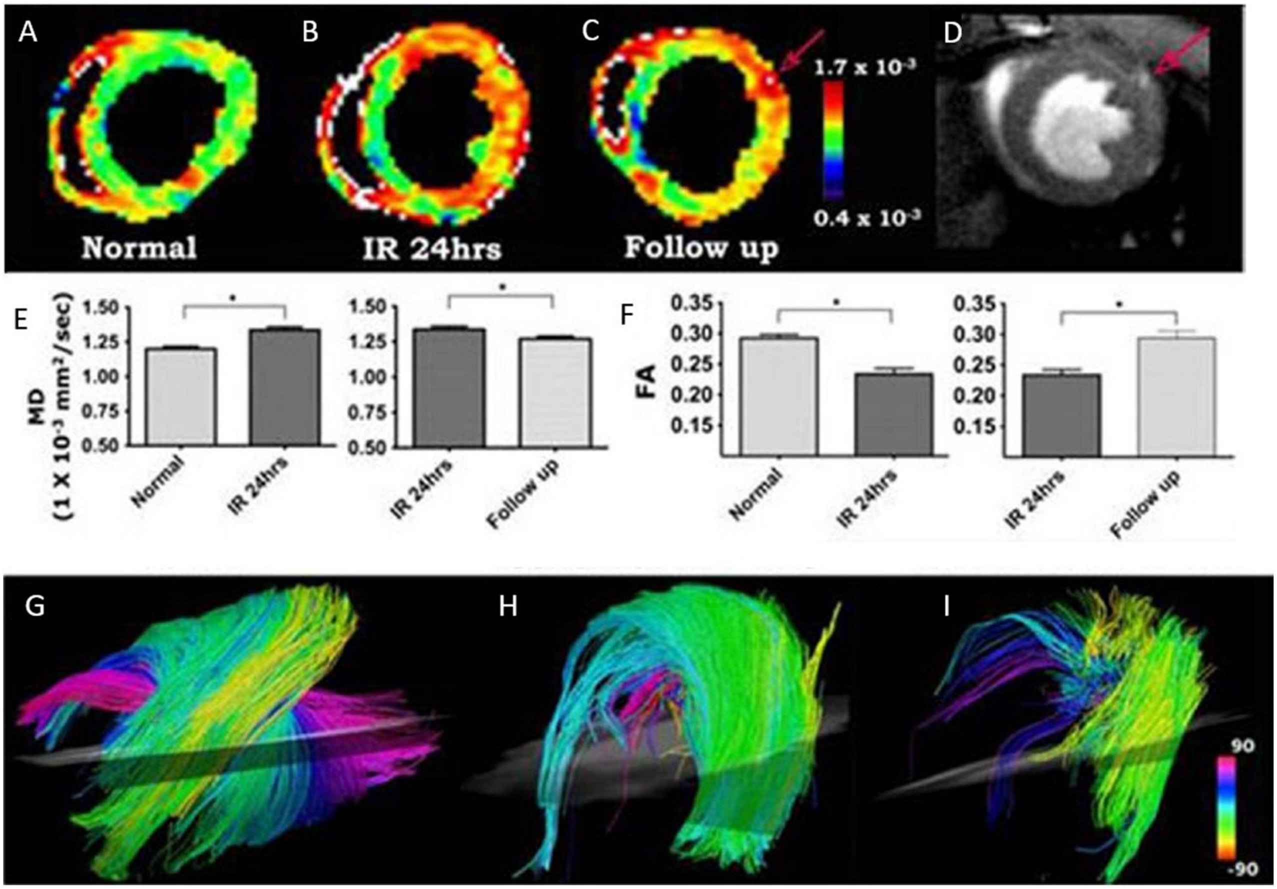


**FIGURE 12 | (A–I)** *In vivo* DTI-tractography of mouse heart at baseline, 24 h after injury and 2–3 weeks after ischemia-reperfusion. The mean diffusivity (MD) maps clearly showed that MD in the injured anterolateral wall increased acutely (24 h after injury) and subsequently returned toward baseline as the myocardium healed **(A–C,E)**. Fractional anisotropy (FA) decreased acutely and returned to baseline 2–3 weeks after injury **(F)**. **(C,D)** The left coronary artery, when present in the image, can be used for internal standardization and control. MD in the vessel and its branches (red arrow, **C,D**) will be significantly higher than MD in normal or healing myocardium. Myofibers passing through a region of interest placed in the anterolateral wall are shown in **(G–I)**. **(G)** Normal mouse heart. The characteristic arrangement of myofibers into an array of crossing helices is clearly visible. **(H)** Mouse exposed to ischemia-reperfusion with severe hypokinesis in the anterolateral wall. However, MD has remained $<1.3 \times 10^{\times}$ $mm^2/s$ and fiber architecture remains reasonably organized. **(I)** Mouse exposed to ischemia-reperfusion, also presenting with severe hypokinesis of the anterolateral wall. MD in this mouse, however, is $<1.3 \times 10^{-3}$ $mm^2/s$ and fiber architecture is severely perturbed. Reproduced with permission from Huang et al. [195].

mainly contain two approaches, single-voxel and chemical shift imaging (CSI). Both contain advantages and limitations. Single-voxel localization is usually performed with image selected *in vivo* spectroscopy (ISIS), which consists of three slice-selective 180° pulses for localization and a single nonselective 90° pulse for signal detection [202]. Bakermans et al. [203] assessed myocardial energy status *in vivo* using single-voxel ISIS-localized $^{31}$P-MRS. Accurate localization and decreased PCr/γ-ATP ratios were observed in TAC mice (**Figure 13**). The $^{31}$P-CSI can be performed in 1D (column of voxel), 2D (plane of voxel), or 3D (block of voxels) mode [200, 204, 205]. CSI employs phase-encoding gradients in different directions and resolves spectra from different locations across the myocardium.

The $^1$H represents the MR-active nuclei with the highest natural abundance and sensitivity in living tissues, and ensures cardiac $^1$H-MRS to be a useful target for quantifying myocardial metabolites, such as triglycerides, lactate, carnitine, myoglobin, and creatine (Cr) levels [206]. Since creatine plays a key role in the creatine kinase system, its measurement can provide additional information about myocardial energy transportation and storage. The high lipid concentration is associated with atherosclerosis and type 2 diabetes mellitus, which results in impaired cardiac function. Due to the technical restriction, it took decades for translating to *in vivo* imaging after first implemented $^1$H-CMRS in a perfused rat heart in Ugurbil et al. [207]. Schneider et al. [208] reported cardiac $^1$H-MRS in a guanidinoacetate N-methyltransferase (GAMT) deficient mouse model *in vivo* using a single-voxel point resolved spectroscopy sequence (PRESS). Various cardiac metabolites were detected in voxels of 2 μl and a clear decreased myocardial creatine level was observed. PRESS is the dominant method for $^1$H-MRS, containing three slice-selective RF pulses (90–180–180°) applied

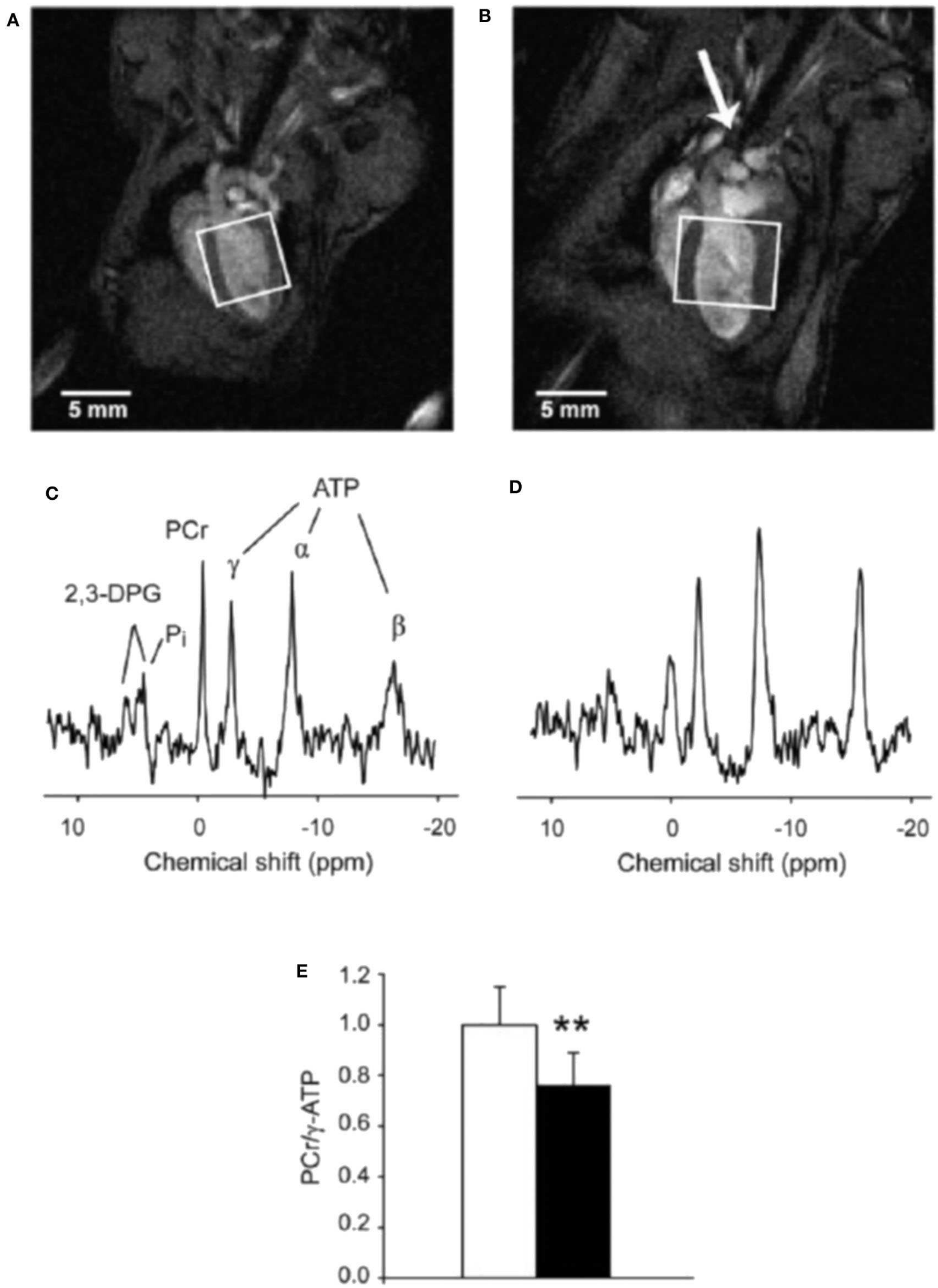


**FIGURE 13 |** End-diastolic left ventricular MR images obtained from a control mouse **(A)** and a mouse with a transverse aortic constriction (TAC) **(B)**. The constriction is indicated by the arrow. Dilated hypertrophic cardiomyopathy is evidenced by increased LV wall thickness and LV cavity volume in the TAC mouse. Rectangles indicate the voxels selected for localized 31P-MRS with 3D ISIS. **(C,D)** display $^{31}$P MR spectra acquired *in vivo* with 3D ISIS in a healthy mouse heart and a TAC heart, respectively. Myocardial PCr/γ-ATP was lower in TAC mice ($n = 8$) compared to healthy controls ($n = 9$) **(E)**. Data are expressed as mean ± SD. $^{**}P < 0.01$. α-, β-, γ-ATP, α-, β-, and γ-phosphate groups in ATP; 2,3-DPG, 2,3-diphosphoglycerate; PCr, phosphocreatine; Pi, inorganic phosphate. Reproduced with permission from Bakermans et al. [203].

concurrently with three mutually orthogonal field gradients [209]. Another technique for $^{1}$H-MRS is STEAM. It is similar to PRESS, but uses three 90° RF pulses. However, $^{1}$H-MRS remains technically challenging due to the superabundance of $^{1}$H in the water molecule, and it will result in baseline distortion and affect the quantification.

$^{23}$Na is an important component in the myocardial signal transduction pathway. The $^{23}$Na signal is increased in myocardial ischemia. Thus, $^{23}$Na-MRS can measure intracellular and extracellular $Na^{+}$ changes to investigate myocardial viability without external contrast agents [210, 211]. Combination with acceleration methods such as CS has been shown [212].

As many metabolites contain carbon, $^{13}$C-MRS is particularly suited to study myocardial metabolism. However, traditional $^{13}$C-MRS is limited by low inherent sensitivity. In the last 10 years, *in vivo* cardiac $^{13}$C-MRS has become feasible with the development of dynamic nuclear hyperpolarization (DNP) technique. DNP is based on transferring electron to nuclear spins thus achieving substantially higher polarization through DNP. It requires the presence of unpaired electrons homogeneously distributed within the sample, which can be achieved by mixing the sample with radicals. To achieve almost 100% polarization of the electrons, DNP works at low temperature and high magnetic fields. Electron-nuclear spin transitions are induced through microwave irradiation. In the solid state, the nuclear polarizations of $^{13}$C can be increased to over 40% [213]. Subsequently, the solid sample is dissolved rapidly to yield a solution of molecules with hyperpolarized nuclear spins [214]. The sensitivity of $^{13}$C-MRS can be increased over 10,000-fold and the metabolism of infused hyperpolarized compounds be visualized *in vivo* [210]. 1-$^{13}$C-pyruvate has been the most widely used DNP hyperpolarized molecules. Pyruvate is the primary metabolites of carbohydrates. After being transported into mitochondria, it is irreversibly converted to acetyl-CoA by the pyruvate dehydrogenase enzyme complex (PDH), then participated into the tricarboxylic acid (TCA) cycle [215]. By labeling pyruvate in a unique carbon position and investigating its metabolism by MRS, insights into myocardial metabolism can be derived. Dodd et al. [216] investigated *in vivo* metabolism of [1-$^{13}$C]pyruvate in the mouse heart and revealed metabolic differences between different mouse strains. Atherton et al. [217] used [2-$^{13}$C]pyruvate to evaluate Krebs cycle metabolism in hyperthyroidism rats and increased anaplerosis was observed in the hyperthyroid heart. With infused hyperpolarized pyruvate, myocardial metabolic processes have been quantified in different rodent models, including diabetes [218], ischemia [219], cardiac inflammation [220], etc.

## CONCLUSIONS

MRI is a tremendously versatile and flexible imaging modality and provides high-resolution images in any arbitrary plane without the risk of ionizing radiation. Especially its accuracy and high reproducibility have made CMR the non-invasive reference modality for deriving myocardial structure, global and regional function, perfusion, tissue characterization and myocardial metabolism in small animal research.

Even though well-established, cardiac imaging in small animals is still challenging especially due to high cardiac and respiratory rates and the small anatomical structures, often demanding dedicated hardware components for providing sufficient image quality in acceptable imaging times. Especially dedicated multielement receiver coils either placed under the chest of the animal or wrapped around its thorax ensure sufficient SNR and reduction of the acquisition time by parallel imaging approaches.

According to the nature of MRI, reliable and highly reproducible information on the cardiac condition of the animal can be obtained. However, the impact of the required general anesthesia and rather long acquisition times on the investigated parameters have to be carefully considered during data interpretation. Inhalation anesthesia is highly recommended, since it provides greater safety, lesser cardiovascular depression, and rapid recovery, and convenient adjustments and maintenance during scanning. The body temperature control of the animal seems mandatory to avoid the deterioration of the derived functional parameters by cardiovascular depression due to cooling out of the animal.

With the availability of reliably working self-gating techniques, assessment of global cardiac function has been proven to be an excellent tool for reliable quantification of systolic dysfunction. However, due to the high heart rates, the assessment of diastolic dysfunction is still challenging and demands long acquisition times to provide sufficient temporal resolution. As in human imaging, regional cardiac function has been addressed by several approaches, and the use of conventional cine images in combination with feature tracking show the potential to enable efficient regional wall motion analysis.

One of the strengths of CMR is its capability for tissue characterization. Identification of scarred tissue by means of delayed contrast enhancement imaging is straight forward using (black-blood) self-gating techniques. Although mapping of relaxation parameters by different means has been reported, it is technically more challenging and well-trained operators are required especially for ensuring accurate and reproducible numbers. More advanced techniques such as (first-pass) perfusion, diffusion-weighted imaging or DTI for deriving myocardial fiber orientation must still be seen as experimental.

Further important information on tissue composition and metabolism can be retrieved from MR spectroscopy and multinuclei imaging. Due to its high natural abundance and sensitivity, $^{1}$H spectroscopy has been efficiently applied to quantifying triglycerides, lactate, carnitine, myoglobin, and creatine (Cr) levels. However, to make full use of the technique, different nuclei like phosphorus ($^{31}$P), Sodium ($^{23}$Na), and Carbon ($^{13}$C) need to be investigated to quantify myocardial metabolism *in vivo*. $^{31}$P-MRS can be used to quantify high-energy phosphates in the heart, $^{23}$Na is an important component in the myocardial signal transduction pathway, and $^{13}$C-MRS is particularly suited to study myocardial metabolism. In general, the multinuclei techniques can be extended to imaging thus providing the chemical composition of each voxel. Due to the low sensitivity and the need to spectrally separate the signal from the different metabolites, multinuclei MRS and MRI are mainly performed at ultra-high field strengths. Even though available in research for decades, due to the long scan times and the expertise required to performing multi-nuclei MRS and MRI in the heart, this technique must still be seen as experimental with unfortunately only little utilization. With the recent introduction of hyperpolarized $^{13}C$ imaging, limitations from the intrinsic low sensitivity may be solved and rapid access to $^{13}C$-labeled metabolites may be enabled at the expense of high related costs.

CMR imaging and spectroscopy is still one of the most promising noninvasive tools for the staging and longitudinal monitoring of cardiovascular diseases in small animals. Due to its versatility, it can be applied to a wide range of translational applications and provide quantitative data from global functional assessment to metabolic characterization of the underlying myocardial substrate. Due to its complexity, the application is currently often limited to global functional assessment and scar imaging. More challenging techniques such as assessing metabolism or the structural organization of the myocardial fibers are still limited by long scan times and may need further technical developments before finally becoming routine in small animal applications.

## AUTHOR CONTRIBUTIONS

HL and VR drafted the manuscript. All authors read and approved the final manuscript.

## ACKNOWLEDGMENTS

The authors would like to thank the Ulm University Center for Translational Imaging MoMAN for its support.

## REFERENCES


1. Wang H, Naghavi M, Allen C, Barber RM, Bhutta ZA, Carter A, et al. Global, regional, and national life expectancy, all-cause mortality, and cause-specific mortality for 249 causes of death, 1980–2015: a systematic analysis for the Global Burden of Disease Study 2015. *Lancet.* (2016) **388**:1459–544. doi: 10.1016/S0140-6736(16)31012-1
2. Joseph P, Leong D, McKee M, Anand SS, Schwalm J-D, Teo K, et al. Reducing the global burden of cardiovascular disease, part 1: the epidemiology and risk factors. *Circ Res.* (2017) **121**:677–94. doi: 10.1161/CIRCRESAHA.117.308903
3. Camacho P, Fan H, Liu Z, He JQ. Small mammalian animal models of heart disease. *Am J Cardiovasc Dis.* (2016) **6**:70–80.
4. Wang K, Long B, Liu F, Wang J-X, Liu C-Y, Zhao B, et al. A circular RNA protects the heart from pathological hypertrophy and heart failure by targeting miR-223. *Eur Heart J.* (2016) **37**:2602–11. doi: 10.1093/eurheartj/ehv713
5. Aherrahrou Z, Schlossarek S, Stoelting S, Klinger M, Geertz B, Weinberger F, et al. Knock-out of nexilin in mice leads to dilated cardiomyopathy and endomyocardial fibroelastosis. *Basic Res Cardiol.* (2016) **111**:6. doi: 10.1007/s00395-015-0522-5
6. Vanhoutte L, Gallez B, Feron O, Balligand J-L, Esfahani H, d'Hoore W, et al. Variability of mouse left ventricular function assessment by 11.7 Tesla MRI. *J Cardiovasc Trans Res.* (2015) **8**:362–71. doi: 10.1007/s12265-015-9638-0
7. Zuo Z, Subgang A, Abaei A, Rottbauer W, Stiller D, Ma G, et al. Assessment of longitudinal reproducibility of mice LV function parameters at 11.7 T derived from self-gated CINE MRI. *Biomed Res Int.* (2017) **2017**:8392952. doi: 10.1155/2017/8392952
8. Lottonen-Raikaslehto L, Rissanen R, Gurzeler E, Merentie M, Huusko J, Schneider JE, et al. Left ventricular remodeling leads to heart failure in mice with cardiac-specific overexpression of VEGF-B $_{167}$ : echocardiography and magnetic resonance imaging study. *Physiol Rep.* (2017) **5**:e13096. doi: 10.14814/phy2.13096
9. Weisell J, Ruotsalainen A, Laakso H, Ylä-Herttuala E, Näpänkangas J, Levonen A, et al. Characterizing valve dynamics in mice by high-resolution cine-MRI. *NMR Biomed.* (2019) **32**:e4108. doi: 10.1002/nbm.4108
10. Wessels A, Sedmera D. Developmental anatomy of the heart: a tale of mice and man. *Physiol Genomics.* (2003) **15**:165–76. doi: 10.1152/physiolgenomics.00033.2003
11. Janiczek RL, Blackman BR, Roy RJ, Meyer CH, Acton ST, Epstein FH. Three-dimensional phase contrast angiography of the mouse aortic arch using spiral MRI. *Magn Reson Med.* (2011) **66**:1382–90. doi: 10.1002/mrm.22937
12. Chen X, Salerno M, Epstein FH, Meyer CH. Accelerated multi-TI spiral MRI using compressed sensing with temporal constraints. In: *19th Annual Meeting of IS*. Montreal, QC (2011). p. 4369.
13. Motaal AG, Noorman N, de Graaf WL, Hoerr V, Florack LMJ, Nicolay K, et al. Functional imaging of murine hearts using accelerated self-gated UTE cine MRI. *Int J Cardiovasc Imaging.* (2015) **31**:83–94. doi: 10.1007/s10554-014-0531-8
14. Hiba B, Richard N, Thibault H, Janier M. Cardiac and respiratory self-gated cine MRI in the mouse: comparison between radial and rectilinear techniques at 7T. *Magn Reson Med.* (2007) **58**:745–53. doi: 10.1002/mrm.21355
15. Lustig M, Donoho D, Pauly JM. Sparse MRI: the application of compressed sensing for rapid MR imaging. *Magn Reson Med.* (2007) **58**:1182–95. doi: 10.1002/mrm.21391
16. Lustig M, Donoho DL, Santos JM, Pauly JM. Compressed sensing MRI. *IEEE Signal Process Mag.* (2008) **25**:72–82. doi: 10.1109/MSP.2007.914728
17. Mistretta CA, Wieben O, Velikina J, Block W, Perry J, Wu Y, et al. Highly constrained backprojection for time-resolved MRI. *Magn Reson Med.* (2006) **55**:30–40. doi: 10.1002/mrm.20772
18. Lindsey ML, Kassiri Z, Virag JAI, de Castro Brás LE, Scherrer-Crosbie M. Guidelines for measuring cardiac physiology in mice. *Am J Physiol Heart Circ Physiol.* (2018) **314**:H733–52. doi: 10.1152/ajpheart.00339.2017
19. Curley D, Lavin Plaza B, Shah AM, Botnar RM. Molecular imaging of cardiac remodelling after myocardial infarction. *Basic Res Cardiol.* (2018) **113**:10. doi: 10.1007/s00395-018-0668-z
20. Gyöngyösi M, Winkler J, Ramos I, Do Q, Firat H, McDonald K, et al. Myocardial fibrosis: biomedical research from bench to bedside. *Eur J Heart Fail.* (2017) **19**:177–91. doi: 10.1002/ejhf.696
21. Constantinides C. Study of the murine cardiac mechanical function using magnetic resonance imaging: the current status, challenges, and future perspectives. In: Andrade AO, Alves Pereira A, Naves ELM, Soares AB, editors. *Practical Applications in Biomedical Engineering.* Rijek: InTech Publications (2012). p. 343–86. doi: 10.5772/51364
22. Epstein FH. MR in mouse models of cardiac disease. *NMR Biomed.* (2007) **20**:238–55. doi: 10.1002/nbm.1152
23. Vanhoutte L, Gerber BL, Gallez B, Po C, Magat J, Jean-Luc B, et al. High field magnetic resonance imaging of rodents in cardiovascular research. *Basic Res Cardiol.* (2016) **111**:46. doi: 10.1007/s00395-016-0565-2
24. Gilson WD, Kraitchman DL. Cardiac magnetic resonance imaging in small rodents using clinical 1.5T and 3.0T scanners. *Methods.* (2007) **43**:35–45. doi: 10.1016/j.ymeth.2007.03.012
25. Bunck AC, Engelen MA, Schnackenburg B, Furkert J, Bremer C, Heindel W, et al. Feasibility of functional cardiac MR imaging in mice using a clinical 3 Tesla whole body scanner. *Invest Radiol.* (2009) **44**:749–56. doi: 10.1097/RLI.0b013e3181b2c135
26. Gabbay-Benziv R, Reece EA, Wang F, Bar-Shir A, Harman C, Turan OM, et al. A step-wise approach for analysis of the mouse embryonic

heart using 17.6 Tesla MRI. *Magn Reson Imaging.* (2017) **35**:46–53. doi: 10.1016/j.mri.2016.08.008
27. Felder J, Celik AA, Choi CH, Schwan S, Shah NJ. 9.4 T small animal MRI using clinical components for direct translational studies. *J Transl Med.* (2017) **15**:264. doi: 10.1186/s12967-017-1373-7
28. Naresh NK, Chen X, Roy RJ, Antkowiak PF, Annex BH, Epstein FH. Accelerated dual-contrast first-pass perfusion MRI of the mouse heart: development and application to diet-induced obese mice: dual-contrast first-pass MRI in Mice. *Magn Reson Med.* (2015) **73**:1237–45. doi: 10.1002/mrm.25238
29. Constantinides C, Angeli S, Gkagkarellis S, Cofer G. Intercomparison of performance of RF coil geometries for high field mouse cardiac MRI. *Concepts Magn Reson.* (2011) **38A**:236–52. doi: 10.1002/cmr.a.20225
30. Doty FD, Entzminger G, Kulkarni J, Pamarthy K, Staab JP. Radio frequency coil technology for small-animal MRI. *NMR Biomed.* (2007) **20**:304–25. doi: 10.1002/nbm.1149
31. Gareis D, Wichmann T, Lanz T, Melkus G, Horn M, Jakob PM. Mouse MRI using phased-array coils. *NMR Biomed.* (2007) **20**:326–34. doi: 10.1002/nbm.1156
32. Schneider JE, Lanz T, Barnes H, Stork L-A, Bohl S, Lygate CA, et al. Accelerated cardiac magnetic resonance imaging in the mouse using an eight-channel array at 9.4 Tesla. *Magn Reson Med.* (2011) **65**:60–70. doi: 10.1002/mrm.22605
33. Wagenhaus B, Pohlmann A, Dieringer MA, Els A, Waiczies H, Waiczies S, et al. Functional and morphological cardiac magnetic resonance imaging of mice using a cryogenic quadrature radiofrequency coil. *PLoS ONE.* (2012) **7**:e42383. doi: 10.1371/journal.pone.0042383
34. Dieringer B, Pohlmann A, Dieringer M, Fuchs K, Els A, Waiczies H, et al. Feasibility and benefit of using a cryogenic radiofrequency coil for functional cardiac magnetic resonance imaging of mice at 9.4 T. *J Cardiovasc Magn Reson.* (2013) **15**:W39. doi: 10.1186/1532-429X-15-S1-W39
35. Flecknell PA. *Laboratory Animal Anaesthesia*. 4th ed. Newcastle upon Tyne: Academic Press (2009).
36. Gargiulo S, Greco A, Gramanzini M, Esposito S, Affuso A, Brunetti A, et al. Mice anesthesia, analgesia, and care, part I: anesthetic considerations in preclinical research. *ILAR J.* (2012) **53**:E55–69. doi: 10.1093/ilar.53.1.55
37. Hildebrandt IJ, Su H, Weber WA. Anesthesia and other considerations for *in vivo* imaging of small animals. *ILAR J.* (2008) **49**:17–26. doi: 10.1093/ilar.49.1.17
38. Berry CJ, Thedens DR, Light-McGroary K, Miller JD, Kutschke W, Zimmerman KA, et al. Effects of deep sedation or general anesthesia on cardiac function in mice undergoing cardiovascular magnetic resonance. *J Cardiovasc Magn Reson.* (2009) **11**:16. doi: 10.1186/1532-429X-11-16
39. Pachon RE, Scharf BA, Vatner DE, Vatner SF. Best anesthetics for assessing left ventricular systolic function by echocardiography in mice. *Am J Physiol Heart Circ Physiol.* (2015) **308**:H1525–9. doi: 10.1152/ajpheart.00890.2014
40. Constantinides C, Mean R, Janssen BJ. Effects of isoflurane anesthesia on the cardiovascular function of the C57BL/6 mouse. *ILAR J.* (2011) **52**:e21–31.
41. Haase A, Frahm J, Matthaei D, Hänicke W, Merboldt KD. FLASH imaging: rapid NMR imaging using low flip-angle pulses. *J Magn Reson.* (2011) **213**:533–41. doi: 10.1016/j.jmr.2011.09.021
42. Rose SE, Wilson SJ, Zelaya FO, Crozier S, Doddrell DM. High resolution high field rodent cardiac imaging with flow enhancement suppression. *Magn Reson Imaging.* (1994) **12**:1183–90. doi: 10.1016/0730-725X(94)90084-5
43. Heijman E, de Graaf W, Niessen P, Nauerth A, van Eys G, de Graaf L, et al. Comparison between prospective and retrospective triggering for mouse cardiac MRI. *NMR Biomed.* (2007) **20**:439–47. doi: 10.1002/nbm.1110
44. van Genderingen HR, Sprenger M, de Ridder JW, van Rossum AC. Carbon-fiber electrodes and leads for electrocardiography during MR imaging. *Radiology.* (1989) **171**:872. doi: 10.1148/radiology.171.3.2717770
45. Choquet P, Goetz C, Aubertin G, Hubele F. Carbon tube electrodes for electrocardiographygated cardiac multimodality imaging in mice. *J Am Assoc Lab Anim Sci.* (2011) **50**:61–4.
46. Sablong R, Rengle A, Ramgolam A, Saint-Jalmes H, Beuf O. An optical fiber-based gating device for prospective mouse cardiac MRI. *IEEE Trans Biomed Eng.* (2014) **61**:162–70. doi: 10.1109/TBME.2013.2278712
47. Schmidt M, Krug JW, Rosenheimer MN, Rose G. Filtering of ECG signals distorted by magnetic field gradients during MRI using non-linear filters and higher-order statistics. *Biomed Tech.* (2018) **63**:395–406. doi: 10.1515/bmt-2016-0232
48. Schmidt M, Krug JW, Rose G. Reducing of gradient induced artifacts on the ECG signal during MRI examinations using Wilcoxon filter. *Curr Dir Biomed Eng.* (2016) **2**:175–8. doi: 10.1515/cdbme-2016-0040
49. Park H, Park Y, Cho S, Jang B, Lee K. New cardiac MRI gating method using event-synchronous adaptive digital filter. *Ann Biomed Eng.* (2009) **37**:2170–87. doi: 10.1007/s10439-009-9764-4
50. Hoerr V, Nagelmann N, Nauerth A, Kuhlmann MT, Stypmann J, Faber C. Cardiac-respiratory self-gated cine ultra-short echo time (UTE) cardiovascular magnetic resonance for assessment of functional cardiac parameters at high magnetic fields. *J Cardiovasc Magn Reson.* (2013) **15**:59. doi: 10.1186/1532-429X-15-59
51. Bovens SM, te Boekhorst BCM, Ouden K den, van de Kolk KWA, Nauerth A, Nederhoff MGJ, et al. Evaluation of infarcted murine heart function: comparison of prospectively triggered with self-gated MRI. *NMR Biomed.* (2011) **24**:307–15. doi: 10.1002/nbm.1593
52. Coolen BF, Abdurrachim D, Motaal AG, Nicolay K, Prompers JJ, Strijkers GJ. High frame rate retrospectively triggered cine MRI for assessment of murine diastolic function. *Magn Reson Med.* (2013) **69**:648–56. doi: 10.1002/mrm.24287
53. Haberkorn SM, Jacoby C, Ding Z, Keul P, Bönner F, Polzin A, et al. Cardiovascular magnetic resonance relaxometry predicts regional functional outcome after experimental myocardial infarction. *Circ Cardiovasc Imaging.* (2017) **10**:e006025. doi: 10.1161/CIRCIMAGING.116.006025
54. Coolen BF, Geelen T, Paulis LEM, Nauerth A, Nicolay K, Strijkers GJ. Three-dimensional T1 mapping of the mouse heart using variable flip angle steady-state MR imaging. *NMR Biomed.* (2011) **24**:154–62. doi: 10.1002/nbm.1566
55. Beyers RJ, Smith RS, Xu Y, Piras BA, Salerno M, Berr SS, et al. T2-weighted MRI of post-infarct myocardial edema in mice. *Magn Reson Med.* (2012) **67**:201–9. doi: 10.1002/mrm.22975
56. Breuer FA, Kellman P, Griswold MA, Jakob PM. Dynamic autocalibrated parallel imaging using temporal GRAPPA (TGRAPPA). *Magn Reson Med.* (2005) **53**:981–5. doi: 10.1002/mrm.20430
57. Griswold MA, Jakob PM, Heidemann RM, Nittka M, Jellus V, Wang J, et al. Generalized autocalibrating partially parallel acquisitions (GRAPPA). *Magn Reson Med.* (2002) **47**:1202–10. doi: 10.1002/mrm.10171
58. Seiberlich N, Ehses P, Duerk J, Gilkeson R, Griswold M. Improved radial GRAPPA calibration for real-time free-breathing cardiac imaging. *Magn Reson Med.* (2011) **65**:492–505. doi: 10.1002/mrm.22618
59. Feng L, Srichai MB, Lim RP, Harrison A, King W, Adluru G, et al. Highly accelerated real-time cardiac cine MRI using K - T SPARSE-SENSE. *Magn Reson Med.* (2013) **70**:64–74. doi: 10.1002/mrm.24440
60. Bollache E, Barker AJ, Dolan RS, Carr JC, van Ooij P, Ahmadian R, et al. k-t accelerated aortic 4D flow MRI in under two minutes: feasibility and impact of resolution, k-space sampling patterns, and respiratory navigator gating on hemodynamic measurements. *Magn Reson Med.* (2018) **79**:195–207. doi: 10.1002/mrm.26661
61. Schnell S, Markl M, Entezari P, Mahadewia RJ, Semaan E, Stankovic Z, et al. K-T GRAPPA accelerated four-dimensional flow MRI in the aorta: effect on scan time, image quality, and quantification of flow and wall shear stress. *Magn Reson Med.* (2014) **72**:522–33. doi: 10.1002/mrm.24925
62. Kido T, Kido T, Nakamura M, Watanabe K, Schmidt M, Forman C, et al. Compressed sensing real-time cine cardiovascular magnetic resonance: accurate assessment of left ventricular function in a single-breath-hold. *J Cardiovasc Magn Reson.* (2016) **18**:50. doi: 10.1186/s12968-016-0271-0
63. Otazo R, Kim D, Axel L, Sodickson DK. Combination of compressed sensing and parallel imaging for highly accelerated first-pass cardiac perfusion MRI. *Magn Reson Med.* (2010) **64**:767–76. doi: 10.1002/mrm.22463
64. Wech T, Seiberlich N, Schindele A, Grau V, Diffley L, Gyngell ML, et al. Development of real-time magnetic resonance imaging of mouse hearts at 9.4 tesla – simulations and first application. *IEEE Trans Med Imaging.* (2016) **35**:912–20. doi: 10.1109/TMI.2015.2501832
65. Frahm J, Voit D, Uecker M. Real-time magnetic resonance imaging: radial gradient-echo sequences with nonlinear inverse reconstruction.

*Invest Radiol.* (2019) **54**:757–66. doi: 10.1097/RLI.0000000000000584
66. Uecker M, Zhang S, Voit D, Karaus A, Merboldt K-D, Frahm J. Real-time MRI at a resolution of 20 ms. *NMR Biomed.* (2010) **23**:986–94. doi: 10.1002/nbm.1585
67. Xue H, Kellman P, LaRocca G, Arai AE, Hansen MS. High spatial and temporal resolution retrospective cine cardiovascular magnetic resonance from shortened free breathing real-time acquisitions. *J Cardiovasc Magn Reson.* (2013) **15**:102. doi: 10.1186/1532-429X-15-102
68. Zhang S, Uecker M, Voit D, Merboldt K-D, Frahm J. Real-time cardiovascular magnetic resonance at high temporal resolution: radial FLASH with nonlinear inverse reconstruction. *J Cardiovasc Magn Reson.* (2010) **12**:39. doi: 10.1186/1532-429X-12-39
69. Dai G, Ding Y, Huang S, simonetti OP, Sosnovik DE. Realtime cine MRI in mice with a single-shot EPI sequence and the karhunen–loeve transform. In: *Proceedings of the 18th Annual Meeting of IS*. Stockholm (2010). p. 1437.
70. Uecker M, Zhang S, Voit D, Merboldt KD, Frahm J. Real-time MRI: recent advances using radial FLASH. *Imaging Med.* (2012) **4**:461–76. doi: 10.2217/iim.12.32
71. Winkelmann S, Schaeffter T, Koehler T, Eggers H, Doessel O. An optimal radial profile order based on the golden ratio for time-resolved MRI. *IEEE Trans Med Imaging.* (2007) **26**:68–76. doi: 10.1109/TMI.2006.885337
72. Wundrak S, Paul J, Ulrici J, Hell E, Geibel M-A, Bernhardt P, et al. Golden ratio sparse MRI using tiny golden angles: golden ratio sparse MRI using tiny Golden Angles. *Magn Reson Med.* (2016) **75**:2372–8. doi: 10.1002/mrm.25831
73. Li H, Abaei A, Lu Q, Rasche V. Tiny golden angle real-time cardiac MRI in the mouse model. In: *27th Annual Meeting of IS.* Montreal, QC (2019). p. 155.
74. Li H, Metze P, Abaei A, Rottbauer W, Just S, Lu Q, et al. Feasibility of real-time cardiac MRI in mice using tiny golden angle radial sparse. *NMR Biomed.* (2020) e4300. doi: 10.1002/nbm.4300. [Epub ahead of print].
75. Donoho DL. Compressed sensing. *IEEE Trans Inform Theory.* (2006) **52**:1289–306. doi: 10.1109/TIT.2006.871582
76. Candes EJ, Romberg J, Tao T. Robust uncertainty principles: exact signal reconstruction from highly incomplete frequency information. *IEEE Trans Inform Theory.* (2006) **52**:489–509. doi: 10.1109/TIT.2005.862083
77. Feng L, Benkert T, Block KT, Sodickson DK, Otazo R, Chandarana H. Compressed sensing for body MRI: compressed sensing for body MRI. *J Magn Reson Imaging.* (2017) **45**:966–87. doi: 10.1002/jmri.25547
78. Feng L, Grimm R, Block KT, Chandarana H, Kim S, Xu J, et al. Golden-angle radial sparse parallel MRI: combination of compressed sensing, parallel imaging, and golden-angle radial sampling for fast and flexible dynamic volumetric MRI. *Magn Reson Med.* (2014) **72**:707–17. doi: 10.1002/mrm.24980
79. Montesinos P, Abascal JFPJ, Cussó L, Vaquero JJ, Desco M. Application of the compressed sensing technique to self-gated cardiac cine sequences in small animals: compressed sensing for self-gated cardiac cine sequences. *Magn Reson Med.* (2014) **72**:369–80. doi: 10.1002/mrm.24936
80. Motaal AG, Coolen BF, Abdurrachim D, Castro RM, Prompers JJ, Florack LMJ, et al. Accelerated high-frame-rate mouse heart cine-MRI using compressed sensing reconstruction. *NMR Biomed.* (2013) **26**:451–7. doi: 10.1002/nbm.2883
81. Wech T, Lygate CA, Neubauer S, Köstler H, Schneider JE. Highly accelerated cardiac functional MRI in rodent hearts using compressed sensing and parallel imaging at 9.4T. *J Cardiovasc Magn Reson.* (2012) **14**:P65. doi: 10.1186/1532-429X-14-S1-P65
82. Buonincontri G, Methner C, Krieg T, Carpenter TA, Sawiak SJ. Functional assessment of the mouse heart by MRI with a 1-min acquisition. *NMR Biomed.* (2014) **27**:733–7. doi: 10.1002/nbm.3116
83. Axel L, Otazo R. Accelerated MRI for the assessment of cardiac function. *BJR.* (2016) **89**:20150655. doi: 10.1259/bjr.20150655
84. Pruessmann KP, Weiger M, Scheidegger MB, Boesiger P. SENSE: sensitivity encoding for fast MRI. *Magn Reson Med.* (1999) **42**:952–62.
85. Deshmane A, Gulani V, Griswold MA, Seiberlich N. Parallel MR imaging. *J Magn Reson Imaging.* (2012) **36**:55–72. doi: 10.1002/jmri.23639
86. Ratering D, Baltes C, Dörries C, Rudin M. Accelerated cardiovascular magnetic resonance of the mouse heart using self-gated parallel imaging strategies does not compromise accuracy of structural and functional measures. *J Cardiovasc Magn Reson.* (2010) **12**:43. doi: 10.1186/1532-429X-12-43
87. Pedersen H, Kozerke S, Ringgaard S, Nehrke K, Kim WY. K-T PCA: temporally constrained K-T BLAST reconstruction using principal component analysis. *Magn Reson Med.* (2009) **62**:706–16. doi: 10.1002/mrm.22052
88. Tsao J, Boesiger P, Pruessmann KP. K-T BLAST and K-T SENSE: dynamic MRI with high frame rate exploiting spatiotemporal correlations. *Magn Reson Med.* (2003) **50**:1031–42. doi: 10.1002/mrm.10611
89. Marshall I, Jansen MA, Tao Y, Merrifield GD, Gray GA. Application of kt-BLAST acceleration to reduce cardiac MR imaging time in healthy and infarcted mice. *Magn Reson Mater Phys.* (2014) **27**:201–10. doi: 10.1007/s10334-013-0392-5
90. Makowski M, Jansen C, Webb I, Chiribiri A, Nagel E, Botnar R, et al. First-pass contrast-enhanced myocardial perfusion MRI in mice on a 3-T clinical MR scanner. *Magn Reson Med.* (2010) **64**:1592–8. doi: 10.1002/mrm.22470
91. Bassett EC, Kholmovski EG, Wilson BD, DiBella EVR, Dosdall DJ, Ranjan R, et al. Evaluation of highly accelerated real-time cardiac cine MRI in tachycardia. *NMR Biomed.* (2014) **27**:175–82. doi: 10.1002/nbm.3049
92. Nahrendorf M, Hiller KH, Hu K, Ertl G, Haase A, Bauer WR. Cardiac magnetic resonance imaging in small animal models of human heart failure. *Med Image Anal.* (2003) **7**:369–75. doi: 10.1016/S1361-8415(03)00011-2
93. Stuckey DJ, Carr CA, Camelliti P, Tyler DJ, Davies KE, Clarke K. *In vivo* MRI characterization of progressive cardiac dysfunction in the mdx mouse model of muscular dystrophy. *PLoS ONE.* (2012) **7**:e28569. doi: 10.1371/journal.pone.0028569
94. Heijman E, Strijkers GJ, Habets J, Janssen B, Nicolay K. Magnetic resonance imaging of regional cardiac function in the mouse. *MAGMA.* (2004) **17**:170–8. doi: 10.1007/s10334-004-0082-4
95. Roberts TA, Price AN, Jackson LH, Taylor V, David AL, Lythgoe MF, et al. Direct comparison of high-temporal-resolution CINE MRI with doppler ultrasound for assessment of diastolic dysfunction in mice. *NMR Biomed.* (2017) **30**:e3763. doi: 10.1002/nbm.3763
96. Le TT, Huang W, Bryant JA, Cook SA, Chin CWL. Stress cardiovascular magnetic resonance imaging: current and future perspectives. *Expert Rev Cardiovasc Ther.* (2017) **15**:181–9. doi: 10.1080/14779072.2017.1296356
97. Saab R, Hage FG. Vasodilator stress agents for myocardial perfusion imaging. *J Nucl Cardiol.* (2017) **24**:434–8. doi: 10.1007/s12350-016-0408-4
98. Charoenpanichkit C, Hundley WG. The 20 year evolution of dobutamine stress cardiovascular magnetic resonance. *J Cardiovasc Magn Reson.* (2010) **12**:59. doi: 10.1186/1532-429X-12-59
99. Wiesmann F, Ruff J, Engelhardt S, Hein L, Dienesch C, Leupold A, et al. Dobutamine-stress magnetic resonance microimaging in mice: acute changes of cardiac geometry and function in normal and failing murine hearts. *Circ Res.* (2001) **88**:563–9. doi: 10.1161/01.RES.88.6.563
100. Tyrankiewicz U, Skorka T, Jablonska M, Petkow-Dimitrow P, Chlopicki S. Characterization of the cardiac response to a low and high dose of dobutamine in the mouse model of dilated cardiomyopathy by MRI *in vivo.* *J Magn Reson Imaging.* (2013) **37**:669–77. doi: 10.1002/jmri.23854
101. Palmer OR, Chiu CB, Cao A, Scheven UM, Diaz JA, Greve JM. *In vivo* characterization of the murine venous system before and during dobutamine stimulation: implications for preclinical models of venous disease. *Ann Anat.* (2017) **214**:43–52. doi: 10.1016/j.aanat.2017.08.004
102. Hao Li, Metze P, Abaei A, Rottbauer W, Just S, Lu Q, Rasche V. Real-time cardiac MRI in the Mice model. In: *23rd Annual Meeting of SCMR.* Orlando, FL (2020).
103. Zerhouni EA, Parish DM, Rogers WJ, Yang A, Shapiro EP. Human heart: tagging with MR imaging–a method for noninvasive assessment of myocardial motion. *Radiology.* (1988) **169**:59–63. doi: 10.1148/radiology.169.1.3420283
104. Axel L, Dougherty L. Heart wall motion: improved method of spatial modulation of magnetization for MR imaging. *Radiology.* (1989) **172**:349–50. doi: 10.1148/radiology.172.2.2748813
105. de Crespigny AJS, Carpenter TA, Hall LD. Cardiac tagging in the rat using a DANTE sequence. *Magn Reson Med.* (1991) **21**:151–6. doi: 10.1002/mrm.1910210119

106. Price AN. Cardiovascular magnetic resonance imaging in experimental models. *TOCMJ.* (2010) **4**:278–92. doi: 10.2174/1874192401004010278
107. Fischer SE, McKinnon GC, Maier SE, Boesiger P. Improved myocardial tagging contrast. *Magn Reson Med.* (1993) **30**:191–200. doi: 10.1002/mrm.1910300207
108. Axel L, Gonçalves RC, Bloomgarden D. Regional heart wall motion: two-dimensional analysis and functional imaging with MR imaging. *Radiology.* (1992) **183**:745–50. doi: 10.1148/radiology.183.3.1584931
109. Prince JL, Gupta SN, Osman NF. Bandpass optical flow for tagged MRI. *Med Phys.* (2000) **27**:108–18. doi: 10.1118/1.598862
110. Liu W, Chen J, Ji S, Allen JS, Bayly PV, Yu X. HARP MRI tagging for direct quantification of lagrangian strain in rat hearts after myocardial infarction. *J Biomech Eng.* (2004) **126**:523–8. doi: 10.1115/1.1785811
111. Delfino JG, Fornwalt BK, Eisner RL, Leon AR, Oshinski JN. Determination of transmural, endocardial, and epicardial radial strain and strain rate from phase contrast MR velocity data. *J Magn Reson Imaging.* (2008) **27**:522–8. doi: 10.1002/jmri.21211
112. Espe EK, Aronsen JM, Skårdal K, Schneider JE, Zhang L, Sjaastad I. Novel insight into the detailed myocardial motion and deformation of the rodent heart using high-resolution phase contrast cardiovascular magnetic resonance. *J Cardiovasc Magn Reson.* (2013) **15**:82. doi: 10.1186/1532-429X-15-82
113. Zhu Y, Drangova M, Pelc NJ. Estimation of deformation gradient and strain from cine-PC velocity data. *IEEE Trans Med Imaging.* (1997) **16**:840–51. doi: 10.1109/42.650880
114. Bernstein MA, Zhou XJ, Polzin JA, King KF, Ganin A, Pelc NJ, et al. Concomitant gradient terms in phase contrast MR: analysis and correction. *Magn Reson Med.* (1998) **39**:300–8. doi: 10.1002/mrm.1910390218
115. Walker PG, Cranney GB, Scheidegger MB, Waseleski G, Pohost GM, Yoganathan AP. Semiautomated method for noise reduction and background phase error correction in MR phase velocity data. *J Magn Reson Imaging.* (1993) **3**:521–30. doi: 10.1002/jmri.1880030315
116. Espe EKS, Aronsen JM, Skrbic B, Skulberg VM, Schneider JE, Sejersted OM, et al. Improved MR phase-contrast velocimetry using a novel nine-point balanced motion-encoding scheme with increased robustness to eddy current effects. *Magn Reson Med.* (2013) **69**:48–61. doi: 10.1002/mrm.24226
117. Rolf MP, Hofman MB, Gatehouse PD, Markenroth-Bloch K, Heymans MW, Ebbers T, et al. Sequence optimization to reduce velocity offsets in cardiovascular magnetic resonance volume flow quantification - a multi-vendor study. *J Cardiovasc Magn Reson.* (2011) **13**:18. doi: 10.1186/1532-429X-13-18
118. McGinley G, Bendiksen BA, Zhang L, Aronsen JM, Nordén ES, Sjaastad I, et al. Accelerated magnetic resonance imaging tissue phase mapping of the rat myocardium using compressed sensing with iterative soft-thresholding. *PLoS ONE.* (2019) **14**:e0218874. doi: 10.1371/journal.pone.0218874
119. Aletras AH, Ding S, Balaban RS, Wen H. DENSE: displacement encoding with stimulated echoes in cardiac functional MRI. *J Magn Reson.* (1999) **137**:247–52. doi: 10.1006/jmre.1998.1676
120. Kim D, Epstein FH, Gilson WD, Axel L. Increasing the signal-to-noise ratio in DENSE MRI by combining displacement-encoded echoes. *Magn Reson Med.* (2004) **52**:188–92. doi: 10.1002/mrm.20109
121. Haggerty CM, Kramer SP, Binkley CM, Powell DK, Mattingly AC, Charnigo R, et al. Reproducibility of cine displacement encoding with stimulated echoes (DENSE) cardiovascular magnetic resonance for measuring left ventricular strains, torsion, and synchrony in mice. *J Cardiovasc Magn Reson.* (2013) **15**:71. doi: 10.1186/1532-429X-15-71
122. Zhong X, Gibberman LB, Spottiswoode BS, Gilliam AD, Meyer CH, French BA, et al. Comprehensive cardiovascular magnetic resonance of myocardial mechanics in mice using three-dimensional cine DENSE. *J Cardiovasc Magn Reson.* (2011) **13**:83. doi: 10.1186/1532-429X-13-83
123. Vandsburger MH, French BA, Kramer CM, Zhong X, Epstein FH. Displacement-encoded and manganese-enhanced cardiac MRI reveal that nNOS, not eNOS, plays a dominant role in modulating contraction and calcium influx in the mammalian heart. *Am J Physiol Heart Circ Physiol.* (2012) **302**:H412–9. doi: 10.1152/ajpheart.00705.2011
124. Aletras AH, Ingkanisorn WP, Mancini C, Arai AE. DENSE with SENSE. *J Magn Reson.* (2005) **176**:99–106. doi: 10.1016/j.jmr.2005.05.010
125. Chen X, Yang Y, Cai X, Auger DA, Meyer CH, Salerno M, et al. Accelerated two-dimensional cine DENSE cardiovascular magnetic resonance using compressed sensing and parallel imaging. *J Cardiovasc Magn Reson.* (2016) **18**:38. doi: 10.1186/s12968-016-0253-2
126. Maret E, Todt T, Brudin L, Nylander E, Swahn E, Ohlsson JL, et al. Functional measurements based on feature tracking of cine magnetic resonance images identify left ventricular segments with myocardial scar. *Cardiovasc Ultrasound.* (2009) **7**:53. doi: 10.1186/1476-7120-7-53
127. Morais P, Marchi A, Bogaert JA, Dresselaers T, Heyde B, D'hooge J, et al. Cardiovascular magnetic resonance myocardial feature tracking using a non-rigid, elastic image registration algorithm: assessment of variability in a real-life clinical setting. *J Cardiovasc Magn Reson.* (2017) **19**:24. doi: 10.1186/s12968-017-0333-y
128. Schuster A, Morton G, Hussain ST, Jogiya R, Kutty S, Asrress KN, et al. The intra-observer reproducibility of cardiovascular magnetic resonance myocardial feature tracking strain assessment is independent of field strength. *Eur J Radiol.* (2013) **82**:296–301. doi: 10.1016/j.ejrad.2012.11.012
129. Morton G, Schuster A, Jogiya R, Kutty S, Beerbaum P, Nagel E. Inter-study reproducibility of cardiovascular magnetic resonance myocardial feature tracking. *J Cardiovasc Magn Reson.* (2012) **14**:43. doi: 10.1186/1532-429X-14-43
130. Kempny A, Fernández-Jiménez R, Orwat S, Schuler P, Bunck AC, Maintz D, et al. Quantification of biventricular myocardial function using cardiac magnetic resonance feature tracking, endocardial border delineation and echocardiographic speckle tracking in patients with repaired tetralogy of fallot and healthy controls. *J Cardiovasc Magn Reson.* (2012) **14**:32. doi: 10.1186/1532-429X-14-32
131. Lapinskas T, Grune J, Zamani SM, Jeuthe S, Messroghli D, Gebker R, et al. Cardiovascular magnetic resonance feature tracking in small animals – a preliminary study on reproducibility and sample size calculation. *BMC Med Imaging.* (2017) **17**:51. doi: 10.1186/s12880-017-0223-7
132. Kober F, Jao T, Troalen T, Nayak KS. Myocardial arterial spin labeling. *J Cardiovasc Magn Reson.* (2016) **18**:22. doi: 10.1186/s12968-016-0235-4
133. Detre JA, Leigh JS, Williams DS, Koretsky AP. Perfusion imaging. *Magn Reson Med.* (1992) **23**:37–45. doi: 10.1002/mrm.1910230106
134. Williams DS, Grandis DJ, Zhang W, Koretsky AP. Magnetic resonance imaging of perfusion in the isolated rat heart using spin inversion of arterial water. *Magn Reson Med.* (1993) **30**:361–5. doi: 10.1002/mrm.1910300314
135. Kwiatkowski G, Kozerke S. Extended quantitative dynamic contrast-enhanced cardiac perfusion imaging in mice using accelerated data acquisition and spatially distributed, two-compartment exchange modeling. *NMR Biomed.* (2019) **32**:e4123. doi: 10.1002/nbm.4123
136. Belle V, Kahler E, Waller C, Rommel E, Voll S, Hiller K, et al. *In vivo* quantitative mapping of cardiac perfusion in rats using a noninvasive MR spin-labeling method. *J Magn Reson Imaging.* (1998) **8**:1240–5. doi: 10.1002/jmri.1880080610
137. Kober F, Iltis I, Cozzone PJ, Bernard M. Myocardial blood flow mapping in mice using high-resolution spin labeling magnetic resonance imaging: influence of ketamine/xylazine and isoflurane anesthesia. *Magn Reson Med.* (2005) **53**:601–6. doi: 10.1002/mrm.20373
138. Kober F, Iltis I, Izquierdo M, Desrois M, Ibarrola D, Cozzone PJ, et al. High-resolution myocardial perfusion mapping in small animals *in vivo* by spin-labeling gradient-echo imaging. *Magn Reson Med.* (2004) **51**:62–7. doi: 10.1002/mrm.10676
139. Vandsburger MH, Janiczek RL, Xu Y, French BA, Meyer CH, Kramer CM, et al. Improved arterial spin labeling after myocardial infarction in mice using cardiac and respiratory gated look-locker imaging with fuzzy C-means clustering. *Magn Reson Med.* (2010) **63**:648–57. doi: 10.1002/mrm.22280
140. Abeykoon S, Sargent M, Wansapura JP. Quantitative myocardial perfusion in mice based on the signal intensity of flow sensitized CMR. *J Cardiovasc Magn Reson.* (2012) **14**:73. doi: 10.1186/1532-429X-14-73
141. Troalen T, Capron T, Cozzone PJ, Bernard M, Kober F. Cine-ASL: a steady-pulsed arterial spin labeling method for myocardial perfusion mapping in mice. Part I. Experimental study. *Magn Reson Med.* (2013) **70**:1389–98. doi: 10.1002/mrm.24565
142. Coolen BF, Moonen RPM, Paulis LEM, Geelen T, Nicolay K, Strijkers GJ. Mouse myocardial first-pass perfusion MR imaging. *Magn Reson Med.* (2010) **64**:1658–63. doi: 10.1002/mrm.22588

143. van Nierop BJ, Coolen BF, Dijk WJR, Hendriks AD, de Graaf L, Nicolay K, et al. Quantitative first-pass perfusion MRI of the mouse myocardium: MRI. *Magn Reson Med.* (2013) **69**:1735–44. doi: 10.1002/mrm.24424
144. van Nierop BJ, Coolen BF, Bax NA, Dijk WJR, van Deel ED, Duncker DJ, et al. Myocardial perfusion MRI shows impaired perfusion of the mouse hypertrophic left ventricle. *Int J Cardiovasc Imaging.* (2014) **30**:619–28. doi: 10.1007/s10554-014-0369-0
145. Bulluck H, Maestrini V, Rosmini S, Abdel-Gadir A, Treibel TA, Castelletti S, et al. Myocardial T1 mapping. *Circ J.* (2015) **79**:487–94. doi: 10.1253/circj.CJ-15-0054
146. Waghorn B, Edwards T, Yang Y, Chuang K-H, Yanasak N, Hu TCC. Monitoring dynamic alterations in calcium homeostasis by $T_1$ -weighted and $T_1$ -mapping cardiac manganese-enhanced MRI in a murine myocardial infarction model. *NMR Biomed.* (2008) **21**:1102–11. doi: 10.1002/nbm.1287
147. Schneider JE, Cassidy PJ, Lygate C, Tyler DJ, Wiesmann F, Grieve SM, et al. Fast, high-resolution *in vivo* cine magnetic resonance imaging in normal and failing mouse hearts on a vertical 11.7 T system. *J Magn Reson Imaging.* (2003) **18**:691–701. doi: 10.1002/jmri.10411
148. Coelho-Filho OR, Shah RV, Mitchell R, Neilan TG, Moreno H, Simonson B, et al. Quantification of cardiomyocyte hypertrophy by cardiac magnetic resonance: implications for early cardiac remodeling. *Circulation.* (2013) **128**:1225–33. doi: 10.1161/CIRCULATIONAHA.112.000438
149. Li W, Griswold M, Yu X. Rapid T1 mapping of mouse myocardium with saturation recovery look-locker method. *Magn Reson Med.* (2010) **64**:1296–303. doi: 10.1002/mrm.22544
150. Li W, Griswold M, Yu X. Fast cardiac $T_1$ mapping in mice using a model-based compressed sensing method. *Magn Reson Med.* (2012) **68**:1127–34. doi: 10.1002/mrm.23323
151. Jiang K, Li W, Li W, Jiao S, Castel L, Van Wagoner DR, et al. Rapid multislice $T_1$ mapping of mouse myocardium: application to quantification of manganese uptake in α-Dystrobrevin knockout mice: myocardial $Mn^{2+}$ uptake in α-Dystrobrevin knockout mice by rapid $T_1$ mapping. *Magn Reson Med.* (2015) **74**:1370–9. doi: 10.1002/mrm.25533
152. Messroghli DR, Radjenovic A, Kozerke S, Higgins DM, Sivananthan MU, Ridgway JP. Modified look-Locker inversion recovery (MOLLI) for high-resolution $T_1$ mapping of the heart. *Magn Reson Med.* (2004) **52**:141–6. doi: 10.1002/mrm.20110
153. Nezafat M, Ramos IT, Henningsson M, Protti A, Basha T, Botnar RM. Improved segmented modified look-Locker inversion recovery $T_1$ mapping sequence in mice. *PLoS ONE.* (2017) **12**:e0187621. doi: 10.1371/journal.pone.0187621
154. Castets CR, Ribot EJ, Lefrançois W, Trotier AJ, Thiaudière E, Franconi J-M, et al. Fast and robust 3D $T_1$ mapping using spiral encoding and steady RF excitation at 7 T: application to cardiac manganese enhanced MRI (MEMRI) in mice: spiral encoding mouse heart 3D $T_1$ mapping. *NMR Biomed.* (2015) **28**:881–9. doi: 10.1002/nbm.3327
155. Neilan TG, Coelho-Filho OR, Shah RV, Abbasi SA, Heydari B, Watanabe E, et al. Myocardial extracellular volume fraction from T1 measurements in healthy volunteers and Mice. *JACC Cardiovasc Imaging.* (2013) **6**:672–83. doi: 10.1016/j.jcmg.2012.09.020
156. Higgins CB, Herfkens R, Lipton JM, Sievers R, Sheldon P, Kaufman L, et al. Nuclear magnetic resonance imaging of acute myocardial infarction in dogs: alterations in magnetic relaxation times. *Am J Cardiol.* (1983) **52**:184–8. doi: 10.1016/0002-9149(83)90093-0
157. Bun SS, Kober F, Jacquier A, Espinosa L, Kalifa J, Bonzi MF, et al. Value of *in vivo* T2 measurement for myocardial fibrosis assessment in diabetic mice at 11.75 T. *Invest Radiol.* (2012) **47**:319–23. doi: 10.1097/RLI.0b013e318243e062
158. Kim PK, Hong YJ, Im DJ, Suh YJ, Park CH, Kim JY, et al. Myocardial T1 and T2 mapping: techniques and clinical applications. *Korean J Radiol.* (2017) **18**:113. doi: 10.3348/kjr.2017.18.1.113
159. Giri S, Chung YC, Merchant A, Mihai G, Rajagopalan S, Raman SV, et al. T2 quantification for improved detection of myocardial edema. *J Cardiovasc Magn Reson.* (2009) **11**:56. doi: 10.1186/1532-429X-11-56
160. Coolen BF, Simonis FFJ, Geelen T, Moonen RPM, Arslan F, Paulis LEM, et al. Quantitative $T_2$ mapping of the mouse heart by segmented MLEV phase-cycled $T_2$ preparation: $T_2$ mapping of the mouse heart. *Magn Reson Med.* (2014) **72**:409–17. doi: 10.1002/mrm.24952
161. Chen Y, Li W, Jiang K, Wang CY, Yu X. Rapid $T_2$ mapping of mouse heart using the carr-purcell-meiboom-gill sequence and compressed sensing reconstruction: rapid $T_2$ mapping of mouse heart. *J Magn Reson Imaging.* (2016) **44**:375–82. doi: 10.1002/jmri.25175
162. Jackson LH, Vlachodimitropoulou E, Shangaris P, Roberts TA, Ryan TM, Campbell-Washburn AE, et al. Non-invasive MRI biomarkers for the early assessment of iron overload in a humanized mouse model of β-thalassemia. *Sci Rep.* (2017) **7**:43439. doi: 10.1038/srep43439
163. van Nierop BJ, Bax NAM, Nelissen JL, Arslan F, Motaal AG, de Graaf L, et al. Assessment of myocardial fibrosis in mice using a T2*-weighted 3D radial magnetic resonance imaging sequence. *PLoS ONE.* (2015) **10**:e0129899. doi: 10.1371/journal.pone.0129899
164. Sosnovik DE, Schellenberger EA, Nahrendorf M, Novikov MS, Matsui T, Dai G, et al. Magnetic resonance imaging of cardiomyocyte apoptosis with a novel magneto-optical nanoparticle. *Magn Reson Med.* (2005) **54**:718–24. doi: 10.1002/mrm.20617
165. Sosnovik DE, Nahrendorf M, Deliolanis N, Novikov M, Aikawa E, Josephson L, et al. Fluorescence tomography and magnetic resonance imaging of myocardial macrophage infiltration in infarcted myocardium *in vivo*. *Circulation.* (2007) **115**:1384–91. doi: 10.1161/CIRCULATIONAHA.106.663351
166. Zhou R, Idiyatullin D, Moeller S, Corum C, Zhang H, Qiao H, et al. SWIFT detection of SPIO-labeled stem cells grafted in the myocardium. *Magn Reson Med.* (2010) **63**:1154–61. doi: 10.1002/mrm.22378
167. Cunningham CH, Arai T, Yang PC, McConnell MV, Pauly JM, Conolly SM. Positive contrast magnetic resonance imaging of cells labeled with magnetic nanoparticles. *Magn Reson Med.* (2005) **53**:999–1005. doi: 10.1002/mrm.20477
168. Mani V, Briley-Saebo KC, Itskovich VV, Samber DD, Fayad ZA. Gradient echo acquisition for superparamagnetic particles with positive contrast (GRASP): sequence characterization in membrane and glass superparamagnetic iron oxide phantoms at 1.5T and 3T. *Magn Reson Med.* (2006) **55**:126–35. doi: 10.1002/mrm.20739
169. Dahnke H, Liu W, Herzka D, Frank JA, Schaeffter T. Susceptibility gradient mapping (SGM): a new postprocessing method for positive contrast generation applied to superparamagnetic iron oxide particle (SPIO)-labeled cells. *Magn Reson Med.* (2008) **60**:595–603. doi: 10.1002/mrm.21478
170. de Jong S, Zwanenburg JJ, Visser F, der Nagel R van, van Rijen HV, Vos MA, et al. Direct detection of myocardial fibrosis by MRI. *J Mol Cell Cardiol.* (2011) **51**:974–9. doi: 10.1016/j.yjmcc.2011.08.024
171. Doltra A, Amundsen B, Gebker R, Fleck E, Kelle S. Emerging concepts for myocardial late gadolinium enhancement MRI. *CCR.* (2013) **9**:185–90. doi: 10.2174/1573403X113099990030
172. Kim RJ, Chen E-L, Lima JAC, Judd RM. Myocardial Gd-DTPA kinetics determine MRI contrast enhancement and reflect the extent and severity of myocardial injury after acute reperfused infarction. *Circulation.* (1996) **94**:3318–26. doi: 10.1161/01.CIR.94.12.3318
173. Yang Z, Berr SS, Gilson WD, Toufektsian M-C, French BA. Simultaneous evaluation of infarct size and cardiac function in intact mice by contrast-enhanced cardiac magnetic resonance imaging reveals contractile dysfunction in noninfarcted regions early after myocardial infarction. *Circulation.* (2004) **109**:1161–7. doi: 10.1161/01.CIR.0000118495.88442.32
174. Thomas D, Dumont C, Pickup S, Misselwitz B, Zhou R, Horowitz J, et al. T1-weighted cine FLASH is superior to IR imaging of post-infarction myocardial viability at 4.7T. *J Cardiovasc Magn Reson.* (2006) **8**:345–52. doi: 10.1080/10976640500451986
175. Ojha N, Roy S, Radtke J, Simonetti O, Gnyawali S, Zweier JL, et al. Characterization of the structural and functional changes in the myocardium following focal ischemia-reperfusion injury. *Am J Physiol Heart Circ Physiol.* (2008) **294**:H2435–43. doi: 10.1152/ajpheart.01190.2007
176. Buonincontri G, Methner C, Krieg T, Carpenter TA, Sawiak SJ. A fast protocol for infarct quantification in mice: fast LGE protocol in Mice. *J Magn Reson Imaging.* (2013) **38**:468–73. doi: 10.1002/jmri.24001

177. Price AN, Cheung KK, Lim SY, Yellon DM, Hausenloy DJ, Lythgoe MF. Rapid assessment of myocardial infarct size in rodents using multi-slice inversion recovery late gadolinium enhancement CMR at 9.4T. *J Cardiovasc Magn Reson.* (2011) **13**:44. doi: 10.1186/1532-429X-13-44
178. Protti A, Sirker A, Shah AM, Botnar R. Late gadolinium enhancement of acute myocardial infarction in mice at 7T: cine-FLASH versus inversion recovery. *J Magn Reson Imaging.* (2010) **32**:878–86. doi: 10.1002/jmri.22325
179. Luo M, Anderson ME. Mechanisms of altered $Ca^{2+}$ handling in heart failure. *Circ Res.* (2013) **113**:690–708. doi: 10.1161/CIRCRESAHA.113.301651
180. Fernandes JL, Storey P, da Silva JA, de Figueiredo GS, Kalaf JM, Coelho OR. Preliminary assessment of cardiac short term safety and efficacy of manganese chloride for cardiovascular magnetic resonance in humans. *J Cardiovasc Magn Reson.* (2011) **13**:6. doi: 10.1186/1532-429X-13-6
181. Skjold A, Kristoffersen A, Vangberg TR, Haraldseth O, Jynge P, Larsson HB. An apparent unidirectional influx constant for manganese as a measure of myocardial calcium channel activity. *J Magn Reson Imaging.* (2006) **24**:1047–55. doi: 10.1002/jmri.20736
182. Skjold A, Vangberg TR, Kristoffersen A, Haraldseth O, Jynge P, Larsson HBW. Relaxation enhancing properties of MnDPDP in human myocardium. *J Magn Reson Imaging.* (2004) **20**:948–52. doi: 10.1002/jmri.20200
183. Toma I, Kim PJ, Dash R, McConnell MV, Nishimura D, Harnish P, et al. Telmisartan in the diabetic murine model of acute myocardial infarction: dual contrast manganese-enhanced and delayed enhancement MRI evaluation of the peri-infarct region. *Cardiovasc Diabetol.* (2016) **15**:24. doi: 10.1186/s12933-016-0348-y
184. Spath NB, Lilburn DML, Gray GA, Le Page LM, Papanastasiou G, Lennen RJ, et al. Manganese-enhanced $T_1$ mapping in the myocardium of normal and infarcted hearts. *Contrast Media Mol Imaging.* (2018) **25**:9641527. doi: 10.1155/2018/9641527
185. Hu TC-C, Bao W, Lenhard SC, Schaeffer TR, Yue T, Willette RN, et al. Simultaneous assessment of left-ventricular infarction size, function and tissue viability in a murine model of myocardial infarction by cardiac manganese-enhanced magnetic resonance imaging (MEMRI). *NMR Biomed.* (2004) **17**:620–6. doi: 10.1002/nbm.933
186. Spath NB, Thompson G, Baker AH, Dweck MR, Newby DE, Semple SIK. Manganese-enhanced MRI of the myocardium. *Heart.* (2019) **105**:1695–700. doi: 10.1136/heartjnl-2019-315227
187. Hsu EW, Muzikant AL, Matulevicius SA, Penland RC, Henriquez CS. Magnetic resonance myocardial fiber-orientation mapping with direct histological correlation. *Am J Physiol.* (1998) **274**:H1627–34. doi: 10.1152/ajpheart.1998.274.5.H1627
188. Jiang Y, Pandya K, Smithies O, Hsu EW. Three-dimensional diffusion tensor microscopy of fixed mouse hearts. *Magn Reson Med.* (2004) **52**:453–60. doi: 10.1002/mrm.20191
189. McGill LA, Ferreira PF, Scott AD, Nielles-Vallespin S, Giannakidis A, Kilner PJ, et al. Relationship between cardiac diffusion tensor imaging parameters and anthropometrics in healthy volunteers. *J Cardiovasc Magn Reson.* (2015) **18**:2. doi: 10.1186/s12968-015-0215-0
190. Basser PJ, Mattiello J, LeBihan D. MR diffusion tensor spectroscopy and imaging. *Biophys J.* (1994) **66**:259–67. doi: 10.1016/S0006-3495(94)80775-1
191. Saggu R, Schumacher T, Gerich F, Rakers C, Tai K, Delekate A, et al. Astroglial NF-kB contributes to white matter damage and cognitive impairment in a mouse model of vascular dementia. *Acta Neuropathol Commun.* (2016) **4**:76. doi: 10.1186/s40478-016-0350-3
192. Argyridis I, Li W, Johnson GA, Liu C. Quantitative magnetic susceptibility of the developing mouse brain reveals microstructural changes in the white matter. *NeuroImage.* (2014) **88**:134–42. doi: 10.1016/j.neuroimage.2013.11.026
193. Scollan DF, Holmes A, Winslow R, Forder J. Histological validation of myocardial microstructure obtained from diffusion tensor magnetic resonance imaging. *Am J Physiol.* (1998) **275**:H2308–18. doi: 10.1152/ajpheart.1998.275.6.H2308
194. Chen J, Song S-K, Liu W, McLean M, Allen JS, Tan J, et al. Remodeling of cardiac fiber structure after infarction in rats quantified with diffusion tensor MRI. *Am J Physiol Heart Circ Physiol.* (2003) **285**:H946–54. doi: 10.1152/ajpheart.00889.2002
195. Huang S, Mekkaoui C, Chen HH, Wang R, Ngoy S, Liao R, et al. Serial diffusion tensor MRI and tractography of the mouse heart *in-vivo*: impact of ischemia on myocardial microstructure. *J Cardiovasc Magn Reson.* (2011) **13**:O28. doi: 10.1186/1532-429X-13-S1-O28
196. Sosnovik DE, Mekkaoui C, Huang S, Chen HH, Dai G, Stoeck CT, et al. Microstructural impact of ischemia and bone marrow–derived cell therapy revealed with diffusion tensor magnetic resonance imaging tractography of the heart *in vivo*. *Circulation.* (2014) **129**:1731–41. doi: 10.1161/CIRCULATIONAHA.113.005841
197. Akki A, Gupta A, Weiss RG. Magnetic resonance imaging and spectroscopy of the murine cardiovascular system. *Am J Physiol Heart Circ Physiol.* (2013) **304**:H633–48. doi: 10.1152/ajpheart.00771.2011
198. Tognarelli JM, Dawood M, Shariff MIF, Grover VPB, Crossey MME, Cox IJ, et al. Magnetic resonance spectroscopy: principles and techniques: lessons for clinicians. *J Clin Exp Hepatol.* (2015) **5**:320–8. doi: 10.1016/j.jceh.2015.10.006
199. Abdurrachim D, Nabben M, Hoerr V, Kuhlmann MT, Bovenkamp P, Ciapaite J, et al. Diabetic db/db mice do not develop heart failure upon pressure overload: a longitudinal *in vivo* PET, MRI, and MRS study on cardiac metabolic, structural, and functional adaptations. *Cardiovasc Res.* (2017) **113**:1148–60. doi: 10.1093/cvr/cvx100
200. Chacko VP, Aresta F, Chacko SM, Weiss RG. MRI/MRS assessment of *in vivo* murine cardiac metabolism, morphology, and function at physiological heart rates. *Am J Physiol Heart Circ Physiol.* (2000) **279**:H2218–24. doi: 10.1152/ajpheart.2000.279.5.H2218
201. Gupta A, Chacko VP, Schär M, Akki A, Weiss RG. Impaired ATP kinetics in failing *in vivo* mouse heart. *Circ Cardiovasc Imaging.* (2011) **4**:42–50. doi: 10.1161/CIRCIMAGING.110.959320
202. Bakermans AJ, Abdurrachim D, Moonen RPM, Motaal AG, Prompers JJ, Strijkers GJ, et al. Small animal cardiovascular MR imaging and spectroscopy. *Prog Nucl Magn Reson Spectrosc.* (2015) **88–89**:1–47. doi: 10.1016/j.pnmrs.2015.03.001
203. Bakermans AJ, Abdurrachim D, van Nierop BJ, Koeman A, van der Kroon I, Baartscheer A, et al. *In vivo* mouse myocardial (31) P MRS using three-dimensional image-selected *in vivo* spectroscopy (3D ISIS): technical considerations and biochemical validations. *NMR Biomed.* (2015) **28**:1218–27. doi: 10.1002/nbm.3371
204. Flögel U, Jacoby C, Gödecke A, Schrader J. *In vivo* 2D mapping of impaired murine cardiac energetics in NO-induced heart failure. *Magn Reson Med.* (2007) **57**:50–8. doi: 10.1002/mrm.21101
205. Rodgers CT, Clarke WT, Snyder C, Vaughan JT, Neubauer S, Robson MD. Human cardiac $^{31}$ P magnetic resonance spectroscopy at 7 tesla: human cardiac $_{31}$ P MR spectroscopy at 7T. *Magn Reson Med.* (2014) **72**:304–15. doi: 10.1002/mrm.24922
206. Faller KME, Lygate CA, Neubauer S, Schneider JE. 1H-MR spectroscopy for analysis of cardiac lipid and creatine metabolism. *Heart Fail Rev*. (2013). 18:657–68. doi: 10.1007/s10741-012-9341-z
207. Ugurbil K, Petein M, Maidan R, Michurski S, Cohn JN, From AH. High resolution proton NMR studies of perfused rat hearts. *FEBS Lett.* (1984) **167**:73–8. doi: 10.1016/0014-5793(84)80835-2
208. Schneider JE, Tyler DJ, ten Hove M, Sang AE, Cassidy PJ, Fischer A, et al. *In vivo* cardiac1H-MRS in the mouse. *Magn Reson Med.* (2004) **52**:1029–35. doi: 10.1002/mrm.20257
209. Klose U. Measurement sequences for single voxel proton MR spectroscopy. *Eur J Radiol.* (2008) **67**:194–201. doi: 10.1016/j.ejrad.2008.03.023
210. Anzawa R, Bernard M, Tamareille S, Baetz D, Confort-Gouny S, Gascard JP, et al. Intracellular sodium increase and susceptibility to ischaemia in hearts from type 2 diabetic db/db mice. *Diabetologia.* (2006) **49**:598–606. doi: 10.1007/s00125-005-0091-5
211. Imahashi K, London RE, Steenbergen C, Murphy E. Male/female differences in intracellular Na+regulation during ischemia/reperfusion in mouse heart. *J Mol Cell Cardiol.* (2004) **37**:747–53. doi: 10.1016/j.yjmcc.2004.06.010
212. Maguire ML, Geethanath S, Lygate CA, Kodibagkar VD, Schneider JE. Compressed sensing to accelerate magnetic resonance spectroscopic imaging: evaluation and application to 23Na-imaging of mouse hearts. *J Cardiovasc Magn Reson.* (2015) **17**:45. doi: 10.1186/s12968-015-0149-6

213. Hurd RE, Yen YF, Chen A, Ardenkjaer-Larsen JH. Hyperpolarized $_{13}$ C metabolic imaging using dissolution dynamic nuclear polarization. *J Magn Reson Imaging.* (2012) **36**:1314–28. doi: 10.1002/jmri.23753
214. Ardenkjaer-Larsen JH, Fridlund B, Gram A, Hansson G, Hansson L, Lerche MH, et al. Increase in signal-to-noise ratio of > 10,000 times in liquid-state NMR. *Proc Natl Acad Sci USA*. (2003) **100**:10158–63. doi: 10.1073/pnas.1733835100
215. Kolwicz SC, Purohit S, Tian R. Cardiac metabolism and its interactions with contraction, growth, and survival of cardiomyocytes. *Circ Res.* (2013) **113**:603–16. doi: 10.1161/CIRCRESAHA.113.302095
216. Dodd MS, Ball V, Bray R, Ashrafian H, Watkins H, Clarke K, et al. *In vivo* mouse cardiac hyperpolarized magnetic resonance spectroscopy. *J Cardiovasc Magn Reson.* (2013) **15**:19. doi: 10.1186/1532-429X-15-19
217. Atherton HJ, Dodd MS, Heather LC, Schroeder MA, Griffin JL, Radda GK, et al. Role of pyruvate dehydrogenase inhibition in the development of hypertrophy in the hyperthyroid rat heart: a combined magnetic resonance imaging and hyperpolarized magnetic resonance spectroscopy study. *Circulation.* (2011) **123**:2552–61. doi: 10.1161/CIRCULATIONAHA.110.011387
218. Le Page LM, Ball DR, Ball V, Dodd MS, Miller JJ, Heather LC, et al. Simultaneous *in vivo* assessment of cardiac and hepatic metabolism in the diabetic rat using hyperpolarized MRS: *In vivo* assessment of both cardiac and hepatic diabetic metabolism. *NMR Biomed.* (2016) **29**:1759–67. doi: 10.1002/nbm.3656
219. Miller JJ, Lau AZ, Nielsen PM, McMullen-Klein G, Lewis AJ, Jespersen NR, et al. Hyperpolarized [1,4-13C2]fumarate enables magnetic resonance-based imaging of myocardial necrosis. *JACC Cardiovasc Imaging.* (2018) **11**:1594–606. doi: 10.1016/j.jcmg.2017.09.020
220. Lewis AJM, Miller JJ, Lau AZ, Curtis MK, Rider OJ, Choudhury RP, et al. Noninvasive immunometabolic cardiac inflammation imaging using hyperpolarized magnetic resonance. *Circ Res.* (2018) **122**:1084–93. doi: 10.1161/CIRCRESAHA.117.312535

**Conflict of Interest:** The authors declare that the research was conducted in the absence of any commercial or financial relationships that could be construed as a potential conflict of interest.

frontiers in Physics

REVIEW
published: 12 June 2020
doi: 10.3389/fphy.2020.00152

Check for updates

# Functional Neuroimaging in Rodents Using Cerebral Blood Flow SPECT

*Anja M. Oelschlegel*[1,2†] *and Jürgen Goldschmidt*[1*]

[1] *Department of Systems Physiology of Learning, Leibniz Institute for Neurobiology, Magdeburg, Germany,* [2] *Institute of Anatomy, Medical Faculty, Otto-von-Guericke University, Magdeburg, Germany*

The brain-wide activation patterns that underlie, generate, and change the behavioral outputs in rodents, the main animal models in biomedical research, are difficult to assess *in vivo*. The standard tool for whole-brain imaging of spatiotemporal activation patterns in rodents is BOLD fMRI, but the technique requires the animals to be immobilized inside the scanners. One of the few methods that can provide *in vivo* images of brain-wide patterns of neural activity from unrestrained animals outside scanner environments is single-photon emission computed tomography (SPECT) imaging of cerebral blood flow (CBF). During ongoing behavior, animals are intravenously injected with $^{99m}$Tc-HMPAO (99m-technetium hexamethylene propyleneamine oxime), a lipophilic tracer that, after accumulation in the brain in a flow-dependent manner, is rapidly converted to a hydrophilic compound that remains trapped in the brain and shows no redistribution. The $^{99m}$Tc brain distribution, reflecting the average blood flow during the time of injection, can be read out in the anesthetized animal after injection. Similar in rationale to $^{18}$F-2-fluoro-2-deoxy-glucose ($^{18}$F-FDG) positron emission tomography (PET), $^{99m}$Tc-HMPAO SPECT provides static images of spatial patterns of neural activity from awake behaving rodents, but the spatial resolution can be higher and the stimulation times substantially shorter. In this review, we present an overview about the underlying rationales and principles of functional CBF SPECT imaging in rodents, give a short summary of the experimental procedures, and discuss the advantages, drawbacks, and perspectives of the technique within the framework of methods for imaging brain-wide activation patterns in awake behaving rodents.

**Keywords: functional neuroimaging, small-animal SPECT, cerebral blood flow, PET, fMRI**

OPEN ACCESS

***Edited by:***
*Adriana Tavares,*
*University of Edinburgh,*
*United Kingdom*

***Reviewed by:***
*Wang Xi,*
*Zhejiang University, China*
*Paul Vaska,*
*Stony Brook University, United States*

***Correspondence:***
*Jürgen Goldschmidt*
*juergen.goldschmidt@lin-magdeburg.de*

***†Present address:***
*Anja M. Oelschlegel,*
*Research Group Neuroplasticity,*
*Leibniz Institute for Neurobiology,*
*Magdeburg, Germany*

***Specialty section:***
*This article was submitted to Medical Physics and Imaging, a section of the journal Frontiers in Physics*

***Received:*** *15 December 2019*
***Accepted:*** *15 April 2020*
***Published:*** *12 June 2020*

***Citation:***
*Oelschlegel AM and Goldschmidt J (2020) Functional Neuroimaging in Rodents Using Cerebral Blood Flow SPECT. Front. Phys. 8:152. doi: 10.3389/fphy.2020.00152*

## INTRODUCTION

Rodents, in particular rats and mice, serve as the main model organisms for studying the structure and function of the mammalian brain in basic and applied neurosciences. With brain sizes in the cubic centimeter range—about 0.5 $cm^3$ in mice and 2 $cm^3$ in rats—these rodents pose particular challenges for neuroimaging techniques, especially techniques for *in vivo* imaging of the entire organ.

Rodent brains are several orders of magnitude larger than the brains of small vertebrates such as the zebrafish or common invertebrate model organisms such as the fruit fly *Drosophila* and the roundworm *Caenorhabditis elegans*. In addition, myelinated fiber bundles traverse the adult rodent brains, strongly increasing the scattering of electromagnetic waves in the visible range. In contrast to the transparent brains of zebrafish larvae or *C. elegans*, which can be optically imaged as a whole at cellular resolution *in vivo* [1, 2], optical *in vivo* imaging of entire rodent brains at this resolution is not possible.

With respect to penetration depths and fields of view, rodent brains can easily be imaged with X-ray CT, MRI, PET, or SPECT, medical imaging techniques developed for human imaging. However, with brain volumes about a thousand times smaller than the human brain, substantial increases in spatial resolution are required if rodent brains should be imaged with at least the same relative resolution—relative to the brain size—as in humans.

Techniques for imaging the entire brain are of particular relevance in neuroscience. Brains are characterized by high degrees of global and local anatomical and functional interconnectivities between single neurons and neuronal ensembles. This network topology implies that, as a general rule, changes in behavioral output are mediated by activation changes in distributed neuron populations. In fact, even apparently simple behaviors, e.g., fear behavior [3], have been shown to be governed by complex brain-wide network activations. Explaining the changes in behavior that genetic alterations or manipulations, protein modifications, pharmacological treatments, and artificial or natural stimulations of cell ensembles might cause requires identification of the network activation patterns.

An ideal method for functional neuroimaging would be able to image *in vivo* brain-wide patterns of neural activity with high spatial (single-cell) and temporal (millisecond) resolution in behaving unrestrained animals. High-throughput imaging, repeated imaging over long time spans, and little to no interferences with experimental set-ups would be additional benefits.

Optical methods in invertebrates and the zebrafish larva as a small vertebrate come close to these demands [1, 2]. For the mouse brain, however, no such methods are available, and it remains dubious whether techniques for single-cell-resolution *in vivo* imaging of the activation patterns of the ∼70 million neurons in the mouse brain [4] can be developed at all. All currently available methods operate at substantially lower resolutions and suffer from more or less severe drawbacks.

The prevailing approach to assessing the brain-wide network behavior in the rodent brain is functional magnetic resonance imaging based on blood-oxygenation-level-dependent contrast (BOLD fMRI). Spatial and temporal resolutions rank among the highest in rodent whole-brain imaging, but animals have to be restrained inside scanners. *In vivo* images of brain-wide activation patterns in unrestrained, behaving rodents can be obtained using tracer techniques. Rodents are injected before or during the behavior of interest with tracers that accumulate in the brain in an activity-dependent manner. Tracers that show no relevant redistribution can be imaged in anesthetized animals after the experiment. Three tracers with three different imaging modalities are commonly used, the glucose analog $^{18}$F-2-fluoro-2-deoxy-glucose ($^{18}$F-FDG) for positron emission tomography (PET) imaging, the calcium analog manganese for manganese-enhanced MRI (MEMRI), and the blood flow tracer $^{99m}$Tc-HMPAO for SPECT imaging. As one of the main drawbacks, these methods can provide only a static view of the average activity during the uptake period. What makes these approaches attractive is that there are few constraints on the behavioral set-ups to be used and the simplicity of the methods with respect to the treatments of the animals.

We here review one of the approaches, functional neuroimaging using CBF SPECT. We first describe the historical development and the rationales of using tracers for imaging cerebral blood flow and give an overview of the principles of SPECT imaging in small animals. We then explain the experimental procedure and discuss the approach in the framework of the diverse techniques for brain-wide functional neuroimaging in rodents.

## IMAGING REGIONAL CEREBRAL BLOOD FLOW USING TRACER TECHNIQUES

Functional neuroimaging has its roots in studies of cerebral blood flow in mammals. In 1948, Kety and Schmidt published a method for quantifying the global cerebral blood flow in humans based on measurements of arteriovenous differences in concentrations of nitrous oxide, a non-metabolized gas [5]. The method solved a problem inherent to earlier attempts of calculating global cerebral blood flow from arteriovenous differences in oxygen concentration. By using an inert gas, the flow could be determined independently from the oxygen metabolism [6]. The inert gas approach, which can be seen as a tracer technique for calculating global cerebral blood flow, led to the development of tracer techniques for imaging regional cerebral blood flow (rCBF). The first method for studying rCBF was published in 1955 [7]. It was based on intravenously injecting cats with $^{131}$I-trifluoroiodomethane, an inert gas radioactively labeled with $^{131}$iodine, and studying the spatial patterns of the flow-dependent wash-in of the gas post-mortem by means of an autoradiographic method. After tracer injection, brains were quickly removed and frozen in order to avoid back-diffusion of the tracer from the brain to plasma. Brain sectioning and autoradiography were performed at −40°C in order to minimize the loss of the volatile compound [6]. By demonstrating the increased blood flow in the visual cortex upon visual stimulation, the method was also the first to provide images of stimulus-induced brain activations [8, 9].

Interestingly, it was not generally recognized at that time that these studies formed the basis for what would later be termed "functional neuroimaging." When the data were presented in 1955 on a meeting of the American Neurological Association, Landau (as quoted from [10]) commented: "Of course we recognize that this is a very secondhand way of determining physiological activity; it is rather like trying to measure what a factory does by measuring the intake of water and the output of sewage. This is only a problem of plumbing and only secondary inferences can be made about function. We would not suggest that this is a substitute for electrical recording in terms of easy evaluation of what is going on."

In fact, in terms of spatial and temporal resolution, measurements of blood flow are orders of magnitude apart from electrophysiological recordings. Nevertheless, the following decades clearly showed the usefulness of this approach for

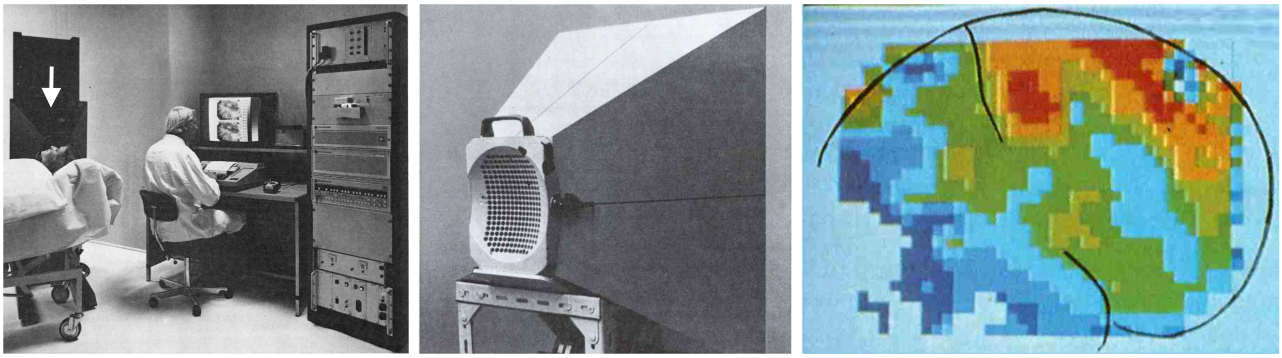

**FIGURE 1 |** Functional neuroimaging in humans started with 2D scintigraphic imaging of cerebral blood flow. An experimental set-up is shown in the left panel. The arrow points to a gamma camera equipped with a cone beam collimator similar to the collimator shown in the middle panel. The cone-beam collimator is placed close to the subject's head. The gamma camera is a 254 detector camera developed by Per Rommer and Edda Sveinsdottir under the leadership of Niels A. Lassen at Meditronic and commercialized by Medimatic under the name "Dynamatic 254" (Images reprinted with permission from Per Rommer). An example of the images obtained with this set-up is shown in the right panel. Brain contours and the central sulcus are outlined in black. The image shows CBF during hand gripping with the contralateral hand. Reprinted with permission from the American Medical Association. Copyright © (1976) American Medical Association. All rights reserved [12].

detecting spatial patterns of neural activity in experimental animals and in humans. The first images of functional brain activity in humans were 2D scintigraphic gamma camera images from subjects intra-arterially injected with the gamma emitter $^{133}$Xe as a tracer, again an inert gas ([11]; **Figure 1**). Groundbreaking work on functional imaging in humans followed using PET with $^{15}$O-H$_2$O as a blood flow tracer [13–15]. The short half-life of $^{15}$O of 2.04 min made it possible to repeatedly image the same subject inside the PET scanner, and the logic of subtracting data sets from different conditions for studying cognitive processes was introduced [10].

The details of the neurovascular coupling are still under debate. Much progress has been made in elucidating signal cascades coupling energy demands in neural tissue to changes in diameter in capillaries or different segments of the arterial system [16], but the interpretation of increased or decreased flow in volumes of mixed populations of excitatory and inhibitory neurons, presynaptic and post-synaptic neuronal elements, and astrocytes has remained unclear. Under simple conditions, an excitatory input may lead to enhanced post-synaptic processing in a volume element, resulting in an increased flow. Conversely, reduced excitatory input under certain stimulus conditions may result in reduced metabolism and flow appearing as a deactivation. The complexity increases, however, when inhibitory interneurons are involved. Subpopulations of inhibitory interneurons, for instance, may have high firing rates and energy demands, but the net effect on energy demands in a volume element will depend on, among others, the densities of excitatory and inhibitory neurons as well as the local effects of the inhibition, factors that vary in different brain regions.

Stimulus-induced changes in cerebral blood flow as measured with $^{15}$O-H$_2$O PET in humans increase up to 30% upon intense stimulation [17]. These changes are relatively large compared to changes in cerebral blood volume (CBV) or in the BOLD response. This may compensate to some degree for the fact that, in contrast to BOLD fMRI or functional ultrasound (fUS) measurements of CBV, usually only one image is taken per individual and condition in CBF studies. Comparisons of the sensitivities of the different methods are difficult, however, as they strongly depend on image noise, which can vary substantially with different imaging protocols and in radionuclide imaging is strongly affected by injected dose and acquisition times.

A number of chemically quite diverse molecules can be used as tracers for imaging cerebral blood flow: inert gases, $^{15}$O-labeled water, or labeled lipophilic compounds such as $^{14}$C-iodoantipyrine [18]. A key feature of all these compounds is that they can readily pass the blood-brain barrier. With all these compounds, the passage through the BBB is bi-directional. In order to measure the blood-flow-dependent wash-in of these compounds into the brain, measurements have to be done quickly after injection—usually within the first minute—as long as there is unidirectional flow of the tracers from plasma to brain. Even if the half-life of $^{15}$O were much longer, $^{15}$O-H$_2$O PET CBF measurements would still have to be done in subjects inside the PET scanner. For autoradiographic measurements in experimental animals, the brains have to be quickly removed after injection [18].

Routine SPECT imaging of CBF differs from these approaches because tracers can be used that are trapped in the brain after passage through the BBB. This makes it possible to image the tracer distributions, or the distributions of the radioactive labels, resp., after trapping. In theory, measurements of CBF using trapped tracers are less straightforward than measurements with inert, non-metabolized compounds, because additional factors come into play, in particular the rates of the trapping reactions and potential redistributions of tracers or trapped labels. In practice, however, the two most commonly used tracers for SPECT imaging of brain perfusion, $^{99m}$Tc-HMPAO [19] and $^{99m}$Tc-ethyl cysteinate dimer ($^{99m}$Tc-ECD), have been shown to rather accurately reflect CBF [18].

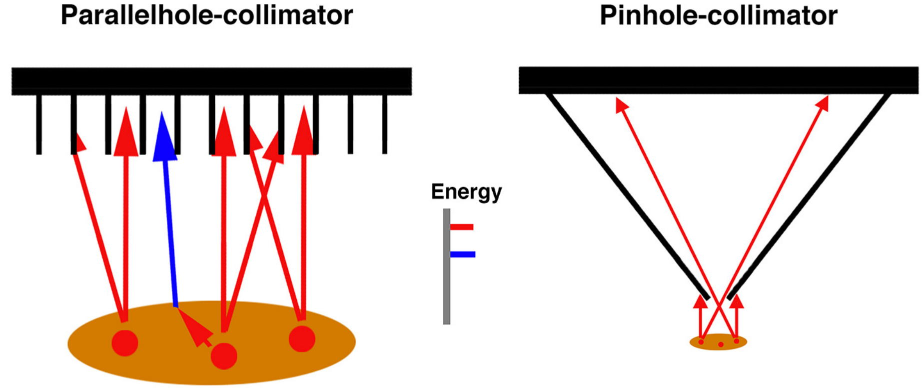


**FIGURE 2 |** Two collimator types used in SPECT imaging. Parallel-hole collimators, frequently used in SPECT imaging in humans, absorb photons that would reach the detector—within limits—at oblique angles after emission from the sources. The sources are depicted in red. Scattered photons (blue, shown only for the parallel-hole collimator) can be distinguished from non-scattered photons due to their lower energy. When pinhole collimators are used, magnified 2D projection images form on the detector if the imaged objects are close to the pinhole.

Both tracers are trapped by rapid conversion to hydrophilic compounds after passage through the BBB. The available data indicate that $^{99m}$Tc-HMPAO is metabolized to hydrophilic compounds in reactions that, at least in part, depend on glutathione and may take place preferentially in astrocytes [20, 21]. $^{99m}$Tc-ECD is metabolized to a monoacid form that is retained in brains of primates. $^{99m}$Tc is not retained in rat and mouse brains after intravenous $^{99m}$Tc-ECD injections [22, 23]. Studies in mice have shown that the $^{99m}$Tc monoacid is quickly extruded by the organic anion transporter OAT3 [24], which is highly expressed in endothelial cells. In addition to the $^{99m}$Tc-labeled tracers, there is also a $^{123}$I-iodine-labeled tracer available for SPECT imaging, $^{123}$I-iodoamphetamine ($^{123}$I-IMP). In humans, the tracer redistributes already within the first hour after administration [25, 26], a fact that has limited its use. To our knowledge, its redistribution has not been studied with small-animal SPECT in rodents, but the tracer has been used for an *ex vivo* SPECT imaging study [27]. Currently, $^{99m}$Tc-HMPAO can be regarded as the tracer of choice for functional neuroimaging using CBF SPECT in rodents.

## PRINCIPLES OF SPECT IMAGING IN SMALL ANIMALS

As mentioned above, the first *in vivo* images of brain activity were 2D scintigraphic images of cerebral blood flow in humans with pixel sizes on the order of 1 cm$^2$. These images were taken with a gamma camera, a device developed in the 1950s by Anger [28, 29].

The traditional Anger camera records the spatial positions and intensities of scintillation events that occur in relatively large crystals—usually flat thallium-activated sodium iodide crystals a few hundred square centimeters in size—upon absorption of gamma photons. In order to relate the spatial position of a scintillation event in the crystal to a restricted volume of possible emission sites in the subject, the cameras are equipped with so-called collimators, a term derived from a false reading of Latin *collineare*, meaning “to direct in a straight line” (Merriam-Webster online dictionary: https://www.merriam-webster.com/dictionary/collimate).

No different from light emitted from a light source, gamma rays are emitted isotropically from gamma ray sources. Collimators, placed between the sources and the scintillation crystal, limit the possible angles at which gamma rays from different positions in the field of view can reach the crystal (for a review on collimators, see [30]). A parallel-hole collimator, for instance, is a sieve-like structure made of heavy metals that absorbs most of the gamma photons reaching the detector at oblique angles (**Figure 2**). The 2D projection image of the source distribution is formed from parallel bundles of gamma rays that can pass through the collimator. Absorptive collimation with different collimator geometries is the prevailing method for forming 2D projection images in SPECT. In general, small fractions of <1% of the gamma photons that could theoretically reach the detector pass through the collimator and can be used for image formation [30].

The first systems for 3D imaging of gamma emitters were developed in the 1960s [31, 32]. Scanners with rotating gamma cameras, similar to currently prevailing clinical scanners, were introduced in the 1970s [31]. The development of SPECT imaging was driven not only by advancements in the imaging technology but also by the discovery of the radionuclide $^{99m}$Technetium [33]. With a physical half-life of 6 h, an energy of the emitted gamma photons of 140 keV, which is low enough for efficient detection with NaI-scintillator crystals but high enough for efficient emissions out of the human body, and easy on-site availability from $^{99m}$Tc generators, this radionuclide proved to be ideal for SPECT imaging. $^{99m}$Tc became the most used radionuclide for diagnostic imaging worldwide [33].

With spatial resolutions in the range of a cubic centimeter in clinical routine, SPECT has been notoriously regarded a low-resolution imaging modality that is inferior to PET in any respect. However, the spatial resolution of SPECT

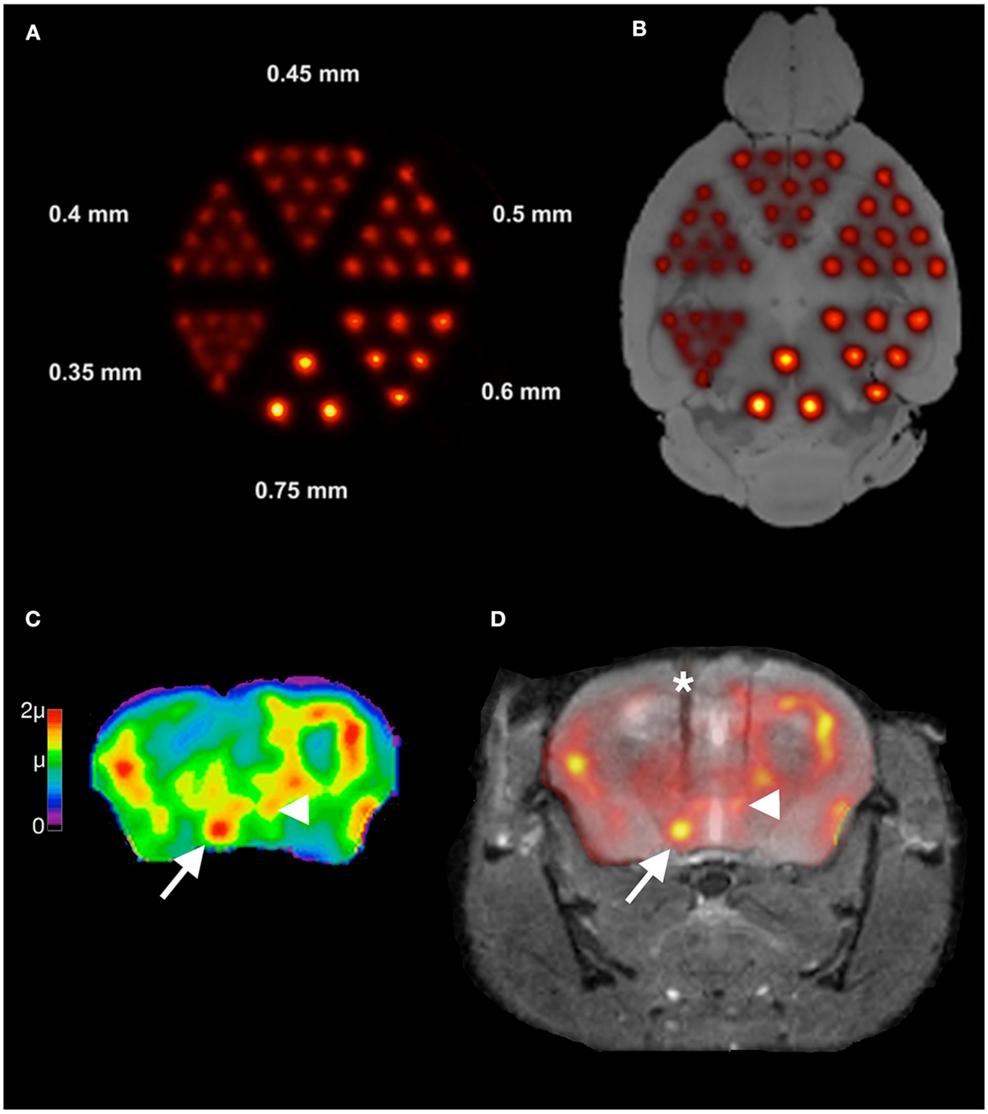


**FIGURE 3 |** Illustration of spatial resolutions with multi-pinhole SPECT imaging in mouse brain. Shown in **(A)** is an image of a SPECT measurement of a micro-Jaszczak hot-rod resolution phantom filled with $^{99m}$Tc. The phantom was scanned with custom-made 0.3 mm multi-pinhole apertures at the Leibniz Institute for Neurobiology. Rods down to the size of 0.4 mm can be resolved. In **(B)**, an overlay of the image in **(A)** onto an anatomical reference MR image [38] of a mouse brain is shown to illustrate these spatial resolutions in relation to the mouse brain anatomy. Resolutions in the range of 0.75 mm that can easily be achieved in SPECT imaging are already quite useful for imaging brain regional tracer distributions. In **(C)** a high-resolution $^{99m}$Tc-HMPAO SPECT image is shown from the CBF of a mouse during intracranial self-stimulation of the medial forebrain bundle (mfb). This image was overlaid on the MR of the same animal in **(D)**. The MR is a post-mortem MR after removal of the self-stimulation setup. The electrode track is marked by an asterisk in **(D)**. Images were taken with the same setup as for the measurement in **(A)**. The color scale in **(C)** is in units of the global mean intensity μ. Note in **(C)** the clear delineation of the mfb (arrow) and the small hypothalamic region with a relatively high uptake (arrowhead).

critically depends on the collimators used and can exceed that of PET.

Magnified projection images of gamma ray sources can be obtained when pinhole collimators (**Figure 2**) are used, with the magnification depending on pinhole-detector and pinhole-object distances and the resolution depending on pinhole diameters and detector resolutions. High system resolutions can be achieved this way even with detector resolutions in the range of a few millimeters. In principle, microscopic resolutions could be achieved [34], the main limiting factor being the decreasing sensitivity with decreasing pinhole diameter. The system's sensitivity increases with increasing number of pinholes for a given field of view, the maximum number of pinholes depending on the geometries of pinhole and detector arrangements. Current commercially available small-animal SPECT scanners make use of this multi-pinhole technology ([35]; for reviews on small-animal SPECT, see also [36, 37]; **Figure 3**). Spatial resolutions down to ca. 250 μm have been reported for *in vivo* imaging [39].

These spatial resolutions cannot be achieved in PET imaging of conventional positron emitters in brain tissue. In clinical routine and in most preclinical scanners, PET imaging is based on coincidence detection of two 511 keV-photons emitted in nearly opposite directions from positron-electron annihilation sites (but see Walker et al. [40] for a preclinical PET scanner with pinhole collimation). Positrons have to lose most of their kinetic energy before an annihilation event is possible. Annihilation events occur at certain distances from the positron emitting radionuclide or tracer molecules labeled with the radionuclide, a factor limiting the spatial resolution of PET, irrespective of the way the emitted photons are detected. The mean distances between the sites of positron emissions and the sites of annihilations, the so-called positron ranges, depend on the kinetic energies at which positrons are emitted and the probabilities with which the emitted positrons can interact with their environment. On average, positron ranges decrease with increasing tissue density. Positrons emitted from $^{18}$F have a favorably low maximum energy of 0.634 MeV [41], and it seems possible to detect this radionuclide in mouse brain at a spatial resolution close to 600 $\mu$m [42]. For comparison, $^{15}$O emits positrons at a maximum energy of 1.732 MeV, resulting in a mean positron range of three millimeters in water [41]. While detection of photons from annihilations rather than detection of photons emitted from radionuclide atoms limits the spatial resolution of PET, there is at the same time a substantial gain in sensitivity when coincidence detection is used, as no collimators are necessary for imaging radionuclide distributions.

In preclinical practice, the spatial resolution advantage of SPECT vs. the sensitivity advantage of PET may in many cases be of minor relevance: Newest-generation small-animal PET scanners approach the fundamental limit in spatial resolution for $^{18}$F, which is similar to the resolutions in many routine measurements with small-animal SPECT. On the other hand, SPECT imaging at a resolution of about 700 $\mu$m is possible with doses that are well within nano- to picomolar ranges. 100 MBq $^{99m}$Tc corresponds to ca. 5 pmol (see [43] for details of calculations). With about 1.5 MBq of this amount reaching the mouse brain in a typical CBF imaging experiment [22, 44], this would correspond to ca. 0.075 pmol/0.5 cm$^3$ brain tissue corresponding to a concentration of 150 pmol/L (assuming 1 cm$^3$ = 1 mL). For estimating pharmacological or toxicological effects, it has to be taken into account that HMPAO labeled with $^{99}$Tc, the decay product of $^{99m}$Tc, also enters the brain. However, even with amounts of $^{99}$Tc-HMPAO exceeding those of $^{99m}$Tc-HMPAO by an order of magnitude, the total concentration of labeled HMPAO would still be outside of the range of pharmacological effects.

In general, the ratio of radioactively labeled tracers vs. tracers labeled with decay products is higher with $^{99m}$Tc-labeled compounds than with PET tracers because of the longer half-life of $^{99m}$Tc and delivery of the radionuclide from $^{99m}$Tc generators at high specific activities, i.e., high amounts of radioactive atoms per total number or mass of the atoms. With activities of $^{99m}$Tc of 1 GBq delivered in a few hundred microliters of physiological saline solution, volume loads usually are also within limits of good practice for i.v. injections in rodents.

Radionuclide contents can be quantified quite accurately in SPECT and PET imaging if the data sets are corrected for the various factors that affect how many of the emitted photons can finally be counted and selected for 3D image reconstructions, e.g., collimator effects in SPECT, random coincidences in PET, and effects of absorption and scattering in the imaged subjects [45]. Underestimations of the true activities due to gamma ray attenuation in the subjects can be more severe in PET than in SPECT imaging despite the higher photon energies in PET, because a true coincidence event is missing if only one of the two annihilation photons does not reach the detector in a line of response [45]. Without attenuation correction, radionuclide contents would be underestimated in small-animal PET imaging by about 40% in rats [46] and 20% in mice [47]. In small-animal SPECT imaging, the combined effects of scattering and absorption can result in underestimations of true activities by about 12% in mice [48, 49] and 23% in rats [50] when using the radionuclide $^{99m}$Tc. Attenuation correction is computationally simpler in PET imaging [45, 51], but algorithms have been developed that reduce the errors in small-animal SPECT imaging to $<5\%$ [50]. It can be expected that the accuracy will increase further when corrections will be based on calculations of attenuation coefficients from X-ray CT scans or more indirectly from MR images of the same individual, as increasingly done in humans [51]. Finally, when using SPECT for functional neuroimaging in rodents, the focus is on comparing differences in radionuclide distributions in brains from animals of different experimental groups. Due to little variations in brain and skull anatomy, absorption and scattering will also differ little within and between the groups. This tends to reduce attenuation effects in voxel-wise statistical comparisons.

The radionuclide doses given per body weight are generally higher in small-animal imaging as compared with human imaging [52], resulting in higher radiation exposures. Data for $^{99m}$Tc-HMPAO in rats [19] and calculations for other $^{99m}$Tc-compounds in mice and rats [52] indicate that whole-body radiation doses in CBF SPECT at commonly used $^{99m}$Tc doses, e.g., 100 MBq in mice, can be estimated to be in the lower to mid centigray range, which is well within usual dose ranges in small-animal PET and SPECT imaging [52].

The choice between PET and SPECT in preclinical imaging may frequently depend on scanner availabilities and suitable tracers for the questions to be studied. The logistics of small-animal SPECT are simpler due to the relatively long half-lives of the radionuclides used. An interesting opportunity in SPECT imaging is dual-isotope SPECT [36, 37]. Two or more tracers can be detected simultaneously if they emit gamma or X-ray photons at energies sufficiently different for being resolved with the detectors used. In principle, images of CBF under two different conditions in the same animal could be obtained by sequentially injecting the two tracers $^{99m}$Tc-HMPAO and $^{123}$I-IMP in one session. Because of potential redistributions of $^{123}$I-IMP, the feasibility of this approach for *in vivo* imaging is currently unclear, but it could be of interest for high-resolution *ex vivo* imaging.

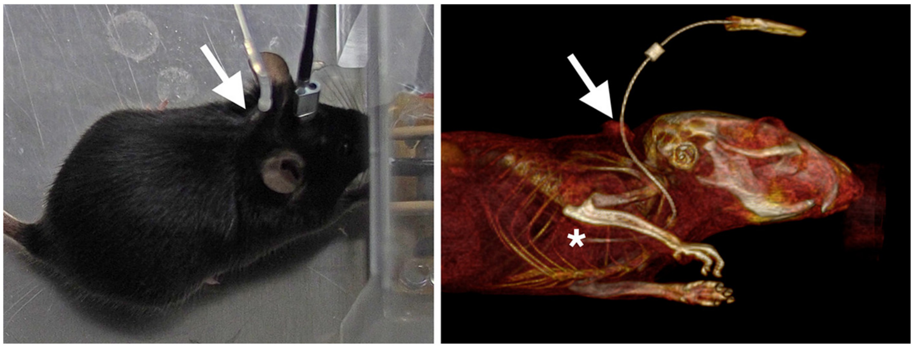

**FIGURE 4 |** Images of mice implanted with chronic external jugular vein catheters. The image on the left shows a mouse during optogenetic stimulation, the image on the right a volume-rendered CT from a mouse that was injected with an X-ray-dense contrast agent during CT acquisition. The arrows point to the dorsal exit of the catheter. The subcutaneous part of the tunneled catheter can be seen in the CT. The tip of the catheter (asterisk) is at or close to the right atrium.

## FUNCTIONAL NEUROIMAGING IN RODENTS USING $^{99m}$Tc-HMPAO SPECT—THE EXPERIMENTAL PROCEDURE

SPECT imaging of cerebral blood flow in rodents dates back to experiments in the 1990s in rats [53, 54]. High-resolution images of cerebral blood flow in mice were demonstrated much later with a multi-pinhole system in 2009 [55].

These experiments were done to demonstrate the spatial resolution of imaging systems using pinhole collimators. $^{99m}$Tc-HMPAO was intravenously injected via the tail vein—the common approach of i.v. injections in rodents. The highly lipophilic compound is rapidly cleared from the plasma. Andersen et al. [56] found a high first-pass extraction of about 80% in rats. The images obtained after a tail vein bolus injection thus mostly represent the mean CBF during the short time span during and shortly after tail vein injection.

In order to make use of the approach for mapping stimulus-dependent changes in blood flow, the tracer has to be injected during the stimulation period. To the best of our knowledge, the first study using a dedicated small-animal SPECT scanner for imaging brain activation patterns was performed by Wyckhuys et al. [57] in restrained rats.

For the method to be used for repeated imaging of unrestrained behaving animals, we developed an approach for continuously injecting the tracer during ongoing behavior via catheters in the right external jugular vein. External jugular vein catheterization is a well-established approach for chronic intravenous injections or blood sampling in rodents (for instance [58–67]). From our experience, the complexity of the approach is frequently overestimated. In experienced hands, the surgery takes about 30 min. The catheters are subcutaneously tunneled and exit shortly behind the scapulae (**Figure 4**). For i.v. injections, the catheters are connected to perfusion pumps via polyethylene tubes with little interference with ongoing behavior. We used this approach in a number of studies including different learning paradigms [68, 69].

We have developed a protocol for simple, inexpensive on-site synthesis of $^{99m}$Tc-HMPAO close to the behavioral setup [44]. $^{99m}$Tc is a so-called generator radionuclide [33]. It is a decay product of $^{99}$Mo-molybdenum, a radionuclide with a half-life of 66 hours. $^{99}$Mo can conveniently be transported over long distances to hospitals for on-site delivery of $^{99m}$Tc. $^{99m}$Tc generators contain the divalent molybdate anion $^{99}MoO4^{2-}$, from which the monovalent pertechnetate anion $^{99m}TcO4^{-}$ forms when $^{99}$Mo decays. The change in valency facilitates separating $^{99m}TcO4^{-}$ from $^{99}MoO4^{2-}$ by elution with NaCl solutions. $^{99m}$Tc generators are present in practically every department of nuclear medicine. The logistics of supplying a small-animal SPECT lab with $^{99m}$Tc are very simple.

For synthesis of $^{99m}$Tc-HMPAO, the solution of $^{99m}TcO4^{-}$ in saline is added to the organic compound exametazime (HMPAO) in the presence of the reducing agent $Sn(II)Cl_2$. HMPAO and $Sn(II)Cl_2$ are commercially available as kit preparations delivered as a lyophilized mixture under nitrogen in amounts for use in humans. For use in rodents, we store aliquots of such a kit preparation frozen in saline solutions. Upon use, we add freshly prepared $Sn(II)Cl_2$ solution in order to compensate for potential losses due to oxidation during storage [44]. $^{99m}$Tc-HMPAO synthesis from kits or stored aliquots takes a few minutes.

We inject the tracer during ongoing behavior over a period, in most experiments, of about five to 10 min. After injection, animals are anesthetized and scanned (for a scheme of the workflow, see **Figure 5**). We use co-registered CT scans as anatomical references. In most studies, we repeatedly image the same animals under different behavioral conditions. We use intervals between the measurements of 2 days. For data analysis, we align the SPECT/CTs to reference MRs and calculate parametric voxel-wise statistical maps from global mean normalized data of brain $^{99m}$Tc content.

In humans, arterial input functions can be determined and cerebral blood flow or glucose metabolism can be fully quantified

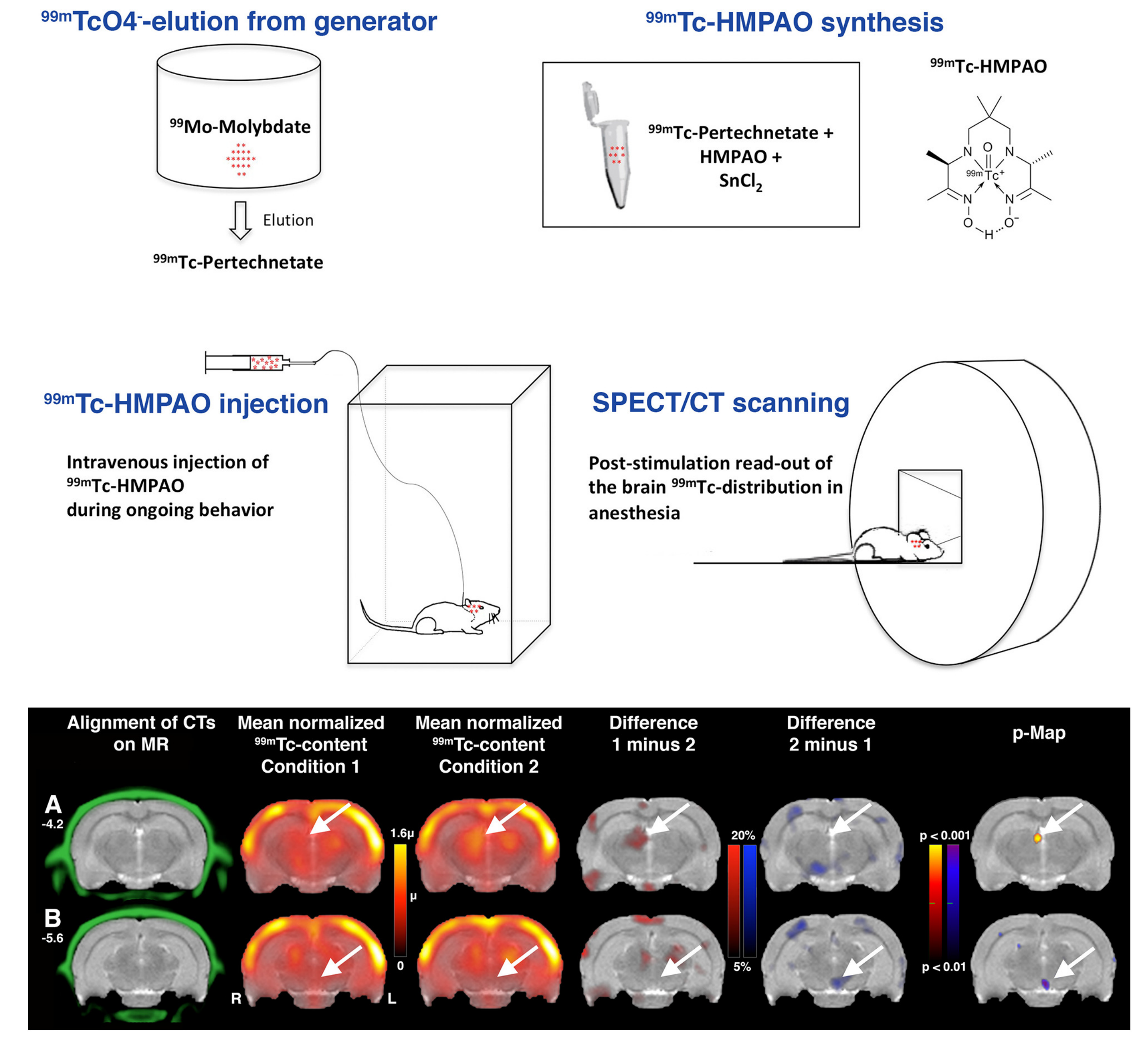


**FIGURE 5 |** Workflow in functional neuroimaging using $^{99m}$Tc-HMPAO SPECT. After elution of $^{99m}$Tc-pertechnetate from the $^{99m}$Tc generator, $^{99m}$Tc-HMPAO can be synthesized on-site in the small-animal SPECT lab. Rodents are intravenously injected with the tracer during ongoing behavior. For SPECT scanning of the distribution of the trapped tracer, the animals are anesthetized. Data analysis starts with aligning of the SPECT data sets to reference MRs or atlases by using the landmarks of the co-registered CT. Here, previously unpublished images from data of a subgroup of rats from the study of innate fear behavior in Vincenz et al. [70] are shown to illustrate the data analysis. Sections at two different Bregma levels are shown (**A** Bregma −4.2; **B** Bregma −5.6). The color scale on the left is in units of the global mean intensity. Arrows point to the habenula and interpeduncular nucleus where significant increases or decreases, resp., in flow were found.

with PET imaging. In rodents, and in particular in mice, arterial blood sampling is difficult and impractical in behaving animals. Therefore, intensity normalization is the standard approach to comparing individual and group data in functional small-animal radionuclide imaging [71, 72]. Especially when used for imaging normal behaving animals, where global metabolic rates and blood flow can be assumed to vary only within narrow limits, the effects of the normalization can be expected to be minor.

## CBF SPECT IN THE CONTEXT OF TECHNIQUES FOR IMAGING BRAIN-WIDE ACTIVATION PATTERNS IN AWAKE BEHAVING RODENTS

We have reviewed above the rationales underlying functional neuroimaging using CBF SPECT in rodents and outlined the experimental procedure that we developed in our lab. We have used this approach in a number of different studies including artificial stimulations—electrical as well as optogenetic [44, 73, 74]—pharmacological manipulations [75], studies of baseline metabolism under physiological or pathological conditions [76], or changes in activation patterns due to sensory stimuli in conjunction with [68] or without [70, 77] learning paradigms. Our findings matched well with data from other groups using other methods as far as such data were available. The involvement of the habenulo-interpeduncular system in innate fear behavior [70], for instance, or of the supramammillary nucleus in food reward [75] as described in our SPECT studies has also been found with optogenetic or electrophysiological methods, resp. [78–80].

The scope of most of our studies was on screening for brain-wide activation patterns in behaving rodents. Many of these studies would have been very difficult or impossible to perform with BOLD fMRI, especially those that require active locomotor behaviors as the intracranial self-stimulation studies or studies with complex learning paradigms [68].

Some of the studies might have been performed with $^{18}$F-FDG PET. In fact, the scopes of applications of $^{18}$F-FDG PET (see, for instance, [71, 72, 81–83]) and $^{99m}$Tc-HMPAO SPECT are very similar. As mentioned above, both methods provide static images of spatial patterns of neural activity averaged or integrated resp. over certain periods of time. However, due to differences in tracer kinetics, the integration times differ considerably between the two methods.

As studied in detail by Sokoloff et al. when they introduced the autoradiographic technique for mapping cerebral glucose metabolism using 2-deoxyglucose (2-DG) labeled with $^{14}$C, it takes about 30–45 min until, after a single bolus injection, sufficient amounts of the tracer are trapped in the brain [84]. 2-DG can enter and leave the brain via facilitated diffusion through glucose transporters in the BBB. The brain regional 2-DG distribution shortly after injection reflects spatial patterns of 2-DG influx in relation to blood flow. In a relatively slow process, 2-DG is phosphorylated to 2-DG-6-phosphate, which is trapped intracellularly and does not redistribute. Images taken earlier than about 30 min reflect to varying degrees the influx, efflux, and phosphorylation of 2-DG. In order to image with $^{18}$F-FDG PET a tracer distribution that solely or at least largely reflects tracer uptake and phosphorylation in the unrestrained awake state outside the scanner and that remains stable during subsequent image acquisition under anesthesia inside the scanner, animals cannot be imaged much earlier than about 30 min after $^{18}$F-FDG injection.

On the other hand, the long uptake and phosphorylation times of $^{18}$F-FDG make it possible to inject a single tracer dose i.v. or i.p. before the behavioral experiment starts. Repeated imaging of the same individual over long time periods such as weeks or months is easier with $^{18}$F-FDG because there is no need for implanting intravenous catheters.

In contrast to $^{18}$F-FDG, $^{99m}$Tc-HMPAO is rapidly cleared from the plasma and rapidly trapped in the brain. We mentioned above the high first-pass extraction of about 80% [56]. In humans, count rates in the brain reach maximum values 30–40 s after injection, then decrease slightly to 91% and remain constant 2 min after injection [85]. The 40-s period until the net uptake of $^{99m}$Tc-HMPAO ceases can be seen as the maximum temporal resolution that might theoretically be achieved when using CBF SPECT for assessing the spatial patterns of neural activity in unrestrained animals outside scanner environments, the limiting factor in practice being the volume load if the dose necessary for imaging at high resolution and high signal-to-noise ratio should be injected in one single bolus. In our routine protocols, we use time spans of several minutes over which $^{99m}$Tc-HMPAO is injected. The time spans might be adjusted to the behavioral paradigms under study.

Among the different tracer techniques for *in vivo* imaging of brain-wide activation patterns in rodents, the highest spatial resolution can be achieved with MEMRI [86], but without opening the BBB, manganese reaches detectable levels only slowly. The long stimulation times on the order of several hours limit the scope of applications.

The static images that are usually acquired with all of these tracer techniques provide insight into temporal dynamics only insofar as the temporal dynamics might affect the average spatial patterns of network activities. In theory, nuclear imaging techniques are well-suited for imaging temporal dynamics. Motion-correction algorithms have been used to obtain images of awake behaving animals inside scanners [87–89], and miniaturized, wearable PET scanners for brain imaging in behaving rats have been developed [90]. The methods can be of high value for imaging tracers that are not trapped and the distribution of which might change under anesthesia as compared with that in the awake state, e.g., neurotransmitter receptor ligands. Imaging at both high spatial resolutions and short acquisition times in the range of seconds or lower would require high sensitivities and/or high radionuclide doses and might be challenging. It remains to be seen whether approaches for 4D functional neuroimaging in awake behaving rodents, based on imaging, e.g., CBF, CBV, or displacement of receptor ligands, might emerge from nuclear imaging techniques and what spatial and temporal resolutions these could provide.

Four-dimensional whole-brain imaging of spatiotemporal patterns of neural activity in behaving rodents is possible with ultrasound imaging of changes in CBV [91]. As a major drawback compared to fMRI, PET, and SPECT, animals have to undergo skull surgery in order to enable ultrasound imaging. Measurements have been performed through the thinned skull in rats [92], ultrasound-clear skull prostheses [93], or large cranial windows in head-fixed mice [94]. In the latter study [94], high spatial resolutions of about 100 $\mu$m in-plane and 300 $\mu$m off-plane have been obtained, but relatively long imaging times were used ranging from 14 min to several hours.

In the context of the array of *in vivo* whole-brain functional neuroimaging techniques, we see the attractiveness of functional CBF SPECT imaging in the combination of minimal invasiveness with relatively high spatial resolution and simple logistics.

The temporal resolution might be improved with stimulus-triggered short bolus injections of $^{99m}$Tc-HMPAO, but it certainly cannot compete with that of BOLD fMRI. When effects of anesthesia or restraints can be tolerated or expected to be minor, BOLD fMRI is certainly the method of choice.

From the underlying physics, the spatial resolution of $^{99m}$Tc-HMPAO SPECT could be further increased, the limiting factor in practice being the limited sensitivity that, to our experience, can make imaging well-beyond the range of about 500 μm difficult for routine use, as it requires injections of large doses or volumes resp. and/or long scan times. It remains to be seen whether technical improvements could increase the sensitivity in small-animal SPECT imaging.

Despite the variety of new methods for *in vivo* imaging of neural activity, there are still only three approaches to non-invasively—in particular without the need for head surgery—obtain images of brain-wide patterns of neural activity in awake unrestrained rodents, $^{18}$F-FDG PET, MEMRI, and $^{99m}$Tc-HMPAO SPECT. Currently, the vast majority of studies aiming at elucidating brain-wide patterns of neural activity in rodents are done by post-mortem readout of the patterns of immediate early genes (IEGs) expressed in an activity-dependent manner *in vivo* [95]. IEG expression patterns can be mapped with cellular resolution, but data acquisition and analysis are time consuming. Similar to tracer techniques, IEG mapping studies provide little information on temporal dynamics on timescales of neuronal signal-processing rates, but the decades of its use demonstrate at the same time the value of this spatial information for elucidating network activation patterns.

Within this array of methods for imaging brain-wide spatial patterns of neural activity in unrestrained rodents, $^{99m}$Tc-HMPAO SPECT is, in our opinion, a highly attractive technique. When aiming at regional spatial resolutions, it provides 3D data sets of functional brain activations at substantially higher throughput than IEG-mapping approaches, and stimulation times in the minute range make the method less sensitive to the effects of behavioral habituation than $^{18}$F-FDG PET and MEMRI.

## ETHICS STATEMENT

All experiments were conducted according to the guidelines of the European Community (Directive 2010/63/EU) and approved by a local ethics committee of the Federal state of Saxony-Anhalt.

## AUTHOR CONTRIBUTIONS

JG and AO conceived the review and wrote the manuscript.

## FUNDING

This work was supported by the German Federal Ministry of Education and Science (BMBF grants 01SF0718 and 03 V0765) and the Deutsche Forschungsgemeinschaft (SFB 779). The publication of this article was funded by the Open Access Fund of the Leibniz Association.

## ACKNOWLEDGMENTS

The authors wish to thank Frank Angenstein for providing the MR image in Figure 3D.

## REFERENCES

1. Venkatachalam V, Ji N, Wang X, Clark C, Mitchell JK, Klein M, et al. Pan-neuronal imaging in roaming *Caenorhabditis elegans. Proc Natl Acad Sci USA*. (2016) **113**:E1082–8. doi: 10.1073/pnas.1507109113
2. Vanwalleghem GC, Ahrens MB, Scott EK. Integrative whole-brain neuroscience in larval zebrafish. *Curr Opin Neurobiol.* (2018) **50**:136–45. doi: 10.1016/j.conb.2018.02.004
3. Vetere G, Kenney JW, Tran LM, Xia F, Steadman PE, Parkinson J, et al. Chemogenetic interrogation of a brain-wide fear memory network in mice. *Neuron.* (2017) **94**:363–74.e4. doi: 10.1016/j.neuron.2017.03.037
4. Herculano-Houzel S, Mota B, Lent R. Cellular scaling rules for rodent brains. *Proc Natl Acad Sci USA.* (2006) **103**:12138–43. doi: 10.1073/pnas.0604911103
5. Kety SS, Schmidt CF. The nitrous oxide method for the quantitative determination of cerebral blood flow in man: theory, procedure and normal values. *J Clin Invest.* (1948) **27**:476–83. doi: 10.1172/JCI101994
6. Kety SS. The measurement of cerebral blood flow by means of inert diffusible tracers. *Keio J Med.* (1994) **43**:9–14. doi: 10.2302/kjm.43.9
7. Landau WM, Freygang WH Jr, Roland LP, Sokoloff L, Kety SS. The local circulation of the living brain; values in the unanesthetized and anesthetized cat. in: *80th Meeting Trans Am Neurol Assoc.* (1955) 125–9.
8. Sokoloff L. Local cerebral circulation at rest and during altered cerebral activity induced by anesthesia or visual stimulation. In: SS Kety, J Elkes, editors. *The Regional Chemistry, Physiology and Pharmacology of the Nervous System* Oxford: Pergamon Press (1961). p. 107–17.
9. Sokoloff L. Preface to volume 1. In: Squire LR, editor. *The History of Neuroscience in Autobiography.* Washington, DC: Library of Congress Catalog Card Number 96-709501996 (2005). p. 454–97.
10. Raichle ME. Behind the scenes of functional brain imaging: a historical and physiological perspective. *Proc Natl Acad Sci USA.* (1998) **95**:765–72. doi: 10.1073/pnas.95.3.765
11. Lassen NA, Ingvar DH, Skinhoj E. Brain function and blood flow. *Sci Am.* (1978) **239**:62–71. doi: 10.1038/scientificamerican1078-62
12. Roland PE, Larsen B. Focal increase of cerebral blood flow during stereognostic testing in man. *Arch Neurol.* (1976) 33:551–8. doi: 10.1001/archneur.1976.00500080029005
13. Fox PT, Mintun MA, Raichle ME, Miezin FM, Allman JM, Van Essen DC. Mapping human visual cortex with positron emission tomography. *Nature.* (1986) **323**:806–9. doi: 10.1038/323806a0
14. Herscovitch P, Markham J, Raichle ME. Brain blood flow measured with intravenous H2O. I. Theory and error analysis. *J Nucl Med.* (1983) **24**:782–9.
15. Raichle ME, Martin WR, Herscovitch P, Mintun MA, Markham J. Brain blood flow measured with intravenous $H_2O$. II. Implementation and validation. *J Nucl Med.* (1983) **24**:790–8.
16. Iadecola C. The neurovascular unit coming of age: a journey through neurovascular coupling in health and disease. *Neuron.* (2017) **96**:17–42. doi: 10.1016/j.neuron.2017.07.030
17. Fox PT, Raichle ME. Stimulus rate dependence of regional cerebral blood flow in human striate cortex, demonstrated by positron emission tomography. *J Neurophysiol.* (1984) **51**:1109–20. doi: 10.1152/jn.1984.51.5.1109
18. Holschneider DP, Maarek JM. Mapping brain function in freely moving subjects. *Neurosci Biobehav Rev.* (2004) **28**:449–61. doi: 10.1016/j.neubiorev.2004.06.007
19. Neirinckx RD, Canning LR, Piper IM, Nowotnik DP, Pickett RD, Holmes RA, et al. Technetium-99m d,l-HM-PAO: a new radiopharmaceutical for SPECT imaging of regional cerebral blood perfusion. *J Nucl Med.* (1987) **28**:191–202.
20. Neirinckx RD, Burke JF, Harrison RC, Forster AM, Andersen AR, Lassen NA. The retention mechanism of technetium-99m-HM-PAO: intracellular reaction with glutathione. *J Cereb Blood Flow Metab.* (1988) **8**:S4–12. doi: 10.1038/jcbfm.1988.27

21. Zerarka S, Pellerin L, Slosman D, Magistretti PJ. Astrocytes as a predominant cellular site of (99m)Tc-HMPAO retention. *J Cereb Blood Flow Metab.* (2001) **21**:456–68. doi: 10.1097/00004647-200104000-00014
22. Apostolova I, Wunder A, Dirnagl U, Michel R, Stemmer N, Lukas M, et al. Brain perfusion SPECT in the mouse: normal pattern according to gender and age. *Neuroimage.* (2012) **63**:1807–17. doi: 10.1016/j.neuroimage.2012.08.038
23. Inoue Y, Momose T, Ohtake T, Nishikawa J, Sasaki Y, Waritani T, et al. Metabolism of technetium-99m-L,L-ethyl cysteinate dimer in rat and cynomolgus monkey tissue. *J Nucl Med.* (1997) **38**:1731–7.
24. Kikuchi T, Okamura T, Wakizaka H, Okada M, Odaka K, Yui J, et al. OAT3-mediated extrusion of the 99mTc-ECD metabolite in the mouse brain. *J Cereb Blood Flow Metab.* (2014) **34**:585–8. doi: 10.1038/jcbfm.2014.20
25. Creutzig H, Schober O, Gielow P, Friedrich R, Becker H, Dietz H, et al. Cerebral dynamics of N-isopropyl-(123I)p-iodoamphetamine. *J Nucl Med.* (1986) **27**:178–83.
26. Yonekura Y, Nishizawa S, Mukai T, Iwasaki Y, Fukuyama H, Ishikawa M, et al. Functional mapping of flow and back-diffusion rate of N-isopropyl-p-iodoamphetamine in human brain. *J Nucl Med.* (1993) **34**:839–44.
27. Zeniya T, Watabe H, Hayashi T, Ose T, Myojin K, Taguchi A, et al. Three-dimensional quantitation of regional cerebral blood flow in mice using a high-resolution pinhole SPECT system and 123I-iodoamphetamine. *Nucl Med Biol.* (2011) **38**:1157–64. doi: 10.1016/j.nucmedbio.2011.04.007
28. Anger HO. Use of a Gamma-Ray Pinhole Camera for *in vivo* Studies. *Nature.* (1952) **170**:200–1. doi: 10.1038/170200b0
29. Anger HO. Scintillation Camera. *Rev Sci Instr.* (1958) **29**:27–33. doi: 10.1063/1.1715998
30. Van Audenhaege K, Van Holen R, Vandenberghe S, Vanhove C, Metzler SD, Moore SC. Review of SPECT collimator selection, optimization, and fabrication for clinical and preclinical imaging. *Med Phys.* (2015) **42**:4796–813. doi: 10.1118/1.4927061
31. Hutton BF. The origins of SPECT and SPECT/CT. *Eur J Nucl Med Mol Imaging.* (2014) **41**(Suppl. 1):S3–16. doi: 10.1007/s00259-013-2606-5
32. Kuhl DE, Edwards RQ. Image separation radioisotope scanning. *Radiology.* (1963) **80**:653–62. doi: 10.1148/80.4.653
33. Eckelman WC. Unparalleled contribution of technetium-99m to medicine over 5 decades. *JACC Cardiovasc Imaging.* (2009) **2**:364–8. doi: 10.1016/j.jcmg.2008.12.013
34. Beekman F, van der Have F. The pinhole: gateway to ultra-high-resolution three-dimensional radionuclide imaging. *Eur J Nucl Med Mol Imaging.* (2007) **34**:151–61. doi: 10.1007/s00259-006-0248-6
35. Deleye S, Van Holen R, Verhaeghe J, Vandenberghe S, Stroobants S, Staelens S. Performance evaluation of small-animal multipinhole muSPECT scanners for mouse imaging. *Eur J Nucl Med Mol Imaging.* (2013) **40**:744–58. doi: 10.1007/s00259-012-2326-2
36. Bernsen MR, Vaissier PE, Van Holen R, Booij J, Beekman FJ, de Jong M. The role of preclinical SPECT in oncological and neurological research in combination with either CT or MRI. *Eur J Nucl Med Mol Imaging.* (2014) **41**(Suppl. 1):S36–49. doi: 10.1007/s00259-013-2685-3
37. Franc BL, Acton PD, Mari C, Hasegawa BH. Small-animal SPECT and SPECT/CT: important tools for preclinical investigation. *J Nucl Med.* (2008) **49**:1651–63. doi: 10.2967/jnumed.108.055442
38. Ma Y, Hof PR, Grant SC, Blackband SJ, Bennett R, Slatest L, et al. A three-dimensional digital atlas database of the adult C57BL/6J mouse brain by magnetic resonance microscopy. *Neuroscience.* (2005) **135**:1203–15. doi: 10.1016/j.neuroscience.2005.07.014
39. Ivashchenko O, van der Have F, Villena JL, Groen HC, Ramakers RM, Weinans HH, et al. Quarter-millimeter-resolution molecular mouse imaging with U-SPECT(+). *Mol Imaging.* (2014) **13**:1–8. doi: 10.2310/7290.2014.00053
40. Walker MD, Goorden MC, Dinelle K, Ramakers RM, Blinder S, Shirmohammad M, et al. Performance assessment of a preclinical PET scanner with pinhole collimation by comparison to a coincidence-based small-animal PET scanner. *J Nucl Med.* (2014) **55**:1368–74. doi: 10.2967/jnumed.113.136663
41. Conti M, Eriksson L. Physics of pure and non-pure positron emitters for PET: a review and a discussion. *EJNMMI Phys.* (2016) **3**:8. doi: 10.1186/s40658-016-0144-5
42. Yang Y, Bec J, Zhou J, Zhang M, Judenhofer MS, Bai X, et al. A prototype high-resolution small-animal PET scanner dedicated to mouse brain imaging. *J Nucl Med.* (2016) **57**:1130–5. doi: 10.2967/jnumed.115.165886
43. Zolle I. Performance and Quality Control of the 99Mo/99mTc Generator. In: Zolle I, editor. *Technetium-99m Pharmaceuticals, Preparation and Quality Control in Nuclear Medicine*. 1 ed. Berlin; Heidelberg: Springer-Verlag (2007). p. 345.
44. Kolodziej A, Lippert M, Angenstein F, Neubert J, Pethe A, Grosser OS, et al. SPECT-imaging of activity-dependent changes in regional cerebral blood flow induced by electrical and optogenetic self-stimulation in mice. *Neuroimage.* (2014) **103**:171–80. doi: 10.1016/j.neuroimage.2014.09.023
45. Bushberg JT, Seibert JA, Boone JM, Leidholdt EM. *The Essential Physics of Medical Imaging.* 3rd ed. Philadelphia, PA: Wolters Kluwer Health/Lippincott Williams & Wilkins (2012) p. 705–47.
46. D'Ambrosio D, Zagni F, Spinelli AE, Marengo M. Attenuation correction for small animal PET images: a comparison of two methods. *Comput Math Methods Med.* (2013) **2013**:103476. doi: 10.1155/2013/103476
47. El Ali HH, Bodholdt RP, Jorgensen JT, Myschetzky R, Kjaer A. Importance of Attenuation Correction (AC) for small animal pet imaging. *Diagnostics.* (2012) **2**:42–51. doi: 10.3390/diagnostics2040042
48. Austin DW, Feng B, Mintzer RA, Chen M, Gregor J, Stuckey A, et al. Validation of CT-based attenuation correction for multi-pinhole PSF reconstruction for small-animal SPECT. In: *IEEE Nuclear Science Symposium Conference Record Nuclear Science Symposium.* Knoxville, TN (2010). p. 3339–42. doi: 10.1109/NSSMIC.2010.5874423
49. Finucane CM, Murray I, Sosabowski JK, Foster JM, Mather SJ. Quantitative accuracy of low-count SPECT imaging in phantom and *in vivo* mouse studies. *Int J Mol Imaging.* (2011) **2011**:197381. doi: 10.1155/2011/197381
50. Gerdekoohi SK, Vosoughi N, Tanha K, Assadi M, Ghafarian P, Rahmim A, et al. Implementation of absolute quantification in small-animal SPECT imaging: phantom and animal studies. *J Appl Clin Med Phys.* (2017) **18**:215–23. doi: 10.1002/acm2.12094
51. Lee TC, Alessio AM, Miyaoka RM, Kinahan PE. Morphology supporting function: attenuation correction for SPECT/CT, PET/CT, and PET/MR imaging. *Q J Nucl Med Mol Imaging.* (2016) **60**:25–39.
52. Funk T. Sun M, Hasegawa BH. Radiation dose estimate in small animal SPECT and PET. *Med Phys.* (2004) **31**:2680–6. doi: 10.1118/1.1781553
53. Ishizu K, Mukai T, Yonekura Y, Pagani M, Fujita T, Magata Y, et al. Ultra-high resolution SPECT system using four pinhole collimators for small animal Studies. *J Nuclear Med.* (1995) **36**:2282–7.
54. Weber DA, Ivanovic M, Franceschi D, Strand SE, Erlandsson K, Franceschi M, et al. Pinhole SPECT: an approach to *in vivo* high resolution SPECT imaging in small laboratory animals. *J Nucl Med.* (1994) **35**:342–8.
55. Pissarek M, Meyer-Kirchrath J, Hohlfeld T, Vollmar S, Oros-Peusquens AM, Flogel U, et al. Targeting murine heart and brain: visualisation conditions for multi-pinhole SPECT with (99m)Tc- and (123)I-labelled probes. *Eur J Nucl Med Mol Imaging.* (2009) **36**:1495–509. doi: 10.1007/s00259-009-1142-9
56. Andersen AR, Friberg H, Knudsen KB, Barry DI, Paulson OB, Schmidt JF, et al. Extraction of [99mTc]-d,l-HM-PAO across the blood-brain barrier. *J Cereb Blood Flow Metab.* (1988) **8**:S44–51. doi: 10.1038/jcbfm.1988.32
57. Wyckhuys T, Staelens S, Van Nieuwenhuyse B, Deleye S, Hallez H, Vonck K, et al. Hippocampal deep brain stimulation induces decreased rCBF in the hippocampal formation of the rat. *Neuroimage.* (2010) **52**:55–61. doi: 10.1016/j.neuroimage.2010.04.017
58. Bardelmeijer HA, Buckle T, Ouwehand M, Beijnen JH, Schellens JH, van Tellingen O. Cannulation of the jugular vein in mice: a method for serial withdrawal of blood samples. *Lab Anim.* (2003) **37**:181–7. doi: 10.1258/002367703766453010
59. De Luca T, Szilagyi KL, Hargreaves KA, Collins KS, Benson EA. Improving the patency of jugular vein catheters in Sprague-Dawley rats by using an antiseptic nitrocellulose coating. *J Am Assoc Lab Anim Sci.* (2018) **57**:520–8. doi: 10.30802/AALAS-JAALAS-18-000017
60. Feng J, Fitz Y, Li Y, Fernandez M, Cortes Puch I, Wang D, et al. Catheterization of the carotid artery and jugular vein to perform hemodynamic measures, infusions and blood sampling in a conscious rat model. *J Vis Exp.* (2015) **2015**:51881. doi: 10.3791/51881
61. Gaud N, Kumar A, Matta M, Kole P, Sridhar S, Mandlekar S, et al. Single jugular vein cannulated rats may not be suitable for intravenous

pharmacokinetic screening of high logP compounds. *Eur J Pharm Sci.* (2017) **99**:272–8. doi: 10.1016/j.ejps.2016.12.025

62. Park AY, Plotsky PM, Pham TD, Pacak K, Wynne BM, Wall SM, et al. Blood collection in unstressed, conscious, and freely moving mice through implantation of catheters in the jugular vein: a new simplified protocol. *Physiol Rep.* (2018) **6**:e13904. doi: 10.14814/phy2.13904
63. Thrivikraman KV, Huot RL, Plotsky PM. Jugular vein catheterization for repeated blood sampling in the unrestrained conscious rat. *Brain Res Brain Res Protoc.* (2002) **10**:84–94. doi: 10.1016/S1385-299X(02)00185-X
64. Onishi S, Kaji T, Machigashira S, Yamada W, Masuya R, Nakame K, et al. The effect of intravenous lipid emulsions and mucosal adaptation following massive bowel resection. *J Pediatr Surg.* (2018) **53**:2444–8. doi: 10.1016/j.jpedsurg.2018.08.019
65. Wang T, Liu C, Wei P, Lv L, Yang Z. The inhibiting effect of intravenous anesthesia on adrenal gland functions under the sepsis condition. *Int J Immunopathol Pharmacol.* (2017) **30**:188–93. doi: 10.1177/0394632017705049
66. Yamada W, Kaji T, Onishi S, Nakame K, Yamada K, Kawano T, et al. Ghrelin improves intestinal mucosal atrophy during parenteral nutrition: an experimental study. *J Pediatr Surg.* (2016) **51**:2039–43. doi: 10.1016/j.jpedsurg.2016.09.035
67. Zhang Y, Li RM, Wang C, Liu N, Lv S, Xiong JY. Etomidate inhibits nuclear factor-kappaB through decreased expression of glucocorticoid receptor in septic rats. *Mol Med Rep.* (2016) **14**:5760–6. doi: 10.3892/mmr.2016.5947
68. Bhattacharya S, Herrera-Molina R, Sabanov V, Ahmed T, Iscru E, Stober F, et al. Genetically induced retrograde amnesia of associative memories after neuroplastin ablation. *Biol Psychiatry.* (2017) **81**:124–35. doi: 10.1016/j.biopsych.2016.03.2107
69. Mannewitz A, Bock J, Kreitz S, Hess A, Goldschmidt J, Scheich H, et al. Comparing brain activity patterns during spontaneous exploratory and cue-instructed learning using single photon-emission computed tomography (SPECT) imaging of regional cerebral blood flow in freely behaving rats. *Brain Struct Funct.* (2018) **223**:2025–38. doi: 10.1007/s00429-017-1605-x
70. Vincenz D, Wernecke KEA, Fendt M, Goldschmidt J. Habenula and interpeduncular nucleus differentially modulate predator odor-induced innate fear behavior in rats. *Behav Brain Res.* (2017) **332**:164–71. doi: 10.1016/j.bbr.2017.05.053
71. Endepols H, Sommer S, Backes H, Wiedermann D, Graf R, Hauber W. Effort-based decision making in the rat: an [18F]fluorodeoxyglucose micro positron emission tomography study. *J Neurosci.* (2010) **30**:9708–14. doi: 10.1523/JNEUROSCI.1202-10.2010
72. Thanos PK, Robison L, Nestler EJ, Kim R, Michaelides M, Lobo MK, et al. Mapping brain metabolic connectivity in awake rats with muPET and optogenetic stimulation. *J Neurosci.* (2013) **33**:6343–9. doi: 10.1523/JNEUROSCI.4997-12.2013
73. Brocka M, Helbing C, Vincenz D, Scherf T, Montag D, Goldschmidt J, et al. Contributions of dopaminergic and non-dopaminergic neurons to VTA-stimulation induced neurovascular responses in brain reward circuits. *Neuroimage.* (2018) **177**:88–97. doi: 10.1016/j.neuroimage.2018.04.059
74. Weidner TC, Vincenz D, Brocka M, Tegtmeier J, Oelschlegel AM, Ohl FW, et al. Matching stimulation paradigms resolve apparent differences between optogenetic and electrical VTA stimulation. *Brain Stimul.* (2019) **13**:363–71. doi: 10.1016/j.brs.2019.11.005
75. Vogel H, Wolf S, Rabasa C, Rodriguez-Pacheco F, Babaei CS, Stober F, et al. GLP-1 and estrogen conjugate acts in the supramammillary nucleus to reduce food-reward and body weight. *Neuropharmacology.* (2016) **110**:396–406. doi: 10.1016/j.neuropharm.2016.07.039
76. Pottker B, Stober F, Hummel R, Angenstein F, Radyushkin K, Goldschmidt J, et al. Traumatic brain injury causes long-term behavioral changes related to region-specific increases of cerebral blood flow. *Brain Struct Funct.* (2017) **222**:4005–21. doi: 10.1007/s00429-017-1452-9
77. Henschke JU, Oelschlegel AM, Angenstein F, Ohl FW, Goldschmidt J, Kanold PO, et al. Early sensory experience influences the development of multisensory thalamocortical and intracortical connections of primary sensory cortices. *Brain Struct Funct.* (2018) **223**:1165–90. doi: 10.1007/s00429-017-1549-1
78. Le May MV, Hume C, Sabatier N, Schele E, Bake T, Bergstrom U, et al. Activation of the rat hypothalamic supramammillary nucleus by food anticipation, food restriction or ghrelin administration. *J Neuroendocrinol.* (2019) **31**:e12676. doi: 10.1111/jne.12676
79. Yang H, Yang J, Xi W, Hao S, Luo B, He X, et al. Laterodorsal tegmentum interneuron subtypes oppositely regulate olfactory cue-induced innate fear. *Nat Neurosci.* (2016) **19**:283–9. doi: 10.1038/nn.4208
80. Zhang J, Tan L, Ren Y, Liang J, Lin R, Feng Q, et al. Presynaptic excitation via GABAB receptors in Habenula cholinergic neurons regulates fear memory expression. *Cell.* (2016) **166**:716–28. doi: 10.1016/j.cell.2016.06.026
81. Michaelides M, Miller ML, Egervari G, Primeaux SD, Gomez JL, Ellis RJ, et al. Striatal Rgs4 regulates feeding and susceptibility to diet-induced obesity. *Mol Psychiatry.* (2018) doi: 10.1038/s41380-018-0120-7
82. Njemanze PC, Kranz M, Amend M, Hauser J, Wehrl H, Brust P. Gender differences in cerebral metabolism for color processing in mice: a PET/MRI Study. *PLoS ONE.* (2017) **12**:e0179919. doi: 10.1371/journal.pone.0179919
83. Rohleder C, Jung F, Mertgens H, Wiedermann D, Sue M, Neumaier B, et al. Neural correlates of sensorimotor gating: a metabolic positron emission tomography study in awake rats. *Front Behav Neurosci.* (2014) **8**:178. doi: 10.3389/fnbeh.2014.00178
84. Sokoloff L, Reivich M, Kennedy C, Des Rosiers MH, Patlak CS, Pettigrew KD, et al. The [14C]deoxyglucose method for the measurement of local cerebral glucose utilization: theory, procedure, and normal values in the conscious and anesthetized albino rat. *J Neurochem.* (1977) **28**:897–916. doi: 10.1111/j.1471-4159.1977.tb10649.x
85. Leonard JP, Nowotnik DP, Neirinckx RD. Technetium-99m-d, 1-HM-PAO: a new radiopharmaceutical for imaging regional brain perfusion using SPECT–a comparison with iodine-123 HIPDM. *J Nucl Med.* (1986) **27**:1819–23.
86. Koretsky AP, Silva AC. Manganese-enhanced magnetic resonance imaging (MEMRI). *NMR Biomed.* (2004) **17**:527–31. doi: 10.1002/nbm.940
87. Angelis GI, Ryder WJ, Gillam JE, Boisson F, Kyme AZ, Fulton RR, et al. Rigid motion correction of dual opposed planar projections in single photon imaging. *Phys Med Biol.* (2017) **62**:3923–43. doi: 10.1088/1361-6560/aa68cd
88. Kyme AZ, Judenhofer MS, Gong K, Bec J, Selfridge A, Du J, et al. Open-field mouse brain PET: design optimisation and detector characterisation. *Phys Med Biol.* (2017) **62**:6207–25. doi: 10.1088/1361-6560/aa7171
89. Baba JS, Endres CJ, Foss CA, Nimmagadda S, Jung H, Goddard JS, et al. Molecular imaging of conscious, unrestrained mice with AwakeSPECT. *J Nucl Med.* (2013) **54**:969–76. doi: 10.2967/jnumed.112.109090
90. Schulz D, Southekal S, Junnarkar SS, Pratte JF, Purschke ML, Stoll SP, et al. Simultaneous assessment of rodent behavior and neurochemistry using a miniature positron emission tomograph. *Nat Methods.* (2011) **8**:347–52. doi: 10.1038/nmeth.1582
91. Deffieux T, Demene C, Pernot M, Tanter M. Functional ultrasound neuroimaging: a review of the preclinical and clinical state of the art. *Curr Opin Neurobiol.* (2018) **50**:128–35. doi: 10.1016/j.conb.2018.02.001
92. Sieu LA, Bergel A, Tiran E, Deffieux T, Pernot M, Gennisson JL, et al. EEG and functional ultrasound imaging in mobile rats. *Nat Methods.* (2015) **12**:831–4. doi: 10.1038/nmeth.3506
93. Bergel A, Deffieux T, Demene C, Tanter M, Cohen I. Local hippocampal fast gamma rhythms precede brain-wide hyperemic patterns during spontaneous rodent REM sleep. *Nat Commun.* (2018) **9**:5364. doi: 10.1038/s41467-018-07752-3
94. Mace E, Montaldo G, Trenholm S, Cowan C, Brignall A, Urban A, et al. Whole-Brain functional ultrasound imaging reveals brain modules for visuomotor integration. *Neuron.* (2018) **100**:1241–51.e7. doi: 10.1016/j.neuron.2018.11.031
95. He Q, Wang J, Hu H. Illuminating the activated brain: emerging activity-dependent tools to capture and control functional neural circuits. *Neurosci Bull.* (2019) **35**:369–77. doi: 10.1007/s12264-018-0291-x

**Conflict of Interest:** The authors declare that the research was conducted in the absence of any commercial or financial relationships that could be construed as a potential conflict of interest.

# Advantages of publishing in Frontiers

**OPEN ACCESS**
Articles are free to read for greatest visibility and readership

**FAST PUBLICATION**
Around 90 days from submission to decision

**HIGH QUALITY PEER-REVIEW**
Rigorous, collaborative, and constructive peer-review

**TRANSPARENT PEER-REVIEW**
Editors and reviewers acknowledged by name on published articles

**Frontiers**
Avenue du Tribunal-Fédéral 34
1005 Lausanne | Switzerland

**Visit us:** www.frontiersin.org
**Contact us:** info@frontiersin.org | +41 21 510 17 00

**REPRODUCIBILITY OF RESEARCH**
Support open data and methods to enhance research reproducibility

**DIGITAL PUBLISHING**
Articles designed for optimal readership across devices

**FOLLOW US**
@frontiersin

**IMPACT METRICS**
Advanced article metrics track visibility across digital media

**EXTENSIVE PROMOTION**
Marketing and promotion of impactful research

**LOOP RESEARCH NETWORK**
Our network increases your article's readership